TASKA-M, A Low Cost, Near Term Tandem Mirror Device for Fusion Technology Testing

B. Badger, F. Arendt, E. Borie, M.L. Corradini, H.G. Dittrich, L. El-Guebaly, G.A. Emmert, T. Fett, J.M. Grover, B. Haferkamp, W. Heinz, E. Hölzchen, K. Kleefeldt, R. Klingelhöfer, P. Komarek, G.L. Kulcinski, M. Kuntze, E.M. Larsen, H.G. Leiste, G.W. Leppelmeier, W. Link, S. Malang, B.M. Manes, W. Maurer, C.W. Maynard, I. Michael, R.A. Müller, G. Neffe, E.K. Opperman, L.J. Perkins, R.R. Peterson, K.E. Plute, J.F. Santarius, M.E. Sawan, J.E. Scharer, K. Schramm, A. Suppan, I.N. Sviatoslavsky, D.K. Sze, S. Taczanowski, M.A. Vogel, W .F. Vogelsang, D. Weinberg, and L.J. Wittenberg

December 1983

UWFDM-600

FUSION TECHNOLOGY INSTITUTE

UNIVERSITY OF WISCONSIN

MADISON WISCONSIN

TASKA-M
A Low Cost, Near Term Tandem Mirror
Device for Fusion Technology Testing

B. Badger[1]

F. Arendt[2]

E. Borie[5]

M.L. Corradini[1]

H.G. Dittrich[2]

L. El-Guebaly[1]

G.A. Emmert[1]

T. Fett[2]

J.M. Grover[4]

B. Haferkamp[2]

W. Heinz[2]

E. Hölzchen[2]

K. Kleefeldt[2]

R. Klingelhöfer[2]

P. Komarek[2]

G.L. Kulcinski[1]

M. Kuntze[2]

E.M. Larsen[1]

H.G. Leiste[2]

G.W. Leppelmeier[3]

W. Link[2]

S. Malang[2]

B.M. Manes[2]

W. Maurer[2]

C.W. Maynard[1]

I. Michael[2]

R.A. Müller[2]

G. Neffe[2]

E.K. Opperman[4]

L.J. Perkins[1,7]

R.R. Peterson[1]

K.E. Plute[1,8]

J.F. Santarius[1]

M.E. Sawan[1]

J.E. Scharer[1]

K. Schramm[2]

A. Suppan[2]

I.N. Sviatoslavsky[1]

D.K. Sze[1,9]

S. Taczanowski[2,6]

M.A. Vogel[4]

W.F. Vogelsang[1]

D. Weinberg[2]

L.J. Wittenberg[1]

----

[1] Fusion Power Associates/University of Wisconsin

[2] Kernforschungszentrum Karlsruhe

[3] Lawrence Livermore National Laboratory

[4] Hanford Engineering Development Laboratory

[5] University of Karlsruhe

[6] University of Kraków

[7] Present Address: Lawrence Livermore National Laboratory

[8] Present Address: Indiana University

[9] Present Address: Argonne National Laboratory

ACKNOWLEDGEMENT

TASKA-M TABLE OF CONTENTS

1. INTRODUCTION

The first complete design study of an integrated engineering test facility based on the tandem mirror concept was successfully completed in 1980/81 and resulted in the TASKA report.[1] Since that time, considerable progress has been made both in physics and in engineering. The theoretical understanding of tandem mirror physics has been progressing steadily while experimental results have been rapidly accumulating from the Phaedrus, Gamma-10, and TMX-U tandem mirrors. The preconceptual design of commercial power plants based on these concepts, such as MARS,[2] has further advanced the engineering understanding of the tandem mirror configuration.

The current experimental and design studies support the previous TASKA concept. A later study, the TDF tandem mirror test facility,[3] upheld the conclusion that the tandem mirror concept offers significant technical and economical advantages over toroidal devices in the area of engineering tests.

Therefore, the present study, TASKA-M, was initiated in 1982 in an attempt to achieve the most important TASKA objectives at a minimum cost. Such an objective includes engineering testing relevant to both mirror and toroidal concepts.

A large amount of solid engineering design features was generated by the INTOR[4] study. This study also identified problem areas, risks, and costs leading to the feeling, in at least part of the fusion community, that INTOR might be too costly a next step. The TFCX study,[5] which has recently begun, is an example of a lower cost and less ambitious option in the tokamak line.

If the next step is limited to this class of devices, then related materials and engineering tests are required in a separate facility which produces a significant neutron flux and fluence. For economic reasons, such a machine will probably not be a tokamak.

Therefore, one of the objectives of TASKA-M is to provide a high flux neutron source, with high reliability and availability, to serve as a test bed for a variety of technologies required for fusion reactors. TASKA-M aims at achieving this in a minimum cost machine which still maintains significant engineering relevance for power reactors. The trade-off between neutron flux and reactor physics relevance was a major consideration of the TASKA-M study. In general, test and cost objectives have taken precedence over reactor

physics relevance, but a great amount of reactor relevant physics still remains.

Since TASKA-M is intended to be a near-term test device, we have relied on existing technologies with only moderate extrapolations. In particular, we have tried to keep close to the present experimental data base in physics and technology. Since the thermal barrier utilized in the earlier studies was a major cost-driver, but is not crucial to engineering testing goals, it is not present in TASKA-M. Locating the high flux test modules over ion density peaks allows a much lower fusion power than in previous devices. Consequently, tritium breeding concepts can be tested but internally bred tritium is not necessary for continued plasma operation. This greatly simplifies the machine.

In summary, TASKA-M meets the above objectives for a moderate direct capital cost investment (~ 400 million dollars). This study provides important ideas and information for the next steps on the path to fusion power.

References for Section 1

1. "TASKA - Tandem Spiegelmaschine Karlsruhe," KfK-3311/FPA-82-1/UWFDM-500, March 1982.

2. "MARS - A Mirror Advanced Reactor Study," to be published 1984.

3. "TDF - A Technology Demonstration Facility," to be published 1983/84 by Lawrence Livermore National Laboratory.

4. "INTOR, the International Tokamak Reactor, Phase One," International Atomic Energy Agency, Vienna, 1982.

5. "TFCX - A Toroidal Fusion Core Experiment," to be published by Princeton Plasma Physics Laboratory, 1984.

2. SUMMARY OF TASKA-M DESIGN

2.1 Introduction

The need for a high neutron fluence, large volume 14 MeV neutron technology test facility has been highlighted in every national and international program plan for the past decade. The first attempt to provide such a facility was the LLNL minimum-B mirror configuration called FERF.[1] This was followed by a 360 MW_t University of Wisconsin tokamak test facility called TETR[2] in 1977, and by the IAEA INTOR[3] 620 MW_t reactor in 1981. In 1982, the 86 MW_t Wisconsin-Karlsruhe tandem mirror test facility study, TASKA,[4] was published. This was followed in 1983 by the LLNL 20 MW_t tandem mirror facility, TDF.[5] While each of these designs did provide valuable test space, the cost of most facilities was rather expensive (e.g., up to $1.5 billion). The purpose of the TASKA-M study is to investigate the smallest and least costly tandem mirror fusion test facility possible, while retaining a considerable degree of reactor technology relevance.

2.2 General Features of TASKA-M

TASKA-M is a tandem mirror with an axisymmetric central cell and two yin-yang cells, as shown in Fig. 2.2-1. The central cell contains hot, magnetically trapped deuterium and tritium ions which react via fusion to produce 14.1 MeV neutrons and 3.5 MeV alpha particles. The central cell contains the blanket and materials test modules, while the plasma in the anchors and connecting transition regions is only deuterium and has a low neutron yield. The hot D and T ion population in the central cell is sustained by injection of energetic neutral beams at an angle of 45° to the magnetic field; this produces a so-called "sloshing-ion" plasma in which the ion density peaks away from the central cell midplane. Such a plasma configuration produces an electrostatic potential well which traps warm ions provided by a low energy neutral beam. The warm ions fill the hole in the loss-cone of the hot ions and thereby provide microstability of the central cell plasma. The non-uniform axial density profile of the hot ions also produces a non-uniform neutron source. Test modules are therefore located near the density peaks to take advantage of the higher neutron wall loading.

In order to provide a sufficiently deep electrostatic well and to minimize the effect of electron drag on the hot ions, the electrons are heated by Landau damping on ion cyclotron waves. These waves are generated by antennae

Fig. 2.2-1. Magnetic field and electrostatic potential configuration of
TASKA-M.
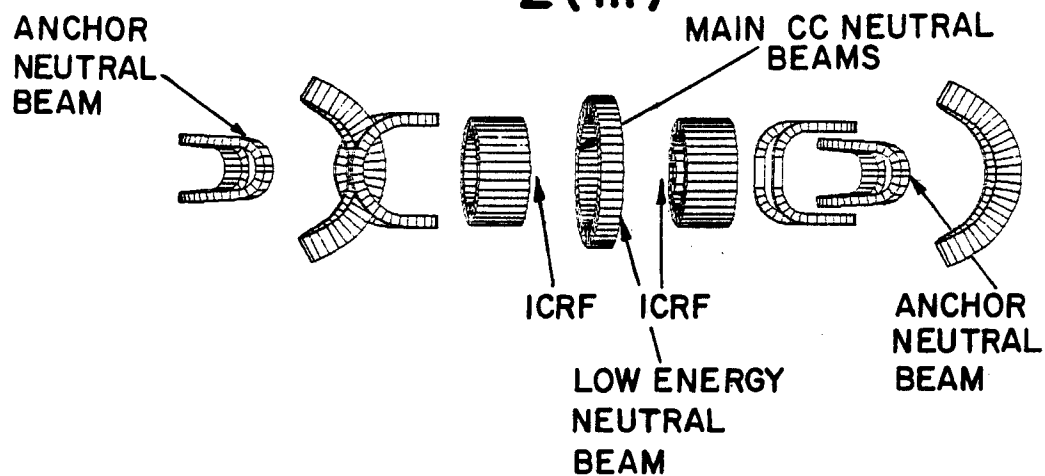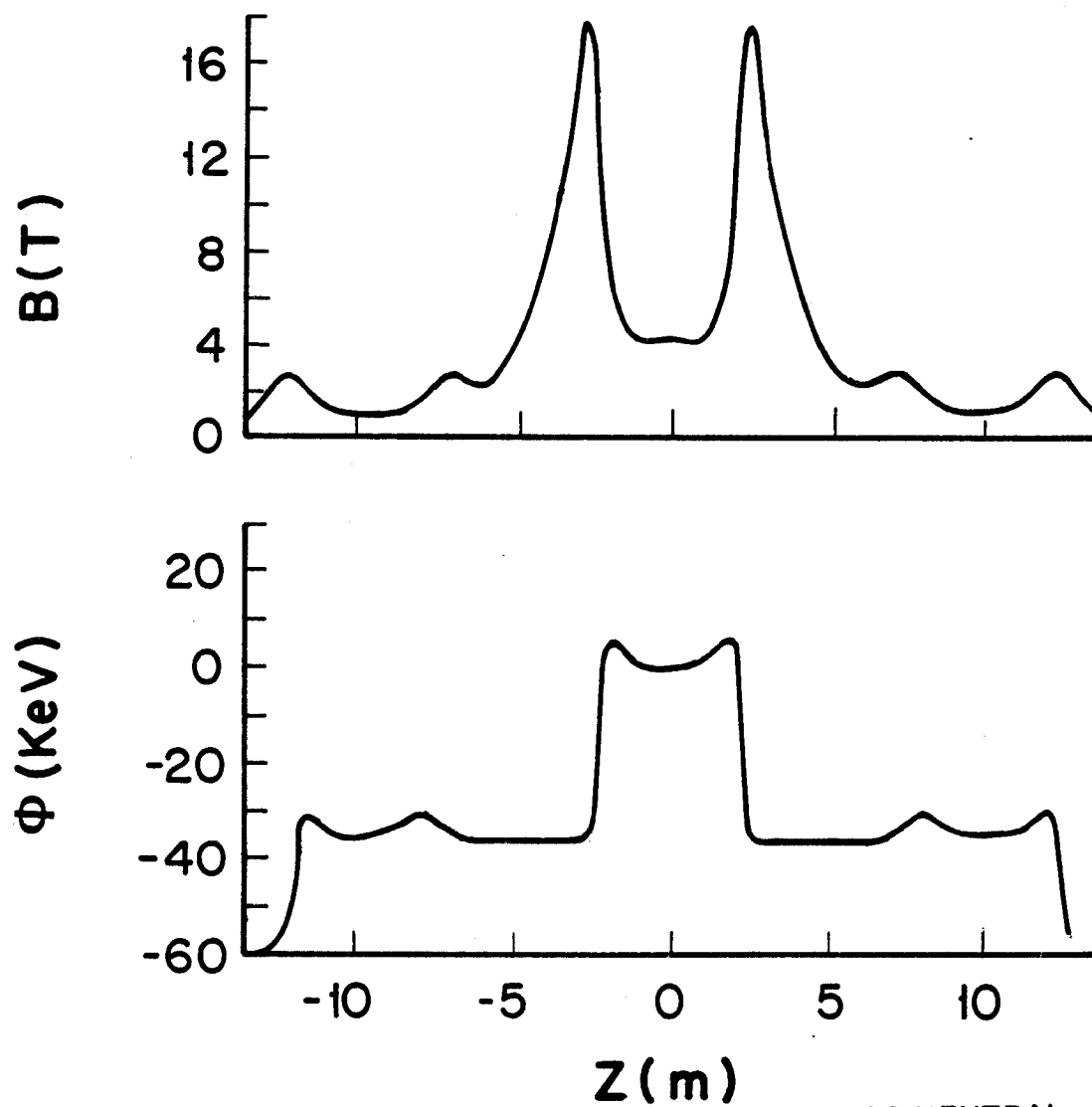
in the central cell. This system utilizes RF power in the ion cyclotron range and avoids the very high frequency (> 84 GHz) associated with ECRH in the central cell. An alternative approach would be the use of fundamental electron cyclotron heating in the lower density magnetic field transition region.

The yin-yang end cells have the sole purpose of providing MHD stability for the entire plasma, and consequently they are called "anchors." Unlike a usual tandem mirror, they do not provide any plugging of the axial loss from the central cell. The anchor plasma is also sustained by energetic neutral beams injected at an angle to produce a sloshing-ion plasma. Trapping of warm plasma from the transition region in the resulting electrostatic well provides microstability for the anchor plasma.

It should be noted that the TASKA-M configuration does not utilize electrostatic end-plugging or a thermal barrier. The reason for this is three-fold. First, a thermal barrier had not been produced in an experiment at the start of the study (January 1982) and it was our desire to keep the physics as simple as possible and to minimize the extrapolation from the present physics data base. (However, at the time of this writing (November 1983), there has been qualitative indication of a thermal barrier on TMX-U.) Second, neutral beam pumping of the thermal barrier in TASKA[4] presented considerable complications and expense. Recently, ideas concerning drift pumping[6] of thermal barriers have emerged. These ideas, however, are also unproven and would, therefore, be inconsistent with our physics philosophy. Third, electrostatic end-plugging is not required for achieving the TASKA-M testing goals within cost constraints.

An overall schematic of the TASKA-M device is shown in Fig. 2.2-2. The basic parameters of TASKA-M are given in Table 2.2-1 and the heating parameters in Table 2.2-2. It should be noted that the fusion power is very low -- only 6.8 MW. The total injected power is 44 MW, of which 35 MW are absorbed. The Q (fusion power/absorbed power) is low (~ 0.2), but this was not a design goal.

The magnetic coil set consists of 3 superconducting (S/C) solenoid coils, 2 normal high field copper choke coil inserts, 2 superconducting yin-yang coil sets (4 coils in all) and 2 superconducting transition coils, as shown in Fig. 2.2-1. All of the superconducting coils in TASKA-M are either state-of-the-

HE - NBI
4×52MW, 90 keV

TEST BLANKETS

BEAM-DUMP

END-DUMP

LE-NBI
0,6 MW, 12 keV

ANCHOR-NBI
3,5 MW, 73 keV

SECTION A-A

EXHAUST TUBE

0 1 2 3 4 5 6 7 8 9 10m
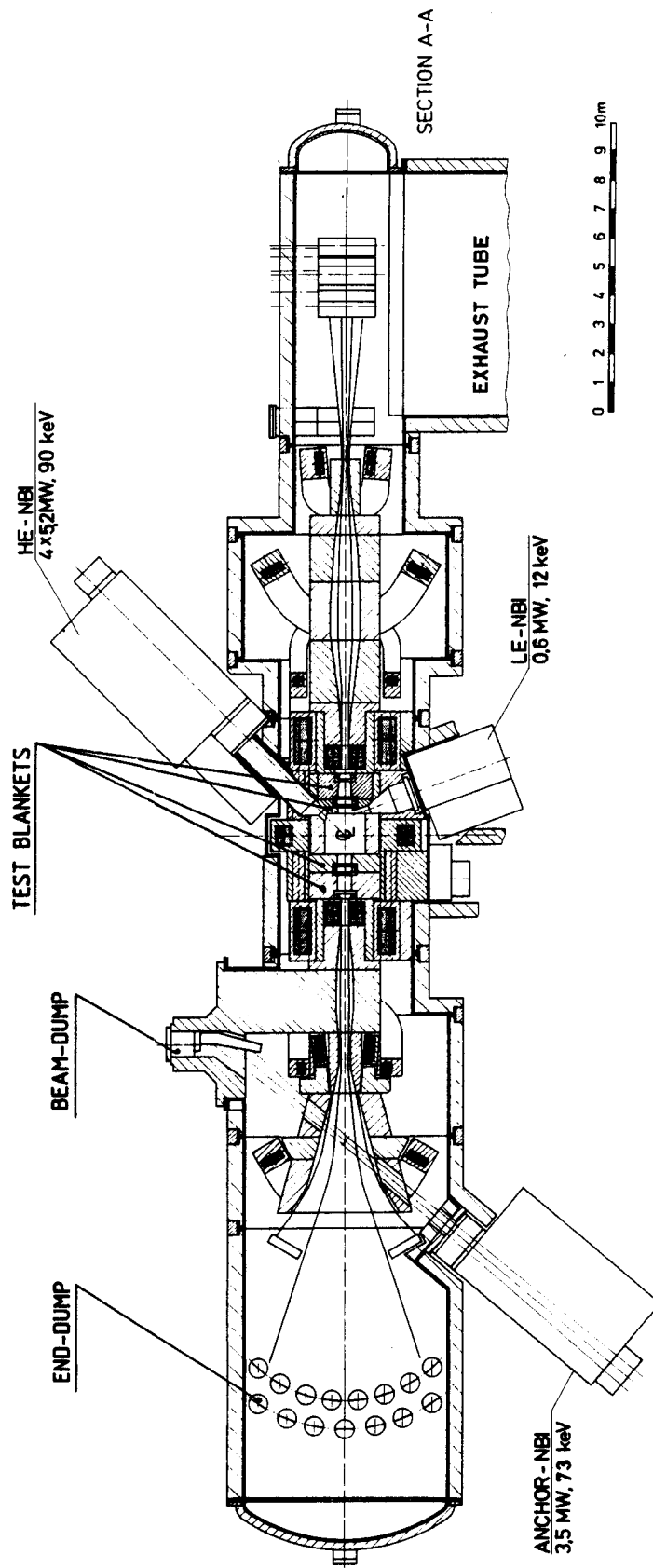
Schematic of TASKA-M Technology Test Facility

Fig. 2.2-2

2.2-4

Table 2.2-1. TASKA-M General Parameters

Neutron Wall Loading

Central cell midplane	0.7 MW/m^2
Central cell maximum	1.3 MW/m^2

Fusion Power   6.8 MW

Magnetic Fields (on axis)

Central cell - midplane	4.2 T
Central cell - maximum	17.5 T
Transition region - minimum	2.2 T
Anchor - midplane	1.0 T
Anchor - maximum	2.7 T

Central Cell Dimensions

Length (between magnetic field peaks)	5.5 m
Plasma length (between density peaks)	3.4 m
Wall radius in the test zone	0.22-0.25 m

Anchor Dimensions

Length (between magnetic field peaks)	5.4 m
Wall radius - midplane	0.37 m

Table 2.2-2. TASKA-M Neutral Beam and RF Heating Parameters

Central Cell

High Energy Neutral Beams

Injection voltage	90 kV
Total injected power	21 MW
Injection angle	45°
Species	0.5 D/0.5 T
Number of beam lines	4

Low Energy Neutral Beam

Injection voltage	12 kV
Total injected power	0.6 MW
Injection angle	70°
Species	D
Number of beam lines	1

Anchor

Medium Energy Neutral Beams

Injection voltage	73 kV
Total injected power/anchor	3.5 MW
Injection angle	50°
Species	D
Number of beam lines/anchor	1

RF Heating

Injected/Absorbed power	15/12 MW
Frequency	15 MHz

----

art today (e.g., the yin-yang coils are of the same size and field strength as the MFTF-B coils already constructed and tested successfully) or should be state-of-the-art by the 1985-1990 period. The S/C solenoid coils are roughly

the same size as the LCP coils and the MFTF-B central cell coils. Only the choke coil represents a development challenge, which is already covered by U.S.-Euratom high field development programs. In addition, Nb_3Sn technology will also be proven by the Westinghouse coil in the LCP.[7]

2.3 Plasma Physics
2.3.1 Sensitivity of TASKA-M to Plasma Physics Parameters

The basic plasma performance of TASKA-M was calculated using a global power and particle balance code, which considers the various species -- hot ions, warm ions, and electrons in each cell. The physics parameters are given in Table 2.3-1. The code was used to perform parametric studies in an attempt to consider various trade-offs between performance and cost. Shown in Fig. 2.3-1 is the increase in the required neutral beam power and electron heating power as the neutron wall loading is increased. In this variation, the plasma beta and magnetic fields are kept constant; higher wall loading is obtained by increasing the plasma radius. Raising the wall loading substantially above the design value requires a considerable increase in power. The present TASKA-M configuration does not have space for an increase in the high energy neutral beam power; this is one of the limiting factors in TASKA-M. Figure 2.3-2 shows the effect of the central cell beta on the required neutral beam and electron heating power. Improvements in beta sharply reduce the neutral beam power; correspondingly, one could obtain a higher wall loading at the same neutral beam power if beta were increased. However, in order to maintain sufficient MHD stability margin, the volume-averaged beta was limited to 30%.

2.3.2 MHD Stability

MHD stability was analyzed using the interchange stability criterion. The curvature of the magnetic field was calculated using the vacuum fields; finite beta effects and ballooning mode stability were not calculated, but were compensated for by not encroaching too close to the interchange stability criterion boundary. The stability boundary is shown in Fig. 2.3-3 in terms of the on-axis central cell, anchor, and transition region beta. The TASKA-M design point is considered to be reasonably prudent with respect to interchange stability.

Table 2.3-1. TASKA-M Plasma Parameters[*]

Central Cell

On-axis β	0.50
Radially-averaged β	0.30
Electron temperature	14 keV
Hot ion density	3.3×10^{14} cm^{-3}
Sloshing ion density ratio	1.59
Mean hot ion energy	84 keV
$(n\tau)$ - hot ions	1.0×10^{13} s/cm^3
Warm ion density	3.0×10^{13} cm^{-3}
Mean warm ion energy	5.8 keV
$(n\tau)$ - warm ions	1.3×10^{12} s/cm^3
Potential (to ground)	59 kV
Warm ion confining potential	5.3 kV
Plasma radius	12 cm

Anchor

On-axis β	0.50
Radially-averaged β	0.30
Hot ion density	2.6×10^{13} cm^{-3}
Sloshing ion density ratio	1.4
Mean hot ion energy	60 keV
$(n\tau)$ - hot ions	3.0×10^{12} s/cm^{-3}
Warm ion density	2.6×10^{12} cm^{-3}
Mean warm ion energy	6.6 keV
$(n\tau)$ - warm ions	6.6×10^{11} s/cm^3
Potential (to ground)	24 keV
Warm ion confining potential	3.4 keV

---

[*]spatially dependent parameters are given on-axis at the midplane.
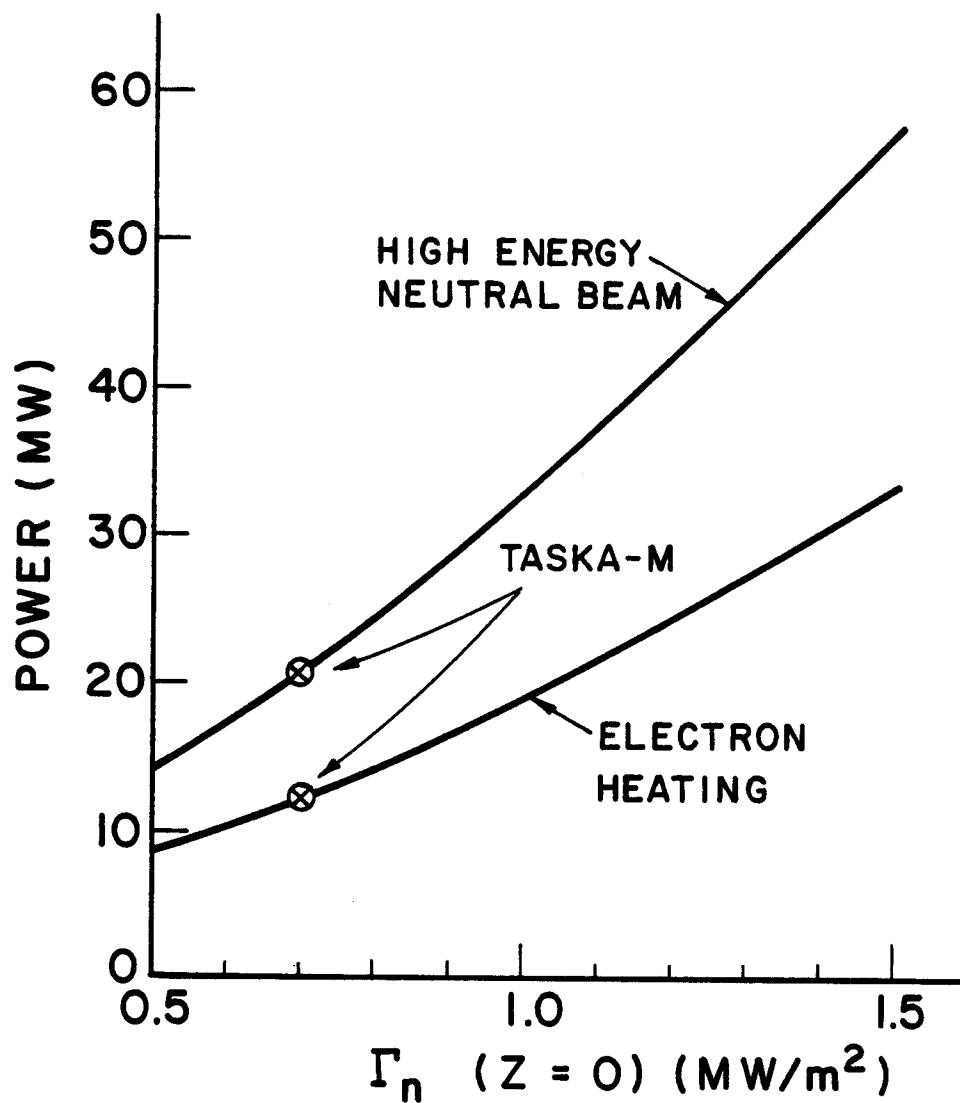
Fig. 2.3-1. Variation of the neutral beam and electron heating power with neutron power density at the midplane of the central cell for a 25 cm radius.
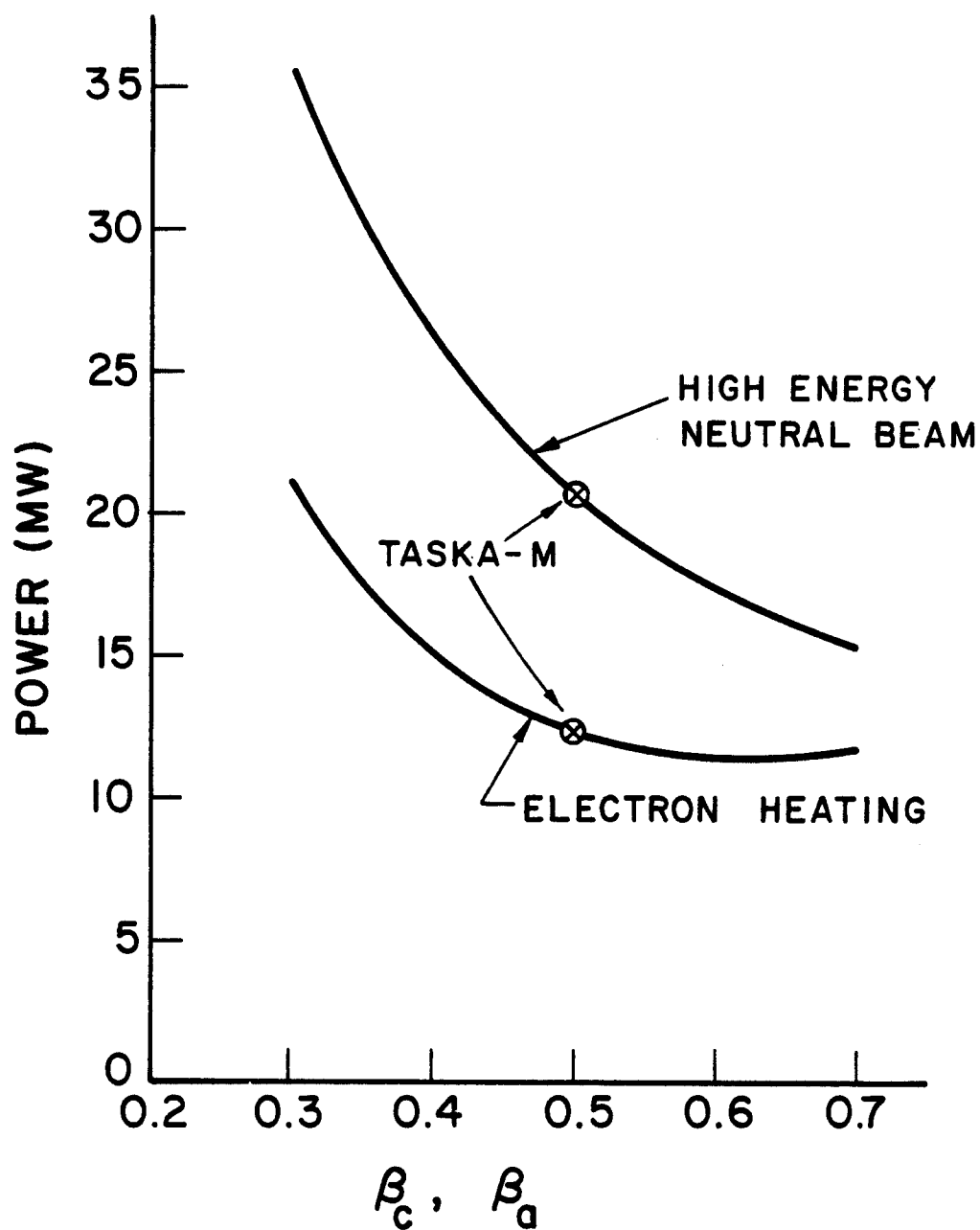
Fig. 2.3-2. Variation of the neutral beam and electron heating power with on-axis beta ($\beta_a = \beta_c$).
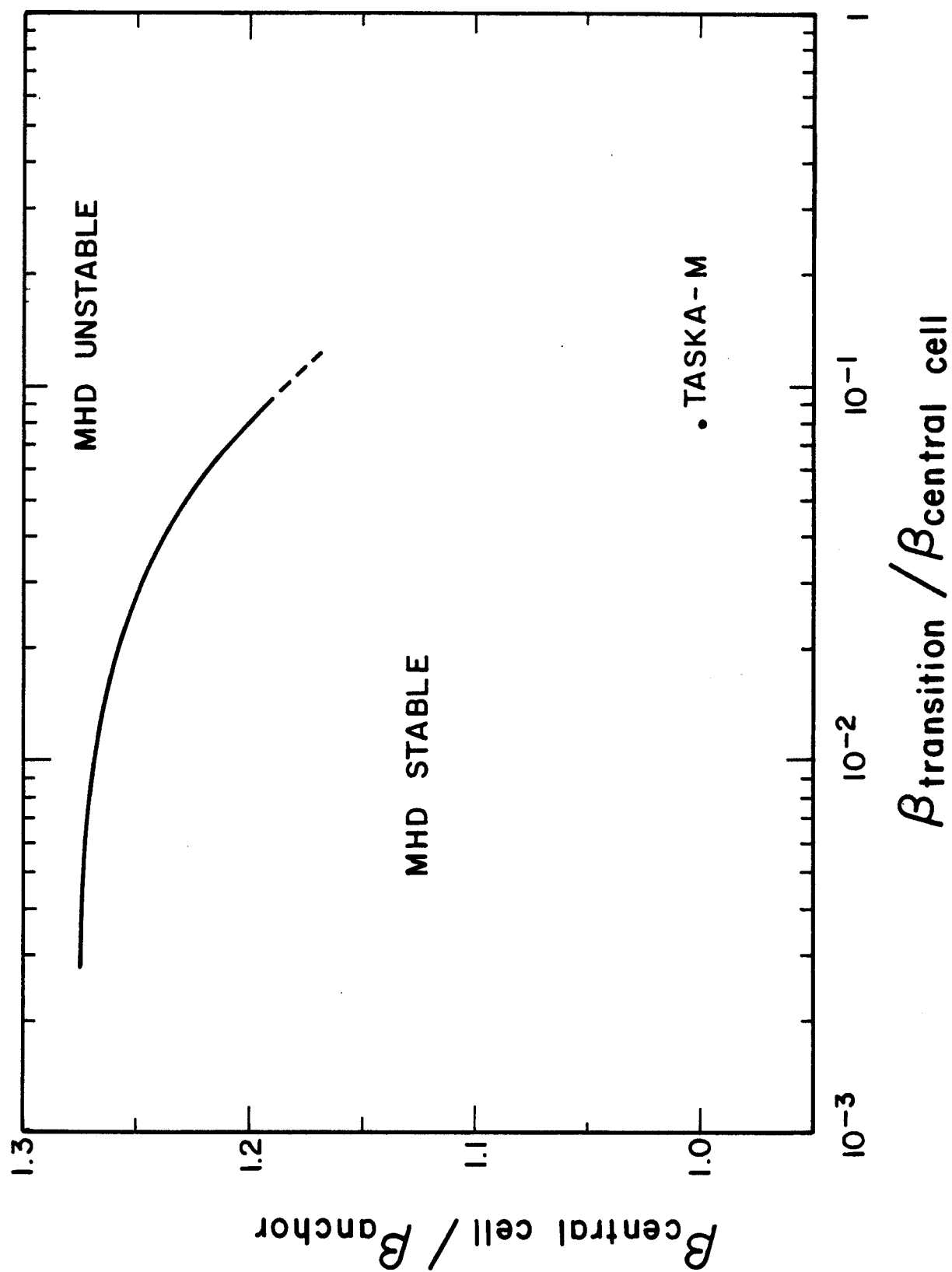
Fig. 2.3-3. MHD interchange stability limit.

2.3.3 Sloshing Ion Distribution

The sloshing ion plasma in the central cell and in the anchors is maintained by injecting the main neutral beams at an angle to the magnetic field. The resulting density profile peaks off the midplane and produces an electrostatic well which traps warm plasma. The density dip is maintained by charge exchange between ions with pitch angle $\simeq 90°$ and neutral atoms in the beam. The neutral beam, since it is injected at the midplane, "charge exchange pumps" the midplane density as well as sustaining the sloshing density. Figure 2.3-4 shows the sloshing ion distribution function at the central cell midplane.

2.3.4 Microstability

Historically, microstability has been the Achilles' heel of mirror-confined plasmas. The approach used in TASKA-M to obtain microstability is the use of a sloshing ion distribution and electrostatic potential well which contains warm plasma created by injection of a low energy neutral beam. The warm plasma density is about 10% of the hot-ion density. According to theoretical calculations, this should be adequate to suppress the drift-cyclotron loss-cone mode, at least between the two peaks of the sloshing-ion density profile. The Alfvén ion-cyclotron mode is also suppressed because of the increased $p_\parallel/p_\perp$ associated with the sloshing distribution. TMX-Upgrade[8] has operated with sloshing-ion plugs and achieved a very low level of fluctuations due to microinstabilities. The uncertainty in microstability occurs in the region between the density peaks and the mirror throats. In this region, the loss-cone is essentially empty. Stability depends on the shortness of this region compared with the localization length of possible modes. This question requires further investigation.

2.3.5 Trapped Particle Stability

A recent theoretical development in tandem mirror physics is the trapped particle instability, which is associated with particles trapped in regions of bad magnetic curvature. This instability is stabilized by maintaining a sufficient fraction of particles which pass between regions of good and bad magnetic curvature. In TASKA-M the anchor plasma density is maintained at a level to satisfy this criterion for low azimuthal mode numbers. There is a possibility of the plasma being unstable at an azimuthal mode number of 4 or 5, but this can be cured by appropriate control of the electrostatic potential
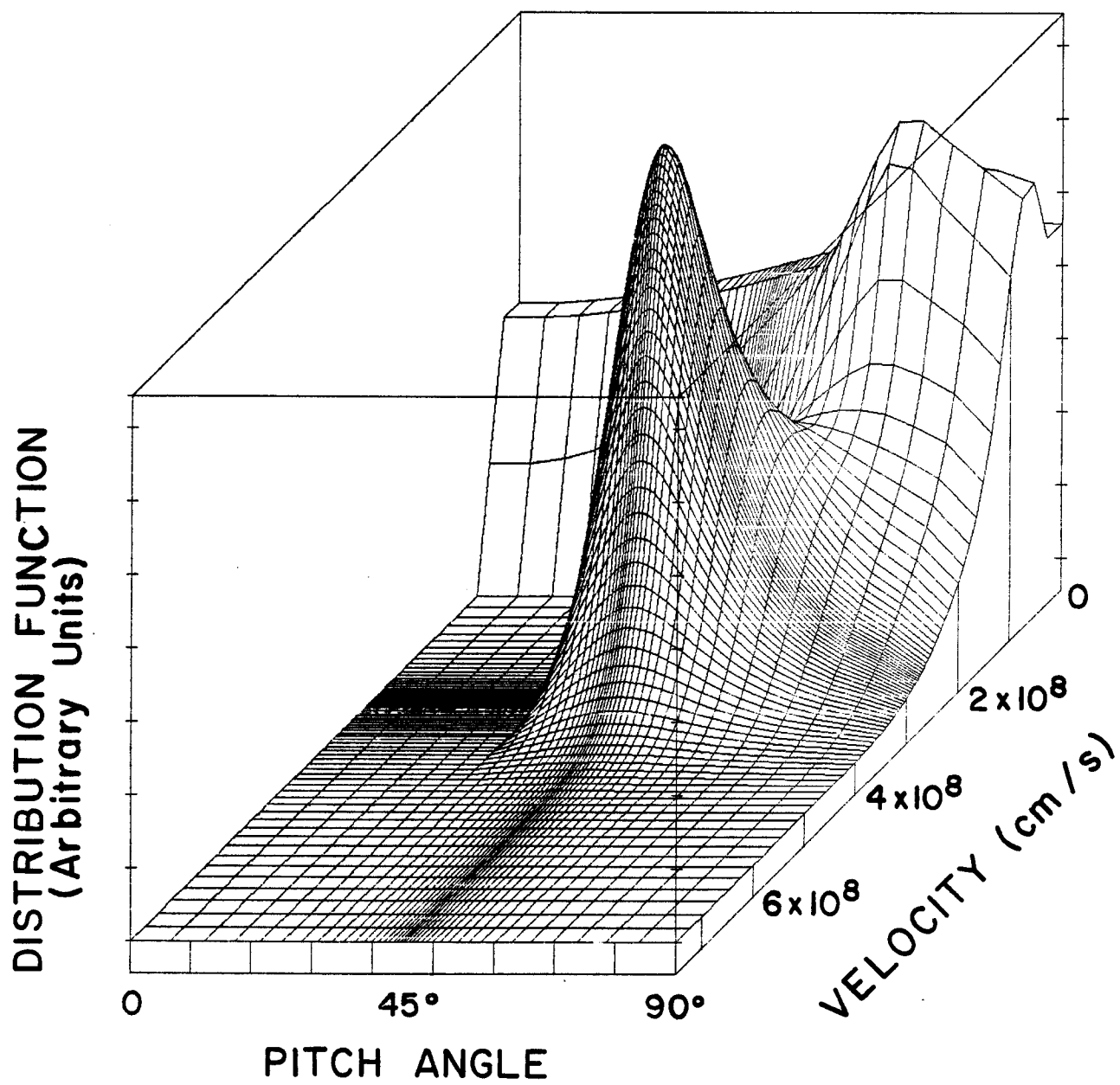
Fig. 2.3-4.   Ion distribution function showing the hot ion and warm ion
              components.

at the end plasma dumps. This instability has not yet been investigated experimentally; the TARA[9] and TMX-U[8] experiments should provide a good test.

2.3.6 Conclusions for Plasma Physics

The preliminary design of TASKA-M shows that an attractive tandem mirror test facility can be designed with a low fusion power and total cost. The plasma physics of this device represents a minimal extrapolation from the present experimental data base. There are unresolved questions concerning microstability and trapped particle stability, but the TMX-Upgrade experiment, which is in operation, and MFTF-B and TARA, which are under construction, should resolve these questions and thereby provide a basis on which to proceed with a TASKA-M type test facility in the late 1980's.

2.4 Neutronics

The neutron wall loading in the 5.6 m long central cell (CC) varies from 0.25 MW/m^2 at the midplane to a peak of 1.34 MW/m^2 at the test modules (see Fig. 2.4-1). The neutron wall loading in the transition and anchor is about four orders of magnitude less than that in the CC. The neutron source is dominated by D-T and D-D neutrons in the transition and anchor regions, respectively.

TASKA-M utilizes a number of superconducting (S/C) coils. This includes a central solenoid, two choke coil solenoids, two transition coils and two anchor yin-yang coil sets. To mirror confine the plasma, a 17.5 T field is produced by hybrid choke coils where a normal insert coil is used. Figure 2.4-2 gives a schematic of the central cell showing the magnets and the neutral beam injector (NBI) ducts.

The limits on the neutron fluence for NbTi and Nb_3Sn are taken to be 3 x 10^{22} and 4 x 10^{22} n/m^2 ($E_n > 0.1$ MeV), respectively. For a reactor life of 7.8 full power years (FPY), a minimum time between anneals of 0.5 FPY, and 70% recovery of the critical current density degradation in NbTi, the fast neutron flux should not exceed 1.1 x 10^{22} n/m^2 per FPY. No recovery with annealing is obtained for Nb_3Sn implying a flux limit of 5.1 x 10^{21} n/m^2 per FPY. Cryostability requires the resistivity of aluminum used in the central and choke coils to not exceed 20 $n\Omega$ cm after irradiation. Allowing for annealing every 0.5 FPY implies a dpa rate limit of 10^{-4} dpa/FPY. Using charts developed for specifying the dpa rate limit for the copper stabilizer (Chapter 5), a 3.1 x
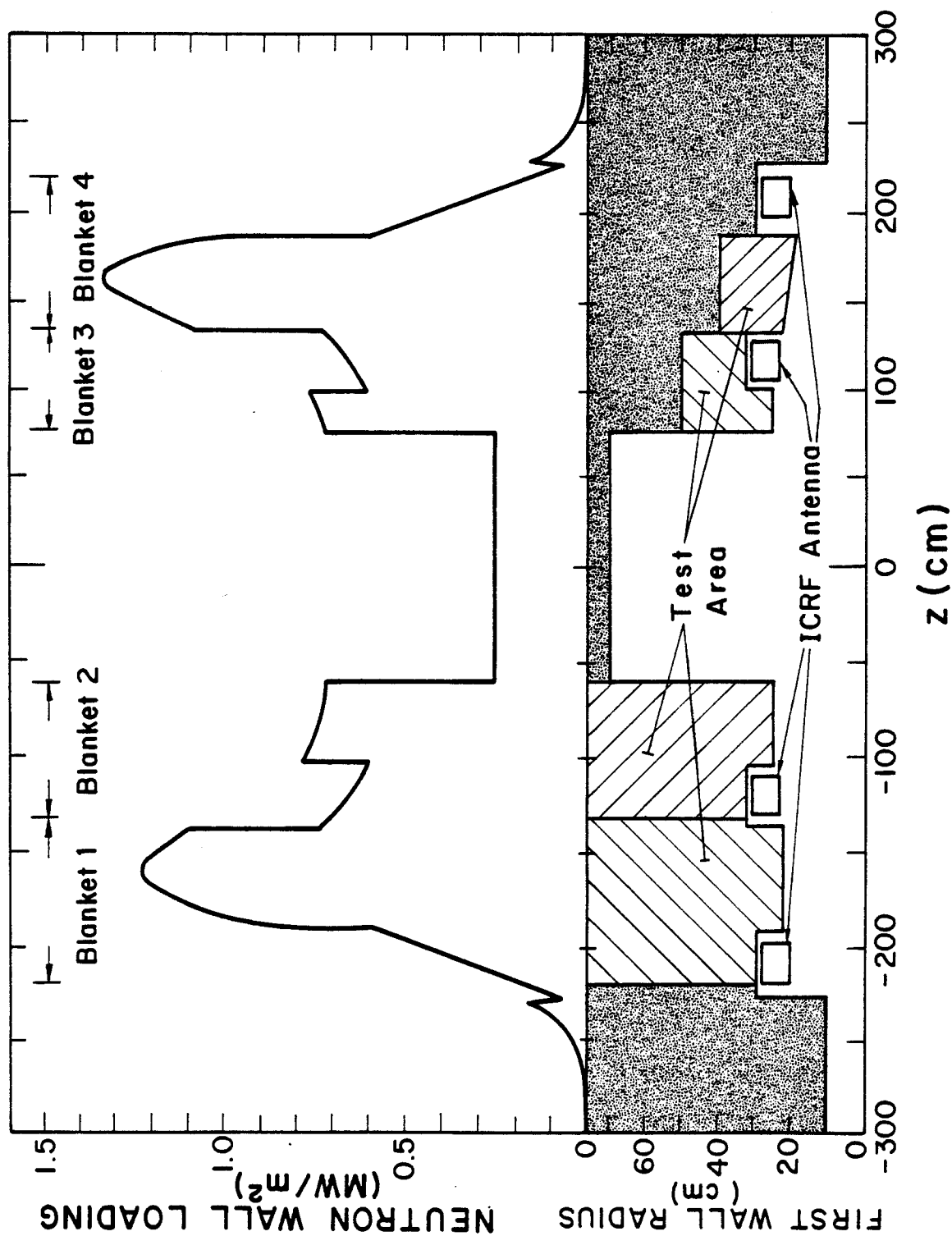
Fig. 2.4-1 Axial variation of neutron wall loading in the central cell.
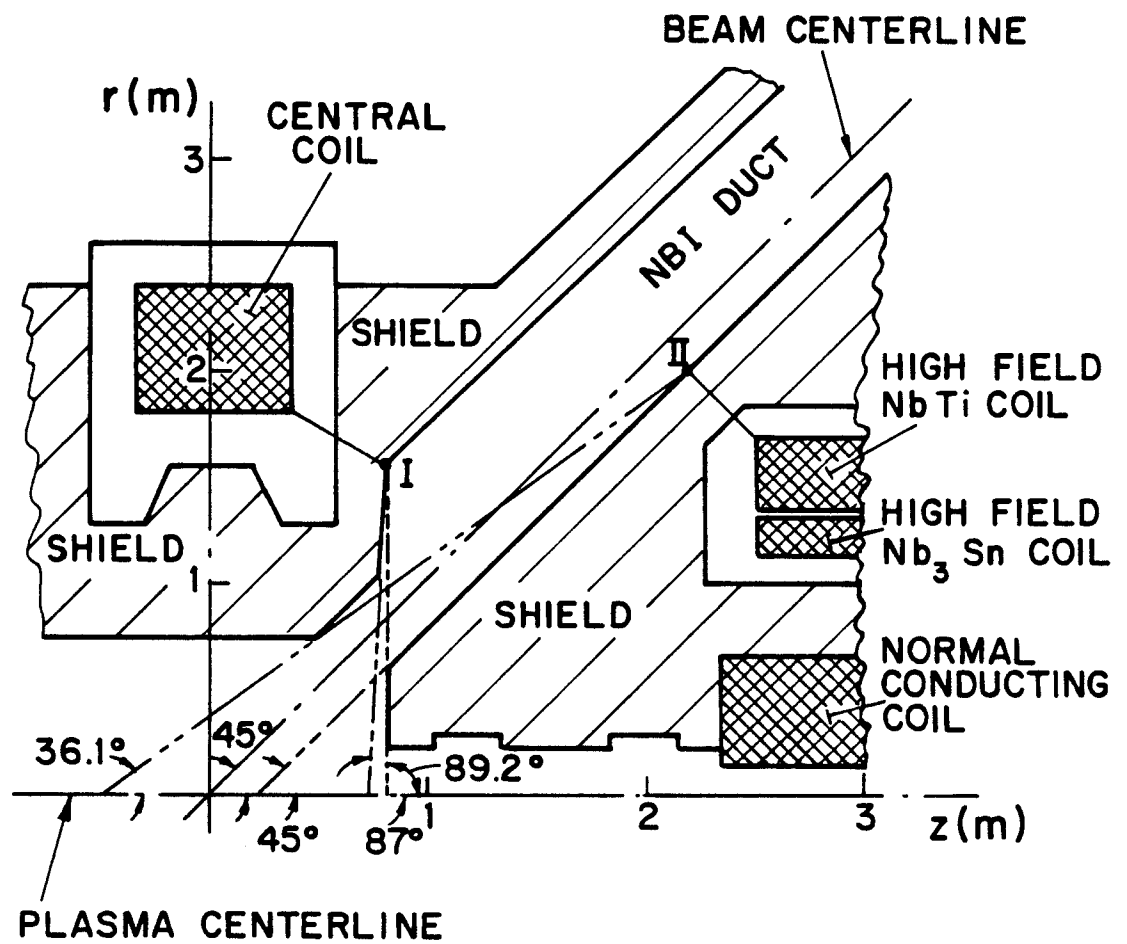
Fig. 2.4-2. Geometrical configuraton of NBI duct and beam dump duct relative to the central cell magnets.

10^{-4} dpa/FPY limit is obtained for the C-shaped coils. Glass fiber filled (gff) epoxy and gff polyimide are used for electrical insulation in the central and end cell coils, respectively. Aluminized Kapton is used for superinsulation. End of life dose limits of 6×10^8, 5×10^9, and 10^{10} rads are used for gff epoxy, gff polyimide, and aluminized Kapton, respectively. A peak winding pack power density limit of 0.1 mW/cm^3 is considered. Finally, in the normal coil, we allow for 10% swelling in the compacted MgO powder insulation of the normal copper insert and this yields a fast neutron fluence limit of 3.5×10^{26} n/m^2.

A series of ONEDANT calculations was performed with data based on ENDF/B-V to determine the optimal shield configuration. The optimum shield in the CC and transition region consists of water-cooled Fe 1422 followed by a B_4C layer. The optimal shield for the anchor coils, where D-D neutrons dominate the source, consists mainly of water with small volume fractions of Fe 1422 and B_4C.

Radiation analysis was performed at the midplane of the central cell and the radiation effects are given in Table 2.4-1. For the choke coil with 0.1 MW/m^2 neutron wall loading, an end of life peak fluence of 3.15×10^{25} n/m^2 is obtained. Hence, there is no need for replacing the unshielded normal insert coil due to radiation damage in the insulator. The radiation effects at the inner bore of the S/C choke coil are given in Table 2.4-1.

Hot spots in the magnets will occur due to radiation streaming into the NBI ducts and their associated beam dump ducts illustrated in Fig. 2.4-2. We developed a fairly accurate calculational method to estimate the magnet radiation effects from streaming radiation. The method results in only a few centimeter overestimate of the required shield thickness compared to the detailed expensive three-dimensional calculation. The first step involves calculating the neutron wall loading at the points on the duct wall closest to the S/C magnets. A one-dimensional calculation is then performed using the calculated wall loading. Adding the bulk shield contribution, the peak radiation effects are given in Table 2.4-1. Although as far as damage in NbTi is concerned, no magnet annealing is required, annealing every 0.5 FPY is required to avoid an excessive increase in stabilizer resistivity that could jeopardize magnet cryostability. The hottest spot in the S/C coils is on the outer edge of the choke coil close to the NBI duct.

Table 2.4-1. Radiation Effects in Superconducting Magnets of TASKA-M

	Inner Bore of Central Coil at Midplane	Inner Bore of Central Coil		Inner Bore of Choke Nb$_3$Sn Coil	Outer Edge of Choke NbTi Coil		Transition Coil	Anchor Coil	Design Limits
		At NBI Duct	At Beam Dump Duct		At NBI Duct	At Beam Dump Duct			
Stabilizer/dpa rate (dpa/FPY)	Al/5.2×10^{-6}	Al/8.1×10^{-5}	Al/2.5×10^{-5}	Al/5.6×10^{-7}	Al/9.8×10^{-5}	Al/4.4×10^{-5}	Cu/4.8×10^{-5}	Cu/6.4×10^{-5}	Al/10^{-4} Cu/3.1×10^{-4}
Electrical Insulator/Dose after 7.8 FPY (rad)	epoxy/6.6×10^{7}	epoxy/1.8×10^{8}	epoxy/9.4×10^{7}	epoxy/9.4×10^{6}	epoxy/1.5×10^{8}	epoxy/6×10^{7}	polyimide/9.6×10^{8}	polyimide/1.3×10^{9}	gff epoxy/6×10^{8} gff polyimide/5×10^{9}
Dose in aluminized Kapton after 7.8 FPY (rad)	1.1×10^{9}	3.2×10^{7}	1.6×10^{9}	3.2×10^{7}	2.9×10^{9}	1.1×10^{9}	2.2×10^{9}	3.1×10^{9}	10^{10}
Power density in winding pack (mW/cm^3)	0.005	0.038	0.0012	0.001	0.047	0.018	0.096	0.088	0.1
Superconductor/Fast neutron flux (n/m^2 per FPY)	NbTi/5×10^{19}	NbTi/6.7×10^{20}	NbTi/2.1×10^{20}	Nb$_3$Sn/3.5×10^{19}	NbTi/8.1×10^{20}	NbTi/3.6×10^{20}	NbTi/6.2×10^{20}	NbTi/7.8×10^{20}	NbTi/1.1×10^{22} Nb$_3$Sn/5.1×10^{21}

The radiation effects in the end cell magnets at locations corresponding to the D-T and D-D peaks are included in Table 2.4-1. Shield thicknesses of 0.17 and 0.12 m are used in the transition and anchor regions, respectively. The results of this analysis imply that the shield design for TASKA-M provides adequate protection for the magnets against both radiation streaming into the penetrations and radiation penetrating the bulk shield.

2.5 Heating and Fueling

Neutral beam injection has been chosen as the method for plasma buildup, plasma fueling and ion heating in the central cell and in the two anchors of TASKA-M. Alternatives to this scheme, for instance building up a hot plasma to full density by filling the vacuum vessel with neutral gas, which is subsequently ionized and heated by radiofrequency waves, cannot be applied in TASKA-M. Since the plasma confinement time τ decreases with temperature, the initial power for startup would be extremely high. Even though a low density startup is possible in principle (since $n \cdot \tau$ does not depend on plasma density n and the low density would lower the power by n^2), fueling would cause a problem as the density increases. Scaling up experimental information on ablation to the TASKA-M regime, the penetration depth of pellets at full density is very small in comparison to the plasma radius of TASKA-M even at the highest pellet velocities which seem to be credible.

To provide a mechanism for suppressing microinstabilities, the beams are injected at 45° and 50° in the central cell and the anchors, respectively. Thus sloshing ion distributions are achieved with density dips in the center of the two regions for the confinement of warm plasma filling the loss cones. The injected power and the energy of the neutrals are 20.8 MW D° + T° at 90 keV in the central cell and 3.5 MW D° at 73 keV in each of the two anchors. A 0.6 MW D°-beam at 12 keV is injected at 70° into the central cell to build up and fuel the warm plasma. In the anchors, warm plasma is expected to be provided by the end losses from the transition zone plasma. The main neutral beam parameters are given in Table 2.2-2. The neutral beams are all positive ion technology and are consistent with the present beam development program for MFTF-B, JET, JT-60, and TFTR.

To decrease the electron drag on the ions which in turn spoils the ion confinement, the plasma electrons are heated separately. Since TASKA-M has no thermal barrier, the electrons will communicate throughout the whole machine. From this point of view the power for heating the electrons could be coupled to the plasma anywhere, preferably outside the central cell to keep the interference with the blanket as small as possible. Choosing ECRH, another advantage of electron heating in the transition region would be the relatively low magnetic field strength. Nevertheless, ECRH was ruled out because of cost considerations and difficulties with wave accessibility and heating of relatively high density plasmas with $\omega_{pe}/\omega_{ce} \approx 1$. The excitation of plasma waves near the ion cyclotron frequency was chosen instead, using the Landau damping mechanism to heat the electrons. Ion heating is avoided by choosing the wave frequency such that ion resonances are avoided. There is a drawback, however, since for absorption of the ICRH to be high enough, a relatively high density must be maintained and the antennae have to be installed in the central cell. The radiofrequency power which has to be coupled to the plasma is 12.5 MW at 15 MHz. The four antennae are located adjacent to the test modules. A detailed schematic of the antennae is shown in Fig. 2.5-1. The design power flux is about 1 kW/cm^2, which is in the range of design values for newer antennae designed for PLT, TFR, JET, Doublet III-D and TFTR.

2.6 Vacuum and Exhaust Systems

The vacuum and exhaust system for TASKA-M is used in two distinct modes:
- for evacuation of the interior of the machine before startup and
- to keep the neutral gas pressure and the content of high-Z material in the plasma chamber at the required low level.

The technical design objectives are mainly determined by the operational, i.e. the exhaust conditions. The particle streams to be exhausted occur as directed neutral particle beams and plasma streams. They are converted to thermal gas on specially designed beam dump (BD) plates which constitute one of the most critical components of the whole machine because of their extraordinary loading conditions. The CC-beam dumps and the anchor beam dumps are exposed by the neutral particle shine through fraction of the NBI's, in contrast to the end dumps, which see plasma particles, i.e. ions and electrons. The design concepts for the CC-BD, the anchor-BD and the end dumps, are all
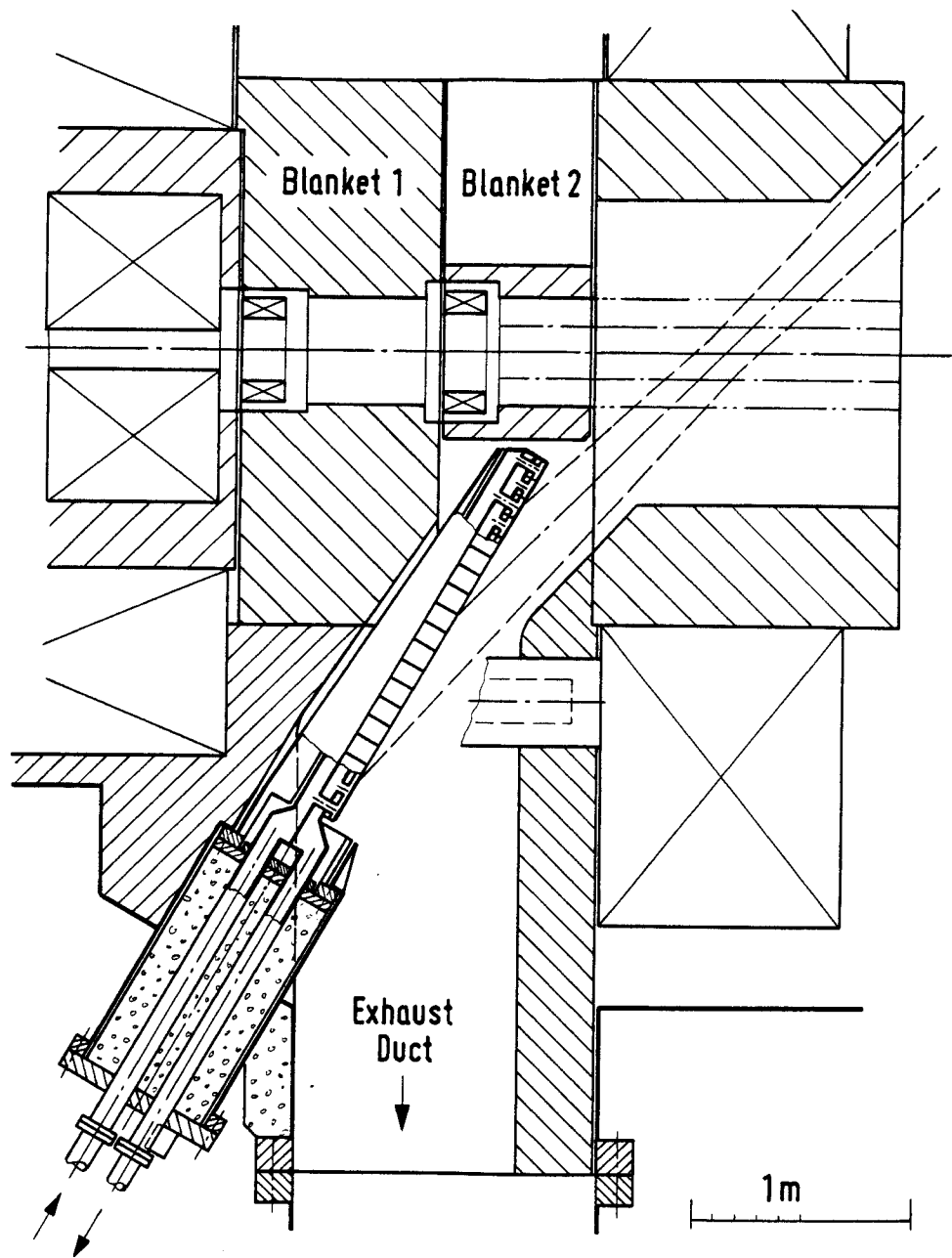
Fig. 2.6-1 TASKA-M CENTRAL CELL BEAM DUMP AND
EXHAUST DUCT CONCEPTUAL DESIGN
(Vertical Cross-Section)
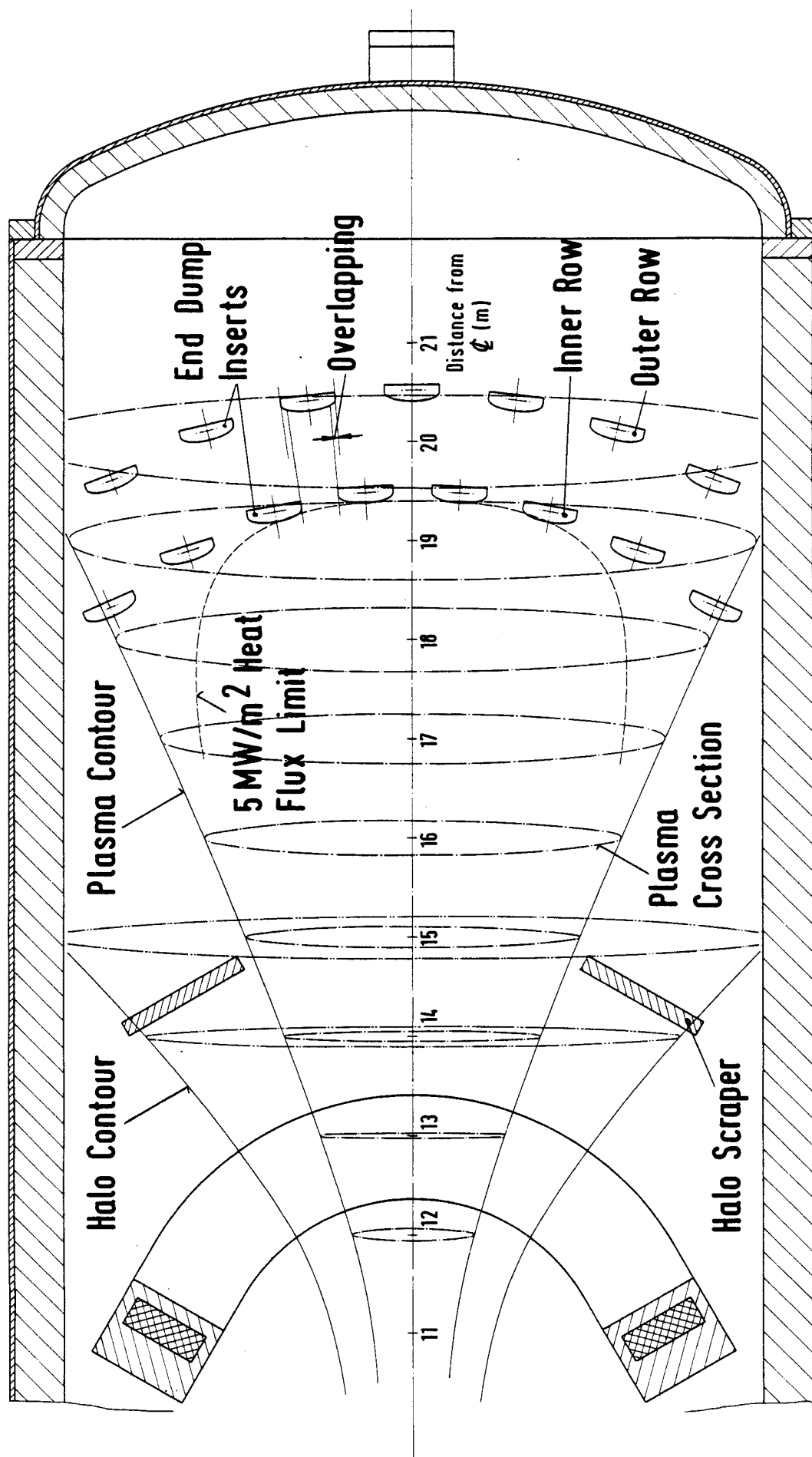
Fig. 2.6-2   SCHEMATIC DIAGRAM OF THE END DUMP ARRANGEMENT

based on the water cooled Hypervapotron technique.[10] The dumps consist of finger like individual inserts, which are easily replaceable. Figure 2.6-1 shows the CC, Fig. 2.6-2 the end cell arrangement.

Three operational modes are considered as design bases:
• normal operation
and for the CC and anchor beam dumps in addition,
• calibration and
• startup.
As a goal, the dumps should withstand normal operation for at least 0.25 full power years.

Without plasma, i.e. during calibration and startup, full power operation of the NBI's for longer durations is not acceptable with respect to the heat loads. In the calibration mode the idea is to turn on the individual sources within each NBI sequentially, so that only one source is burning at a time, leading to a much lower time average power at the dumps. During startup, as the third operational mode, the full injected power is needed, and the plasma is expected to ramp up from zero to nominal within about 80 ms. It is assumed that the beam dumps are exposed to the rated injected beam power during the startup mode, which is terminated by either a normal operation mode or a shutdown, if the plasma is not developing as specified. Calibration and startup in this sense do not affect the end dumps.

One of the most important parameters is the maximum allowable heat flux at the dump surface. Primarily with reference to the experience gained in the NBI development for JET,[10] a maximum heat flux of 5 MW/m^2 for the normal operation mode and 10 MW/m^2 for the calibration mode has been chosen. The first figure is equal to half the design value adopted for JET (10 MW/m^2) and reflects additional margin for the continuous operation of TASKA-M. For the startup mode, no maximum heat flux is established because of the thermal inertia effects. The maximum surface temperature will be the limiting factor.

The end dumps have to dissipate the high power of 14.8 MW per end, more than 99% being in the plasma region and the rest in the halo region. To accommodate this power at acceptable heat fluxes, the strong spread of the plasma fan in the end cells is used at the expense of a large collector area which, in essence, will face an elliptical footprint with a high aspect ratio. A modular end dump collector similar to the BD design is proposed, consisting

of parallel overlapping inserts (Fig. 2.6-2). The central inserts can be removed for plasma direct convertor tests. In the halo region a simpler design is sufficient, since the heat flux is very low.

The maximum heat flux at the CC-BD during normal operation (2.5 MW/m^2) is only half as high as the design limit established, however, during calibration, 8.7 MW/m^2 is obtained, which is close to the design limit. The anchor-BD's are loaded close to the design limit in normal operation, whereas during calibration there is a margin of more than a factor 2. Even the transient heat flux of 8.6 MW/m^2 could be dissipated continuously. The end dumps are located in such positions that the heat loads are close to the design limit of 5 MW/m^2 in normal operation.

The erosion rate due to physical sputtering for copper as the reference material and for molybdenum as a candidate plating material and the corresponding lifetime amounts to

	CC-BD		Anchor-BD		End Dump	
	Cu	Mo	Cu	Mo	Cu	Mo
Maximum Wall Erosion Rate (10^{-9} cm/s)	3.8	3.5	4.0	3.8	.43	.4
Sputtering Life Time (FPY)	0.8	0.9	0.8	0.8	7.4	8.0
Total Volume Sputter Rate (cm^3/FPY)	190	180	580	560	400	380

A maximum material loss of 1 mm is considered in the lifetime calculation. It should be noted the the uncertainty of this assessment may be half an order of magnitude to both sides, which would have to be compensated for by adjusting the accumulated operating time and the allowable material loss, respectively, in the final analysis.

The gas pumping requirements during operation are met with appropriate pump chains, consisting of cryopumps, turbomolecular pumps, booster pumps and metal bellows pumps. The gas pumping requirements during evacuation before startup require some additional pump sets.

Three different kinds of pump trains satisfy the exhaust requirements during operation:

• the D, T end cell trains which pump the majority of the gases

- the He end cell trains using the Ar cryotrapping process
- the D, T central cell trains.

For preoperation evacuation of the plant down to a pressure of approximately 10^{-3} mbar ($\sim 10^{-3}$ torr) an additional startup vacuum system is provided, which feeds its effluent to the radioactive off-gas systems.

The end cell cryopumps are installed within the vacuum boundary of the machine. In this way large gas ducts on the suction side of these pumps are avoided. In contrast the central cell cryopumps are located outside because of space and neutron shielding requirements. Ducts of relatively large cross section are necessary here.

Regeneration of the cryopumps must take place during plant operation. To allow for this, the total cryosurface of each subsystem is subdivided into a number of independent modules. In each end cell 8 pumps with 10 m^2 cryosurface each are installed. The CC evacuation system consists of 6 pumps with 14 m^2 cryosurface each. The cycle time of cryopumps must be defined with regard to (1) the maximum amount of tritium stored on the cryosurfaces, (2) the risk potential in case of a major leakage with air intake and (3) the reduction of the pumping speed by an increasing layer of solid matter on the cryosurfaces. For the actual conditions the last two arguments are relatively unimportant because they are applicable only with extremely long cycle times or abnormal operating conditions. Otherwise, short cycle times tend to increase cryogenic consumption. A duty time of 8 hours and a time interval of 2 hours to carry out the regeneration process was chosen and seems to be an acceptable relation for all cryopumps.

The operational sequence during the evacuation process and the total time required to reach the startup conditions is strongly determined by the design concept of the main vacuum boundary. Unlike most of the previous experimental fusion facilities the "outer wall" concept is selected here, similar to that used in the US Tandem Mirror Fusion Test Facility (MFTF). The advantage of the "outer wall" concept is avoidance of vacuum tight welds with highly irradiated materials close to the plasma and allowance of volumetric and geometric changes of the materials and structural parts by irradiation induced swelling and creep.

2.7 Fuel Cycle

The fueling system supplies D/T fuel of the proper composition and purity at the rate required of 1.03 g T and 0.7 g D per day to sustain the fusion power. Because burnup of fuel per transit through this experimental test facility is very low, 0.3%, considerable recycle and fuel is necessary. In addition, about 80% of the fuel supplied to the NBI's must be recycled because of the low gas efficiencies of the NBI's. Because of the need to recycle a large amount of fuel, fuel purification and isotopic adjustment systems must be constructed as part of the fuel cycle system. In addition, TASKA-M does not breed tritium for use as fuel; therefore, sufficient tritium must be stored in a safe manner in order to keep the facility operational.

Figure 2.7-1 indicates the flow rates of D/T to each of the components of the fuel cycle system. Each of these components has a residual tritium inventory during operation. These tritium inventories, Table 2.7-1, are kept as low as possible in order to reduce the initial cost and the radioactive hazard potential of tritium. The total active inventory in these components is ~ 207 g T. If all these components functioned satisfactorily, the machine could be started using the active inventory to saturate these components in ~ 4 FPd. During this time the reactor would consume 4.12 g T. With a 30 day supply of fuel as a minimum, the facility could be started with ~ 242 g T. At the present cost of 10^4/g T this represents an initial cost of 2.4 million dollars. After startup, the test facility would require 380 g T/yr for an operational tritium fuel cost of 3.8 million dollars/FPY.

The sole method of fuel delivery to the plasma is by means of the 4 high energy NBI's in the central cell. The total beam flux of 258 A delivers a 50:50 composition of D + T particles. Most of the fuel must be recovered by the vacuum systems in the two end plasma dumps as specified in Table 2.7-1. Because the gas efficiencies of the NBI's are only 20%, fuel accumulates on the NBI cryopumps at the rate of 5.35 mmoles/s (D_2 + T_2). In addition, these cryopumps capture impurity gases, particularly protium, which drift into the beam duct from the halo gas surrounding the plasma. In order to maintain the H atomic fraction of the fuel < 10^{-3}, a 1% sidestream of the cryopump recycle is diverted to the fuel cleanup and isotopic separation system. The cryopumps for the other NBI's containing only deuterium, also collect protium and tritium gases which drift up the beam ducts from the halo gas. In this case it is
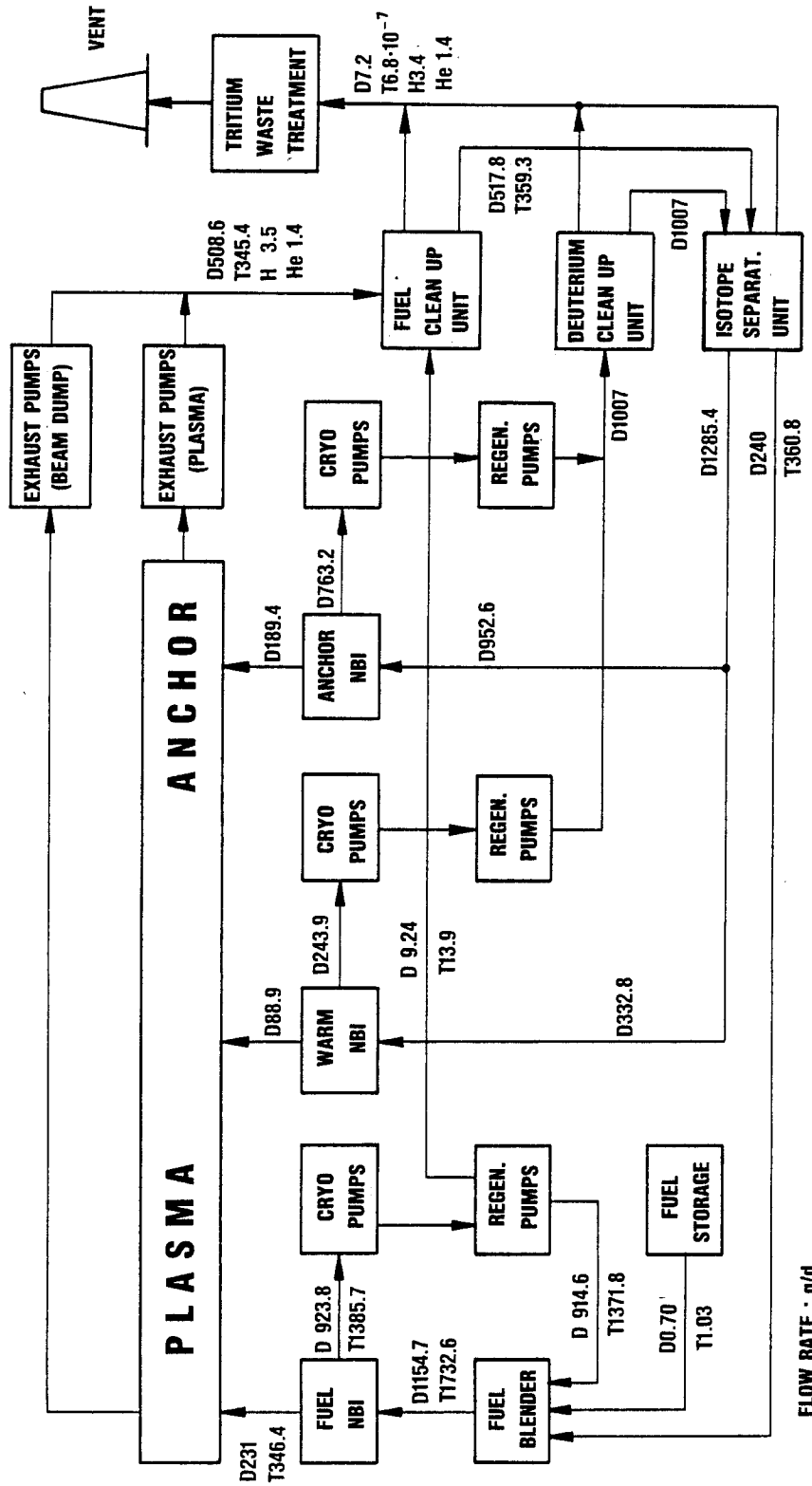
TASKA-M REPROCESSING CYCLE

Fig. 2.7-1

Table 2.7-1. Tritium Inventory

Location	T (g)
Active inventory	206.7
HE-NBI cryopanels	115.5
Central cell cryopanels	4.2
End plasma exhaust	
D/T cryopanels	49
He cryopanels	5.5
Fuel cleanup unit	2.5
Isotope separation system	30.0
Inactive inventory	66.
Fuel storage (30 day supply)	31.0
Structure (end-of-life)	< 1.0
Coolant water (end-of-life)	34.0
Blanket test modules	
Liquid lithium	5.8
Liquid LiPb	0.01
Ceramic pellets/yr	25.0

desirable to keep the T/D ratio < 10^{-3} in order to minimize the tritium con-
tamination of the NBI; therefore, 100% of the recycle gases from these NBI's
is sent to fuel cleanup (Table 2.7-1).

The method of fuel purification is based upon adsorption of impurity
gases during passage through molecular sieve columns at 77°K. A cryogenic
distillation system composed of three columns is utilized for isotopic sepa-
ration of the hydrogen isotopes. Tritium is stored principally on UT_3 beds.

Tritium contamination of the coolant water occurs at the end plasma
dumps, the HE-NBI beam dumps, and the central cell insert, due to energetic
tritium ions impinging upon the structural material. These ions are implanted
into the structure and permeate to the coolant water. Based upon preliminary
models, ~ 117 Ci/d permeates initially into the water from these three
sources; however, the neutron flux to the HE-NBI beam dumps and the central
cell insert causes radiation damage which produce tritium traps. These triti-
um traps would capture large quantities of tritium if they remained in place
over the lifetime of the reactor. Because of the unknown structural effects
caused by the large D and T concentrations, these components are changed fre-
quently so that little tritium trapping occurs.

2.8 Magnet System

The design of the TASKA-M magnets follows the same guidelines as in the
original TASKA study and uses the same constraints in the magnetic data. The
aim of TASKA-M was to decrease cost while retaining a reasonable test volume
compared with TASKA. Since another plasma configuration is used in TASKA-M,
the magnets are smaller, less numerous and therefore less expensive.

The field requirement in the central cell is 4.2 T at the midplane and
the high field hybrid mirror coil gives 17.5 T at the mirror throat. The
minimum field in the transition region is required to be about 2.2 T and the
anchors have a mirror ratio of 2.5 to 3 with a minimum field of about 1 T.
This high mirror ratio was required to provide good confinement on the
sloshing ions in the anchors.

The magnet set of TASKA-M consists of
- 1 central cell coil (CCC)
- 2 high field hybrid mirror coils (choke coils). Each consists of a normal
  conducting insert, a Nb_3Sn part and a NbTi outer part (BC1, BC2).
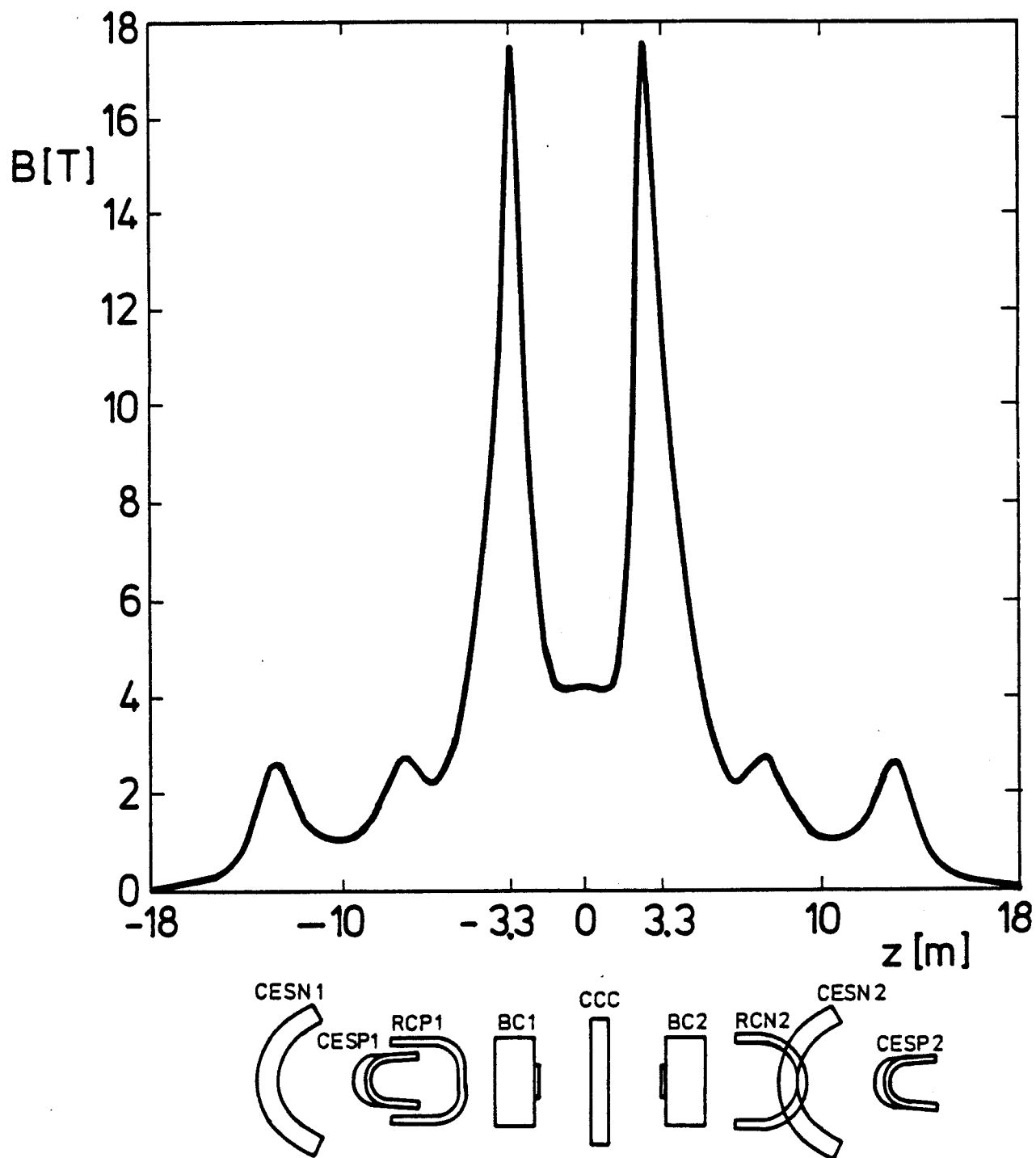
Fig. 2.8-1. Magnet system of TASKA-M and magnetic field.
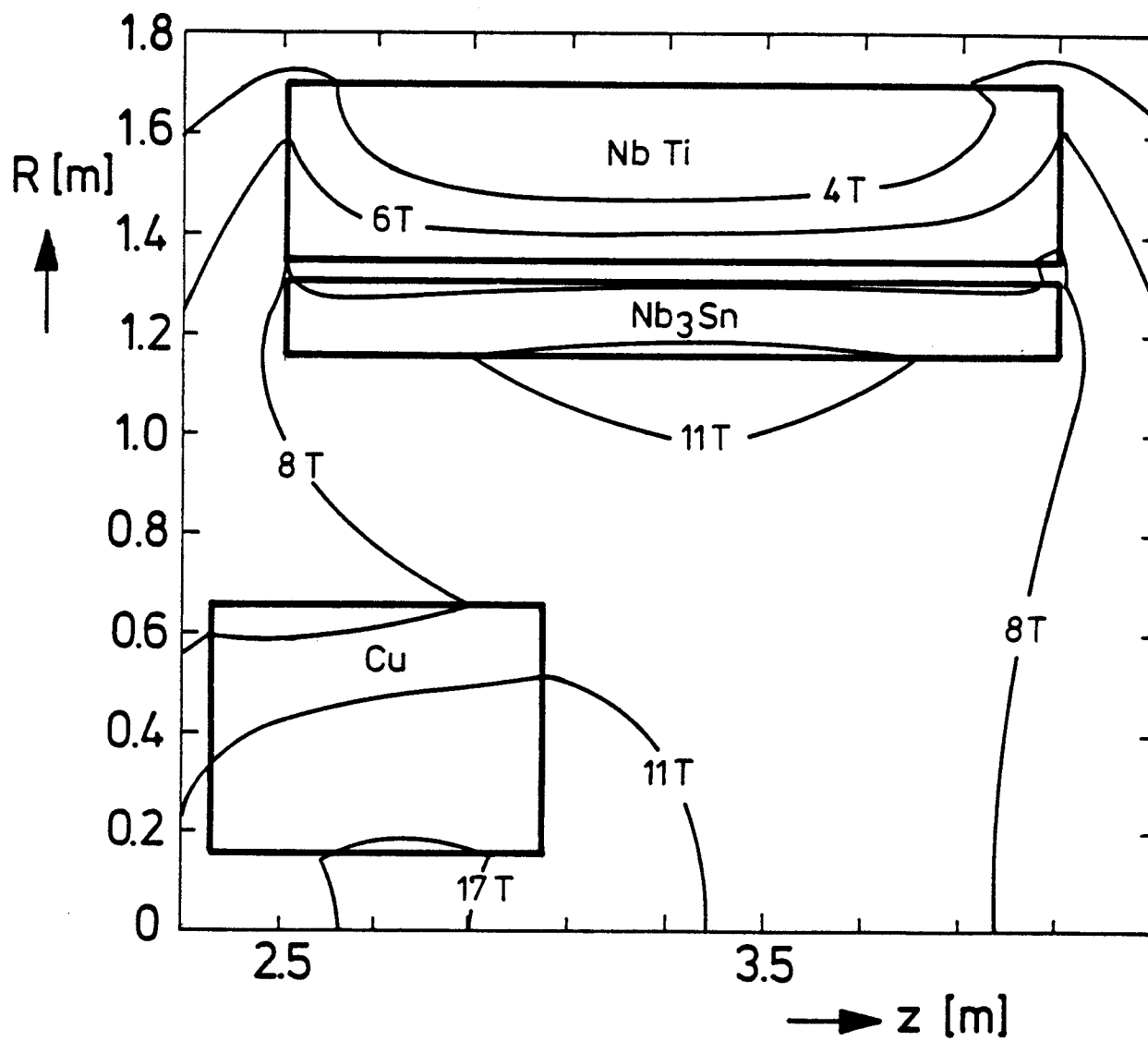
Fig. 2.8-2. Contours of the magnetic field strength in the vicinity and within the choke coil.

- 2 transition coils (RCP1, RCN2).
- 2 Yin-Yang sets (CESN1, CESP1 and CESN2, CESP2).

Figure 2.8-1 shows a computer drawing of the magnet set with the names of the magnets and the magnetic field magnitude B along the z-axis (machine axis). The central cell coil and the choke coil are solenoidal type magnets. All the anchor magnets are C-shaped coils. The magnet system in TASKA-M is much simpler than that used for the TASKA design. In particular the choke coil is smaller and cheaper, because the plasma radius is lower and the field requirement is 17.5 T in TASKA-M instead of 20 T in TASKA. The goal to have only 12 T at the Nb_3Sn conductor is attained (as shown in Fig. 2.8-2) and the electrical data are comparable with Nb_3Sn coils already tested. However, the diameter of tested coils is characterized by a half meter bore.

All the NbTi superconducting coils have electrical data comparable with existing tested magnets. The size of the magnets is also on the same order of magnitude as for tested magnets.

One area of concern is the lack of a data base for the normal conducting insert coil, especially for the behavior of the ceramic insulation in a high magnetic field and high 14 MeV neutron flux environment. In this respect, more experimental work is needed. However, extrapolation from existing data indicates that the inserts will operate the whole life of the machine. In case of earlier failures, a replacement is possible in a time period comparable to that needed for the change of blanket modules.

2.9 Testing Modules
2.9.1 Introduction

A primary function of the TASKA-M facility is to provide a nuclear test bed for the magnetic fusion program. This role is meant to complement other ex-reactor facilities and provide an integrated test of components in a complex nuclear environment. TASKA-M will provide a test bed for large specimens in a thermal, stress and chemical environment similar to that of a fusion power reactor, where a large volume, high fluence and high energy neutron environment is required. It also provides a test bed for fusion blanket designs in which the synergistic effects of corrosion, stress, neutron induced mechanical property changes, and tritium breeding, confinement and extraction can be tested and evaluated. Finally, TASKA-M will also be a test bed for

high heat flux components such as beam dumps, as well as neutral beams, ICRF antennas, vacuum pumps, superconducting and normal magnets and a variety of other systems.

Figure 2.9-1 is a cross section of the TASKA-M central cell showing the four testing facilities provided. These are a liquid metal blanket module designated as blanket 1, a solid breeder module designated blanket 2 and two material test modules designated blankets 3 and 4. A brief summary of each module will be given in the following sections.

2.9.2 Liquid Metal Test Module

Two liquid metal blanket modules, one utilizing $Li_{17}Pb_{83}$ and the other Li are designed to fit in the same slot within the central cell and will be tested consecutively. Both are made of the ferritic steel, HT-9, and are self-cooled once-through tubular designs with a single inlet and outlet header.

The liquid metal blanket test module consists of rows of tubes distributed axially, running from an upper manifold to a lower manifold as shown in the module assembly in Fig. 2.9-2. Breeding material comes in through a horizontal header at the top, distributes axially within the upper manifold with the aid of the magnetic field, then flows through the tubes around the plasma collecting in the lower manifold and exiting through the outlet header. The inner radius is 22 cm, the axial length is 83 cm and the thickness is 45 cm for the $Li_{17}Pb_{83}$ module and 64 cm for the Li module. All the tubes have an outer diameter of 7.04 cm and a wall thickness of 1.6 mm. The axial spacing from tube center to center is 7.3 cm and the radial spacing is 6.32 cm. At the point where they connect to the manifold, the tubes neck down to a diameter of 5.2 cm. This provides more space for welding on the inside of the manifold.

Figure 2.9-2 shows the liquid metal blanket module as part of the assembly used to support it and insert it into the test reactor. The assembly consists of the module, integral reflector/shield and the seal flange. Horizontal insertion is used to fit the assembly into the test reactor. The Li blanket module will have ten rows of tubes per side instead of seven. A completely new assembly will be needed to accommodate it. However, the space within the reactor and the components in it will not need to be modified.
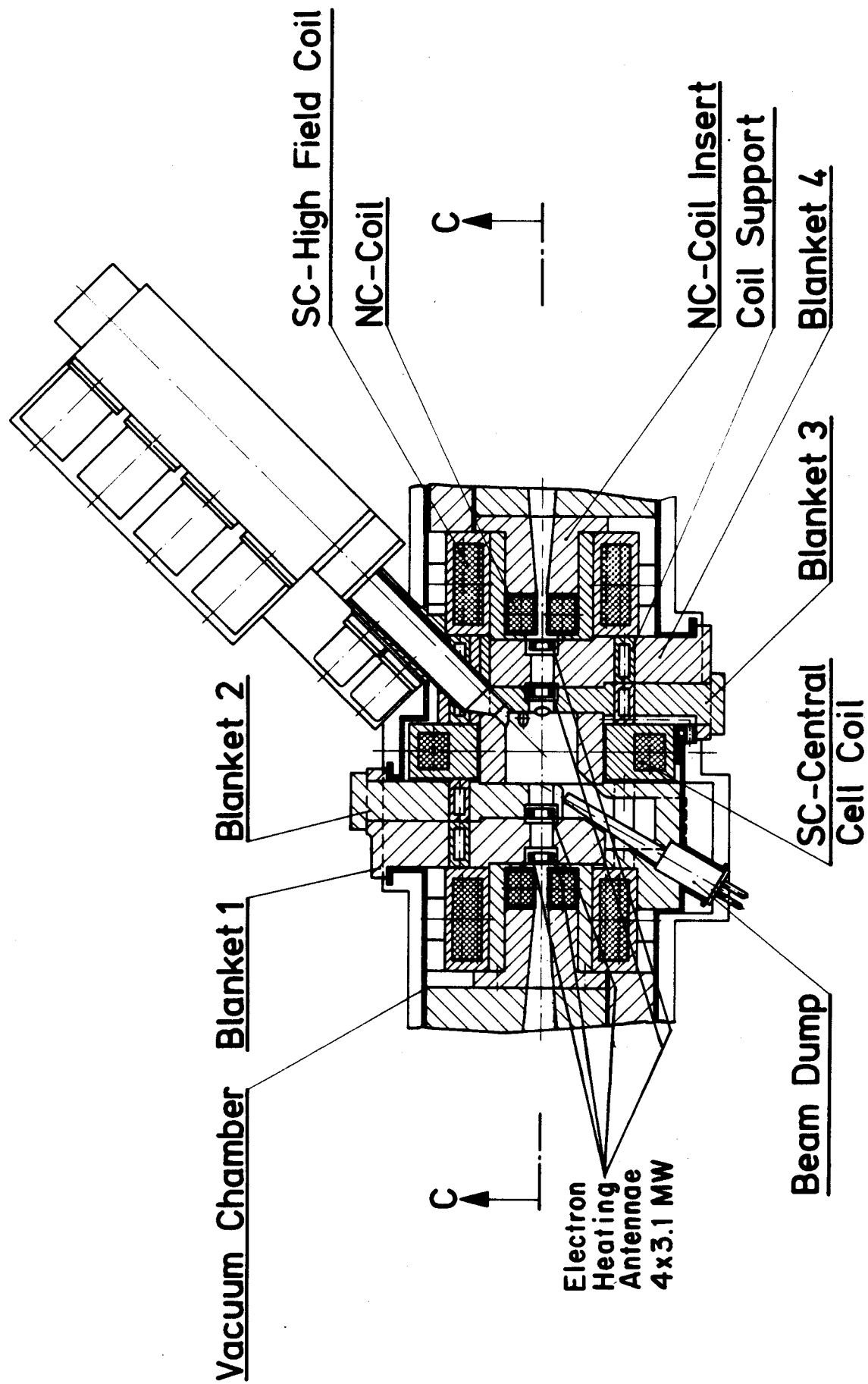
Fig. 2.9-1. Plan view of central cell.

Vacuum Chamber Blanket 1 Blanket 2

SC-High Field Coil

NC-Coil

C

NC-Coil Insert

Coil Support

Blanket 4

Blanket 3

SC-Central
Cell Coil

Beam Dump

Electron
Heating
Antennae
4x3.1 MW

C
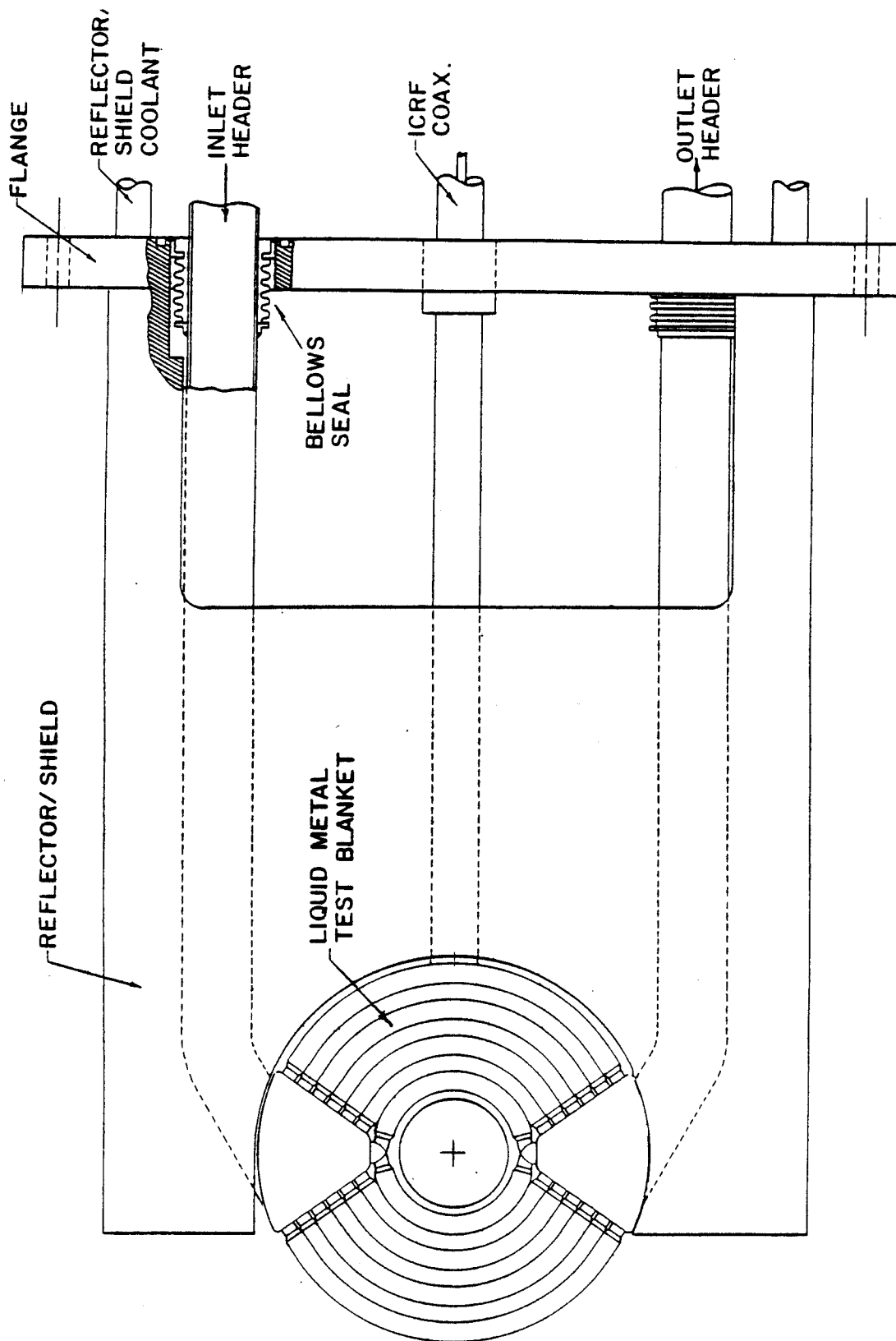
Fig. 2.9-2. View of liquid metal blanket module assembly.

Plasma heating by ICRF requires that antennae be situated within the central cell in close proximity to the plasma. One of the antennae falls within the axial span occupied by the liquid metal module. To accommodate the ICRF antenna, four of the front tubes have to be eliminated, to provide space on the sides and in the back of the antenna.

The blanket modules are supported on the bottom manifold with the load path going through the reflector, vacuum chamber and then to external structure supporting the central cell. An analysis has been made to determine the stresses on the front tubes for the $Li_{17}Pb_{83}$ case. The maximum stress occurs at the upper connection and is equal to ~ 44 MPa. Table 2.9-1 gives the parameters of the two liquid metal modules.

Neutronics analysis has been performed for the liquid metal test blankets using an average blanket volumetric composition of 73% liquid metal, 7% HT-9, and 20% void. The neutron wall loading has strong axial variation with peak and average values of 1.22 and 0.85 MW/m^2, respectively. The primary goal of the neutronics analysis is to design blanket test modules which have reactor relevant neutronics parameters. Local tritium breeding ratios $\geqslant$ 1.15 and energy multiplications $\geqslant$ 1.3 are required. A reflector made of Fe-1422 and cooled by 5 vol.% water is used in this design.

A series of one-dimensional neutronics calculations has been performed to determine the proper enrichment and thickness for the Li and $Li_{17}Pb_{83}$ blanket test modules. The total blanket and reflector thickness was fixed at 90 cm. In the calculations, a 50 cm thick shield was used. The one-dimensional discrete ordinates code ONEDANT was used to model the problem in cylindrical geometry. The P_3S_8 approximation with a coupled 46 neutron-21 gamma group cross section library based on the VITAMIN-C data library and the MACKLIB-IV-82 response library was used for this study. Our results indicate that the best neutronics performance in which large values of tritium breeding ratio and blanket energy multiplication can be obtained simultaneously can be achieved when highly enriched lithium is used in $Li_{17}Pb_{83}$. On the other hand, there is no incentive for increasing the enrichment in the liquid lithium blanket beyond the natural occurrence of 7.42% ^6Li. A blanket thickness of 63.9 cm which corresponds to ten rows of tubes was chosen for the liquid lithium module. This yields a tritium breeding ratio of 1.19. For the LiPb module a thickness of 45 cm is used with seven rows of tubes resulting in a

Table 2.9-1. Parameters of Liquid Metal Blanket Modules

	LiPb	Li
First wall radius, cm	22	22
Axial extent, cm	83	83
Blanket thickness, cm	45	63.9
Number of tube rows/side	7	10
Total number of tubes	148	210
Tube outer diameter, cm	7.04	7.04
Tube inner diameter, cm	6.72	6.72
Axial tube spacing, cm	7.30	7.30
Radial tube spacing, cm	6.32	6.32
Transition section OD, cm	5.20	5.20
Transition section ID, cm	4.92	4.92
Mass of full module, tonnes	7.50	1.60
Mass of empty module, tonnes	0.54	0.94

tritium breeding ratio of 1.15. Table 2.9-2 gives a summary of the design parameters, tritium production and nuclear heating results for both modules.

Due to the large axial variation of the neutron wall loading along the first wall of the blanket module, the power density in the module will vary axially as well as radially. The radial variation obtained from the one-dimensional calculations was coupled with the axial variation of wall loading to get an estimate for the r and z dependence of the power density for the LiPb blanket module and the Li blanket module.

Magnetohydrodynamic effects have been evaluated for the test modules. The dominant force on a conducting fluid across magnetic field lines is the MHD force. The effect of the MHD force is to increase the pressure drop and retard heat transfer by suppressing turbulence. In TASKA-M, the first wall surface heat load is ≤ 10 W/cm^2. Consequently, the effects of MHD on heat transfer are not critical and calculations can be carried out by assuming no turbulence. The MHD pressure drop will slightly increase the stresses in the blanket and also increase pumping power. The total MHD pressure drop in the reactor is 0.57 MPa, which corresponds to a pumping power requirement of 2.3

Table 2.9-2. Comparison Between Design Parameters and Tritium Production Results for Li and Li-Pb Blanket Modules

	LiPb	Li
Lithium enrichment (% ^{6}Li)	90	7.42
Blanket thickness (cm)	45	63.9
Number of tube rows	7	10
Reflector thickness (cm)	45	26.1
Tritium breeding (tritons/fusion)		
^{6}Li(n,α)t	1.15	0.67
^{7}Li(n,n'α)t	0.002	0.52
Total	1.15	1.19
Tritium production rate (tritons/s) per 1 MW/m^2 wall loading per 1 m width	7.04×10^{17}	7.28×10^{17}
Nuclear heating (MeV/fusion)		
Blanket		
Neutron	7.31	11.85
Gamma	6.41	2.95
Total	13.72	14.80
Reflector		
Neutron	0.70	0.61
Gamma	4.53	3.93
Total	5.23	4.54
Total recoverable	18.95	19.34
Energy multiplication	1.344	1.371
Power per unit width (MW/m) for 1 MW/m^2 wall loading		
Blanket	1.35	1.45
Reflector	0.51	0.45
Total	1.86	1.90
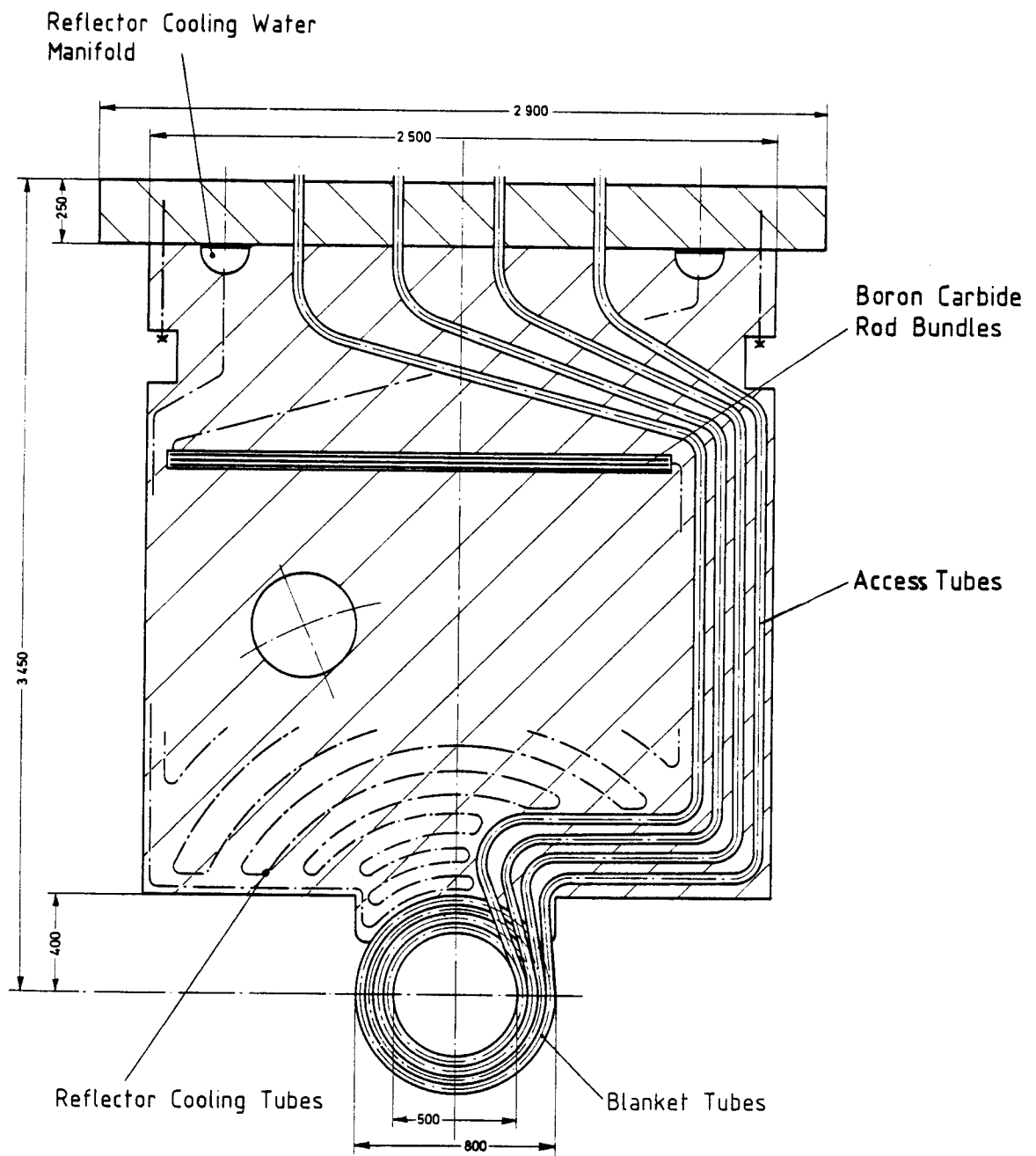
Fig. 2.9-3. Liquid metal blanket module assembly.

kW. The maximum blanket pressure is 0.42 MPa. This value is smaller than the total MHD pressure drop because much of the drop occurs in the inlet header.

The temperature profile in the coolant tube can be calculated by assuming only conduction. The most severe heat transfer problems occur in the first row of tubes. The energy deposited in the first row of tubes consists of a volumetric component due to nuclear heating and a surface heating load from the plasma. A slab geometry with a constant velocity, constant surface heat flux and exponential volumetric heat flux was used to calculate the temperature profile. Table 2.9-3 gives the thermal hydraulic parameters for the two liquid metal blanket modules.

Table 2.9-3. Liquid Metal Testing Module Thermal - Hydraulic Parameters

	LiPb	Li
Average wall loading, MW/m^2	0.84	0.84
Peak wall loading, MW/m^2	1.22	1.22
Energy production rate, MW/m / MW/m^2	1.35	1.45
Module width, m	0.83	0.83
Magnetic field, tesla	4.2	4.2
Module neutron power, MW	0.96	0.96
Blanket power, MW	0.95	1.02
Coolant temperature, °C	300/450	300/450
Coolant flow rate, kg/hr	1.37×10^5	5.8×10^3
Maximum structural temp., °C	512	500
Maximum coolant velocity, cm/s	2.5	1.8
MHD pressure drop (MPa)	0.57	0.45
Maximum blanket pressure (MPa)	0.42	0.35
Pumping power, kW	2.3	1.4
Reflector power, MW	0.36	0.32
Reflector coolant	H_2O	H_2O

2.9.3 Solid Breeder Test Module

Blanket module no. 2 in Fig. 2.9-1 was designated for testing all kinds of solid breeder materials. Because of limited space, it is therefore not intended to represent a typical fusion reactor blanket and does not attain a local breeding ratio greater than one.

The design consists of four layers of 316 SS coiled tubes, each having nine windings as shown in Figs. 2.9-3 and 2.9-4. The inner radius of the blanket is 25 cm and the outer, 40 cm. Tube outer diameter is 4 cm and the wall thickness is 3 mm. The breeding material is contained in spherical shells also made of 316 SS. The spheres are 3 cm in diameter and are confined in the coiled tubes around the plasma. Adding and replacing the balls is accomplished simply by pushing them through the coiled tubes, such that as new balls are added, some are extracted on the exit end. The content of each layer of coils can be exchanged separately to avoid mixing the breeding balls which have been exposed to different neutron fluences. There are 4 inlet and outlet tubes penetrating the vacuum flange. Welding is done only on the outside of the vacuum chamber. Each layer of tubes contain up to 850 spheres. Water flowing through the tubes in the spaces around the spheres provides the cooling. Table 2.9-4 gives the physical parameters of the solid breeder module.

The reflector and the shield zone are composed of flat steel plates which are bolted together. Cooling tubes are located between the plates and are embedded in grooves of non-circular cross section.

There is a large heat flux to the front surface of the reflector facing the neutral beam ducts, caused by charge exchange particles. This surface is covered by separate cooling tubes.

The average neutron wall loading in the solid breeder test blanket is 0.73 MW/m^2. Assuming a surface heat flux density of 5% of the neutron wall load the surface heat load to the first row of tubes is 22 kW. The average volumetric heat generation in the first 3.75 cm (equivalent to the homogenized first row of tubes) is 4.67 W/cm^3. This leads to a volumetric heat generation of 112 kW. The total heat input to the first row therefore amounts to 134 kW. Between inlet and outlet a coolant temperature rise of 50 K has been chosen, resulting in a mass flow rate of 0.6 kg/s. The total heat generation in the
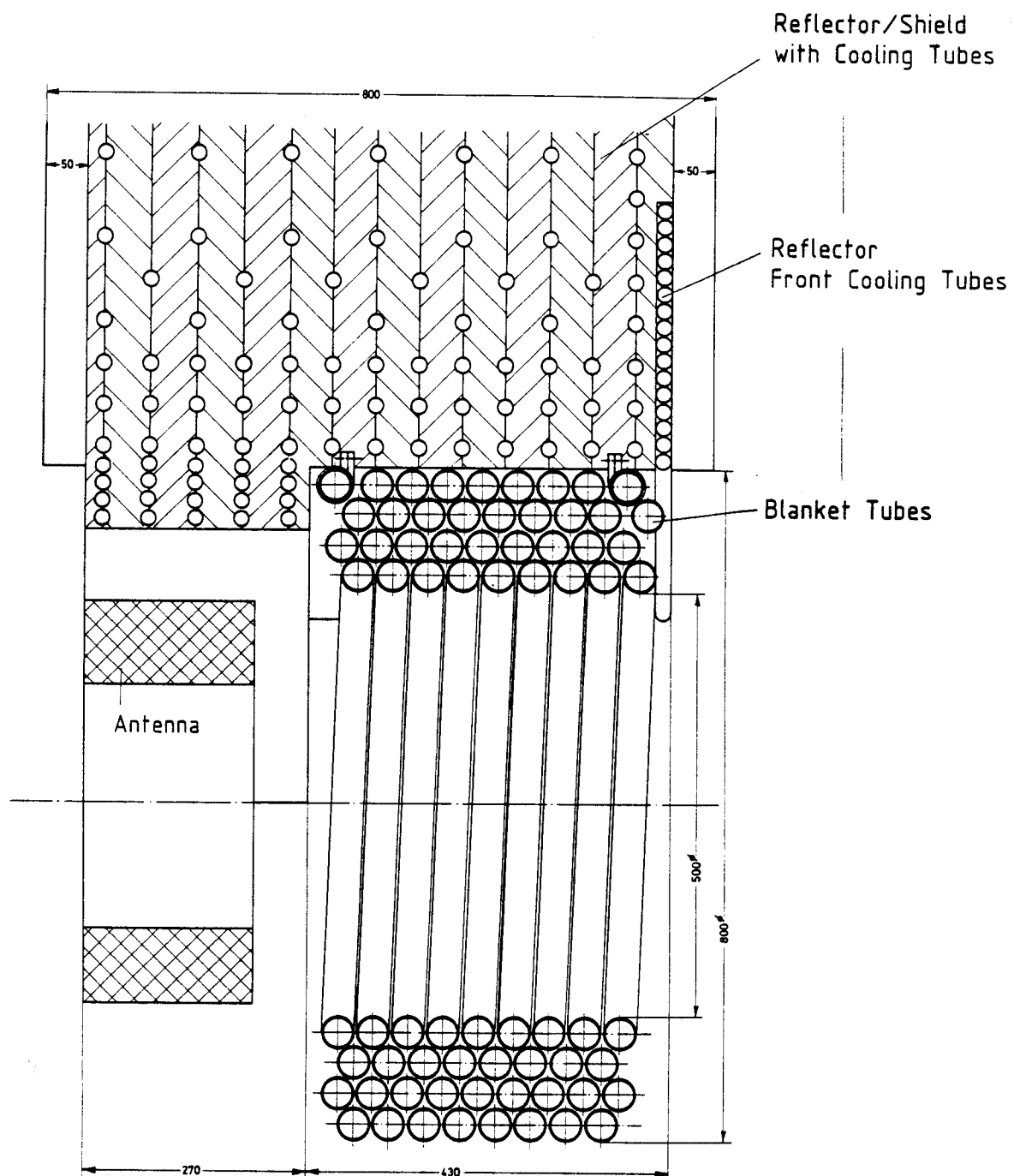
Fig. 2.9-4 Basic arrangement of the blanket and the reflector/shield.

Table 2.9-4. Physical Parameters of Solid Breeder Module

Breeding zone

Outer diameter, cm	40
Inner diameter, cm	25
Axial length, cm	40
Tube outer diameter, cm	4
Tube wall thickness, mm	3
Tube material	316 SS
Breeding ball outer diameter, cm	3
Breeding ball wall thickness, mm	2
Ball shell material	316 SS
Breeding material	Li_2O
Breeding material fraction, %	20
Steel fraction, %	32
Water fraction, %	28
Void fraction, %	20
He mass flow, kg/s	1.8

breeding region is 380 kW, leading to a total coolant mass flow (at $\Delta T = 50$ K) of 1.8 kg/s.

The breeder balls have a diameter of 30 mm and fit into the pressure tube with a radial gap of 2 mm. This is a rather complicated coolant channel geometry where the calculated velocity varies between $w_{max} = 3.6$ m/s and $w_{min} = 0.8$ m/s. The pressure drop is caused mainly by flow separation in the zone where the velocity decreases, leading to a small pressure recovery. It is rather difficult to theoretically estimate a recovery factor and the friction pressure drop for the given case. For this reason, a benchmark experiment has been performed in a 1:1 geometry to determine the drag coefficient. A drag coefficient of $\xi = 0.5$ has been calculated from the measured data for one ball and the given Re-number of 10^5. Using this coefficient, the pressure drop in the inner blanket tube containing about $n = 750$ balls is 20 bar.

In the neutron and gamma transport calculations, the one-dimensional discrete ordinates code, ONEDANT, is used with the University of Wisconsin 46-neutron, 21-gamma group cross section set condensed from the ENDF/B-IV based Vitamin C and MACKLIB libraries. The actual shape of the solid breeder test modules is modeled in the code by cylindrical geometry with homogenized regions. The breeding zone contains 32% SS 316, 28% H_2O, 20% breeding medium (Li_2O) and 20% void. The reflector/shield consists of 95% SS and 5% water. The objective of the calculations is to provide necessary data for the design of the blanket cooling system and to give an indication of the breeding ratio expected.

The energy multiplication factor was determined to be 1.31 for the blanket region and 1.33 for the antenna region. The total breeding ratio using 30% enriched ^6Li at 90% theoretical density is 0.71 and is made up of 0.66 for ^6Li and 0.05 for ^7Li. Table 2.9-5 gives the thermal hydraulic parameters of the solid breeder module.

Table 2.9-5. Thermal Hydraulic Parameters of Solid Breeder Module

Average neutron wall loading, MW/m^2	0.73
Total heat generation in breeding zone, kW	380
Heat in reflector/shield, kW	130
Heat in reflector/shield and behind antenna, kW	270
Water flow rate in breeding zone, kg/s	1.8
Inlet pressure, bar	50
Inlet temperature, °C	150
Pressure drop, bar	20
Water temperature rise, °C	50
Water flow in reflector/shield, kg/s	2
Inlet pressure, bar	30
Inlet water temperature, °C	40
Water temperature rise, °C	50

Each of the 8 access tubes in the blanket is closed by a separate valve block, containing two double valves for closing the cooling water line and the ball exchange line. The refilling machines are flanged to those valve blocks after removing blank flanges. All flanges are designed for remote handling.

A main advantage of a breeding ball concept is that the bred tritium remains inside the steel shell of the breeding ball, and thus the tritium extraction can be separated from the cooling process. A high retention -- meaning a minimum of tritium loss through the steel shell -- is achieved in the following way:

• At the operating conditions of up to 300°C a thin oxide layer will be established at the outer surface of the steel shell. This will reduce the permeability of T by a factor of 10 to 100 compared to pure steel.

• By adding to the solid breeder material a small amount of Nb as a getter material, the partial pressure of T inside the ball can be drastically reduced.

The tritium extraction can be easily done by heating the balls up to 800°C in a special recovery system outside the reactor.

2.9.4 Material Test Modules

The material test modules are designated nos. 3 and 4 in Fig. 2.9-1. Although neutronic analysis has been performed for both modules, only no. 4 was designed in detail and will be described here.

The main goal in the materials test modules is to provide a large volume test zone for testing specimens in a high fusion neutron flux. To that end we tried to maximize the exposure of the specimens to the neutron environment while maintaining reasonable access to the test cells. The TASKA-M materials test matrix specifies the type of materials tests with detail on specimen numbers, irradiation temperatures, fluences, stress, changeout frequencies and post-irradiation testing conditions. The test matrix provides a means to compare the volume needed to carry out a specific materials testing scenario with the volume available for testing in TASKA-M. Also the frequency of specimen changeout can be quantified and its effect on the overall reactor availability estimated. The test matrix is shown in Table 2.9-6.

The major components of the TASKA-M materials test module, shown in Fig. 2.9-5, are the helium cooled heat sink (annular test module), the biological shield and the specimen capsules. The temperature within each of the 180

Table 2.9-6. Materials Test Matrix for TASKA-M
Module 4

Test Types	Mat.[a] Var.	Dup.[b]	Temp.[c]	Fluence[d]	Postirradiation Conditions	Total Specimens (Assume 50-50 Mix of Ferritic & Austenitic Alloys)	Total Capsules[e]	Sub-Total
Material Qualification								
Tensile/Ductility	3	2	4	3	4 Rate/Temp.	288	14	
Fatigue Life	2	2	4	3	2 Strain Levels	96	3	
Fatigue Crack Growth	2	2	4	3	2 Stress Levels	96	1	
Fracture Toughness								
-- Charpy	2	2	6	2	6 Temperatures	288	2	
-- Compact Tension	2	2	3	2	2 Temperatures	48	4	24
Engineering Scoping								
Tensile/Ductility	5	3	6	4	4 Rate/Temp.	1440	6	
Fatigue Life	5	2	4	2	2 Strain Levels	160	4	
Fatigue Crack Growth	5	2	4	4	2 Stress Levels	320		
Fracture Toughness								
-- Charpy	3	2	6	4	6 Temperatures	864	4	
-- Compact Tension	3	2	2	4	2 Temperatures	96	1	
Swelling/Microstructure	10	5	10	5	2	5000	1	
Creep/Stress Rupture	6	2	4	[6]	6 Stress Levels	288	2	18
Other Materials[f]								
Fatigue Life	5	2	4	4	2 Strain Range	320	8	
Tensile/Ductility	15	3	6	4	4 Rate/Temp.	4320	16	
Dimensional Stability	15	4	6	3	3 Post-Tests	7200	36	
Creep/Creep Rupture	10	2	6	[4]	4 Stress Levels	480	2	
Fracture Toughness	3	2	2	2	6 Temperatures	144	2	
Electrical Properties	6	3	3	4	3 Tests	648	4	
Thermal Conductivity	6	3	4	4	2 Tests	576	6	74
						22,576	116	
						Total No. of Specimens	Total No. of Capsules to Hold Specimens	

Module 4 only: Module 3 used for surface effects and dynamic in-situ testing.
[ ] 1 specimen used to obtain 6 fluence measurements.

[a]Materials x variations

[b]Duplication

[c]Number of irradiation temperatures

[d]Fluence Levels

[e]Capsule volume-390 cm^3

[f]Ceramics, electrical, and heat sink materials

2.9-15

Table 2.9-7. Design Values for Test Module #4

REACTOR OPENING
- Maximum axial opening of 90 cm

TEST MODULE
- Material of Construction: HT-9
- Size: Inside radius - 18 to 22 cm (conical)
        Outside radius - 38 to 42 cm (conical)
        Length - 55 cm (end to end) 42.4 cm straight section
- No. of Capsule Tubes: 180
- Total Heat Generation: 572 kW
- Coolant: Helium at 3448 kPa and 125°C
- Flow Rate: 33.7 x 10^3 ℓ/min
- Coolant Pipe Size: 12.5 cm diameter
- Instrumentation Per Capsule Tube: 2 pair thermocouple leads - chromel
                                                                alumel

    2 gas leads - 0.158 cm diameter for
                gas gap control

SPECIMEN CAPSULE
- Material of Construction: 316 SS
- Size: 5 cm diameter by 20 cm long
- Specimens: Various shapes packed to 50% of capsule volume in NaK
              (22/78)
- Instrumentation: (2) 0.168 cm diameter stainless steel sheathed MgO
                    insulated thermocouples
- Sealing: All welded construction with bellows for NaK expansion
- Gas Gap: Variable annulus 0.018 - 0.100 cm filled with helium or neon
            or mixtures of the two gases

TASKA-M
TEST MODULES

ARRANGEMENT OF TEST MODULES IN CENTRAL CELL

PLASMA AXIS

MATERIALS TEST BLANKET NO. 4

MATERIALS TEST BLANKET NO. 3

INSTRUMENT AND COOLANT LINE SHIELD PLUG

TEST SPECIMEN CAPSULE

MATERIALS TEST BLANKET NO. 4

ANNULAR CONICAL CYLINDER TEST MODULE WITH 180 CAPSULE TUBES

VACUUM SHROUD

MODULE SHIELD PLUG
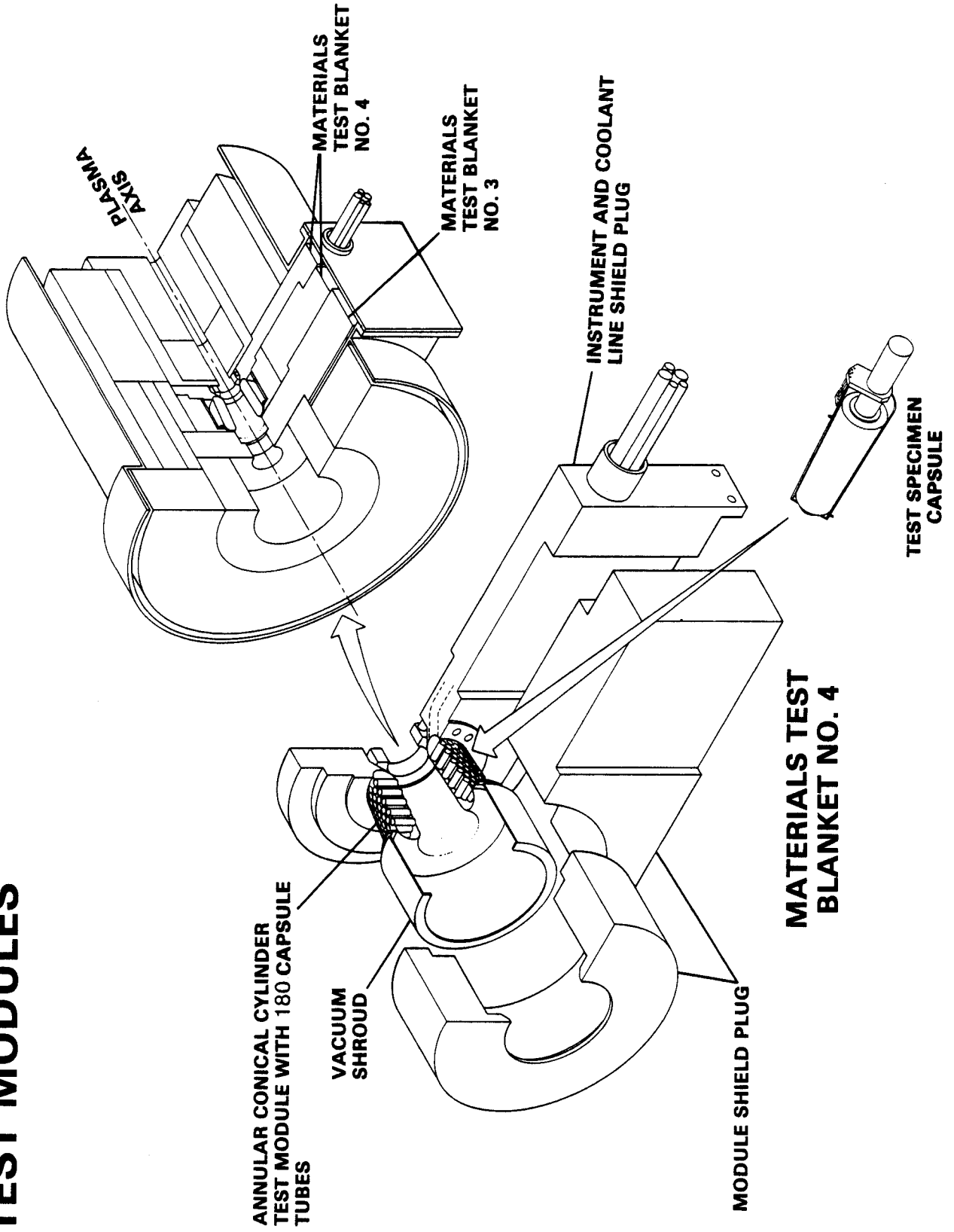
Fig. 2.9-5. Major components of materials test module #4.
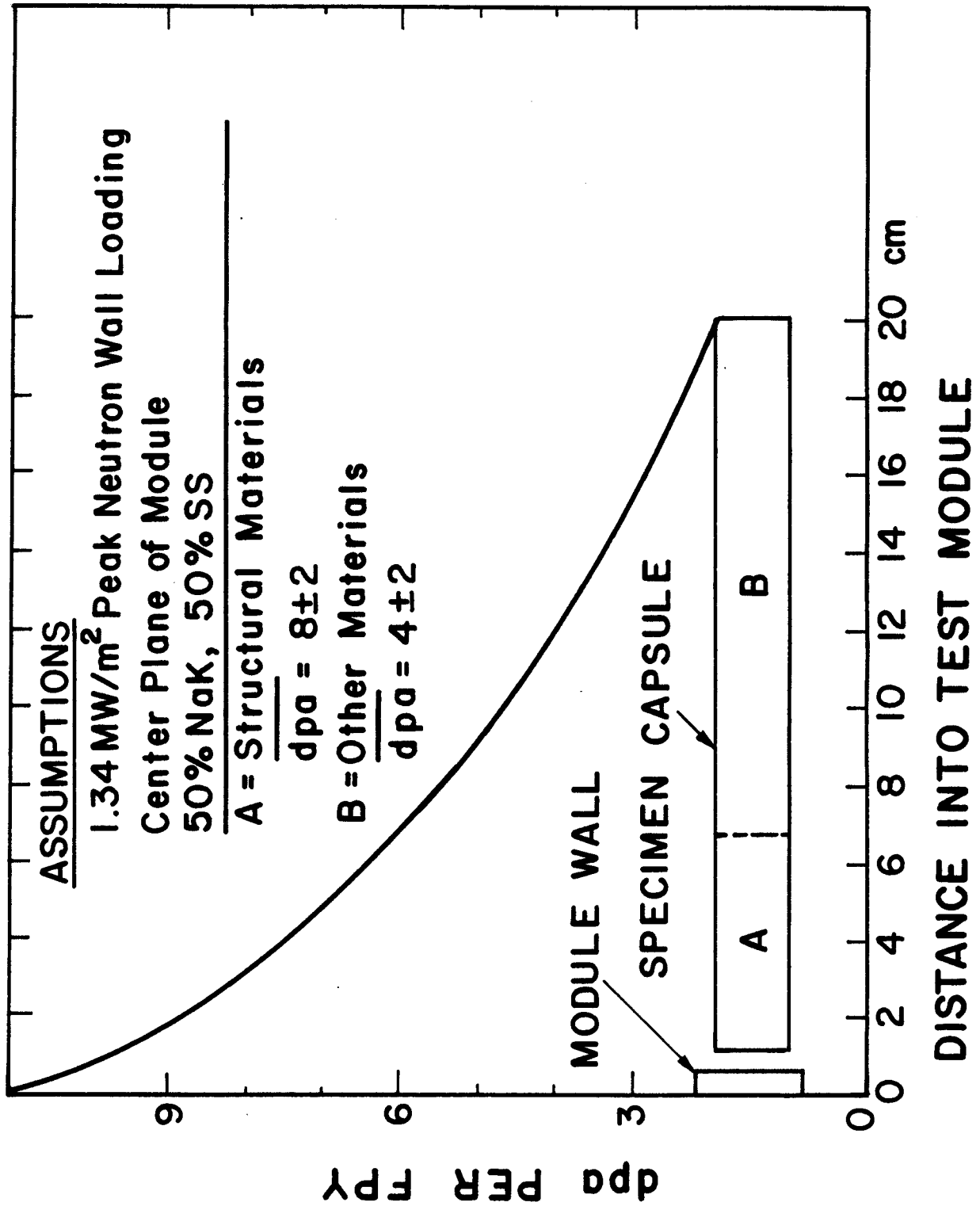
Fig. 2.9-6. Dpa profiles in the two material test modules.
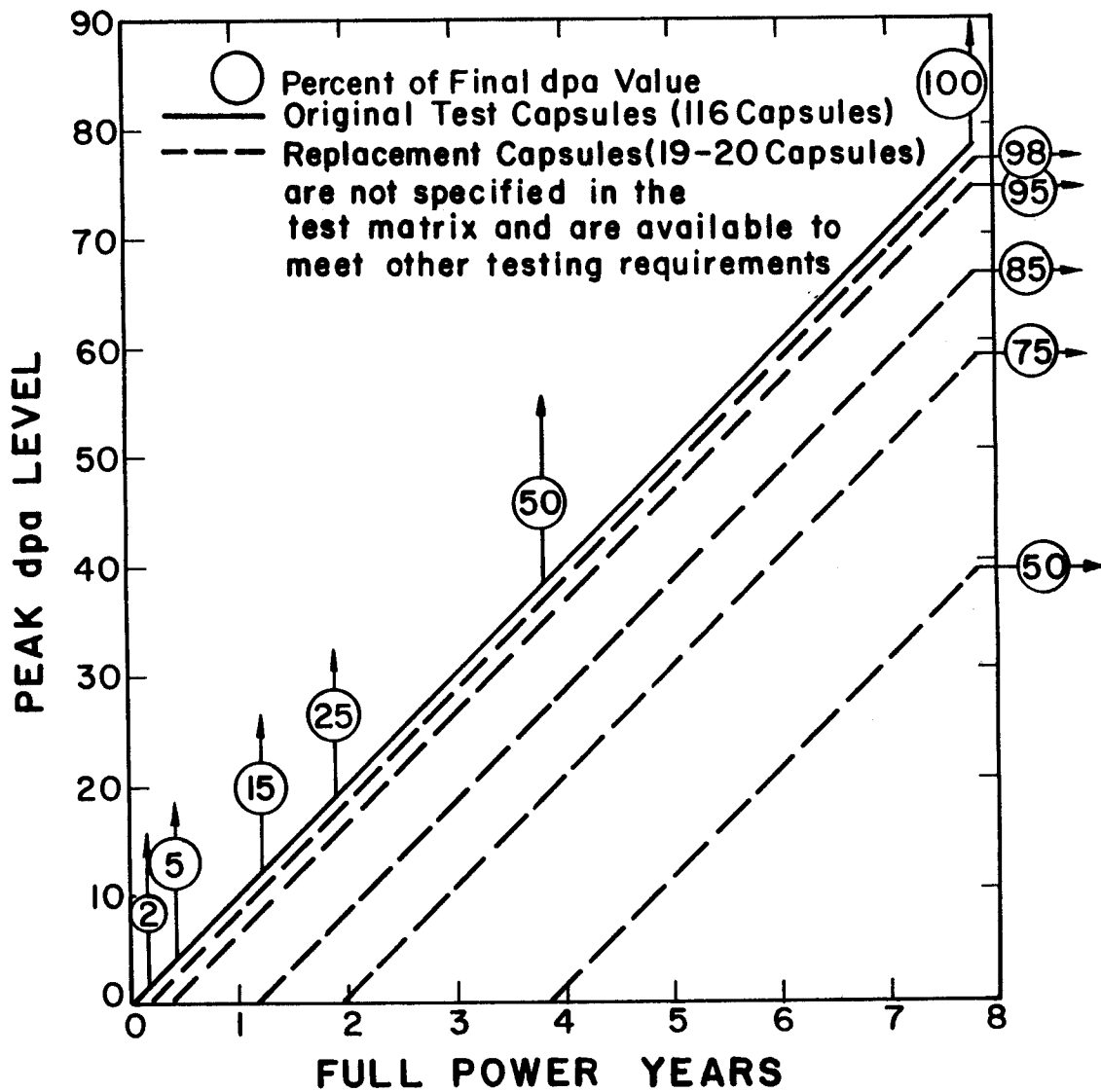
Fig. 2.9-7 The capsule discharge scheme.
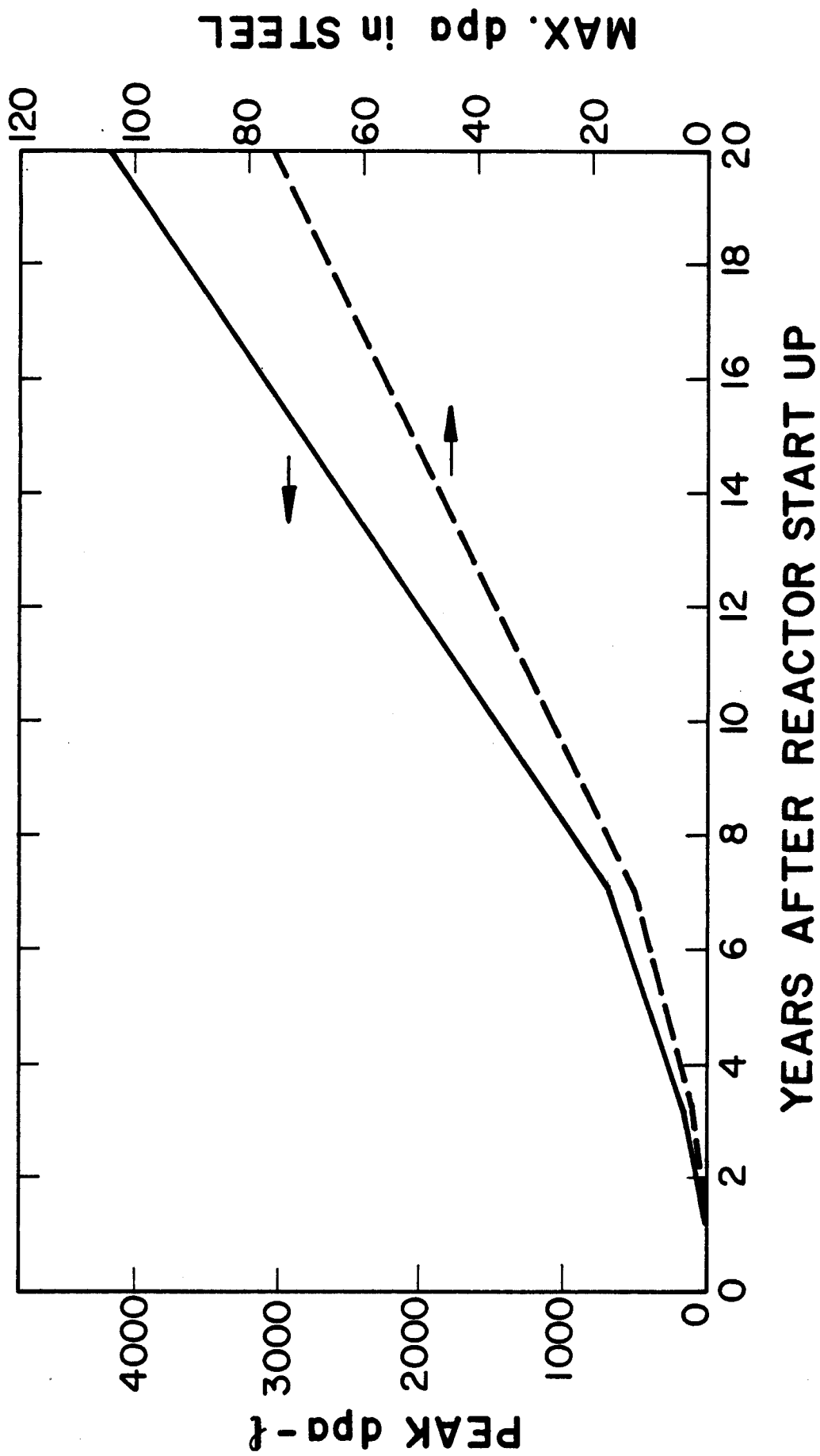
Fig. 2.9-8 . Accumulated damage parameters for TASKA-M.

specimen capsules is predetermined by engineering the thermal barrier between the specimen capsule and the heat sink. Individual capsules can be independently accessed and are designed to operate at a predetermined temperature within the range of 350 to 650°C. The total irradiation volume within the module is 70.6 liters. Table 2.9-7 lists the detailed test module design values determined during the initial conceptual design.

Neutronics calculations have been performed to determine the specimen damage profiles and testing capability of the materials testing modules in blankets #3 and #4. Profiles of the power density resulting from neutron and gamma heating in the modules have also been determined as they are required for proper design of the cooling system. The capsules are assumed to consist of 50 vol.% NaK, which is used as a thermal contact material, and 50 vol.% 316 SS, which represents the specimens and capsule structural material. The module structure is assumed to represent 20% of the module volume and is made of HT-9. The helium gas coolant occupies the remaining volume of the test module.

The dpa and helium production profiles in modules #3 and #4 have been obtained from three-dimensional Monte Carlo calculations. These profiles reveal that the peak dpa and He production rates in the test modules are 10 dpa/FPY and 120 He appm/FPY, respectively. The dpa rates drop to a value of ~ 1.5 dpa/FPY at the back of the module and the helium production rate drops to ~ 10 He appm/FPY. Figure 2.9-6 shows the dpa profile in one of the capsules.

Finally, the accumulated damage and capsule discharge schedule is given in Fig. 2.9-7. At the present time only 116 capsules are required and the potential of module 4 is for 180 capsules. This leaves room for even more testing capability than that outlined in Table 2.9-6. The materials community should welcome the additional space and we have no doubt that it will be used. Finally, the cumulative damage and dpa·ℓ figure of merit is shown in Fig. 2.9-8. As stated previously the over 4000 dpa·ℓ product is an indication of the ultimate usefulness of TASKA-M compared to lower volume test sources.

2.10 Maintenance

In order to guarantee sufficient availability of TASKA-M, a maintenance scheme on the basis of remote handling systems was evaluated. It is expectedthat all its elements can be designed and provided for operation of the device in the 1990's.

The major subsystems and components of TASKA-M are categorized into four general maintenance classes according to their lifetime.

Class 1: Components which have a full lifetime, such as buildings, support structures, shielding, superconducting magnets.

Class 2: Components with a lifetime of more than 3 full power years, such as central cell insert, ICRF antennas.

Class 3: Components with a lifetime of less than 3 full power years such as ion sources, test blanket inserts, diagnostic equipment, neutral beam dumps.

Class 4: Parts with a very short lifetime or scheduled operating time such as samples in materials test blankets. The parts in this class can be exchanged quickly.

The requirements on the maintenance equipment are essentially posed by the sizes and weights to be handled and by the radiation environment in which an operation takes place.

The problem of radiation doses can be solved without the use of a shielded protection containment. It will be sufficient to increase the wall thickness of the reactor hall as a biological shield and carry out all the operations inside remotely, if the radiation dose level is unacceptably high for manned access.

Sizes and weights of parts are given in Table 2.10-1. They are significantly reduced in comparison to TASKA, in agreement with the overall objectives of TASKA-M.

In order to minimize machine downtime, maintenance schemes were developed for Class 2 and 3 components which do not break the vacuum boundary outside of magnets and shield. An example is given in the following description of the test blanket maintenance. In order to change Class 1 equipment (such as the central cell magnet or Yin-Yang magnets), the vacuum boundary must be opened. This is possible because the vacuum vessel is segmented and joined by bolts and renewable lip welds.

Table 2.10-1. Main Components - Estimated Sizes and Removable Weights[*]

	Size (m)	Removable Weight (t)
Vacuum chamber (section)	5.5 x 4.5 x 4	17
Breeding test blanket	4.45 x 2.50 x 0.88	35
Central cell coil	5.16 Ø x1.06	110
High field coil	3.70 Ø x2.06	73
Yin-Yang coil	6.5 x 3.2 x 2.95	52
Transition coil	4.05 x 3.85 x 3.45	35
Beam dump	0.65 Ø x3.5	6
Central cell insert	2.45 Ø x1.36	38
NC-coil insert	1.95 Ø x2.1	40

[*] may include shields, supports, etc.

Ø = diameter

Maintenance of Blankets. The blankets inside the vacuum chamber face the plasma directly, thus forming the first wall with their innermost parts. Besides their replacement according to the maintenance schedule, the exposure to extreme thermal and radiation loads may necessitate frequent exchange, in addition to scheduled maintenance. The main operations are:
• breaking the blanket seal,
• removing the blanket,
  transporting the blanket to a storage cell or hot cell,
• transporting and installing a new blanket,
• restoring vacuum tightness.

    To fulfill the requirements of vacuum tightness, a combination of a welded joint and a metal gasket is proposed. After first inserting the blanket, the gasket flange with the gasket is forced against the vacuum chamber flange by means of flange bolts. This operation can be performed by tools inside the protection containment. Then the containment can be removed and the joint can be welded. The metal gasket protects the vacuum chamber from such impurities as welding vapor and allows tightness checks to be made.
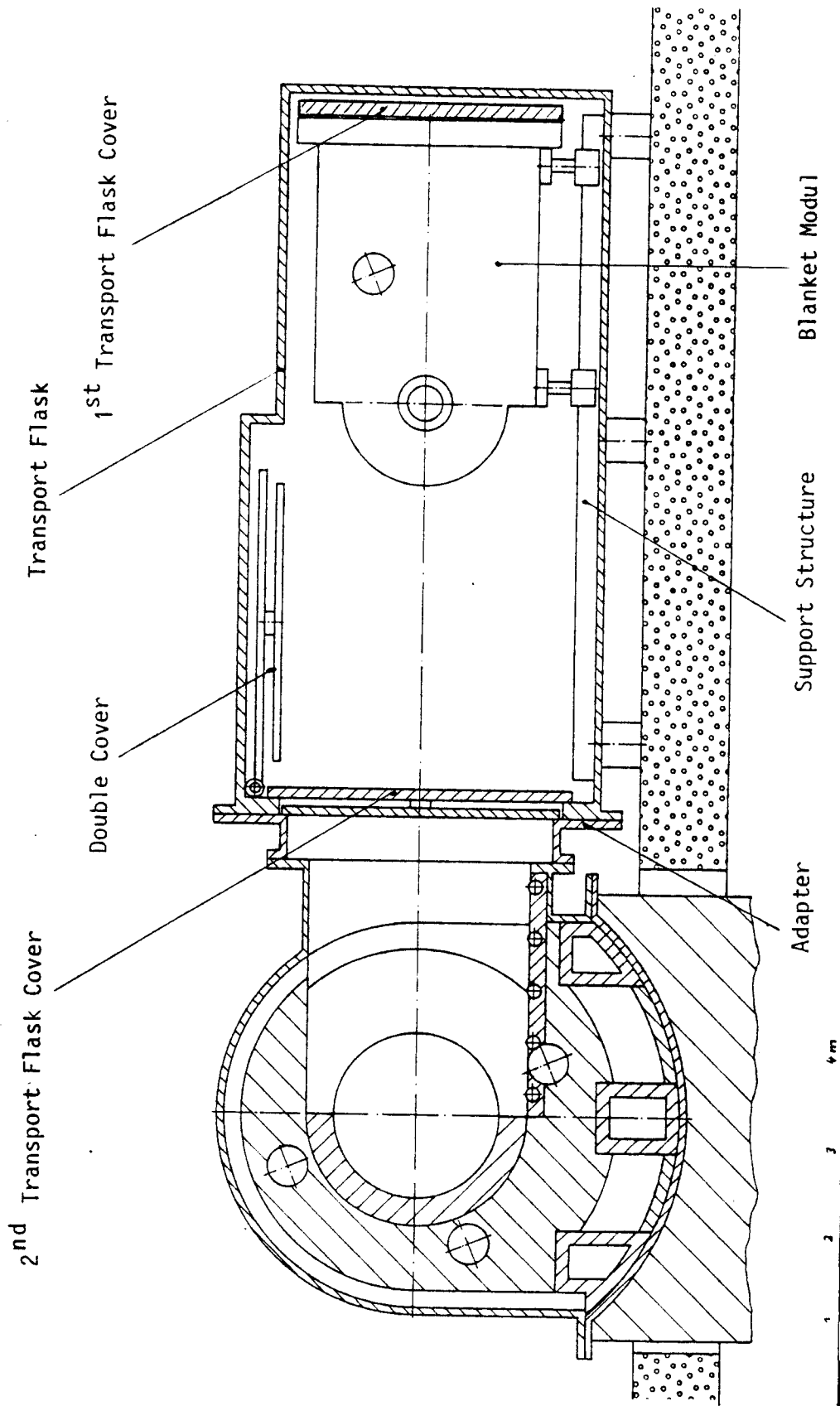
Fig. 2.10-1. Exchange of blanket module.

Transport Flask

1st Transport Flask Cover

2nd Transport Flask Cover

Double Cover

Blanket Modul

Support Structure

Adapter

To break the blanket seal, first the gasket flange is tightened by the flange bolts, and then the welded joint is cut. Next the protective containment is attached to the machine; after unbolting, the blanket can be withdrawn.

Various methods of blanket handling were investigated in previous studies. The use of roller rails permanently installed on the blanket or in the vacuum chamber is critical because of lubricant in the vacuum. One method could be the use of roller chains. To remove the blanket, a pair of chains is introduced through blanket openings normally closed. Then the guide track for the chain mounted at the bottom of the vacuum chamber is mechanically lifted from the outside and the blanket can be withdrawn.

Flasks can be used to transport blankets. Because of the high radiation level of blankets after an operating time of 2 or 3 full power years, the shielding would have to be very thick to permit access of the personnel during transport. Therefore, remotely controlled transport in less shielded transport flasks is preferred. The transport flasks can simultaneously serve as a protective containment. For this purpose, the transport flask is attached directly to the machine (Fig. 2.10-1). Double covers close the machine and the flask; tools and devices for sealing the blanket opening as well as exchange equipment are integrated. Consequently, the transport flask is large, heavy and also quite expensive. If more than one flask is used all transport flasks must be fully equipped for the exchange of blankets. As an alternative, a transfer unit may be set up between the machine and the transport flask. It contains all the exchange equipment and is equipped with double covers at each end. The unit remains attached to the machine during the blanket exchange.

2.11 Costs
2.11.1 Direct Costs
The costing format for TASKA-M follows that established for INTOR. The unit costs and cost algorithms were obtained from INTOR (FEDC-M-81-062), PNL-2987, ORNL and Westinghouse document (WFPS-TN-057) and the recent detailed costing of TDF. A summary of the total direct costs is given in Table 2.11-1.

In addition to the direct costs, certain percentages for indirect costs such as engineering, assembly and contingency have to be included. As an

Table 2.11-1. Summary of Accounts

		$ x 10^6
1.1	Vacuum tank blanket/shield	21.27
1.2	Magnets	58.70
1.3	Plasma heating	91.12

Support Systems

2.1	Electrical	31.00
2.2	Auxiliary cooling	16.36
2.3	Instrumentation and control	25.00
2.4	Fuel handling	22.74
2.5	Maintenance equipment	19.66
2.6	Heat transport	12.45
2.7	Reactor vacuum	16.37
2.8	Radwaste treatment	3.00
2.9	Thermal dumps	0.54
2.10	Reactor support structure	7.50
2.11	Special Materials	2.20
2.12	Miscellaneous plant	10.00
3.0	Buildings	67.27
	Total Direct Costs	405.18

example, in INTOR, these consisted of 45% and 15% of the direct costs for engineering and assembly respectively, and 30% of the direct and indirect costs for contingency.

2.11.2 Operating Costs

The operating costs for TASKA-M consist of operation and maintenance, tritium costs and power costs. Tritium costs are based on the annual burnup and the decay. Power requirements are estimated at 166 MWe during operation and 12 MWe during downtime. The availability for TASKA-M is the same as in INTOR with the final (50% availability) period extended from 15 to 20 years.

The levelized annual operating cost for the 20 years is $42.8 x 10^6. The total tritium costs over the 20 year life of the plant would be 30 million dollars or a levelized cost of ~ 1.5 million dollars per year.
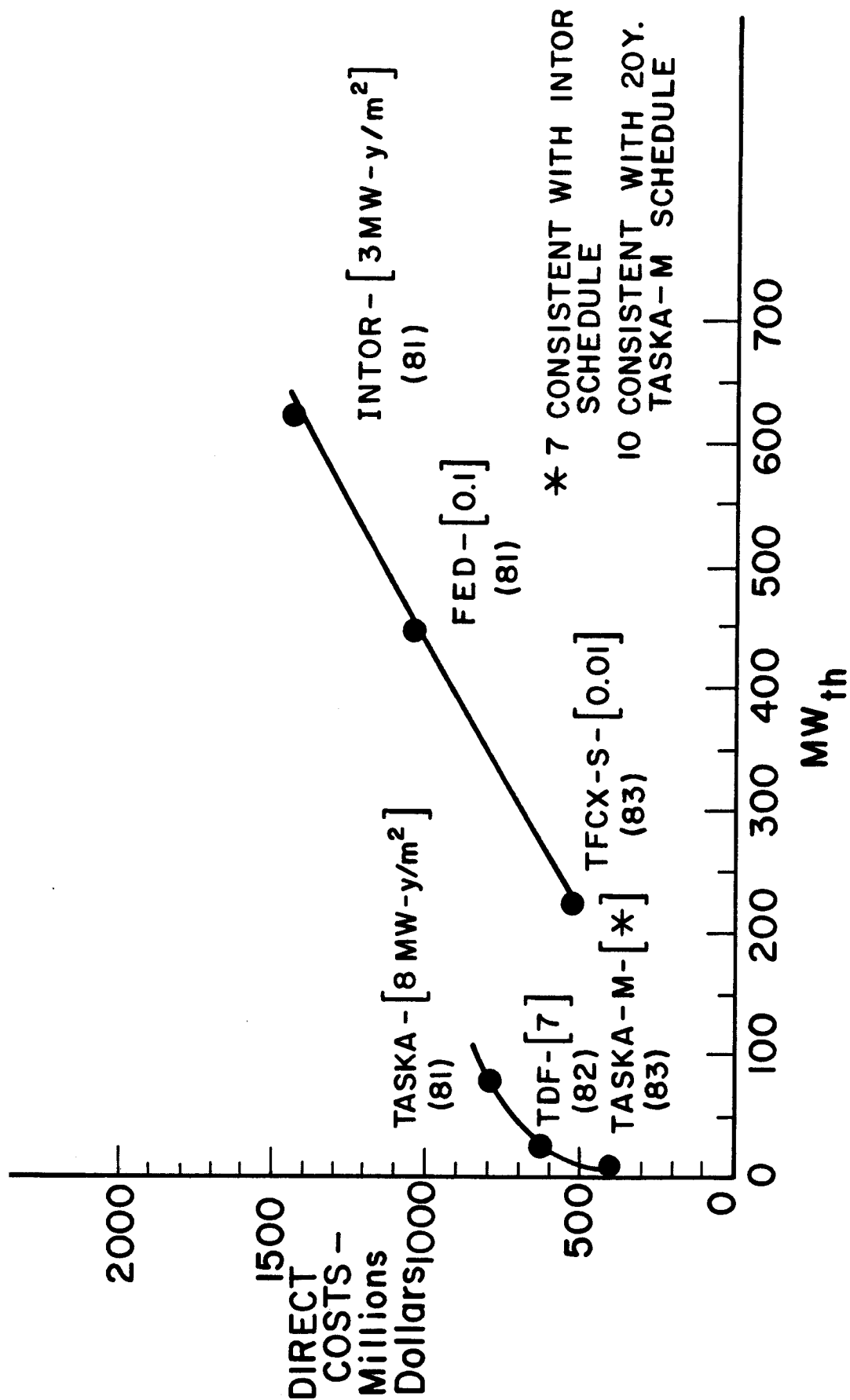
Fig. 2.11-1 Comparison of near term test facilities.

In either case, on the basis of capital costs or operating costs, TASKA-M is well within the capability of any major fusion research program or it could be built and/or operated as part of an international collaborative effort.

2.11.3 Comparison to Other Test Facilities

A final comparison of TASKA-M can be made to other recent test reactor proposals. Figure 2.11-1 graphically displays the quoted direct costs of 3 tokamak test facilities (INTOR, FED, and TFCX-S) and 3 tandem mirror test facilities (TASKA, TDF and TASKA-M). Also quoted on the figure is the year the cost estimates were made (1981-1983) and the cumulative maximum neutron fluence to the test modules in $MW-y/m^2$ (0.01-10). It can be seen that the tandem mirrors and tokamaks separate into two categories. Progressing from TFCX-S at 230 MW and 530 M$ one notes that only 0.01 $MW-y/m^2$ of neutron fluence is expected over the lifetime of the device. The FED device increased the neutron exposure by a factor of 10 to 0.1 $MW-y/m^2$ but the direct cost in 1981 $ exceeded 1 billion dollars. To get a respectable neutron fluence (3 $MW-y/m^2$) the INTOR device direct cost exceeded 1.4 billion dollars.

On the other hand, Fig. 2.11-1 demonstrates that tandem mirror facilities could achieve rather high neutron fluence levels (7-10 $MW-y/m^2$) at direct costs of 400-800 million dollars. The main difference between TASKA-M and TASKA is the inclusion of the thermal barrier. While such a design is more reactor relevant, one must examine whether or not it is worth the extra 400 million dollars in the test phase of the fusion program. The final point of note in Fig. 2.11-1 is that the total DT power of the tandem mirror can be made quite small, reducing the problems of handling tritium, thermal power and large reactor components. It also relieves the necessity of breeding tritium for continued plant operation.

References for Chapter 2

1. T. Batzer et al., Lawrence Livermore National Laboratory Report UCRL-51617, 1974.

2. B. Badger et al., "TETR - A Tokamak Engineering Test Reactor," University of Wisconsin Fusion Engineering Program Report UWFDM-191, 1977.

3. W.M. Stacey et al., "INTOR," Georgia Institute of Technology Report No. USA-INTOR/81-1, 1981.

4. B. Badger et al., "TASKA - A Tandem Mirror Fusion Engineering Facility," Karlsruhe Nuclear Laboratory Report 3311, 1982.

5. K.I. Thomassen and J.N. Doggett, J. Fusion Energy 3, 109 (1983).

6. B.G. Logan et al., "Mirror Advanced Reactor Study - Interim Design Report," Lawrence Livermore National Laboratory Report UCRL-53333, 1983.

7. P.N. Haubenreich et al., 7th Symp. on Engr. Prob. of Fusion Research, IEEE Pub. No. CH1441-5/79/0000-1140, 1979.

8. T.C. Simonen et al., Phys. Rev. Lett. 50, 1668 (1983).

9. J. Kesner et al., Nuclear Fusion 22, 549 (1982).

10. R. Haange, "Design of Calorimeter and Ion Dump for JET Neutral Injection Beam Line," Proc. 9th Symposium on Engineering Problems of Fusion Research, Chicago, October 1981, IEEE 81CH1715-2 NPS, p. 1352.

3. PLASMA PHYSICS

3.1 Introduction

The basic configuration of TASKA-M consists of an axisymmetric central cell and two yin-yang end cells, as shown in Fig. 3.1-1. The central cell contains hot, magnetically trapped deuterium and tritium ions which react via fusion to produce 14.1 MeV neutrons and 3.5 MeV alpha particles. The hot D and T ion population in the central cell is sustained by injection of energetic neutral beams which are trapped by impact ionization and charge exchange. These neutral beams are injected at an angle to the magnetic field in order to produce a so-called "sloshing ion plasma"; the hot ion density peaks away from the central cell midplane. This produces an electrostatic potential well at the central cell midplane; this potential well traps warm ions which are provided by a low energy neutral beam. The warm ions fill the loss-cone of the hot ions and thereby provide microstability of the central cell plasma.

In order to provide a sufficiently deep electrostatic well and to minimize the effect of electron drag on the hot ions, the electrons are heated by RF power. Rather than use electron cyclotron resonance heating (ECRH) which would require very high frequency gyrotrons because of the high magnetic field strength, we propose to heat the electrons using Landau damping of ion cyclotron waves. These waves are generated by antennas which are driven with RF power at frequencies in the ion cyclotron range. Electron heating is discussed in Chapter 6.

The yin-yang end cells have the sole purpose of providing plasma in a magnetic field with good curvature and thereby provide MHD stability for the entire plasma. Consequently they are called "anchors." Unlike a usual tandem mirror, they do not provide any plugging of the axial loss from the central cell. Since the plasma in the anchor cells is also mirror-confined, the neutral beams sustaining this plasma are also injected at an angle to produce a sloshing-ion plasma and electrostatic well. Trapping of warm plasma in this electrostatic well fills in the loss-cone distribution of the hot ions and provides for microstability of the anchor plasma. Good connection between the central cell and anchor plasma is required in order to assure both MHD stability and trapped particle stability of TASKA-M. This requires feeding gas into the transition region between the central cell and anchor in order to maintain a sufficient plasma density there. This plasma is electrostatically

Fig. 3.1-1.   The TASKA-M configuration and the magnetic and potential profiles.
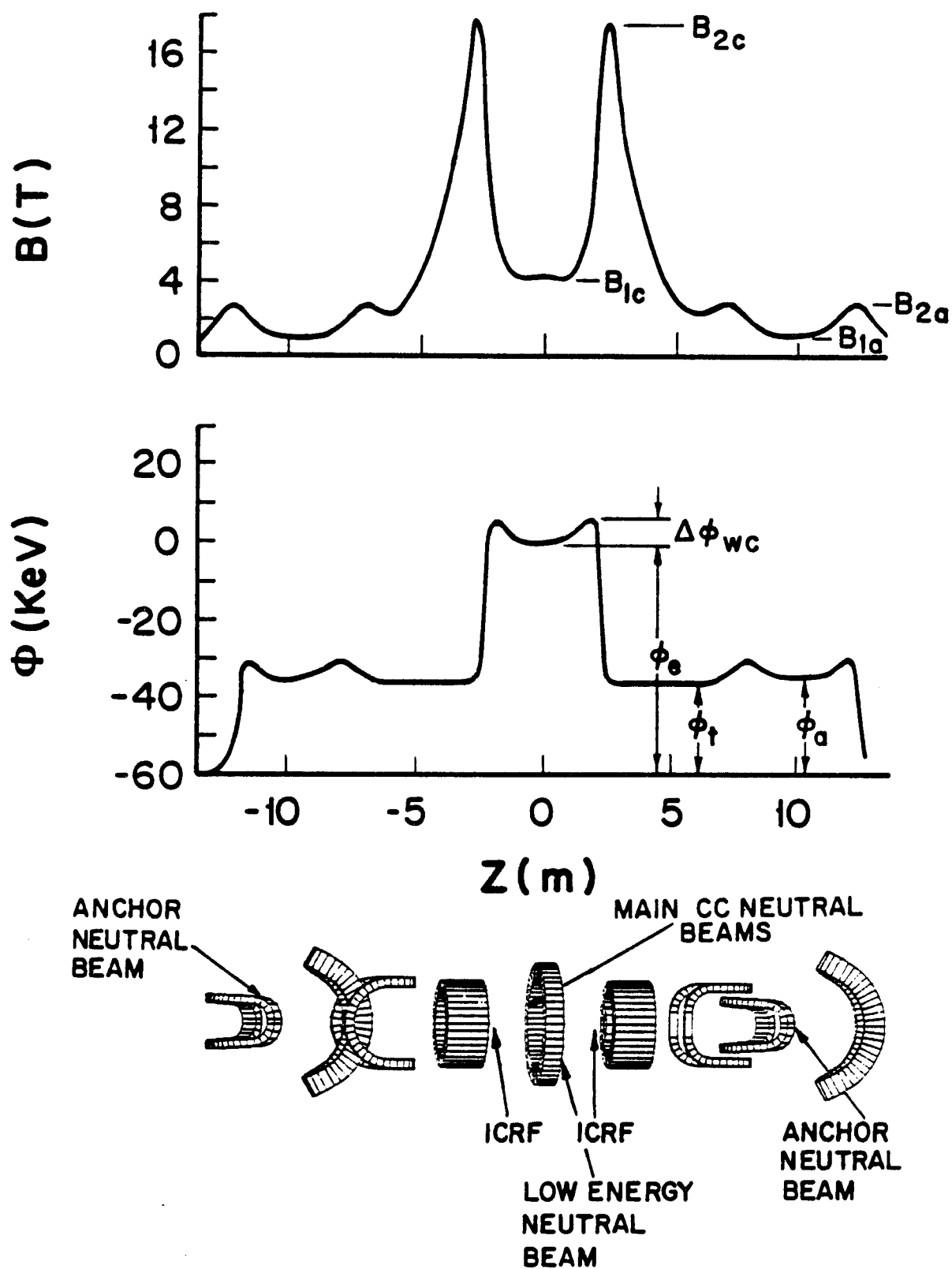
contained by the anchor; some of it can scatter into the electrostatic well in the anchor. This is the source of the warm plasma required to maintain micro-stability of the anchor plasma.

The basic configuration of TASKA-M therefore consists of three separate mirror-confined plasmas; a central cell and two anchors. Unlike usual tandem mirrors, electrostatic confinement of the dominant plasma components is not utilized. An electrostatic potential is used only to trap a warm plasma which is roughly 10% of the total density. The plasma in each cell is separately microstable, but the connection of the three plasmas is required for overall MHD stability. Electron heating in the central cell is assumed to heat all electrons because of good electron thermal transport along the magnetic field. The central cell plasma is 50:50 deuterium-tritium and therefore provides the neutrons for the test modules; the anchor cell plasmas are essentially 100% deuterium and therefore generate few neutrons. This reduces the shielding required for the yin-yang magnets and transition magnet.

The TASKA-M configuration makes considerable use of sloshing-ions to generate electrostatic wells and trap warm plasma for microstability. A sloshing-ion plasma has been produced in TMX-Upgrade[1] and the associated improved microstability has been observed. Direct electron heating by Landau damping of ion cyclotron waves has not been attempted, although the effect is well-founded in theory. Experimental observations of electron heating by RF in the TFR[2] tokamak have been interpreted as due to Landau damping. Backup options for electron heating are ECRH in the transition region or electron Landau damping of lower hybrid waves.

Finally, it should be noted that the TASKA-M configuration does not contain a thermal barrier. The reason for this is two-fold. First, a thermal barrier has not yet been produced (as of the writing of this report) and it was our desire to keep the physics as simple as possible and to minimize the extrapolation from the present data base. Second, neutral beam pumping of the thermal barrier in TASKA[3] presented considerable complications and expense. It was our objective in TASKA-M to minimize the cost. Recently, ideas con-cerning drift pumping[4] of thermal barriers have emerged. These, however, are untested experimentally and are not completely evaluated from the point of view of theory. Consequently, to incorporate a thermal barrier based on drift orbit pumping would be inconsistent with our physics philosophy.

In the following sections of this chapter we present the detailed physics analysis of TASKA-M. These include the power balance model (Section 3.2) and the design point chosen using this model (Section 3.3), Fokker-Planck calculations of the sloshing-ion plasma (Section 3.4), MHD stability (Section 3.5), central cell microstability (Section 3.6), trapped particle stability (Section 3.7), and the halo plasma (Section 3.8) surrounding the hot plasma. Finally, in Section 3.9, we present some work on the startup of the TASKA-M plasma.

References for Section 3.1

1. T.J. Orzechowski, S.L. Allen, J.H. Foote, et al., Phys. Fluids $\underline{26}$, 2335 (1983).

2. Equipe TFR, "Dominant Role of Wave Conversion Mechanism in TFR Ion Cyclotron Heating Experiments," 9th IAEA Conf. on Plasma Physics and Controlled Nuclear Fusion Research, 1-8 Sept. 1982, Baltimore, MD, Vol. II, p. 17.

3. B. Badger et al., "TASKA - A Tandem Mirror Fusion Engineering Test Facility," Kernforschungszentrum Karlsruhe, Report KfK 3311 and University of Wisconsin UWFDM-500 (1982).

4. B.G. Logan, C.D. Henning, G.A. Carlson, et al., "Mirror Advanced Reactor Study - Interim Design Report," Lawrence Livermore National Laboratory Report UCRL-53333 (1983).

3.2 Power Balance of TASKA-M

The basic performance of TASKA-M has been calculated using a zero-dimensional model for the power and particle balance of the plasma. It treats two distinct regions of the machine (central cell and anchor) and includes power and particle flows required to sustain the various hot ion, warm ion, and electron species. A zero-dimensional model was chosen for this study since, in addition to being tractable, it permits quick solution of the system of equations and is therefore well-suited to design studies. This approach requires some approximations; these will be discussed where appropriate. All formulas are written in SI units except certain selected formulas which are written in plasma engineering units (cm, keV, tesla, s, except that power is measured in MW and neutron wall loading in MW/m^2). These are noted where they occur.

3.2.1 General Considerations

There is assumed to be one electron population with density n_{ec} at the midplane of the central cell and density n_{eA} at the midplane of the anchor. The electron temperature, T_e, is assumed to be the same in both regions. The four ion species are: (1) hot, magnetically trapped in the central cell (n_{Hc}, E_{Hc}); (2) warm, electrostatically trapped in the central cell (n_{wc}, E_{wc}); (3) hot, magnetically trapped in the anchor (n_{HA}, E_{HA}); and (4) warm, electrostatically trapped in the anchor (n_{wA}, E_{wA}). Here E refers to the mean ion energy and not the temperature, and n is the corresponding density.

The radial density profile of each species is assumed to be

$$n(r) = n(0)\left(1 - (r/a)^m\right) \qquad (3.2-1)$$

where $n(0)$ is the on-axis density and a is the plasma radius. The profile exponent, m, is taken to be three in this work. The mean ion energy and electron temperature is assumed to be independent of radius up to the plasma edge. These profiles are assumptions which need to be checked by either experiment or detailed radial beam deposition and plasma transport calculations. They are qualitatively in agreement with experiments so far. Consequently the pressure profile, $p(r)$, is the same as the density profile and the fusion power density varies only as $n^2(r)$. Finite β corrections to the magnetic field strength are calculated using the "long-thin" approximation:

$$\frac{B^2(r)}{2\mu_0} + p(r) = \text{constant} .$$

Because of the radial variation of $B(r)$ and the axial variation of $\beta = p/(B^2/2\mu_0)$, the axial mirror ratio is a function of radius. In evaluating the confinement time of mirror-trapped ions, the mirror ratio calculated using the radial-averaged β is used. The radial-averaged β is given by

$$\langle\beta\rangle = \frac{4\pi\mu_0 T \int_0^a n(r)\, r dr}{\pi a^2 B^2} = \frac{\beta(0)m}{m + 2} \tag{3.2-2}$$

where m is the profile exponent and $\beta(0)$ is the on-axis β.

A quantity appearing in many of the equations is the volume average of the square of the plasma density. We assume the density $n(r,z)$ can be written as a separable function of r and z:

$$n(r,z) = n(0,0)(1 - (r/a)^m)\, f(z) . \tag{3.2-3}$$

Thus $\quad \int n^2\, dV = n^2(0,0) \int_0^a 2\pi r[1 - (\tfrac{r}{a})^m]^2\, dr \int dz\, f^2(z) .$

We define the effective volume, V_p, such that

$$\int n^2\, dV = n^2(0,0)\, V_p . \tag{3.2-4}$$

Thus $\quad V_p = \pi a^2 \dfrac{m^2}{(m + 1)(m + 2)} \int dz\, f^2(z) . \tag{3.2-5}$

The axial density profile is normalized such that $f(0) = 1$. We can also define an effective plasma length, L_p, by

$$L_p = \int dz\, f^2(z) . \tag{3.2-6}$$

For a sloshing ion plasma, $f(z)$ rises above unity at the density peaks. In this case L_p can be longer than the physical length of the plasma. In the following sections, we drop the argument $(0,0)$ and let n represent the on-axis density at the midplane.

3.2.2 Central Cell Ions

Hot ions in the central cell are produced by ionization and trapping of the high energy neutral beams injected into the central cell. A low energy beam is also injected in order to produce a population of warm ions filling the loss-cone of the hot ions and thereby providing microstability. Both neutral beams interact with both the hot and warm components of the plasma by charge exchange, as well as by ion and electron impact ionization. Consequently, hot and warm charge exchange neutrals are generated; these have a finite probability of escaping from the plasma. Pitch angle scattering and energy diffusion also cause hot and warm ions to become untrapped and escape axially.

Let n_{Hb} and n_{wb} be the density of hot and warm beam neutrals, respectively, in the plasma. Also, let V_b be the volume in which the beams interact with the plasma. Then, particle conservation on the hot ion component gives

$$\frac{n_{Hc}^2 V_{Hc}}{(n\tau)_{Hc}} = n_{ec} n_{Hb} V_b^H (<\sigma v>_e + <\sigma v>_i^H) + n_{wc} n_{Hb} V_b^H <\sigma v>_{cx}^H$$

$$\quad (3.2-7)$$

$$+ \; n_{Hc} n_{Hb} V_b^H <\sigma v>_{cx}^H (1 - f_e^H) - n_{Hc} n_{wb} V_b^W <\sigma v>_{cx}^H f_e^H \; .$$

The left side is the axial loss of hot ions; $(n\tau)_{Hc}$ is the confinement product of the hot ions and is discussed later. The first term on the right side is the source due to electron and ion impact ionization of the high energy neutral beam. The second term is the source of hot ions due to charge exchange of the high energy beam with the warm plasma. The third term is the hot ion source due to charge exchange of the high energy beam with the hot ions; a fraction f_e^H of the hot charge exchange neutrals escapes the plasma and a fraction $(1 - f_e^H)$ is re-ionized before escaping. The fourth term is the loss of hot ions because of charge exchange of hot ions with the warm beam injected into the plasma. In Eq. (3.2-7) and elsewhere, $<\sigma v>_e$, $<\sigma v>_i$, $<\sigma v>_{cx}$ are the rate coefficients for electron and ion impact ionization, and charge exchange, respectively. The superscript H or w denotes the mean energy at which $<\sigma v>_i$ and $<\sigma v>_{cx}$ are evaluated.

Particle conservation for the warm ion component gives

$$\frac{n_{wc}^2 V_{wc}}{(n\tau)_{wc}} + \frac{n_{Hc} n_{wc}}{(n\tau)_{wHc}} V_{wc} = n_{ec} n_{wb} V_b^W \langle\sigma v\rangle_e + n_{wc} n_{wb} V_b^W \langle\sigma v\rangle_i^W + n_{Hc} n_{wb} V_b^W \langle\sigma v\rangle_i^H$$

(3.2-8)

$$+ n_{wc} n_{wb} V_b^W \langle\sigma v\rangle_{cx}^W (1 - f_e^W) + n_{Hc} n_{wb} V_b^W \langle\sigma v\rangle_{cx}^H - n_{wc} n_{Hb} \langle\sigma v\rangle_{cx}^H V_b^H f_e^W \ .$$

The first term on the left represents the loss of warm ions due to Coulomb collisions among themselves. Since these ions are trapped in an electrostatic well, the confinement product, $(n\tau)_{wc}$, is calculated using the Pastukhov formula; this is discussed in a later section. The second term on the left is the loss of warm ions due to Coulomb collisions of warm ions with hot ions; $(n\tau)_{wHc}$ is the appropriate confinement product for this process. The first, second, and third terms on the right are the sources due to electron, warm ion, and hot ion impact ionization of the warm neutral beam, respectively. The fourth term is the source due to charge exchange between the warm neutral beam and the warm plasma; a fraction f_e^W of the warm charge exchange neutrals escapes before re-ionization. The fifth term is the warm ion source due to charge exchange of the warm neutral beam with the hot ions. The last term is the loss which occurs when warm plasma charge exchanges with the high energy neutral beam.

The neutral atom densities, n_{Hb} and n_{wb}, in the beams are obtained from the trapping rates of the neutral beams. Let I_H and I_w be the injected currents of the high and low energy neutral beams, respectively, and f_t^H and f_t^W be the corresponding fraction of the incident currents that are trapped (i.e., interact with the plasma). Then

$$I_H f_t^H = e n_{ec} n_{Hb} V_b^H \left[\langle\sigma v\rangle_e + \langle\sigma v\rangle_i^H + \langle\sigma v\rangle_{cx}^H \right]$$

(3.2-9)

$$I_w f_t^W = e n_{wb} V_b^W \left[n_{ec} \langle\sigma v\rangle_e + n_{wc} \langle\sigma v\rangle_i^W + n_{wc} \langle\sigma v\rangle_{cx}^W \right.$$

(3.2-10)

$$\left. + n_{Hc} \langle\sigma v\rangle_i^H + n_{Hc} \langle\sigma v\rangle_{cx}^H \right] \ .$$

Using Eqs. 3.2-9 and 3.2-10, we can eliminate $n_{Hb}V_b$ and $n_{wb}V_b$ from Eqs. 3.2-7 and 3.2-8. This gives us two equations for the injection currents I_H and I_W required to sustain the plasma. These equations can be solved to yield

$$I_H f_t^H = eD_H \left(\frac{a_{22}b_1 - a_{12}b_2}{\det a} \right) \tag{3.2-11}$$

$$I_w f_t^W = eD_W \left(\frac{a_{11}b_2 - a_{21}b_1}{\det a} \right) \tag{3.2-12}$$

where the elements of the matrix a are

$$a_{11} = n_{ec}\left(\langle\sigma v\rangle_e + \langle\sigma v\rangle_i^H\right) + n_{wc}\langle\sigma v\rangle_{cx}^H + n_{Hc}\langle\sigma v\rangle_{cx}^H\left(1 - f_e^H\right) \tag{3.2-13}$$

$$a_{12} = -n_{Hc}\langle\sigma v\rangle_{cx}^H f_e^H \tag{3.2-14}$$

$$a_{21} = -n_{wc}\langle\sigma v\rangle_{cx}^H f_e^W \tag{3.2-15}$$

$$a_{22} = n_{ec}\langle\sigma v\rangle_e + n_{wc}\langle\sigma v\rangle_i^W + n_{Hc}\langle\sigma v\rangle_i^H + n_{wc}\langle\sigma v\rangle_{cx}^W\left(1 - f_e^W\right)$$
$$\tag{3.2-16}$$
$$+ n_{Hc}\langle\sigma v\rangle_{cx}^H \; .$$

The elements of the vector b are

$$b_1 = \frac{n_{Hc}^2 V_{Hc}}{(n\tau)_{Hc}} \tag{3.2-17}$$

$$b_2 = \frac{n_{wc}^2 V_{wc}}{(n\tau)_{wc}} + \frac{n_{Hc} n_{wc} V_{wc}}{(n\tau)_{wHc}} \; . \tag{3.2-18}$$

The coefficients D_H and D_W are

$$D_H = n_{ec}\left(\langle\sigma v\rangle_e + \langle\sigma v\rangle_{cx}^H + \langle\sigma v\rangle_{cx}^H\right) \tag{3.2-19}$$

3.2-5

$$D_W = n_{ec}\langle\sigma v\rangle_e + n_{we}\left(\langle\sigma v\rangle_{cx}^W + \langle\sigma v\rangle_i^W\right) + n_{Hc}\left(\langle\sigma v\rangle_{cx}^H + \langle\sigma v\rangle_i^H\right) . \qquad (3.2\text{-}20)$$

Equations 3.2-11 to 3.2-20 are sufficient to determine the required currents of the high and low energy neutral beams.

In addition to the various particle source and loss terms, we have to consider energy sources and sinks as well. A power balance on the hot ion component gives

$$\frac{1}{4} n_{Hc}^2 \langle\sigma v\rangle_f \ f_i Q_\alpha V_{Hc} + n_{ec}n_{Hb}V_b E_{Hb}\left(\langle\sigma v\rangle_e + \langle\sigma v\rangle_i^H + \langle\sigma v\rangle_{cx}^H\right)$$

$$= \frac{n_{Hc}^2 V_{Hc} E_{out}}{(n\tau)_{Hc}} + n_{Hc}n_{Hb}V_b\langle\sigma v\rangle_{cx}^H f_e^H E_{Hc} + n_{Hc}n_{wb}V_b\langle\sigma v\rangle_{cx}^H f_e^H E_{Hc} \qquad (3.2\text{-}21)$$

$$+ \ n_{Hc}\nu_{eH}^C V_{Hc}\left(E_{Hc} - 1.5 \ T_e\right) + n_{Hc}\nu_{Hw}^C V_{wc}\left(E_{Hc} - E_{wc}\right) ,$$

The first term is the alpha power deposited in the hot ions; Q_α is the energy of the fusion born alpha particles and f_i is the fraction of this energy going to the ions, $f_i = 1 - 0.91 \exp(-T_e/102)$, where T_e is in keV. The second term on the left is the power deposited by the high energy beam in the hot ions due to ionization and charge exchange of the beam. The energy E_{Hb} is not the full energy component, but a mean energy which takes into account the current in the one-half and one-third energy components of the beam. The first term on the right is the power carried by ions escaping axially; they leave with mean energy E_{out}. The second and third terms represent the loss due to charge exchange of the hot plasma with the hot and warm neutral beams. The charge exchange neutrals are assumed to have the mean hot plasma energy, E_{Hc}, and an escape probability f_e^H. The fourth term is the cooling of the hot plasma by electron drag and the fifth term is the cooling by the drag of the hot ion component on the warm ion component.

A power balance on the warm plasma yields

$$n_{ec} n_{wb} V_b E_{wb} \langle \sigma v \rangle_e + n_{wc} n_{wb} V_b E_{wb} (\langle \sigma v \rangle_i^W + \langle \sigma v \rangle_{cx}^W) + n_{Hc} n_{wb} V_b E_{wb} (\langle \sigma v \rangle_i^H + \langle \sigma v \rangle_{cx}^H)$$

$$= n_{wc} n_{Hb} V_b E_{wc} \langle \sigma v \rangle_{cx}^H f_e^W + n_{wc} n_{wb} V_b E_{wc} \langle \sigma v \rangle_{cx}^W f_e^W \qquad (3.2\text{-}22)$$

$$+ \left(\frac{n_{wc}^2}{(n\tau)_{wc}} + \frac{n_{wc} n_{Hc}}{(n\tau)_{wHc}} \right) V_{wc} \left(\Delta\phi_{wc} + \frac{2}{3} E_{wc} \right) - n_{wc} \nu_{ew}^C (1.5 \, T_e - E_{wc}) \, V_{wc}$$

$$- n_{wc} n_{Hc} \nu_{Hw}^C V_{wc} (E_{Hc} - E_{wc}) \, .$$

The terms on the left side of Eq. 3.2-22 represent the power deposited in the warm ions by the low energy neutral beam; deposition occurs by ionization and charge exchange processes with both the warm and hot plasma components. The first two terms on the right are the power losses due to the escape of warm charge exchange neutrals; these are created by charge exchange of the warm plasma with the high energy and low energy neutral beams, respectively. The third term is the energy carried out by warm ions upscattering in energy and escaping the confining potential well. $\Delta\phi_{wc}$ is the potential confining the warm ions. The fourth and fifth terms represent the heating of the warm plasma by Coulomb collisions with electrons and hot ions, respectively.

The neutral beam intensities, $n_{Hb} V_b$ and $n_{wb} V_b$, in Eqs. 3.2-21 and 3.2-22 can be eliminated using Eq. 3.2-9 and 3.2-10. The resulting equations can then be used to solve for either the mean ion energies, E_{Hc} or E_{wc} for given neutral beam injection energies, or solved for the required injection energies to sustain given mean ion energies.

The $(n\tau)_{Hc}$ product of the hot sloshing ion plasma component is calculated using the Logan-Rensink model[1] but with the coefficients modified by fitting the $(n\tau)_{Hc}$ and mean ion energy, E_{Hc}, to Fokker-Planck code calculations for the sloshing ions for parameters in the range expected for TASKA-M. Thus, we write

$$(n\tau)_{Hc} = \left[\frac{\ln \Lambda_i (m_D/m_i)^{1/2}}{C_1 E_{inj}^{3/2} \log_{10} R_{eff}} + \frac{\ln \Lambda_{ei} (m_H/m_i)}{10^{13} T_e^{1.5} \ln (E_{inj}/E_{out})} \left(1 - \frac{3T_e}{2E_{Hc}} \right) \right]^{-1} \qquad (3.2\text{-}23)$$

where E_{inj} is the full energy component of the injected beam, $\ln \Lambda_i$ and $\ln \Lambda_{ei}$ are the Coulomb logarithms for ion and electron scattering, respectively, m_H and m_D are the proton and deuteron masses, respectively, m_i is the ion mass, and C_1 is a coefficient to be determined. Equation 3.2-23 is written in plasma engineering units. R_{eff} in Eq. 3.2-23 is the effective mirror ratio and is defined as

$$R_{eff} = \frac{R_m \sin^2\theta_{inj}}{1 + (\phi_e - \phi_t)/E_{inj}} \qquad (3.2-24)$$

where R_m is the beta-corrected mirror ratio

$$R_m = \frac{B_2}{B_1 \sqrt{1 - \langle\beta_c\rangle}} \; ,$$

θ_{inj} is the injection angle, ϕ_e is the potential at the central cell midplane, and ϕ_t is the potential at the mirror throat. We define a cutoff energy

$$E_c = \frac{\phi_e - \phi_t}{R_m \sin^2\theta_{inj} - 1} \; . \qquad (3.2-25)$$

Then the mean ion escape energy is given by

$$E_{out} = \frac{\left(E_{inj} + E_c \frac{\tau_i}{\tau_d}\right)}{\left(1 + \frac{\tau_i}{\tau_d}\right)} \qquad (3.2-26)$$

where τ_i/τ_d, the ratio of the ion collision time to the electron drag time, is given by

$$\frac{\tau_i}{\tau_d} = C_2 \left(\frac{E_{inj}}{T_e}\right)^{3/2} \frac{\log_{10}(R_{eff})}{\ln(E_{inj}/E_{out})} \left(\frac{\ln \Lambda_{ei}}{\ln \Lambda_i}\right)\left(\frac{m_D}{m_i}\right)^{1/2} \; . \qquad (3.2-27)$$

C_2 is a second adjustable constant. The coefficients C_1 and C_2 are obtained by fitting the $(n\tau)_{Hc}$ confinement product and mean energy E_{Hc} to Fokker-Planck results, as described in Section 3.4. The values chosen are

$$C_1 = 1.4 \times 10^{12} \; s/cm^3/(keV)^{3/2}$$

and $\qquad C_2 = 0.055$.

The warm ion confinement product $(n\tau)_{wc}$ is simply the Pastukhov[2] formula as corrected and expanded by Cohen[3]

$$(n\tau)_{wc} = \frac{3.51 \times 10^{11} \ E_{wc}^{3/2}}{\ln \Lambda_i} \ (\frac{m_i}{m_H})^{1/2} \ \frac{\Delta\phi_c}{E_{wc}} \ \exp (\frac{\Delta\phi_c}{E_{wc}}) \ \frac{G(R_w/2)}{I(E_{wc}/\Delta\phi_c)} \qquad (3.2\text{-}28)$$

in plasma engineering units, where

$$G(x) = \frac{\sqrt{\pi}}{4} \ (1 + \frac{1}{x})^{1/2} \ \ln \ [\frac{(1 + \frac{1}{x})^{1/2} + 1}{(1 + \frac{1}{x})^{1/2} - 1}] \ , \qquad (3.2\text{-}29)$$

$$I(x) = \frac{1 + \frac{x}{2}}{1 + \frac{x^2}{4}} \qquad (3.2\text{-}30)$$

and R_w is the mirror ratio between the midplane of the central cell and the turning point of the sloshing ions,

$$R_w = \frac{1}{\sin^2\theta_{inj}} \ . \qquad (3.2\text{-}31)$$

The confinement product $(n\tau)_{wHc}$ is the effect of Coulomb collisions between the warm ions and the hot ions on the loss rate of the warm ions. For this $n\tau$ we use

$$(n\tau)_{wHc} = (n\tau)_{wc} \ (\frac{E_{Hc}}{E_{wc}})^{3/2} \qquad (3.2\text{-}32)$$

since the relative speed between the warm and hot ions is determined primarily by the hot ion energy.

The rate of cooling of the hot ions by collisional exchange of energy with the electrons is determined by the coefficient ν_{eH}^c, which in plasma engineering units is given by

$$\nu_{eH}^c = \frac{1.03 \times 10^{-13} \ n_{ec} \ \ln \Lambda_{ei}}{T_e^{1.5}} \ (\frac{m_H}{m_i}) \ . \qquad (3.2\text{-}33)$$

The same expression is also used for ν_{ew}^c, the collisional transfer between the electrons and warm ions. For the energy transfer between hot and warm ions, we use

$$\nu_{Hw}^C = \frac{4.4 \times 10^{-12} \, n_{wc} \, \ln \Lambda_i}{(2 \frac{m_i}{m_H})(E_{Hc} \frac{m_H}{m_i} + \frac{E_{Hc}}{2})^{1.5}} \, . \tag{3.2-34}$$

The warm plasma is taken to be pure deuterium, whereas the hot plasma is a 50:50 mixture of deuterium and tritium. Thus we take $m_i/m_H = 2.5$.

3.2.3 Hot and Warm Ions in the Anchor

The same considerations apply to the ions in the anchor as to the central cell ions. The one exception to this is the ion population in the transition region; these ions are electrostatically contained by the anchor potential relative to the transition region. Upon being detrapped by Coulomb collisions they pass through the anchor with low velocity on their way out of the machine. Since they "dribble" through the anchor, they have a reasonable probability of being trapped in the anchor; this trapping process provides a source of warm plasma for the anchor. For this reason, we do not use a low energy neutral beam in the anchor to provide warm plasma. The only beam injected into the anchor is the high energy sloshing ion beam. With this change, the analysis in Section 3.2.2 for the central cell ions also applies to the anchor ions. The same basic formulae are used for the various $n\tau$'s and E_{out} in the particle and energy conservation equations.

3.2.4 Electrostatic Potential

Since the electrons are taken to be Maxwellian along magnetic field lines, the potential differences between various points in the plasma is obtained by the Boltzmann relation

$$\phi_2 - \phi_1 = T_e \ln (n_2/n_1)$$

where ϕ and T_e are measured in the same units. This relationship is used to determine the potential profile in the central cell and anchor assuming a starting value, ϕ_e, for the potential at the midplane of the central cell relative to the end wall; we take the end wall potential to be zero here, al-

though its value is arbitrary. The potential ϕ_e is found by assuming ambipolarity of the particle fluxes to the end walls. Since only the net flux and not the axial flux is required to be ambipolar, this assumption is based on another assumption -- either the radial particle loss is separately ambipolar or that it is negligible compared with the axial loss. In TASKA-M, most of the particles are contained in the central cell, which is axisymmetric. Hence, we do not expect an enhanced ion radial loss due to non-axisymmetric effects for these particles. Furthermore, the ion distribution is sloshing and therefore poorly confined against pitch angle scattering leading to axial loss. Consequently we expect the axial loss to dominate over the radial loss. The MHD anchor is a yin-yang configuration and therefore is not axisymmetric, but has a quadrupole component. The drift surfaces of trapped ions, however, coincide with the flux surfaces, at least to lowest order. Consequently, a large radial loss is not anticipated. The axial loss should dominate because the ions are only mirror-confined in a modest mirror ratio and have a sloshing distribution.

For the above reasons, we consider only axial losses in the ambipolarity condition determining the potential ϕ_e. Equating the electron current to the ion current at the end wall gives the equation

$$\frac{n_{Hc}^2 V_{Hc}}{(n\tau)_{Hc}} + \left(\frac{n_{wc}^2}{(n\tau)_{wc}} + \frac{n_{Hc}n_{wc}}{(n\tau)_{wHc}}\right) V_{wc} + 2\frac{n_{HA}^2 V_{HA}}{(n\tau)_{HA}} + 2\left(\frac{n_{wA}^2}{(n\tau)_{wA}} + \frac{n_{wA}n_{HA}}{(n\tau)_{wHA}}\right) V_{wA}$$

$$= \frac{\int n_e^2 \, dV}{(n\tau)_e}$$

(3.2-35)

where the integral is over the entire plasma. We take

$$\int n_e^2 \, dV = n_{Hc}^2 V_{Hc} + 2n_{HA}^2 V_{HA} + n_{wc}(n_{wc} + 2n_{Hc})V_{wc}$$

$$+ 2n_{wA}(n_{wA} + 2n_{HA})V_{HA} \; .$$

(3.2-36)

For the electron confinement product $(n\tau)_e$ we use the Pastukhov formula,

$$(n\tau)_e = \frac{4.09 \times 10^9 \, T_e^{3/2}}{\ln \Lambda_e} \left(\frac{\phi_e}{T_e}\right) \exp\left(\frac{\phi_e}{T_e}\right) \frac{G(R_m)}{I(T_e/\phi_e)} \qquad (3.2-37)$$

where R_m is the beta-corrected mirror ratio in the central cell, and G and I are defined in Eqs. 3.2-29 and 3.2-30. Equation 3.2-35 gives us a transcendental equation for ϕ_e. Alpha particles are neglected since their current is small compared with the other currents.

3.2.5 Electron Power Balance

The remaining consideration in the power balance model is the electron power balance. This determines the amount of electron heating, P_E, required to maintain a given electron temperature. This gives the result

$$P_e = \frac{\int n_e^2 \, dV}{(n\tau)_e} (\phi_e + T_e) + P_x - \frac{n_{Hc}^2}{4} V_{Hc} \langle \sigma v \rangle_f Q_\alpha f_e - n_{Hc} \nu_{eH}^C (E_{Hc} - 1.5 \, T_e) V_{Hc}$$

$$- 2 n_{HA} \nu_{eH}^A (E_{HA} - 1.5 \, T_e) V_{HA} - n_{wc} \nu_{eH}^C (E_{wc} - 1.5 \, T_e) V_{wc} \qquad (3.2-38)$$

$$- n_{wA} \nu_{eH}^A (E_{wA} - 1.5 \, T_e) V_{wA} \; .$$

The first term on the right of Eq. 3.2-38 is the power carried by the axial electron loss; the electrons are assumed to carry energy ($\phi_e + T_e$) as they leave the plasma. P_x is the bremsstrahlung radiation; the third term is the alpha heating power transferred to the electrons. We take

$$f_e = 0.88 \exp(-T_e/67.4) \; , \qquad (3.2-39)$$

where T_e is in keV, as the fraction going to the electrons. The remaining term in Eq. (3.2-38) is the collisional energy transfer between the electrons and the various ion species.

3.2.6 Neutral Beam Trapping Fraction

The trapping fraction, f_t, is defined as that fraction of the incident neutral atoms in the beam which upon hitting the plasma, are either ionized or undergo charge exchange with the plasma ions. The shine-through fraction, f_s,

is that fraction which traverses the plasma without interaction. Thus $f_t + f_s = 1$ in our definitions. If the beam were a pencil beam (i.e., zero transverse size) then we would get

$$f_t = 1 - \exp\left\{-\int \frac{n(s)<\sigma v>_T}{v_b}\, ds\right\}$$

where the integral is along the beam path, $<\sigma v>_T$ is the total rate coefficient, and v_b is the beam velocity. Realistic neutral beams for mirror devices, however, have beam dimensions on the order of the plasma size and thus the trapping fraction along different "beamlets" varies greatly. We have to consider the finite beam and plasma size to get an accurate estimate of the net trapping fraction.

We assume that the plasma is cylindrical with a radial density profile

$$n = n_0(1 - (r/a)^m) , \qquad r < a$$

and is uniform in z, the cylindrical axis, at least over the section intercepted by the beam. The beam axis is assumed to be in the x-z plane and to intercept the z-axis at an angle θ; $\theta = \pi/2$ corresponds to normal incidence. The incident beam is assumed to have negligible angular divergence at the plasma, but a finite extent in the plane perpendicular to its axis. Consider an infinitesimal beamlet at height y and axial coordinate z at the midplane (x = 0). All such beamlets see the same plasma over their path length and hence have the same trapping fraction. Thus we can write the beamlet trapping fraction as

$$f_t(y) = 1 - \exp\left\{- \int_{-x_1}^{x_1} n(x,y) \frac{<\sigma v>_T}{v_b} \frac{dx}{\sin \theta}\right\}$$

where the integral along the beam path has been transformed to an integral over x; the limits $\pm x_1$ are given by

$$x_1^2 + y^2 = a^2 .$$

Now
$$\int_{-x_1}^{x_1} n(x,y)\, dx = 2 \int_{y}^{a} n(r) \frac{dx}{dr}\, dr = I(y)$$

3.2-13

and
$$\frac{dx}{dr} = \frac{r}{x} = \frac{r}{\sqrt{r^2 - y^2}}$$

since $r^2 = x^2 + y^2$. We let $u = r/a$, $u_0 = y/a$ and use the radial profile for $n(r)$ to get

$$I(y) = 2n_0 am \int_{u_0}^{1} u^{m-1} \sqrt{u^2 - u_0^2} \, du \ ,$$

after integrating by parts. This can be evaluated analytically, but there is no single form for all m. We let

$$I(y) = \frac{2n_0 am}{m + 1} I_m(u_0)$$

where
$$I_m = (m + 1) \int_{u_0}^{1} u^{m-1} \sqrt{u^2 - u_0^2} \, du \ .$$

I_m is tabulated in Table 3.2-1 for $m = 2, 3, 4$.

The trapping fraction of an individual beamlet at height y is thus

$$f_t(y) = 1 - \exp \left(-\alpha I_m \left(\frac{m}{m + 1} \right) \right) \tag{3.2-40}$$

where
$$\alpha = \frac{2n_0 a \langle \sigma v \rangle_T}{v_b \sin \theta} \ .$$

We now integrate over the beam cross section to get the net trapping fraction. Let (x', y') be Cartesian coordinates in the plane perpendicular to the beam axis, with $y' = y$, and integrate the beam current density over x' to get

$$I(y) = \int J(x', y') \, dx' \ .$$

As a model, we take

$$I(y) = \begin{cases} J_0 e^{-(y/\lambda)^2} \ , & |y| < \lambda \\ 0 & , \quad |y| > \lambda \ . \end{cases}$$

Table 3.2-1. The Function $I_m(u_o)$

m	$I_m(u_o)$
2	$(1 - u_o^2)^{3/2}$
3	$(1 - u_o^2)^{3/2} + \dfrac{u_o^2}{2} (1 - u_o^2)^{1/2} - \dfrac{u_o^4}{4} \ln \left(\dfrac{1 + \sqrt{1 - u_o^2}}{u_o} \right)$
4	$(1 - u_o^2)^{5/2} + \dfrac{5}{3} u_o^2 (1 - u_o^2)^{3/2}$

The beam is to be collimated at a height λ. The net trapping fraction is then

$$f_t = \frac{\displaystyle\int_o^{y_{max}} dy \; e^{-(y/\lambda)^2} f_t(y)}{\displaystyle\int_o^{\lambda} dy \; e^{-(y/\lambda)^2}} \qquad (3.2\text{-}42)$$

where y_{max} is the lesser of λ and a. The integral to evaluate f_t has to be done numerically and depends on the choice for m and a/λ. Figure 3.2-1 shows f_t versus α for $m = 3$ and various values of a/λ. In the TASKA-M power balance code we use $m = 3$ and $\lambda = 0.8a$ to get the trapping fraction of the various neutral beams.

3.2.7 Neutron Wall Loading

The neutron wall loading is nonuniform axially because of the density profile of the hot ions in the central cell. A simple estimate of the local wall loading, $\Gamma(z)$, can be gotten using the long-thin approximation:

$$\Gamma(z) = \frac{n_{Hc}^2(z) \langle \sigma v \rangle_f Q_n r_p^2(z)}{8 r_w(z)}$$

where $r_p(z)$ is the local plasma radius, $r_w(z)$ is the local wall radius, $\langle \sigma v \rangle_f$ is the D-T fusion reaction rate, and $Q_n = 14.1$ MeV. TASKA-M is defined so
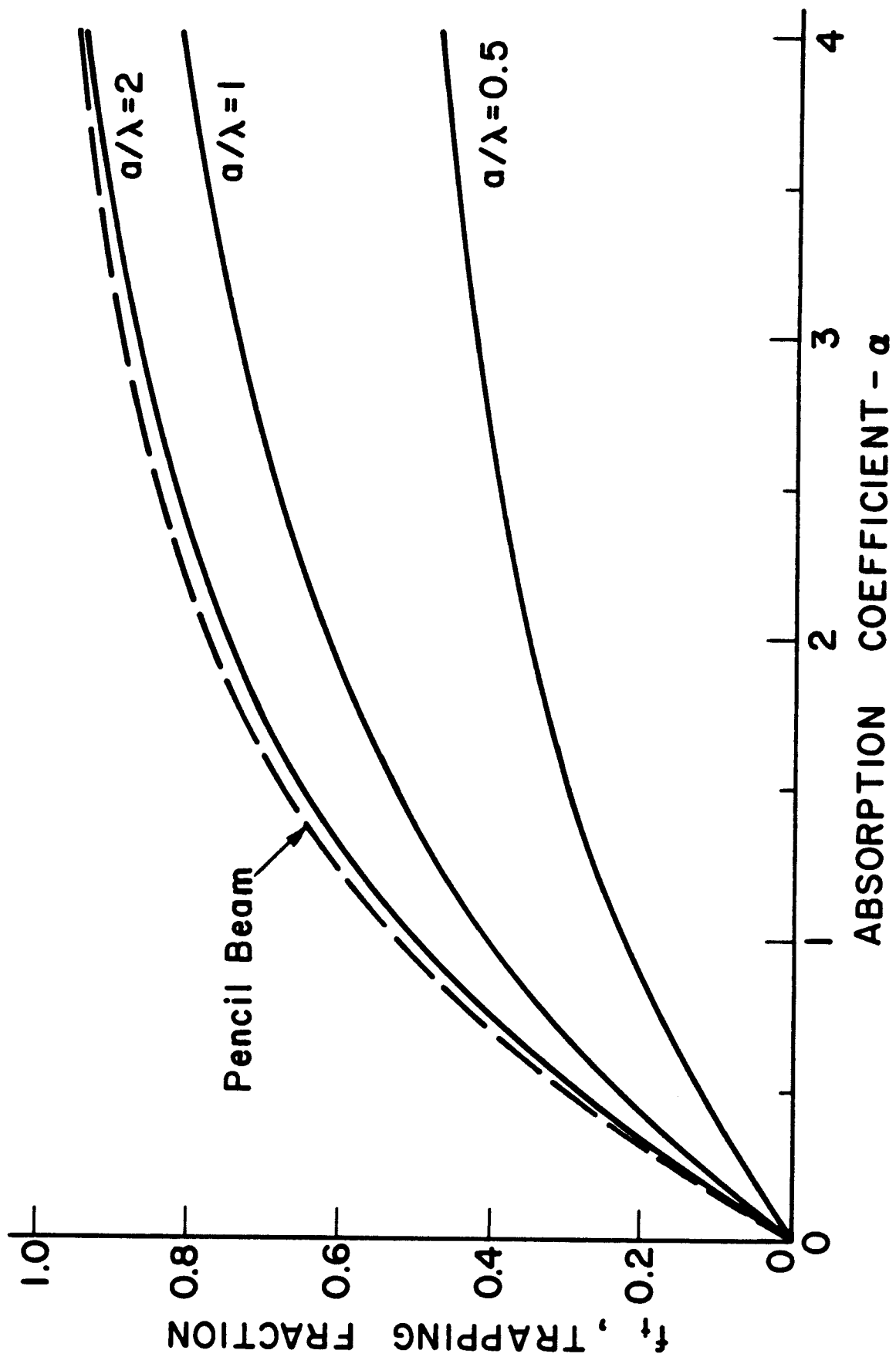
Fig. 3.2-1. The trapping fraction as a function of the absorption coefficient, α, for various neutral beam widths, λ. Also shown is the pencil beam for comparison.

that $r_w(z)$ is greater than $r_p(z)$ by one gyrodiameter of a 3.5 MeV alpha particle; this avoids direct bombardment of the first wall by energetic alpha particles.

The above estimate for the local wall loading overestimates the peak wall loading by about 20%. This is because the long-thin approximation fails near the peak; the wall radius is comparable to the axial extent of the peak. Consequently, a more accurate expression for the local wall loading has been developed. The plasma is assumed to be a line source at $r = 0$ which emits $Q(z_0)$ neutrons isotropically per unit length per second at the source point $z = z_0$. The number of neutrons emitted at z_0 and passing through an annular ring at z is then

$$dN = Q(z_0) \, dz_0 \, \frac{d\Omega}{4\pi}$$

where $d\Omega$ is the solid angle subtended by the ring; see Fig. 3.2-2. Now, the incremental wall loading at z due to the source at z_0 is

$$d\Gamma = \frac{dN}{dA} \, Q_n = \frac{Q(z_0) \, dz_0 \, d\Omega}{4\pi \, dA}$$

where $d\Omega = 2\pi \sin\theta \, d\theta$, $dA = 2\pi r \, dz$, $R \, d\theta = \sin\theta \, dz$, and $R^2 = r^2 + (z - z_0)^2$. Thus

$$d\Gamma(z) = \frac{r}{[r^2 + (z - z_0)^2]^{3/2}} \frac{Q(z_0)}{4\pi} \, dz_0 \, Q_n \, .$$

Integrating over the line source gives

$$\Gamma(z) = \frac{r(z)}{4\pi} \int_{z_1}^{z_2} dz_0 \, \frac{Q(z_0) \, Q_n}{[r^2(z) + (z - z_0)^2]^{3/2}} \, . \qquad (3.2\text{-}43)$$

The source strength is simply

$$Q(z_0) = \frac{n_{Hc}^2(z_0)}{4} \langle \sigma v \rangle_f \pi r_p^2(z_0) \, . \qquad (3.2\text{-}44)$$

This allows us to compute a better approximation for the local wall loading.
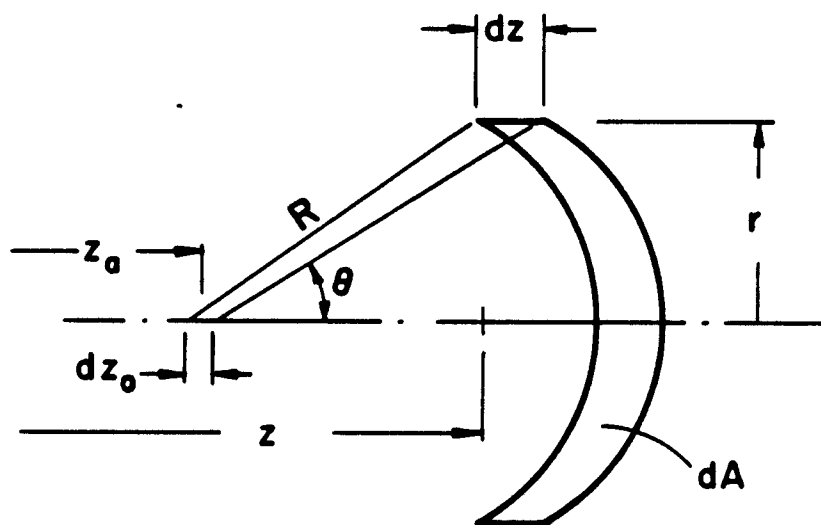
Fig. 3.2-2. Notation for computing the wall loading of a nonuniform line
source.

The neutron source strength $Q(z_0)$ is also used in the neutronics calculations in Chapter 5.

3.2.8 Structure of the Power Balance Code

The power balance code solves the relevant equations in Sections 3.2.1-3.2.6 for a solution consistent with the objectives of TASKA-M. The input data are of three types. First, there are the machine parameters: vacuum magnetic field everywhere, energy and injection angle of the high energy central cell beams, injection angle of the anchor beams, species of the various injected particles. Second, there are plasma parameters: electron temperature; beta in the central cell and in the anchor; the ratio of the potential of the anchor, ϕ_a, to the central cell potential, ϕ_e (this determines the anchor density relative to the central cell density). Finally, we have various parameters which are obtained or inferred from other codes. The bounce-average Fokker-Planck code yields values for the density ratio, $n_H(z)/n_h(0)$, of the sloshing ions in the central cell and anchor. This, combined with the magnetic field profile, yields the effective length of the hot and warm ion species. A neutral atom transport code gives estimates for the escape probability f_e^H of the hot neutrals.

The neutron wall loading at the midplane of the central cell is also input data. The code then solves in an iterative fashion for the plasma density, plasma radius, and wall radius to yield this wall loading consistent with the other input data. The warm plasma required for microstability is evaluated self-consistently using the analysis described in Section 3.6.4. A rough flow diagram of the power balance code is shown in Fig. 3.2-3. The final convergence test is that all iteration loops between points 1 and 4 be passed on the first try with an error criteria of 10^{-3} since the last time point 1 was reached.

Fig. 3.2-3. Flow diagram of the power balance code.

INITIALIZATION
OF PARAMETERS

INITIAL GUESSES
FOR E_{Hc}, E_{OUT}, ϕ_e

① ← ③

COMPUTE $r_p(z), r_w(z), n_{Hc}$

LOGAN-RENSINK MODEL
FOR CENTRAL CELL

HAS E_{OUT} CONVERGED — NO

YES

WARM PLASMA REQUIREMENTS

CENTRAL CELL BEAM
REQUIREMENTS

CALCULATE E_{Hc} → ②

CENTRAL
CELL
CALCULATIONS
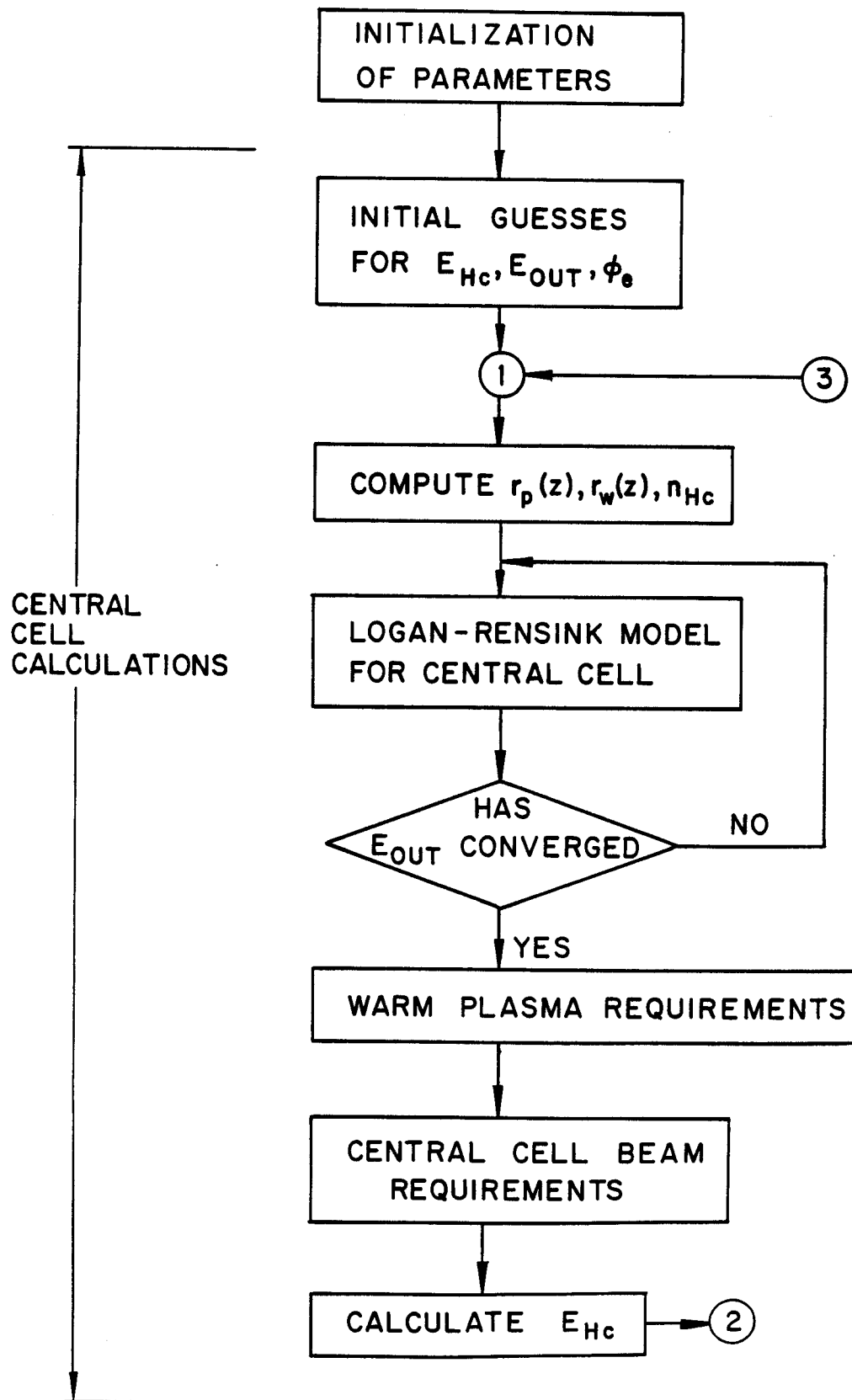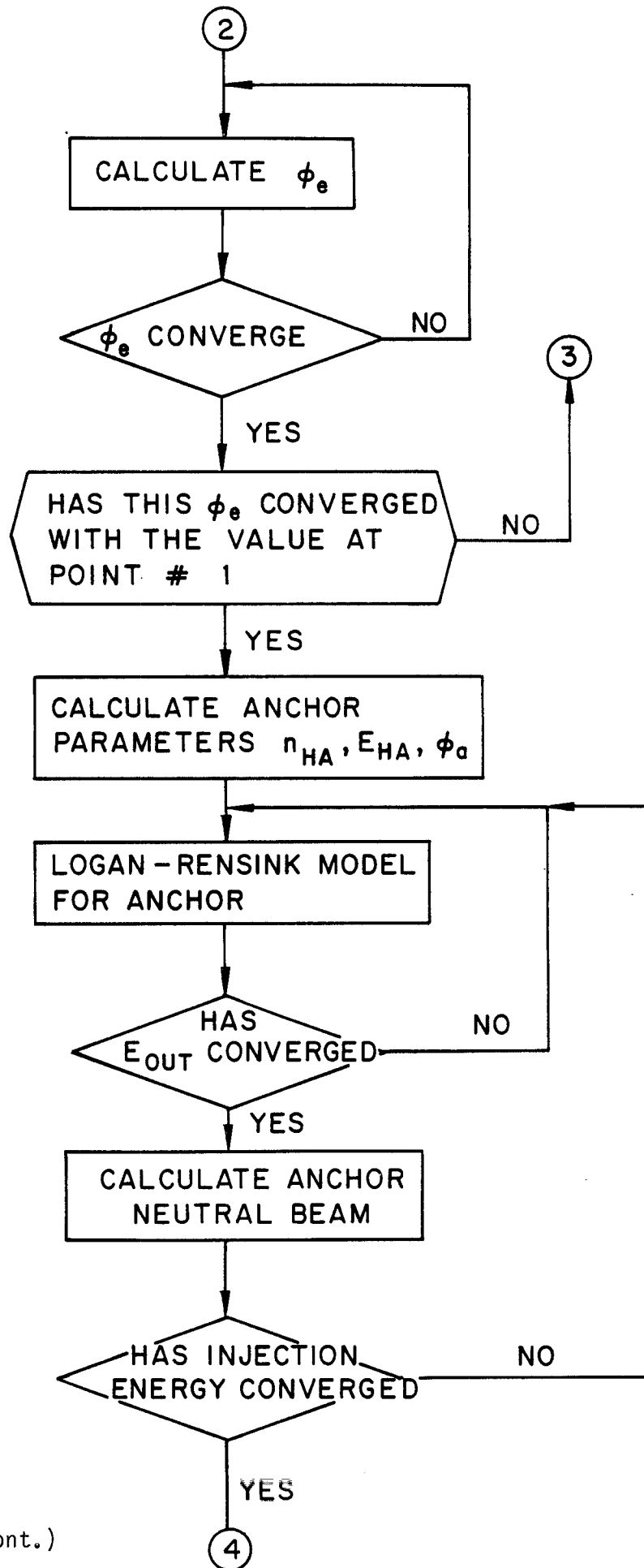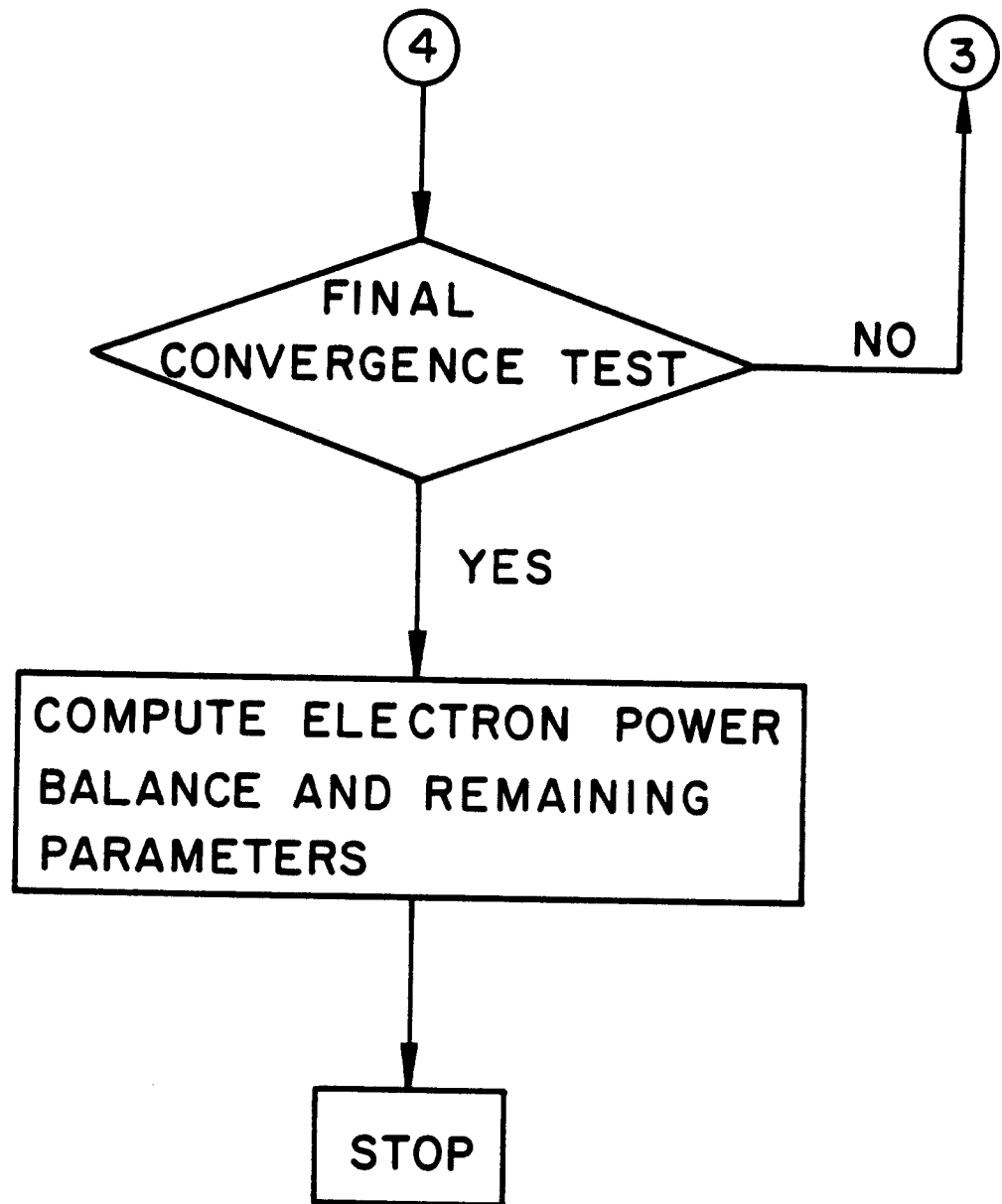
Fig. 3.2-3 (cont.)

Fig. 3.2-3 (cont.)

References for Section 3.2

1. B.G. Logan, A.A. Mikin, M.E. Rensink, Nuclear Fusion 20, 1613 (1980).

2. V.P. Pastukhov, Nuclear Fusion 14, 3 (1974).

3. R.H. Cohen, M.E. Rensink, T.A. Cutler, and A.A. Mirin, Nuclear Fusion 18, 1229 (1978).

4. R.P. Drake et al., "Radial Transport in the Central Cell of the Tandem Mirror Experiment," Lawrence Livermore National Laboratory Report UCRL-85872, March 12, 1982 (submitted to Phys. Fluids).

3.3 The TASKA-M Design Point

The power balance model described in Section 3.2 was used to compute the required plasma parameters, neutral beam powers, and electron heating power to achieve a given neutron wall loading at the midplane of the central cell. With this code, one can perform a series of parametric calculations to "optimize" the TASKA-M parameters. In addition to minimizing the injected power for a given magnetic field and neutron wall loading, one has to consider other aspects of the design point. For example, there are limitations on how much neutral beam power can be injected through a single beam line, or how much RF power can be applied to a single antenna. The number of beam lines and antennas is limited by the space available. One also needs to retain sufficient space (with good access) for blanket and materials test modules. There are also plasma physics considerations not incorporated into the power balance model; these are usually checked after some possible design points are selected for more detailed examination. These include MHD interchange stability criteria, Fokker-Planck calculations of the sloshing-ion plasma, microstability of the mirror-confined ions, and trapped particle stability. These considerations may suggest changes in the plasma parameters; the process is then iterated again.

The above process was used to "zero-in" on the TASKA-M design point selected. First we give the details for this design point and then present results in which some of the design parameters are varied. Table 3.3-1 lists the main machine and power parameters of TASKA-M. Table 3.3-2 presents the main plasma physics parameters, and Table 3.3-3 lists the neutral beam and RF heating parameters. The neutron wall loading is 0.7 MW/m^2 at the central cell midplane and rises to a peak value of 1.3 MW/m^2 at the density maximum; the wall loading profile is shown in Fig. 3.3-1. This is calculated using Eq. 3.2-43 and assuming the local wall radius follows the local plasma radius with a separation of 2 alpha particle gyroradii. The actual first wall radius of the machine is somewhat different for construction simplicity, and hence the wall loading used in the neutronics analysis is different in some regions. Shown in Fig. 3.3-2 is the effect of varying the wall loading; other design parameters (e.g., β, magnetic fields, neutral beam injection energy, etc., are held constant). We see a sharp rise in the injected power and the electron heating power with increasing wall loading. In this parametric variation, the

Table 3.3-1. TASKA-M General Parameters

Neutron Wall Loading

Central cell midplane (at 0.25 m radius)	0.7 MW/m^2
Central cell maximum	1.3 MW/m^2

Fusion Power
6.8 MW

Magnetic Fields

Central cell - midplane	4.2 T
Central cell - maximum	17.5 T
Transition region - minimum	2.2 T
Anchor - midplane	1.0 T
Anchor - maximum	2.7 T

Central Cell Dimensions

Length between magnetic field peaks	5.5 m
Length between density peaks	3.4 m
Wall radius in the test zone	0.22-0.25 m

Anchor Dimensions

Length between magnetic field peaks	5.4 m
Length between density peaks	3.4 m
Wall radius - midplane	0.37 m

Table 3.3-2.   TASKA-M Plasma Parameters*

Central Cell

On-axis β	0.50
Radially-averaged β	0.30
Electron temperature	14 keV
Hot ion density	3.3×10^{14} cm^{-3}
Hot ion sloshing density ratio	1.59
Mean hot ion energy	84 keV
Mean hot ion escape energy	67 keV
$(n\tau)_{HC}$ - hot ions	1.0×10^{13} s/cm^3
Warm ion density	3.0×10^{13} cm^{-3}
Mean warm ion energy	5.8 keV
$(n\tau)_{WC}$ - warm ions	1.3×10^{12} s/cm^3
Potential (to ground)	59 kV
Warm ion confining potential	5.3 kV
Plasma radius	12 cm
Radial profile exponent	3

Anchor

On-axis β	0.50
Radially averaged β	0.30
Electron temperature	14 keV
Hot ion density	2.6×10^{13} cm^{-3}
Hot ion sloshing density ratio	1.4
Mean hot ion energy	60 keV
Mean hot ion escape energy	56 keV
$(n\tau)_{HA}$ - hot ions	3.0×10^{12} s/cm^3
Warm density	2.6×10^{12} cm^{-3}
Mean warm ion energy	6.6 keV
$(n\tau)_{WA}$ - warm ions	6.6×10^{11} s/cm^3
Potential (to ground)	24 keV
Warm ion confining potential	3.4 keV
Plasma radius	24 cm
Radial profile exponent	3

---

* spatially dependent parameters are given on-axis at the midplane.

Table 3.3-3. TASKA-M Neutral Beam and RF Heating Parameters

Central Cell
  High Energy Neutral Beams

Injection voltage	90 kV
Total injected power	21 MW
Injection angle	45°
Species	0.5 D/0.5 T
Trapping fraction	0.92
Number of beam lines	4

  Low Energy Neutral Beam

Injection voltage	12 kV
Total injected power	0.60 MW
Injection angle	70°
Species	D
Trapping fraction	1
Number of beam lines	1

Anchor
  Medium Energy Neutral Beams

Injection voltage	73 kV
Total injected power/anchor	3.5 MW
Injection angle	50°
Species	D
Trapping fraction	0.37
Number of beam lines/anchor	1

RF Heating

Absorbed power	12 MW
Frequency	25 MHz
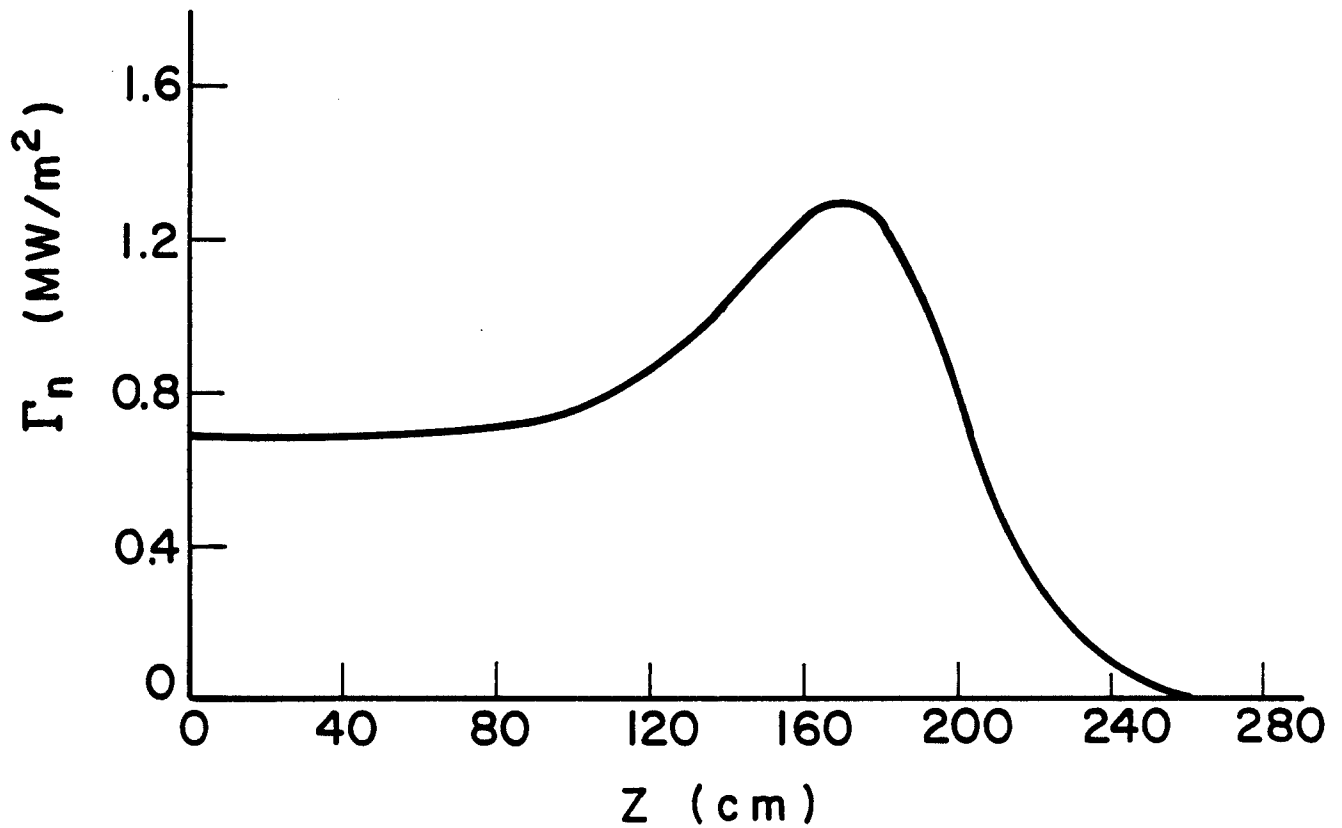
Fig. 3.3-1. Axial profile of the 14.1 MeV neutron wall loading assuming the wall follows the plasma radius with a separation of 2 alpha particle gyroradii.
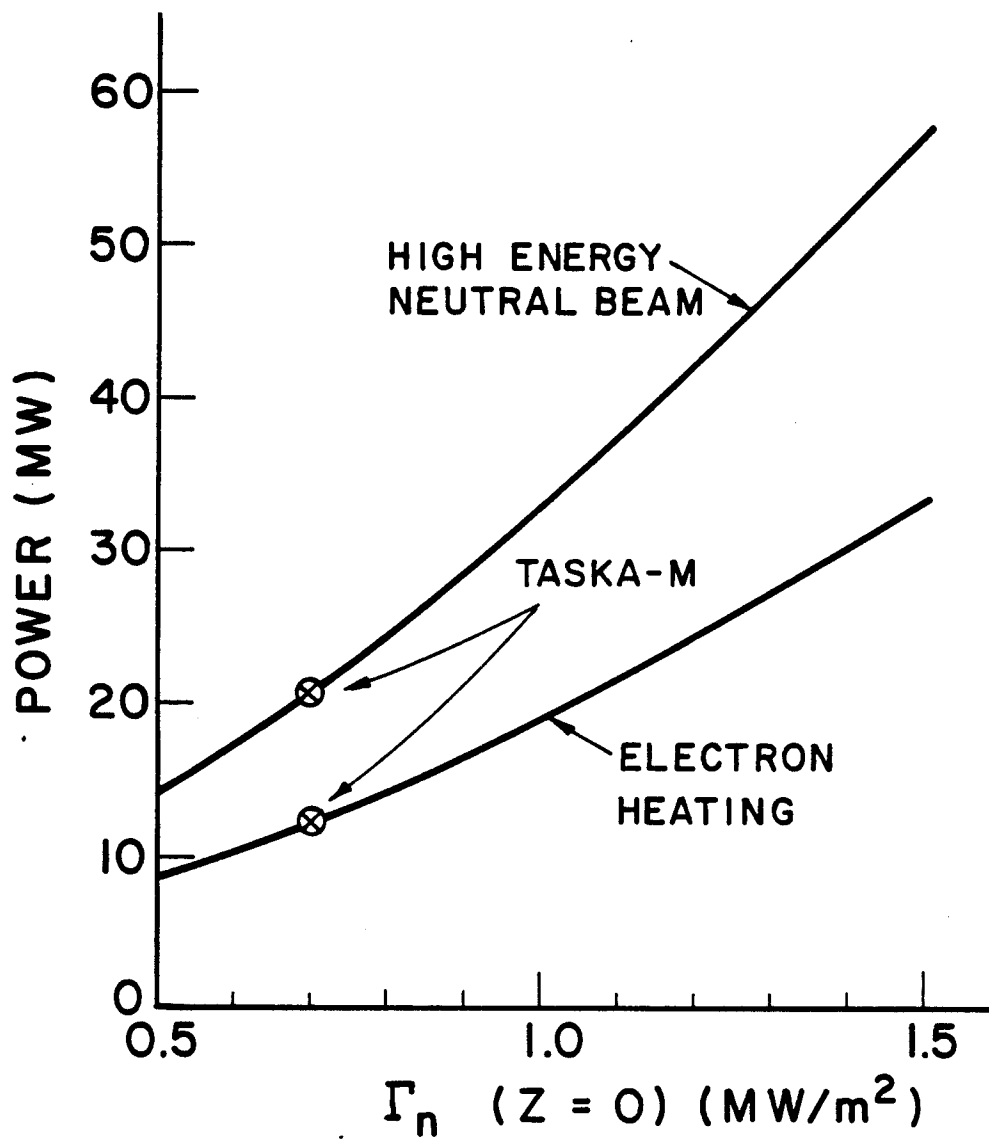
Fig. 3.3-2. Variation of the high energy neutral beam power and electron heating power with the midplane neutron wall loading.

primary change is in the plasma radius, which has to increase to produce the higher wall loading. The neutral beam power and electron heating power increase because of the increased plasma volume.

The hot ion sloshing density ratio of 1.59 in the central cell is typical of values obtained from the Fokker-Planck calculations described in Section 3.4. This density ratio is very sensitive to the injection angle. With the present configuration it is difficult to get an injection angle less than 45° without lengthening the central cell. A smaller injection angle and a higher density ratio would yield a greater wall loading near the peak and allow a reduced electron temperature for a given warm ion confining potential.

The sloshing density ratio is maintained by the high energy neutral beams. Charge exchange between the incident neutral beam atoms and the plasma removes ions with pitch angles near 90° and replaces them with ions at the injection angle. Consequently, the density dip is pumped by charge exchange while being filled by collisional scattering. Because charge exchange decreases with increasing energy in the energy range of interest, the effectiveness of this process decreases with increasing beam energy. Raising the beam energy also reduces the plasma density for a given β and thereby reduces the fusion power density. On the other hand, too low a beam energy leads to high collisional losses per unit volume. Shown in Fig. 3.3-3 is the effect of changing the high energy neutral beam energy in the central cell. The sloshing ion density ratio is held constant in this variation; this is not realistic but not enough Fokker-Planck calculations have been done in order to parameterize this effect. There is little effect of the beam energy on the beam power; the electron power decreases somewhat with increasing beam energy. A compensating effect not included in this graph is the reduced neutralization efficiency with increasing beam energy.

TASKA-M is designed with an electron temperature of 14 keV. Decreasing the electron temperature reduces the required RF power to sustain the electrons. This also reduces the electron contribution to the beta and thereby allows a higher plasma density and smaller radius for a given wall loading. On the other hand, one gets a smaller potential, $\Delta\phi_w$, in which to confine the warm plasma. Figure 3.3-4 shows the effect of electron temperature on the neutral beam and electron heating power and on $\Delta\phi_w/E_{wc}$. Because of concern about $\Delta\phi_w/E_{wc}$, we chose T_e to be 14 keV.
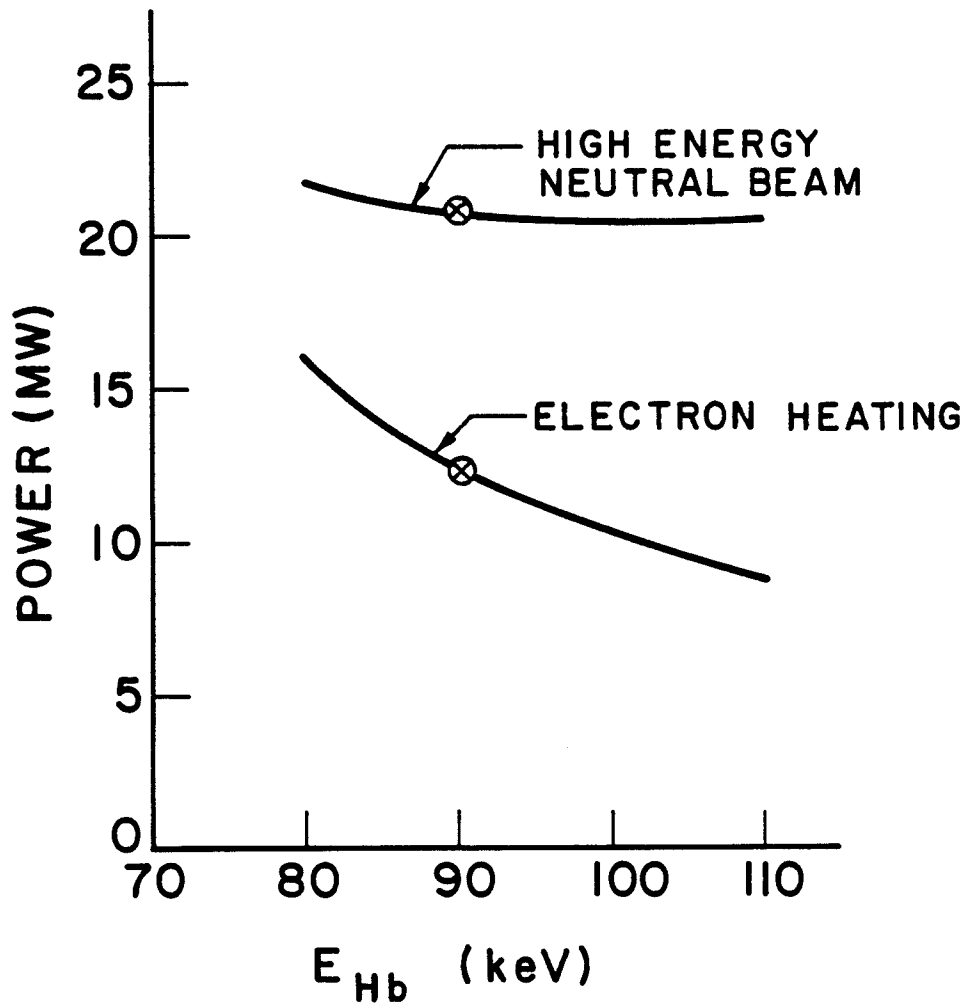
Fig. 3.3-3. Variation of the high energy neutral beam power and electron heating power with the energy of the high energy beam.
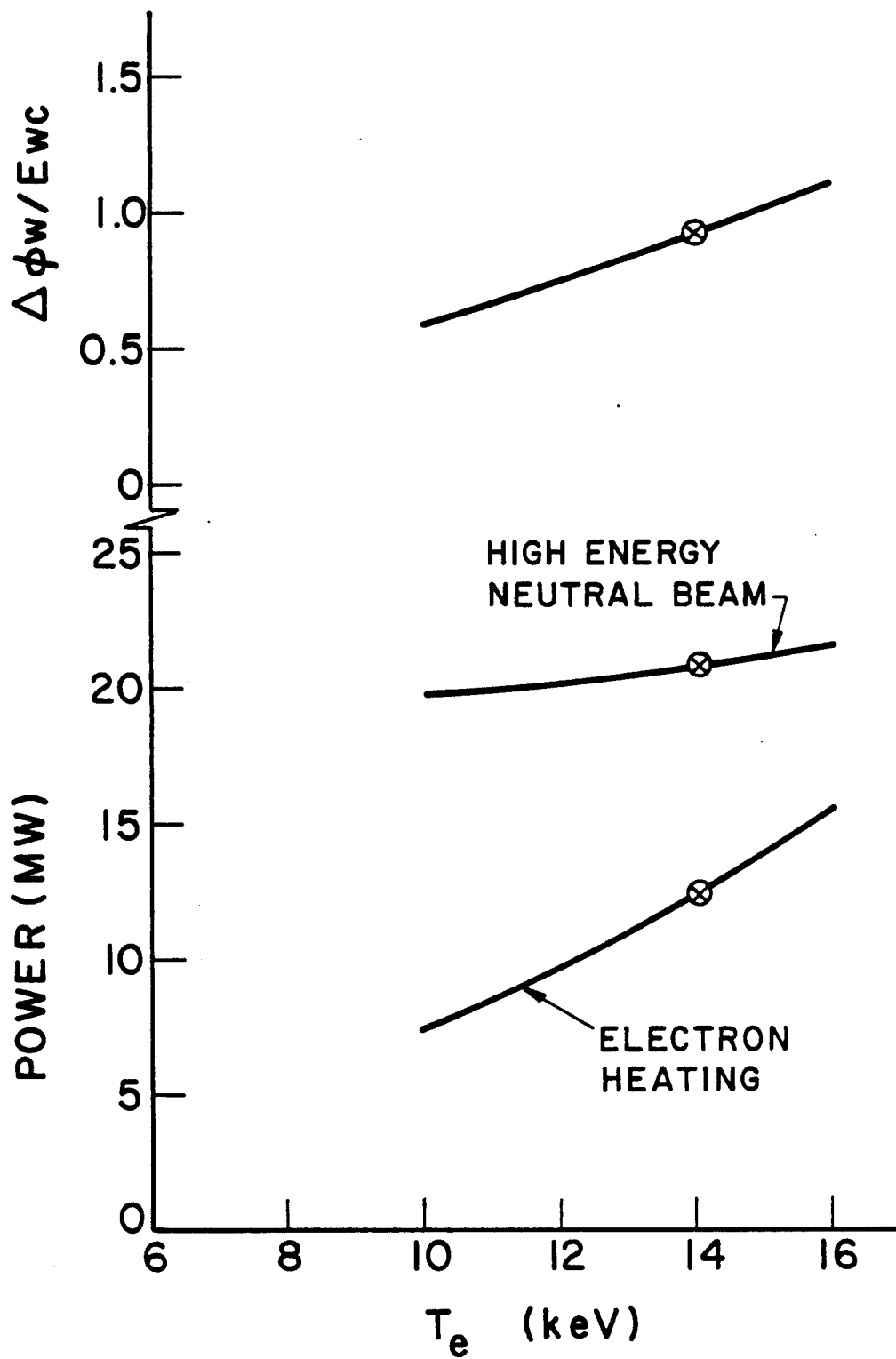
Fig. 3.3-4. Variation of high energy beam power, electron heating power, and warm ion confining potential with electron temperature.

The warm ion density in the central cell and anchor is determined by microstability requirements, as described in Section 3.6.4. The power balance code gives a warm ion neutral beam energy of 7 keV and a current of 14 amps to sustain the warm ion plasma. The warm ion beam energy has been raised to 12 keV in order to improve penetration and because low energy neutral beams are difficult to make. The neutral beam current has also been raised to 50 amps because of a concern that only a small fraction of the 12 keV ions will down-scatter into the 5 keV warm plasma population. The power balance model described in Section 3.2 uses the Pastukhov time for the warm plasma confinement time. This assumes the warm plasma is essentially Maxwellian with $\Delta\phi_{WC}/E_{WC} \gtrsim 1$. Because a higher energy was chosen for the warm plasma neutral beam, this model is not directly applicable for determining the required beam current. Figure 3.3-5 shows the velocity space in the vicinity of the warm plasma energy at the central cell midplane. Assuming the beam ions are initially spread isotropically by interaction with both the hot and warm plasma, about half of the injected particles will enter the warm part of velocity space. Some of these will be lost by scattering into the loss-cone before getting very deep into warm plasma region. In addition, charge exchange losses further reduce the fraction getting to the warm plasma region. Based on these considerations, the current of the warm plasma neutral beam has been raised to 50 amp at an energy of 12 keV. This is still only 500 kW of injected power, and thus this power level is not a major concern.

Finally, we consider the effect of varying the beta of the central cell and anchor simultaneously. We keep $\beta_C = \beta_A$ in this variation in order to preserve the beta ratio of the plasma in good curvature in the anchor to the plasma in bad curvature in the central cell. Shown in Fig. 3.3-6 is the effect on the neutral beam power and electron power of changing β. As can be expected, increasing β reduces the required power. We have chosen $\beta_C = \beta_A = 0.5$ in order to have margin for stability against ballooning modes, as well as interchange stability.

The TASKA-M design point was mainly chosen from these considerations. It does not represent an optimum configuration (it is not even clear what functional to optimize), but represents a reasonable choice in order to obtain a design which is credible from both a physics and an engineering viewpoint.
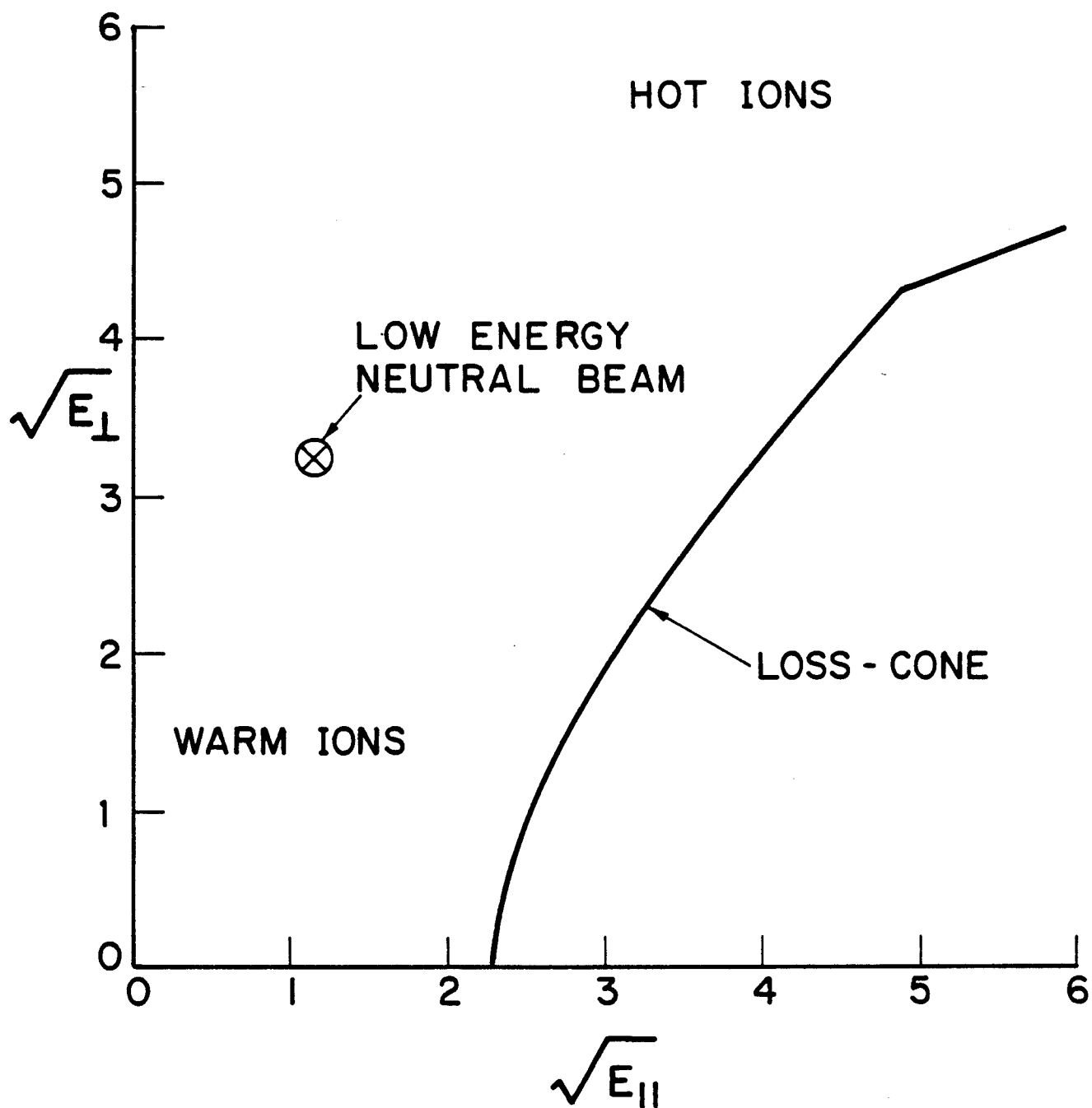
Fig. 3.3-5. Velocity space at the central cell midplane showing the low energy neutral beam and the loss-cone.
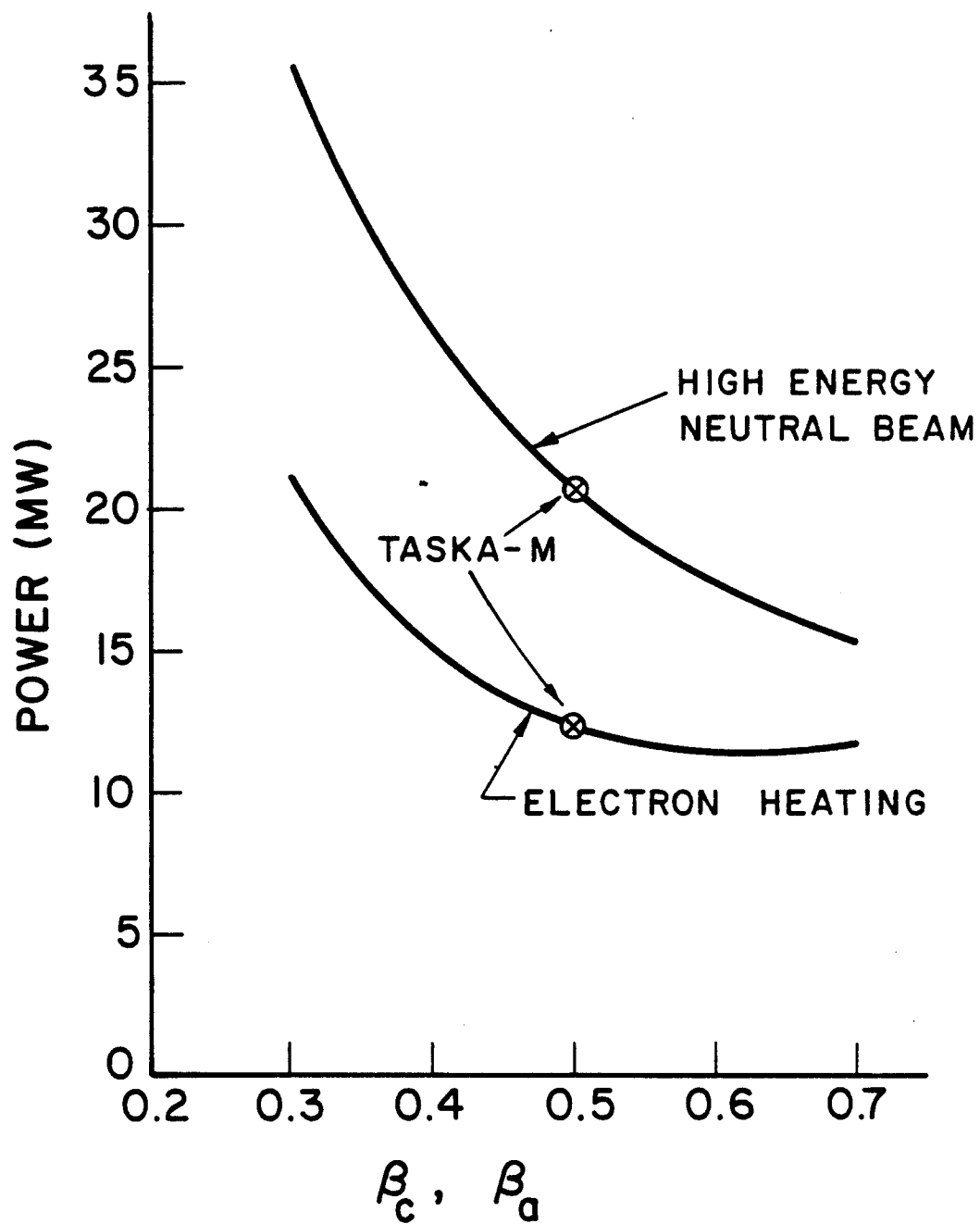
Fig. 3.3-6. Variation of the high energy beam power and electron heating power with β. In this variation, central cell and anchor beta are kept equal.

Further analysis may suggest ways TASKA-M could be modified to be less expensive or have higher performance for the same cost.

3.4 Fokker-Planck Calculations for Ion Distribution Function

3.4.1 Introduction

The ion velocity space distribution function in TASKA-M is important for two reasons:

1. Detailed design of the blanket and material test modules depends on the neutron wall loading profile which, in turn, depends on the density profile derived from the distribution function.

2. Microinstabilities which will possibly degrade plasma confinement can occur if the ion distribution function does not fit certain criteria discussed in Section 3.6.

Only the central cell neutral beams are investigated here, since they possess the largest amount of power and the end cell beam physics should be similar. Also, the reference case gives the ion distribution function for the 90 keV neutral beams, but neglects the effect of the 12 keV beams. Although it would clearly be desirable to have that effect included, the presence of a low energy component in the ion distribution alters the fundamental time scale on which processes occur which, in turn, causes Fokker-Planck codes to require inordinate amounts of computer time. Since the low energy component is only about 10% of the total ion density, neglecting it should not alter the basic hot ion distribution function. Thus, the neutron wall loading profile should be reasonably accurate. For microstability calculations, however, warm ions must be added in an ad hoc way.

The goals of these calculations were to:

1. Model the physical processes involved with reasonable accuracy.

2. Find a reference case which was close to the plasma physics power balance and magnetic field reference case values.

3. To the extent possible, optimize the ion distribution function for microstability and wall loading criteria.

The method used to find the distribution function is to run the LLNL Bounce-Average Fokker-Planck computer code (BA code).[1] The essence of the physics of bounce-average Fokker-Planck calculations is straightforward, although the calculations are typically very time consuming. The basic assumption is that the plasma collisionality is sufficiently small so that particle bounce times are much less than collision times. The distribution function along the axis of a mirror machine (z direction) thus depends only on the

distribution function at the midplane. The evolution of the distribution function in time may then be calculated by bounce averaging the collision operator and applying the resulting operator to the midplane distribution function. For details of how this procedure is implemented in the BA code, the reader is referred to Ref. 1.

Section 3.4.2 describes the models used for magnetic field, electrostatic potential, and neutral beams. Section 3.4.3 presents some of the cases which were run in the process of choosing reference case parameters for TASKA-M. The reference case ion distribution function and plasma properties derived from it are given in Section 3.4.4.

3.4.2 Models for Electrostatic Potential, Magnetic Field, and Neutral Beams

Although the BA code is able to self-consistently solve for the electro-static potential, it is extremely time-consuming when it does so. Therefore, the cases presented in the next sections were run with a constant axial po-tential profile, and a check for self-consistency with density and temperature was done at the end of the run. The model potential profile and the computed density profile for the reference case are shown in Fig. 3.4-1, which shows that they correspond qualitatively quite well to the electrostatic potential calculated from the Boltzmann relation $e\phi = T_e \ln n/n_0$. Also, the electron temperature is 14 keV, giving a potential dip of 5.2 keV, so quantitative agreement is also very good.

It was originally assumed that a parabolic axial magnetic field profile would be sufficiently accurate for investigating density profiles. As dis-cussed in the next section, however, more accuracy was required. The model magnetic field compared to the actual field generated by the detailed magnet analysis of Chapter 9 is shown in Fig. 3.4-2.

Accurate modeling of the interaction of the neutral beams with the plasma is a difficult task, and only a very simple model is used here. Ideally, a realistic beam profile, plasma profile, and reionization of charge exchanged neutrals would be included in the analysis. A radial transport equation would then have to be solved in order to find a self-consistent plasma profile. Since the BA code is a velocity space code with only axial space dependence, another code would have had to be written in order to analyze radial depen-dence. The compromise chosen for TASKA-M was to use a simple mean free path attenuation of the beam to some nominal radius (chosen here to be 6 cm) as
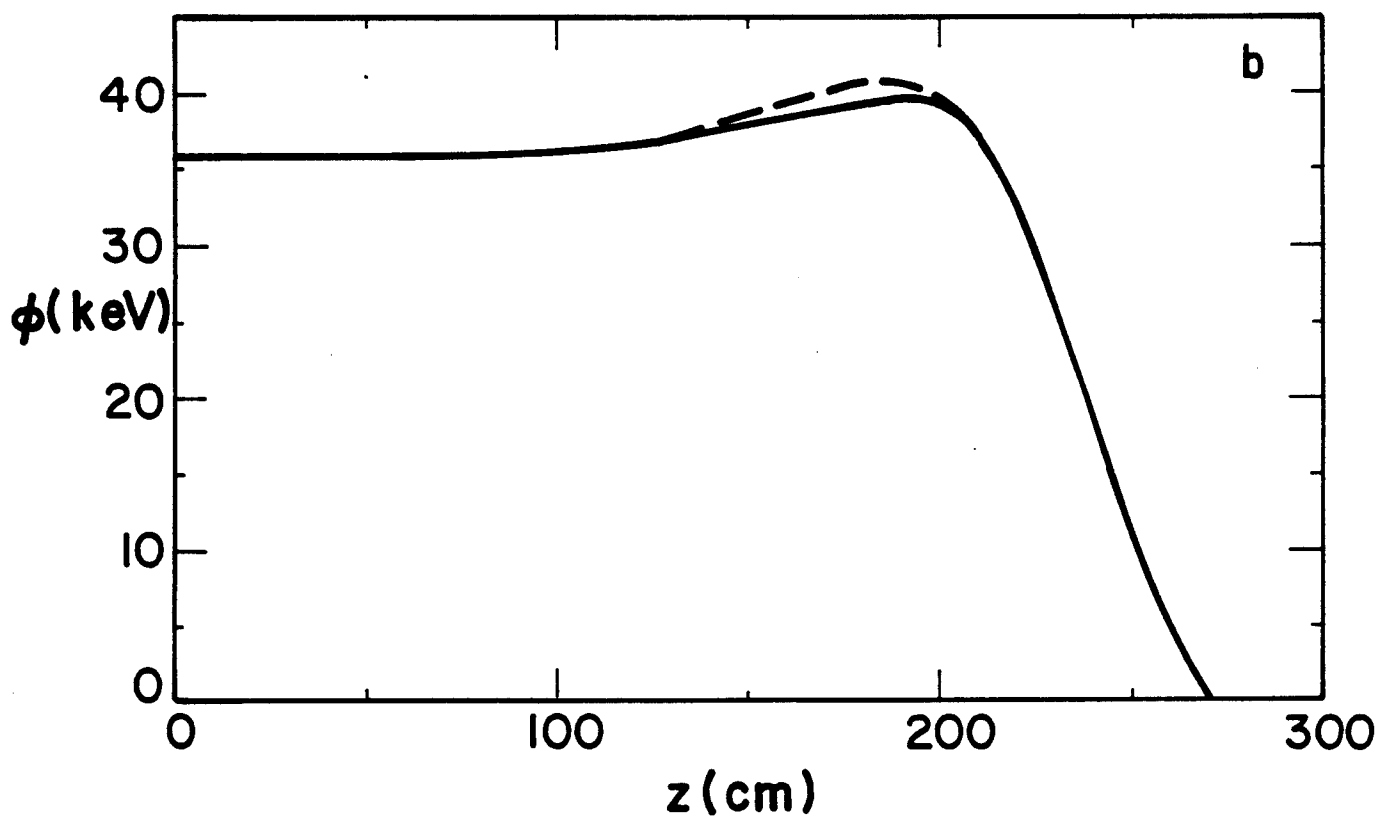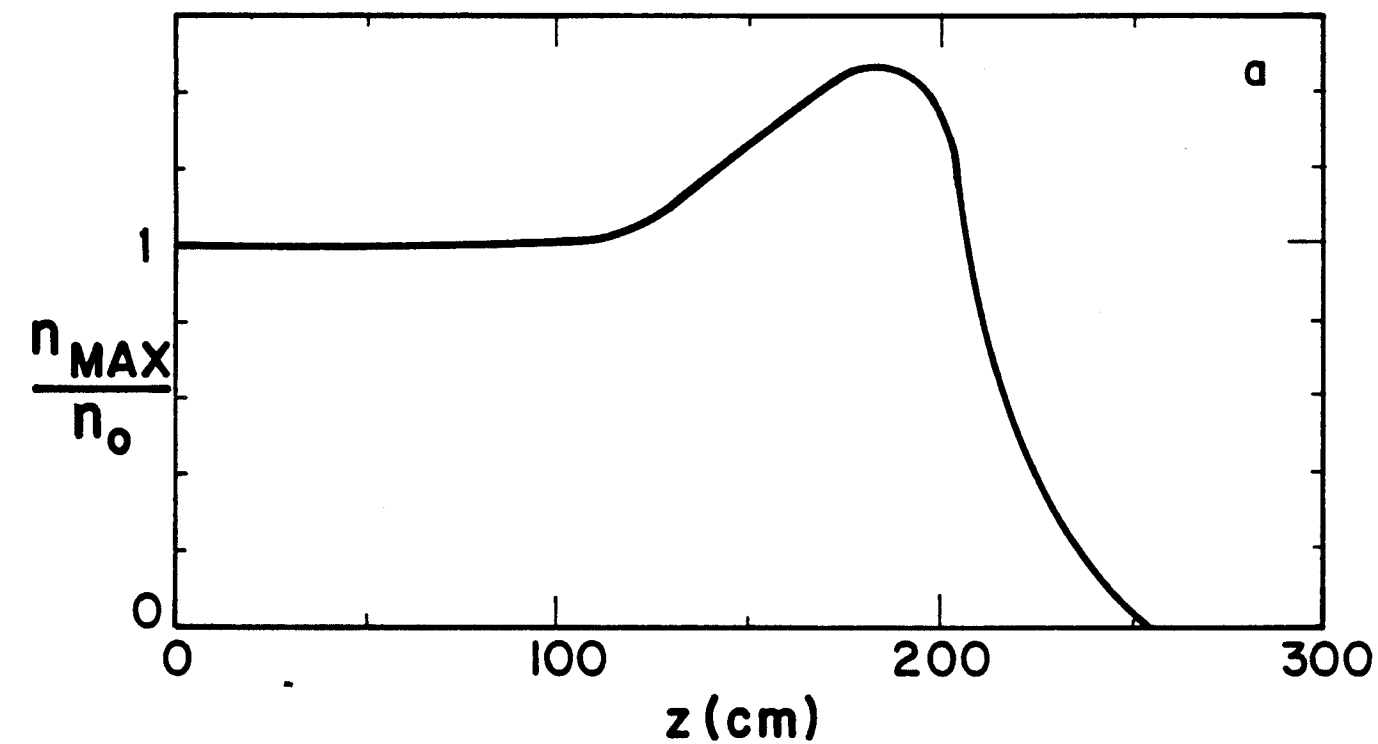
Fig. 3.4-1. (a) Reference case density profile. (b) Model potential profile (solid) and potential profile calculated from $\phi(z) = T_e \ln n(z)/n_0$ (dashed).
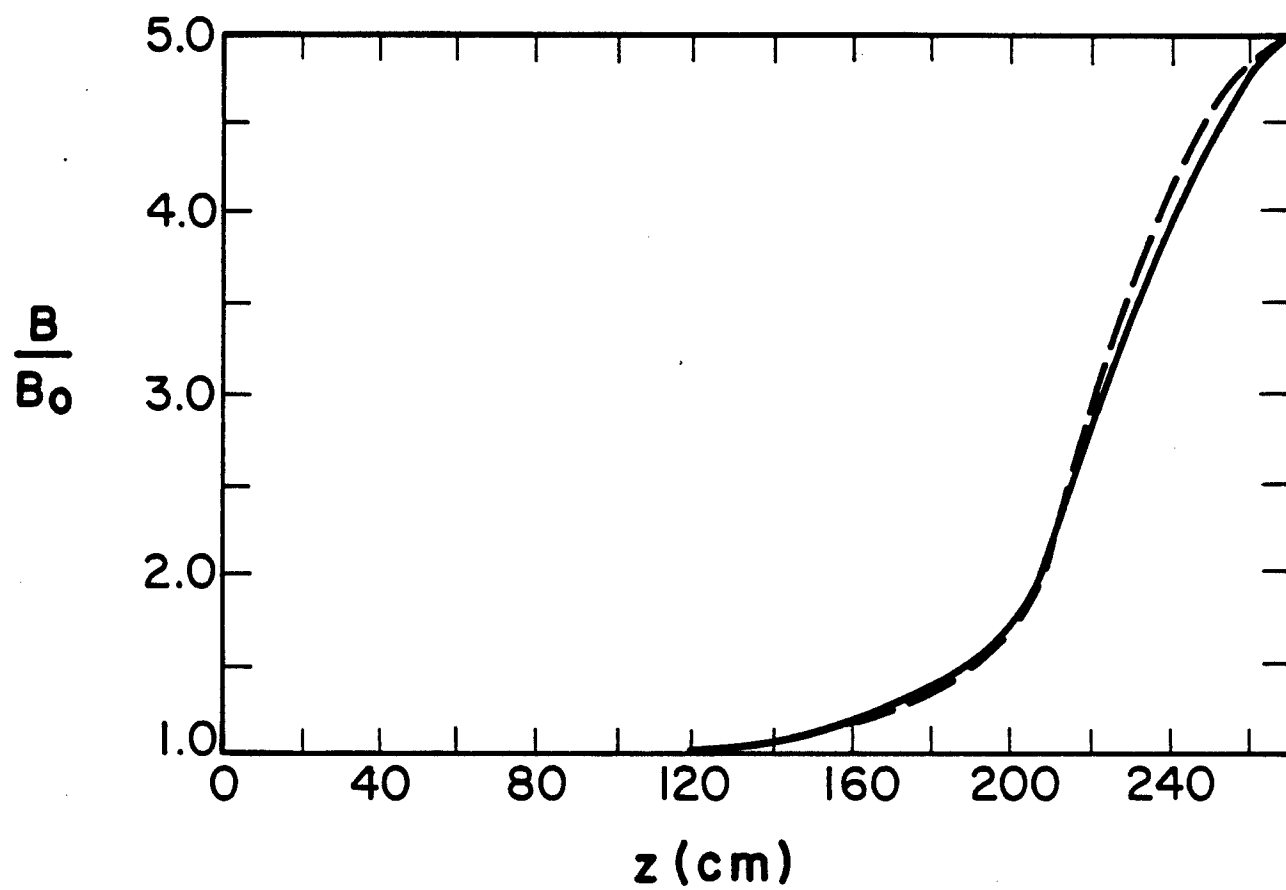
Fig. 3.4-2. Model magnetic field (solid) and magnet design field (dashed) versus z.

input to the BA code, and to use the resulting approximate ion distribution function for subsequent analysis. Absolute plasma density values, therefore, need to be calculated by other means, as described in Section 3.2, although axial profiles and the general shape of the ion distribution function should be reasonably accurate. A brief description of the calculational method used here follows.

Initially, the neutral beam source is taken to be composed of 90% atomic D and T, and 5% each of two- and three-atom molecules. When dissociated, this leads to a beam with 78.3% full energy, 8.7% one-half energy, and 13% one-third energy components. When divergence due to the thermal spread in energy of the beam components is considered, the energy composition of the neutral beams becomes 87.4%, 6.0% and 6.6%. These divergences were calculated for a beam with a thermal energy, T, of 10 eV in the ion source, a 10 cm beam radius, a beam energy of 100 keV, and a 10 m beam path length. The final TASKA-M reference case (see Chapter 6) is close to these parameters, and refining them is not warranted, since the uncertainty due to charge exchange effects is much larger. The beam divergence angle is approximately given by arcsin $[(T/E_{inj})^{1/2}]$. The density of the neutral beam at radius r is assumed to be given by $n(r) = n_0 e^{-\lambda(r)}$ where

$$\lambda(r) = 7.15 \times 10^{-7} \ n_0 \mu_i^{1/2} \ \frac{\langle \sigma v \rangle_{tot}}{E_{inj}^{1/2}} \int_r^{r_c} \frac{dr}{\sin \theta_{inj}} \ [1 - (\frac{r}{r_c})^3]$$

$$(3.4-1)$$

$$= 7.15 \times 10^{-7} \ \frac{n_0 \mu_i^{1/2} \langle \sigma v \rangle_{tot}}{E_{inj}^{1/2} \sin \theta_{inj}} \ (\frac{3}{4} r_c - r + \frac{r^4}{4r_c^3})$$

where n_0 is the on-axis plasma density in cm^{-3}, E_{inj} is the neutral beam injection energy in eV, θ_{inj} is the neutral beam injection angle, μ_i is the ion mass divided by the proton mass, $\langle \sigma v \rangle_{tot}$ is the total charge exchange plus ionization rate, and a cubic radial density profile has been assumed. The overall attenuation of the neutral beams is about 92% (see Section 3.3) so, when attenuating to the r = 6 cm point, only the near side of the plasma is considered. The neutral beams are assumed to have Gaussian radial profiles, giving the effective area of a 10 cm radius beam as

$$A_b \equiv 2\pi \int_0^{10} r \, dr \, e^{-r^2/10^2} \approx 200 \text{ cm}^2 . \qquad (3.4-2)$$

The beam current is taken to be given by $I_b = P_b/\langle E \rangle_b$, where $\langle E \rangle_b$ is the average beam energy. The total beam density at the plasma edge is then given by

$$n_{bs} = \sum_E \frac{f_E I_b}{v_E A_b} \qquad (3.4-3)$$

where the sum is over all energy components, f_E is the fraction of the beam, and v_E is the velocity of an ion with energy E. The BA code requires ionization and charge exchange rates as input. These are given by

$$S_{iE} = n_{bs} e^{-\lambda(r=6\text{cm})} \langle \sigma v \rangle_{iE} f_E \qquad (3.4-4)$$

and

$$S_{cxE} = n_{bs} e^{-\lambda(r=6\text{cm})} \langle \sigma v \rangle_{cxE} f_E \qquad (3.4-5)$$

where S_{iE} is the ionization rate for a beam with energy E, S_{cxE} is the charge exchange rate, and the $\langle \sigma v \rangle$'s are defined similarly.

The detailed Monte Carlo calculations of Section 6.2.3 give a reionization rate of about 30% for charge exchanged neutrals. To model the effect of this on the ion distribution function, an extra beam is included with 30% of the charge exchange rate of the original beams. The energy spread of this beam will be larger than the very monoenergetic original beams, consequently reducing the sloshing ion density ratio. This is clearly rough, but is probably within the accuracy of the calculations for which the distribution function will be used.

3.4.3 Special Cases

As the physics parameters of TASKA-M evolved, a variety of Fokker-Planck cases were run. In particular, the electrostatic potential went through considerable evolution. Since the BA code is very time-consuming, little parametric variation could be done but, within a limited range, the following items were investigated: neutral beam species mix, electron temperature, beam injection angle, beam energy, magnetic field axial profile, and reionization. Reionization was modeled for a few cases (in a rather ad hoc way). When varying a parameter, other parameters remain approximately constant unless stated

3.4-6

Table 3.4-1. Case Used for Varying Parameters -- NOT the Reference Case

Average ion energy	102 keV
Average ion $n\tau$	8.0×10^{12} cm^{-3} s
Electron temperature	14.7 keV
Midplane magnetic field (beta-corrected)	3.5 T
Peak magnetic field	17.5 T
Mirror half-length	270 cm
Neutral beam source radius	10 cm
Midplane to mirror-peak potential	32.4 keV
Potential dip	11.3 keV

	Neutral Beam Component		
Computer Code Input	100 keV	50 keV	33 keV
Ionization source, s^{-1}	944	52	46
Charge exchange source, s^{-1}	891	49	44
Velocity spread, keV	1	0.5	0.33
θ-spread parameter (see Eq. 3.4-6)	200	200	200

otherwise. Most of the variation was done around the case presented in Table 3.4-1; the final reference case is presented in the next section.

Beam species mixes for ion source components at 90:5:5, 75:15:10, and 50:25:25 were tried, where the numbers represent the percentage of the ion source in one-atom, two-atom, and three-atom molecules, respectively. The results are plotted in Fig. 3.4-3. Both the average ion energy and the average $n\tau$ values increased as the full energy fraction of the beam rose; the maximum sloshing ion peak to midplane density ratio also rose slightly. Therefore, the 90:5:5 mix was chosen for the reference case. This species mix is on the borderline of present day technology for neutral beams.
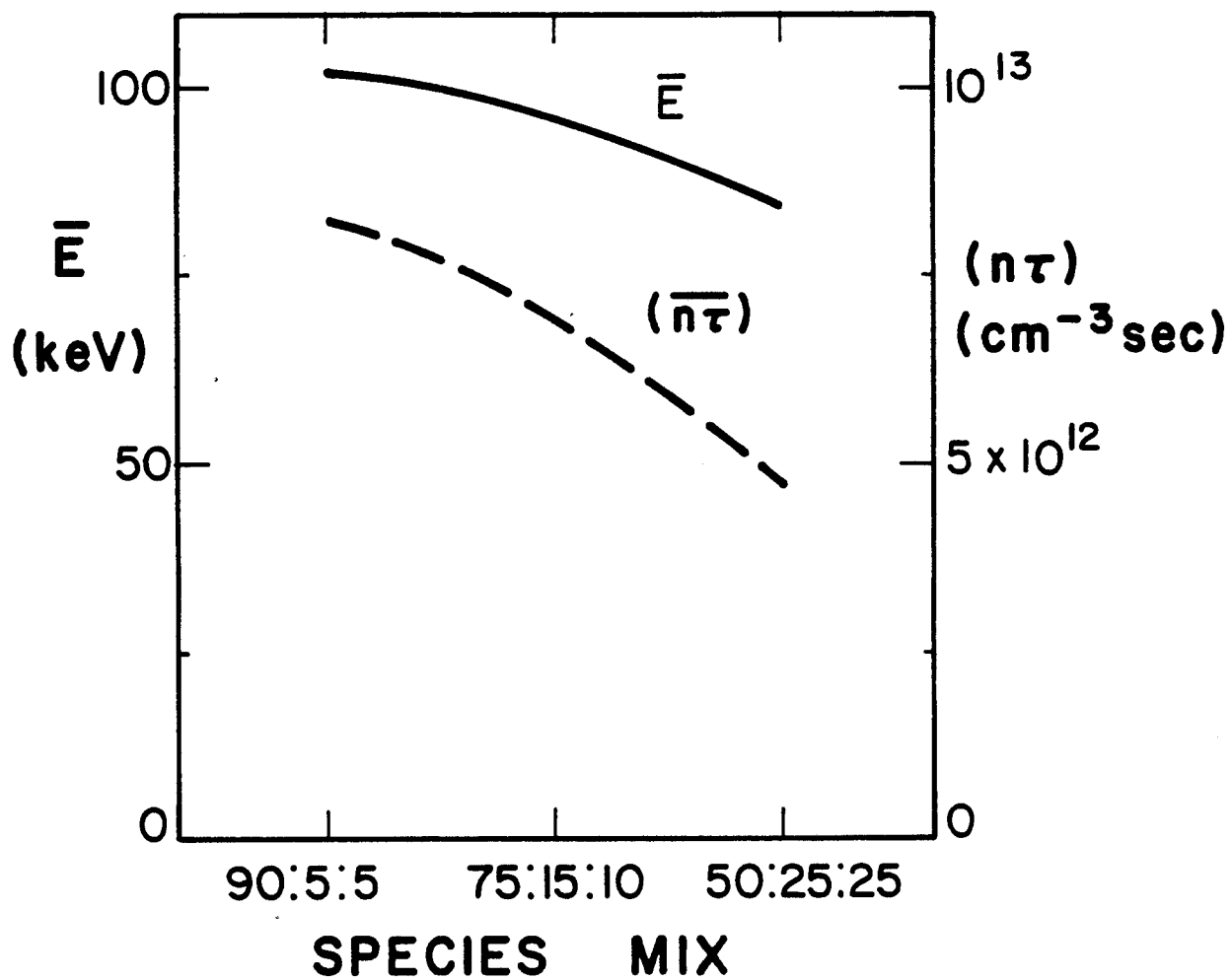
Fig. 3.4-3. Average ion energy and average (nτ) versus neutral beam species
mix.

The electron temperature, T_e, was varied from 10 to 20 keV in order to test whether a small change in T_e would give a significant change in the sloshing ion density ratio. As expected, due to reduced electron drag on the ions, the average ion energy and $n\tau$ values rose as T_e rose, but there was less than a one percent change in the density ratio. From plasma power balance considerations, a value of $T_e = 14$ keV was eventually chosen.

Details of the magnetic field axial profile have a large effect on the ion distribution. When cases were run for both a parabolic magnetic field and for the actual design magnetic field, the sloshing ion density ratio changed dramatically, although the average ion energy and $n\tau$ values did not. The parabolic magnetic field case had a sloshing ion density ratio of 1.81 while the actual field case had a density ratio of 1.57 and a 20% lower midplane density for the same ionization and charge exchange rates. Note that these test cases are not the final reference case. The reasons for this behavior are not fully understood, and the reference case used the actual magnetic field, since it is more accurate in any case. The strong dependence on magnetic field implies, however, that it may be desirable to tailor the magnetic field, if possible, in future designs.

The neutral beam injection angle, θ_{inj}, is a very important parameter, as shown in Fig. 3.4-4, where a 10° change in θ_{inj} is seen to give a 60% change in the sloshing ion density ratio. Unfortunately, it is difficult to inject the neutral beams at a lower angle than the 45° reference case because of engineering considerations.

The neutral beam injection energy affects parameters primarily through the fact that charge exchange and ionization rates depend strongly on E_{inj}. Higher energy, as expected, also gives better $n\tau$ values due to the consequent lower collisionality. However, as energy rises, the charge exchange cross section falls, making it more difficult for the beam to pump ions and maintain the sloshing ion distribution. A difficulty with the BA code is that ionization and charge exchange rates are not calculated self-consistently for given beam and plasma characteristics. In practice, a plasma ion energy is chosen, from which rates are found by the procedure given in Section 3.4.2, then the BA code is run and gives an average plasma ion energy. The ionization and charge exchange rates must then be iterated with the plasma ion energy until a self-consistent case results; this is done by hand and can be
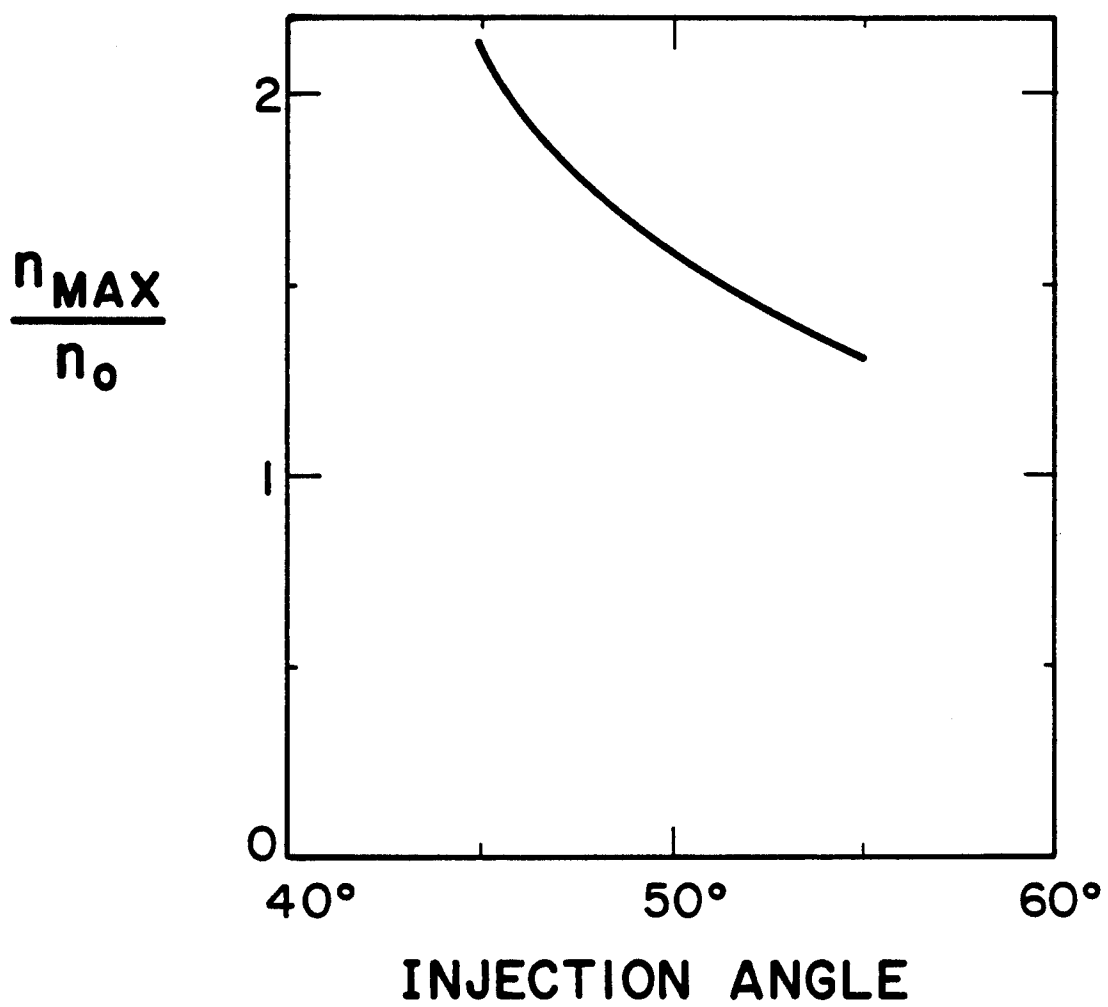
Fig. 3.4-4. Sloshing ion density ratio versus neutral beam injection angle.

extremely time consuming. The reference case given in the next section uses E_{inj} = 90 keV with an average plasma ion energy of 90 keV for calculating rates, while the output plasma ion energy is 98 keV. These appear to be close enough for practical purposes. The plasma physics power balance calculations are based on a fit to Fokker-Planck code runs called the Logan-Rensink plug model, but with modified coefficients (see Section 3.2).[2] That model gives numbers qualitatively similar, but not equal, to the results of running the BA code for the reference case.

To model the effects of reionization of charge exchange neutrals on the ion distribution, results are used from a separate analysis (Section 6.2.3) indicating that the total reionization fraction for the plasma power balance reference case is 30%. A case with reionization is generated by using ionization and charge exchange rates calculated from the total beam current, beam energy mix, and attenuation to r = 6 cm in the plasma. 30% of the charge exchange is then subtracted from each of the components at full, half, and third energy and is put into a beam with the average ion energy of the plasma. The angle and velocity spreads of the added beam are difficult to estimate, since the cross section for charge exchange is peaked at low energy and, therefore, the rate is higher for plasma ions traveling in the same direction as the beam. The added beam must have spreads somewhere between those of the plasma and the original beam. For the cases given here, a velocity spread of 5 keV is used, and the angle distribution is modeled by

$$F(\theta) \sim e^{-S_\theta (\cos\theta_{inj} - \cos\theta)^2} \tag{3.4-6}$$

with S_θ = 80 for the added beam, as opposed to S_θ = 200 for the original beam. The effect of reionization is strong. With reionization, the reference case sloshing ion density ratio is 1.45, without reionization, the ratio is 1.80.

3.4.4 Reference Case

The reference case for the TASKA-M ion distribution function is given in Table 3.4-2. The case chosen models reionization in the way discussed in the previous section. Attempts to use the BA code to model the physics of the low energy neutral beam have been less successful. When a significant amount of low energy plasma is present, the characteristic time scale drops by approximately the ratio $(T_w/E_{hc})^{1.5} \sim 0.03$, and the BA code takes a very long time to

Table 3.4-2. TASKA-M Fokker-Planck Calculation Reference Case

Average ion energy	98 keV
Average ion $n\tau$	7.4×10^{12} cm^{-3} s
Electron temperature	14 keV
Midplane magnetic field (beta-corrected)	3.5 T
Peak magnetic field	17.5 T
Mirror half-length	270 cm
Neutral beam source radius	10 cm
Midplane to mirror-peak potential	35.4 keV
Potential dip	5.5 keV

	Neutral Beam Component			
Computer Code Input	90 keV	45 keV	30 keV	90 keV "Reionization"
Ionization source, s^{-1}	727	40	35	288
Charge exchange source, s^{-1}	609	33	29	0
Velocity spread, keV	0.9	0.45	0.3	5
θ-spread parameter	200	200	200	80
(see Eq. 3.4-6)				

reach equilibrium. Therefore, only a few cases have been run, and a case that reasonably approximates the plasma power balance reference case has not been found. However, the BA code qualitatively supports the concept of trapping warm plasma in a potential dip. Figure 3.4-5 shows a 3-D plot of the ion distribution function versus velocity and pitch angle ($\theta \equiv \arccos v_\parallel/v$) when the low energy beam is included. Although this case failed to adequately model TASKA-M, the presence of warm ions is clear.

Figure 3.4-1 shows that the density computed by the BA code for the reference case input parameters compares quite well with the model potential. Recall that the density should satisfy
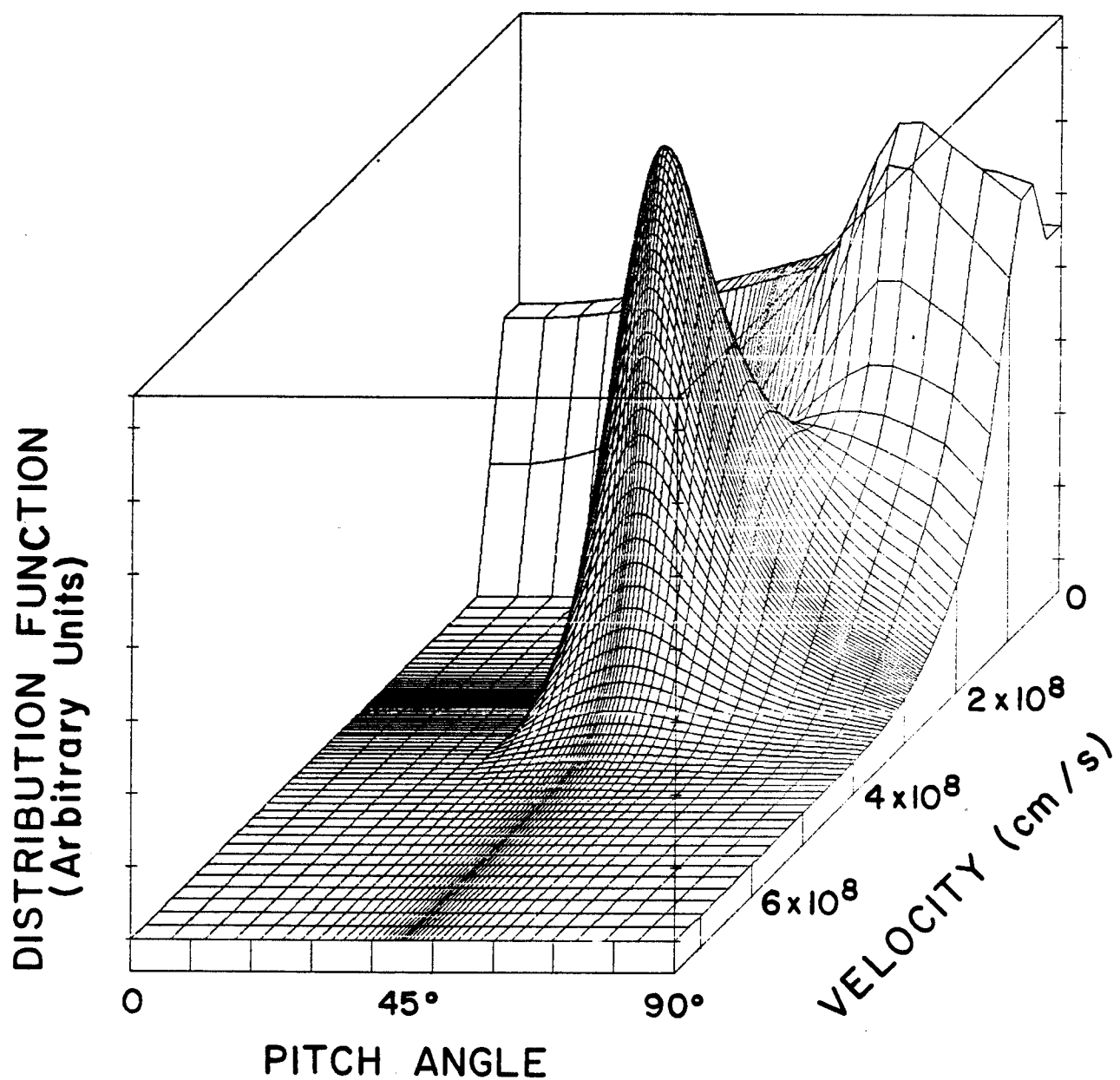
Fig. 3.4-5. Ion distribution function versus velocity and pitch angle, $\theta \equiv$ arccos $(v_{\parallel}/v)$, when 10 keV beam is present.

$$\phi(z) = T_e \ln \left[\frac{n(z)}{n_o}\right] \qquad (3.4-7)$$

where ϕ = 0 at the reference density n_o. Figure 3.4-2 compares the model magnetic field to that calculated from the magnet design of Chapter 9. The ion distribution function as a function of velocity and pitch angle, $\theta \equiv$ arccos $(v_\parallel/v)$, is shown in Fig. 3.4-6. Its "sloshing" ion nature is clearly brought out there. A contour plot of $f(v_\parallel, v_\perp)$ at the midplane is shown in Fig. 3.4-7. An important quantity for microstability analysis is the integral of the distribution function over the parallel velocity, $F(v_\perp)$; it is shown in Fig. 3.4-8, which also gives the analogous quantity, $F(v_\parallel)$.

Experimental evidence for the sloshing ion concept exists from the TMX-U experiment.[3] Figure 3.4-9a shows the angular distribution of the charge exchange flux in one TMX-U end plug; it is clearly peaked near the neutral beam injection angle of 47°. The BA code was used to model this flux, with the result shown as the solid line in Fig. 3.4-9a. The experimental data points fit the curve quite well. Figure 3.4-9b shows the sloshing ion axial density profile calculated from the charge exchange data. Other experimental support of the concept, particularly with regard to microstability, would be very useful.

The average ion energy of 98 keV is somewhat higher than the power balance value of 84 keV, while the bounce averaged $n\tau$ is lower, at 7.4×10^{12} cm^{-3} s compared to 1.0×10^{13} cm^{-3} s. Given the approximate nature of both calculations, however, the difference does not appear to be significant.

In summary, the model of TASKA-M physics used in the bounce average Fokker-Planck code reproduces the essential details of the configuration. The calculations also support the plasma power balance analysis used in Section 3.2 to choose the reference case operating point. Areas with the most potential for improvement in future designs are the neutral beam injection angle and the magnetic field axial profile.
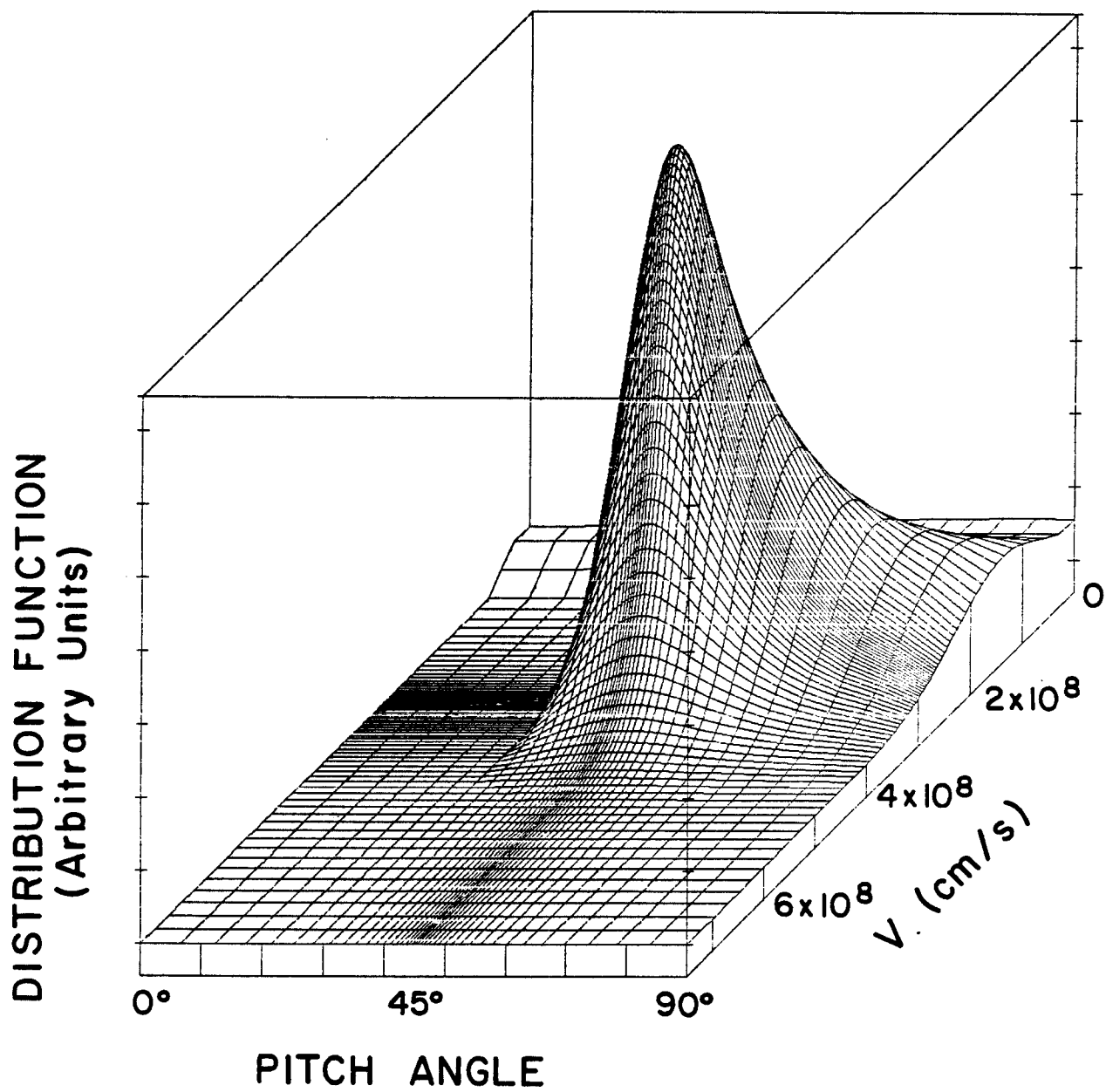
Fig. 3.4-6. Reference case ion distribution function versus v and θ.
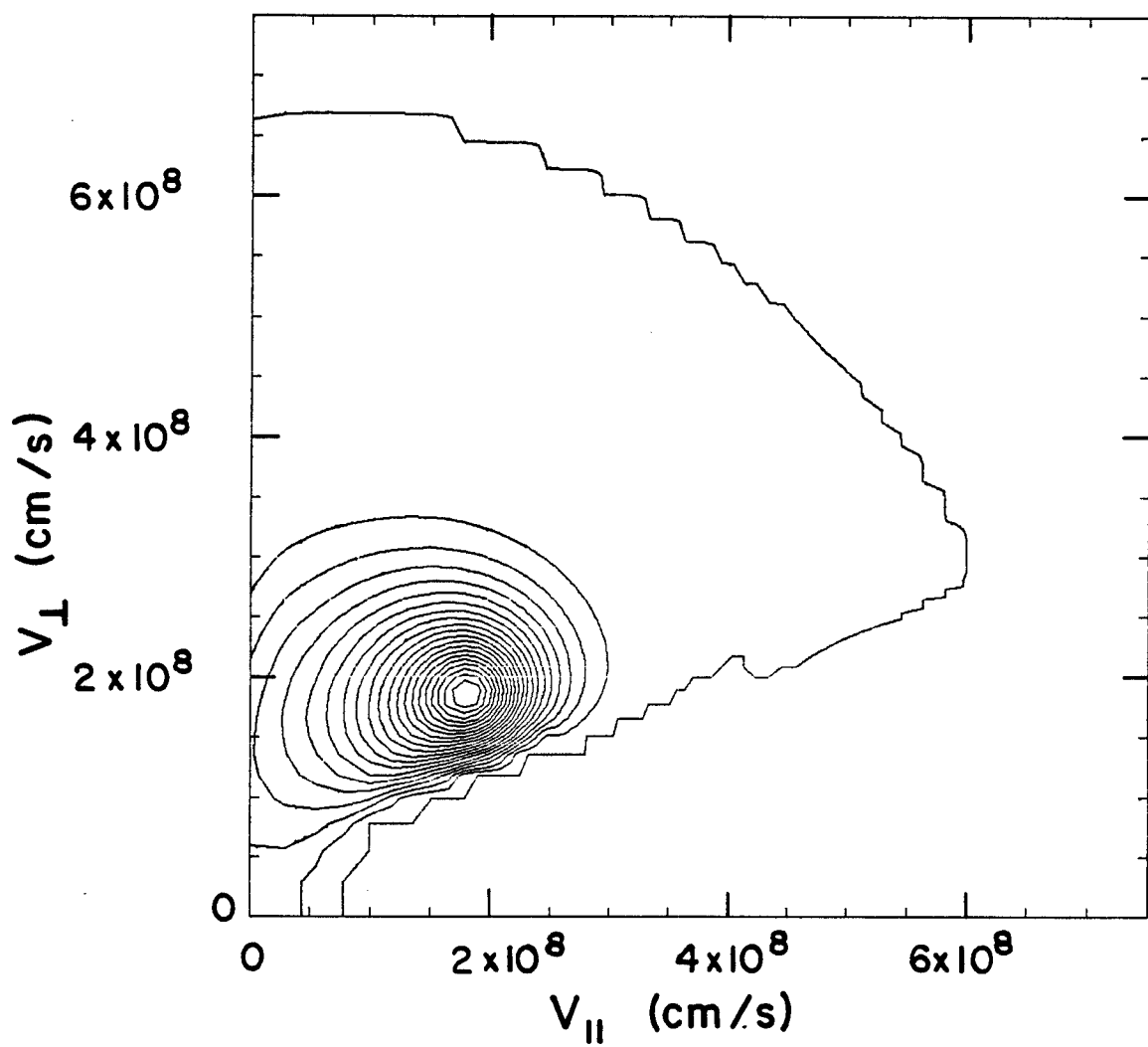
Fig. 3.4-7. Reference case ion distribution function versus $v_{\parallel}$ and $v_{\perp}$.
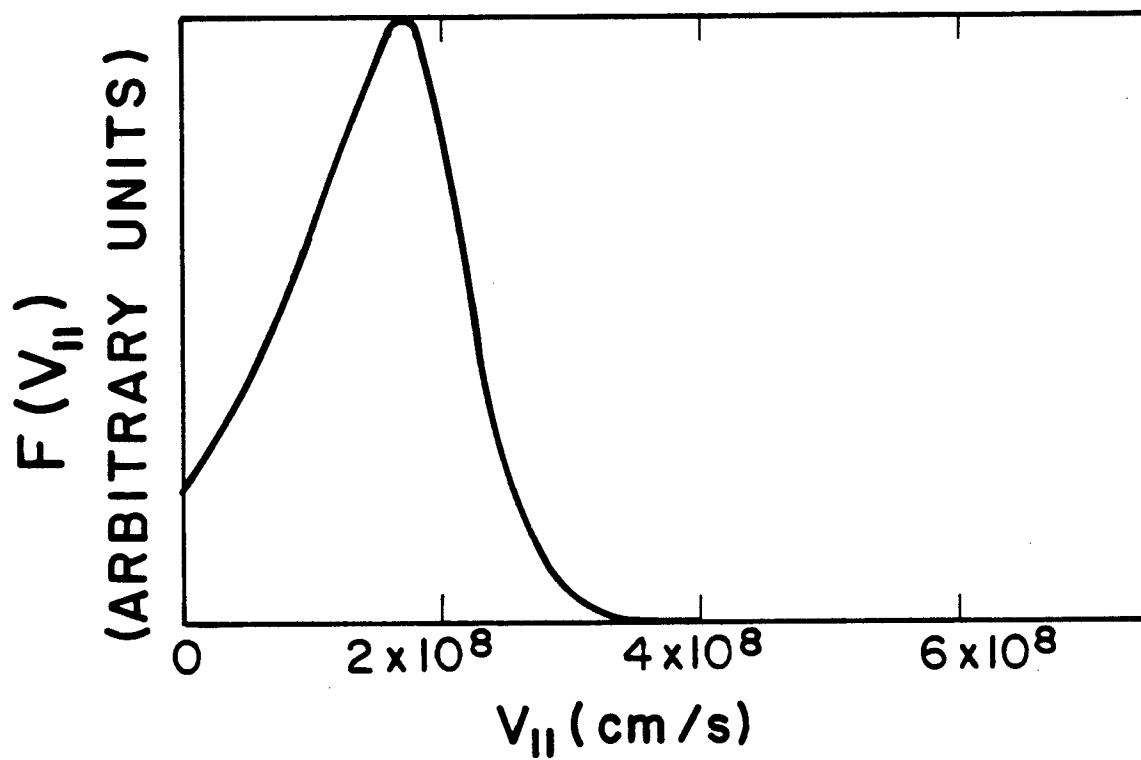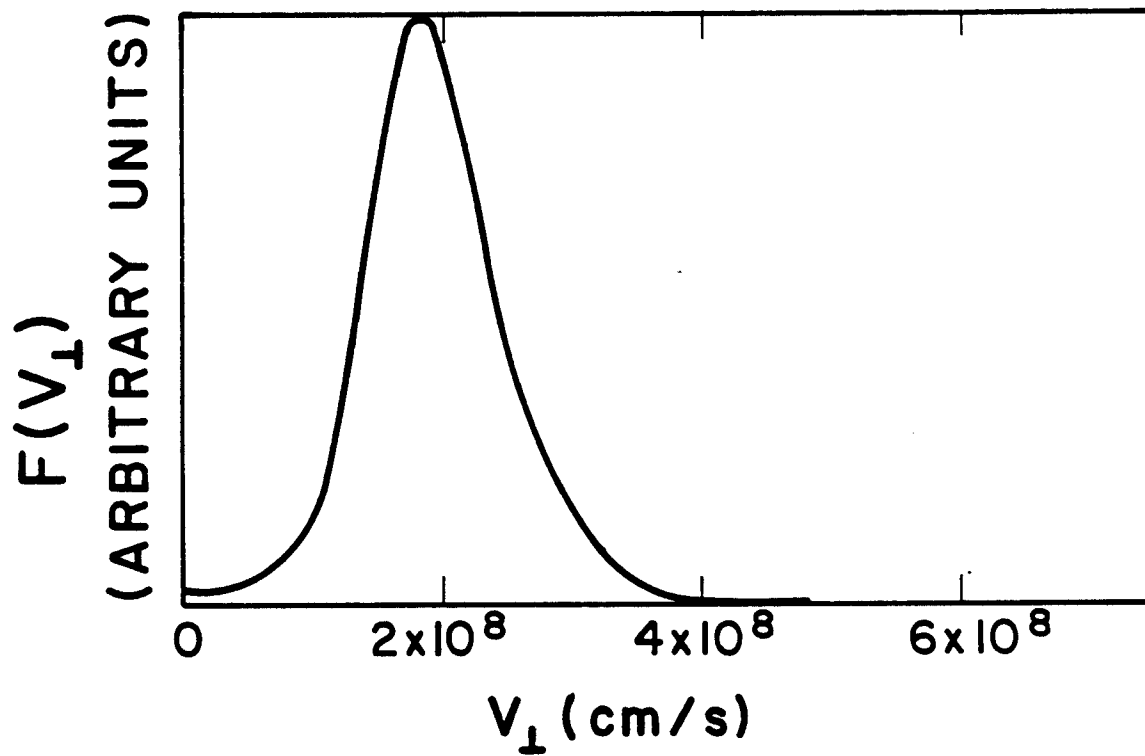
Fig. 3.4-8. (a) Distribution function integrated over $v_{\parallel}$. (b) Distribution function integrated over $v_{\perp}$.
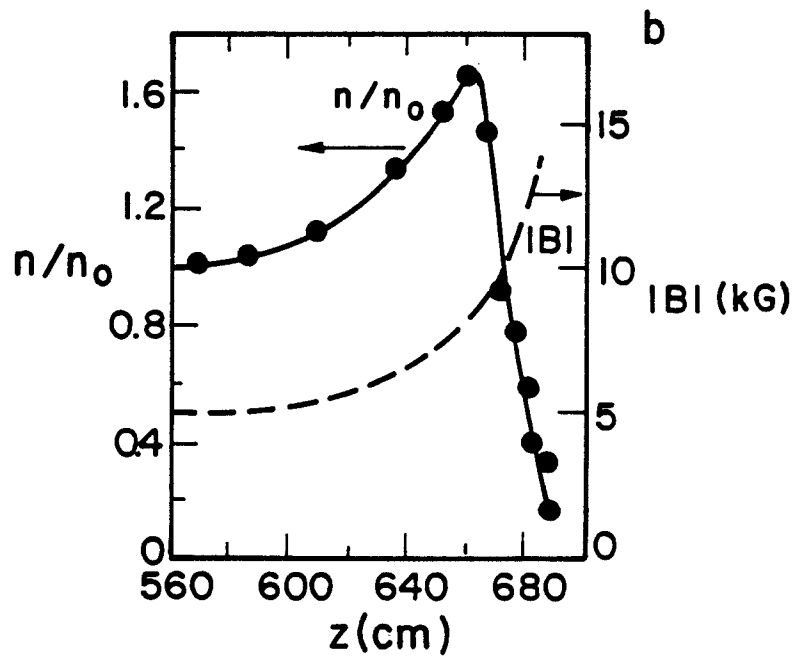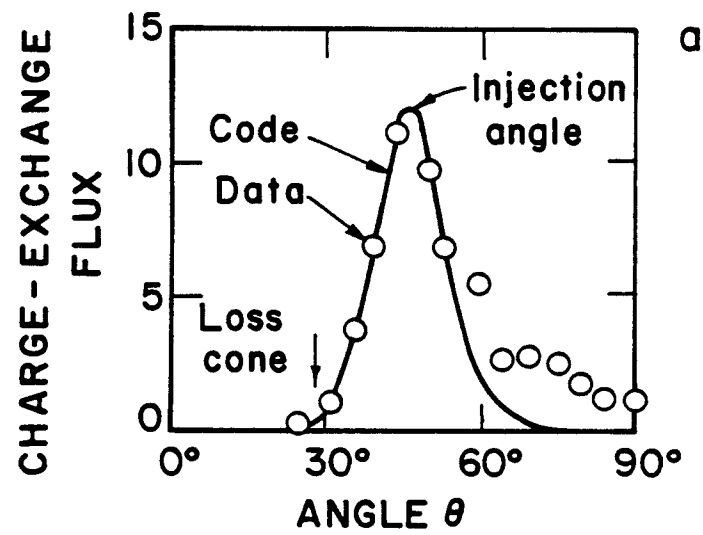
Fig. 3.4-9. (a) Angular distribution of TMX-U charge exchange flux.
(b) Sloshing ion axial density profile.

References for Section 3.4

1. T. Cutler, L.D. Pearlstein and M.E. Rensink, "Computation of the Bounce-Average Code," LLNL Report UCRL-52233 (1977).

2. B.G. Logan, A.A. Mirin, M.E. Rensink, Nucl. Fusion 20, 1613 (1980).

3. T.C. Simonen et al., Phys. Rev. Lett. 50, 1668 (1983).

3.5 MHD Stability

3.5.1 Introduction

The magnets and plasma of TASKA-M must be designed so that the plasma is MHD stable. As in TASKA,[1] only the interchange instability has been analyzed. Because of finite gyroradius effects, ballooning modes are expected to be stable unless one gets too close to the interchange stability boundary. The magnets, shown in Fig. 3.5-1, have been optimized so that the curvature of the magnetic field lines is good in the anchors where the plasma pressure is high and the magnetic field is low. For the optimized magnet set, the plasma pressure profile is varied to investigate the dependence of the MHD interchange mode stability on plasma parameters. The general result of this investigation is that TASKA-M in its base case plasma configuration is stable against MHD interchange modes.

3.5.2 Anchor Magnet Design

The anchor magnets have been designed to provide good curvature,

$$\kappa \equiv x \, \frac{\partial^2 x}{\partial z^2} + y \, \frac{\partial^2 y}{\partial z^2} \, , \qquad\qquad (3.5-1)$$

in the center of the anchor and a mirror ratio in the anchor of about 2.7. The minimum magnetic field in the center of the anchor has been set at 1 tesla by design. The anchor magnets have also been designed in such a way that a magnetic flux tube which is circular in the central cell is nearly circular in the center of the anchor.

The end magnets are shown in Fig. 3.5-1. The magnetic field profile is shown in Fig. 3.5-2. Each end cell magnet set consists of an inboard recircularizing coil between the yin-yang magnets and the high field central cell magnets. These recircularizers roughly cancel the quadrupole moments of the inside magnets of the yin-yang sets so that the flux tube is close to circular at the center of the anchor. There are no outboard recircularizers because, with the adopted end dump design, a circular plasma is not needed at the end dumps.

The magnetic field shown in Fig. 3.5-2 for the magnet set shown in Fig. 3.5-1 for half of the machine, has good curvature over most of the anchor cell. The curvature is very good on the outside half of the anchor cells which, as the following discussion shows, leads to global stability against
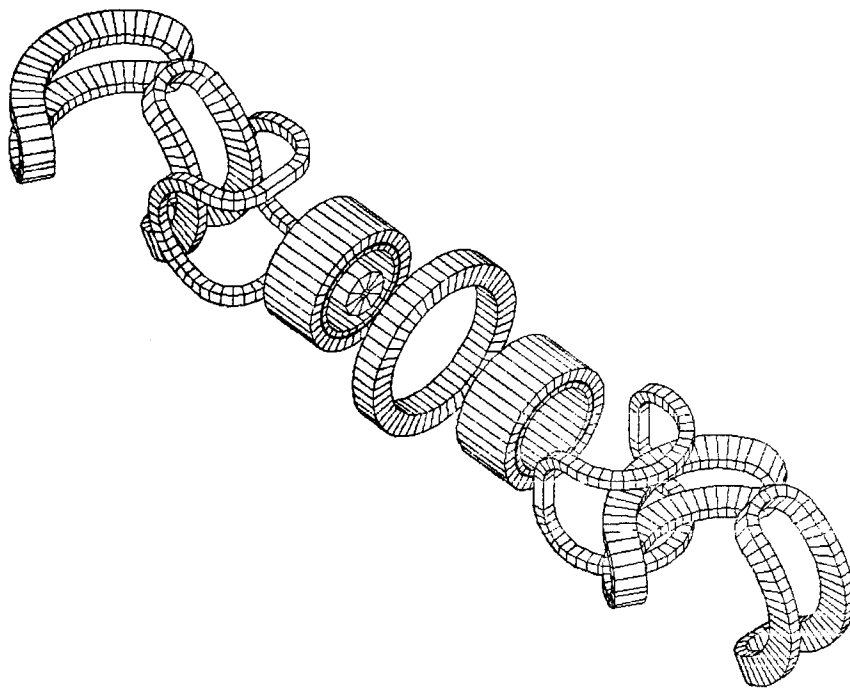
Fig. 3.5-1.   TASKA-M magnet coils.
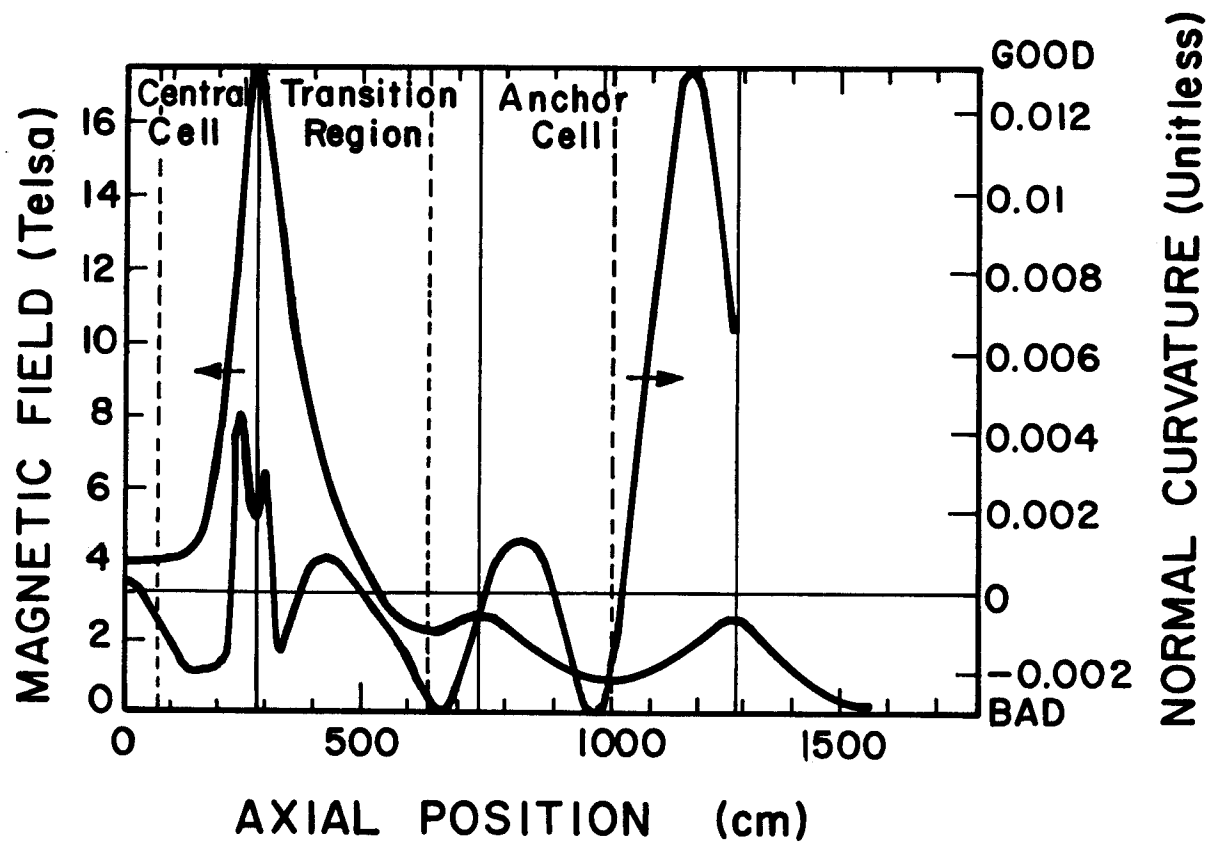
Fig. 3.5-2. Magnetic field and normal curvature of a TASKA-M flux line going through x = 5 cm, y = 5 cm, z = 0.

the MHD interchange mode. Figure 3.5-3 shows the positions of a flux line in the x-z and y-z planes where z is parallel to the axis of the machine. The reason for the worsening curvature on the inboard side of the anchor can be seen from these plots: the recircularizing coils and the rather large distance between the two yin-yangs on each side lead to a slight bowing out of the flux lines on the inside half of the anchor cells.

3.5.3 Plasma Pressure

Since the driving term for the MHD interchange instability is proportional to the plasma pressure times the curvature of the flux lines, it is required that the plasma pressure profile be known.

A model has been developed for the plasma pressure that considers three different regions: the central cell, the transition region and the anchor cell. The model uses components of the plasma ion pressure parallel and perpendicular to the local magnetic fields as calculated with the bounce-averaged Fokker-Planck computer code described in Section 3.4, which are denoted $P_{\parallel}$ and $P_{\perp}$ respectively. It has been assumed that the central cell has neutral beams injected at 45° while the anchor cells have 50° injection and $P_{\parallel}$ and $P_{\perp}$ are calculated accordingly for the different regions. The Fokker-Planck code provides $P_{\perp}$, $P_{\parallel}$ and the plasma density n as functions of $\psi \equiv B(z)/B_{min}$ where B_{min} is the minimum field in the magnetic mirror cell under consideration. Since B(z) is known from Fig. 3.5-2, $P_{\parallel}$, $P_{\perp}$ and n can be found as functions of z. In all regions, the plasma pressure has both electron and ion components. In the central cell the ion pressure is

$$P_{ion} = max \begin{cases} \frac{1}{2} \left(P_{\perp\,45^0}(z) + P_{\parallel\,45^0}(z) \right) \\ \\ \frac{1}{2} n_t T_e \end{cases}, \qquad (3.5-2)$$

where T_e is the electron temperature and n_t is the density in the transition region. The electron pressure in the central cell is

$$P_{el} = max \begin{cases} n(z)\ T_e \\ \\ n_t T_e \end{cases}. \qquad (3.5-3)$$
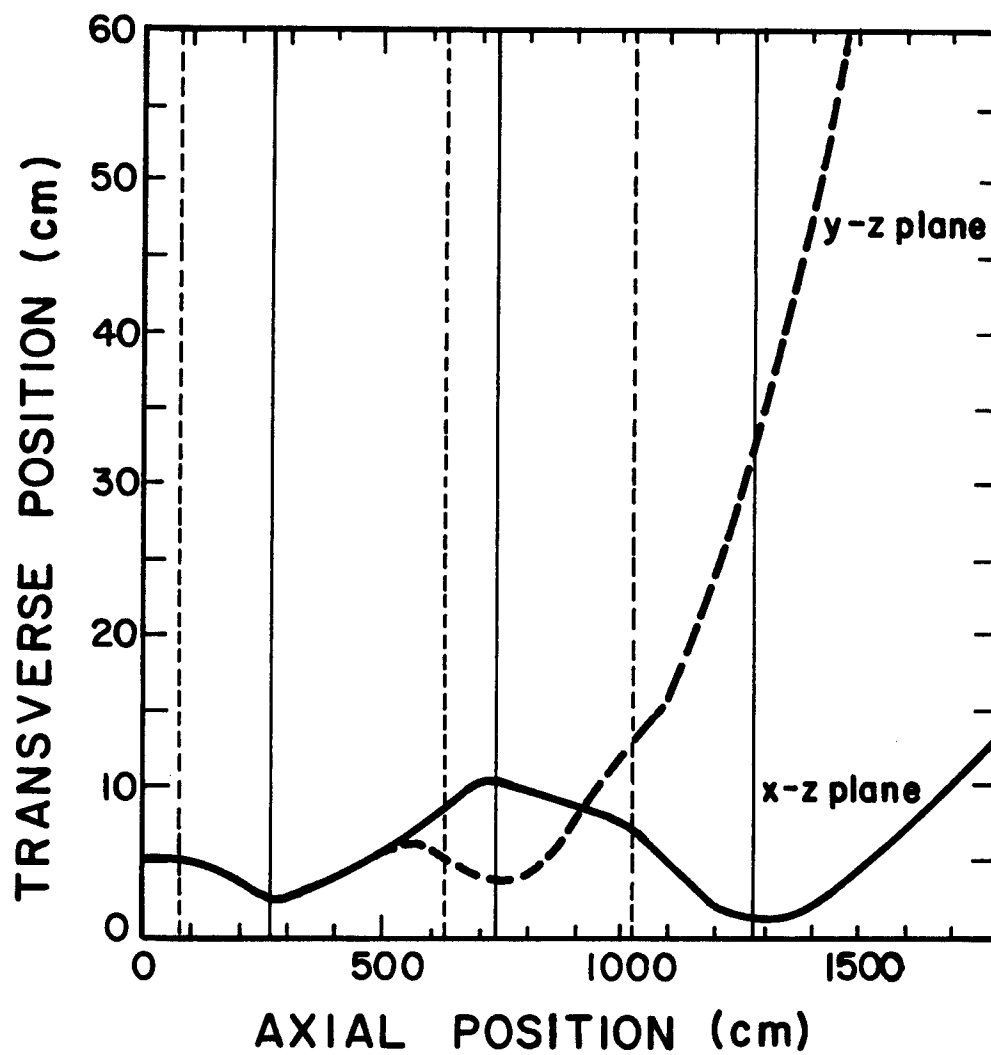
Fig. 3.5-3. Position of flux lines on TASKA-M in x-z and y-z planes.

In the transition regions, the pressure is assumed to be isotropic and the ion temperature is assumed to be half the electron temperature. The plasma density is assumed to be constant at n_t. The ion and electron pressures in the transition regions are thus

$$P_{ion} = \frac{1}{2} n_t T_e \qquad (3.5-4)$$

and

$$P_{el} = n_t T_e , \qquad (3.5-5)$$

respectively. In the anchor cells, the electron pressure is taken to be the same as in the transition regions expressed in Eq. 3.5-5. In fact, the electron density in the anchor should vary like the ion density but this will not make much difference to the TASKA-M base case. The ion pressure is

$$P_{ion} = \frac{1}{2} \frac{E_{HA}}{E_{HC}} \frac{n_t}{n_c} \left(P_{\perp 50^0}(z) + P_{\parallel 50^0}(z) \right) , \qquad (3.5-6)$$

where E_{HA} is the average energy of the ions in the anchor and E_{HC} is the average energy of ions in the central cell, where it has been assumed both here and in Eq. 3.5-1 that the Fokker-Planck calculations are done to yield an average ion energy of E_{HC}. If the Fokker-Planck calculations yield an average ion energy of something other than E_{HC}, the ion pressures must be appropriately scaled in average ion energy.

The pressure profile for the TASKA-M base case is shown in Fig. 3.5-4. The corresponding plasma density profile is shown in Fig. 3.5-5. Notice that the sloshing ions in the central cell and the anchor cells cause peaks in the pressure at the points where the ions are turning against increasing magnetic fields. This effect is very important in the outside halves of the anchor cells where the pressure peaks coincide with the peaks in good curvature. The importance of this to the MHD interchange stability is made clear when one examines the product of the pressure and the curvature divided by the magnetic field plotted against axial position in Fig. 3.5-6. One should notice the dominating peak at the outside edge of the anchor which stabilizes TASKA-M against MHD interchange modes. The peak in the pressure in the central cell is seen to be not a great problem because the bad curvature at the pressure peak is not large compared to the good curvature in the anchor. Also the
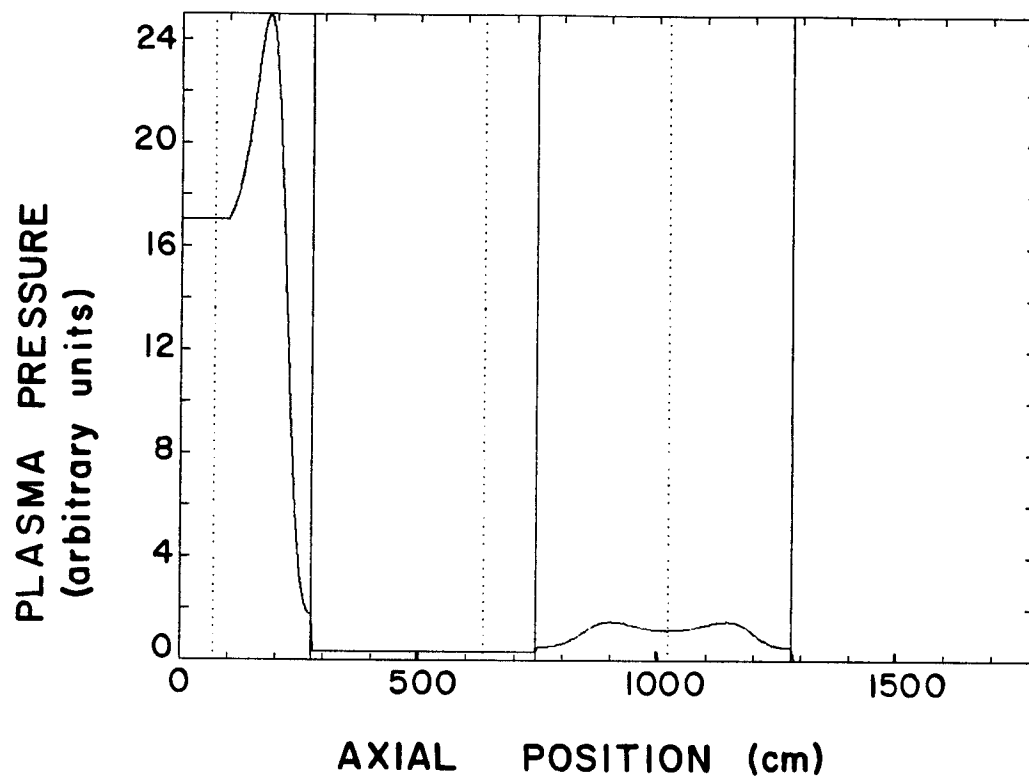
Fig. 3.5-4 Plasma pressure for TASKA-M base case.
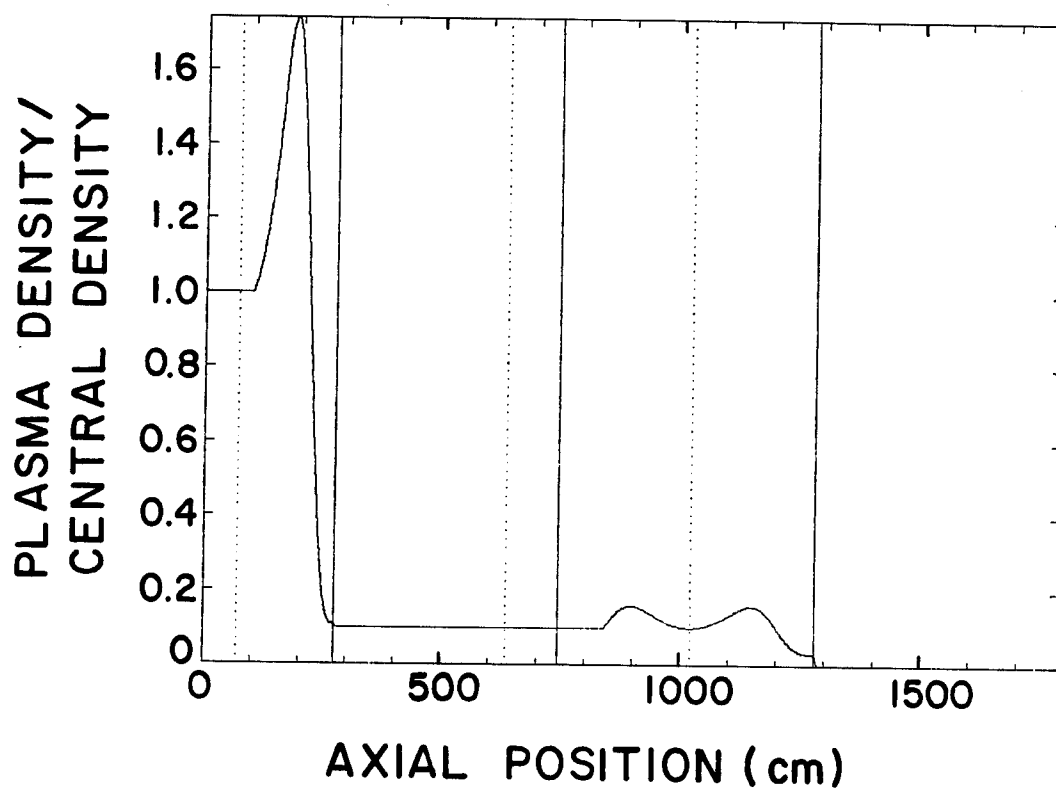
Fig. 3.5-5 Plasma density divided by plasma density in center of machine for TASKA-M base case.
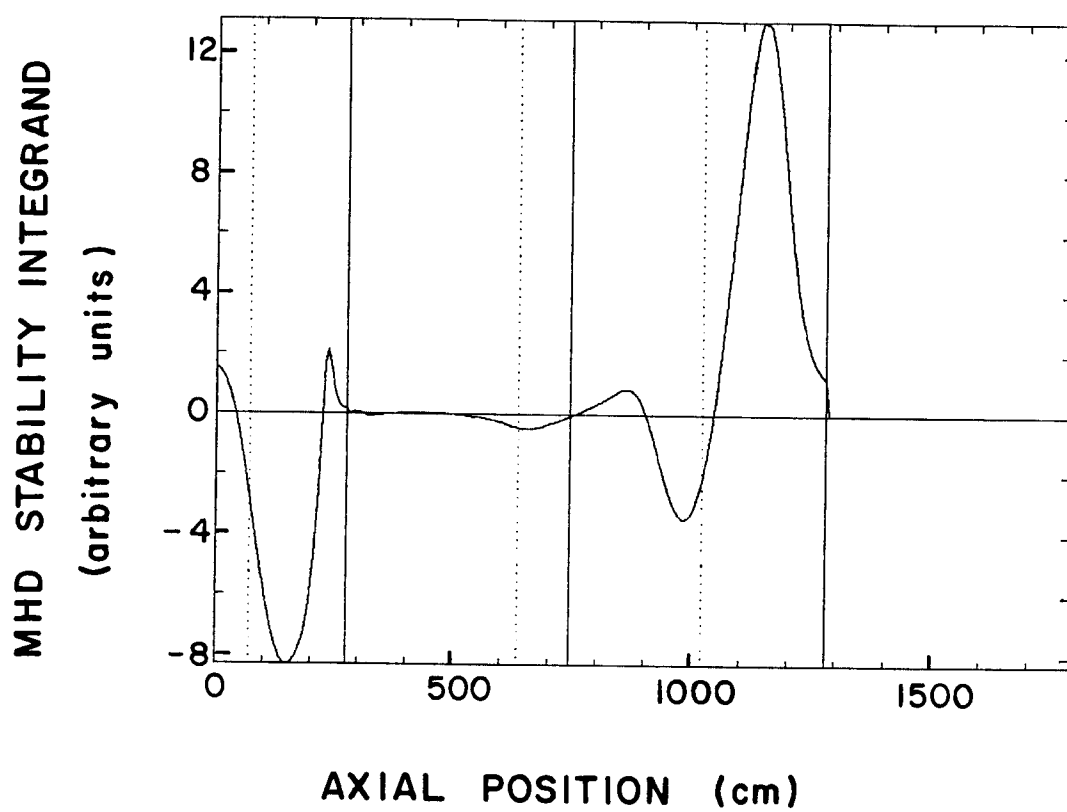
Fig. 3.5-6 Pressure divided by magnetic field, weighted curvature, $P\kappa/B$, for TASKA-M base case.

magnetic field is lower in the anchor, increasing the importance of the good curvature in the anchor.

3.5.4 MHD Stability Analysis

The stability of TASKA-M to the MHD interchange instability is analyzed by considering the integral

$$I \equiv \int_0^L ds \, K(s) \, P(s)/B(s) \, , \tag{3.5-7}$$

where s is the distance along the flux line of interest and L is the length of that flux line, starting at the center of the machine. The flux line which passes through the point x = 5 cm, y = 5 cm at the center of the machine (z = 0) is considered to be most useful for MHD stability calculations. When I > 0 the machine is stable, if I < 0 it is MHD unstable.

This is done with the code called STAB5, which has been created from one of the STAB series codes developed at LLNL.[2] STAB5 searches for the value of the average ion energy in the anchor cells, E_{HA}, which makes I = 0 for a given value of n_t/n_{cc}. This is the condition for a so-called marginally stable case. As one can see from this scheme and from the plasma pressure model described in Section 3.5.3, the plasma density in the anchor remains in the same proportion with the plasma density in the transition.

One particular marginally stable case has n_t = 0.01 n_c and E_{HA} = 1.14 keV. The plasma pressure in the anchor required for this case to be stable is low because there is such large good curvature in the anchor. This leads to the low value for the minimum E_{HA} required for stability. It has been found that the most destabilizing part of the integral in Eq. 3.6-7 occurs at the points in the central cell where the sloshing ions are turning while the sta-bilizing part is due almost completely to the good curvature in the outer part of the anchor cells.

A series of calculations have been carried out with STAB5 for a variety of values for n_t/n_c. The values of E_{HA} giving marginal stability are plotted against n_t/n_c in Fig. 3.5-7. This value for E_{HA} decreases with increasing n_t/n_c because the density of the anchor is tied to n_t and when the anchor and transition regions are taken as a single cell, this cell has net good curva-ture. Thus, increasing n_t increases the plasma density in a net good curva-ture region and reduces the required temperature of the region. One should
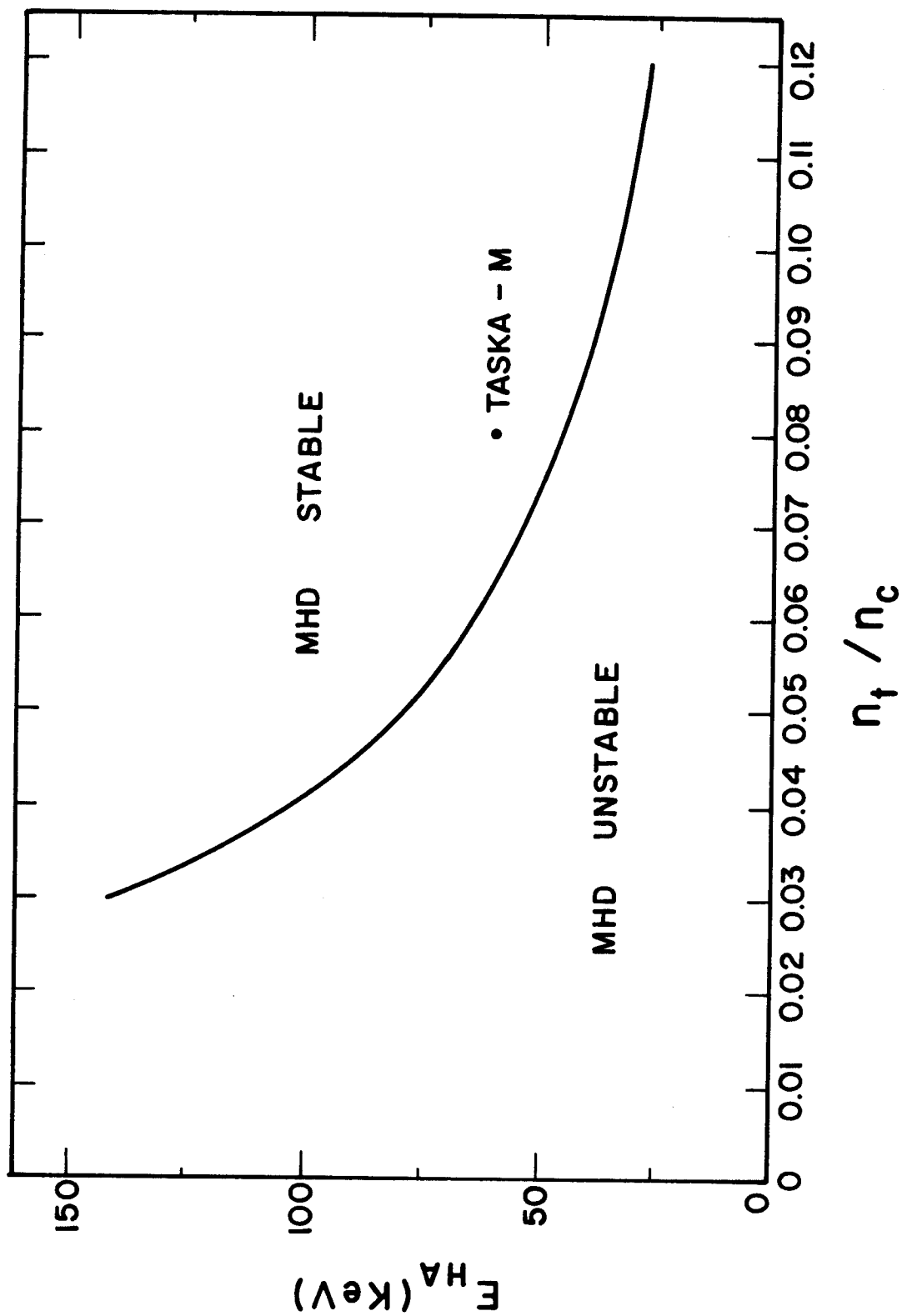
Fig. 3.5-7. Stability diagram for TASKA-M in E_{HA} versus n_t/n_c plane.
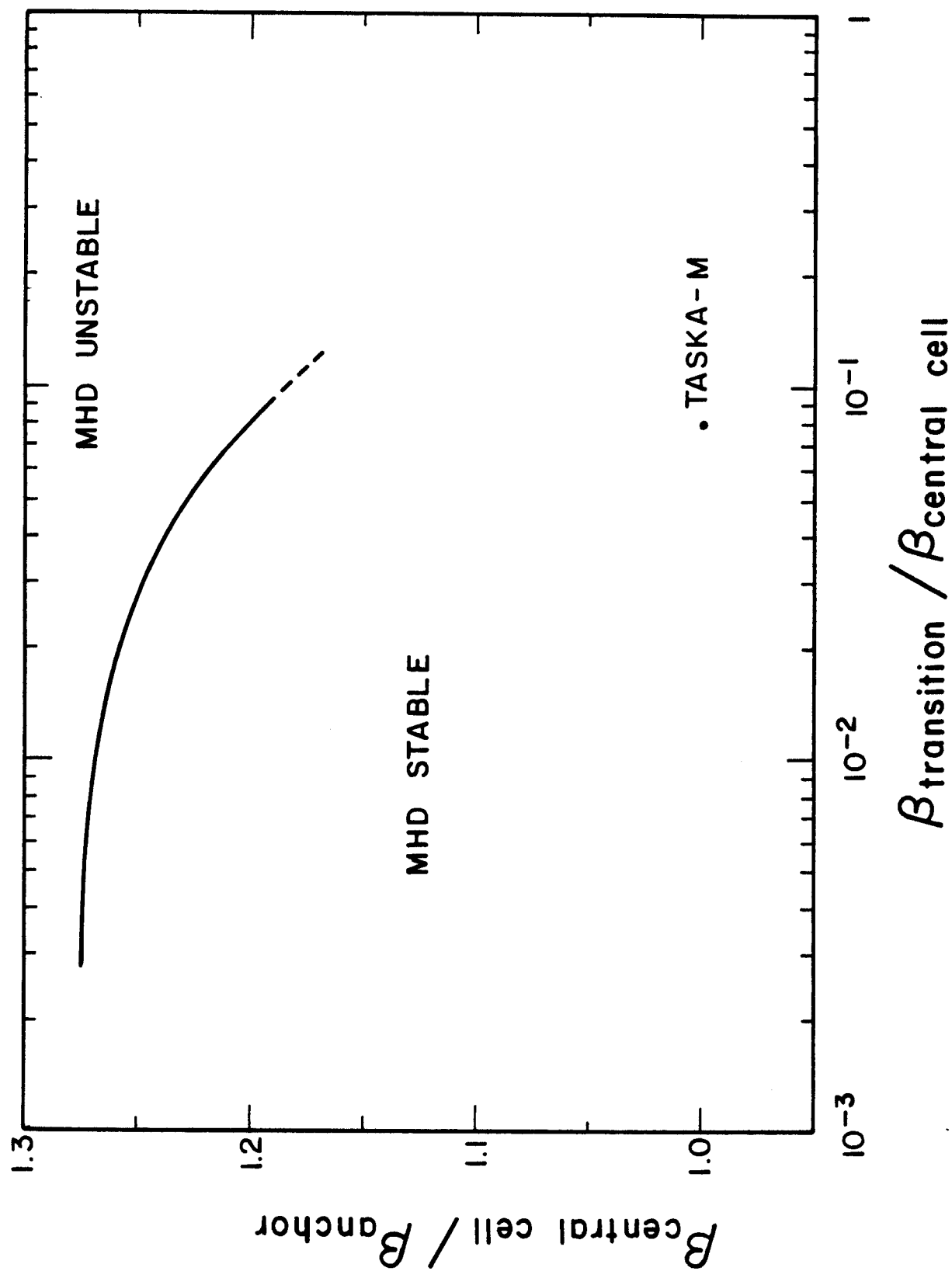
Fig. 3.5-8. Conventional stability diagram for TASKA-M.

notice the point for TASKA-M which is very far into the stable region of the curve.

A more conventional stability curve is given in Fig. 3.5-8, where $\beta_{central\ cell}/\beta_{anchor}$ is plotted against $\beta_{transition}/\beta_{central\ cell}$. If the TASKA-M base case point could be put on this plot, it would show that TASKA-M is very stable against the MHD interchange mode. The base case has $\beta_{transition}/\beta_{central\ cell} = 0.1$ and $\beta_{central\ cell}/\beta_{anchor} = 1.0$, which is well below the marginal stability curve.

Thus, the results shown in Figs. 3.5-5, 3.5-7 and 3.5-8 strongly show that TASKA-M is stable against MHD interchange modes. The temperature or density of the central cell could be increased or the magnetic field lowered in the central cell and the plasma would remain stable.

References for Section 3.5

1. R.R. Peterson, "MHD Stability Analysis for TASKA," Fusion Power Associates Report FPA-83-1 (February 1983).

2. Brad Johnson, LLNL, private communication.

3.6 Central Cell Microstability

3.6.1 Overview

The term microinstabilities covers a wide variety of modes, the common feature being that the plasma distribution as a function of velocity and space is not in equilibrium. In physical terms, this generally implies ion temperature anisotropy, $T_\perp > T_\parallel$, an inverted ion energy population, $df/dv_\perp^2 > 0$, or free energy for radial expansion, ∇n, $\nabla T \neq 0$. The concern with microinstabilities in TASKA-M is that, if they appear, ion loss will be enhanced and will lead to increased power requirements. This section will discuss a small part of the vast literature on microinstabilites, but the reader is referred to Ref. 1 for a more complete treatment and a guide to further references. Much of the discussion which follows is based on Ref. 1.

Physically, microinstabilities arise from the coupling of a plasma wave with a dissipative effect. Dissipation breaks phase relationships and allows growth of a wave which would otherwise oscillate at a constant amplitude. A variety of waves may be present in a plasma; the main ones which contribute to microinstability are ion drift waves, electron plasma waves, Alfvén waves, ion Bernstein waves, and lower hybrid waves. Note, however, that mode names are merely guides, since distinctions blur as the plasma gets farther removed from theoretical conditions and idealized limits. Dissipative effects of importance are electron Landau damping, ion cyclotron and cyclotron harmonic damping, collisional damping, and turbulence-induced damping. The instabilities which are presently thought to be the most potentially dangerous are the drift cyclotron loss cone mode (DCLC), the axial loss cone mode (ALC) or its convective version (CLC), the Alfvén ion cyclotron mode (AIC), the negative energy wave (NEW), the drift cyclotron instability (DCI), the two component mode, and the lower hybrid mode (LH). The relationships between the instabilities, the waves, and the dissipative effects are shown in Fig. 3.6-1.[1]

Most of the analysis presented in this section will concentrate on loss cone modes, since their mode of relaxation is to try to fill the loss cone. Anisotropy-driven modes, on the other hand, tend to remove the anisotropy, which may or may not lead to particle loss. The evolution of the modes in time is that unstable ion distributions modify themselves naturally to remove the anisotropy, or partially fill the loss cone to achieve marginal stability.

Dissipation \ Wave	Electron plasma	Ion drift	Ion Bernstein	Lower hybrid	Alfvén	
Electron Landau damping			Negative energy wave }NEW			
			Length			Controlling feature

Ion cyclotron damping	Electron plasma	Ion drift	Ion Bernstein	Lower hybrid	Alfvén	
	Convective loss-cone mode }CLC	Drift cyclotron / Lower hybrid drift	Dory Guest Harris }DGH[a]	Modified negative mass[b]	Alfvén ion cyclotron }AIC	
	Length Beta	Radius Beta Density	Density / Peaked energy / Field-line fanning	Density Anisotropy	Beta Anisotropy Length	Controlling feature
	Axial loss-cone mode }ALC	Drift cyclotron loss cone }DCLC		Two-component		
	Length Beta Density	Radius Beta Density	Temperature ratio Density			Controlling feature

a Strictly speaking, this mode was not destabilized by cyclotron damping, but did arise from the negative-energy nature of the medium.

b Here the anisotropy was the drive, but the mode also required the inclusion of the ion-bounce motion.

Fig. 3.6-1. Relationships between microinstabilities, waves, and dissipative effects.

The theoretical results presented here must be kept in perspective: In general, experimental results are encouraging and the plasma tends to be more stable than theory predicts. There are numerous explanations for this, but most arguments are qualitative, and a single, comprehensive theory including all effects neither exists nor is likely to exist for some time. Some considerations include:

- Geometry can be crucial. Almost all of the theory is highly idealized, yet details of the modes and, in particular, stability boundaries often depend strongly on geometry.

- Stability boundaries are sensitive to the choice of model ion distribution function. Analytical work utilizes a variety of models, none of which reproduces all of the details of distribution functions as given by the Fokker-Planck codes. Figures 3.6-2, 3.6-3 and 3.6-4 compare the ion distribution function given by the BA code (see Section 3.4) to the most common models. Further discussion will follow.

- Most existing theory uses linearized equations. This is adequate for finding unstable modes, but says nothing about the amplitude level at which the mode saturates due to nonlinear effects. Some modes may remain at levels with insignificant degradation of plasma confinement. A possible example of this appears in the present TMX-U experiment at Lawrence Livermore National Laboratory (LLNL), where low level fluctuations at about 1.8 times the ion cyclotron frequency were observed but did not appear to cause enhanced losses.[2]

- The next step beyond linear theory is quasilinear theory, in which fluctuations maintain the plasma at marginal stability.[3] The theory has had some success but, being a diffusive theory, predicts a broad spectrum[4] in contrast to the observed single frequency of the mode in TMX-U.[2]

- Other nonlinear processes are possible, such as nonlinear Landau damping, nonlinear frequency shifts, particle trapping in waves, three wave resonances, and orbit diffusion.[1] Microstability theory has only begun to examine most of these effects.

TASKA-M achieves microstability through two features: an ion distribution peaked off-midplane (sloshing ions) and a warm plasma component trapped in the resulting potential dip. This differs from other designs such as the MARS thermal barrier tandem mirror reactor design and the TMX-U experiment,
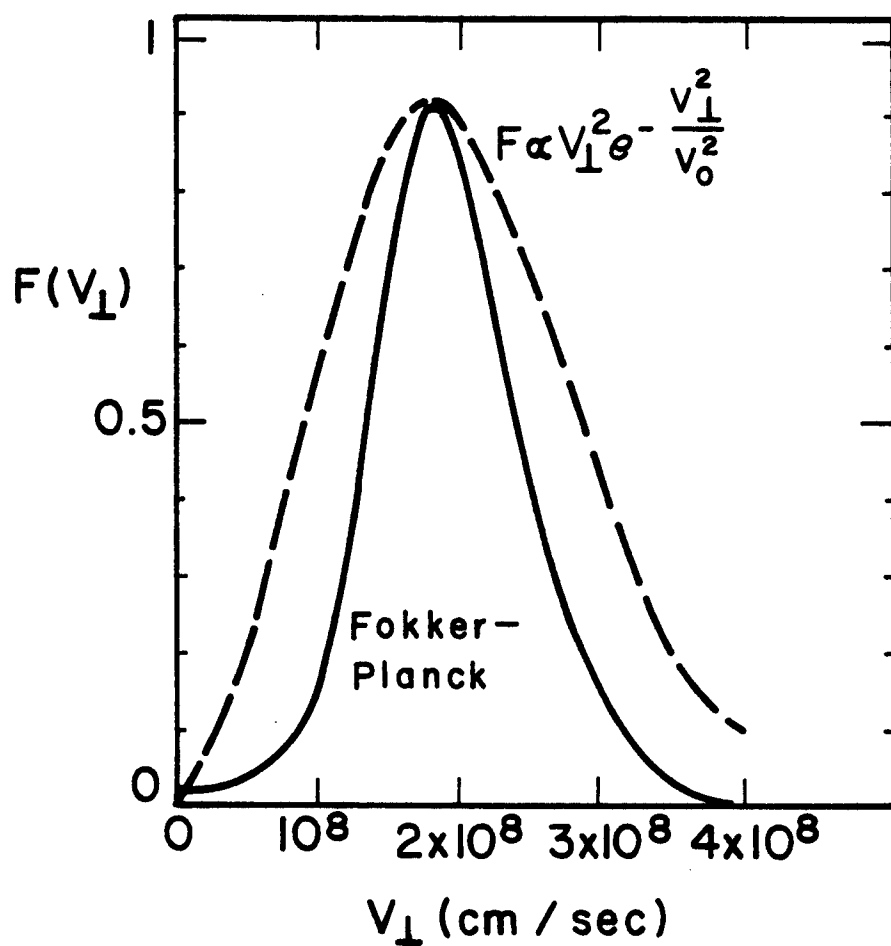
Fig. 3.6-2.   Model ion distribution function $F(v_\perp) \sim v_\perp^2 \exp(-v_\perp^2/v_0^2)$ compared to Fokker-Planck code result.
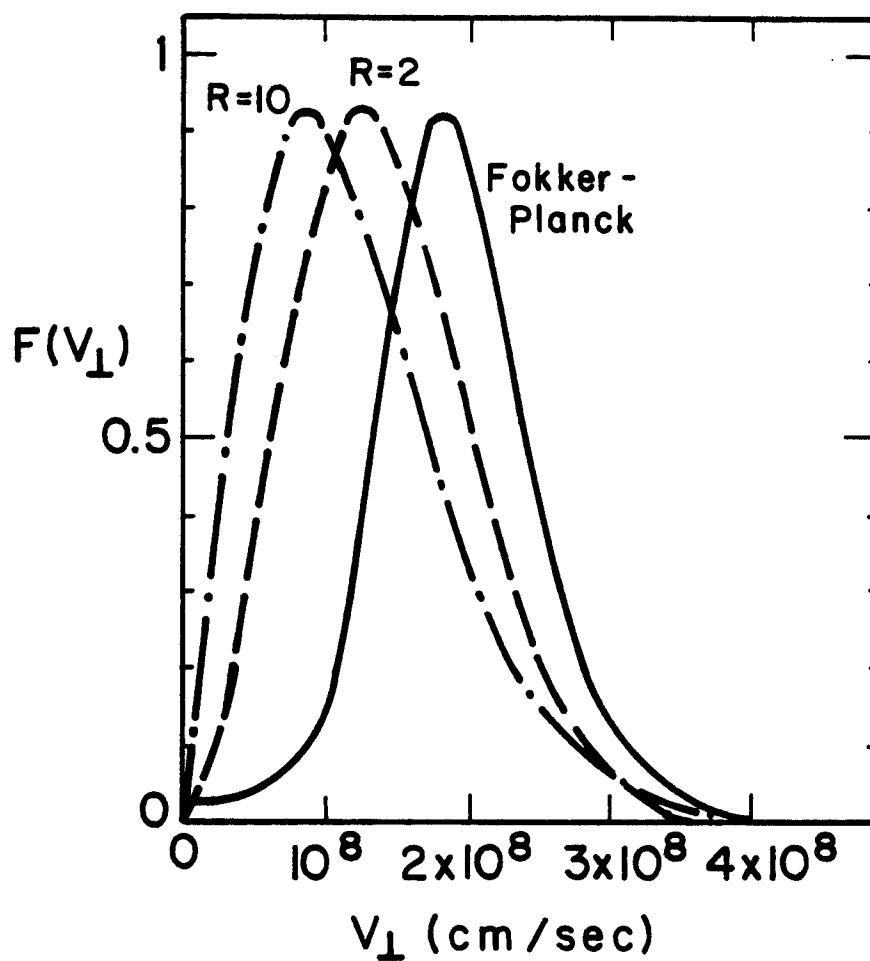
$$F(V_\perp) \propto e^{-\frac{V_\perp^2}{V_H^2}} - e^{-R\frac{V_\perp^2}{V_H^2}}$$

CORRECT $\bar{E}_\perp$

INCORRECT PEAK LOCATION

Fig. 3.6-3.   Fokker-Planck result compared to model ion distribution function (Eq. 3.6-8) normalized for average energy and peak $F(v_\perp)$.

$$F(V_\perp) \propto e^{-\frac{V_\perp^2}{V_H^2}} - e^{-R\frac{V_\perp^2}{V_H^2}}$$

CORRECT PEAK LOCATION

INCORRECT $\bar{E}_\perp$
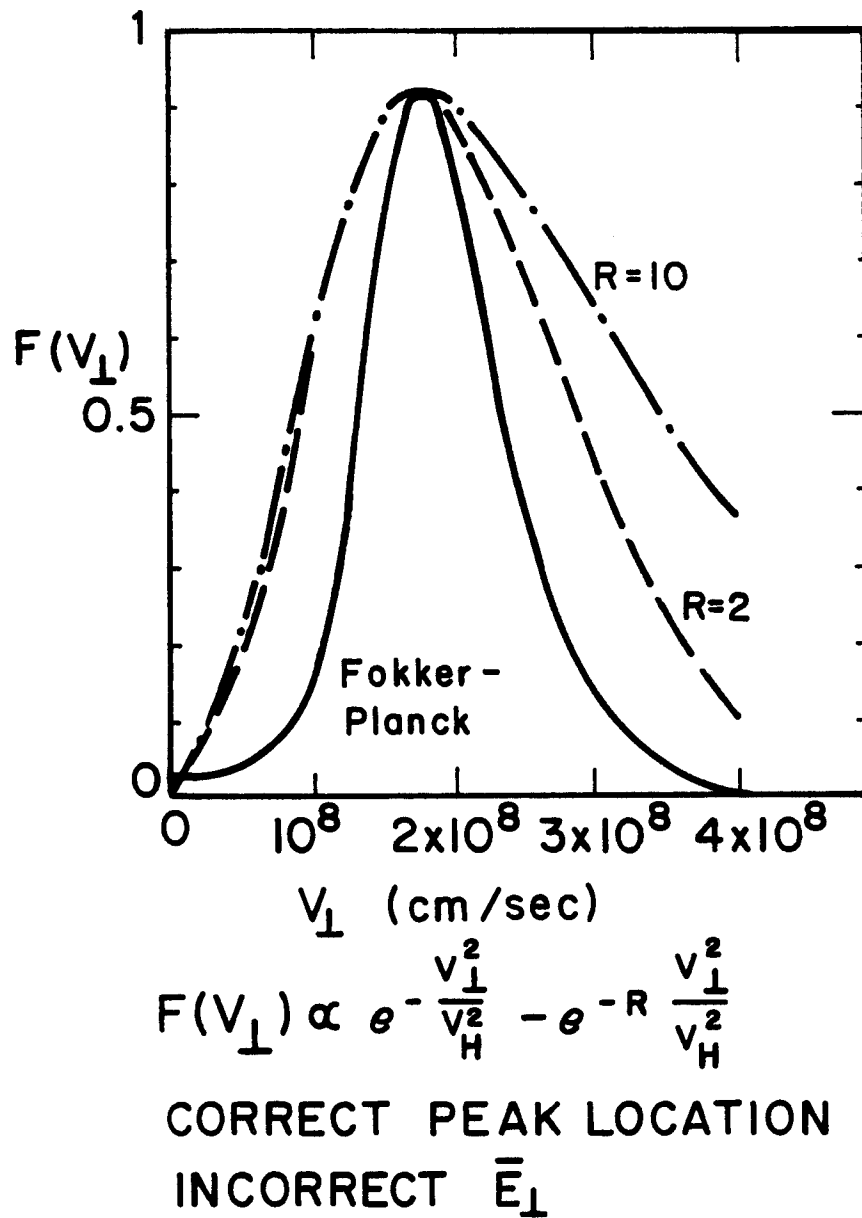
Fig. 3.6-4. Fokker-Planck result compared to model ion distribution function
(Eq. 3.6-8) normalized to peak $F(v_\perp)$ and peak $v_\perp$.

where warm ions partially fill the loss cone at one of the density peaks. The lack of warm plasma at the peaks prompts the question of whether modes localized there can arise. No analytic criteria are available, such as exist for the DCLC flute mode. Therefore, numerical solution of a complicated differential equation with the LLNL MICE code[5,6] or the MIT microstability code[7] is required. However, versions of the MICE code exist only without electostatic potentials for the original 2XIIB configuration or for thermal barrier tandem mirrors such as MFTF-B. No code completely suitable for TASKA-M is extant. Attempts were made to approximate TASKA-M physics with both the 2XIIB and MFTF-B versions of MICE, but an acceptable resolution of the question was not attained. For the purposes of this study, therefore, the question of microstability was approached by utilizing existing analytic theory and by extrapolating as needed. The area is clearly one worthy of major effort in future studies, since the microstability of a single cell has implications for many applications. Since the theoretical models are very complicated, experimental results will, eventually, provide the only completely reliable answers.

An outline of relevant microstability theory will now be presented. The reader is referred to Refs. 1, 8 and 9 for derivations and further details.

At its most basic level, the analysis starts with the linearized Vlasov equation and Maxwell's equations. Combining these eventually leads to an equation for the perturbed electrostatic potential along the magnetic field:[9]

$$\omega_{ci} \frac{d}{ds} \left(\frac{k_\perp^2 c^2}{k_\perp^2 c^2 + \omega_{pe}^2} \right) \frac{\omega_{pe}^2}{\omega^2 \omega_{ci}} \frac{d\phi}{ds} - k_\perp^2 \{\phi + F_e\phi + F_i\phi\} = 0 \qquad (3.6-1)$$

where s measures distance along B. The imaginary part of the solution for ω gives growth or damping depending on sign. The first term is the fluid electron response along the magnetic field, F_e gives the electron response, and $F_i\phi$ gives the ion response. The notation is standard and is given in Ref. 9. An eikonal approximation,

$$\phi \sim \phi(r,s)e^{ik_\perp r} ,$$

where $\phi(r,s)$ varies slowly with r, has been used since the modes of interest tend to have short perpendicular wavelengths, $k_\perp \rho_i > 1$. The electron response is given by[5]

$$F_e = \frac{\omega_{pe}^2}{\omega_{ce}^2} + \frac{1}{k_\perp^2 \lambda_D^2} \left\{ (1 - \frac{\omega_{*i}}{\omega})(1 + \frac{1}{2} [\frac{1 - \frac{\beta}{2}\phi_2 - \frac{\omega}{\omega_{ci}}(1 + \phi_2)}{1 - \frac{\omega}{\omega_{ci}}(1 + \phi_2)}]) \right\} \qquad (3.6-2)$$

where

$$\phi_2 \equiv -\int_0^\infty dv_\perp^2 \, f_e(v_\perp^2)(\frac{\omega - \omega_{*e}}{\omega + \omega_{*e}v_\perp^2 \frac{\beta}{2}}) . \qquad (3.6-3)$$

The first term arises from electron polarization, while the second gives electromagnetic contributions. For the ions, $F_i\phi$ may be written

$$F_i\phi = \sum_n M^n\phi \qquad (3.6-4)$$

and two cases exist:

1. For ω not near ω_{ci}, a fluid approximation suffices, in which parallel kinetic effects are ignored and only perpendicular kinetic effects are retained,

$$M^n_{fluid} = \frac{\omega_{pi}^2}{k_\perp^2} \int d^2v_\perp \, (n\omega_{ci} \frac{\partial f}{\partial v_\perp^2} - \frac{\partial f}{\partial x_\perp} \frac{k_\perp}{\omega_{ci}}) \frac{J_n^2(k_\perp v_\perp/\omega_{ci})}{\omega - n\omega_{ci}} . \qquad (3.6-5)$$

2. For $\omega \approx n\omega_{ci}$, parallel ion thermal effects must be considered, leading to

$$M^n_{res} = -i \frac{\omega_{pi}^2}{k_\perp^2} \int d^3v \, (\frac{\partial f}{\partial v_\perp^2} n\omega_{ci} - \frac{\partial f}{\partial x_\perp} \frac{k_\perp}{\omega_{ci}}) J_n^2(k_\perp v_\perp/\omega_{ci})$$

$$\qquad (3.6-6)$$

$$\times \int_{-\infty}^t dt' \exp\{i \int_{t'}^t dt'' [\omega - n\omega_{ci}(t'')]\} .$$

Various limits of these equations lead to the results to be discussed in the following sections.

In order to solve the dispersion relation, Eq. 3.6-1, model ion distribution functions are required. However, in order to make the problem amenable to analytic solution, models are used which do not necessarily fit the Fokker-Planck code distribution functions very well. In particular, the TASKA-M central cell ion distribution is not closely approximated by any of the standard models. Figure 3.6-2 shows the BA code distribution function (see Section 3.4) and one of the simplest models,

$$F(v_\perp) \equiv \int_{-\infty}^{\infty} dv_\parallel \, f(v_\parallel, v_\perp) \sim v_\perp^2 \, e^{-v_\perp^2/v_0^2} \qquad (3.6\text{-}7)$$

where $v_0^2 = 2\overline{E}_\perp$, $\overline{E}_\perp$ is the average energy, and mass is normalized to one. Obviously, neither the velocity spread nor $dF/dv_\perp$ is very close for the model. The model used for most of the DCLC/ALC references given here and for the MICE code is (in its essential form)

$$F(v_\perp) = \frac{1}{v_H^2 - v_h^2} \left[e^{-v_\perp^2/v_H^2} - e^{-v_\perp^2/v_h^2} \right] \qquad (3.6\text{-}8)$$

where $v_h^2 = v_H^2/R$ and R is a parameter. The average perpendicular ion energy resulting from this distribution is

$$\overline{E}_\perp = \frac{v_H^2}{2} + \frac{v_h^2}{2} = \frac{v_H^2}{2} \left(\frac{R+1}{R}\right)$$

and the distribution peaks at

$$v_\perp = \left(\frac{R \ln R}{R^2 - 1}\right)^{1/2} \left(2\overline{E}_\perp\right)^{1/2} .$$

The best fit to the BA code distribution function is given by matching $\overline{E}_\perp$ and the peak $F(v_\perp)$ value (Fig. 3.6-3) rather than having the distributions peak at the same $v_\perp$ (Fig. 3.6-4), but neither alternative is particularly attractive. The values of $dF/dv_\perp$ appear close in Fig. 3.6-3, but they occur at different velocities. The distribution functions in Fig. 3.6-4 are normalized to the same peak value of $F(v_\perp)$, but this leads to very high average ion energies.

If the model $F(v_\perp)$'s in Fig. 3.6-4 were normalized in $E_\perp$ by dropping the peak, the $dF/dv_\perp$ values would be even farther from the BA code case.

The AIC mode has been analyzed using a number of distribution function models.[10] A contour plot of $f(v_\parallel, v_\perp)$ for the model which most closely approximates the TASKA-M case is given in Fig. 3.6-5. The TASKA-M ion distribution function, taken from Section 3.4, appears in Fig. 3.6-6, on a different scale. The functional dependence of f is given by

$$f = \frac{2}{3\pi^{3/2}} \left(\frac{1}{2E_{Hc}}\right)^{5/2} v^2 \, e^{-v^2/2E_{hc}} \, K[H(\xi) - \pi)]$$

$$\times \left\{ \exp\left[-\frac{(\xi - \xi_i)^2}{2\Delta^2}\right] + \exp\left[-\frac{(\pi - \xi - \xi_i)^2}{2\xi^2}\right] \right\}$$

(3.6-9)

where $\xi = \arccos v_\parallel/v$, ξ_i is the pitch angle at the peak, and $H(\xi)$ is the Heavyside step function.

$$K \equiv -\frac{1}{2^{1/2}\Delta} \left(\text{Re}\left\{\exp[-a\xi_i^2] \, Z(\zeta_+) - \exp[i\pi - a(\pi - \xi_i)^2] \, Z(\zeta_-) \right\} \right)^{-1}$$

$$a = (2\Delta^2)^{-1}$$

$$\zeta_+ = \frac{1}{2} a^{-1/2} - i a^{1/2} \, \xi_i$$

$$\zeta_- = \frac{1}{2} a^{-1/2} + i a^{1/2} (\pi - \xi_i)$$

and Z is the plasma dispersion function.

Section 3.6.2 treats the DCLC and ALC modes, since they are related and are the most worrisome. The AIC mode is treated in Section 3.6.3. The treatment of microstability as a constraint on the power balance analysis of Section 3.2 is discussed in Section 3.6.4. Section 3.6.5 summarizes the results.

3.6.2 DCLC and ALC Modes

These modes are driven by the inverted ion population characteristic of a mirror-confined plasma. The distinction between them rests primarily in terminology -- the DCLC mode is sometimes defined as the lowest order eigen
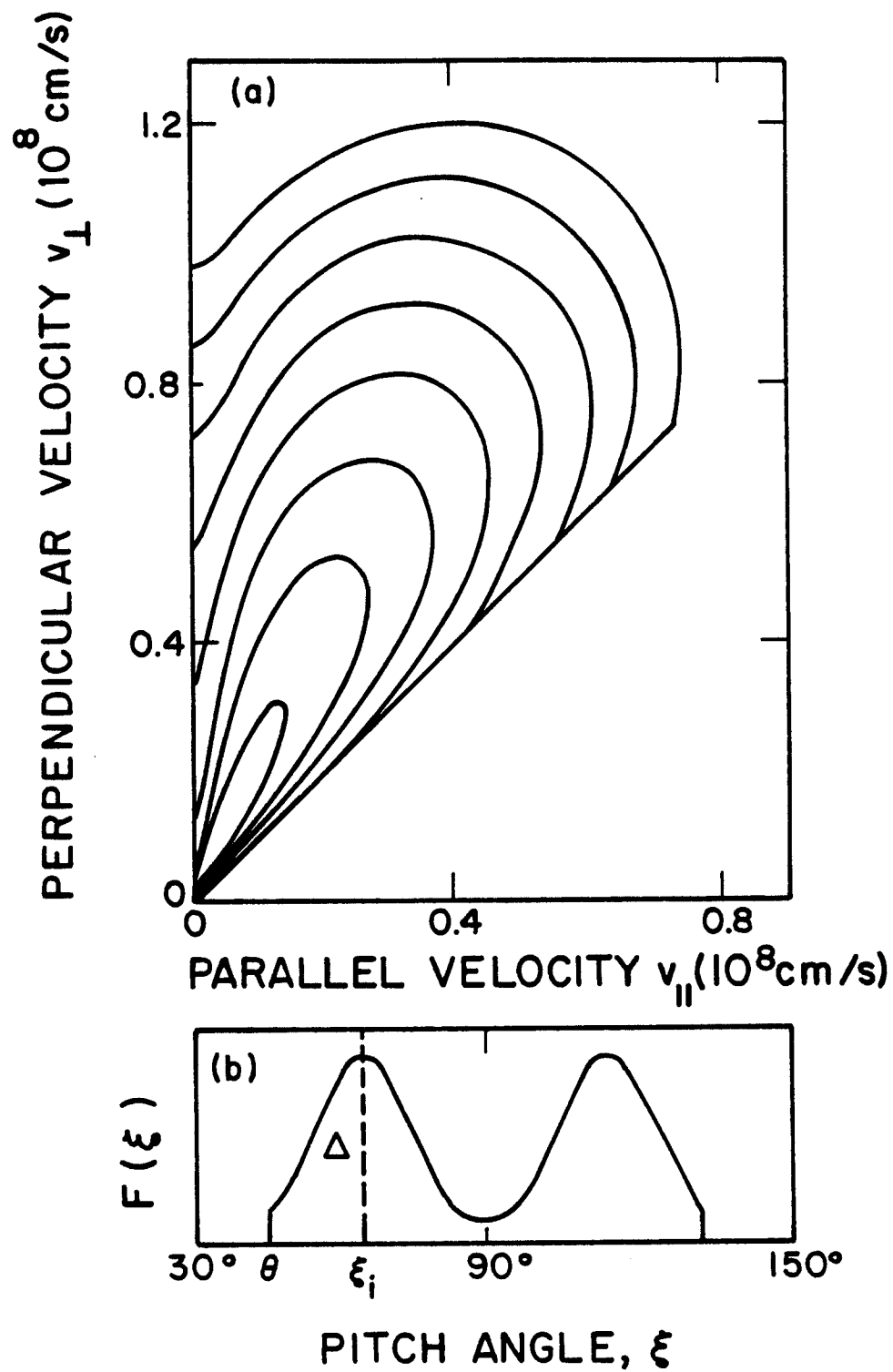
Fig. 3.6-5.   Model ion distribution function for the AIC calculations.
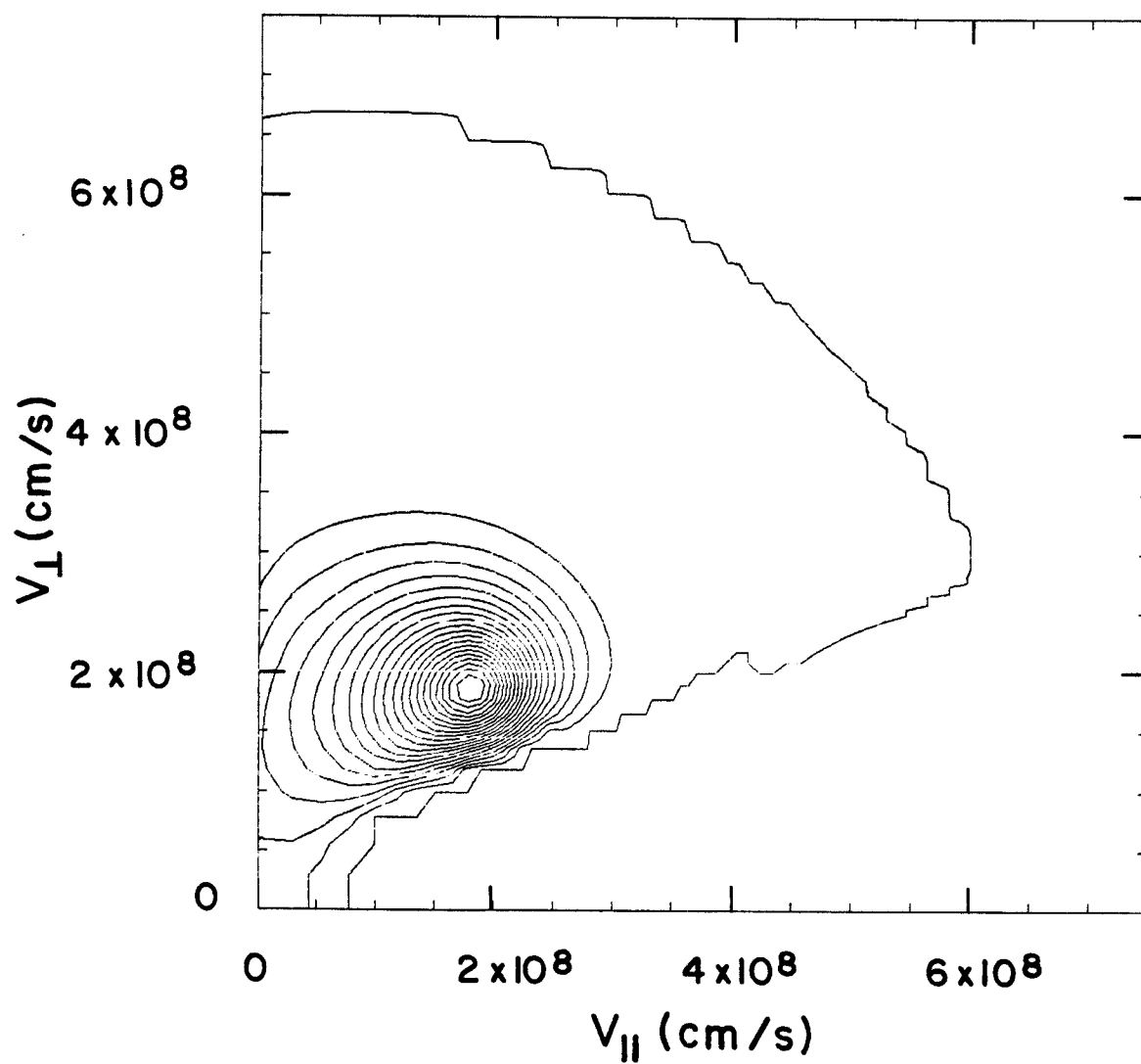
Fig. 3.6-6.   Contour plot of $f(v_{\parallel}, v_{\perp})$ from the Fokker-Planck calculations.

mode in the family of ALC modes. Historically, the "DCLC mode" is a flute ($\underline{k} \cdot \underline{B} = 0$) mode in a symmetric magnetic well,[11] but the lowest eigenmode in wells with sloshing ions tends to localize around density peaks, where few warm ions exist. There is some physical justification for the difference in nomenclature: The ALC modes invoke reflection and transmission at resonances along the magnetic field to produce standing waves; processes which detune the system may significantly alter the details or even existence of the instabilities. For the purposes of this section, the DCLC mode will be defined as the lowest order unstable eigenmode for a system without warm plasma. This will generally be a flute-like mode, but it may be localized to the density peaks.

Papers on the DCLC flute mode abound, but there has been relatively little work on the more difficult question of the ALC modes. The reason for this is that, for flute modes, derivatives along the magnetic field may be neglected and the differential equation 3.6-1 becomes a relatively simple root solving problem.

The minimum amount of warm ion density required for warm plasma stabilization of the DCLC flute mode may be set by fairly well-defined criteria.[3,12-14] Reference 12 found the most effective stabilization to occur when the warm plasma had a Maxwellian distribution with density satisfying

$$\frac{n_w}{n_H} > 3.4 \left(\frac{\rho_i}{r_s}\right)^{3/2} (R^{-1/2} - R^{-1})^{1/2} \tag{3.6-10}$$

and temperature satisfying

$$1 > \left(\frac{T_w}{T_H}\right)^{3/2} \frac{n_H/n_w}{(R^{-1/2} - R^{-1})} , \tag{3.6-11}$$

where $r_s \equiv (dn/d \ln r)^{-1}$. Reference 3 found that, at finite beta, in the TASKA-M regime where

$$\beta^2 \frac{v_h}{v_H} \lesssim \frac{\rho_{iH}}{L_n} \lesssim \frac{v_h}{v_H} , \tag{3.6-12}$$

the required warm density was

$$\frac{n_w}{n_H} \gtrsim 2 \left(\frac{v_h}{v_H}\right)^{1/2} \left(\frac{\rho_{iH}}{L_n}\right)^{3/2} , \tag{3.6-13}$$

where ρ_{iH} is the hot ion gyroradius. The TASKA-M reference case satisfies these criteria. A subsequent paper[14] pointed out that the required warm density should be corrected for the fact that the warm plasma fills a smaller volume along the axis than the hot plasma does. In TASKA-M, the magnetic field and electrostatic potential are fairly flat near the midplane and only rise near the central cell ends, so the warm plasma will fill over half of the hot plasma volume and stability should be satisfied.

Analytic work on the ALC mode concentrates primarily on the case of an empty loss cone. It is even harder to stabilize the ALC mode than the DCLC mode when no warm plasma is present; the maximum stable plasma length is

$$L \approx 10 \, \rho_i / \beta^{1/2}$$

which is not satisfied by any present tandem mirror design.

The only analytic model for warm plasma that has been used is that of a stream of plasma, which gives a Maxwellian component to the distribution function. Within that model, the 9.2% warm plasma in TASKA-M should be sufficient.[15] Again, however, the question is whether modes arise which are localized at the sloshing ion density peaks where there is no warm plasma. A quantitative answer requires a suitable version of the MICE code.

We have chosen to use the DCLC mode rather than the ALC mode as a constraint on the TASKA-M design because of the following reasons:

- The ALC mode has not been identified experimentally, although the PR-6 experiment[16] should have been in the ALC unstable regime. Figure 3.6-7a shows magnetic field, density, and potential profiles used in the theoretical calculation. Figure 3.6-7b shows the DCLC and ALC stability boundaries for PR-6. The results are sensitive to the values chosen for R, T_{hot}, and β, but, as a rough guide, the plot is encouraging.

- The analysis of the ALC mode is very complicated, and depends on details of wave reflection at magnetic field resonances. It is, therefore, rather sensitive to the assumptions required to make the analysis tractable.

- ALC theory is relatively young, and a number of effects may alter stability boundaries. These include Landau damping, magnetic field ellipticity, electron bounce resonances, nonlinear saturation, and density gradients.
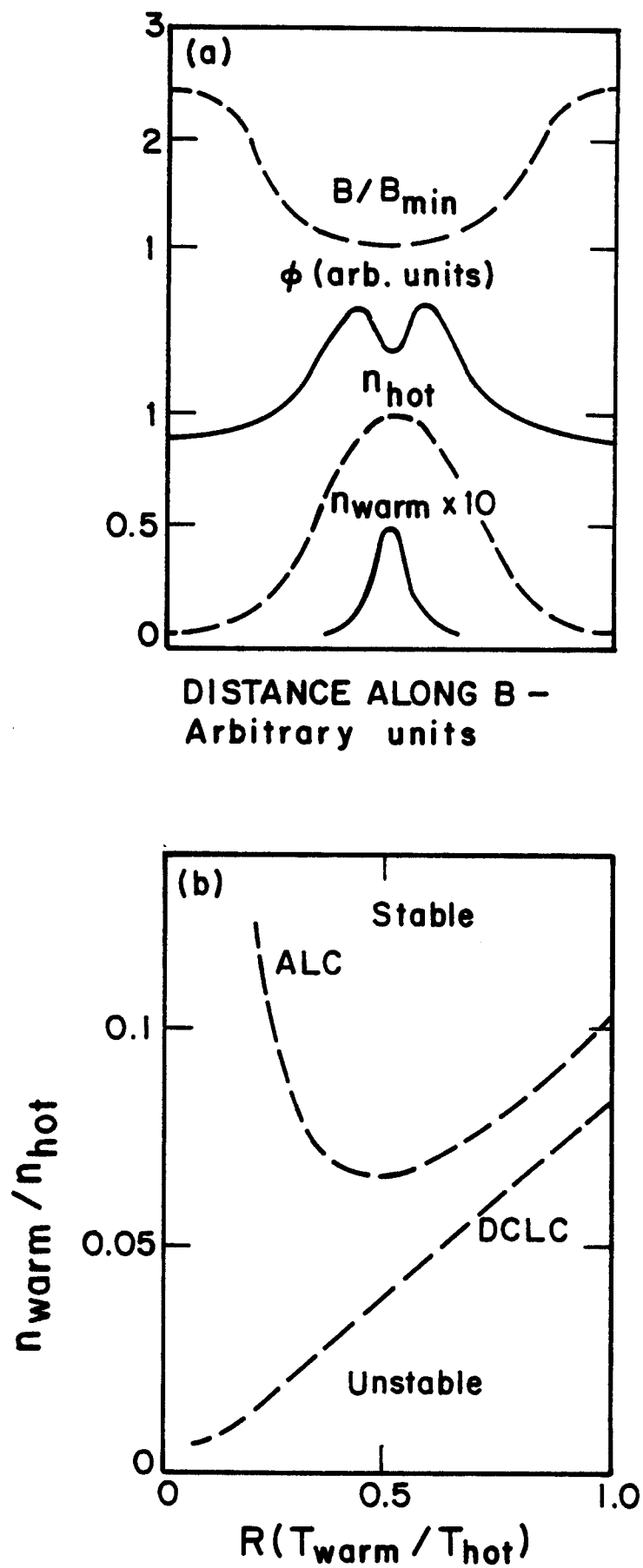
Fig. 3.6-7.   (a) Magnetic field, density, and electrostatic potential model profiles for the PR-6 calculations. (b) DCLC and ALC stability boundaries for PR-6.

Some guidance regarding TASKA-M stability to the DCLC and ALC modes may be drawn from published results of the MICE code for 2XIIB and MFTF, although the differences in configuration create difficulties of interpretation. Also, most of the MICE cases were run with the parameter $R = T_{hot}/T_{hole} = 10$, while $R = 2$ is perhaps more realistic for TASKA-M (see Fig. 3.6-3). The stability boundary for 2XIIB, which was a single mirror cell with warm neutral beam injection perpendicular to the magnetic field at the midplane, is shown in Fig. 3.6-8. The stability boundary for MFTF is shown in Fig. 3.6-9. Note that

$$R \frac{T_{warm}}{T_{hot}} = \frac{T_{warm}}{T_{hole}} \approx 0.41$$

for TASKA-M, where $T_{warm} = 5.8$ keV and $T_{hole} = 14$ keV. Also, $n_{warm}/n_{hot} \approx 0.09$. Thus, if the DCLC and ALC microstability analysis for 2XIIB or MFTF applies to TASKA-M, TASKA-M will be stable. It is encouraging to note that the two-component mode, which is the closest boundary to the TASKA-M operating point, is highly localized to the midplane[9] and should, therefore, be susceptible to stabilization by warm plasma localized there.

The analysis of the axicell version of MFTF-B[5] is not so encouraging. The stability boundaries are shown in Fig. 3.6-10. The amplitude and phase as a function of z are given in Fig. 3.6-11, where the flute nature of the $n_z = 0$ ("DCLC") mode and the strongly localized nature of the $n_z = 1$ ("ALC") mode are clear. However, from the MFTF-B axial profiles for potential and other quantities shown in Fig. 3.6-12, it is obvious that TASKA-M is a very different configuration. In particular, the extremely deep potential well from plug midplane to sloshing ion peak in MFTF-B implies that it will be very difficult for warm plasma to reach the peak. In contrast, the shallow potential dip in TASKA-M should mean that much less warm plasma is required.

A recent, qualitative result from particle simulations of ion cyclotron loss cone instabilities is also encouraging.[17] Sloshing ion distributions with a potential dip at the midplane and a warm ion density component show significant improvement in fluctuation levels over the empty loss cone case. Figure 3.6-13a shows the parameterization of the potential dip, while Fig. 3.6-13b shows the reduction in $\tilde{\phi}^2$, the amplitude of the fluctuations in potential. Although the assumptions required to do the simulations make the
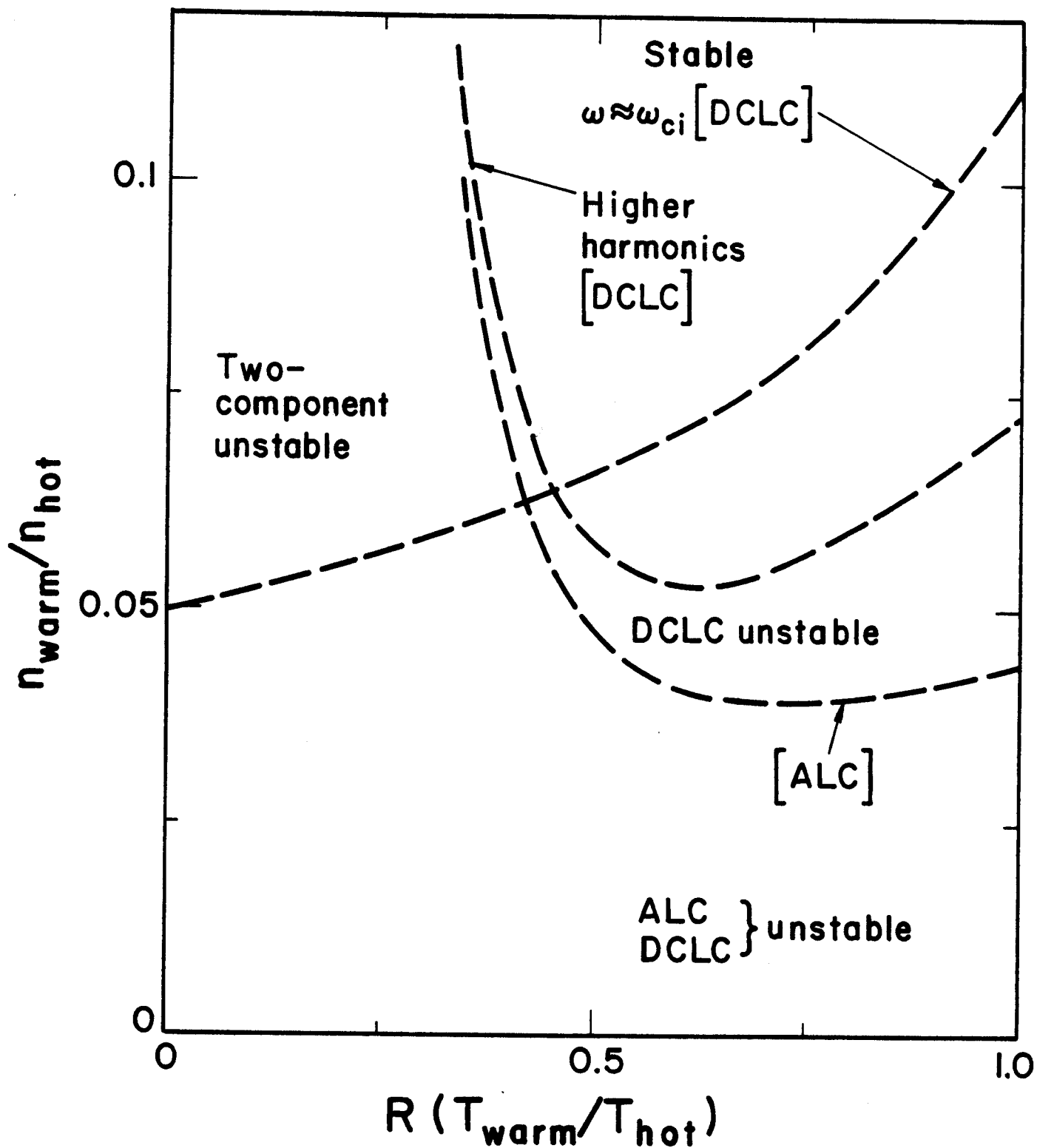
Fig. 3.6-8.   Stability boundaries for 2XIIB.
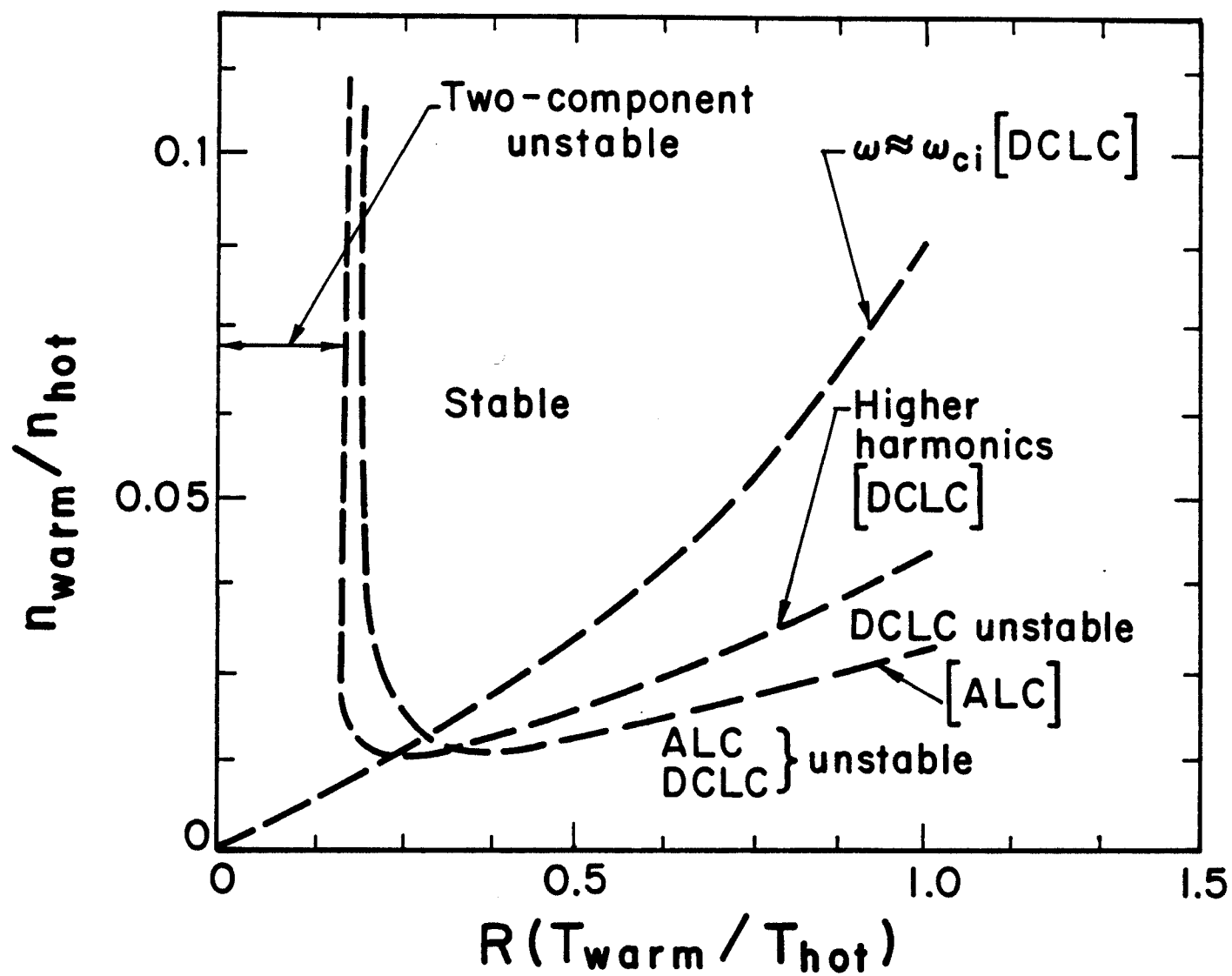
Fig. 3.6-9. Stability boundaries for MFTF.
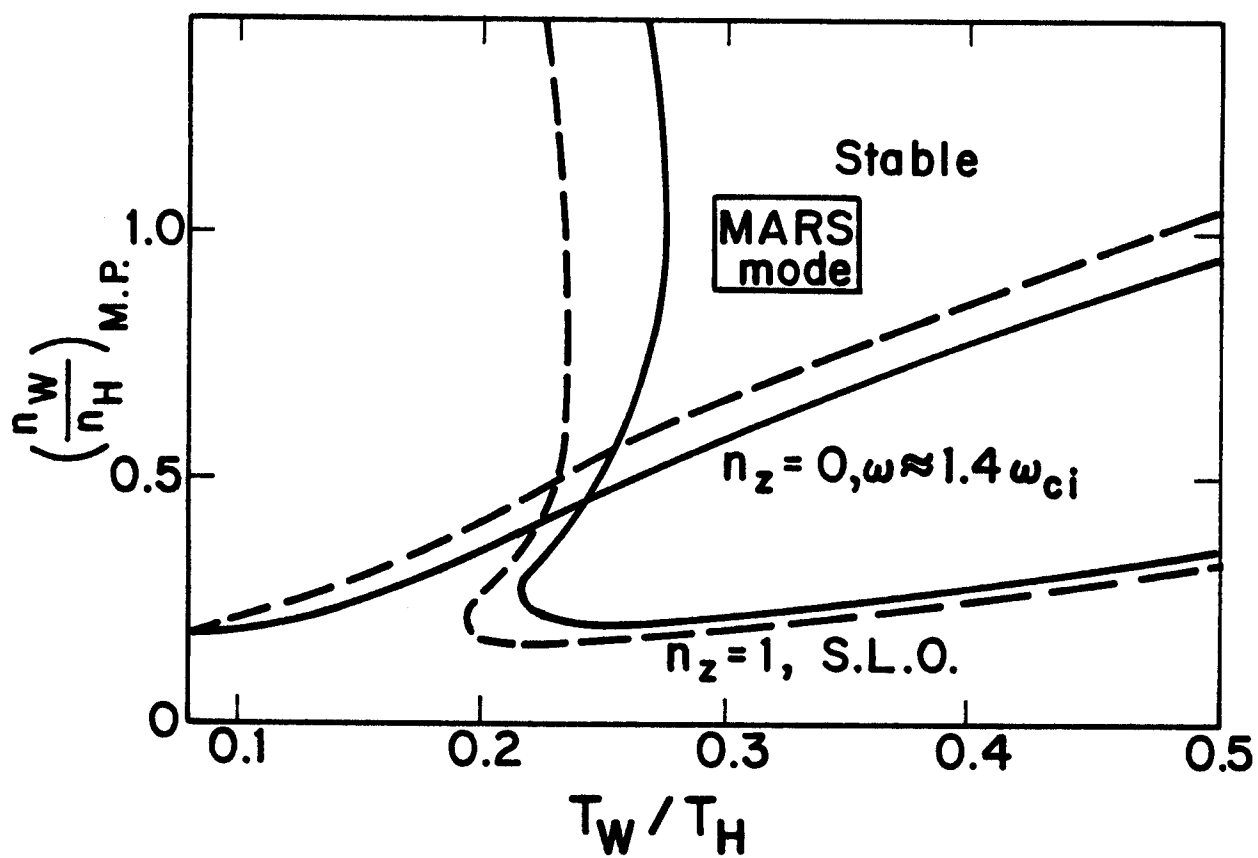
Fig. 3.6 -10

Fig. 3.6-10. Stability boundaries for axicell version of MFTF-B.
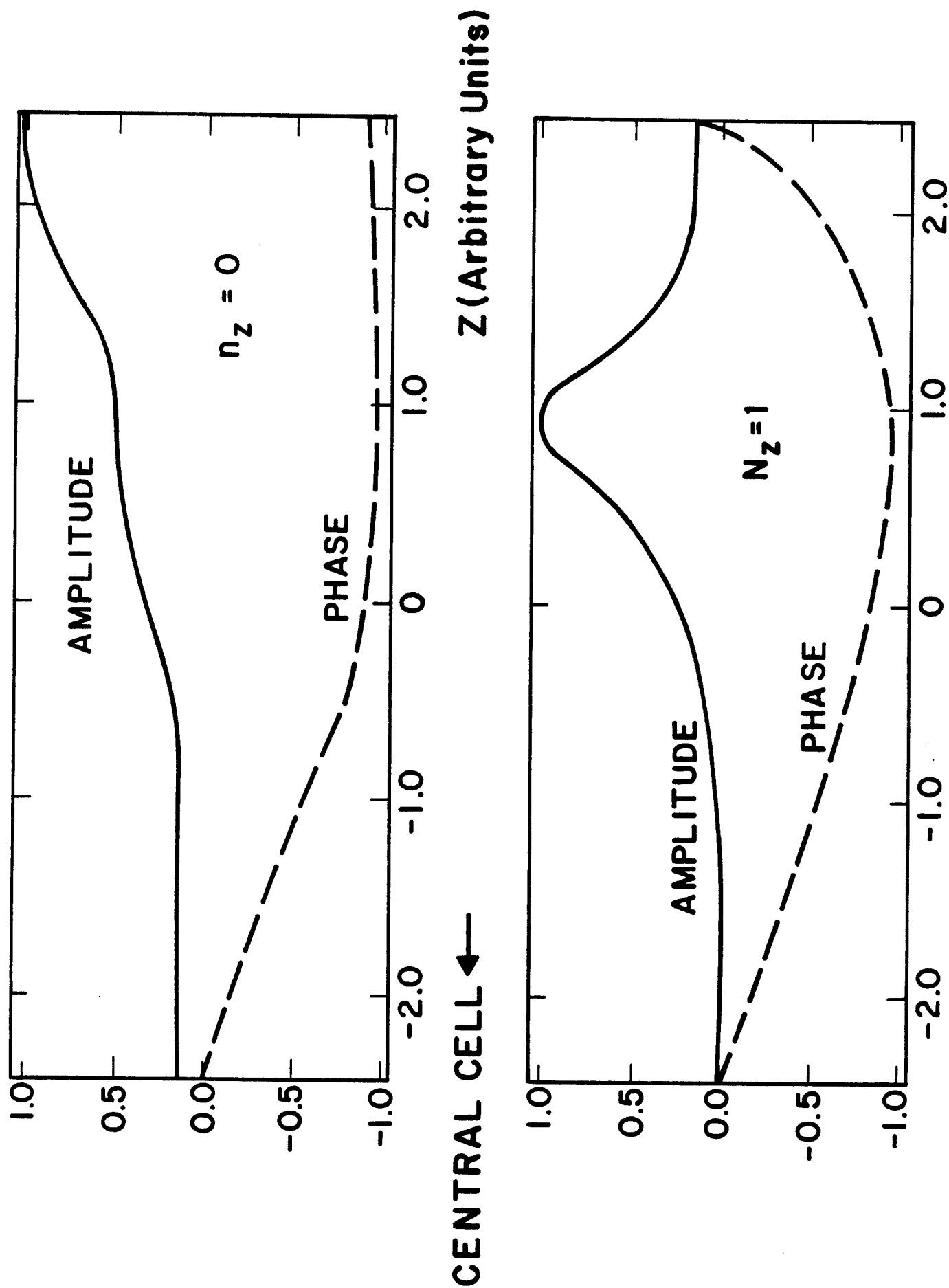
Fig. 3.6-11. Amplitude and phase of the lowest MFTF-B eigenmodes.
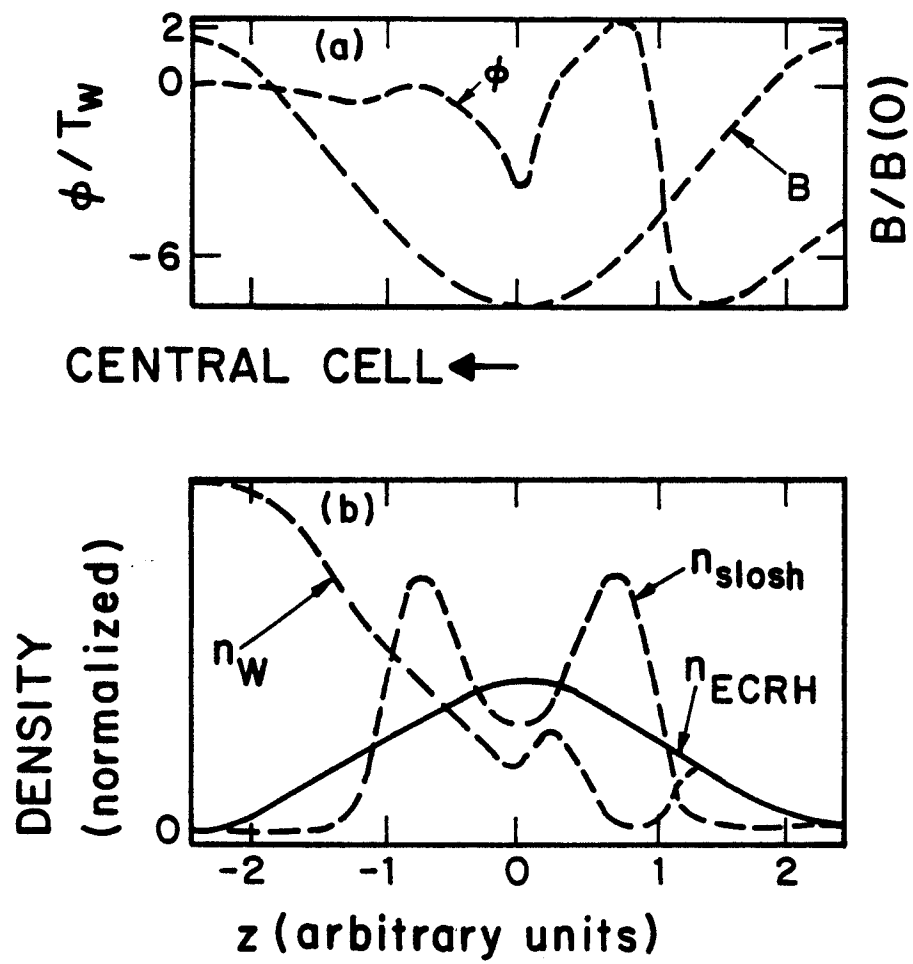
Fig. 3.6-12. MFTF-B axial profiles.

results only qualitative, simulations are presently the only means of treating some nonlinear effects, so the results support the general approach.

3.6.3 AIC Mode

In contrast to the theory of the DCLC and ALC modes, where a multitude of references treat various aspects of the problem, a concise summary of the state of the art in AIC mode theory is given in Refs. 10 and 18. For high beta plasmas with anisotropic pressure distribution functions, this mode can be unstable. Except for very anisotropic plasmas, the instability is produced by waves resonating with ions and satisfying

$$v_{\parallel} = \frac{(\omega - \omega_{ci})}{k} .$$

It is an electromagnetic mode which propagates mainly along magnetic field lines. The results presented here are taken from Ref. 10, and the reader is referred to that reference for details of the dispersion relation and its solution.

In general, the stability criterion for the AIC mode is not that it be completely stable, but that it be convective (growing in space) rather than absolute (growing in time). The deleterious effect of the instability is mitigated in the convective case when the plasma length is less than a few times the spatial e-fold growth length of the wave, since the wave then propagates to a region where it is evanescent.

Figure 3.6-5 shows the model ion distribution function. In order to analyze stability, a measure of the pitch angle spread, Δ, is required. Roughly estimating from Fig. 3.6-14, where contours are separated by a factor of 0.5, and using the full width at half maximum value of Δ, $\Delta_{FWHM} = 2.35 \Delta$, gives $\Delta \approx 13°$. AIC mode stability boundaries are shown in Fig. 3.6-15 for a variety of beta values.[10] Thus, TASKA-M is nominally in the absolutely unstable regime. However, two strongly stabilizing effects discussed in Ref. 18 are present in TASKA-M. First, the presence of both deuterium and tritium causes the effective beta for the AIC mode analysis to be about one-half of the nominal value. Second, the finite magnetic field scale length lowers the required Δ considerably. Thus, TASKA-M is expected to be stable to the AIC mode.[19]
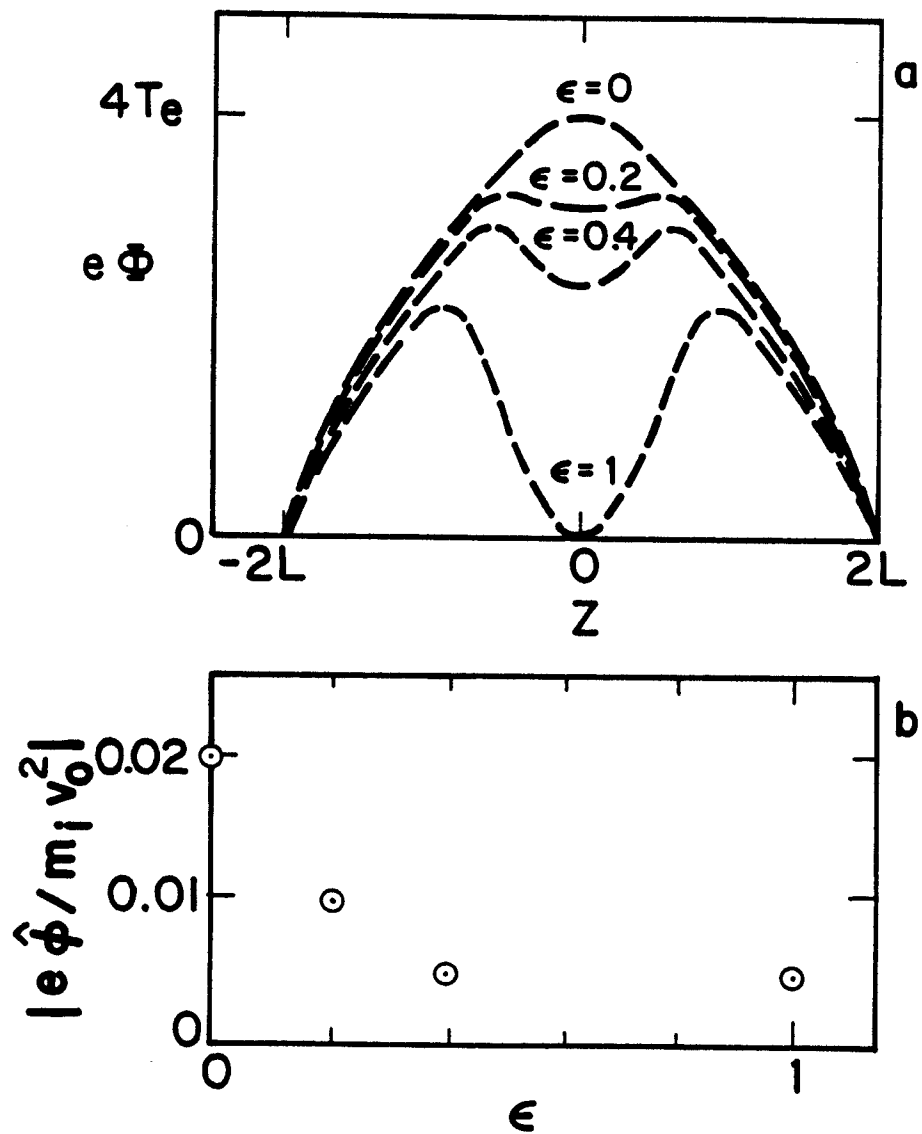
Fig. 3.6-13. (a) Electrostatic potential dip versus ε. (b) Fluctuation level, $\tilde{\phi}^2$ versus ε.
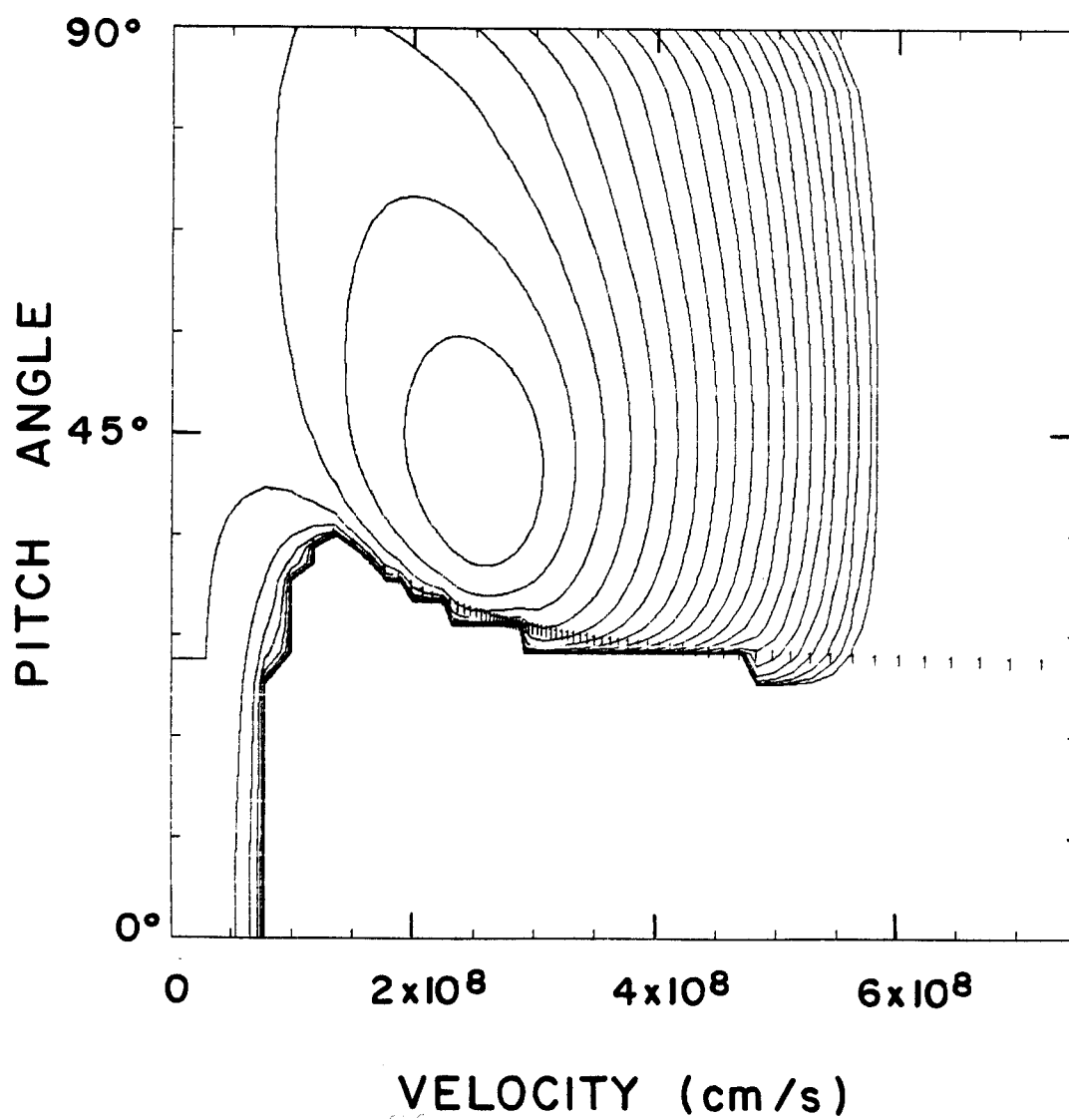
Fig. 3.6-14. Contour plot of f(v,θ) from the Fokker-Planck calculations.
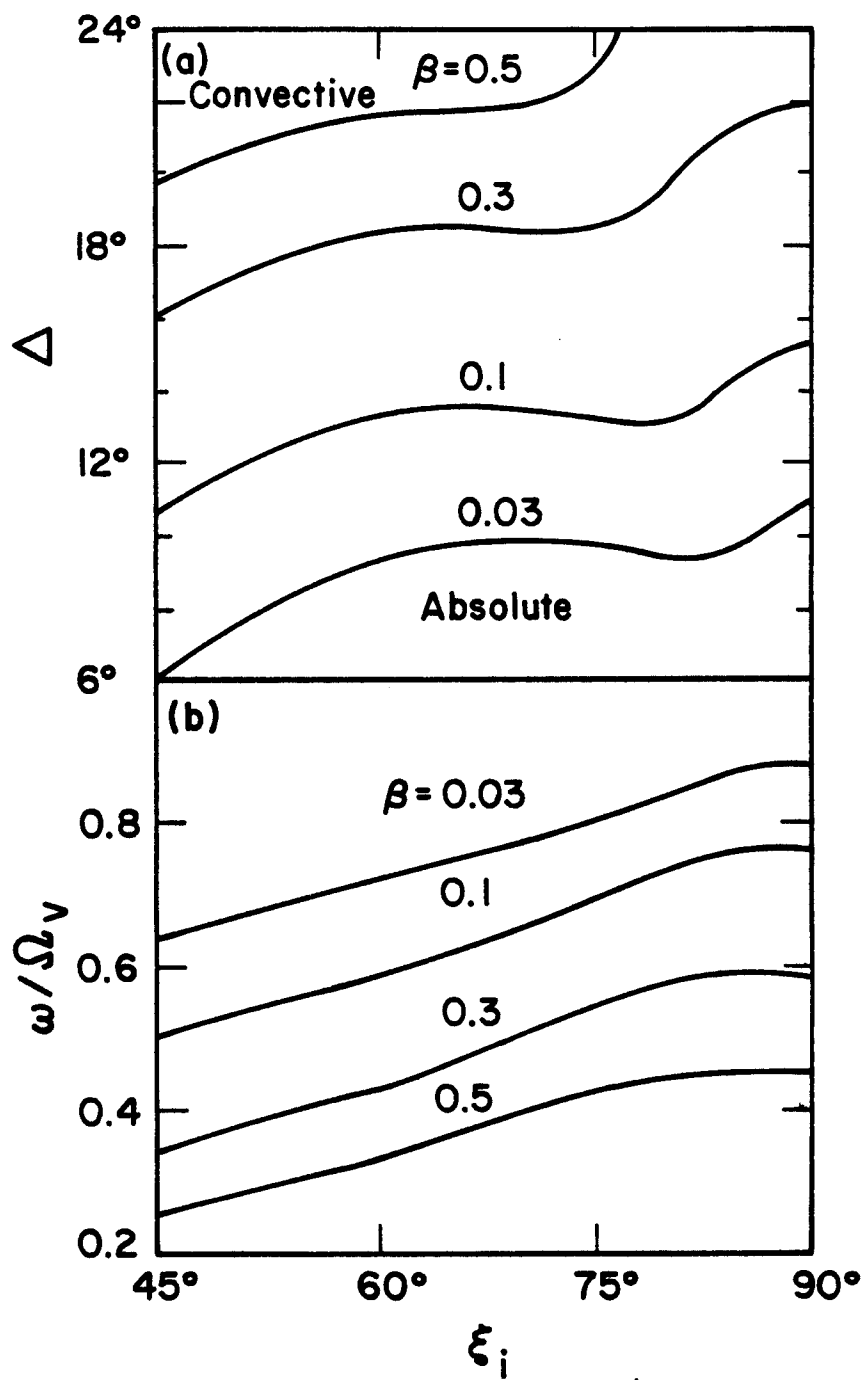
Fig. 3.6-15. AIC stability boundaries.

3.6.4 Microstability Constraints on Power Balance

The power balance code, described in Section 3.2, uses the analysis of Baldwin, Berk, and Pearlstein[3] for the evaluation of the amount of warm plasma required to stabilize the DCLC mode. This analysis uses the model distribution function given in Eq. 3.6-8. In this expression, v_H is <u>not</u> to be interpreted as the r.m.s. ion speed; it is simply a parameter of the model. The velocity v_h determines the size of the "hole" in $F(v_\perp)$ at low $v_\perp$.

The important parameters determining stability are

$$\varepsilon = \frac{v_H}{\Omega r_s}$$

$$\Delta = \frac{n_{wc}}{n_{Hc}}$$

and the ion beta,

$$\beta_i = \mu_0 \frac{n_H M v_H^2}{B^2} .$$

Here Ω is the ion cyclotron frequency, M is the ion mass, r_s is the radial scale length for the density gradient, n_{wc} is the warm ion density, and n_{Hc} is the hot ion density. The parameter ε is effectively the ratio of the ion gyroradius to the scale length r_s.

The marginal stability criteria for the density and temperature of the warm plasma depend on ε and divide into three regions, as given in Table 3.6-1. The expressions in this table are only approximate and meant to apply in the middle of the regions; they do not join well at the boundaries between the regions. Since one expects that Δ should be a monotonically increasing function of ε, "humps" in $\Delta(\varepsilon)$ are smoothed out in the power balance code. In Table 3.6-1, v_w is the mean perpendicular speed of the warm ions filling the loss-cone of the hot ions. The temperature, T_w, of the warm ions is then given by $T_w = \frac{1}{2} M v_w^2$.

For application to TASKA-M, the power balance code assumes that

$$v_h = 0.7 \ v_H \ ,$$

$$R_s = r_p/2$$

Table 3.6-1. Marginal Stability Criteria

Region	Range	Δ	v_w/v_h
I	$\varepsilon_0 < \varepsilon < \varepsilon_1$	$2 \dfrac{v_H}{v_h} \left(\dfrac{\varepsilon}{\beta}\right)^3$	$\varepsilon \dfrac{v_H}{v_h}$
II	$\varepsilon_1 < \varepsilon < \varepsilon_2$	$2 \left(\dfrac{v_h}{v_H} \varepsilon^3\right)^{1/2}$	$\left(\varepsilon \dfrac{v_H}{v_h}\right)^{1/2}$
III	$\varepsilon_2 < \varepsilon$	$\dfrac{1}{2} \left(\dfrac{v_h}{v_H}\right)^2$	1

$$\varepsilon_0 = 2\left(\beta_i \frac{m_e}{M} + \beta_i \frac{\Omega^2}{\omega_{p_i}^2}\right)^{1/2} \; ; \qquad \omega_{p_i}^2 = \frac{n_{Hc}e^2}{M\varepsilon_0}$$

$$\varepsilon_1 = \beta^2 \frac{v_h}{v_H}$$

$$\varepsilon_2 = \frac{v_h}{v_H}$$

- - - - - - - - - - - - - -

and
$$\langle v_\perp^2 \rangle = \frac{2E_{Hc}}{M} \sin^2\theta_{inj} \; .$$

This allows us to calculate the parameters v_H, v_h, and ε for a given E_{Hc} and injection angle for the sloshing ions. The expressions in Table 3.6-1 are then used to determine the amount, Δ, of warm plasma, and the warm ion temperature, $T_w = \frac{1}{2} M v_w^2$. TASKA-M operates in Region II in this table.

This value of the warm ion temperature is used as one estimate; a second estimate is gotten by considering MICE calculations for MFTF-B[9] and TMX-U.[2] These suggest that T_w should be greater than $\sim 0.25\ E_{Hc} \sin^2\theta_{inj}$ in order to avoid the two-component mode. The latter criterion normally gives a higher criterion for T_w and is difficult to satisfy. In order to not deviate far from either criterion, the power balance code uses the geometric mean of these

two estimates for T_w. Figure 3.6-16 shows the effect of different T_w on the net $F(v_\perp)$ of the ions when 9.2% warm plasma is included. (This example is for TASKA-M parameters.) All three distributions have a region of positive slope to some degree. The hole is largest for $T_w = 11.2$ keV, which is from the two-component mode criteria. The DCLC criteria can tolerate a hole in $F(v_\perp)$ to a certain degree; the criterion for stability is[1]

$$\int_0^\infty dv_\perp \frac{\partial F}{\partial v_\perp^2} J_n^2 \left(\frac{k_\perp}{\Omega}\right) < 0$$

where J_n is the Bessel function. The two lower values for T_w have a smaller hole and therefore provide a larger safety margin. TASKA-M is designed using $T_w = 5.8$ keV since it is difficult to obtain a suitable warm plasma source at lower energies.

3.6.5 Summary

TASKA-M is microstable to the DCLC and ALC modes when related calculations are extrapolated. However, uncertainties exist which can only be removed by extensive, numerical calculations and, ultimately, by experiment. Experimental and numerical results support the basic TASKA-M approach to microstability.

The AIC mode is expected to be stable. However, even if unstable, it would probably evolve to a marginally stable distribution without significant degradation of plasma confinement.

Thus, there is considerable reason for optimism that TASKA-M will be microstable, but only experimental verification of the theoretical results can adequately address the issue.
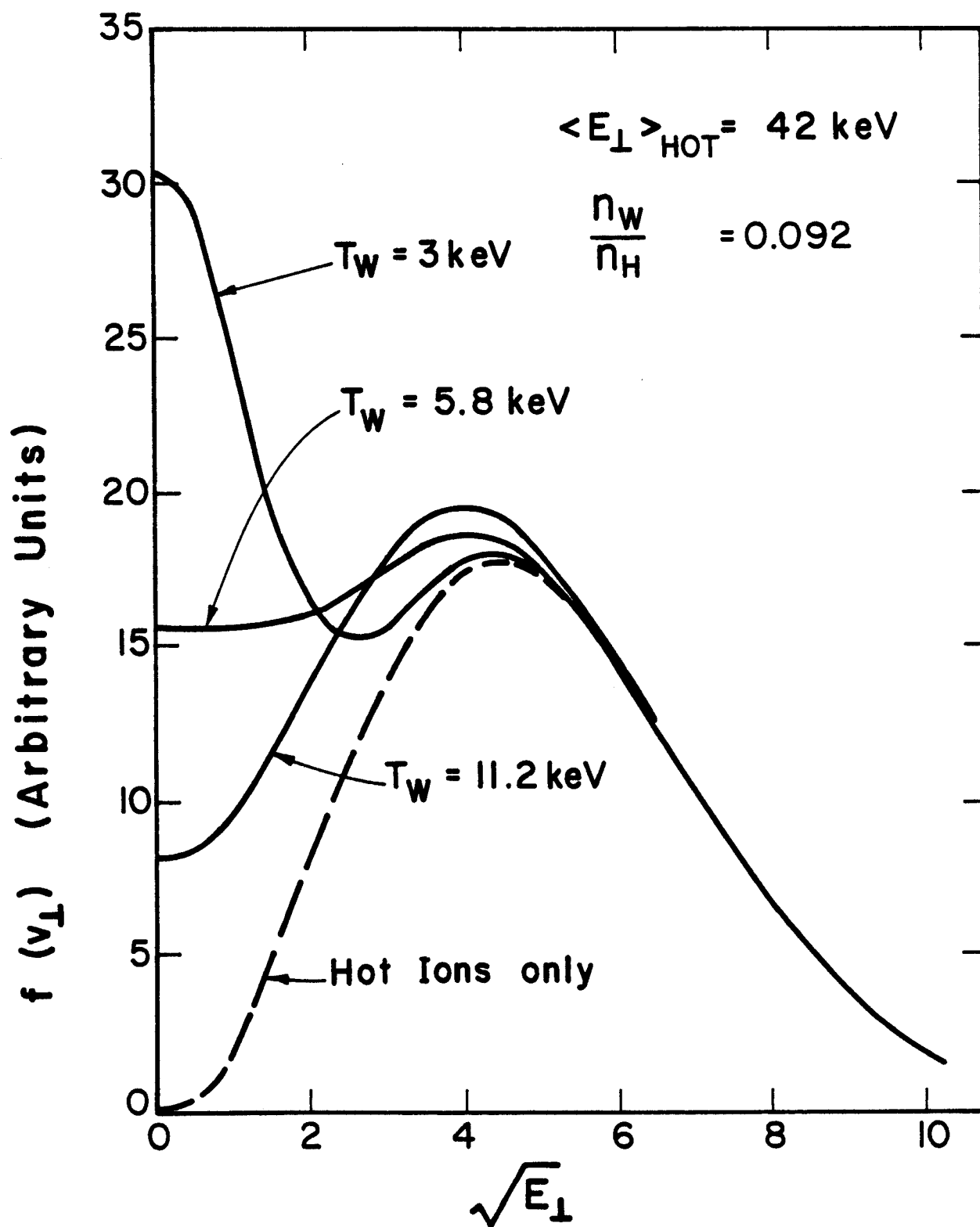
Fig. 3.6-16. Model ion distribution function (Eq. 3.6-8) with warm plasma included.

References for Section 3.6

1. B.I. Cohen et al., "Status of Mirror Fusion Research, 1980," LLNL Report UCAR-10049-80-Rev. 1 (1980).

2. T.C. Simonen et al., Phys. Rev. Lett. $\underline{50}$, 1668 (1983).

3. D.E. Baldwin, H.L. Berk and L.D. Pearlstein, Phys. Rev. Lett. $\underline{36}$, 1051 (1976).

4. W.C. Turner, E.J. Powers and T.C. Simonen, Phys. Rev. Lett. $\underline{39}$, 1087 (1977).

5. D.E. Baldwin and B.G. Logan, editors, "Physics Basis for an Axicell Design for the End Plugs of MFTF-B," LLNL Report UCID-19359 (1982).

6. L.D. Pearlstein, private communication (1983).

7. M.J. Gerver, private communication (1983).

8. D.E. Baldwin, Rev. Mod. Phys. $\underline{49}$, 317 (1977).

9. D.E. Baldwin, B.G. Logan and T.C. Simonen, editors, "Physics Basis for MFTF-B," LLNL Report UCID-18496 (1980).

10. Gary R. Smith, "Alfvén Ion-Cyclotron Instability in Tandem Mirror Plasmas. I.," LLNL Report UCRL-89676 (1983).

11. M.N. Rosenbluth and R.F. Post, Phys. Fluids $\underline{8}$, 547 (1965).

12. M.J. Gerver, Phys. Fluids $\underline{19}$, 1581 (1976).

13. H.L. Berk and M.J. Gerver, Phys. Fluids $\underline{19}$, 1646 (1976).

14. D.E. Baldwin and R.A. Jong, Phys. Fluids $\underline{22}$, 119 (1979).

15. M.J. Gerver, Phys. Fluids $\underline{23}$, 755 (1980), and references contained therein.

16. B.I. Kanaev, Nucl. Fusion $\underline{19}$, 347 (1979).

17. B.I. Cohen, N. Maron, and W.M. Nevins, "Simulation of Drift-Cyclotron-Loss-Cone Modes in Tandem Mirrors with Sloshing Ions," LLNL Report UCRL-88728 (1983).

18. Gary R. Smith, William McKay Nevins, and William M. Sharp, "Alfvén Ion Cyclotron Instability in Tandem-Mirror Plasmas II," LLNL Report UCRL-90108 (1983).

19. G.R. Smith, private communication (1983).

3.7 Trapped Particle Stability

In 1982, Rosenbluth[1,2] found, from theoretical calculations, a new instability which can affect tandem mirror performance. This instability is related to particles trapped in regions of bad magnetic curvature and hence is known as a trapped particle instability. This instability is related to trapped particle instabilities in toroidal devices, e.g. tokamaks. Trapped particle instabilities in tokamaks have small growth rates compared with MHD growth rates and hence their effects are not as serious. In fact, trapped particle instabilities have not yet been experimentally identified in tokamaks, although moderate level fluctuations in the appropriate frequency range are observed. The trapped particle instability in a tandem mirror is potentially more dangerous because, at least in some configurations, a majority of the particles can be trapped in regions of bad magnetic curvature and the resulting growth rate can be of the order of the MHD growth rate. The design implication is that one needs to maintain a sufficient fraction of particles which pass from regions of bad curvature to the good curvature region in the anchor. These passing particles provide connection between the plasma in the good and bad curvature regions and thereby stabilize the plasma in the bad curvature region. In this section we consider the implication of the trapped particle instability for TASKA-M.

The trapped particle instability is an electrostatic mode in which the fluctuating potential localizes in regions of bad magnetic curvature. Using a slab model to describe the plasma, the dispersion relation can be written as

$$
0 = \sum_j \frac{q_j^2}{m_j} \int d\varepsilon \int d\mu \ \tau_{Bj} \frac{\partial f_{oj}}{\partial \varepsilon} \ [\overline{(\phi - \overline{\phi})_j^2}(1 - \frac{\omega_{*j}}{\omega})
$$

$$
(3.7\text{-}1)
$$

$$
+ k^2 \rho_j^2 (1 - \frac{\omega_{*j}}{\omega}) \ \overline{\phi}^2 + \frac{\omega_{*j} \omega_{Dj}}{\omega^2} \ \overline{\phi}^2]
$$

where $\phi(\ell)$ is the amplitude of the fluctuating potential and is a function of ℓ, the coordinate along $\vec{B}$. $\overline{\phi}$ is the bounce-averaged value of ϕ

$$
\overline{\phi} = \frac{1}{\tau_B} \int \frac{d\ell}{v_\parallel(\ell)} \ \phi(\ell)
$$

where $v_\parallel(\ell)$ is the parallel velocity of the particle and τ_B is the bounce period. In Eq. 3.7-1, q and m are the charge and mass of a given species of particles, ε and μ are the energy and magnetic moment per unit mass, ω_* is the diamagnetic frequency, ω_D is the curvature drift frequency, ρ is the gyroradius, and ω and k are the mode frequency and wave-number perpendicular to $\vec{B}$. The sum in Eq. 3.7-1 is over the various types of particle trajectories and the various species of particles.

Assuming a Maxwellian distribution for f_0,

$$\frac{1}{m} \int d\varepsilon \int d\mu \int \frac{d\ell}{v_\parallel} \frac{\partial f_0}{\partial \varepsilon} = -\frac{1}{T} \int \frac{d\ell}{B} n$$

for each species j. Then the dispersion relation can be written as

$$\sum_j \left[\overline{(\phi - \bar{\phi})^2_j}\left(1 - \frac{\omega_{*j}}{\omega}\right) \frac{1}{T_j} \int_j d\ell \frac{n_{pass}}{B} + \frac{k^2 \rho_j^2}{T_j}\left(1 - \frac{\omega_{*j}}{\omega}\right) \bar{\phi}^2 \int_j d\ell \frac{n}{B} \right.$$

$$\left. + \frac{\omega_{*j}\omega_{Dj}}{\omega^2} \frac{1}{T_j} \bar{\phi}^2 \int_j d\ell \frac{n}{B} \right] = 0 .$$

(3.7-2)

The term involving $\overline{(\phi - \bar{\phi})^2}$ is nonzero only for passing particles; for particles trapped in the central cell or anchor, $\phi = \bar{\phi}$. Consequently, for these particles $n \to n_{pass}$, the density of particles passing into the anchor.

For the axial variation of the fluctuation potential ϕ, we take $\dot{\phi} = \phi_c$ equal to a constant in the central cell and transition region, and $\phi = 0$ in the anchor. We also use square-well approximations for each cell. In TASKA-M only electrons pass from the anchor to the central cell; ions leaving the central cell are on unconfined orbits and are lost out the ends. Then

$$\int \frac{d\ell}{B} n_{pass} = \frac{n_c L_c}{B_{2c}} e^{-\Delta\phi/T_e} + 2n_A \left(\frac{L_a}{B_{2a}} + \frac{L_t}{B_{1t}}\right)$$

where $\qquad \Delta\phi = \phi_e - \phi_t$,

n_c and n_A are the electron density in the central cell and anchor, respective-

ly, the effective lengths of the central cell, anchor, and transition region are L_c, L_a, and L_t, respectively, and the other symbols are as defined in Section 3.2. For passing electrons

$$\bar{\phi} = \frac{\phi_c(\tau_c + 2\tau_t)}{\tau_c + 2\tau_t + 2\tau_a} \; ,$$

where τ_c, τ_t, τ_a are the transit time through the central cell, transition region, and anchor, respectively. Then, for the passing electrons

$$\overline{(\phi - \bar{\phi})^2} = \frac{2\tau_A\tau_B}{\tau_T^2} \phi_c^2$$

where
$$\tau_B = \tau_c + 2\tau_t$$
$$\tau_T = \tau_B + 2\tau_a \; .$$

For electrons or ions trapped in the central cell, we have

$$\int d\ell \, \frac{n}{B} = \frac{n_c L_c}{B_{1c}}$$

and $\bar{\phi}^2 = \phi_c^2$. For ions trapped in the anchor, we have

$$\int d\ell \, \frac{n}{B} = \frac{2n_a L_a}{B_{La}}$$

and $\bar{\phi}^2 = 0$.

We put these expressions into the dispersion relation, Eq. 3.7-2, and write it as a quadratic equation for ω,

$$\omega^2(1 + \frac{A_1}{m^2}) - \omega\omega_{*i}[(m - 1) - \frac{A_2}{m}] + \gamma_c^2 = 0 \qquad (3.7\text{-}3)$$

where γ_c is the MHD growth rate,

$$\gamma_c^2 = \frac{\omega_{*i}(\omega_{Di} - \omega_{De})}{k^2 \rho_i^2}$$

$$A_1 = \frac{\overline{(\phi - \overline{\phi})^2}}{\phi_c^2} \frac{T_i}{T_e} \frac{r^2}{\rho_i^2} \frac{\int d\ell \frac{n_{pass}}{B}}{\int_c d\ell \frac{n}{b}}$$

$$A_2 = \frac{T_e}{T_i} A_1 \; .$$

To get Eq. 3.7-3 we have neglected the finite gyroradius correction of the electron and invoked the transformation to cylindrical geometry, so that

$$k \to \frac{m}{r} \qquad \text{or} \qquad \frac{m - 1}{r}$$

as appropriate. Here m is the azimuthal mode number and r is the plasma radius. The ion diamagnetic frequency in Eq. 3.7-3 is defined for m = 1, so that Eq. 3.7-3 shows the m-dependence explicitly.

Writing the dispersion relation as

$$A\omega^2 + B\omega + C = 0 \; ,$$

we see that the plasma is stable if

$$B^2 - 4AC > 0 \; .$$

The effect of finite ion gyroradius stabilizing the plasma is the first term in B and vanishes for m = 1. The A_2 term in B comes from the electrons passing between the central cell and anchor. If the connection were by ions instead of electrons, the sign in front of A_2 in Eq. 3.7-3 would be positive instead of negative. The passing electron contribution in A_2 can stabilize the plasma for m = 1 if A_2 is large enough. For higher azimuthal mode numbers, m, B^2 decreases at first and then increases when

$$A_2 = m(m - 1) \; .$$

This leads to the possibility of an unstable window in m. This arises because the passing electron contribution defeats the finite gyroradius stabilization for some m.

Applying this analysis to the TASKA-M design point, we get

$$\omega_{*i} = 9.2 \times 10^5 \text{ s}^{-1}$$

$$A_1 = 64$$

$$A_2 = 16$$

$$\gamma_c = 3.3 \times 10^5 \text{ s}^{-1} \ .$$

With these parameters, we get stability for m = 1, 2, 3, and m ⩾ 6. The dispersion relation predicts a trapped particle instability for the azimuthal mode number, m, equal to 4 and 5. For these values of m, the growth rate is about $1.4 \times 10^5 \text{ s}^{-1}$, which is about one-half the MHD growth rate. This result is a basis for concern about trapped particle instability in TASKA-M. The analysis, however, is only approximate; a number of complicating effects have not been considered. Furthermore, the nonlinear consequences of the trapped particle instability are unknown. Presumably, the fluctuations caused by the instability would lead to enhanced radial transport. Because of the large azimuthal mode number (m ≃ 4-5), the transport should be considerably smaller than for lower mode number instabilities.

This model assumes the plasma is azimuthally symmetric and therefore modes with different m values are independent in the linear regime. In TASKA-M, however, the anchors have a quadrupole moment. If this were taken into account, one should get a coupling between various mode numbers. It is possible that the unstable mode numbers could be stabilized by coupling to neighboring stable mode numbers. An analysis of this effect is beyond the scope of this study, however.

A recent theoretical development impinges on the trapped particle stability of TASKA-M. It has been found in an analysis of trapped particle stability of the TARA experiment that a small negative electric field in the radial direction can stabilize the trapped particle stability.[3] The stabilizing effect comes from the Coriolis force associated with plasma rotation and increases in strength with mode number. Although the analysis is not directly applicable to TASKA-M, the TARA experiment (presently under construction) is similar to TASKA-M with respect to trapped particle effects, and consequently the same effect should be operative here as well. The negative radial

electric field can be obtained by biasing the end plasma dump negative relative to the side walls and the halo. The present end dump design in TASKA-M does not allow this, but it could be accommodated with a modified end dump design.

We conclude from this analysis that trapped particle stability in TASKA-M is an open question requiring further theoretical analysis and experimental confirmation. The TARA experiment should provide a good experimental data base on which one can make more definitive statements about TASKA-M.

References for Section 3.7

1. M.N. Rosenbluth, H.L. Berk, D.E. Baldwin, H. Vernon Wong, T.M. Antonsen, "Fast Growing Trapped Particle Modes," Sherwood Theory Mtg., Santa Fe, NM (1982), paper 3A2.

2. H.L. Beck et al., "Fast Growing Trapped-Particle Modes in Tandem Mirrors," Institute for Fusion Studies Report IFSR Δ59 (1982).

3. J. Kesner and B. Lane, "Effect of Equilibrium Radial Electric Field on Trapped Particle Stability in Tandem Mirrors," MIT Report PFC/JA-83-21 (1983).

3.8 Plasma Halo

3.8.1 Introduction

The plasma halo is a low density, low temperature plasma filling the volume between the core central cell plasma and the first wall. It serves to shield the core plasma from cold, neutral hydrogen atoms and from impurities. These arise from processes such as outgassing of the chamber walls, sputtering from beam dumps, and cold gas streaming down neutral beam lines. A halo plasma is generally required in magnetic fusion devices in order to protect the core plasma from losses due to charge exchange and impurity radiation.

The halo model used for TASKA-M aims at predicting the shielding and vacuum pumping properties of the halo. Both of these depend only weakly on the halo plasma temperature (for halos above about 20 eV) through ionization and charge exchange rates. Density dependence enters primarily through integrals of density over radial profiles, so it may be adequately approximated by an average value. Therefore, the halo is modeled very simply as a single zone of constant plasma density and temperature. Halo ions and electrons are assumed to have the same temperature. The results for quantities such as first wall surface heat load, shielding from sputtered atoms, and vacuum pumping speed by the halo are rough due both to the simple model and to uncertanties in cold gas sources and sputtering rates. Further refinement of the model is not warranted because of those uncertainties. However, should modification of the halo density be required, added cold gas sources or vacuum pumping could be used.

The geometry used for the TASKA-M halo calculations is shown in Fig. 3.8-1. The halo extends from the core plasma radius at 12.1 cm to the largest radius (18 cm) flux tube which passes through the choke coils at the central cell ends. Beyond that radius, magnetic field lines intersect the wall at or before the choke coils. Thus, electron thermal conduction keeps the region too cold to ionize gas, and essentially no plasma forms. In the cold gas zone, diffusion is assumed to distribute the gas fairly uniformly along the z direction and to smooth out the effects of the varying wall radius.

The shielding of the core plasma from cold gas and sputtered atoms will be estimated first. Second, halo particle and power balance will be discussed. Third, TASKA-M halo reference parameters will be given. Finally, calculations of vacuum pumping by the halo will be presented.
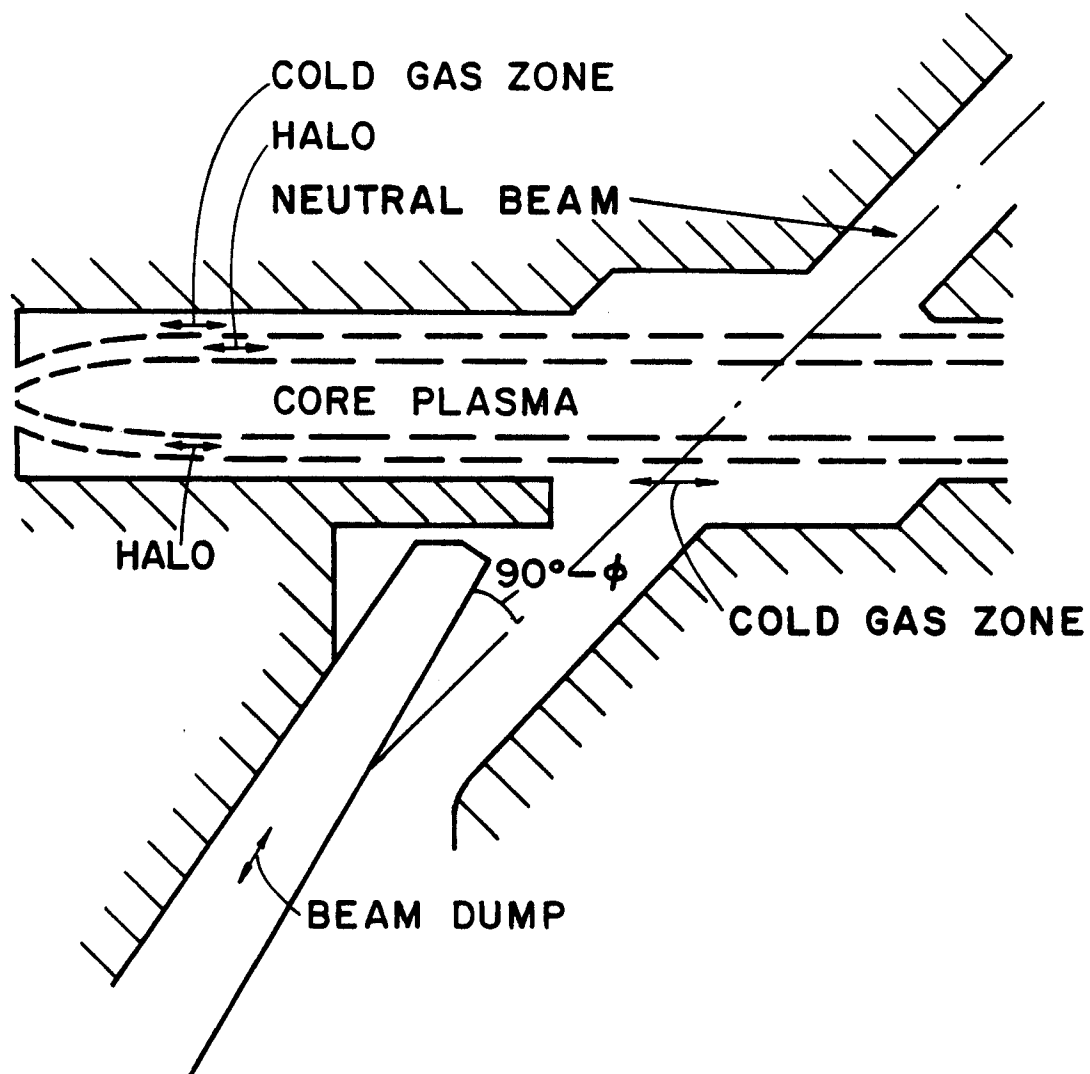
Fig. 3.8-1. Geometry of the beam dump.

Units used are cgs, except that energies will be in eV and powers will be in watts unless stated otherwise.

3.8.2 Shielding from Sputtered Beam Dump Atoms

The analysis presented here consists of two parts: First, the amount of sputtering due to shine-through neutral beam atoms impacting the beam dumps is estimated using the analysis of Bohdansky.[1,2] Second, the number of sputtered atoms which reach the core plasma is approximated by geometric arguments. Both calculations are rough, but they suffice since shielding requirements are defined by the pessimistic assumption that all sputtered atoms reaching the core are absorbed by the core.

The central cell neutral beams total 20.9 MW of power and nominally have three energy components: 87.4% at 90 keV, 6.0% at 45 keV, and 6.6% at 30 keV. The values used here differ slightly from the reference case values given in Chapter 6, but the differences do not alter the final results significantly. This gives an average energy of 83.3 keV and total current of 251 amperes or 1.6×10^{21} atoms/s. Of this current, 92% is trapped in the core plasma. Conservatively, neglecting the trapping fraction in the halo, about $\dot{N}_{bd} = 1.3 \times 10^{20}$ atoms/s impact the beam dumps. The beam dumps are assumed to be molybdenum, but results for other choices such as copper will be very similar. Figure 3.8-2 gives the sputtering yield of Mo per incident deuterium atom for normal (0°) incidence. Examining Fig. 3.8-2 indicates that tritium should give sputtering yields about a factor of two larger than those of deuterium. Roughly extrapolating to the 10 to 100 keV energy range, the total sputtering yield for normal incidence should be approximately $Y_0 = Y_D + Y_T = 3Y_D = 1.1 \times 10^{-3}$ atoms/incident particle.

Sputtering yield depends on the incident beam angle as[1]

$$Y(\phi) = Y(0) \cos^{-f} \phi \qquad (3.8-1)$$

where f ranges from one to two. f is one when incident atoms penetrate so deeply that the resulting, scattered atoms have randomized direction. f = 1.8 will be used here. In the reference case, the beam dump is inclined at $\phi = 71°$ to the neutral beams in order to minimize the surface heat load.

Sputtering yield is proportional to E^{-2} and peaks in energy at about $E = 2E_b/3$, where E_b is the surface binding energy.[1] For very high
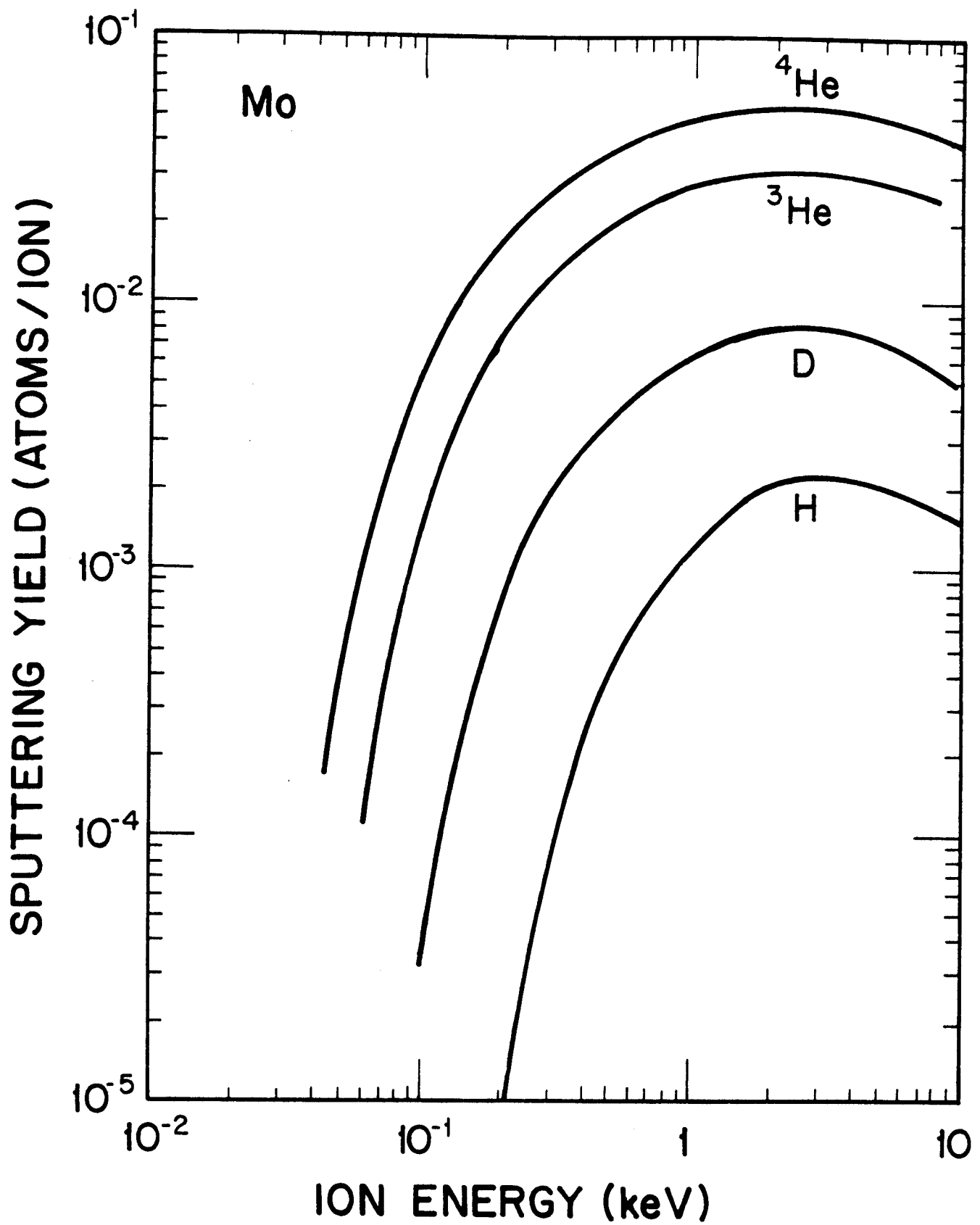
Fig. 3.8-2. Sputtering yield of molybdenum per incident atom for normal
incidence versus incident atom energy.

energy incident particles (90 keV is borderline), the sputtered atoms have a $\cos\theta \cos\zeta$ distribution, where θ and ζ are $0°$ normal to the surface.

Figure 3.8-1 shows the geometry of the beam dump. Assuming that the neutral beam is highly localized in intensity at its axis (adequate for the level of approximation used in this halo model), sputtered atoms can potentially impact the core plasma if $62° \lesssim \theta \lesssim 80°$ and if $\zeta = \arctan(r_c/170$ cm$) \lesssim 4.1°$. r_c is the radius of the core central cell plasma.

The probability that a sputtered atom with energy E penetrates the halo is assumed to be $\exp(-\lambda)$, where λ is the ratio of path length in the halo to mean free path, given by

$$\lambda = 7.15 \times 10^{-7} \frac{n \ell \langle\sigma v\rangle_{Mo} \mu_{Mo}^{1/2}}{E^{1/2}} \qquad (3.8\text{-}2)$$

where μ_{Mo} is the ratio of the mass of Mo to the proton mass. Although the path length, ℓ, depends on θ and ζ, the ranges of θ and ζ are small and ℓ is taken to be a constant here. $\langle\sigma v\rangle_{Mo}$ is the ionization rate for Mo and is given by[3]

$$\langle\sigma v\rangle_{Mo} = \frac{10^{-5} (T_e/I_{Mo})^{1/2}}{I_{Mo}^{3/2} (6 + T_e/I_{Mo})} \exp(-I_{Mo}/T_e) \qquad (3.8\text{-}3)$$

where T_e is the halo electron temperature, $I_{Mo} = 7.3$ eV is the ionization potential for Mo, and the reaction rate has been averaged over Maxwellian electrons.

The number of sputtered Mo atoms per second which reach the core plasma is therefore given by

$$\dot{N}_{Mo}^S = \frac{\dot{N}_{bd} Y_o E_b}{\cos\phi \; 4} \int_0^{4.1°} d\zeta \int_{62°}^{80°} d\theta \int_{E_b}^{E_{inj}} dE \frac{\cos\theta \cos\zeta}{E^2} e^{-\lambda}$$

$$\qquad (3.8\text{-}4)$$

$$= \frac{2.8 \times 10^{27}}{(n \ell \langle\sigma v\rangle_{Mo})^2} (1 + \lambda) e^{-\lambda} \Bigg|_{E=E_b}^{E=E_{inj}}$$

where $\dot{N}_{bd}$ is the particle source to the beam dump, a normalization factor of $9E_b/16$ has been included, and n is understood to be the halo density. Note, however, that most of the Mo atoms which reach the core plasma edge will be quickly ionized and lost out the ends since the axial potentials are small at large radii. $\dot{N}^s_{Mo}$ thus probably gives an overestimate of the number of Mo atoms which actually are trapped in the core plasma.

Since Mo is a high-Z material and sputtered Mo atoms hit the core plasma inside the central cell potential dip, the end loss time is very long. Classical radial transport, therefore, sets the Mo loss rate. The radial loss time is approximately

$$\tau_{Mo} \sim \frac{r_c^2}{2D_\perp^{Mo}} \sim 2.8 \text{ s} \tag{3.8-5}$$

where

$$D_\perp^{Mo} \sim \nu_\perp \rho_{Mo}^2 \sim 2.3 \times 10^{-11} \frac{n_{Hc}}{E_{Hc}^{1/2}} \sim 26 \text{ cm}^2/\text{s} \tag{3.8-6}$$

is the classical radial diffusion coefficient, r_c is the central cell radius, $\nu_\perp$ is the 90° scattering time, ρ_{Mo} is the Mo gyroradius, n_{Hc} is the core hot ion density, and E_{Hc} is the core hot ion energy. The radial loss rate is thus

$$\dot{N}^r_{Mo} \sim f_{rp1} \frac{n_{Mo}}{\tau_{Mo}} V_c \approx 9.8 \times 10^4 \; n_{Mo} \text{s}^{-1} \tag{3.8-7}$$

where $f_{rp1} = 0.6$ is the radial profile factor for cubic profiles, and V_c is the effective central cell volume.

The particle balance for Mo, given by

$$\dot{N}^r_{Mo} = \dot{N}^s_{Mo} \; , \tag{3.8-8}$$

then sets the equilibrium density, n_{Mo}, of Mo in the core plasma. Recall that this is probably an overestimate. Since the energy of the core plasma is high enough to completely strip the Mo, the fusion power reduction factor due to a given density of Mo is

$$1 - (1 - \frac{Z_{Mo} n_{Mo}}{n_c})^2 \; .$$

3.8-6

3.8.3 Shielding from Neutral Gas

The attenuation of neutral gas for a given $\int n \, d\ell$ is given in Fig. 3.8-3.[4] From that figure, assuming a constant density halo, the proportionality constant relating $\int n \, d\ell$, the density of neutral gas at the outer edge of the halo, n_w, and the density of neutral gas a distance ℓ into the halo, n_g, is

$$C_A = \frac{n_w}{n \ell n_g} \sim 5.5 \times 10^{-12} \ .$$

At the edge of the core plasma, the neutral gas density is therefore

$$n_{wc} = \frac{n_w}{C_A n (r_h - r_c)} \ . \qquad\qquad (3.8-9)$$

where r_h is the outer radius of the halo.

The quality of shielding of neutral gas done by the halo may be measured by the amount of charge exchange which occurs between neutral gas and the core plasma. The amount of charge exchange is estimated as follows. Effectively no attenuation occurs in the core plasma until $C_A n(r) \ell = 1$, where $n(r)$ here is the core plasma density given by

$$n(r) = n_0 \left[1 - \left(\frac{r}{r_c} \right)^3 \right]$$

with n_0 the plasma density on axis. Define r_A by the condition that

$$C_A n(r_A) \ell = 1 \ . \qquad\qquad (3.8-10)$$

Then, n_{wc} will be assumed constant for $r_A < r < r_c$; this is rough, but so is the radial density profile.

Total ionization of neutral gas in the core plasma is then given by

$$\dot{N}_{igc} = 2\pi L_c \int_0^{r_A} r \, dr \, \frac{n_{wc} \langle \sigma v \rangle_{ig}}{C_A (r_c - r)} + 2\pi L_c \int_{r_A}^{r_c} r \, dr \, n_{wc} n(r) \langle \sigma v \rangle_{ig}$$

$$(3.8-11)$$

$$= \frac{2\pi L_c}{C_A} n_{wc} \langle \sigma v \rangle_{ig} \left[r_c \ln \left(\frac{r_c}{r_c - r_A} \right) - r_A \right] + 2\pi L_c n_{wc} n_c \langle \sigma v \rangle_{ig} \left[\frac{r^2}{2} - \frac{r^5}{5 r_c^3} \right]_{r_A}^{r_c}$$
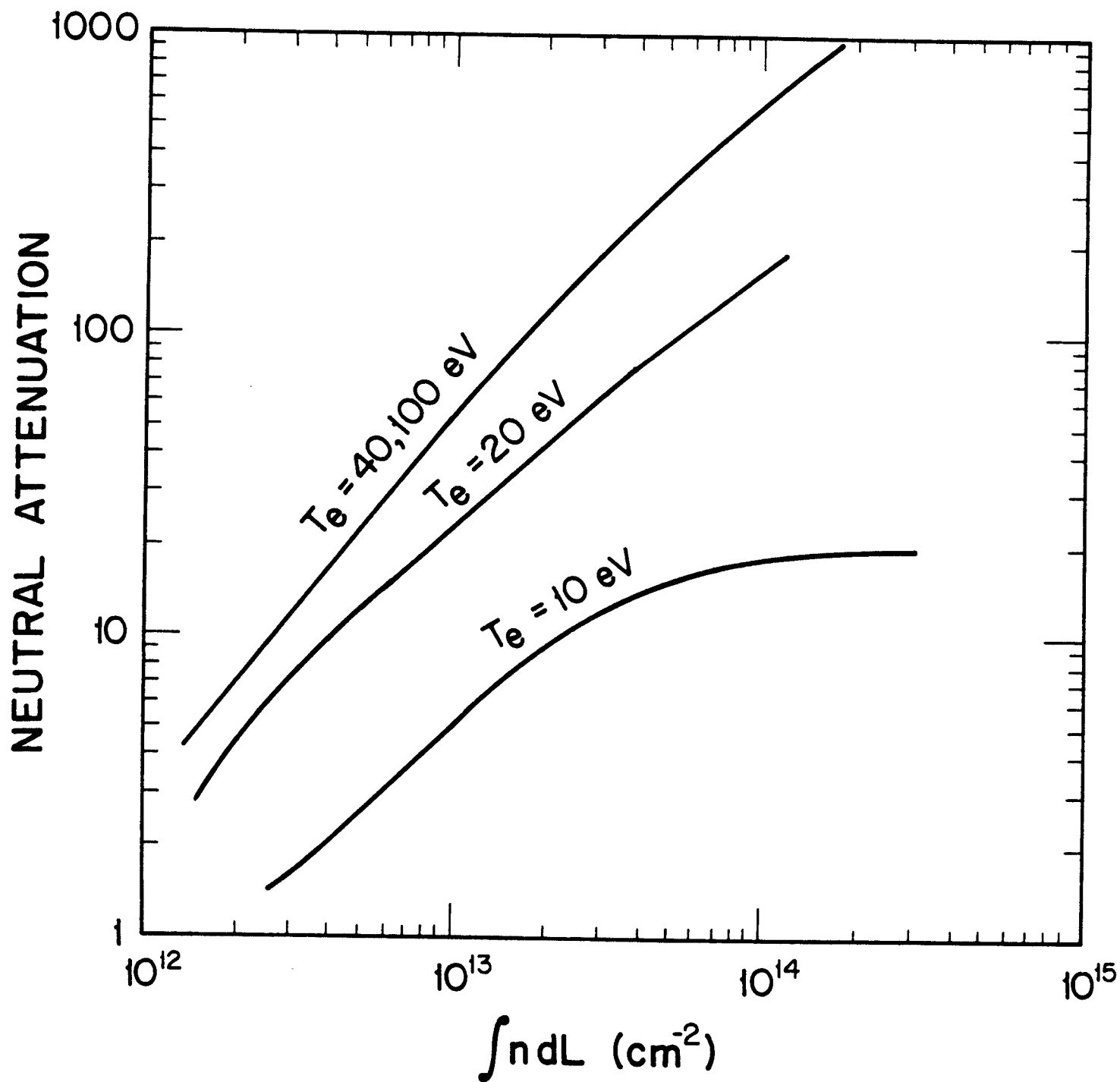
Fig. 3.8-3. Attenuation of neutral gas versus $\int n \, d\ell$.

where $\langle\sigma v\rangle_{ig}$ is the ionization rate for neutral gas and L_c is the effective central cell length. Total charge exchange, by a similar argument, is

$$\dot{N}_{cxgc} = \frac{\langle\sigma v\rangle_{cxg}}{\langle\sigma v\rangle_{ig}} \dot{N}_{igc} . \qquad (3.8\text{-}12)$$

3.8.4 Halo Particle Balance

Since the central cell magnetic fields are axisymmetric, classical radial transport may be assumed. Only hot central cell ions are considered because they are both hotter and denser than the warm ion population. The central cell ion radial transport coefficient is thus

$$D_r \sim \nu_\perp \rho_{iH}^2 \approx \frac{0.105\, n_{Hc}}{E_{Hc}^{1/2}\, B_c^2} \sin^2\theta_{inj} = 33\ cm^2/s \qquad (3.8\text{-}13)$$

where n_{Hc} is the central cell hot ion density, θ_{inj} is the neutral beam injection angle, E_{Hc} is the hot ion energy, B_c is the central cell magnetic field, $\nu_\perp$ is the 90° scattering time, and ρ_{iH} is the hot ion gyroradius. The radial loss time may be approximated by

$$\tau_r \sim \frac{r_c^2}{2D_r} \approx 2.2\ s$$

giving a radial loss from the central cell to the halo of

$$\dot{N}_{r0} \sim f_{rpl} \frac{n_{hc}}{\tau_r} V_c \approx 2.0 \times 10^{19}\ s^{-1} . \qquad (3.8\text{-}14)$$

Radial transport to the cold gas zone from the halo is, similarly,

$$D_r \sim \frac{0.053\, n}{T^{1/2}\, B_c^2} .$$

By an argument analogous to that of Section 3.8.3 for ionization of neutral gas in the core plasma, ionization of neutral gas in the halo is given by

$$\dot{N}_{ig} = \frac{2\pi L_c}{C_A} n_w \langle \sigma v \rangle_{ig} \left[r_w \ln\left(\frac{r_w - r_c}{\Delta r}\right) - (r_w - r_c - \Delta r) \right]$$

(3.8-15)

$$+ \pi L_c n_w n \langle \sigma v \rangle_{ig} \left[2 r_w \Delta r - (\Delta r)^2 \right]$$

where
$$\Delta r \equiv \frac{1}{C_A n} .$$

Also
$$\dot{N}_{cxg} = \frac{\langle \sigma v \rangle_{cxg}}{\langle \sigma v \rangle_{ig}} \dot{N}_{ig} .$$

(3.8-16)

Note that the $\langle \sigma v \rangle$'s here are not the same as those for the central cell. Attenuation of the neutral beams in the halo is modeled by

$$f_{nb} \sim 1 - e^{-\lambda_{nb}}$$

(3.8-17)

where f_{nb} is the neutral beam trapping fraction in the halo and the ratio of path length to mean free path is given by

$$\lambda_{nb} = 7.15 \times 10^{-7} \left(\frac{m_i}{m_H}\right)^{1/2} \frac{n\ell(\langle \sigma v \rangle_{inb} + \langle \sigma v \rangle_{cxnb})}{E_{inj}^{1/2}}$$

(3.8-18)

where ℓ is the path length on one side of the halo, $\langle \sigma v \rangle_{inb}$ is the ionization rate, $\langle \sigma v \rangle_{cxnb}$ is the charge exchange rate, E_{inj} is the neutral beam energy, m_i is the ion mass, and m_H is the proton mass. The total trapping rate in the halo on both sides of the core plasma is thus given by

$$\dot{N}_{nb} \approx \left[f_{nb} + f_{nb}(1 - f_{nb})(1 - f_{trf}) \right] I_{nb}$$

(3.8-19)

where I_{nb} is the incident current and f_{tr} is the trapping fraction in the core plasma. The fraction of this current which ionizes and fuels the halo is

$$\dot{N}_{nbi} = \frac{\langle \sigma v \rangle_{inb}}{\langle \sigma v \rangle_{inb} + \langle \sigma v \rangle_{cxnb}} \dot{N}_{nb} .$$

(3.8-20)

Similarly, the fraction which charge exchanges with the halo is

$$\dot{N}_{nbcx} = \frac{\langle \sigma v \rangle_{cxnb}}{\langle \sigma v \rangle_{inb} + \langle \sigma v \rangle_{cxnb}} \dot{N}_{nb} .$$

(3.8-21)

3.8-10

Some neutrals from charge exchange events in the halo will reionize in the halo. The model used here is rough, but should suffice for the accuracy of this calculation. The two chief assumptions are that the core plasma may be neglected due to its smaller volume, and that slab geometry may be used.

The mean free path for reionization of a charge exchanged neutral is

$$\lambda_{mfp} \approx \left[\frac{E^{1/2}}{7.15 \times 10^{-7} \, n \langle \sigma v \rangle_i (m_i/m_H)^{1/2}} \right] \qquad (3.8\text{-}22)$$

where $\langle \sigma v \rangle_i$ is the ionization rate and E is the neutral's energy. The very simple assumption utilized here is that the neutral escapes if its path length, ℓ, to escape the halo is longer than λ_{mfp}. The following conceptual picture is used in the analysis: $\ell = r_h - r_{cx}$ is greater than λ_{mfp} if the tip of its velocity vector lies on a zone of height h on a sphere of radius λ_{mfp}. The geometry is shown in Fig. 3.8-4a. The ionization probability, f_{ion}, is then the area of the zone divided by the total surface area of the sphere. The three possible cases are shown in Fig. 3.8-4b. For case 1, $\lambda_{mfp} < r_h - r_{cx}$, and $f_{ion} = 1$. For case 2, $r_h - r_{cx} < \lambda_{mfp} < r_h + r_{cx}$, and $f_{ion} = 0.5 + (r_h - r_{cx})/2\lambda_{mfp}$. For case 3, $r_h + r_{cx} < \lambda_{mfp}$, and $f_{ion} = r_h/\lambda_{mfp}$.

The source of halo ions due to reionization of charge exchanged neutrals is then

$$\dot{N}_{icx} = f_{ion} \left(\dot{N}_{nbcx} + \dot{N}_{cxg} \right) . \qquad (3.8\text{-}23)$$

These particle sources are balanced primarily by end loss. Two regimes may be defined, rather arbitrarily, as collisionless and collisional. They are delineated by the ratio of ion-ion scattering time, $\tau_\perp$, to bounce time, $\tau_\parallel$. For $\tau_\perp < \tau_\parallel$, the halo is collisional and a simple flow time may be used:

$$(n\tau)_{flow} \approx \frac{nR_c L_c/2}{(2T/\pi m_i)^{1/2}} \qquad (3.8\text{-}24)$$

where R_c is an appropriate mirror ratio and the π comes from taking a directed Maxwellian velocity distribution. For $\tau_\parallel < \tau_\perp$, the halo is collisionless and

$$(n\tau)_{scat} \approx (n\tau)_{ii} \ln R_c \qquad (3.8\text{-}25)$$

A

B
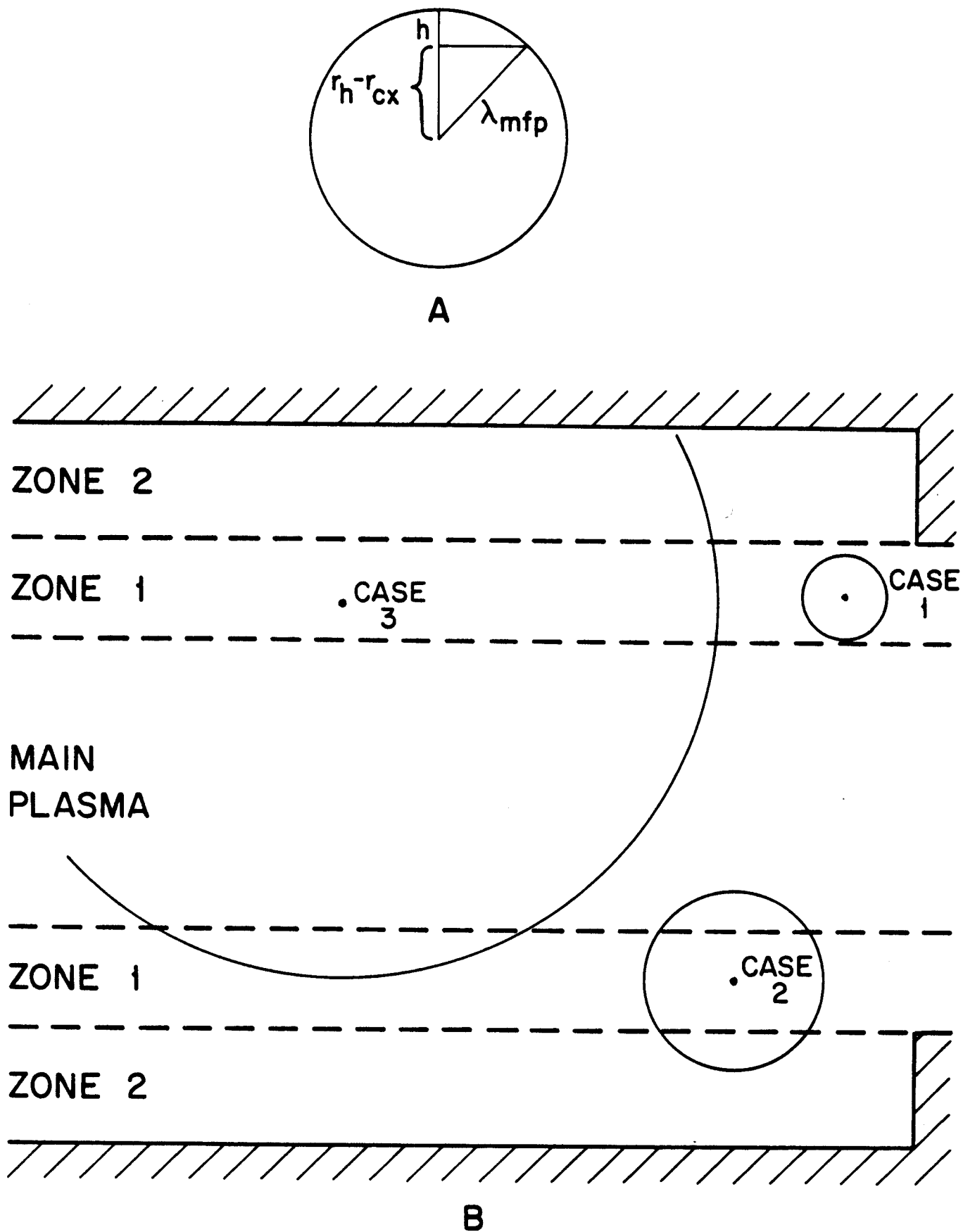
Fig. 3.8-4. (a) Geometry for reionization model argument. (b) Possible cases.

where the ion-ion scattering time is

$$\tau_{ii} \approx 4.9 \times 10^5 \frac{T^{3/2}}{n} . \tag{3.8-26}$$

End loss is then given by

$$\dot{N}_{e\ell} = \frac{n^2}{(n\tau)_{e\ell}} V_h . \tag{3.8-27}$$

Finally, total particle balance requires

$$\dot{N}_{ro} + \dot{N}_{nbi} + \dot{N}_{ig} + \dot{N}_{icx} = \dot{N}_r + \dot{N}_{e\ell} . \tag{3.8-28}$$

3.8.5 Halo Power Balance

Somewhat surprisingly, halo power balance is not dominated by the ~ 90 keV brought into the halo when a neutral beam particle ionizes or charge exchanges. The reason is that often the hot ion charge exchanges with neutral gas before it slows down appreciably. The pertinent times are

$$\tau_{cx} \approx \frac{1}{n_n \langle \sigma v \rangle_{cx}} \tag{3.8-29}$$

$$\tau_{dr} \approx \frac{(m_i/m_H)T^{3/2}}{3.2 \times 10^{-8} n} . \tag{3.8-30}$$

Total halo power drain on the neutral beams is $\dot{N}_{nb}E_{inj}$, but the effective power given to the halo may be approximated by:

$$P_{nb} \approx \dot{N}_{nb}E_{inj} - \left(\dot{N}_{nb} + \dot{N}_{nbcx}\right) \frac{3}{2} T \tag{3.8-31}$$

for $\tau_{dr} < \tau_{cx}$, and

$$P_{nb} \approx \dot{N}_{nb}E_{inj} \frac{\tau_{cx}}{\tau_{dr}} - \left(\dot{N}_{nb} + \dot{N}_{nbcx}\right) \frac{3}{2} T \tag{3.8-32}$$

for $\tau_{cx} < \tau_{dr}$.

Another possibly important term stems from alpha particle orbits intersecting the halo. Whether significant halo heating occurs depends on the relative thermal equilibration times for alpha particles in the halo and in the core plasma. In the core plasma,[3]

$$\tau_E \sim \frac{(m_e E_\alpha + m_\alpha T_{ec})^{3/2}}{1.8 \times 10^{-19} (m_e m_\alpha)^{1/2} Z_\alpha^2 n_e \ln \Lambda} \sim 0.08 \text{ s} \tag{3.8-33}$$

while in the halo,

$$\tau_E^h \sim \frac{(m_e E_\alpha + m_\alpha T)^{3/2}}{1.8 \times 10^{-19} (m_e m_\alpha)^{1/2} Z_\alpha^2 n \ln \Lambda} \sim \frac{24}{n} (3.5 \times 10^6 + 7300\, T)^{3/2} \text{ s} \tag{3.8-34}$$

where $\ln \Lambda \approx 20$ is the Coulomb logarithm. $\tau_E^h \sim 0.15$ s for the reference case. For the purposes of this analysis, the region with the smaller τ_E will be assumed to absorb the alpha particle power. The amount of power absorbed in the halo may be reduced to the geometric question of what fraction of the alpha particle orbits intersects the halo. A slab model and analysis analogous to the reionization model of Section 3.8.4 will be used. Then, for an alpha particle born at radius r with angle θ with respect to the magnetic field, two cases exist:

$$0 < r < 2\rho_\alpha - r_c \qquad f_\alpha(r) = \frac{r_c}{2\rho_\alpha} \tag{3.8-35}$$

$$2\rho_\alpha - r_c < r < r_c \qquad f_\alpha(r) = \frac{1}{2}\left(1 - \frac{r_c - r}{2\rho_\alpha}\right) \tag{3.8-36}$$

where $f_\alpha(r)$ is the fraction of alpha particles at radius r which have orbits intersecting the halo, and ρ_α is the maximum alpha particle Larmor radius. For the cubic radial profile of the reference case, the fraction of total alpha particle orbits which intersects the halo is

$$f_{\alpha h} \approx \int_{r_c - 2\rho_\alpha}^{r_c} \frac{r\, dr}{r_c^2} \left[1 - \left(\frac{r}{r_c}\right)^3\right] f_\alpha(r) . \tag{3.8-37}$$

Total power to the halo is thus at most

$$P_\alpha \approx 0.2 \, P_{fus} f_{\alpha h} \, . \qquad (3.8-38)$$

For the reference case, $\tau_E < \tau_E^h$, so no halo heating due to alpha particles is assumed.

The most important heating mechanism for the halo turns out to be radial transport from the central cell. Core plasma radial transport gives a halo particle gain rate of $\dot{N}_{ro}$ as discussed earlier. The corresponding energy gain is

$$P_{ro} \approx \dot{N}_{ro} E_{hc} \approx 0.27 \text{ MW} \, . \qquad (3.8-39)$$

Unless T_e is very high, the hot, radially transported ions will deposit their energy in the halo before being lost, since their thermal equilibration time is less than their loss time. The loss time for the hot ions once they are in the halo is

$$\tau_\ell \sim \frac{4.4 \times 10^5 \, E_{hc}^{3/2}}{n} \ln R_c = 4.3 \text{ s} \, . \qquad (3.8-40)$$

Their energy equilibrium time with the halo is

$$\tau_E \sim \frac{5.6 \times 10^{18}}{n \ln \Lambda} \left[\frac{1}{m_{DT}^{1/2}(E_{hc} + T)^{3/2}} + \frac{(m_e m_{DT})^{1/2}}{(m_e E_{hc} + m_{DT} T)^{3/2}} \right]^{-1} \, . \qquad (3.8-41)$$

$\tau_E \sim 0.17$ s for the reference case.

Charge exchange with background gas will contribute an important term to power balance. The charge exchange rate, $\dot{N}_{cxg}$, was computed in the previous section, and the power lost will thus be

$$P_{cxg} = \frac{3}{2} \dot{N}_{cxg} (T - T_g) \qquad (3.8-42)$$

where $T_g = 3$ eV is taken as typical of Frank-Condon neutrals.

Similarly, reionization of charge exchanged neutrals will take away

$$P_{icx} = \frac{3}{2} \dot{N}_{icx} T .$$
(3.8-43)

Estimating roughly,[5] neglect of line radiation appears to be a good assumption.

The largest power loss term is generally due to end loss. Using the particle end loss term from the previous section, the end loss power is simply

$$P_{e\ell} = \frac{3}{2} \dot{N}_{e\ell} T .$$
(3.8-44)

3.8.6 First Wall Surface Heat Load

An important consideration for the TASKA-M LiPb blanket test module is that the first wall surface heat load be kept below about 10 watts/cm^2, since the first wall is cooled by circulating LiPb. This section discusses the contribution to that heat load from processes related to the halo only. These are:

1. Neutral gas penetrating the halo and charge exchanging with the core plasma.

2. Ions resulting from neutral beam charge exchange with or ionization on the halo and subsequent charge exchange with the neutral gas.

3. Halo ions charge exchanging with neutral gas and the initial charge exchange events of the neutral beam with the halo.

The heat load due to the first process may be calculated using the charge exchange rate found in Section 3.8.3:

$$\Gamma_{E_{hc}} = \frac{\dot{N}_{cxgc} E_{hc}}{2\pi r_w L_c} .$$
(3.8-45)

The second term, using $\dot{N}_{nbcx}$ from Section 3.8.4 is approximately

$$\Gamma_{E_{inj}} = \frac{\dot{N}_{nb} E_{inj} - P_{nb}}{2\pi r_w L_c} .$$
(3.8-46)

The final term is given by that part of the charge exchanged halo ions which

is not reionized:

$$\Gamma_T = \frac{\frac{3}{2}(1 - f_{ion})(\dot{N}_{nbcx} + \dot{N}_{cxg})T}{2\pi r_w L_c} \;.$$ (3.8-47)

The distribution of the surface heat load over the first wall is related to the ratio of the bounce time for trapped neutral beam ions,

$$\tau_b \approx \frac{L_c}{V_\parallel} \approx \frac{L_c}{(2E_{inj}/m_i)^{1/2} \sin \theta_{inj}}$$ (3.8-48)

to the charge exchange time

$$\tau_{cx} \approx \frac{1}{n_n \langle \sigma v \rangle_{cxnb}} \;.$$ (3.8-49)

Since $\tau_b \lesssim \tau_{cx}$, the surface heat load is assumed to be distributed evenly over the whole first wall.

3.8.7 Halo Reference Case

The TASKA-M halo reference case is given in Table 3.8-1 and 3.8-2. Almost the only available knob to turn in choosing a reference case is the base pressure, which gives the neutral gas density at the first wall. Furthermore, since it is convenient to have the halo do all of the vacuum pumping, essentially no freedom in picking parameters exists. Therefore, it is fortuitous that the final reference case satisfies all necessary criteria.

As stated in the introduction to this section, the main constraint on the choice of a reference case is that the halo must shield the core plasma from neutral gas and sputtered beam dump atoms. The other major consideration is that surface heat load should be as low as possible. A secondary effect of that is to keep the neutral beam attenuation small, which is also desirable.

The dependence of halo density and temperature on the base pressure is shown in Fig. 3.8-5. For cases with base pressures, P_b, below about 5×10^{-5} torr, the halo is in the collisionless regime. The input power is almost totally due to radial transport from the central cell and is, therefore, constant. Since the particle source to the halo is primarily due to ionization and charge exchange (with subsequent reionization) of neutral gas, it is proportional to the base pressure. Constant power and a lower particle source combine to give a rising temperature as base pressure falls. The approximate-

Table 3.8-1. General Halo Parameters

Density, n	3.5×10^{12} cm^{-3}
Temperature, T	615 eV
Inner radius, r_c	12.1 cm
Outer radius, r_h	18 cm

Surface heat to first wall (r_w = 25 cm) from halo

at ~ 90 keV	3.0 W/cm^2
at ~ 84 keV	0.8 W/cm^2
at 615 eV	1.8 W/cm^2
Total	5.6 W/cm^2

Particle flux to first wall

at ~ 90 keV	2.1×10^{14} cm^{-2} s^{-1}
at ~ 84 keV	5.7×10^{13} cm^{-2} s^{-1}
at 615 eV	1.2×10^{16} cm^{-2} s^{-1}

Neutral density

at core plasma edge	2.1×10^9 cm^{-3}
at first wall	2.4×10^{11} cm^{-3}
Base pressure at wall	7.2×10^{-6} torr

Charge exchange of neutral beam ions

Charge exchange time, τ_{cx}	4.7×10^{-6} s
Drag time, τ_{dr}	0.34 s
Bounce time, τ_b	2.7×10^{-6} s

Reionization of charge-exchanged neutrals

Mean free path	238 cm
Reionization fraction	0.076

Beam dump sputtering

Beam dump material	Mo
Surface binding energy, E_b	86 eV
Maximum fusion power degradation	0.1%

Table 3.8-2. Halo Particle and Power Balance Parameters

Confinement parameters

End loss, $(n\tau)_{e\ell}$ 7.5×10^9 cm^{-3} s

Collisional flow, $(n\tau)_{flow}$ 2.9×10^8 cm^{-3} s

Mirror loss, $(n\tau)_{scat}$ 7.5×10^9 cm^{-3} s

Particle gain

Radial transport, $\hat{N}_{r\phi}$ 2.0×10^{19} s^{-1}

Neutral beam ionization, $\hat{N}_{nbi}$ 8.7×10^{18} s^{-1}

Neutral gas ionization, $\hat{N}_{ig}$ 3.5×10^{20} s^{-1}

Reionization of CX neutrals, $\hat{N}_{icx}$ 7.7×10^{19} s^{-1}

Particle loss

Radial transport, $\hat{N}_r$ 2.1×10^{16} s^{-1}

End loss, $\hat{N}_{e\ell}$ 4.5×10^{20} s^{-1}

Power gain

Radial transport, $P_{r\phi}$ 272 kW

Alpha particles, P_α 0 kW

Reionization of CX neutrals, P_{icx} 11 kW

Neutral beams, P_{nb} 0 kW

Power loss

Radial transport, P_r 0 kW

Neutral gas CX, P_{cxg} 149 kW

End loss, $P_{e\ell}$ 134 kW

Neutral beam attenuation in halo   1.0%

Halo pumping speed   21 ℓ s^{-1} cm^{-2}
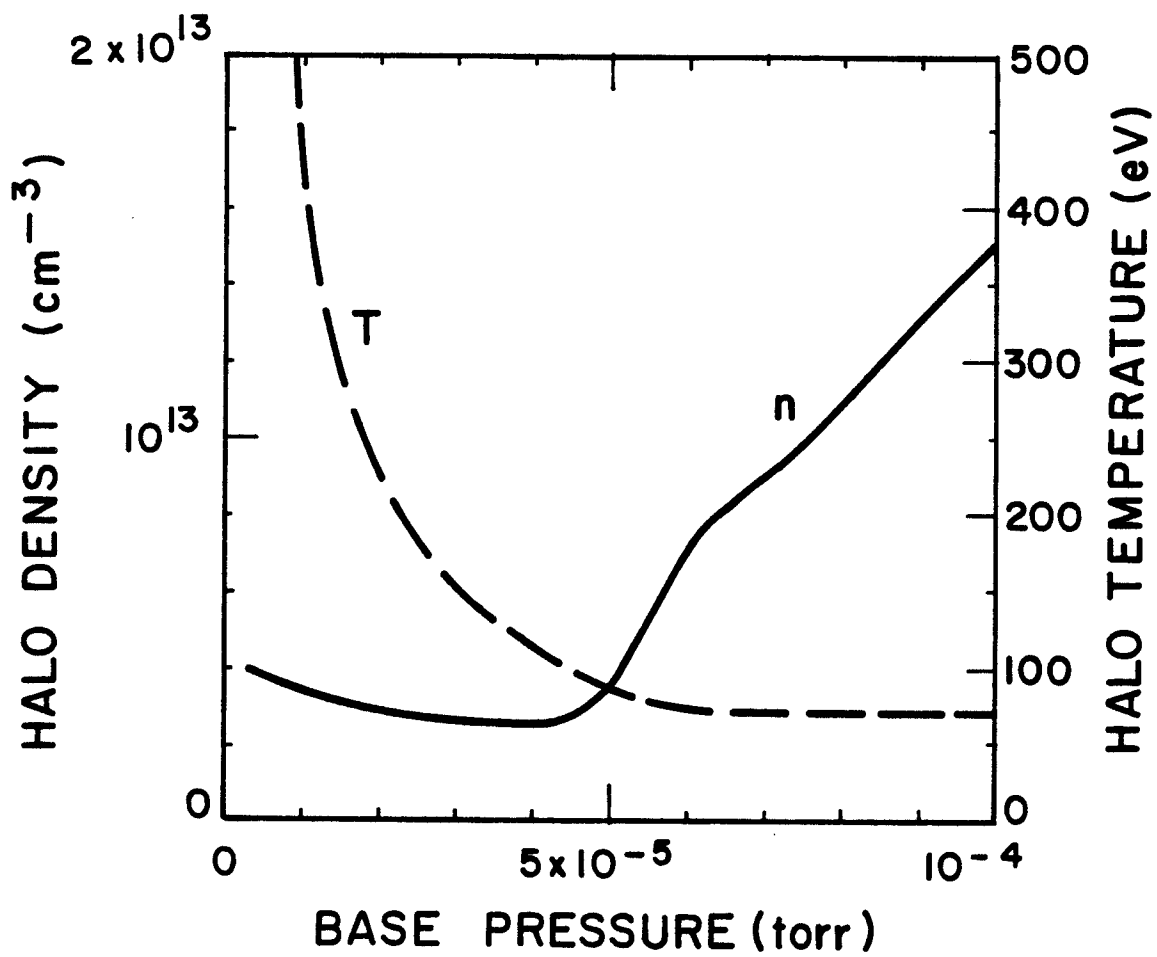
Fig. 3.8-5. Halo density and temperature versus base pressure.

ly constant density in this regime is due to the strong increase in confinement time with temperature. When P_b is greater than 5×10^{-5} torr, the halo is in the collisional regime, where the confinement time is almost independent of density. Thus, since the particle source is rising with base pressure, the density also rises. Also, attenuation of the neutral beams becomes a significant contributor to power balance, with power to the halo rising linearly with density. Because both power and particle sources are rising approximately with density, the halo temperature remains essentially constant.

The most important conclusion to be drawn from Fig. 3.8-5, however, is that considerable leeway exists in the TASKA-M halo operating regime. If, for example, unexpected cold gas sources lead to a reference base pressure as much as a factor of six higher than that used here and calculated in the next section, the shielding properties of the halo remain essentially unchanged. Thus, we may have good confidence that the TASKA-M halo will shield the core plasma and vacuum pump central cell cold gas, despite the rough nature of the model.

3.8.8 Vacuum Pumping of the Central Cell by the Plasma Halo

3.8.8.1 Introduction.
In view of the fact that the nominal density and temperature of the halo ions are $\sim 3.5 \times 10^{12}$ cm^{-3} and 615 eV, respectively, it might be expected that the plasma halo would provide a vacuum pumping surface for cold background gas in the central cell. It is the purpose of this section to quantify the pumping properties of the halo and, given the expected gas loads into the central cell, determine typical steady-state gas pressures under operation. It will be demonstrated that the plasma halo is a very effective pumping medium and is capable of maintaining the central cell pressure at $< 10^{-5}$ torr under operation.

3.8.8.2 The Halo Pumping Equation.
We begin with the ideal gas law

$$PV = NkT \qquad (3.8-50)$$

where k is Boltzmann's constant and N is the total number of gas molecules in system. At constant temperature, the total differential with respect to time is

$$\frac{d}{dt}(PV) = P \left(\frac{\partial V}{\partial t}\right)_P + V \left(\frac{\partial P}{\partial t}\right)_V = kT \frac{dN}{dt} . \qquad (3.8-51)$$

Since TASKA-M has, under steady-state, a well defined plasma radius, we are pumping a central cell of constant volume V. Therefore, Eq. 3.8-51 becomes

$$V \frac{dP}{dt} = kT \frac{dN}{dt} .$$ (3.8-52)

The rate of change of gas molecules in the system will be equal to the gain due to all source terms of cold input gas (dN_s/dt) minus the loss rate due to the halo pumping (dN_h/dt). Therefore,

$$V \frac{dP}{dt} = kT \left(\frac{dN_s}{dt} (P) - \frac{dN_h}{dt} (P) \right) .$$ (3.8-53)

Note that the input and pumping rates have been written as pressure dependent terms. The source term expressing the throughput of cold gas to the central cell may be written

$$q_s(P) = q_{cx} + q_{og} + q_{nb}(P) + q_0(P)$$

(3.8-54)

$$= \frac{1}{kT} \left(\frac{dN_{cx}}{dt} + \frac{dN_{og}}{dt} + \frac{dN_{nb}}{dt} (P) + \frac{dN_0}{dt} (P) \right)$$

where q_{cx} = throughput due to reflux of cold charge-exchange gas from first wall,

q_{og} = throughput due to general outgassing from wall materials etc.,

q_{nb} = throughput due to influx of gas from beam lines,

q_0 = throughput from any other subsidiary sources.

Note that q_{cx} and q_{og} are independent of system pressure. Customary units of q are torr ℓ s^{-1}.

In terms of particle rates, Eq. 3.8-54 becomes

$$q_s(P) = kT (dN_s(P)/dt) .$$ (3.8-55)

To solve Eq. 3.8-53 for pressure as a function of time in the system, we need a functional relationship for the halo pumping rate as a function of pressure. The analysis in Section 3.8 indicates a reasonably linear relationship between the halo pumping rate and the cold gas pressure, thus

3.8-22

$$\frac{dN_h}{dt} (P) \sim cP \tag{3.8-56}$$

where c is a constant. Accordingly, from Fig. 3.8-6 in the low pressure region of interest, we obtain $c \sim 7.2 \times 10^{25}$ torr^{-1} s^{-1} (atomic). This constant expresses the effective pumping speed of the halo. A plot of the halo pumping rate versus cold gas pressure is given in Fig. 3.8-6.

Substituting Eq. 3.8-56 into Eq. 3.8-53 gives the first order differential equation

$$\frac{dP(t)}{dt} + \frac{ckT}{V} P(t) = \frac{kT}{V} \frac{dN_s}{dt} (P(t)) . \tag{3.8-57}$$

To solve Eq. 3.8-55 we make the simplifying assumption that the cold gas throughput in Eq. 3.8-54 above is dominated by the first two terms, i.e. q_{cx} and q_{og}; this is an excellent assumption as will be seen later. Accordingly, we can relax the pressure dependence of the RHS of Eq. 3.8-55 and solve the resulting linear equation as follows

$$P(t) = \{P_o - \frac{1}{c} \frac{dN_s}{dt}\} e^{-(ckT/V)t} + \frac{1}{c} \frac{dN_s}{dt} \tag{3.8-58}$$

where P_o is the equilibrium system pressure at t = 0 (i.e., before the plasma is turned on).

3.8.8.3 Application of the Halo Pumping Equation to TASKA-M. Application of Eq. 3.8-58 leads to the following scenario. The system vacuum at t < 0 is maintained at P_o by some external method (e.g., cryopanels in the end cell, etc.). At t = 0 the beams turn on, the plasma is initiated, the halo begins to pump, and we disconnect all auxiliary vacuum pumps. The time behavior of the system pressure then follows Eq. 3.8-58. At equilibrium, the system will have attained a final pressure given by

$$P_{final} = \frac{1}{c} \frac{dN_s}{dt} \tag{3.8-59}$$

which is dependent on the effective halo pumping speed c and the cold gas input rate dN_s/dt. The rate at which the halo effects the pressure transition from the original base pressure P_o to the final equilibrium pressure P_{final} is dependent on the exponential term in Eq. 3.8-58. This rate will evidently be
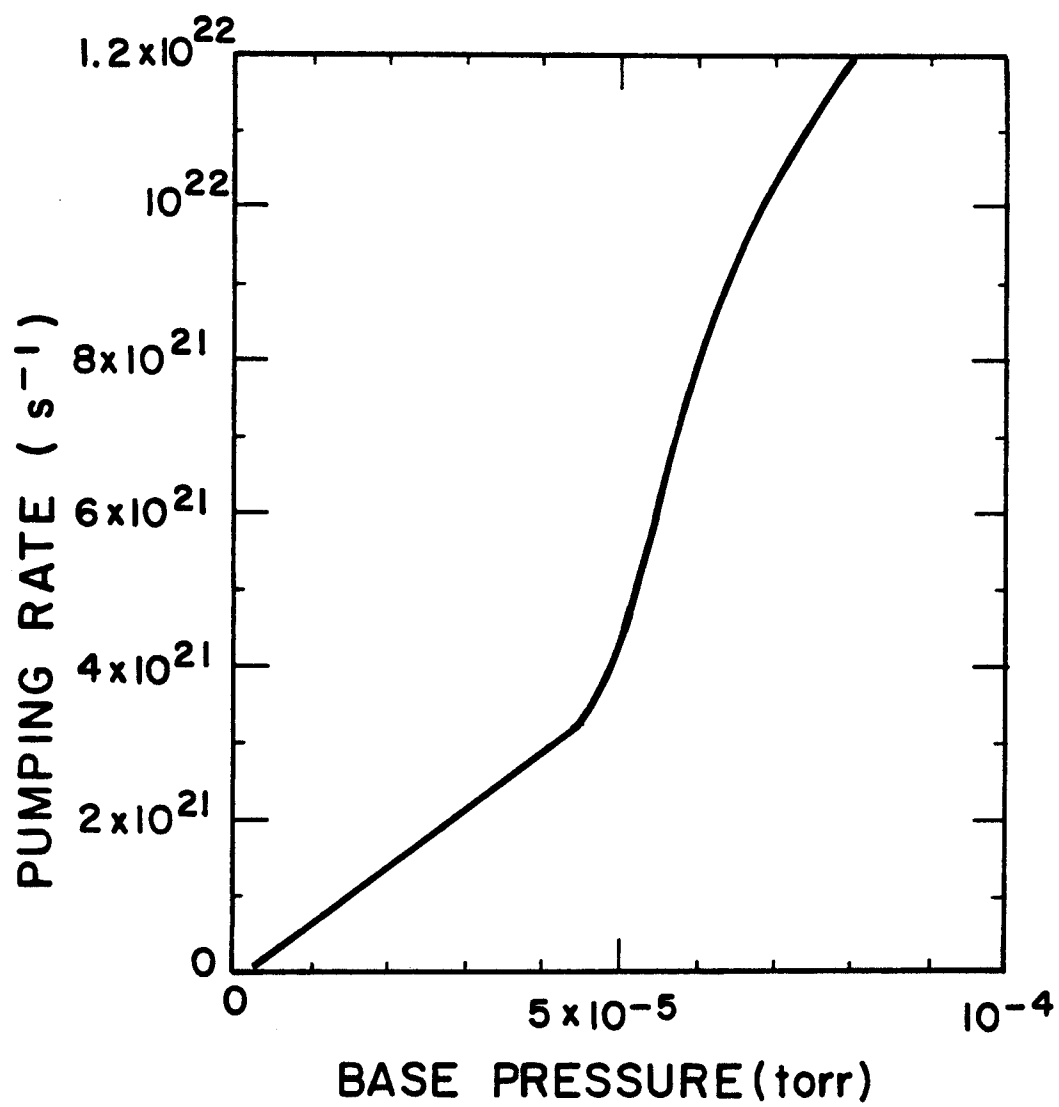
Fig. 3.8-6. Halo pumping rate versus base pressure.

rapid for a large halo speed c, a high temperature T or a small system volume V.

Computation of P_{final} for TASKA-M requires computation of q_s (i.e., dN_s/dt) via Eq. 3.8-54. From Section 6.2.3, the cx particle intensity to the first wall is 3.40 x 10^{20} s^{-1} (atomic). In equilibrium, this is equal* to cold gas reflux rate, thus $dN_{cx}/dt = q_{cx}/kT = 1.70$ x 10^{20} s^{-1} (molecular). A typical outgassing constant for stainless steel after bakeout[6] is ~ 5 x 10^{-9} torr ℓ s^{-1} per cm^2 of surface area. A worst-case upper bound for the convoluted surface area in the central cell for outgassing purposes is ~ 396 m^2 which yields a total outgassing particle rate of 6.8 x 10^{17} s^{-1} (molecular) into the vacuum chamber.

To estimate the cold gas contribution from the beam line, we note that the system base pressure P_0 before operation of the beams and plasma is maintained at typical machine pressure (~ 10^{-5}-10^{-6} torr). Since the beam line exit ducts are maintained at a quiescent pressure of the same order of magnitude by the beam line pumping system, q_{nb} will certainly be small relative to q_{cx} and can be neglected here.

Our final source term for input gas is q_0 in Eq. 3.8-54 which accounts for all other sources of gas input. Normally, excepting large leaks into the vacuum chamber, other sources of gas will be small compared with q_{cx} and q_{og}. However, for completeness, we could assume that the beam dumps are not supplied with an auxiliary pumping system. From Section 6.2.3, we have a total shine-through particle intensity of 1.825 x 10^{20} s^{-1} (atomic). Therefore, under equilibrium conditions, we obtain an equivalent cold gas reflux from the dump surfaces of 9.125 x 10^{19} s^{-1} (molecular).

Our source term for the total cold gas input to the central cell is, therefore, dN_s/dt ~ 2.6 x 10^{20} s^{-1} (molecular). Substituting this into Eq. 3.8-59 yields a final system pressure under halo pumping of ~ 7.2 x 10^{-6} torr. Note that if the beam dump gas reflux were to be accommodated by a separate auxiliary pump, this equilibrium pressure would be maintained at 4.7 x 10^{-6} torr by the halo.

---

*The fraction which diffuses to the back surface of the first wall is less than 10^{-4} of the implantation rate so the vast majority is emitted as cold gas reflux to the vacuum chamber.

3.8.8.4 <u>Discussion</u>. It appears from above that the plasma halo provides a very effective vacuum pump, and is capable of maintaining the central cell pressure at less than 10^{-5} torr under operation without the need for other pumping systems. Auxiliary pumps would, however, be required for initial pumpdown before the plasma (and thus the halo) is initiated.

A quantitative figure of merit for the pumping capabilities of the halo can be obtained if we transform the speed constant c in Eq. 3.8-56 from units of torr^{-1} s^{-1} to units of liters per second and, thereby, obtain a conventional pumping speed. Accordingly, we obtain $c \equiv 1.0 \times 10^6$ ℓ s^{-1}. With a mean halo radius of ~ 15 cm and an effective central cell plasma length of 495 cm, this gives a specific pumping speed per unit area of halo "surface" of ~ 21 ℓ s^{-1} cm^{-2}. This is a very large pumping speed and should be compared with typical speeds for D and T exhibited by present day cryopanels of ~ 5 ℓ s^{-1} cm^{-2}, and Zr-Al getter panels of ~ 0.9 ℓ s^{-1} cm^{-2}.[7] This clearly demonstrates the potential of the plasma halo as affording a very effective vacuum pumping medium for the central cell.

References for Section 3.8

1. J. Bohdansky, "Important Sputtering Yield Data for Tokamaks: A Comparison of Measurements and Estimates," J. Nucl. Mat. <u>93 & 94</u>, 44 (1980).

2. J. Roth, J. Bohdansky, and W. Ottenberger, "Data on Low Energy Light Ion Sputtering," Max-Planck-Institut für Plasmaphysik Report IPP 9/26 (1979).

3. D.L. Book, <u>NRL Plasma Formulary</u>, Naval Research Laboratory, (1980).

4. T.C. Simonen, "TMX-U Sloshing Ion Density Buildup," LLNL Memo (6/25/82).

5. D.E. Post et al., Atomic Data and Nuclear Data Tables <u>20</u>, 397 (1977).

6. H.A. Steinhertz, <u>Handbook of High Vacuum Engineering</u>, Reinhold Publishing Co., New York (1963), pp. 7-9.

7. H. Von Hagn, S.A.E.S. Getters U.S.A. Inc., Colorado Springs, CO, private communication (1981).

3.9 Plasma Startup

The plasma physics and engineering considerations so far have dealt with only the steady-state, or burn, phase of operation. In this section we discuss startup of the plasma, i.e. the process of bringing the plasma to its desired operating point. The startup phase involves creation of an initial target plasma, turning on the various neutral beams and programming the electron heating power. A related consideration is the "thermal" stability of the desired operating point. We address these issues in this section with a time-dependent rate code which calculates the evolution of the central cell density and electron temperature.

An initial target plasma can be created either by injection of plasma along the magnetic field from a stream gun in the end walls, or by injecting gas into the discharge chamber and applying low power microwaves at the electron cyclotron frequency to ionize the gas and make a target plasma. The latter method is preferred because it gives a cleaner plasma which is not so strongly connected to the end walls. Creation of a target plasma by ECRH has been accomplished in the TMX-Upgrade and Phaedrus tandem mirror experiments. A suitable target plasma for TASKA-M would have a density of $\sim 5 \times 10^{12}$ cm^{-3}, an electron temperature of ~ 30 eV, and an ion temperature of ~ 10 eV. These parameters have been obtained in Phaedrus, for example. This could be achieved with an initial ECRH pulse of a few kilowatts of power lasting for ~ 10 ms. The best point for application of the ECRH microwave power would be either in the transition region, or in the anchor, where the magnetic fields are lower and the required frequency is therefore smaller.

Given an initial target plasma, we model the evolution of the hot plasma by rate equations for the hot ion density and electron temperature. In order to reduce the number of rate equations to be solved simultaneously, we consider only the startup of the central cell plasma; starting up the anchor is conceptually the same problem. Our two rate equations are

$$\frac{d}{dt} \left(n_{Hc} V_{Hc} \right) = I_{Hb} f_p - \frac{n_{Hc}^2 V_{Hc}}{(n\tau)_{Hc}} \tag{3.9-1}$$

$$\frac{d}{dt}\left(\frac{3}{2}n_e T_e V_{Hc}\right) = P_e + \frac{n_{Hc}^2}{4}\langle\sigma v\rangle_f Q_\alpha f_e - \int \frac{n_e^2}{(n\tau)_e}dV - P_x$$

$$\text{(3.9-2)}$$

$$+ n_{Hc}\nu_{eH}^C(E_{Hc} - 1.5\ T_e)V_{Hc} + 1.5\ n_s\nu_{es}^C(T_s - T_e)V_{Hc}\ .$$

The notation is the same as in Section 3.2. n_s and T_s are the density and ion temperature of the target plasma, respectively. I_{Hb} is the injected high energy neutral beam current and f_p is a trapping fraction, which is calculated differently than in Section 3.2.6. We use the pencil beam approximation for f_p,

$$f_p = 1 - e^{-\alpha} \tag{3.9-3}$$

where

$$v_b\alpha = \int ds\ \left(n_{HC}(\langle\sigma v\rangle_i + \langle\sigma v\rangle_e) + n_s(\langle\sigma v\rangle_i + \langle\sigma v\rangle_e + \langle\sigma v\rangle_{cx})\right) \tag{3.9-4}$$

and the integral is along the beam path. In this expression for α, we consider trapping by ion and electron impact ionization with the hot plasma and cold target plasma, and by charge exchange with the cold ions. Charge exchange of a beam atom with a hot ion does not lead to an additional trapped ion, and is therefore not included. This effectively assumes the escape probability of the hot charge exchange neutrals is unity. This is true in the early phase of startup but underestimates the trapping by charge exchange as the design point is approached. On the other hand, the pencil beam overestimates the trapping coefficient to some extent (see Fig. 3.2-1) so these effects compensate each other to some degree. The effect of the warm plasma neutral beam is also neglected in Eqs. 3.9-1 and 3.9-2. An additional simplification is that ϕ_e/T_e, which is contained in $(n\tau)_e$, is not solved for self-consistently, but is replaced by its value at the design point, as given in Section 3.3. These simplifications are made in order to increase the computational speed for solving the rate equations; a consequence of these approximations is that the steady-state solution predicted by Eq. 3.9-1 and 3.9-2 will not precisely reproduce the solution of the more complicated power balance equations given in Section 3.2. This is not a major disadvantage,

since the purpose of this analysis is to establish the gross startup requirements and feasibility; minor differences will not negate the basic conclusions.

Equations 3.9-1 and 3.9-2 are solved using a predictor-corrector technique with the initial conditions:

$$n_{Hc}(0) = 0$$
$$T_e(0) = 30 \text{ eV}$$
$$n_s(0) = 5 \times 10^{12} \text{ cm}^{-3} \text{ .}$$

The target plasma density $n_s(t)$ is allowed to decay in such a way that $n_e(t)$,

$$n_e(t) = n_{Hc}(t) + n_s(t) \qquad\qquad (3.9-5)$$

is constant until $n_s(t)$, as calculated from Eq. 3.9-5, becomes zero. From then on, $n_s(t)$ is set to zero and $n_e(t) = n_{Hc}(t)$.

Figure 3.9-1 shows the result of a startup simulation with no RF heating of electrons. The beam is turned full on at t = 0; all other input parameters are given in Tables 3.3-1 to 3.3-3. The rise in the electron temperature to about 6 keV is due to heating by drag on the hot ions. This is an important effect since electron heating by Landau damping is ineffective at low electron temperature and low density. Hence, we need the high energy beams to both raise the total density and the electron temperature before RF heating is applied.

Next we consider startup with RF electron heating. A rough model for the coupling efficiency, η_e, of the heating process is obtained by putting

$$\eta_e = \eta_1(n_e) \, \eta_2(T_e) \text{ .}$$

The dependence of η_1 on n_e and η_2 on T_e is shown in Fig. 3.9-2. With this model, we get little heating with $n_e < 10^{13} \text{ cm}^{-3}$ or $T_e < 2.5$ keV. The coupled power is given by

$$P_e = \eta_e P_{RF} \text{ ,}$$
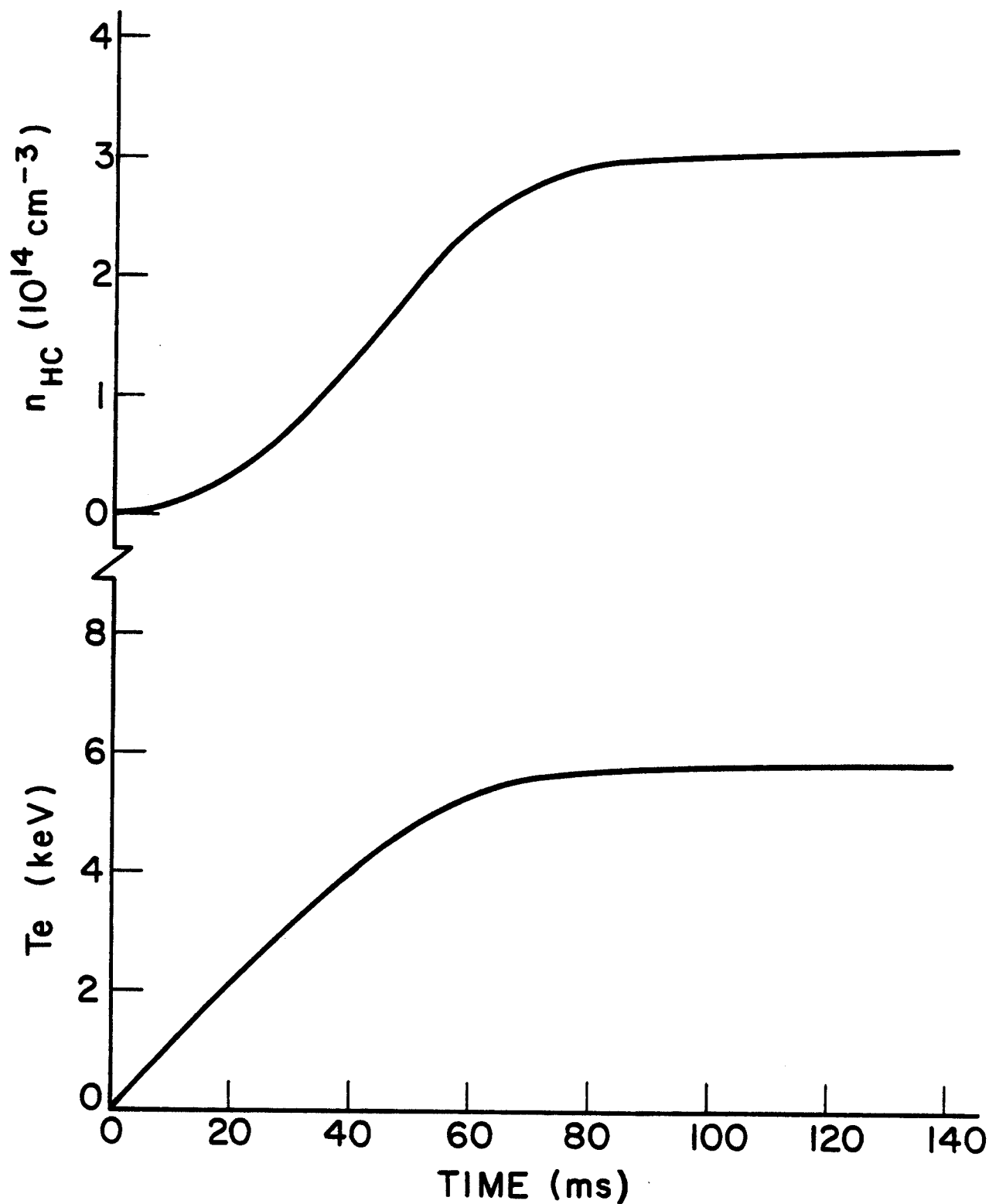
Fig. 3.9-1. Rise of the hot ion density and the electron temperature; the
high energy beam is turned on at t = 0. There is no RF heating
of electrons in this simulation.
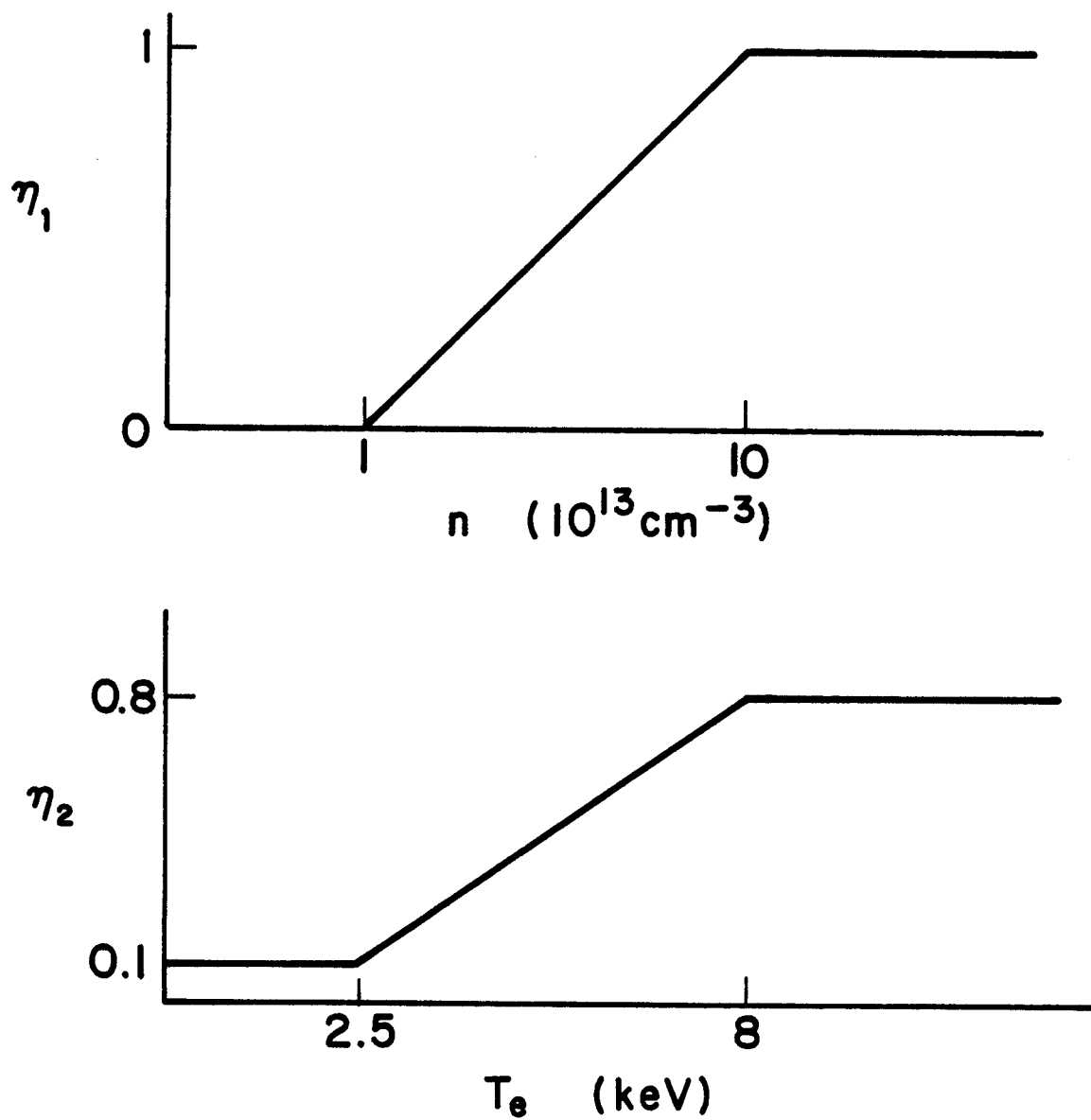
Fig. 3.9-2. The factors used in determining the coupling of the RF power to the electrons.

where P_{RF} is the applied RF power. In order to avoid overheating the electrons when the density is low, the applied power has to be programmed in time during the starting phase. Figure 3.9-3 shows the results of a startup simulation when

$$P_{RF} = \begin{cases} 0 & t < 0.05 \text{ s} \\ 7.5 \text{ MW} & 0.05 < t < 0.1 \text{ s} \\ 15 \text{ MW} & t > 0.1 \text{ s} . \end{cases}$$

We see that the density and electron temperature both rise to plateau values which are reasonably close to the design values. The final density is slightly above the design value; this can be attributed to the neglect of the low energy neutral beam which causes a loss of hot ions by charge exchange. The final electron temperature is slightly below the design value. This can be attributed to the density being too high. The humps in the $T_e(t)$ curve occur at the steps in the RF heating power. A smoother T_e curve could be obtained by a more gradual rise of $P_{RF}(t)$. This calculation is sufficient, however, to demonstrate a successful startup of TASKA-M using only the beams and RF systems required in the burn phase, except for the initial ECRH pulse. The neutral beams are not programmed; they are turned full on at $t = 0$. Programming of the RF power is required in order to avoid overheating the electrons at low density, but this is not a technological difficulty.

We also have found that the plasma comes up to its steady-state values and sits there. Hence, the design equilibrium is thermally stable; a complicated feedback system is not required to maintain the plasma at the desired burn point. A control system will be required, of course, to adjust for slow variations in the input beams and RF power.

The variation of the trapping fraction, f_p, with time is shown in Fig. 3.9-4. The trapping fraction is low for the first 40 ms, but is essentially at its design value after 60 ms. Hence, the beam dumps only have to take the full incident neutral beam power for about 50 ms; this is a consideration in the design of the beam dumps.
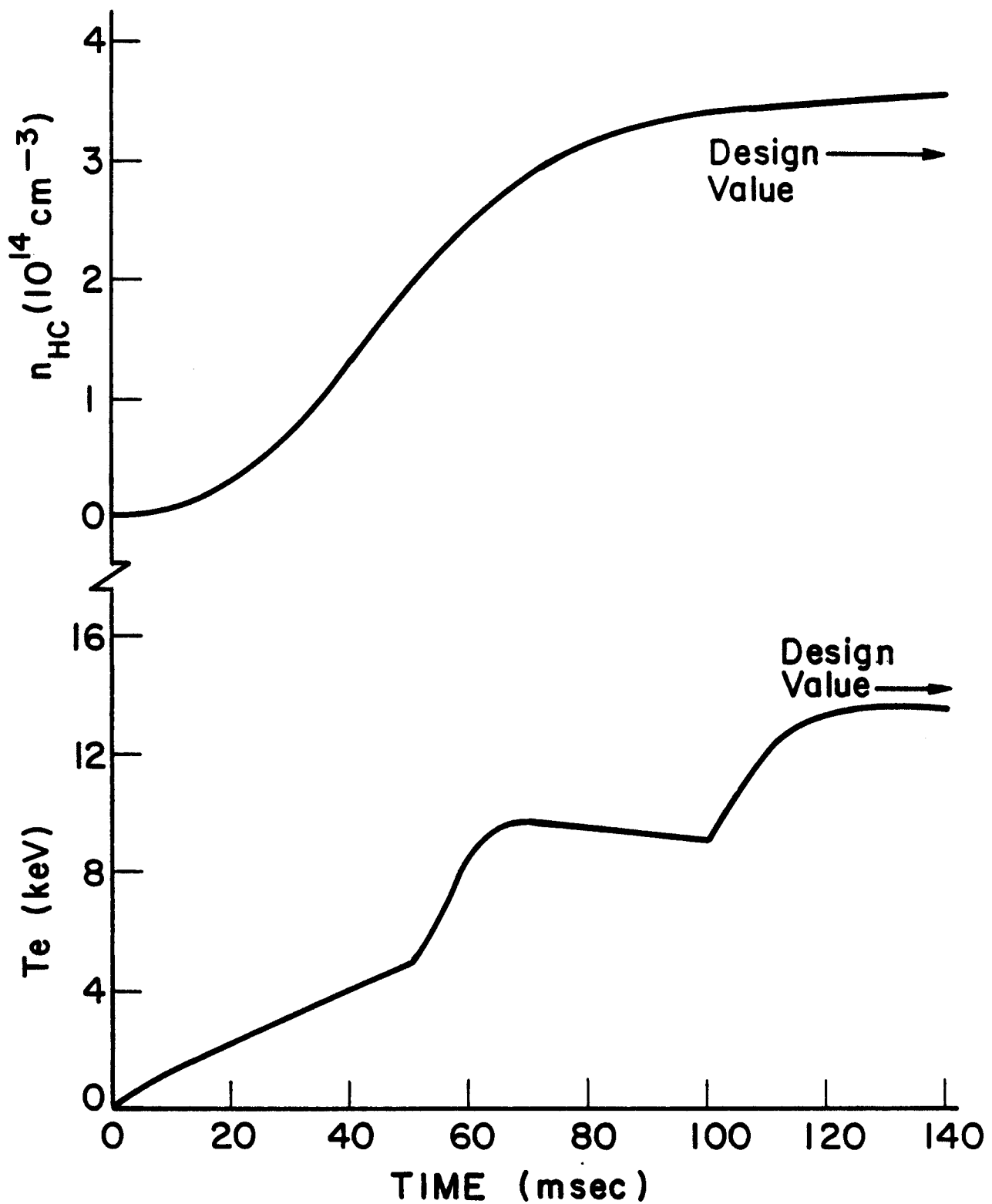
Fig. 3.9-3. The rise of the hot ion density and the electron temperature with both beam injection and RF electron heating.
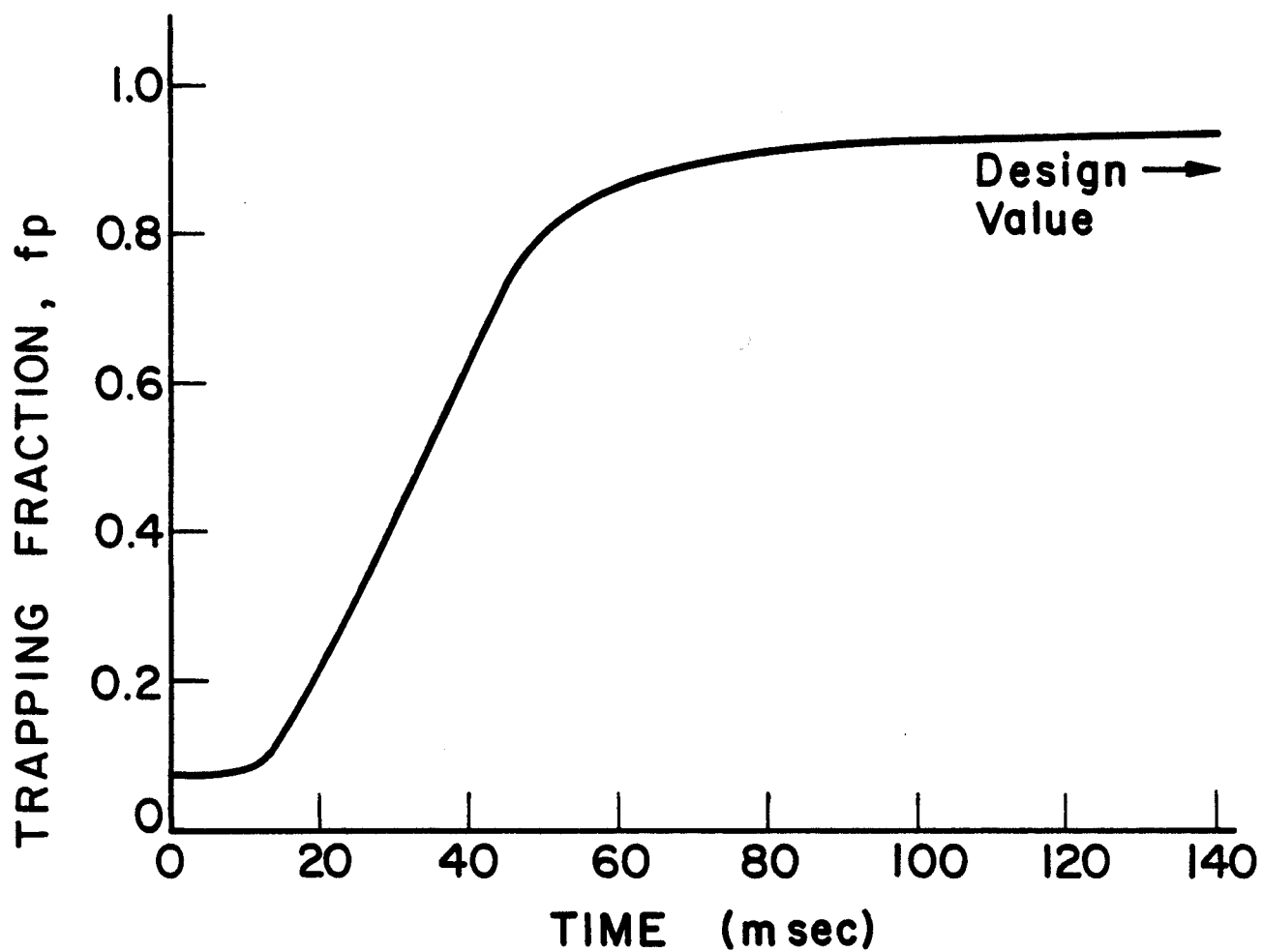
Fig. 3.9-4. The increase of the high energy neutral beam trapping fraction as the hot ion density builds up.

4. Overall Design

4.1 Introduction and Overview

The TASKA-M test facility (Fig. 4.1-1) is a triple mirror with a
solenoidal central cell and MHD-stability anchors. No electrostatic
plugging is provided. The central cell is used only as a zone for testing
both materials and breeding blankets. In order to reduce the capital cost,
there is no tritium production. In contrast to a power reactor, energy
conversion ist not provided. However a space at the end dump is reserved
for experimental purposes.

The overall length of the facility is approximately 50 m subdivided into
an 8.7 m central cell length, two 9.1 m anchor regions, and two 11.5 m end
dumps. While the maximum plasma radius is 0.12 m in the central cell an
average wall diameter of approx. 0.4 m is needed in the test zones.

Fueling and heating of the plasma is accomplished with ICRF and neutral
beam injection (NBI). The ICRF antennae in the central cell are integrated
into the blankets.

The neutral beam injectors are located in the central cell and in the
anchor regions. In the central cell there are four high energy beam lines
(HE-NBI) aimed of the midplane of the central cell and a low energy beam
line (LB-NBI) with the injection point axially displaced by 0.60 m from
the midplane. The radial arrangement of the HE-NBI and the LE-NBI is shown
in Fig. 4.1-2. Each of the two anchor regions have a single medium energy
neutral beam injector (ME-NBI) with the injection point between the Yin
and Yang coils.

The distance from the extraction grids of the ion sources to the plasma
axis is 12 m for the HE-NBI and ME-NBI, and about 5 m for the LE-NBI.
Opposite each NBI, except for the LE-NBI, there is a beam dump for the
particles which are not trapped by the plasma (Fig. 4.1-3).

Fig.4.1-1 TASKA-M OVERVIEW

SECTION A-A

SECTION B-B

HE-Neutral Beam Injector

LE-Neutral Beam Injector

ICRH-Antennae   CC-Insert

SECTION C-C

SECTION A-A

Exhaust Duct

SC-High Field Coil

NC-Coil

NC-Coil Insert
Coil Support

Blanket 4

Blanket 3

Blanket 2

Vacuum Chamber   Blanket 1

SC-Central
Cell Coil

Beam Dump
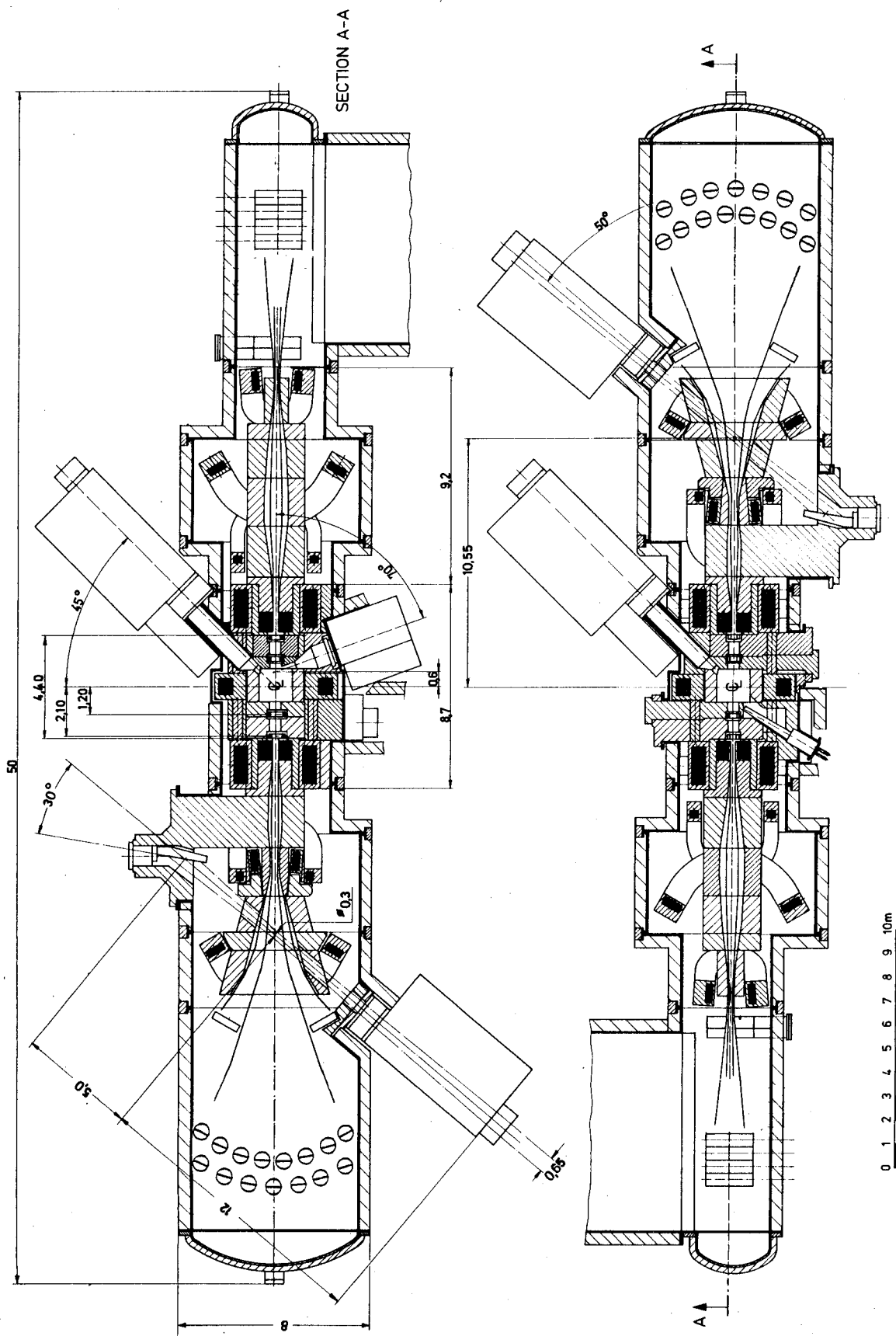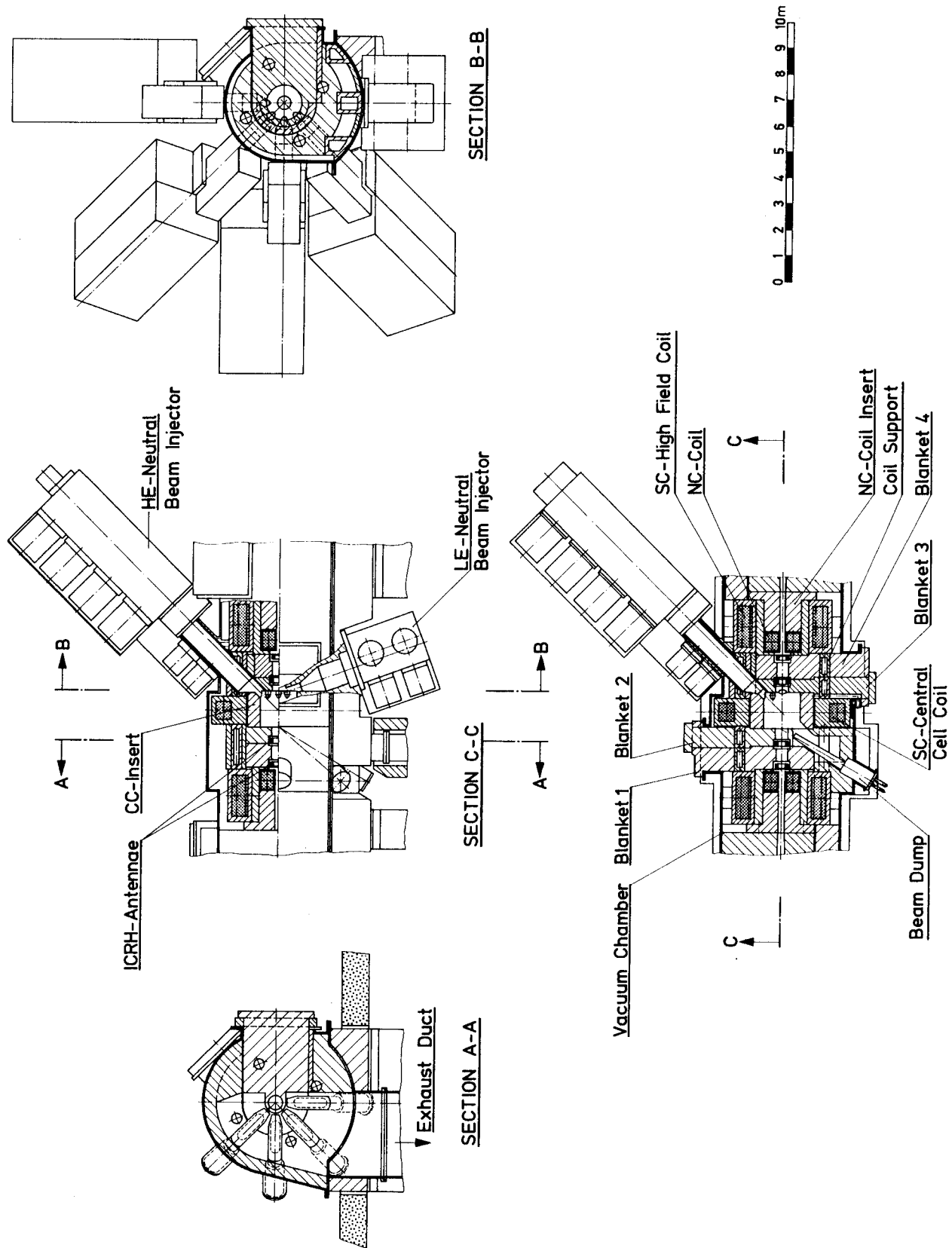
Fig.4.1-2 Overview of Central Cell

0 1 2 3 4 5 6 7 8 9 10m

Vacuum Chamber Blanket 1 Blanket 2 SC-High Field Coil NC-Coil

C

Beam Dump SC-Central Cell Coil Blanket 3 NC-Coil Insert Coil Support Blanket 4

C
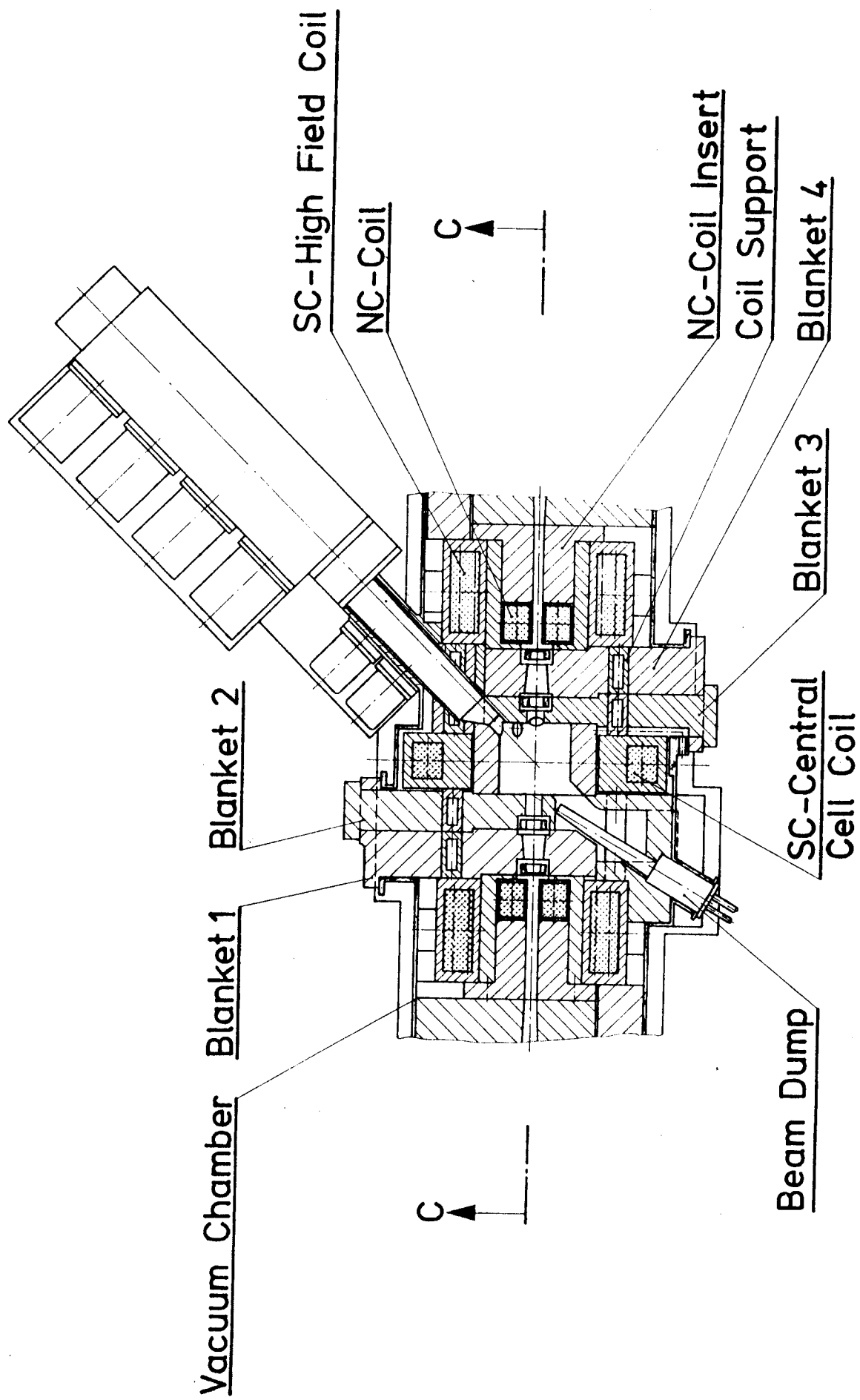
Fig.4. 1-3 Central Cell

The end cells are characterized by dumps for the plasma and the plasma-halo.

Locating the vacuum boundary represented by the vacuum chamber outside the blankets, reflector, shield and coils was an important decision, which provids, the advantage of a cold support structure between the magnets and easier assembly and maintenance of the vacuum chamber, especially for coil replacement.

The vacuum chamber with an average radius of 2.5 m in the central cell region and 4 m in the anchor regions consists of a lower and an upper shell (see Fig. 4.1-2). The lower shell, designed as a box section, rests on pillars and carries the support structures for all the internals, i.e. blankets, coils, shield etc. The upper shell, reinforced against atmospheric external pressure, is divided into segments and will be fitted to the lower shell after the installation of those internals which cannot be inserted through blanket or insert openings. The lower and the upper shells, as well as the segments, are connected by clamps and by lip welding to achieve good tightness.

For better handling and maintenance, the reactor hall level was made about 1 m below the vacuum chamber separation line. Since the neutral beam injectors had to be arranged around the machine, some of them are installed in the basement, as are some of the beam dumps, which are inserted from the bottom. This requires that maintenance of some of the injectors and beam dumps be carried out from the basement.

The basement also contains the vacuum systems for the beam dumps and the end dumps. The cryopumps of the neutral beam injectors and beam ducts, however, are located outside the injector boxes and ducts.

4.2   Central Cell

4.2.1   General

The central cell consists of a cylindrical structure bounded on both ends by the high field coils. It is composed of the vacuum chamber, in which the central cell coil and its support structure, as well as parts of the reflector and the shielding, are permanently installed. The super-conducting central cell solenoid and the two superconducting high field choke coils provide the confining field within the central cell. Between these magnets there are zones for breeding and materials test modules. In addition the large exhaust duct for the central cell vacuum chamber and for the thermalized gas from the beam dumps is located there. The duct goes downward into the basement where the vacuum pumpes are also located.

4.2.2   Blanket

Figure 4.1-3 shows the layout of the central cell with the blankets numbered 1 to 4, with an additional insert which fits inside the central cell magnet and protects the solenoid from radiation. As can be seen in Fig. 4.2-1 blanket test modules 1 and 4 are inserted horizontally, with their flanges providing closures for the blanket openings in the vacuum chamber.

Test modules 2 and 3 in turn are inserted into the modules described above. Figure 4.2-2 and 4.2-3 show the test modules in more detail. Blanket module 2 is reduced in size to leave more space for the neutral beam dumps and the exhaust duct. Table 4.2-1 shows the room temperature dimensions and locations of each module. The axial distance is measured from the center of the central cell, where negative numbers indicate locations left of the centerline. The spacing between the modules is 2 cm to accommodate thermal expansion and neutron induced swelling. Additional blanket parameters are given in Table 4.2-2, while the central cell engineering parameters are given in Table 4.2-3.

SECTION B-B

2.20
2.50
14

SECTION C-C

SECTION A-A

3.30
2.70
3.30
2.70
3.30

B
A
B
A

.09 .120 .120 .09
.09 .120 .120 .09
.90

C
C
C

φ 0.80
φ 2.46
φ 3.04
φ 4.20

60°
45°
70°
45°
45°
45°
45°
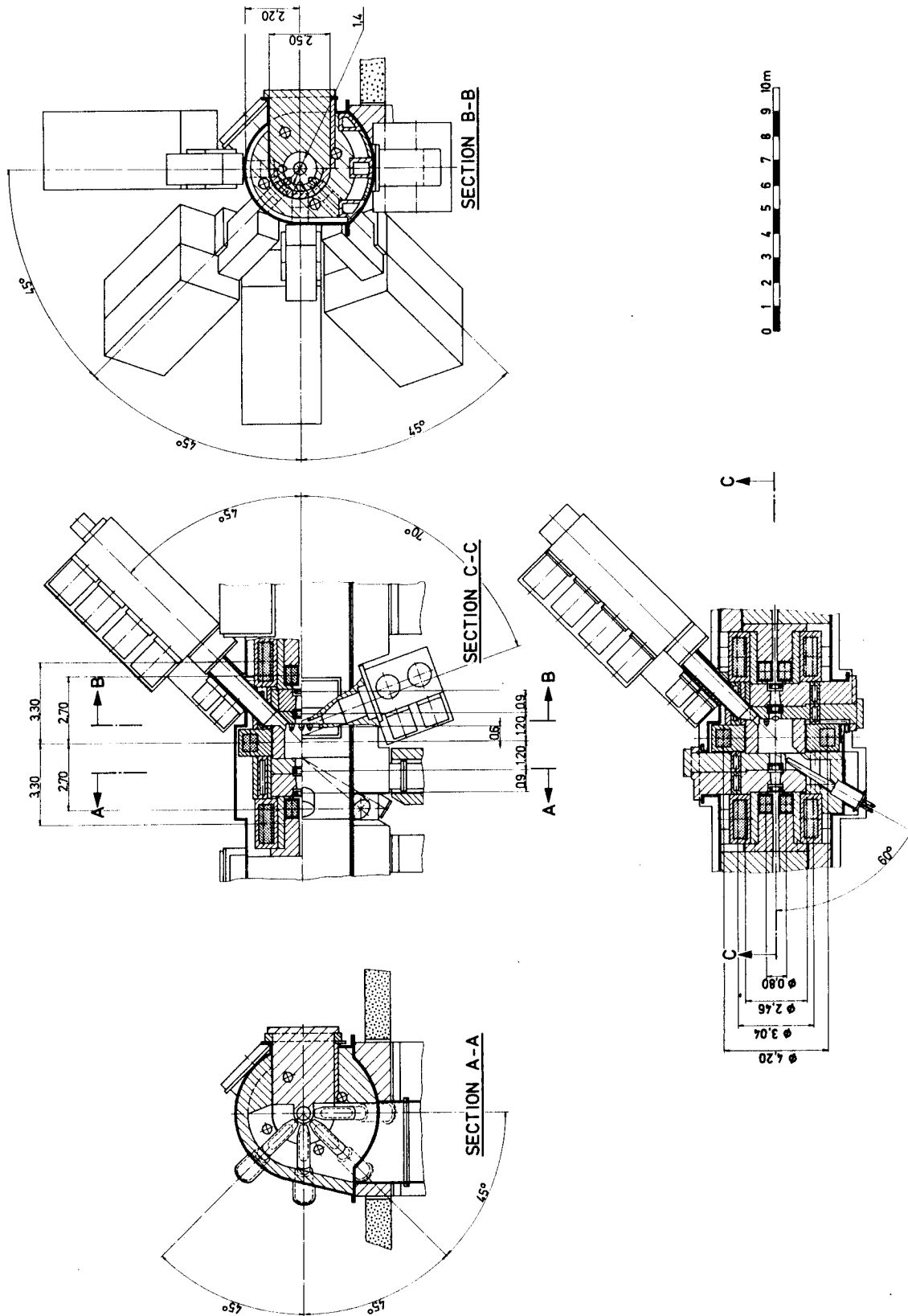
Fig.4.2-1 Details of Central Cell

0 1 2 3 4 5 6 7 8 9 10m
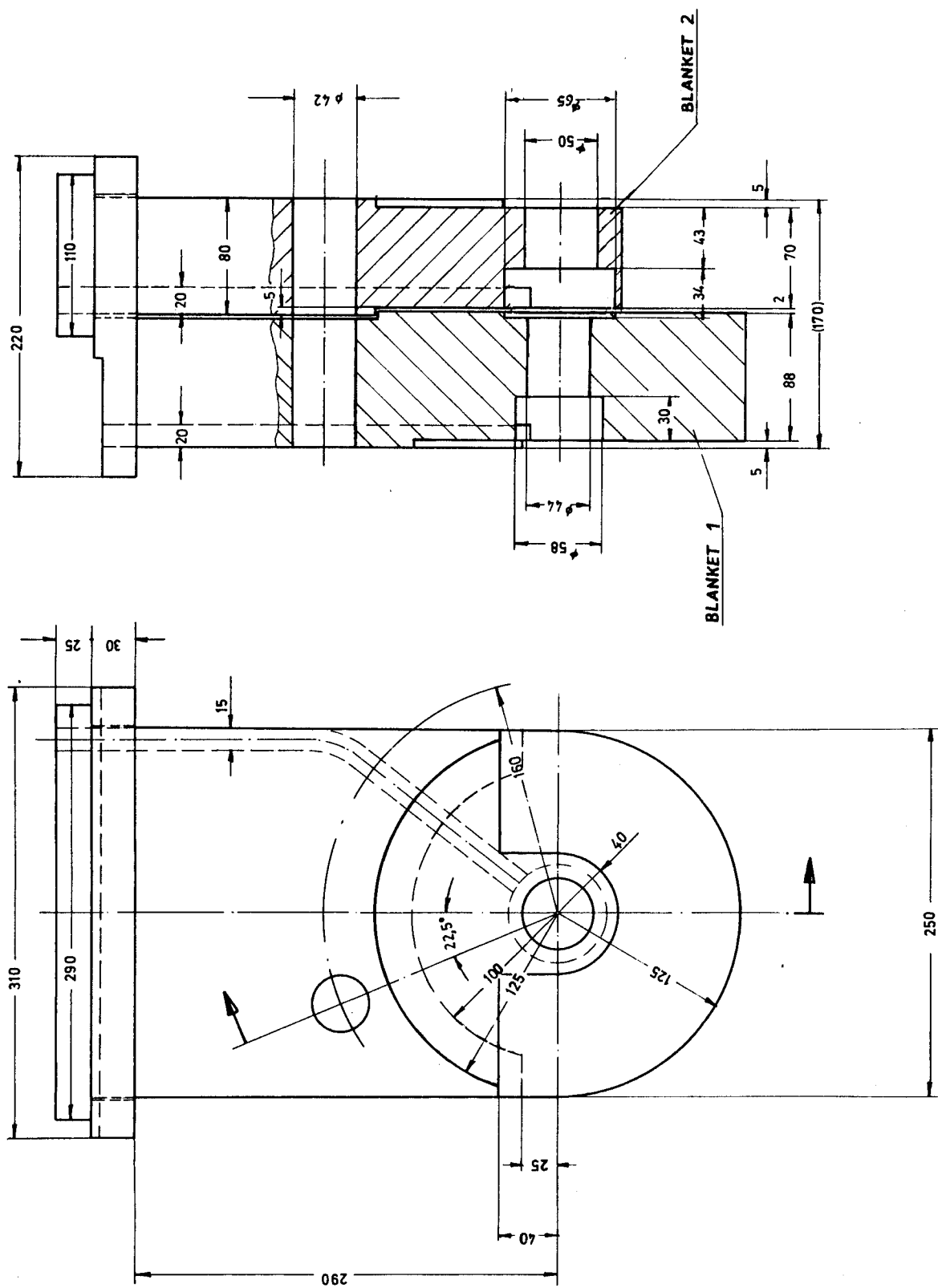
Fig. 4.2-2 BLANKET 1 + 2
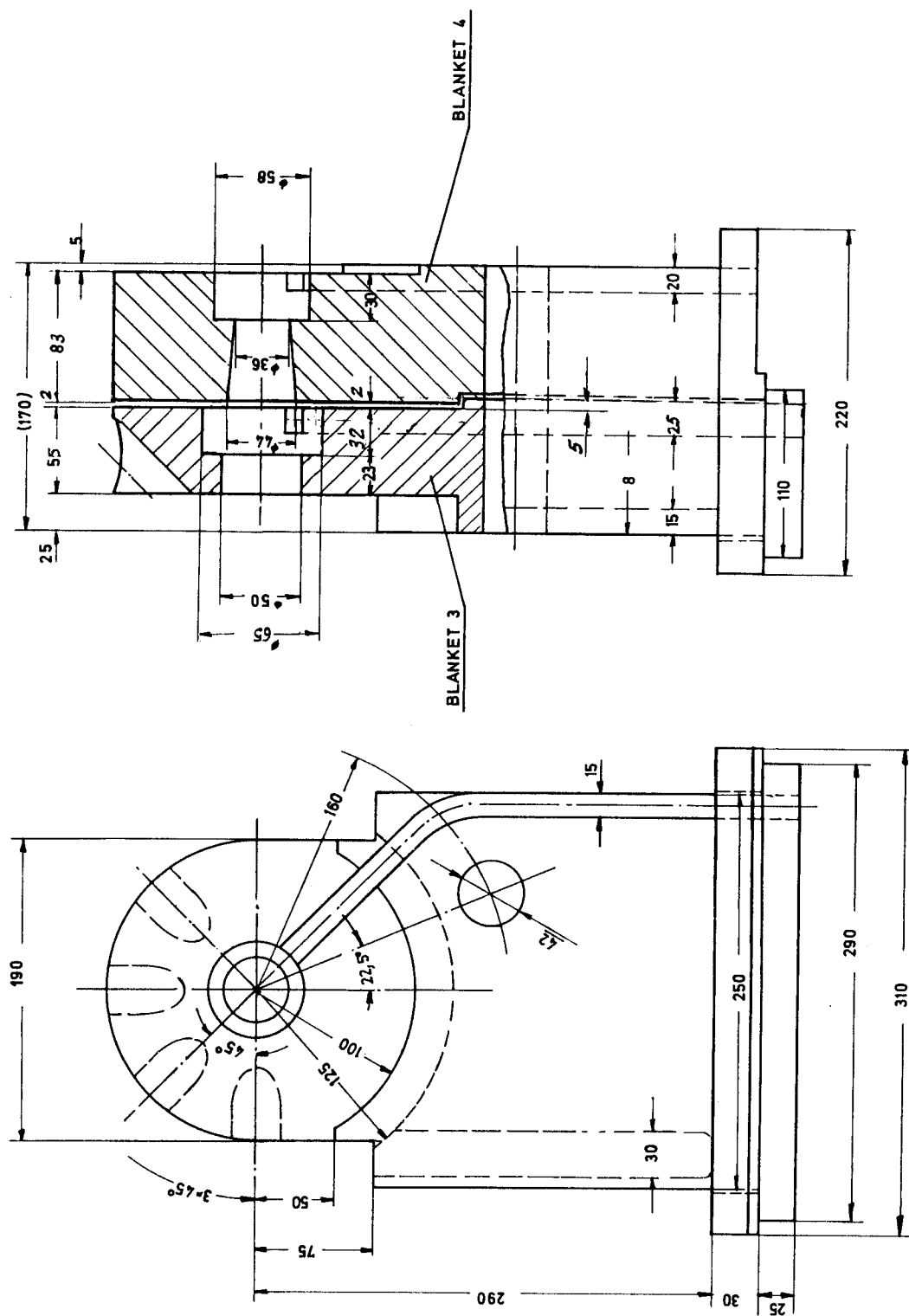
Fig. 4.2-3 BLANKET 3 + 4
(Material Test Region)

4.2-4

Table 4.2-1   Blanket Module and Insert Dimensions and Locations

BLANKET MODULE NUMBER	LOCATION OF MODULE CENTER LINE (CM)	AXIAL LENGTH (CM)	INNER DIAMETER (CM)	R E M A R K S
BL. 1	-176	88	44/58	BREEDING TEST BLANKET (LIQUID)
SPACE		2		
BL. 2	-95	70	50	BREDDING TEST BLANKET (SOLID)
SPACE		2		
INSERT	+10	136	140	CENTRAL CELL SHIELD INSERT
SPACE		2		
BL. 3	+105	55	50	MATERIAL TEST BLANKET ⎫
SPACE		2		⎬ ONE UNIT
BL. 4	+175	83	36/44	MATERIAL TEST BLANKET ⎭

Table 4.2-2   First Wall Parameters at the Central Cell Insert

First Row of Tubes

Plasma Side
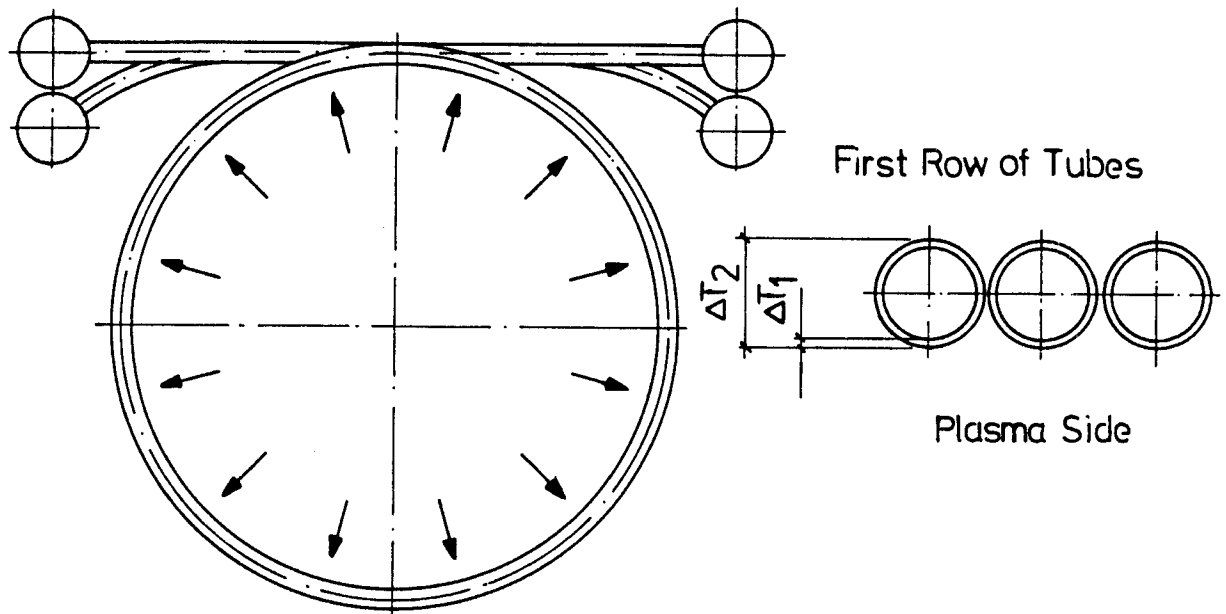
Heat Flux	140 W/cm²
Peak Pressure	4 bar
Inlet Temperature	30 °C
Outlet Temperature	60 °C
Velocity	3.26 m s^{-1}

Tubular Design	
First Wall Radius	70 cm
Coolant Tubes Material	HT 9
Inner Radius	0,7 cm
Wall Thickness	0,3 cm
$\triangle T_1$ Wall	31,8 K
$\triangle T_2$	57,3 K
Maximum Surface Temperature	117,3 °C

Table 4.2-3 Central Cell Engineering Parameters

	Unit	Dimension
Central cell length	m	4.4
Central cell insert diameter	m	1.4
Blanket inner diameter (average)	m	0.47
Length of blanket test module 1	m	0.88
Length of blanket test module 2	m	0.7
Length of CC-insert	m	1.36
Length of materials test module 3	m	0.5
Length of materials test module 4	m	0.88
Total ICRF zone length	m	1.0
Area of blanket test module 1	m^2	0.66
Area of blanket test module 2	m^2	0.67
Area of materials test module 3	m^2	0.36
Area of materials test module 4	m^2	0.66
Total ICRF launching area	m^2	0.08
Blanket 1 thickness	m	0.45/0.64
Blanket 2 thickness	m	0.15
Number of high energy-neutral beam injectors (HE-NBI)		4
Number of low energy-neutral beam injectors (LE-NBI)		1
Angle between adjacent NBI's	deg.	45
Injection angle (HE-NBI's)	deg.	45
Injection angle (LE-NBI)	deg.	70
Point of intersection (HE-NBI's)	m	0
Point of intersection (LE-NBI's)	m	0.6
Footprint diameter (HE-NBI's and LE-NBI)	m	0.2

4.2.3 ICRF Antennae

The four ICRF antennae are integrated into the blanket modules. They are arranged at distances of ± 1.2 m and ± 2.1 m from the midplane. In case of failure they can be extracted together with the corresponding blankets.

4.2.4 Central Cell Coils and Coil Supports

Figure 4.2-4 shows the symmetrical arrangement of the central cell coils. The high field magnets are composed of two superconducting coils enclosed in a common casing, and normally conducting insert coils. The normal coils are assembled as one unit together with their casings and shield. They fit inside the bore of the superconducting coils and protect them from radiation. The dimensions and locations of the coils are given in Chapter 9.

The schematic diagram shwon in Figure 4.2-4 gives the axial forces acting on the coils, both under operating conditions and when the coils are de-energized. The maximum axial force occurs at the central cell coil, when one of the high-field coils fails. Quench detection and parallel discharge of the other central cell solenoids make this force somewhat academic. Therefore, it is not taken into consideration in our stress calculation. The critical components are the support struts and the coil casings.

Figure 4.2-5 is a schematic diagram of the central cell magnet. It is composed of the superconductor and the electrical insulation surrounded by a steel casing. Six cm of kapton between this casing and the dewar vessel provides thermal insulation. The superconductor is cooléd with liquid helium, while the dewar vessel and the support struts are cooled with liquid nitrogen. The dewar vessels are not insulated on the outside and, therefore, act as cryopumps. Poisoning of these surfaces can be avoided by insuring that central cell components are always replaced under vacuum conditions, unless the magnets are warmed up initielly.

SC-Choke Coils   Central Cell Coil   Support Strut
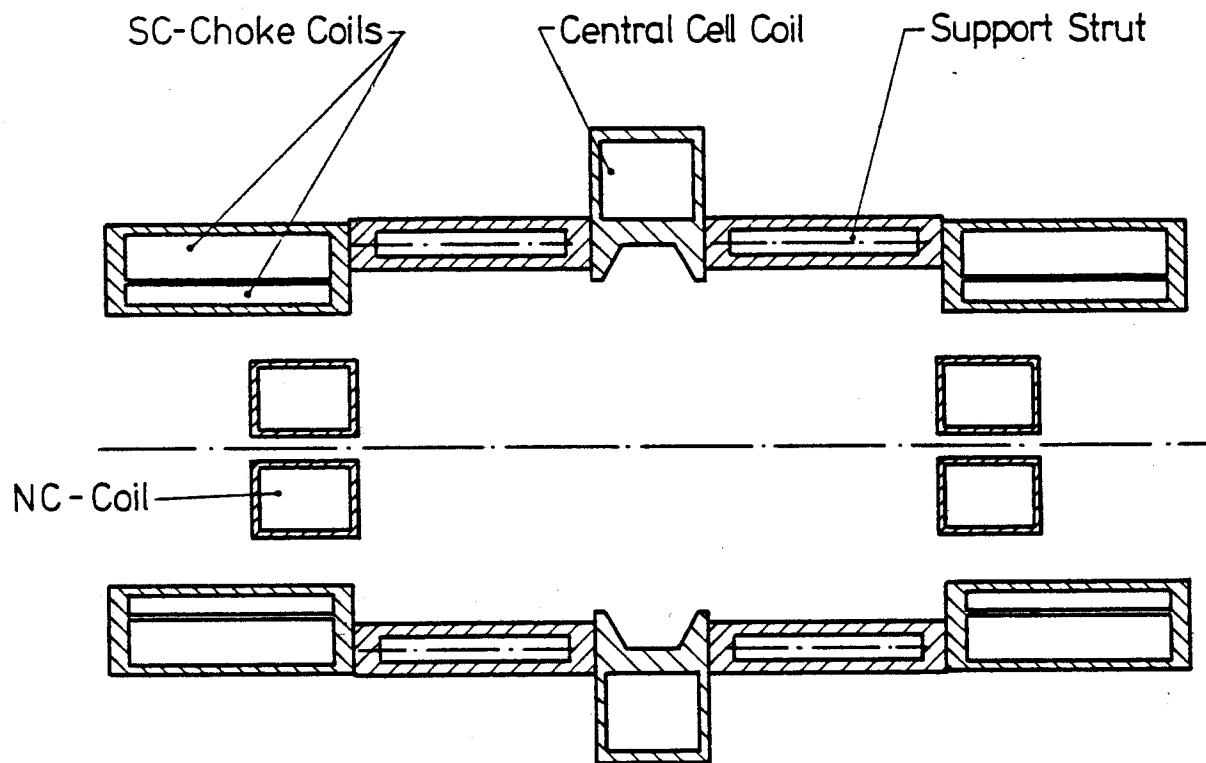
NC-Coil

Axial forces of the central cell solenoids

	Central Cell Coil	SC Choke Coil		NC Coil
		(NbTi)	(Nb$_3$Sn)	
Axial force normal (MN)	0	60	47	2
Working conditions				
Max. axial force single (MN)	85	60	47	2
Coils not energized				

Fig. 4.2-4 Central Cell Coil

Dewar Casing
integrated LN$_2$ schield

Kapton Insulation

Steel Casing

Electrical Insulation

SC-Winding

Pressure Plates
(Low Thermal Conductance)

Support Strut
with Cooling

Center Line
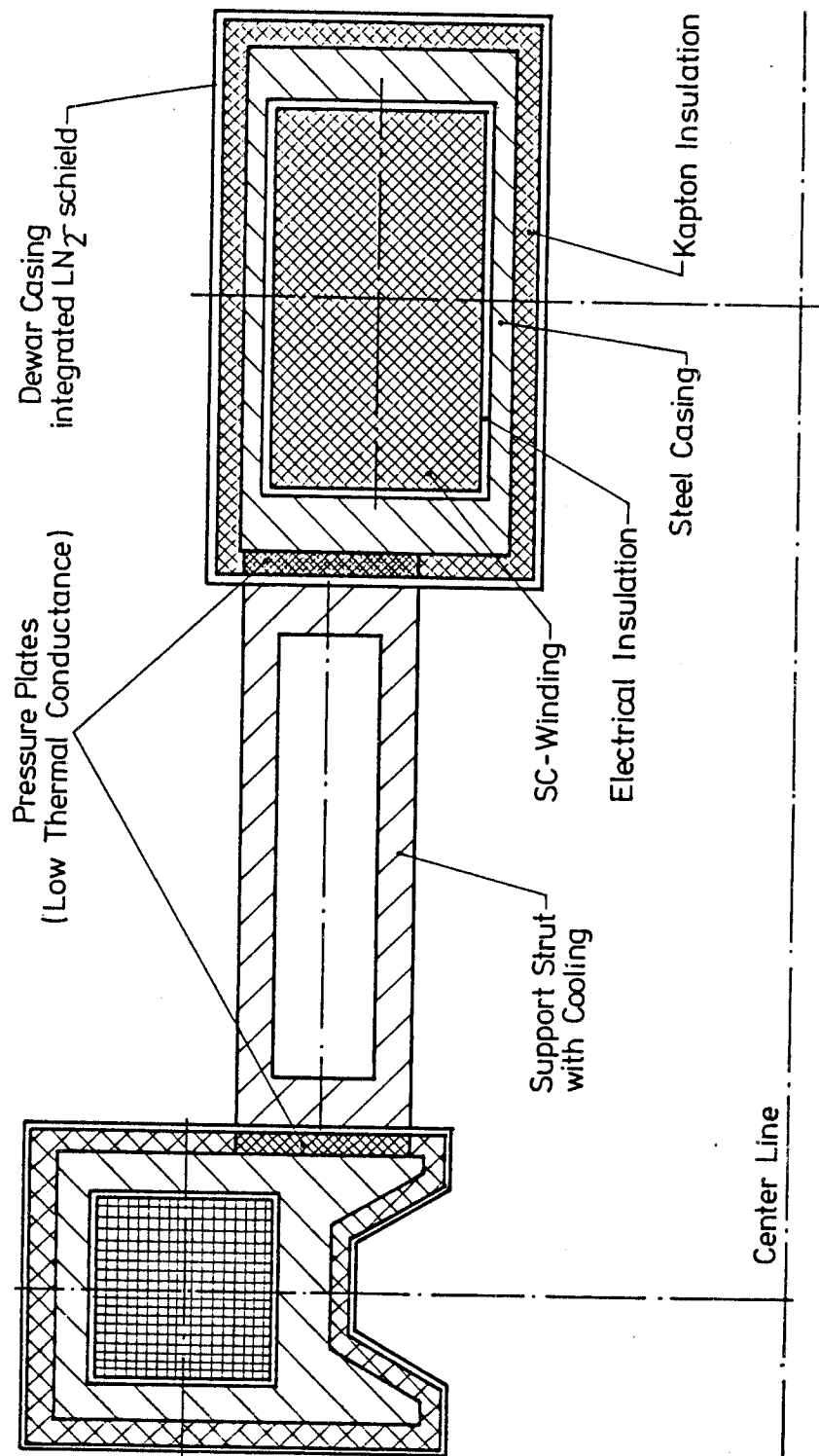
Fig. 4. 2 - 5 Central Cell Coil Casing

- Support struts

  Four 40 cm diameter steel struts on both sides of the central cell
  coils are arranged symmetrically between the central cell coil and
  superconducting choke coils.
  The calculated compressive stress of 300 MPa can be tolerated for steel
  at liquid nitrogen temperature.

- Casing of superconducting choke coils

  It can be assumed that the mechanical loads are reacted by the steel
  coil casings and the hoop stresses, by the windings or the winding
  reinforcement. In this case, the maximum reference stress will be 260
  MPa, an acceptable value for steel at the low temperature of the
  casings. The maximum reference stress is produced by the bending
  moments and shear forces acting on the coil casing in the regions of
  the support struts.

4.2.5 Central Cell Shield Insert

The central cell insert is arranged inside a tube which is part of the
central cell coil casing. Although the plasma radius in this region is
only 12.1 cm, the wall radius is set at 70 cm because of the heat flux
originating from charge exchange from the neutral beams. As Table 4.2-4
indicates, the heat flux will be 140 W/cm^2 on the first wall, which is
water cooled and composed of tubes arranged cylindrically with manifolds
extending in the axial direction. Both are made from HT9. The inner radius
of the coolant tubes is 0.7 cm, the thickness 0.3 cm, and the peak coolant
pressure 4 bar. Water cooling for the insert is dictated by the nuclear
heating in the shiel and is summarized in Chapter 5.

Since the insert is designed to last the lifetime of the facility, it will
have to be exchanged only in case of failure. The insert can be replaced,
however, in the same manner as the blankets, after modules 3 and 4 have
been removed.

4.3 Anchor and Transition Region

The main components of the anchor and transition region are a pair of Yin
Yang coils and the transition coil which are all superconducting. Each of
them is enclosed in a dewar vessel, which is cooled by liquid nitrogen and
acts as a cryopump. Figure 4.3-1 shwos that the inner steel casings of the
magnets are reinforced. The additional support struts are provided to
compensate for the bending forces.

Figure 4.3-2 shows that the center of the transition coil is placed at a
distance of 6.35 m from the midplane of the central cell. The remaining
Yin Yang coils which have no common coil centers, are placed at 9.85 m and
10.45 m respectively.

Unlike TASKA /1/, where the Yin Yang coils were surrounded by a common
dewar, the Yin Yang coils in TASKA-M are contained in separate dewars.
This concept was chosen for the following reasons:

- The coils can be exchanged independently;
   consequently, the coils can be assembled and dismantled
   outside the facility.

- The coils can be tested externally before installation in the machine.

The advantages of the TASKA design were

- A common dewar would permit a solid support
   structure between the coils to react the magnetic
   forces acting on the magnets,

- Cold support structure between the coils prevents thermal
   heat transfer.

TRANSITION COIL SUPPORT STRUCTURE YIN YANG COILS

PLASMA

0 1 2 3 4 5m

CONDUCTOR

ELECTR. INSULATION

THERM. INSULATION

LIQUID N_2-SHIELD

CASING

0 0,5 1m
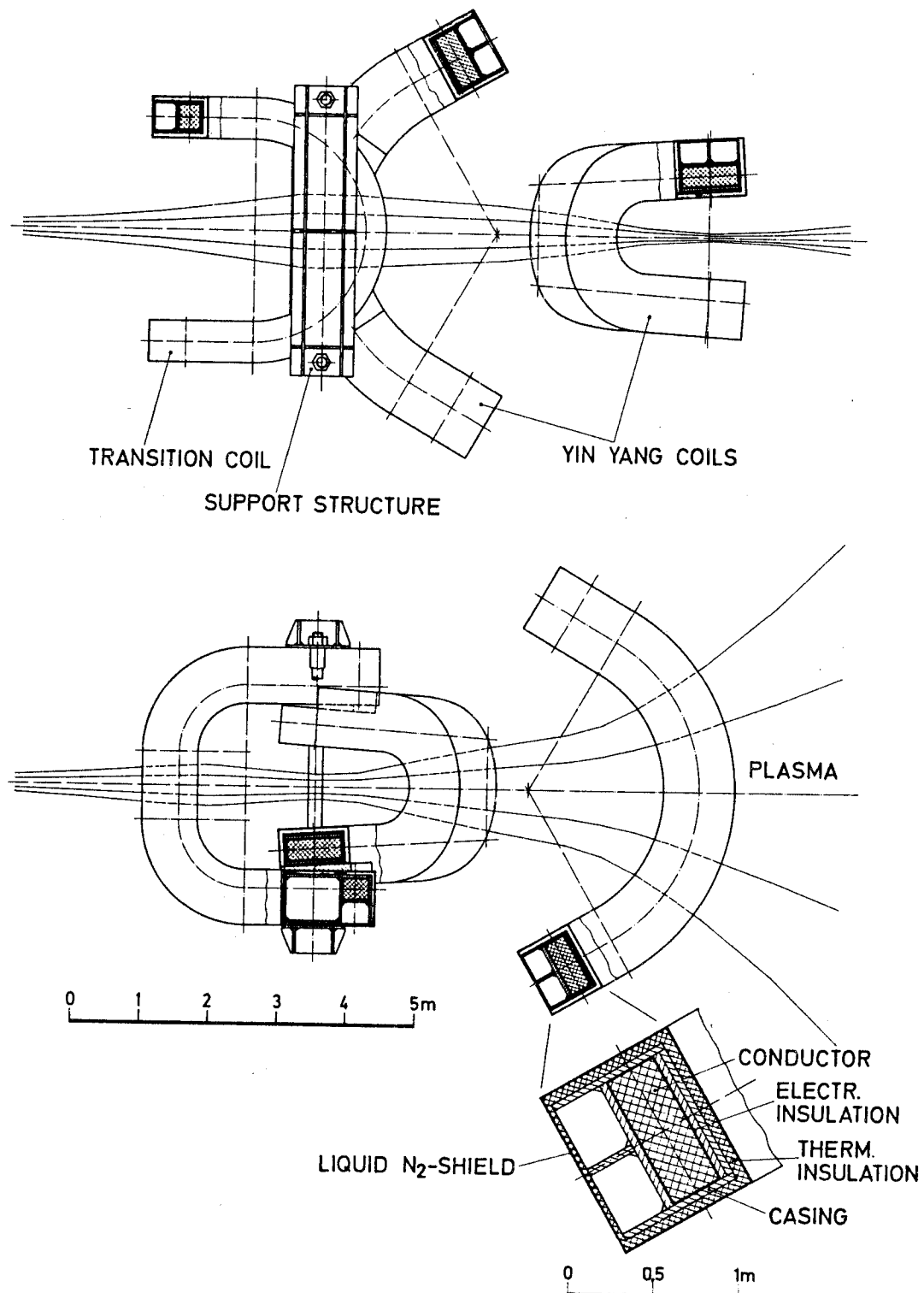
Fig 4.3-1 ANCHOR REGION MAGNETS

LIP WELDING

VACUUM CHAMBER

330   6.35   9.85

TRANSITION COIL

YIN YANG COILS

SHIELD AND
SUPPORT STRUCTURE

HIGH FIELD COIL   INNER SHIELD

NEUTRAL BEAM INJECTOR

10.45
10.55

BEAM DUMP

0 1 2 3 4 5 6 7 8 9 10m
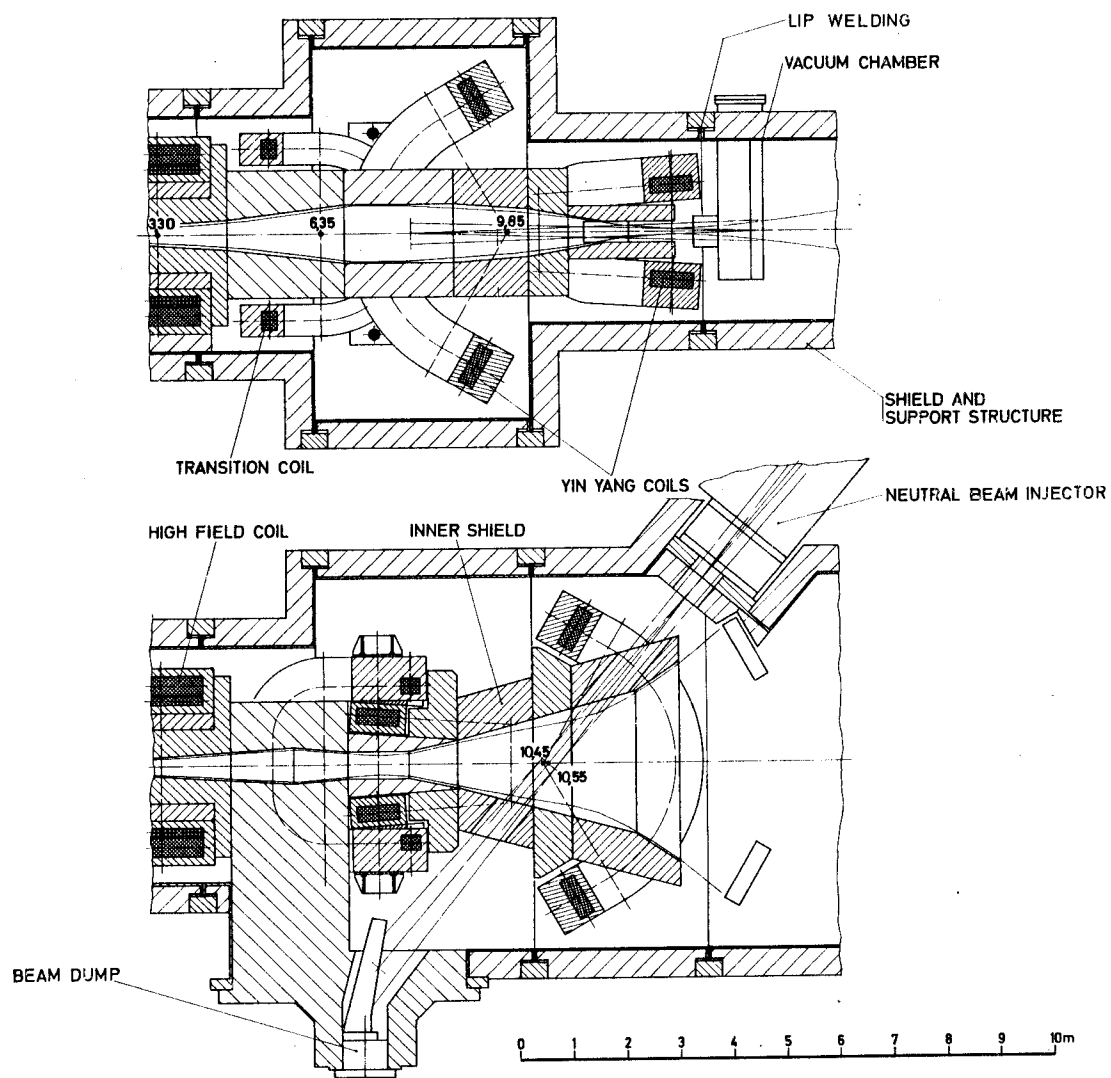
The numbers show the distance in m
from the midplane of the central cell

Fig. 4.3-2 Anchor and Transition Region

Thus, in order to avoid these drawbacks in the TASKA-M concept, additional coil supports are provided by wedges located between the dewars, while plates of synthetic carbon fibre resin transfer the loads from the inner casing to the dewar wall. Thermal conductance through such composits is low enough to prevent excessive heat transfer between the dewar vessel and the inner casing.

To protect the coils from radiation, shielding is provided between the plasma and the coils. The shielding is divided in sections and can be removed in case of coil failure. An additional biological shield is located outside the coils. The upper vessel shell and the shield are mounted independently and can therefore be removed without difficulty in order to provide access to the coils.

Two medium-energy neutral beam injectors are arranged in the anchor regions. The neutral beams intersect the plasma axis at a distance of 10.55 m from the centerline of the facility. The neutral beam duct penetrates through the vacuum vessel and the biological shielding. The beams are arranged in this manner because of the shape of the Yin Yang support structure and the shielding. The divergence of the neutral beam leads to a footprint of 25 cm diameter at the focal plane. At the injection point, the plasma has dimensions of 34.8 x 72 cm. It is theoretically possible to shift the point of injection to the center of the Yin-Yang coils but this would require openings in the magnet support structure and reduce the magnet shielding.

The neutral beam dumps are similar to those locard in the central cell, but they do not have a separate exhaust systems, because the anchor regions are connected to the end dump zones and will be evacuated by the exhaust systems in these regions.

REFERENCES to Chapter 4

1.   TASKA-Team:
     "TASKA Tandem Spiegelmaschine Karlsruhe", Chapt. V.8
     Kernforschungszentrum Karlsruhe and University of Wisconsin /
     Fusion Associates, KfK 3311/1-2, UWFDM-500 (June 1982)

5. NEUTRONICS

5.1 Neutron Wall Loading

5.1.1 Central Cell

The central cell length in TASKA-M is 5.5 m (peak B to peak B). In this relatively short central cell, the D-T neutron source has a strong axial variation. The source is symmetric about the reactor midplane ($z = 0$). The axial variation of the linear neutron source strength is shown in Fig. 5.1-1. Also included is the axial variation of the plasma radius.

Although a first wall radius of 25 cm can be used in the central part of the central cell, the wall is recessed to 70 cm to reduce the surface heat flux due to charge exchange between the incoming beams and the central cell plasma. TASKA-M utilizes four test modules, two of which are devoted to blanket tests (blankets #1 and #2) and the other two to materials tests (blankets #3 and #4). In order to accommodate the ICRF antennas, the first wall is recessed at four locations.

Table 5.1-1 gives the axial locations for the different test modules as well as the wall radius and width for the different segments of each module. The average neutron wall loading in each segment is also given. The method used to calculate the neutron wall loading is described in Section 3.2.7. The average wall loading in the liquid metal breeder test zone in blanket #1 is 0.85 MW/m^2. The corresponding value for the solid breeder test zone is 0.73 MW/m^2. The two materials test modules in blankets #3 and #4 have average wall loadings of 0.69 and 1.23 MW/m^2, respectively. Figure 5.1-2 shows the axial variation of the neutron wall loading in the central cell. While a uniform wall radius is used in the liquid and solid breeder test modules, the wall radius is tapered in the material test module of blanket #4 to achieve a peak neutron wall loading of 1.34 MW/m^2. The peak neutron wall loadings in the liquid metal and solid breeder test modules are 1.22 and 0.78 MW/m^2, respectively. The ICRF antennas are expected to reduce the neutron wall loading behind them by less than 10%.

5.1.2 Anchor and Transition Regions

Two neutron sources exist in the anchor and transition regions of TASKA-M. One source is due to D-T fusion reactions and the other is due to D-D fusion reactions. The anchor plasma is 100% deuterium and, hence, D-D reactions producing 2.45 MeV neutrons are important. The transition region is fueled by

Table 5.1-1. Geometrical Configuration and Average Wall Loading
for the Test Modules

Blanket	Axial Location (cm)	Segment	Axial Width (cm)	Wall Radius (cm)	Average Wall Loading (MW/m^2)
Blanket #1	-220 $\leqslant$ Z $\leqslant$ -132	liquid breeder test	30	29	0.39
		liquid breeder test	53	22	1.11
		shield	5	32.5	0.72
Blanket #2	-130 $\leqslant$ Z $\leqslant$ -60	shield	27	32.5	0.64
		solid breeder test	43	25	0.73
Blanket #3	80 $\leqslant$ Z $\leqslant$ 135	materials test	23	25	0.74
		materials test	32	32.5	0.65
Blanket #4	137 $\leqslant$ Z $\leqslant$ 220	materials test	53	18-22	1.23
		shield	30	29	0.39

deuterium, but it has been assumed for neutronics purposes that there is a 5% tritium background as well. This can arise from tritium in the halo diffusing into the core of the transition region. Since the transition region plasma is cool ($T_i \sim 7$ keV), the reaction rate is small. A peak in the DT reaction rate occurs in the overlap region between the transition zone and the anchor. Interaction between the cooler tritium in the transition zone and the hotter sloshing-ion deuterium plasma yields an increased production rate of DT neutrons. The axial variation of the linear source strength due to D-T and D-D neutrons in the transition and anchor regions of the end cell is shown in Fig. 5.1-3. The axial variation of the horizontal (a) and vertical (b) half widths for the plasma and first wall is illustrated in Fig. 5.1-4. The plasma has an elliptical shape with varying ellipticity in these regions. The first wall closely follows the plasma boundary and allows for the required spacing for the halo region.

Due to the ellipticity of the first wall, an azimuthally nonuniform neutron wall loading is obtained at a given axial location. Figure 5.1-5 shows the axial variation of the maximum neutron wall loading. The contributions from D-T and D-D fusion neutrons are given. Notice that the neutron wall loading is defined as the energy flux resulting from the uncollided
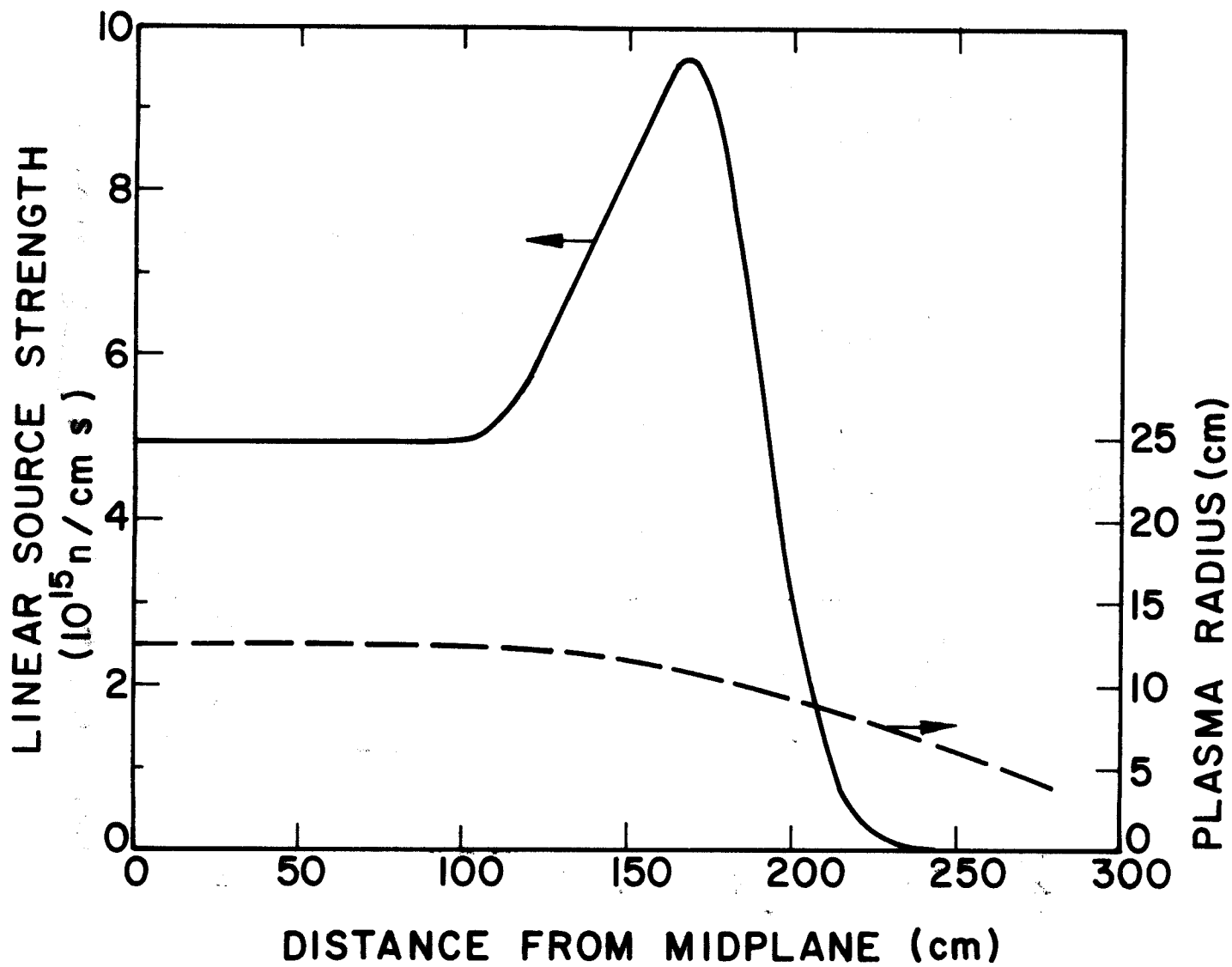
Fig. 5.1-1.   Axial variation of the neutron source in the central cell.
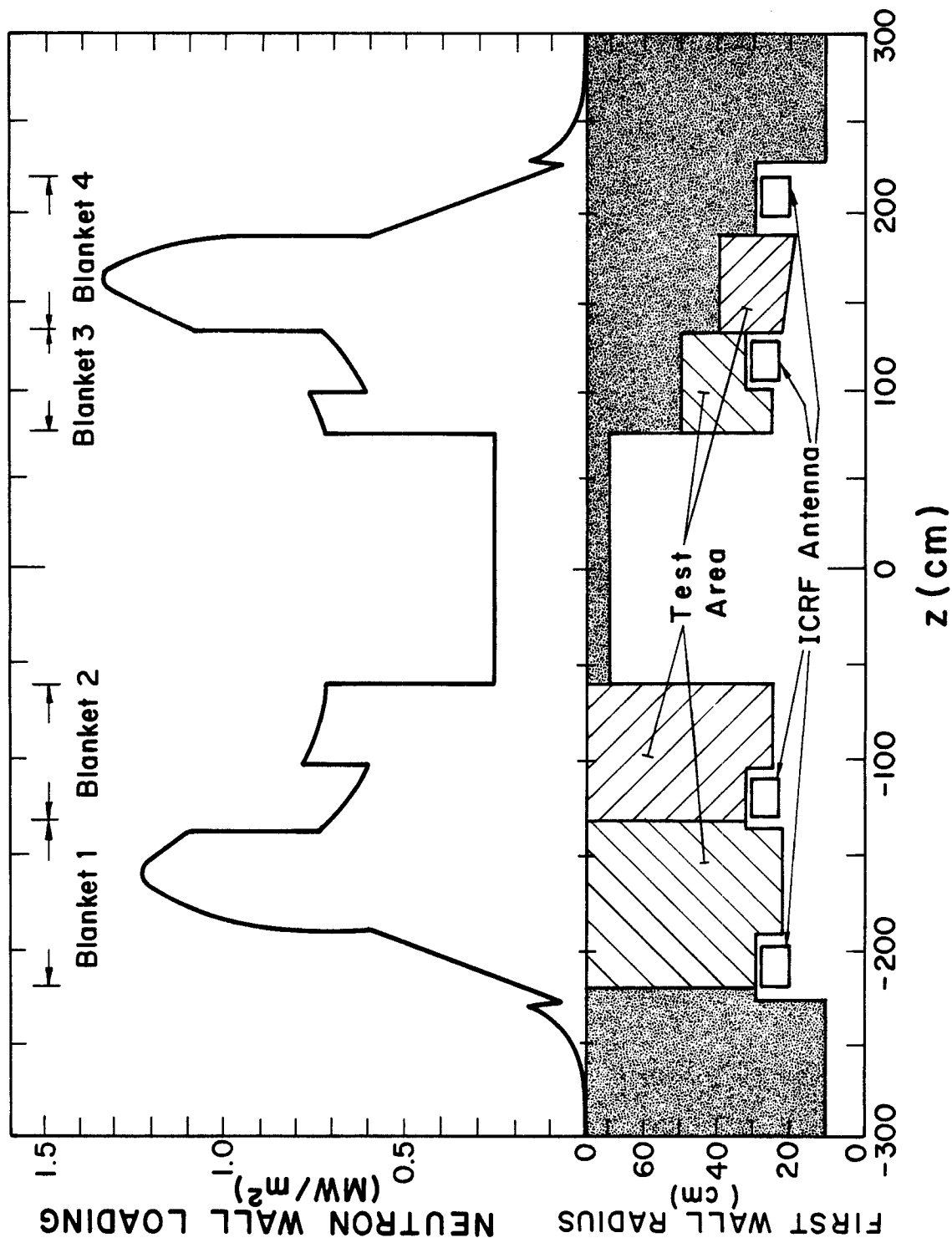
Fig. 5.1-2. Axial variation of neutron wall loading in the central cell.
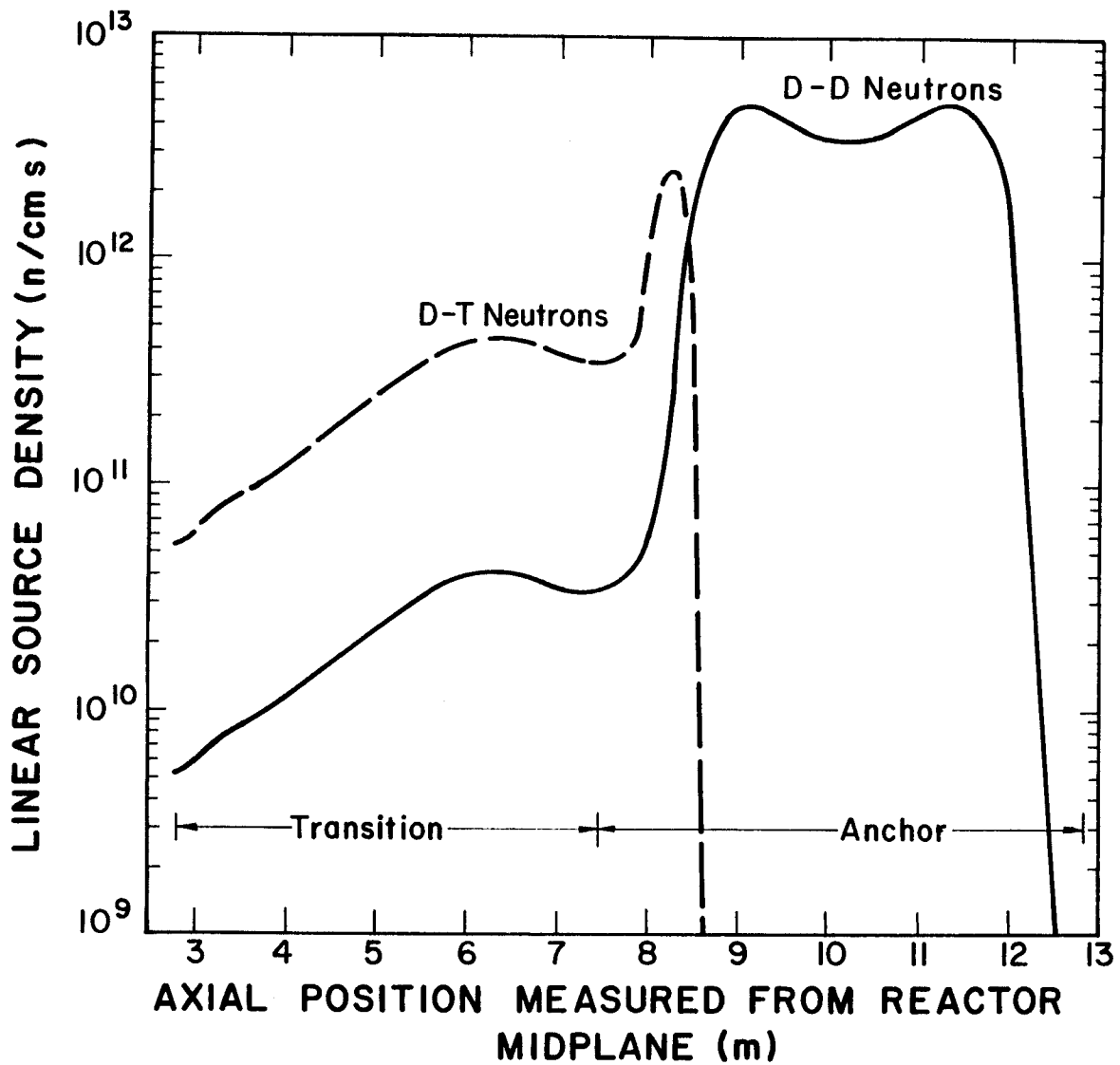
Fig. 5.1-3. Axial variation of the neutron source in the transition and anchor regions.
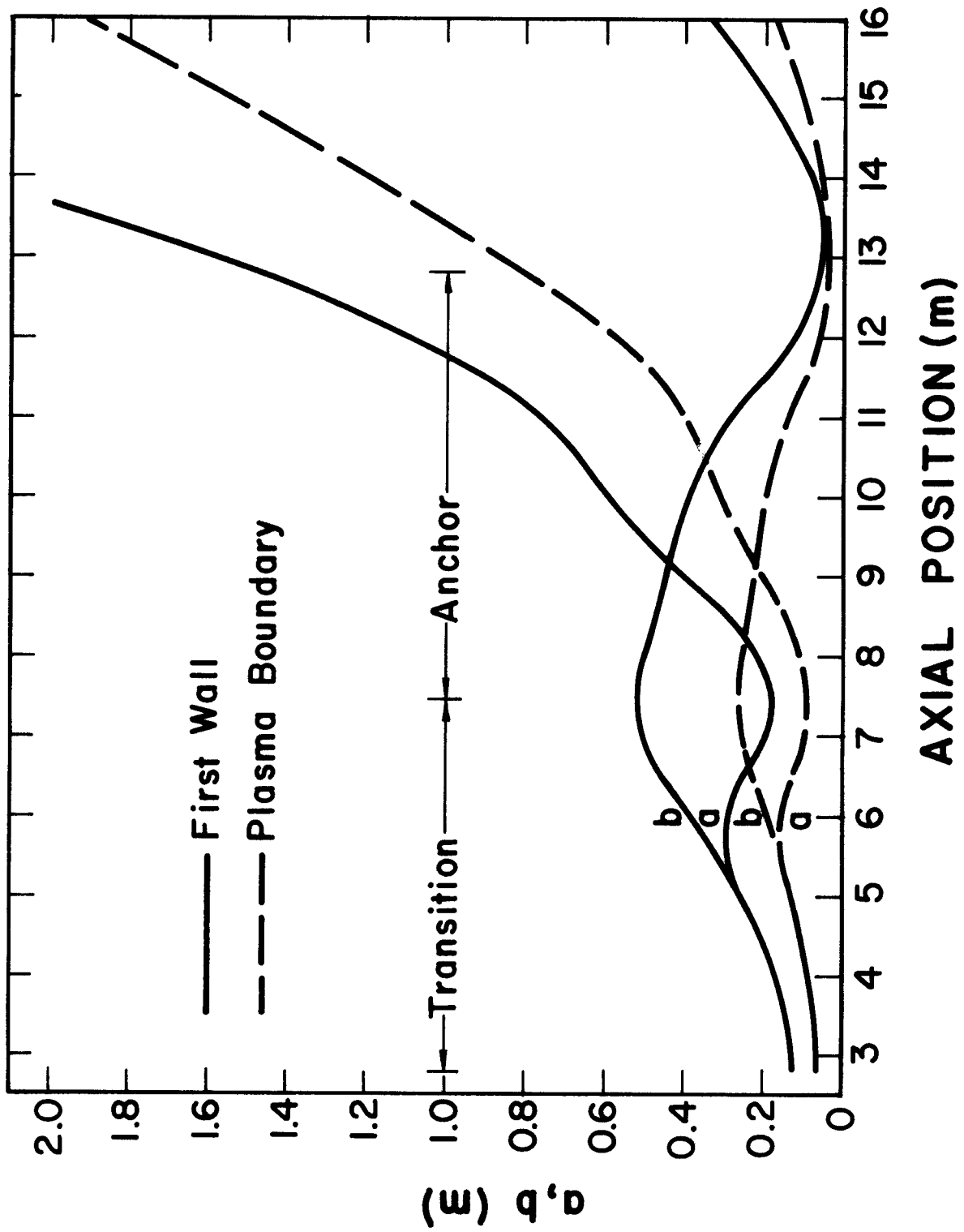
Fig. 5.1-4. Axial variation of the plasma and first wall dimensions in the transition and anchor regions. a and b are the horizontal and vertical half widths.
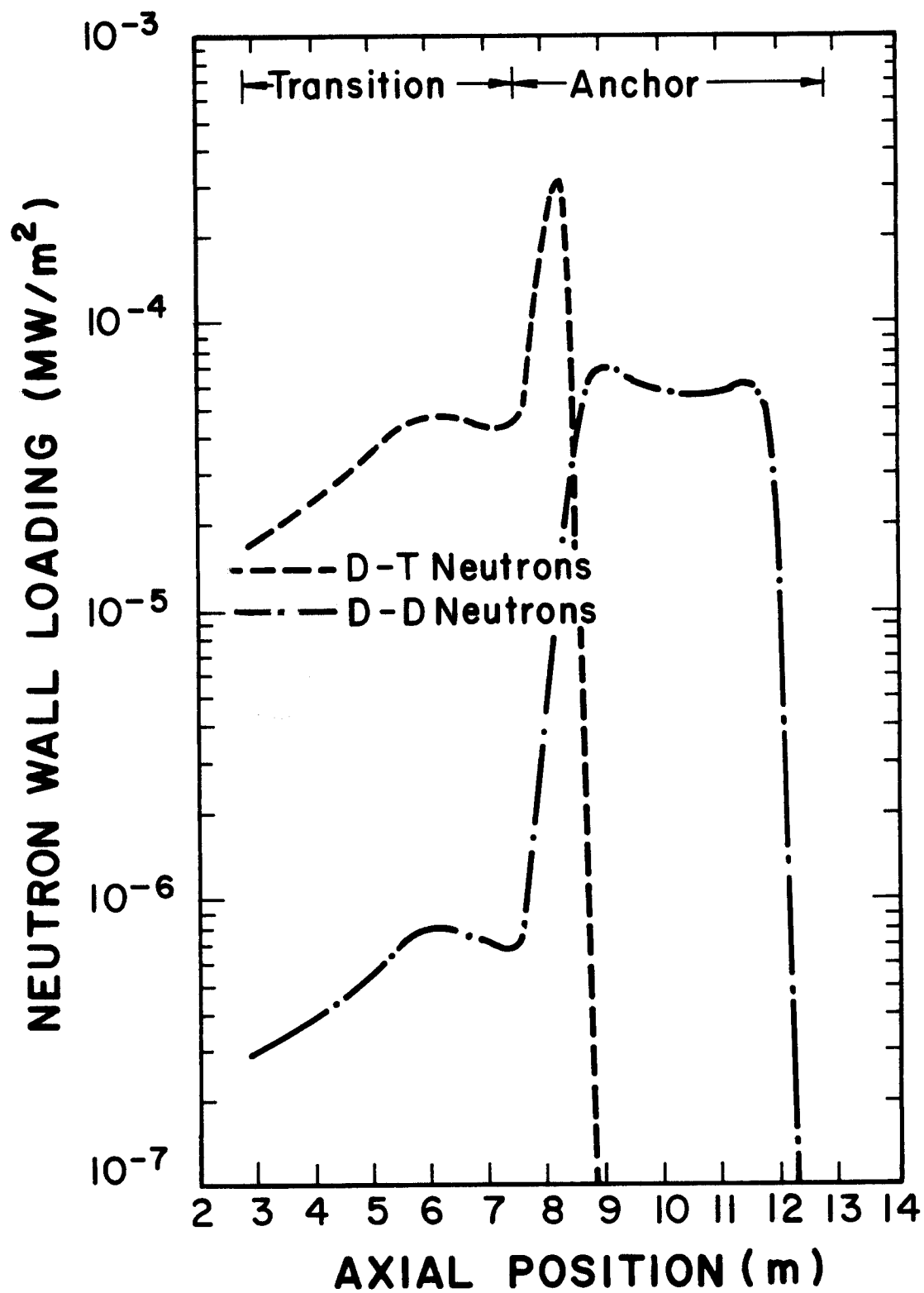
Fig. 5.1-5. Axial variation of the peak neutron wall loading in the transition and anchor regions.

source neutrons whether they are 14.1 MeV D-T neutrons or 2.45 MeV D-D neutrons. The neutron wall loading in the anchor and transition regions is about four orders of magnitude less than that in the central cell.

5.2 Magnet Shielding

This section focuses on the shielding requirements to protect all magnets in the central cell and transition and anchor regions which include the central cell, choke, transition, and anchor Yin-Yang coils. The general arrangement of these coils is described in Chapter 9 and Table 5.2-1 summarizes their material compositions. The production of the high axial magnetic field (17.5 T) to mirror confine the plasma requires the use of hybrid choke coils with an outer superconducting (S/C) part and an inner normal conducting (N/C) insert coil. The N/C is located coaxially with respect to the outer S/C magnet and is positioned with no intervening shield between its coil case and the plasma. Shielding is placed between the two coils to ensure the operational integrity of the S/C magnet.

The radiation transport problem was modeled for a one-dimensional discrete ordinates code to investigate the various responses of interest. In the normal coil there is concern with the mechanical degradation of the ceramic insulation. Problems of concern in the S/C magnets are the atomic displacement (dpa) rate in the stabilizer of the conductor, the nuclear heating in the S/C magnet, the neutron fluence in the superconductor, and the dose to the insulators.

5.2.1 Radiation Limits

Shielding is required to protect the magnets from neutron and gamma radiation. The shielding requirement is determined by the radiation limits for the different magnet components. The components most sensitive to radiation damage in a S/C magnet are the superconductor, the stabilizer, and the insulators. All S/C magnets in TASKA-M use NbTi except for the inner part of the high field choke S/C magnet where Nb_3Sn is used because of the high field requirement. Irradiation of the superconducting material results in degradation of the critical current density. The critical current density for NbTi decreases rather slowly with neutron fluence. In this work we consider the limit on the peak neutron fluence (E > 0.1 MeV) to be 3 x 10^{22} n/m^2 which corresponds to a 10% decrease in the critical current density on the average for commercial alloy with optimized pinning behavior.[1] There are indications that 70% of this effect will anneal out at room temperature.[2] TASKA-M is expected to have a total lifetime of 7.8 full power years (FPY) (see Section 10.2). The operating schedule allows for room temperature magnet

Table 5.2-1 Material Compositions of TASKA-M Magnets

Central cell and outer S/C choke coil	60 v/o	304 SS
	15 v/o	Al
	5 v/o	NbTi
	10 v/o	He
	10 v/o	GFF epoxy
Inner S/C choke coil	47 v/o	304 SS
	21 v/o	Al
	12 v/o	Nb_3Sn
	10 v/o	He
	10 v/o	GFF epoxy
Normal insert coil	60 v/o	Cu
	25 v/o	MgO (90% d.f.*)
	15 v/o	H_2O
C coils	76.6 v/o	Cu
	3.4 v/o	NbTi
	10 v/o	He
	10 v/o	GFF polyimide

*d.f. = density factor

annealing every 0.5 FPY. For the fluence not to exceed the limit at the end of life, it is therefore required that the fast neutron fluence after 0.5 FPY of operation does not exceed 5.5×10^{21} n/m^2. Hence, the fast neutron flux (E > 0.1 MeV) should not exceed 1.1×10^{22} n/m^2 FPY. For Nb_3Sn, following an initial critical current density increase with fluence, J_c starts to drop rapidly at a neutron fluence (E > 0.1 MeV) of 4×10^{22} n/m^2.[3] This effect does not recover by room temperature annealing, implying that for the fluence not to exceed the limit at the end of 7.8 FPY's of operation, the fast neutron flux must not exceed 5.1×10^{21} n/m^2 FPY.

The central cell and choke coils utilize aluminum as a stabilizer while the transition and anchor magnets use copper. Upon irradiation of the stabilizer at cryogenic temperatures, immobile point defects are produced resulting in an increased resistivity. For the magnet to be cryostable, the resistivity increase must be limited such that the I^2R heat generated in the stabilizer can be removed by the normal helium (LHeI) coolant. The unirradiated resistivity of the Al stabilizer is taken to be 5 nΩ cm. For cryostability conditions to be satisfied, the resistivity of Al after irradiation is not allowed to exceed 10 nΩ cm implying that the limit on the radiation induced resistivity is 5 nΩ cm. Abdou[4] used experimental data to derive the formula

$$\Delta\rho_r = 800 \; [1 - \exp(- \; 366 \; d)] \; n\Omega \; cm, \qquad (5.2-1)$$

that relates the radiation induced resistivity in Al to the atomic displacements (d). Using Eq. 5.2-1 yields a dpa limit of 1.7×10^{-5} dpa. Complete recovery of the radiation induced defects in Al can be achieved by room temperature annealing. Considering an operating schedule that allows for annealing every 0.5 FPY, a dpa rate limit of 3.4×10^{-5} dpa/FPY is obtained. At several locations in the magnets, namely the outer bore of the choke coil and the inner bore of the central cell coil, where the field is low and a large contribution from neutron streaming exists, the limit on the total Al resistivity is increased to 20 nΩ cm yielding a dpa rate limit of 1.0×10^{-4} dpa/FPY.

The situation is quite different for Cu stabilizer due to the strong dependence of magnetoresistivity on magnetic field and Cu purity[5] and the fact that only 80-90% of the radiation induced defects are removed by room temperature annealing.[6] Charts based on a Kohler plot for Cu were generated to determine the maximum allowable dpa rate for the magnet to be cryostable.[7] These charts account for the partial damage recovery with annealing. We assume that half hard copper with a residual resistivity ratio RRR = 80 and a residual resistivity of 19.3 nΩ cm is used in the transition and anchor coils. Considering a limit of 120 nΩ cm for the total resistivity and a maximum field in these coils of 6 tesla, the charts yield a dpa limit of 5×10^{-4} dpa which should not be exceeded any time during the reactor life. For an annealing

recovery fraction of 0.85, 0.5 FPY between anneals, and a total reactor life-time of 7.8 FPY, the charts give a dpa rate limit of 3.1×10^{-4} dpa/FPY.

Mechanical strength tests of irradiated magnet insulators have shown that polyimides are 5 to 10 times more radiation resistant than comparably prepared epoxies.[8] Glass fiber filled (GFF) polyimide is used for electrical insula-tion in the transition and anchor coils. However, the factor of three cheaper GFF epoxy is used in the central cell and choke coils where low doses are ob-tained. Aluminized Kapton (a polyimide), which is about 100 times more radi-ation resistant than aluminized Mylar[9] is used for thermal insulation. Radiation effects on organic insulators are not reversible and it is essential that they last for the whole reactor life. An end of life dose of 10^{10} rad is considered to be the limit for the thermal insulator. The dose limits for GFF polyimide and GFF epoxy electrical insulators were taken to be 5×10^9 and 6×10^8 rads, respectively.

The limit on the cryogenic heat load resulting from nuclear heating in the magnet is design dependent. Although peak power densities in the winding pack as large as ~ 200 mW/cm^3 can be accommodated without exceeding the heat flux limit of 0.2 W/cm^2 that can be handled by LHeI, much lower power densi-ties are required to assure stable operation and to avoid excessively high cryogenic refrigeration and plant cost. A peak power density limit of 0.1 mW/cm^3 is used in this study.

As for the normal copper coils, five radiation mechanisms can degrade the performance of the coils.[10] These are: (1) the resistivity degradation of the insulator under instantaneous dose rates, (2) mechanical and structural degradation of the insulator under long-term neutron fluence, (3) radiolytic dissociation of the coolant water leading to corrosion product formation, (4) resistivity increase in the copper conductor due to radiation damage and neutron-induced transmutations, and (5) mechanical and structural degradation in the copper conductor under long-term neutron fluence. The analysis per-formed for the MARS[11] normal insert coils indicated that of these five mechanisms only two are seen as determining the minimum coil lifetime, namely neutron damage to the copper conductor and neutron-induced swelling in the ceramic insulator.[10] Due to the lack of high fluence irradiation data for copper alloys, the first mechanism is rather unknown and the swelling of the ceramic insulator is considered to determine the lifetime for TASKA-M normal

conducting insert coils. Compacted MgO powder insulation is used in TASKA-M. A packing fraction of 0.9 is assumed implying that a local swelling of 10% is tolerable. The reported irradiation swelling data for MgO indicates a swelling of 2.6-3% for a fast fission irradiation of 2.1×10^{26} n/m^2 at 430 K.[12] With the rather conservative assumption that the harder degraded fusion spectrum will enhance the swelling by a factor of two, and assuming a tolerable swelling of 10%, the limit on the fluence will be 3.5×10^{26} n/m^2 (E > 0.1 MeV).

5.2.2 Shield Optimization

Optimizing the shield satisfies one of the design goals as the thinner the shield the less expensive the magnets and consequently the reactor. The purpose of this optimization study is to reduce the magnet radiation effects by using an optimal combination of several layers of shielding materials, including Fe, B_4C, H_2O, and Pb.

The linear neutron source distributions in the central cell and transition and anchor regions are given in Fig. 5.1-1 and 5.1-3, respectively. In the transition and anchor regions, the D-T neutron source is ~ 4 orders of magnitude less than the central cell source and drops to a negligible value in the anchor region, while the D-D neutron source is characterized by two relative peaks. The second branch of the D-D reaction leads to the production of tritium which reacts with the deuterium and produces a 14.1 MeV neutron source which is ~ 2 orders of magnitude less in strength than the D-D neutron source in the anchor region.

Two sets of shield optimization studies were performed: the first set is for the D-T neutron source (at 14.1 MeV), and the second set is for the D-D neutron source (at 2.45 MeV). In the central cell and the choke coil region the neutron source is mainly from the D-T reaction and the design driver for the shield optimization study was the peak dpa rate in the Al stabilizer of the S/C coils. The D-D neutrons in the anchor region dominate the source and the primary motive for the second set of the optimization studies was to minimize the peak power density in the Yin-Yang magnets. The shield design driver for these coils is the peak power density rather than the stabilizer dpa rate as a result of using copper with its lower radiation induced resistivity. Higher resistivity values were also allowed for Cu (see Section 5.2.1).

A series of one-dimensional (1-D) calculations was performed to determine the optimal shield configuration using the discrete ordinates code ONEDANT,[13] the cross section library XSLIB (30 neutron and 12 gamma energy groups) based on the ENDF/B-V evaluation, and the P_3-S_8 approximation in cylindrical geometry. The shield was configured originally in three layers: first, an Fe-shield (Fe 1422 and H_2O) to slow down the high energy neutrons; next a B_4C-shield (B_4C [87% d.f.], Fe 1422 and H_2O) to moderate the neutrons further and absorb the low energy neutrons; and finally a thin Pb-shield (Pb, Fe 1422, and H_2O) to reduce the gamma heating in the S/C magnets. The Fe and Pb-shields are 10 vol.% water cooled and the structural material (Fe 1422) in the B_4C and Pb-shields was kept at 10 vol.%. The relative content of the B_4C to the water in the B_4C-shield was varied in the optimization study.

The central cell S/C magnet has the most severe radiation effects as the first wall is recessed to a 0.7 m radius to reduce the surface heat flux due to charge exchange and, as a result, the shield is constrained to 0.78 m. The central cell coil and its associated cryostat are represented schematically by Fig. 5.2-1. The shield was optimized in several steps. First, the Pb-shield was varied in thickness and the proportion of the Fe-shield to the B_4C-shield thickness was kept the same. Figure 5.2-2 indicates that the Pb-shield is not helpful and a shield consisting of B_4C and Fe is more effective in reducing the dpa rate in the Al stabilizer. Second, the thickness of the B_4C-shield was varied under the constraint that the total shield thickness remains 0.78 m. Figure 5.2-3 shows that 0.68 m of Fe-shield backed by 0.1 m of B_4C-shield is the optimal combination of the shield. Finally, the B_4C content in the B_4C-shield was found to barely affect the dpa rate and a reasonable value of 10 vol.% B_4C was chosen to avoid excessive dose in the insulator and heating in the magnet.

In the anchor region the same optimization scheme was followed for the D-D neutron source. In agreement with the previous analysis, the Pb-shield has proven to be useless in minimizing the peak power density in the Yin-Yang magnets as illustrated by Fig. 5.2-4. Moreover, replacing the Fe-shield by the B_4C-shield is significantly helpful as shown in Fig. 5.2-5. It is of interest to notice in Fig. 5.2-6 the drop in the radiation damage resulting from replacing the B_4C by water in the B_4C-shield. In conclusion, the shield

RADIUS (m)   THICKNESS (cm)

0 ————————— · ————————— · ————————   12.25

                PLASMA

0.1225 —— —— —— —— —— —— —— ——   12.25

                HALO   57.75

0.70 ————————————————————————————————

                FIRST WALL   2

0.72 ————————————————————————————————

                SHIELD   78

1.50 ————————————————————————————————

                VOID   2

1.52 ————————————————————————————————

                STEEL   1

1.53 ————————————————————————————————

                5v/o KAPTON   6

1.59 ————————————————————————————————

                COIL CASE   20

1.79 ————————————————————————————————

                GFF EPOXY   1

1.80 ————————————————————————————————

                S/C COIL   60

2.40 ————————————————————————————————
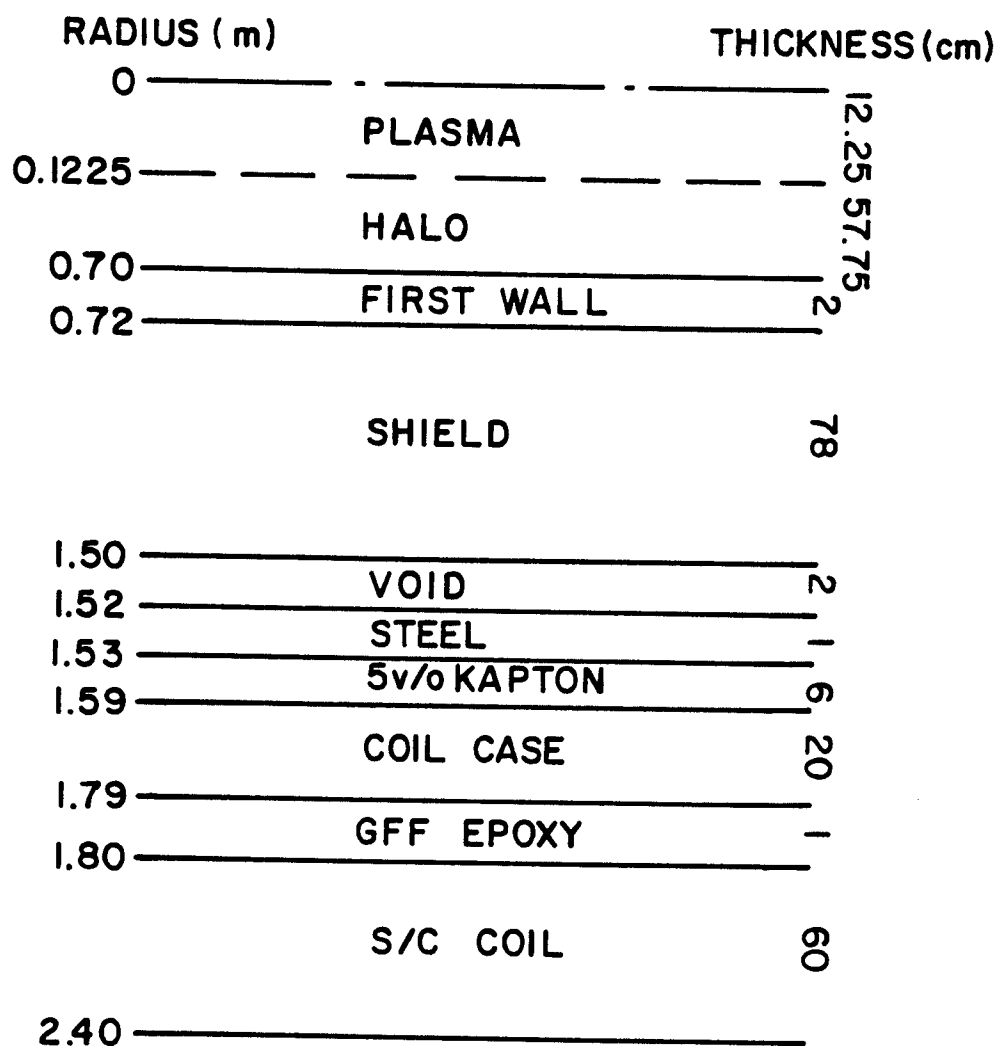
Fig. 5.2-1. Schematic of the central cell magnet and shield at the reactor
             midplane.
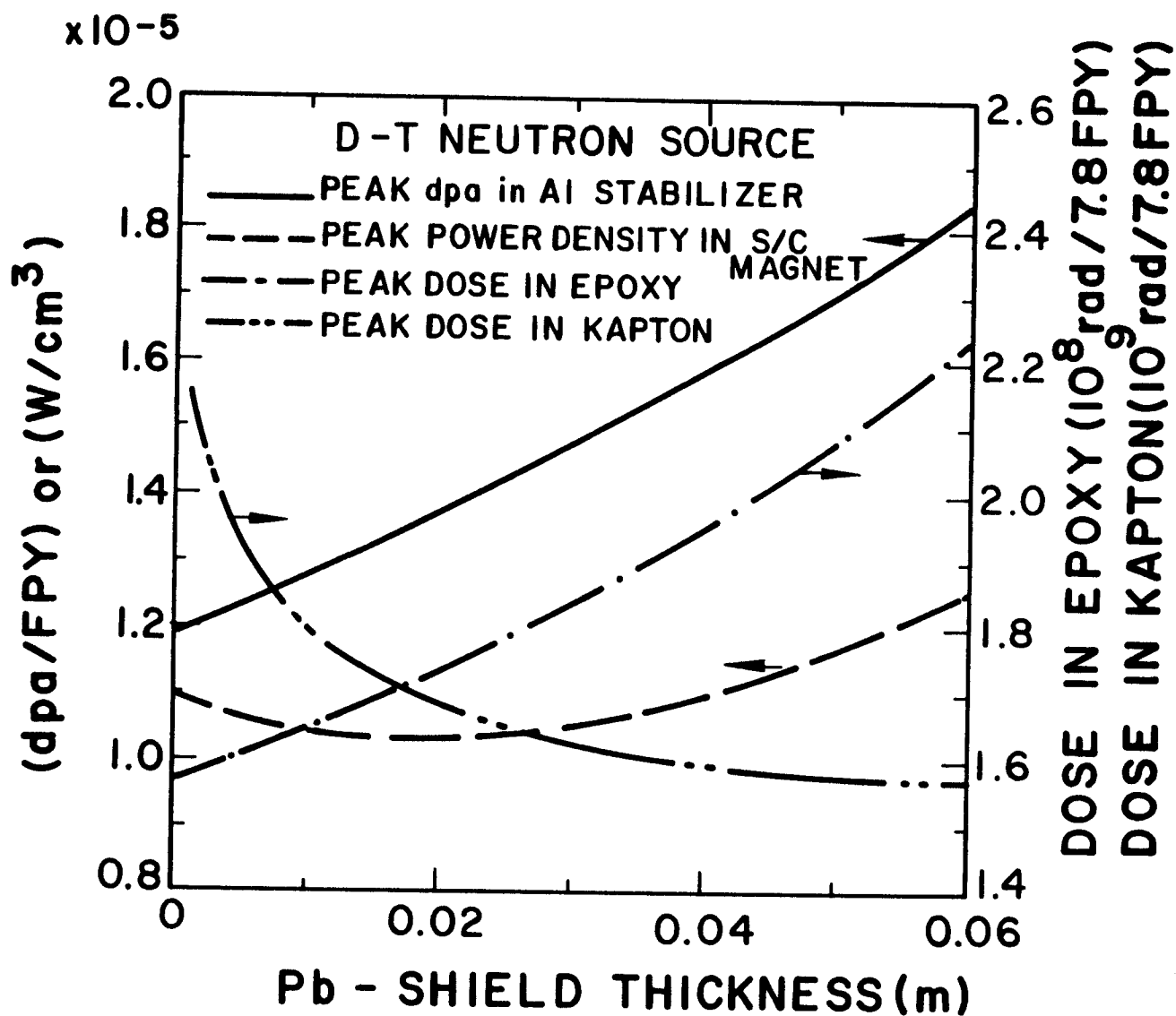
Fig. 5.2-2. Variation of the radiation effects in the central cell magnet with the Pb-shield thickness in a 0.78 m thick shield.
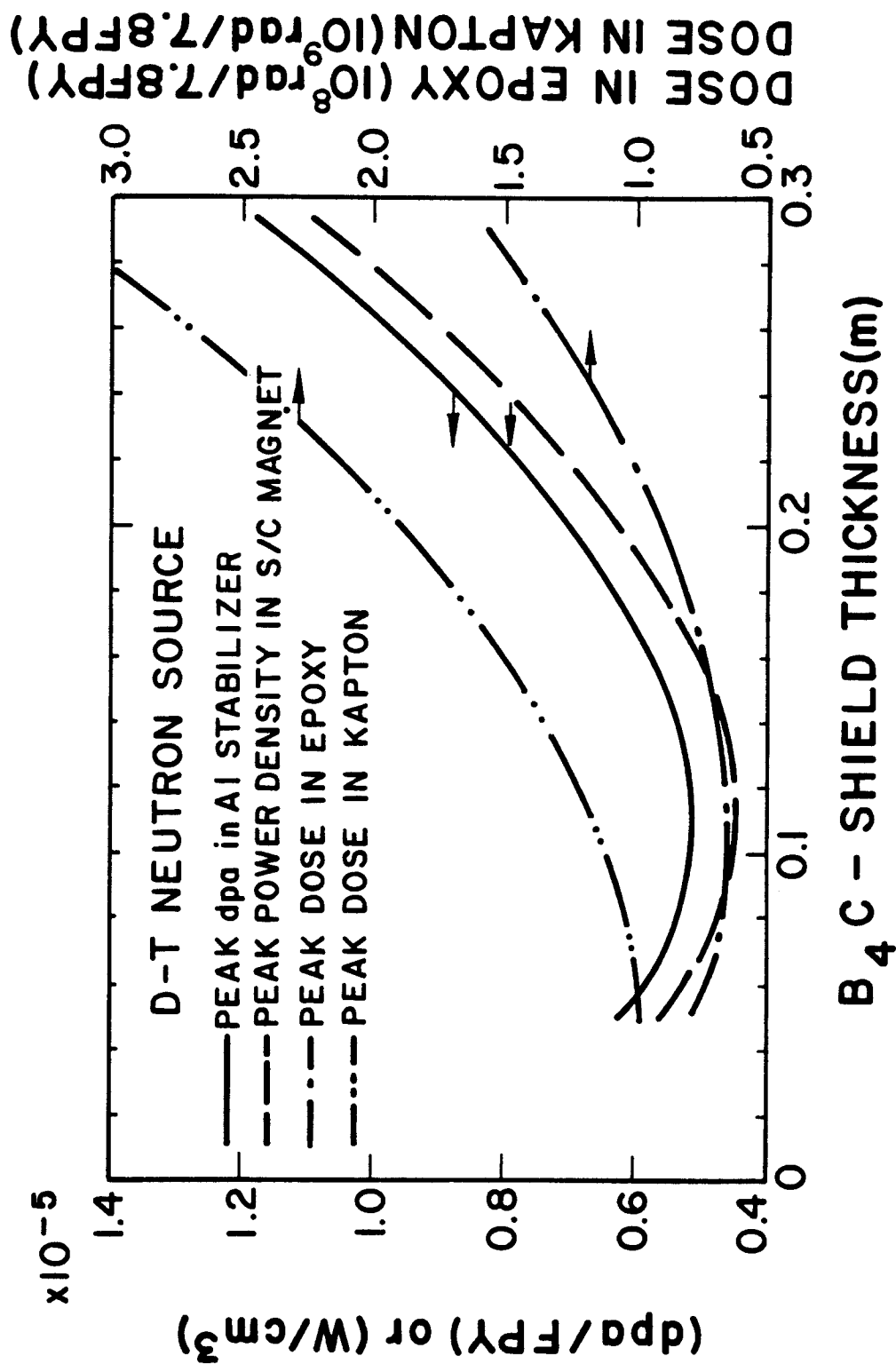
Fig. 5.2-3. Effect of replacing the Fe-shield by B_4C-shield on the damage in the central cell magnet for a 0.78 m thick shield.
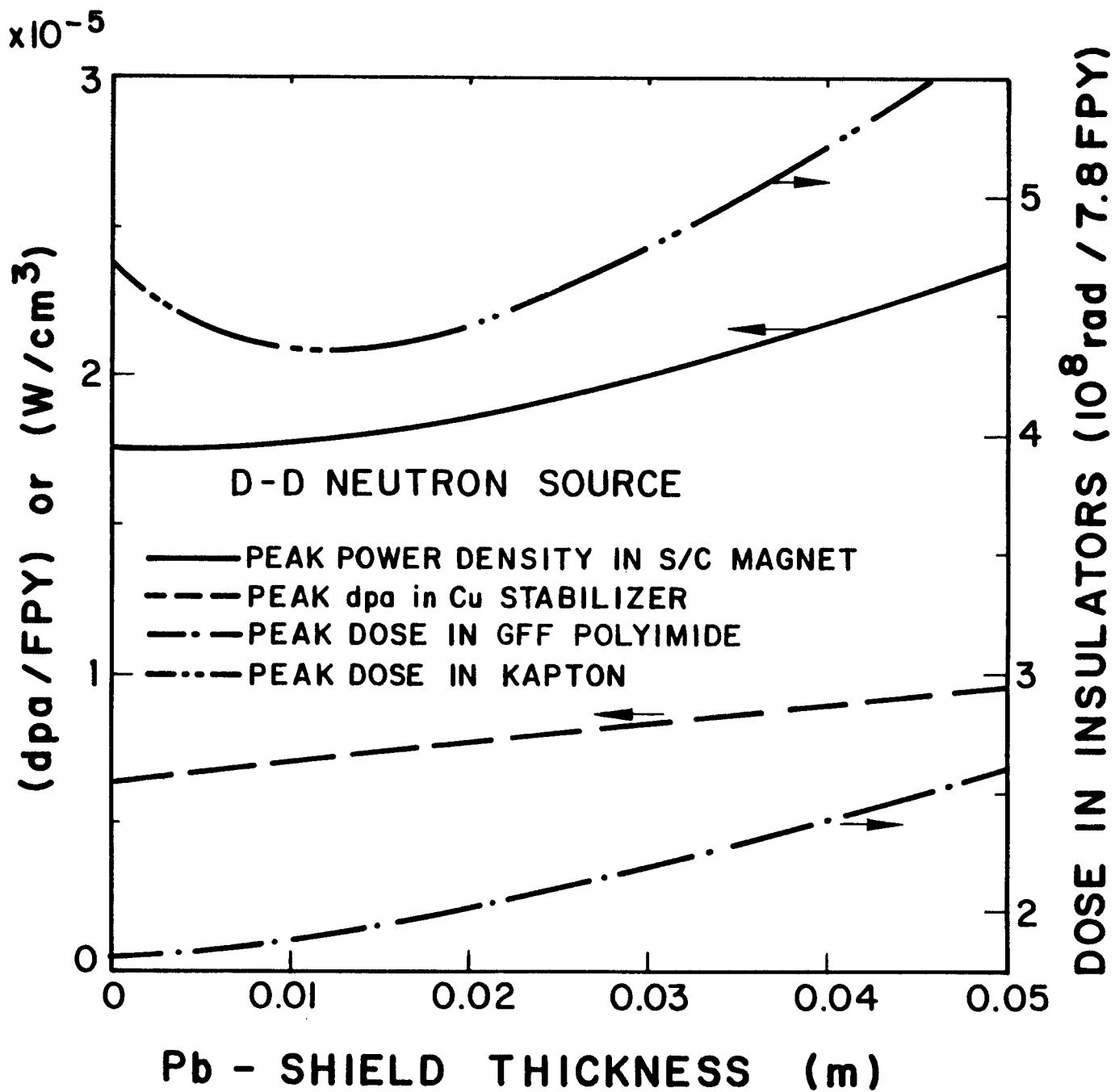
Fig. 5.2-4. Variation of the radiation effects in the C magnets with the Pb-
shield thickness in a 0.32 m thick shield.
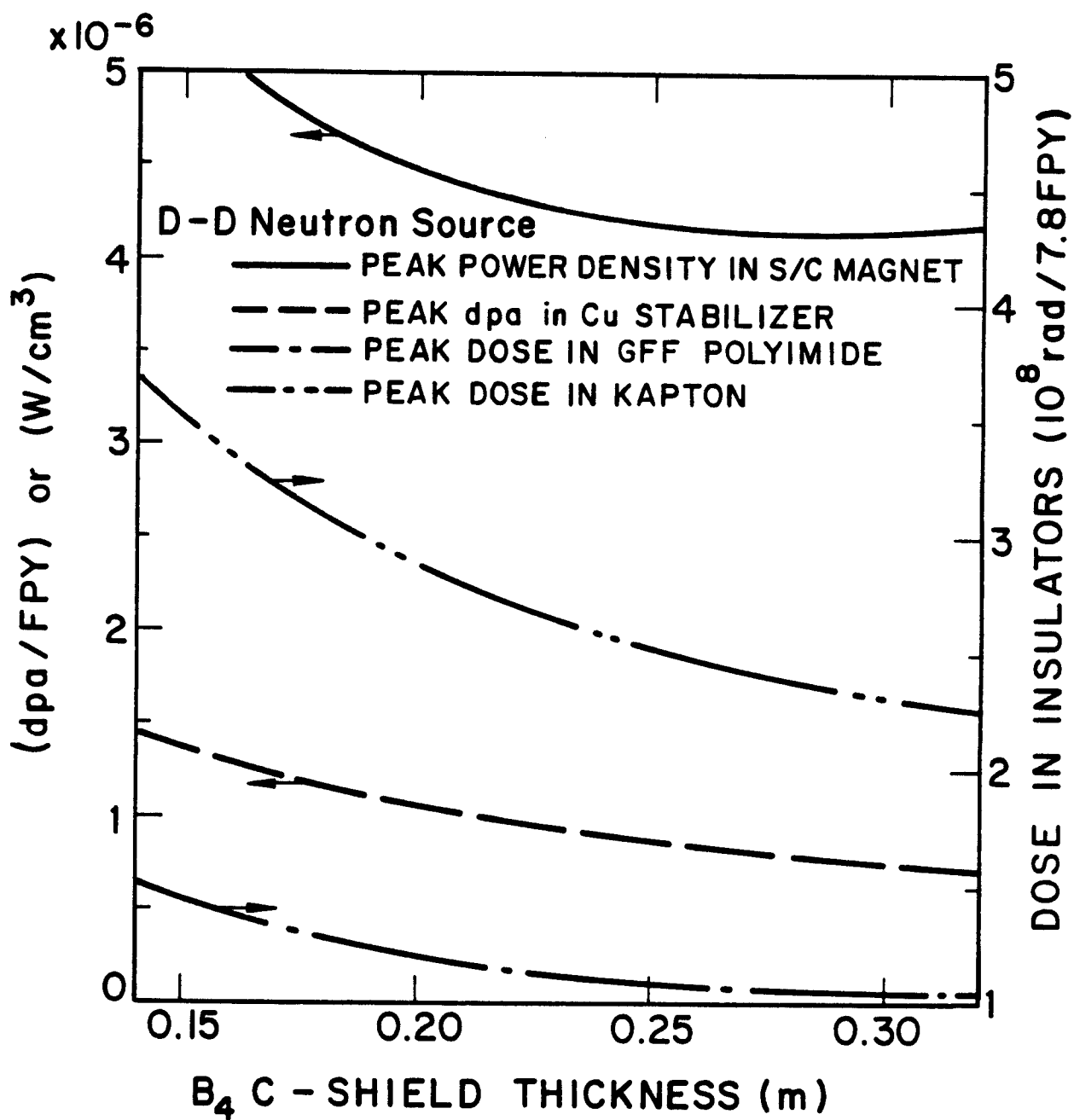
Fig. 5.2-5. Effect of replacing the Fe-shield by B₄C-shield on the damage in the C magnets for a 0.32 m thick shield.
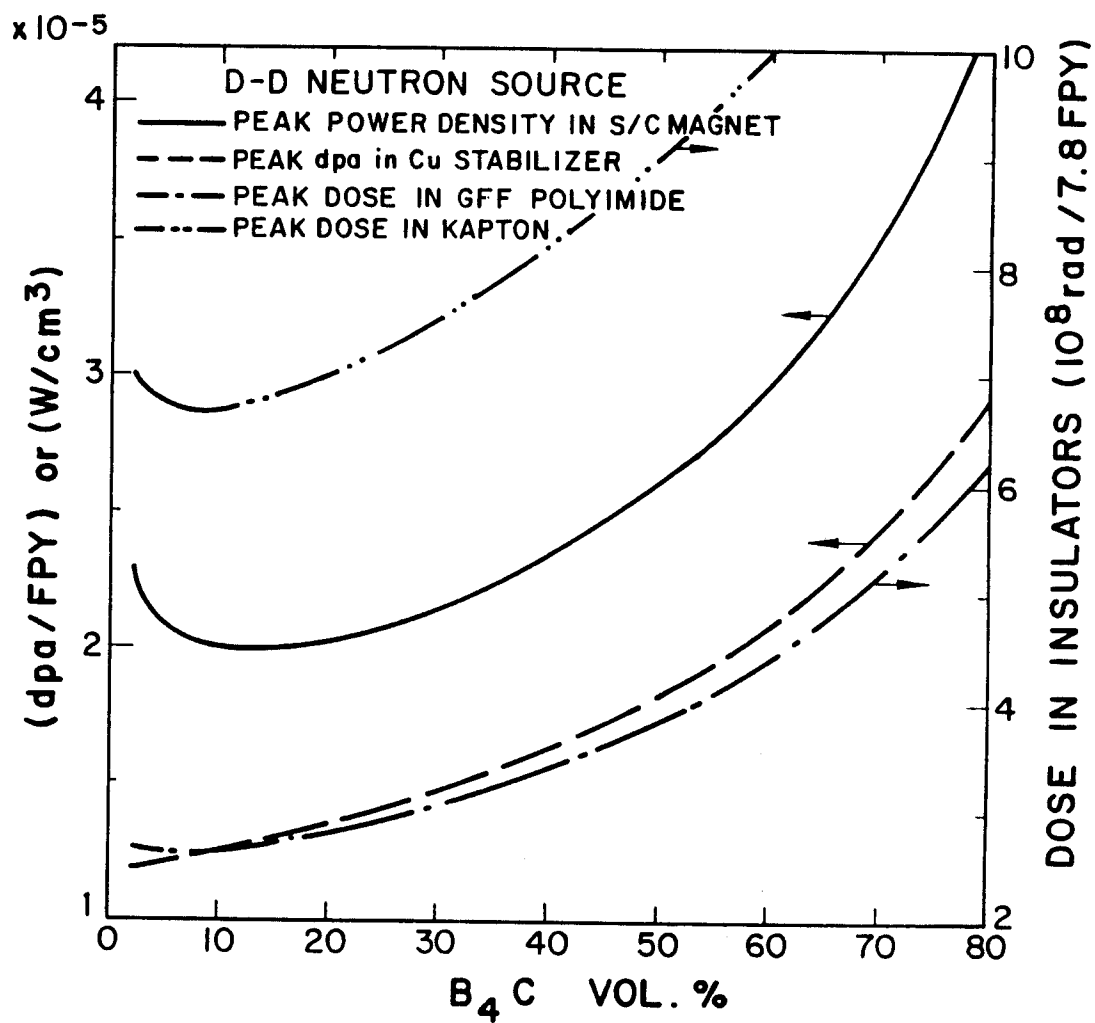
Fig. 5.2-6. Effect of reducing the B_4C content in a 0.2 m thick B_4C-shield on the damage in the C magnets.

required for the D-D neutron source is mainly water with 10 vol.% structure and 15 vol.% B_4C.

5.2.3 Central Cell Magnet

As mentioned before, the radiation analysis was carried out at the mid-plane of the reactor where the shield is constrained to 0.78 m. The optimal shield configuration for the D-T neutrons was used in the 1-D calculations and the radiation effects in the S/C magnet are summarized in Table 5.2-2 along with the design limits for the different responses. The optimal combination of the Fe and B_4C actually provides more shielding than the design goals and to avoid redesigning the magnet the first wall could be recessed by ~ 0.07 m to further lower the surface heat flux due to charge exchange. The dpa rate implies that magnet annealing is required every 3.3 FPY of operation or two anneals are necessary during the test facility life.

5.2.4 Choke Coils

Of the five radiation mechanisms likely to degrade the performance of the normal magnet, only one is seen as lifetime limiting for the coil design, namely the swelling in the compacted powder MgO (90% d.f.) ceramic insulator. The fluence limit to the MgO for the swelling design limit of 10 vol.% was found to be 3.5×10^{26} n/m^2 for $E_n > 0.1$ MeV. The peak neutron wall loading at the normal magnet is 0.1 MW/m^2. The 1-D calculation results in a peak neutron fluence in the MgO of 3.15×10^{25} n/m^2 at the end of the reactor life. Therefore, there should be no need to replace the normal insert coil during the 7.8 FPY designed life of the reactor due to radiation damage in the insulator.

The S/C choke coils seem to be overprotected and the radiation effects are reported in Table 5.2-3 at the inner and outer bore of the coils. The same design limits given in Table 5.2-2 are applied here except for the neutron fluence limit in the Nb_3Sn superconductor which is used in the inner S/C choke coil. This limit is 4×10^{22} n/m^2 for $E_n > 0.1$ MeV at the end of the reactor life. The results show that no anneal is required for the S/C choke coils. However, radiation damage due to neutron streaming through the penetrations of the central cell will require magnet annealing every 0.5 FPY as explained in Section 5.3.

Table 5.2-2. Radiation Effects in the Central Cell Magnet

		Design Limits
Peak dose in kapton (rad/7.8 FPY)	1.12×10^9	10^{10}
Peak dose in epoxy (rad/7.8 FPY)	6.58×10^7	6×10^8
Peak power density in S/C magnet (mW/cm^3)	4.47×10^{-3}	0.1
Peak dpa rate in Al stabilizer (dpa/FPY)	5.15×10^{-6}	3.4×10^{-5}
Peak neutron flux ($E_n > 0.1$ MeV) in NbTi (n/m^2 FPY)	4.94×10^{19}	1.1×10^{22}

Table 5.2-3. Radiation Effects in S/C Choke Magnets

	Inner Bore	Outer Bore
Peak dose in kapton (rad/7.8 FPY)	3.23×10^7	1.21×10^4
Peak dose in epoxy (rad/7.8 FPY)	9.39×10^6	2.62×10^4
Peak power density in S/C magnet (mW/cm^3)	9.14×10^{-4}	1.39×10^{-6}
Peak dpa rate in Al stabilizer (dpa/FPY)	5.56×10^{-7}	2.52×10^{-9}
Peak neutron fluence ($E_n > 0.1$ MeV) in superconductor (n/m^2-7.8 FPY)	3.52×10^{19}	1.96×10^{17}

5.2.5 Anchor and Transition Magnets

The D-T neutron source, shown in Fig. 5.2-1, extends axially up to 8.5 m from the midplane, while the D-D neutrons are mainly generated in the axial positions from 8.5 to 12.5 m. Accordingly, the same compositions and relative thicknesses as those of the central cell shield are used up to an axial distance of 8.5 m, and the D-D neutron source optimized shield is used to protect the rest of the C coils. In both cases, the shield configuration and the coil bundle were modeled for the 1-D code to determine the shield performance and the radiation effects in the magnets. In the modeling, a space of 0.13 m was reserved for the cryostat of the C coils. It consists of 0.03 m as a vacuum dewar followed by 0.02 m superinsulation, 0.06 m 304 SS coil case, and then 0.02 m GFF polyimide insulation. A clearance of 0.03 m was left between the shield and the S/C magnet.

Our results indicate that a negligible contribution to the damage in the Yin-Yang magnets comes from the 14.1 MeV neutron source generated from the

other branch of the D-D reaction (see Section 5.2.2) in the anchor region, even when the D-D neutron source optimized shield was used. Hence, the D-D neutron source drives the shielding design for the Yin-Yang magnets in the anchor region. Calculations for several shield thicknesses yield the radiation damage results shown in Figs. 5.2-7 and 5.2-8 using the peaks of the D-T and D-D neutron sources, respectively. To meet the heat load requirements of the S/C magnets, the shield thicknesses were set at 0.17 and 0.12 m in the two zones described above. This is not expected to cause any problem since in the magnet design a space of 0.35 m was left to accommodate the shield and the magnet cryostat. Other data of interest are reported in Table 5.2-4. The resulting peak dpa rate implies that no anneal is required for the C coils during the reactor life.

Table 5.2-4. Radiation Effects in C Coils

Region	Transition	Anchor	Design Limits
Neutron source	D-T	D-D	
Required shield thickness (m):	0.17	0.12	
Fe-shield	0.148	---	
B_4C-shield	0.022	0.12	
Peak power density in S/C magnet (mW/cm^3)	0.1	0.1	0.1
Peak dpa rate in Cu stabilizer (dpa/FPY)	4.78×10^{-5}	6.4×10^{-5}	3.1×10^{-4}
Peak dose in GFF polyimide (rad/7.8 FPY)	9.65×10^8	1.31×10^9	5×10^9
Peak dose in Kapton (rad/7.8 FPY)	2.20×10^9	3.14×10^9	10^{10}
Peak neutron fluence ($E_n > 0.1$ MeV in NbTi conductor (n/m^2 per 7.8 FPY)	4.82×10^{21}	6.09×10^{21}	3×10^{22}
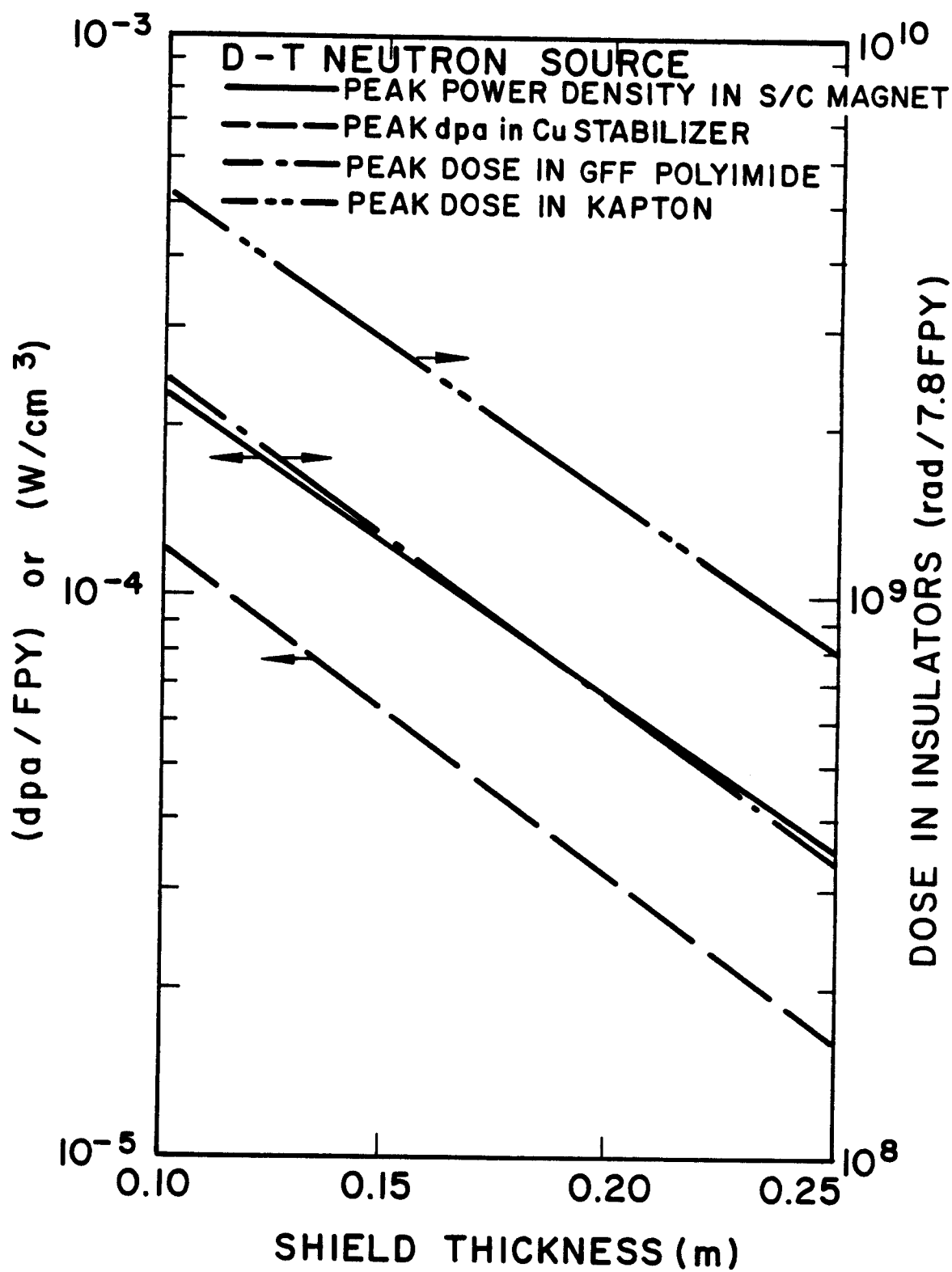
Fig. 5.2-7. Shield thickness effect on the D-T neutron radiation damage in
the C magnets.
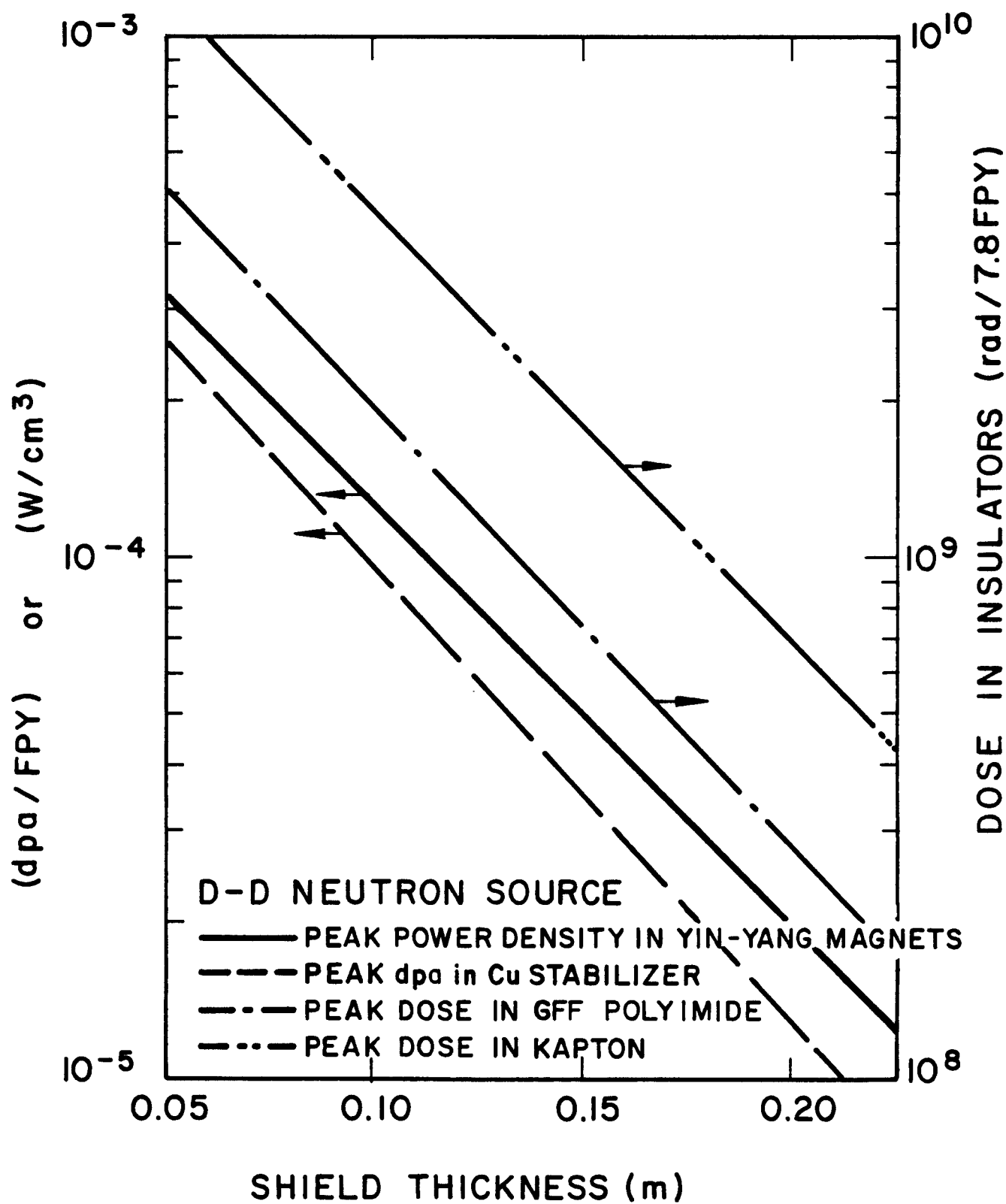
Fig. 5.2-8. Shield thickness effect on the D-D neutron radiation damage in the C magnets.

References for Section 5.2

1. M. Söll, "Influence of Radiation Damage on the Maximum Attainable Magnetic Field for Toroidal Fusion Magnet Systems," J. Nucl. Matl. 72, 168 (1978).

2. B. Brown, "Radiation Effects in Superconducting Fusion Magnet Materials," J. Nucl. Matl. 97, 1 (1981).

3. R.A. Van Konynenburg and M.W. Guinan, "Relative Radiation Sensitivity of Insulators, Stabilizers, and Superconductors," Lawrence Livermore National Laboratory, UCID-19292 (1982).

4. M. Abdou, "Radiation Considerations for Superconducting Fusion Magnets," J. Nucl. Matl. 72, 147 (1978).

5. F. Fickett, "Magnetoresistivity of Copper and Aluminum at Cryogenic Temperatures," Proc. of 4th Intl. Conference on Magnet Technology, CONF-720908, p. 539 (1972).

6. B. Brown, T. Blewitt, T. Scott and A. Klank, "Low Temperature Fast-Neutron Radiation Damage Studies in Superconducting Magnet Materials," J. Nucl. Matl. 52, 215 (1974).

7. M.E. Sawan, "Charts for Specifying Limits on Copper Stabilizer Damage Rate," Proc. of 3rd Topical Meeting on Fusion Reactor Materials, Albuquerque, NM, 19-22 September 1983.

8. R. Coltman and C. Klabunde, "Mechanical Strength of Low-Temperature-Irradiated Polyimides: A Five-To-Tenfold Improvement in Dose-Resistance Over Epoxies," J. Nucl. Matl. 103 & 104, 717 (1981).

9. C. Long, R. Coltman, Jr., C. Klabunde and R. Kernohan, "Effects of Radiation at 5 K on Organic Insulators for Superconducting Magnets," Special Purpose Materials Annual Progress Report, U.S. Dept. of Energy Report DOE-ER-0048/1, p. 73 (1980).

10. L.J. Perkins, "Materials Considerations for Highly Irradiated Normal-Conducting Magnets in Fusion Reactor Applications," Proc. of 3rd Topical Meeting on Fusion Reactor Materials, Albuquerque, NM, 19-22 September 1983.

11. MARS Final Report, Lawrence Livermore National Laboratory, to be published.

12. G.F. Hurley, J.C. Kennedy and F.W. Clinard, "Structural Properties of MgO and $MgAl_2O_4$ After Fission Neutron Irradiation Near Room Temperature," LA-UR 81-2078, Los Alamos National Laboratory (1981).

13. R.D. O'Dell et al., "User's Manual for ONEDANT: A Code Package for One-Dimensional, Diffusion-Accelerated, Neutral-Particle Transport," Los Alamos National Laboratory LA-9184-M (1982).

5.3 Radiation Streaming

5.3.1 Calculational Model

The central cell shield has penetrations for four high energy heating and fueling neutral beams and one low energy beam together with their associated beam dumps. Furthermore, there are two anchor neutral beam penetrations in the anchors. These penetrations must fit between the magnets. Radiation streaming into these penetrations can lead to adverse radiation effects in the superconducting magnets. It is, therefore, essential to provide sufficient shielding between the penetration wall and the magnets. Since the neutron wall loading in the anchor is about four orders of magnitude less than that in the central cell, only radiation streaming into the central cell penetrations is considered.

The most serious streaming problem in the central cell occurs due to the large (32 cm diameter at the first wall) penetrations for the high energy neutral beams. These beams have injection angles of 45° with the plasma axis. For vacuum pumping considerations the beam ducts open to a width of 67 cm resulting in a limited shielding space between the duct wall and the central and high field superconducting coils. Also, significant radiation effects can result in the magnets due to streaming into the large beam dump exhaust ducts which are about 1 meter wide. The radiation effects in the magnets due to streaming into these penetrations will be assessed in the following two sections. Streaming into the low energy beam duct has not been analyzed because of its relatively small size and the large injection angle of 70° which results in larger shielding space between the duct and the magnets as compared to the space available at the high energy beam ducts.

In general, detailed three-dimensional neutronics calculations are required to determine the radiation effects in the magnets due to radiation streaming. This tends to be very expensive and time consuming particularly when iterations are required between plasma physics, magnet design and neutronics calculations to produce a workable design that satisifies both plasma and magnet shielding requirements. An approximate calculational method was developed to estimate the shield required for protecting the magnets against streaming radiation in the penetrations of tandem mirror reactors.[1] The approach involves using a one-dimensional model to represent the actual three-dimensional problem. The problem is simplified further by developing

simple analytical forms based on the buildup factors to represent the one-dimensional results. The formulas can be integrated with the plasma physics models to perform a complete parametric study. The method was applied to the MARS axicell design and was found to give damage rates only a factor of ~ 1.3 higher than those obtained from the detailed three-dimensional calculation.[1] This results in overestimating the required shield thickness by only a few centimeters. This fairly accurate method was used to evaluate the magnet radiation effects due to streaming in TASKA-M. The calculational method is explained below.

A schematic showing a duct with injection angle θ_i that fits between two superconducting magnets is given in Fig. 5.3-1. The points on the duct wall closest to the left and right superconducting magnets are denoted I and II, respectively. The peak radiation effects in these magnets will result from the neutrons impinging on the duct wall around these points. The first step in the present approach is to calculate the neutron wall loadings at these points. This gives a measure of the energy current of the fusion neutrons coming directly from the plasma.

Assuming a line source of fusion neutrons along the plasma centerline, the neutron wall loading at either point I or II on the duct wall is given by

$$\Gamma = \left(\frac{r_w \Gamma_w}{2R}\right) \left| \cos(\theta_i - \theta_{min}) - \cos(\theta_i - \theta_{max}) \right| , \qquad (5.3-1)$$

where Γ_w is the wall loading at a first wall radius r_w in the plasma chamber, R is the radius of the point under consideration and θ_i is the angle between the duct wall and the plasma centerline. The angles θ_{min} and θ_{max} correspond to the boundaries of the plasma zone that will contribute direct neutrons to the point of interest on the duct wall. This formula can be used for any duct shape which will impact only the values of θ_{min} and θ_{max}.

The calculated wall loading gives only the contribution from the primary source neutrons produced in the plasma. It does not include the secondary component resulting from neutrons having collisions in the plasma chamber and succeeding in streaming into the duct. Although as many secondary neutrons as primary neutrons can stream into the duct, these secondary neutrons have a much softer spectrum and their contribution to the energy current is small. In addition, the softer spectrum leads to smaller shield penetration.
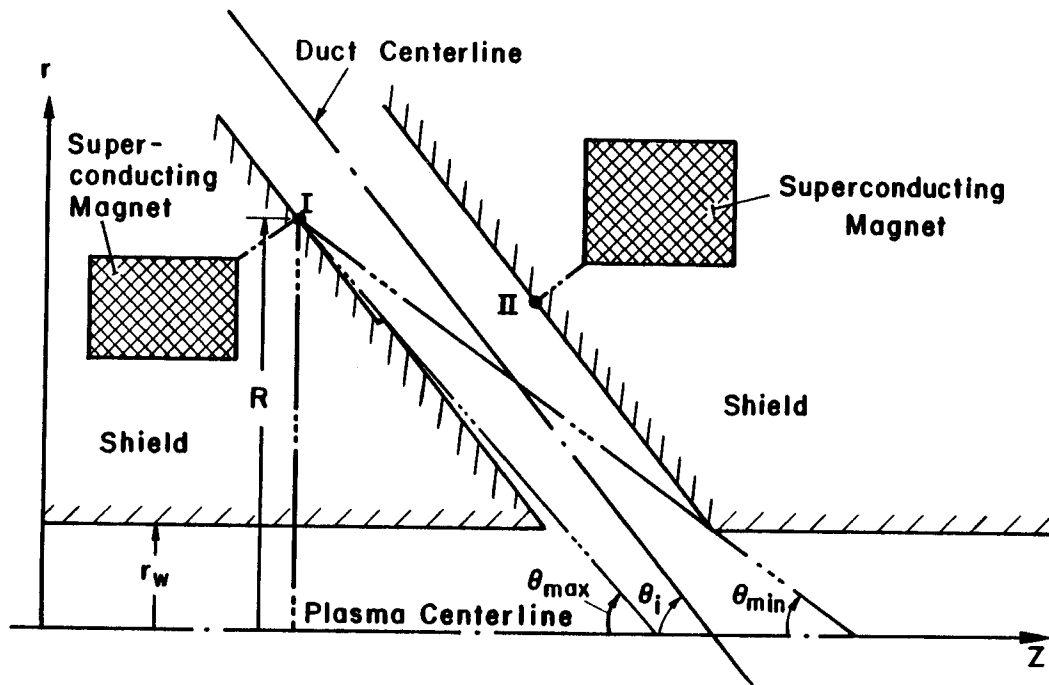
Fig. 5.3-1. A schematic of a neutral beam injector duct fitting between two superconducting magnets in a tandem mirror reactor.

The problem can then be modeled as a one-dimensional problem with a neutron source at the duct center that gives the same wall loading (at the point on the duct wall which has the largest contribution to the radiation effects in the magnet) as the one resulting from the actual neutron source. Notice that modeling the duct in a one-dimensional calculation will also account for the contribution of secondary neutrons and gamma photons resulting from primary streaming neutrons impinging on all of the duct walls. Using this approach will result in conservatively large shield thickness requirements because in the one-dimensional model most source neutrons are incident perpendicularly to the duct wall while in the actual case they are incident at an angle. This is expected to overestimate the required shield thickness by a distance on the order of a transport mean free path which is the distance beyond which the neutron "forgets" its original direction. However, the amount of overestimate will be decreased due to neglecting the contribution from secondary neutrons streaming from the plasma chamber in the wall loading calculation. Notice that the radiation effects calculated using this model represent only the contribution due to streaming. A conservative estimate for the total radiation effects can be obtained by adding the bulk shield contribution evaluated in Section 5.2.3 and 5.2.4.

A homogenized shield composition of 79.7 vol.% Fe-1422, 1.3 vol.% B_4C and 19 vol.% H_2O, which corresponds to the optimized central cell shield discussed in Section 5.2.2, was used in the calculations. The magnet cryostat and the beam dump were included in the model to account for their shielding contribution. The one-dimensional discrete ordinates code ONEDANT[2] was used to perform the one-dimensional calculations in cylindrical geometry. The P_3S_8 approximation was used together with the LANL 30 neutron-12 gamma group cross section data based on the ENDF/B-V evaluation.

5.3.2 Streaming into the Neutral Beam Injector Duct

As discussed before, the duct has a diameter of 32 cm at the first wall and opens to a width of 67 cm at the back. The injection angle between the beam centerline and the plasma centerline is 45°. Figure 5.3-2 illustrates the beam duct relative to the surrounding magnets. The largest radiation effects from streaming neutrons will occur at the inner corner of the central coil (r = 1.8 m and z = 0.35 m) and the outer corner of the high field coil (r = 1.7 m and z = 2.5 m). The points on the duct wall closest to these
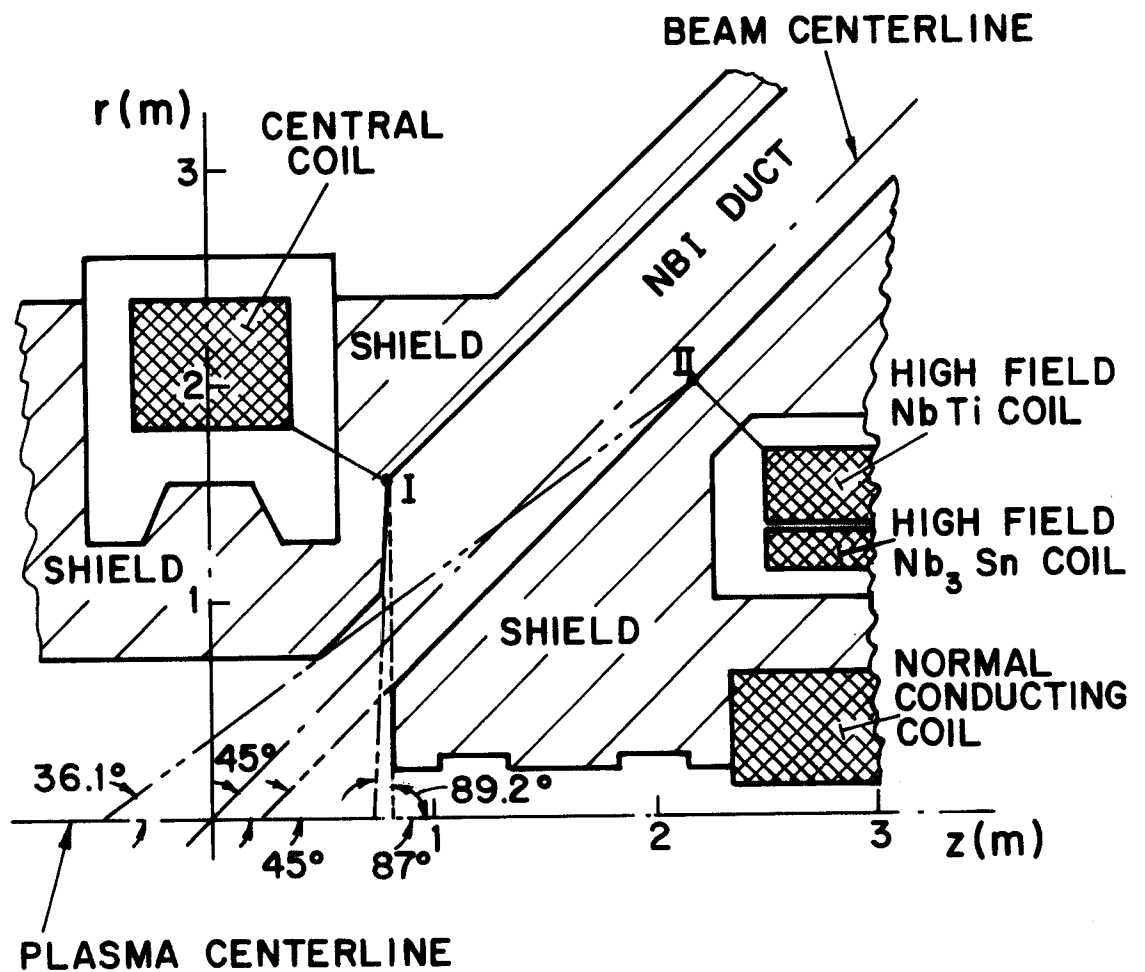
Fig. 5.3-2. Geometrical configuration of the NBI duct relative to the central and high field coils.

corners are designated I and II in Fig. 5.3-2. Point I has the radial and axial coordinates of 1.47 and 0.8 m, respectively. The corresponding values for point II are 1.97 and 2.24 m. The angles θ_{min} and θ_{max} defined in Fig. 5.3-1 are 87° and 89.2°, respectively, for point I and 36.1° and 45° for point II. Using the neutron wall loading of 0.25 MW/m^2 for a wall radius of 70 cm at the reactor midplane (z = 0), Eq. 5.3-1 yields values for the neutron wall loading at points I and II of 1.56 x 10^{-3} and 5.35 x 10^{-4} MW/m^2, respectively.

The distance between point I on the duct wall and the inner corner of the central coil is 55 cm. 32 cm of this space is utilized by the shield. In the remaining 23 cm space for the magnet case and cryostat, an effective 304 SS thickness of 13.3 cm exists. The distance between point II and the outer corner of the high field coil is 37.7 cm. The useful shield thickness at this section is 24.25 cm while the effective stainless steel thickness in the case and cryostat is 10 cm. Notice that the corner of the cryostat was cut to allow for a thicker shield which is more effective in reducing the magnet radiation effects. A summary of the parameters at points I and II used in the neutronics calculations is given in Table 5.3-1.

One-dimensional calculations have been performed for the sections at points I and II to calculate the peak radiation effects in the central and high field coils, respectively, resulting from radiation streaming into the NBI duct. The results are given in Table 5.3-2. The radiation limits discussed in Section 5.2.1 are also included. The value for the resistivity of Al after 0.5 FPY of operation before the first magnet anneal is based on an initial unirradiated resistivity of 5 nΩ cm and a radiation induced resistivity calculated using Eq. 5.2-1. It is clear that the stabilizer dpa rate is slightly lower than the limit while all other radiation effects are well below the corresponding design limits. Although as far as damage to the NbTi superconductor is concerned no magnet annealing is needed during the whole reactor life of 7.8 FPY, annealing every 0.5 FPY is required to avoid excessive increase in stabilizer resistivity that could jeopardize magnet cryostability.

Since in this calculation only radiation effects resulting from streaming into the NBI duct are considered, the extra contributions from the bulk shield must be accounted for. The bulk shield contributions are given in Sections 5.2.3 and 5.2.4. Adding these contributions, the peak radiation effects in

Table 5.3-1. Parameters at Points I and II on Duct Wall Used in Neutronics Calculations

	Point I	Point II
Radius (cm)	147	197
Axial location (cm)	80	224
Neutron wall loading (MW/m^2)	1.56×10^{-3}	5.35×10^{-4}
Distance to magnet corner (cm)	55	37.7
Shield thickness (cm)	32	24.25
Effective SS thickness in case and cryostat (cm)	13.3	10

Table 5.3-2. Peak Radiation Effects in Central and High Field Coils at the NBI Duct

	Central Coil		High Field Coil[*]	Design Limit
	Streaming Contribution	Streaming & Bulk Shield Contribution	Streaming & Bulk Shield Contributions	
Dpa rate in Al stabilizer (dpa/FPY)	7.63×10^{-5}	8.14×10^{-5}	9.8×10^{-5}	10^{-4}
Resistivity of Al after 0.5 FPY (nΩ cm)	16.1	16.8	19.2	20
Dose in epoxy after 7.8 FPY (rad)	1.1×10^8	1.8×10^8	1.5×10^8	6×10^8
Dose in Kapton after 7.8 FPY (rad)	2.1×10^9	3.2×10^9	2.9×10^9	10^{10}
Power density in winding pack (mW/cm^3)	0.034	0.038	0.047	0.1
Neutron flux (E > 0.1 MeV) (n/m^2 per FPY)	6.2×10^{20}	6.7×10^{20}	8.1×10^{20}	1.1×10^{22}

[*] Negligible contribution from the bulk shield.

the central and high field coils at the NBI duct have been calculated and are given in Table 5.3-2. We notice that the bulk shield contribution to the peak radiation effects at the outer corner of the high field coil is negligible and is about four orders of magnitude lower than the contribution from streaming radiation. This is attributed to the large shielding provided by the normal copper insert coil and the superconducting magnet itself. On the other hand, the bulk shield contributes about 10% of the total radiation effect at the inner corner of the central coil. Comparing the results to the radiation limits, it is clear that all limits are satisfied and adequate protection is provided for the central and high field coils against radiation streaming into the NBI duct and radiation penetrating the bulk shield.

5.3.3 Streaming into the Beam Dump Duct

Streaming into the beam dump duct can result in large radiation effects in the central and high field coils. The exhaust duct at the beam dump is 1 m wide. The beam dump makes an angle of 60° with the plasma centerline. The beam dump and its associated duct are shown in Fig. 5.3-3 relative to the surrounding magnets. As in the case for the NBI duct, the largest radiation effects occur in the inner corner of the central coil and the outer corner of the high field coil. Point I on the duct wall is the closest point to the central coil while point II on the beam dump is the closest point to the high field coil. Point I has the radial and axial coordinates of 1.2 and -0.9 m, respectively. The duct wall at this point makes an angle of 47° with the plasma axis. The values of θ_{min} and θ_{max} at this point are 47° and 74°, respectively. Using a neutron wall loading of 0.25 MW/m^2 for a wall radius of 70 cm at the reactor midplane, Eq. 5.3-1 yields a neutron wall loading of 8 x 10^{-3} MW/m^2 at point I. Point II has the radial and axial coordinates of 2.15 and -1.77 m, respectively. The values of θ_{min} and θ_{max} are 47° and 57°, respectively. The calculated neutron wall loading at point II is 10^{-3} MW/m^2.

The distance between point I on the duct wall and the inner corner of the central coil is 80 cm. 50 cm of this space is occupied by the shield while the remaining magnet case and cryostat has an effective 304 SS thickness of 19.1 cm. The distance between point II on the beam dump and the outer corner of the high field coil is 85 cm with only 20 cm of it devoted to the shield. The effective thickness of 304 SS in the magnet case and cryostat at this section is 18.5 cm. The beam dump at this section can be represented by a
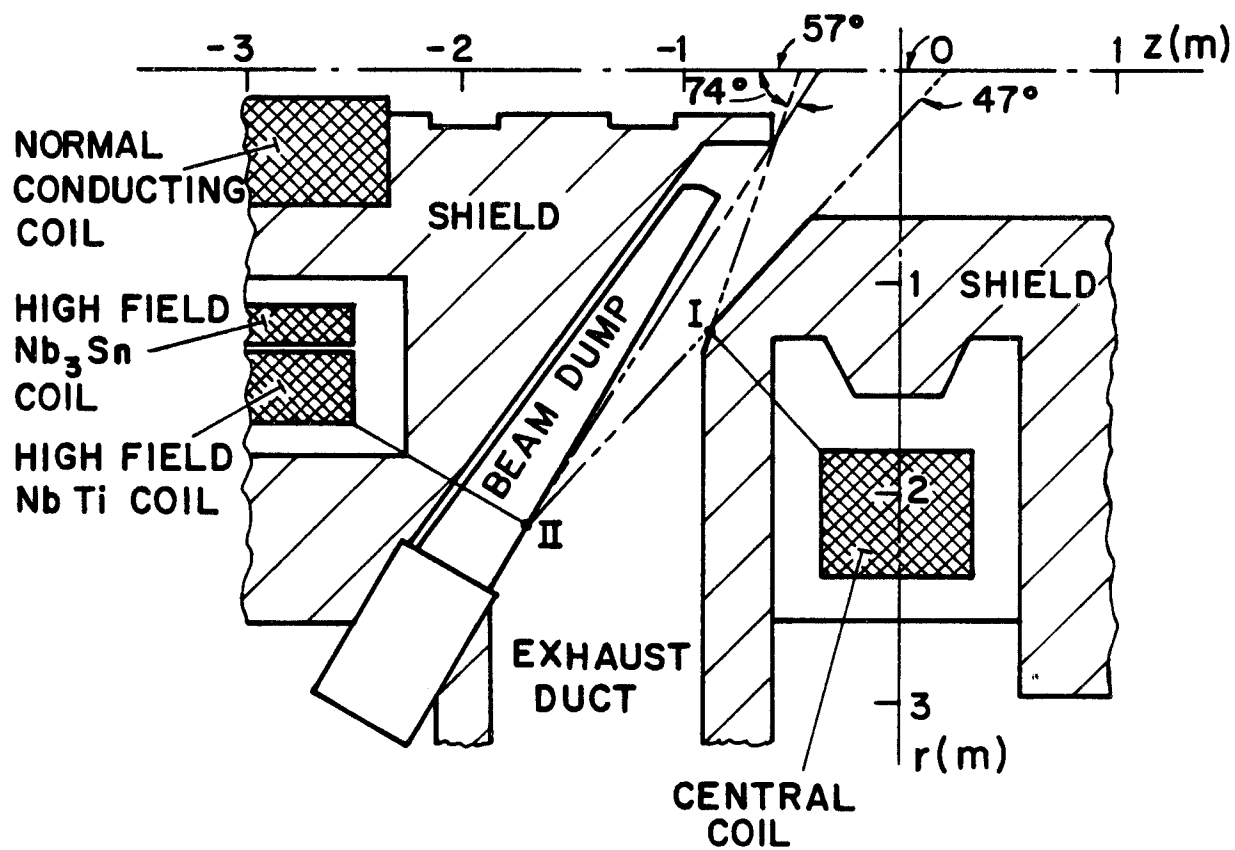
Fig. 5.3-3. Geometrical configuration of the beam dump and exhaust duct relative to the surrounding magnets.

1 cm thick Cu layer followed by a 2 cm thick H_2O layer, 1 cm thick Cu layer, 2 cm thick 304 SS layer and a 5 cm thick H_2O layer. A summary of the parameters at points I and II used in the neutronics calculations is given in Table 5.3-3.

The results for the peak radiation effects at the magnet corners obtained by performing one-dimensional calculations at the sections through points I and II are given in Table 5.3-4. The peak radiation effects obtained by adding the bulk shield contributions are also given. It is clear that all radiation effects are well below the corresponding design limits. Comparing the results of Tables 5.3-2 and 5.3-4, we notice that the hot spots in both the central and high field coils occur in the zones close to the NBI duct.

Table 5.3-3. Parameters at Points I and II in the Beam Dump Penetration Used in the Neutronics Calculations

	Point I	Point II
Radius (cm)	120	215
Axial location (cm)	-90	-177
Neutron wall loading (MW/m^2)	8×10^{-3}	10^{-3}
Distance to magnet corner (cm)	80	85
Shield thickness (cm)	50	20
Effective SS thickness in case and cryostat (cm)	19.1	18.5
Effective beam dump thickness (cm)	---	1 cm Cu
		2 cm H_2O
		1 cm Cu
		2 cm 304 SS
		5 cm H_2O

Table 5.3-4. Peak Radiation Effects in Central and High Field Coils at the Beam Dump Duct

	Central Coil		High Field Coil[*]	Design Limit
	Streaming Contribution	Steaming & Bulk Shield Contributions	Streaming & Bulk Shield Contributions	
Dpa rate in Al (dpa/FPY)	2×10^{-5}	2.5×10^{-5}	4.4×10^{-5}	10^{-4}
Al resistivity after 0.5 FPY (nΩ cm)	8	8.7	11.4	20
Dose in epoxy after 7.8 FY (rad)	2.8×10^{7}	9.4×10^{7}	6×10^{7}	6×10^{8}
Dose in Kapton after 7.8 FPY (rad)	5.3×10^{8}	1.6×10^{9}	1.1×10^{9}	10^{10}
Power density in winding pack W/cm^3)	0.008	0.0012	0.018	0.1
Neutron flux (E > 0.1 MeV) (n/m^2 per FPY)	1.6×10^{20}	2.1×10^{20}	3.6×10^{20}	1.1×10^{22}

[*]Negligible contribution from bulk shield.

References for Section 5.3

1. M. Sawan, C. Maynard, and L. El-Guebaly, "Buildup Factors for Magnet Shielding in Tandem Mirror Fusion Reactors," Proc. 6th International Conf. on Radiation Shielding, Tokyo, Japan, 16-20 May 1983.

2. R. O'Dell, E. Brinkley, Jr., and D. Marr, "User's Manual for ONEDANT: A Code Package for One-Dimensional Diffusion-Accelerated, Neutral-Particle Transport," LA-9184-M, Los Alamos National Laboratory (1982).

6. HEATING AND FUELING

6.1 Introduction

As described in more detail in section 3.9, neutral beam injection is the method chosen for plasma build-up, plasma fueling and ion heating in the central cell and in the two anchors. Alternatives to this scheme, for instance the method to build up a hot plasma at full density by filling the vacuum vessel with neutral gas, ionizing and heating it by radiofrequency cannot be applied in TASKA-M. Since the plasma confinement time τ decreases with temperature, the initial power for startup would be extremely high. Even though a low density startup is possible in principle since $n \cdot \tau$ does not depend on plasma density n and would lower the power by n^2, fueling would cause a problem as the density rises. According to the ablation law found experimentally, the penetration depth of pellets at full density is very small in comparison to the plasma radius of TASKA-M even at the highest pellet velocities which seem to be credible.

To provide a mechanism suppressing microinstabilities, the beams are injected at 45° and 50° in the central cell and the anchors respectively. Thus sloshing ion distributions are achieved with density dips in the center of the two regions for the confinement of warm plasma filling the loss cones. The injected power and the energy of the neutrals are 20.8 MW $D^o + T^o$ at 90 keV in the central cell and 3.5 MW D^o at 73 keV in each of the two anchors. A 0.6 MW D^o-beam at 12 keV is injected at 70° into the central cell to build up and fuel the warm plasma. In the anchors, warm plasma is expected to be provided by the end losses from the transition zone plasma.

To decrease the electron drag on the ions which spoils the ion confinement the plasma electrons are heated separately. Since TASKA-M has no thermal barrier the electrons should communicate in the whole machine. From this point of view the power for heating the electrons could be coupled to the plasma anywhere, preferably outside the central cell to keep the interference with the blanket as small as possible. Choosing ECRH, another advantage of electron heating in the transition region would be relatively low magnetic field strength. Nevertheless, ECRH

was ruled out because of cost considerations and difficulties with wave accessibility and heating of relatively high density plasmas with $\omega_{pe}/\omega_{ce} \approx 1$. The excitation of plasma waves near the ion cyclotron frequency was chosen instead, using the high efficiency Landau damping mechanism to heat the electrons. There is a drawback however since for absorption of the ICRH to be high enough, a relatively high density must be maintained and the antennae have to be installed in the central cell. The radio-frequency power which has to be coupled to the plasma is 12,5 MW at 25 MHz.

6.2 Neutral Beam Injection

6.2.1 General

The initial hot ion build up, plasma fueling and ion heating in both the
central cell and in the two anchors is achieved by neutral beam injection
(NBI). The overall neutral beam injection requirement is divided into
several beam lines because of spatial constraints for the beam ducts by
the blanket and by the magnetic field coils. The number of sources for
each beamline is given by cooling and by breakdown limitations of both
the extraction area and the power density. The steady state NBI system
for TASKA-M includes four high energy beam lines (HE-NBI) and one medium
energy beam line (ME-NBI) to buildup and to maintain the plasma in the
central cell and in each of the two anchors respectively. The beams are
injected at 45° and at 50° to the axis of symmetry respectively to build
up sloshing ion distributions in order to suppress microinstabilities.
Meanwhile it has been proven qualitatively in the TMX-upgrade plasma
that the sloshing-ion scheme works as expected /1/.

In order to fill the potential dip of the sloshing ion distribution with
warm plasma, which is required for the stabilization of the DCLC- and
the ALC-modes, an additional low energy beam (LE-NBI) is injected into
the central cell at 70°. The warm plasma for the stabilization of the an-
chors is expected to be provided by the end losses from the transition
zone plasma. The general layout of the whole NBI-system on the TASKA-M
vessel is shown in Fig. 4.1-1. The specific NBI equivalent current and
energy requirements for each region and each function in TASKA-M are the
result of a set of parametric code studies of plasma equilibrium (except
the LE-NBI) needed for the neutron wall loading goal (described in chap-
ter 3). The procedure used to determine the design data of the LE-beam
is outlined in chapter 3.

The specific NBI parameters needed to produce the specific incident (on
plasma) neutral beam current and power for TASKA-M are given in Table 6.2-1,
including the estimated ion source high voltage power supply current re-

quirements. For simplicity in initial wide ranging parameter studies, the equilibrium code calculations and the resultant NBI parameter listing in Table 6.2-1 are both based upon a beam composition of 90 % D^+, 5 % D_2^+, and 5 % D_3^+ and similarly for the tritium. Taking into account the differences in neutralization efficiencies and divergence for these species, the HE-NB incident on plasma is composed of 83.3 % full energy particles, 7.5 % of half and 9.2 % of one third energy. Therefore, some revisions are to be expected in the NBI requirements of Table 6.2-1 when more refined equilibrium and self-consistent NBI calculations are made using the actual detailed output species composition from the ion sources.

6.2.2 Design of the beam line components and determination of their physical parameters

Since the basic considerations concerning the design of the beam-lines are the same as in TASKA, they are not repeated here and the reader is referred to /2/.

It should be mentioned that 80 kV, 60 A H^+-beams extracted from an $\approx 10^3$ cm^2 surface multiaperture single source (JET) can be considered as the state of the art. Therefore to be conservative, the values of the size and of the power density of the TASKA-M-sources do not exceed the corresponding data of the JET NBI-system. According to these considerations the number of sources per beamline was chosen to be three for the He-NBI system and two for the ME- and the LE-NBI system. Also the operation of longpulse sources (30 s) with actively cooled grids has been demonstrated /3/ (JET sources: ≈ 10 s), thus steady state beams as necessary for TASKA-M seem to be credible. However, although the total power and the power densities at the injection point of a JET- and a TASKA-M-beamline are comparable for 24 cm diameter beams (6.9 kW and 5.2 kW, 15 kW/cm^2 and 11.5 kW/cm^2 respectively) there is a considerable difference between the port areas ($\approx 40 \times 100$ cm^2 and 804 cm^2 circular hole respectively) increasing the risk of beam choking. The diameter of the TASKA-M ports cannot be increased because of the relatively small diameters of the vacuum vessel and of the

plasma. However basically the port and the beams may be elongated in the direction parallel to the plasma axis to descrease the risk of choking but not without other problems arising due to the increased perforation of the blanket with enhanced neutron streaming and due to the rather limited space available between the coils.

Because of this and, because the design is well within the state of the art with respect to all other NBI-parameters the relatively narrow ducts and ports are accepted for now.

The parameters of the LE-Beam are determined by considerations discussed in Sec. 3.2 and 3.3. The required current is 50 Amp. and the required primary energy is 12 keV. Applying the neutralization efficiency of a 12 keV-beam and the transfer efficiency of the beam lines, the final electrical power extracted from the LE-beam sources will be $\approx$ 1 MW.

The pumping system of the beam lines was changed, as compared to that in TASKA; cryopumps instead of getter pumps are used (s. 6.2.4.). Special attention was given to a beam dump for the particles which are not captured by the plasma (see chapter 7). Since the shine through of the HE-beam in the central cell plasma is 8% at full plasma density, the resulting wall loading would be prohibitive if a beam dump were not used.

Table 6.2-1 TASKA-M Neutral Beam Injector Requirements

	Units	HE - NBI	ME - NBI	LE - NBI
Location		central cell	anchors	central cell
Injection angle	Degrees	45	50	70
Primary energy	kV	90	73	12
Mean energy of neutral atom	keV	81	66	11
Transmission efficiency		0,7	0,7	0,6
Neutralization efficiency		0,57	0,57	0,9
Neutral atom current /NBI	A_o	64 $D°+T°$	53 $D°$	50 $D°$
Power/NBI	MW	5,2	3,5	0,55
No. of ion sources per NBI		3	2	2
Total No. of NBI		4	2	1
I^+ per source	A	46,7	57,5	41,7
Total electric power p	MW	50,4	16,8	1,0
Extraction area per source	cm²	20x50	20x50	20x50
Current density at source	A/cm²	0,047	0,058	0,042
Beam divergence	Degrees	±0,5	±0,6	±1x±2

6.2.3 Charge-Exchange First Wall Heat Fluxes from the Central Cell Neutral Beams

6.2.3.1 Introduction. For a given power of neutral particles injected into the plasma, a fraction will penetrate the plasma with no interaction and will "shine through" to be absorbed by the beam dumps. The remaining neutrals will either undergo ionization and become trapped or experience charge-exchange reactions with the plasma ions. In turn, the secondary neutral atoms formed in the charge-exchange (CX) process will either escape and bombard the first wall or undergo ionization or further CX interactions within the plasma. Therefore, from considerations of particle and energy balance, a fraction of the incident beam is absorbed in the plasma, a fraction escapes as shine-through to the beam dumps and the remainder appears as CX neutral bombardment of the surrounding first wall surface. These processes are illustrated schematically in Fig. 6.2-1.

As we shall see, the CX neutral power to the first wall can be a significant fraction of the incident beam power. Accordingly we are faced with the following potential problem areas:

- High local power densities to the first wall of up to several kW cm^{-2} with corresponding requirements for sophisticated high heat flux surfaces.

- Sputtering of the first wall surface resulting in reduced lifetimes.

- Tritium implantation and diffusion through first wall surfaces.

- Additional heat loads to the neutral beam dumps over and above the non-interacting shine-through fraction.

- Resulting reflux of cold neutral CX gas to the plasma chamber.

- Constraints on location of RF antennas, blanket modules and plasma instrumentation.

With regard to the last point above we should note that blanket modules which do not have an efficiently cooled first wall exhibit a fairly low tolerance for surface heat fluxes. This is especially true for liquid-metal-cooled blankets where, due to the poor heat transfer properties of a liquid metal in a strong magnetic field, maximum permissible surface heat fluxes are in the vicinity of ~ 10 W cm^{-2}. Similarly, RF antennas and sensitive plasma diagnostic instrumentation at the first wall are also limited in their surface

Fig. 6.2-1. Schematic of neutral beam interaction with a plasma. Of the incident beam, a fraction f_S penetrates the plasma with no inter-action, a fraction f_A is absorbed in the plasma and a fraction f_W appears as charge-exchange neutral bombardment of the surrounding first wall.

heat flux accommodation and, therefore, cannot be positioned too near the neutral beam interaction region.

Therefore, in TASKA-M, which requires appreciable neutral beam injection power, it is important to accurately model the production and transport of CX neutrals and thereby predict the power density distribution of the CX flux over the first wall surface. Accordingly, it is the purpose of this section to illustrate the application of Monte Carlo methods to the modeling of neutral-beam-driven charge-exchange phenomena. Further details of the methodology can be found in Ref. 4.

6.2.3.2 The Need for Monte Carlo Methods. Modeling the beam/plasma/wall system in three spatial dimensions is, in general, a very complex process. In the past, various simple analytic and numerical investigations have been performed which have incorporated various simplifying assumptions regarding system parameters.[5-7] For example, in their analytical study of neutral beam injection into the FERF minimum-B mirror machine, Carlson and Hamilton[5] employed the simplifying assumptions of a uniform ion density, a single plasma species, an isotropic angular distribution of plasma ion velocities, an infinitesimal beam diameter, and a spherical plasma geometry. Unlike the simpler model of Hovingh and Moir,[7] Carlson and Hamilton's analysis did allow for re-ionization of CX neutrals within the plasma, but second and subsequent generations of CX neutrals were not considered.

However, if formal investigation of charge-exchange phenomena is required in a three-dimensional system with the retention of all major phase space anisotropies inherent in the interaction of multiple neutral beams with a multispecies mirror-confined plasma, then recourse is necessary to Monte Carlo methods. In particular, as we shall see, the CX surface heat fluxes at the first wall exhibit severe local hot spots due to the complex dependence of the CX angular distribution on beam and plasma properties. Realistic modeling of these heat fluxes can, therefore, only be obtained via Monte Carlo techniques. In this respect, Miller[8] has pointed out the similarity of neutral particle transport in a complex plasma medium and neutron transport in a three-dimensional neutron scattering medium and has underlined the need for analogous Monte Carlo methodology. In his study, Miller employed Monte Carlo tracking techniques to study energetic neutral-beam heating of a minimum-B mirror plasma. Hughes and Post[9] have employed similar Monte Carlo methods

in their analysis of charge-exchange and ionization of neutral gas in toka-
maks.

Accordingly, a Monte Carlo neutral beam interaction code MCNEUT is em-
ployed here to model CX production and transport. In addition to computing
general particle and power balances for neutral beam interaction, CX power
density distributions are mapped over the first wall surface in both the axial
and azimuthal directions.

6.2.3.3 Application of the MCNEUT Monte Carlo Code to TASKA-M.

The Monte
Carlo code MCNEUT was originally generated by Kaiser at Lawrence Livermore
National Laboratory for the purpose of modeling the energy spectra of CX
fluxes to CX detectors in the 2XIIB minimum-B mirror device.[10] The code was
configured for a single-species beam incident on a single-species plasma and
has been modified here to accommodate multispecies beams (i.e., mixed
deuterium-tritium) incident on multispecies plasmas and to allow for multiple
beam directions.

In the code, a large number of neutral particle histories ($\sim$ 40,000 for
this study) are followed in three dimensions from their emission from the
neutral beam injector through a mirror-confined target plasma. The beam
geometry is configured to match that of the beam injector under consideration
and incorporates the Gaussian angular divergence of the source. The plasma
can be represented either by a specific bi-Maxwellian characteristic of the
beam interaction point or by a generalized mirror loss-cone distribution
function, and is taken to be in steady state with respect to the neutral beam
input. Electron/ion ionization and charge exchange of transported neutrals
are simulated via Monte Carlo techniques similar to those employed by Hughes
and Post.[9] Descendent generations of charge-exchange neutrals are followed
through phase space until each particle is either ionized and integrated into
the background plasma or escapes to bombard the first wall. Charge-exchange
events between neutral particles and plasma ions are simulated in MCNEUT via a
Monte Carlo sample collision scheme. Both ion and electron ionization events
are incorporated by decreasing the statistical weight of a neutral particle
each time it undergoes a charge exchange by the ratio of the ionization col-
lision frequency to total collision frequency. A series of charge-exchange
events are treated as equivalent changes in the phase-space coordinates of the

primary neutral with appropriate flagging of the mass of the particle after each collision (i.e., deuteron or triton).

Further details on the application of the code to tandem mirror plasmas can be found in Ref. 4.

Application of MCNEUT to two neutral beam systems in TASKA-M was made, namely the four high energy (90 keV) central cell beams and the single low energy (12 keV) central cell beam. CX fluxes from the anchor beams were considered to present little problem and, as such, will not be considered further in this section. The major plasma, beam and first wall parameters employed in MCNEUT for these two beam systems are shown in Table 6.2-2. In each case, the plasma was modeled as a long cylinder with axial extent large relative to the characteristic beam attenuation length such that end effects could be neglected.

In MCNEUT, the beams are configured to intersect at the midpoint of the z-axis of the cylindrical plasma model. For convenience, this intersection point will be designated z = 0 for defining the axial location of CX flux distribution. This point should not be confused with the z = 0 datum coordinate which is conventionally employed as the center midplane of the machine.

The plasma radial density profile was accommodated by radially portioning the target plasma into 32 annular zones in each of which the plasma properties were assumed constant. Escaping CX neutrals were scored on a cylindrical first wall detector grid having 36 azimuthal bins in the θ direction and, depending on the resolution required, between 20 and 40 axial bins in the z direction.

6.2.3.4 Results. We now consider the CX heat fluxes obtained from MCNEUT at the "detector" grids on the first wall surface. As discussed in Section 6.2.3.2 above, the detector grid was discretized into N_θ = 36 azimuthal bins in the θ direction with a resulting bin width of $\Delta\theta$ = 10°. In the z direction, a value of N_z in the range 20 to 40 was employed, depending on the axial extent required, with bin widths of Δz = 5 to 10 cm depending on the resolution required. Therefore, at each of the N_z discrete axial z positions measured from the beam intersecton point (z = 0), a slice is obtained of the first wall in the xy plane with 36 discrete values of the CX power density spaced 10° apart around the surface.

Table 6.2-2. Principal Input Parameters to the Monte Carlo Code MCNEUT

	High Energy Central Cell Beam	Low Energy Central Cell Beam
Number of Beam Lines	4	1
Total Injected Power (MW)	20.8	0.6
Injection Angle[1]	45°	70°
Azimuthal Angle Between Beam Lines	45°	N/A
Beam Voltage (kV)	90	12
Mean Beam Energy	82.49	11.0
Beam Components[2] (%)	83.3/7.5/9.2	83.3/7.5/9.2
Beam Species	D (50%), T (50%)	D (100%)
Beam Profile	Gaussian	Gaussian
Beam Divergence	0.5°	1.0°
Plasma Species	DT	DT
Plasma Geometry	Cylindrical	Cylindrical
Plasma Radius (cm)	12	12
Plasma Radius Profile	Gaussian	Gaussian
Midplane Ion Density[5] ($\times 10^{14}$ cm^{-3})	3.6	3.8
T_{perp} (keV)	26.07	26.07
$T_{parallel}$ (keV)	25.76	25.76
Electron Temperature (keV)	14.0	14.0
B-Field at Midplane[3] (T)	4.2	4.2
First Wall Radius (cm)	25 [4]	25
Grid Azimuthal Bin Width $\Delta\theta$	10°	10°
Grid Axial Bin Width Δz (cm)	10	5
No. of Neutral Histories	40,000	40,000

---

1. Angle between beam line and negative z axis.
2. Percentage of full, half and third beam energy components.
3. For computation of ion gyroradii.
4. Original design value. This was subsequently increased in the vicinity of the beam interaction region due to high CX heat fluxes (see later).
5. Composite density of hot and warm population at injection point.

Figure 6.2-2 is a polar plot of the first wall CX power density distribution in the xy plane at a z coordinate of $z = -5.2$ cm from the beam injection point for the high energy central cell beams. Two distributions are shown in Fig. 6.2-2. The inner distribution is that for a single beam (beam number 1 in the figure); note that the angular distribution is backward-peaked relative to the incident beam direction. The outer distribution is the corresponding polar plot obtained when all four beams are included; note the position of the four beams spaced 45° apart. The maximum power density is seen to be ~ 440 W cm^{-2} and occurs at backward angles between beams 2 and 3 as expected.

Given the MCNEUT output, it is possible to construct polar plots similar to Fig. 6.2-2 for each of the axial (z) grid positions along the first wall surface. However, it is more instructive here to preprocess this data and, for each separate polar plot, extract the maximum, minimum and average CX power densities and plot these as a function of the corresponding z coordinates. Accordingly, these data are shown in Fig. 6.2-3. Peak values of the maximum, minimum and average power density distributions are seen to be ~ 470, 330 and 390 W cm^{-2}.

For brevity here not reproduced are the individual CX polar distributions for the low energy central cell beam. Suffice it to say that they exhibit maximum values in the backward and sideways directions (i.e., at 180° and 90°/270° relative to the incident beam direction). The important engineering parameter here is the variation of the maximum, minimum and average first wall heat flux relative to the beam injection point ($z = 0$); this is shown in Fig. 6.2-4. The peak value of the maximum CX heat flux is seen to be ~ 190 W cm^{-2} at $z \sim -2.5$ cm. Note that at $z = 20$ cm from the beam injection point (i.e., $z = 80$ cm from the machine midplane, the position of the inside edge of the materials test module) the maximum heat flux is still ~ 90 W cm^{-2}.

Typical CPU times on a CRAY 1S computer required for the runs in this study were ~ 3-4 minutes. With a detector grid of $N_\theta \times N_z \sim 36 \times 20$ elements and 40,000 neutral particles followed in one run, this is equivalent to ~ 5 ms per neutral history.

6.2.3.5 Discussion of Results and Their Engineering Implications. One of the major features of Fig. 6.2-2 is the backward peaking of the CX flux distribution for the single beam. This should be contrasted to the CX flux distri-
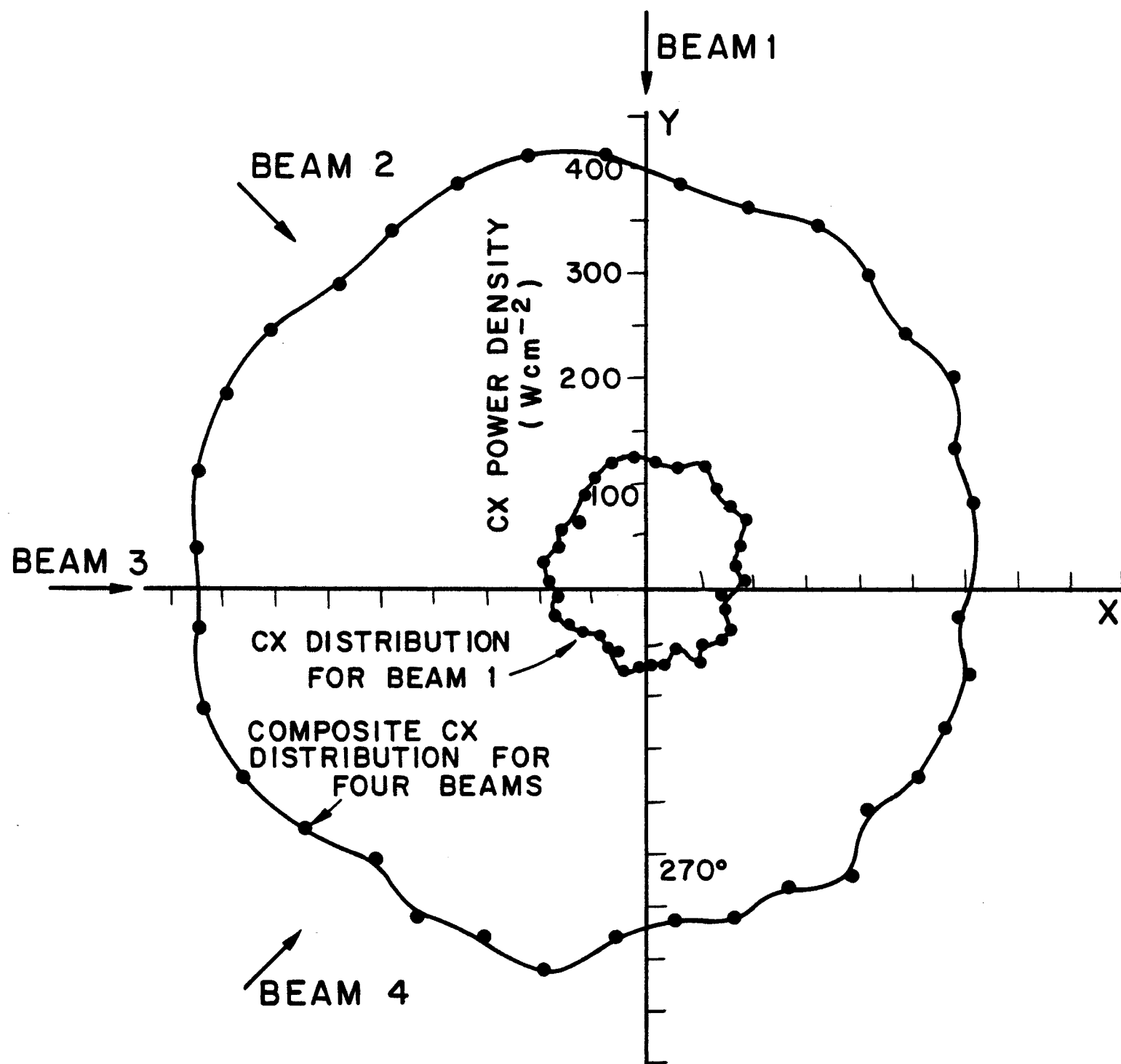
Fig. 6.2-2. Polar distribution of CX heat flux at the first wall (r_w = 25 cm) for the high energy central cell beams. The distribution for one beam is shown together with the composite distribution for all four beams.
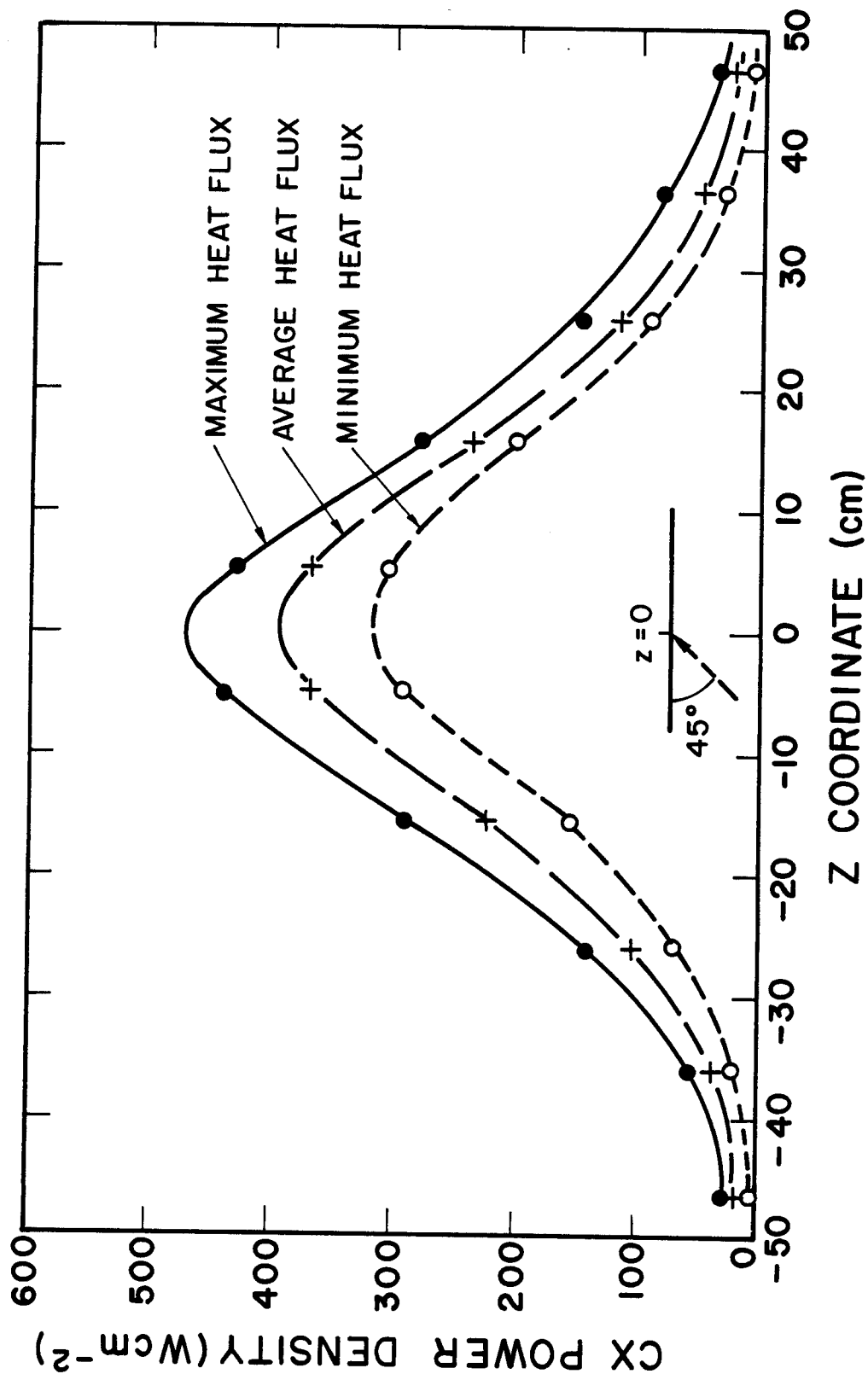
Fig. 6.2-3. Variation of maximum, minimum and average first wall CX heat fluxes as a function of the axial (z) coordinate for the high energy central cell beams. The beam intersection point is at z = 0.
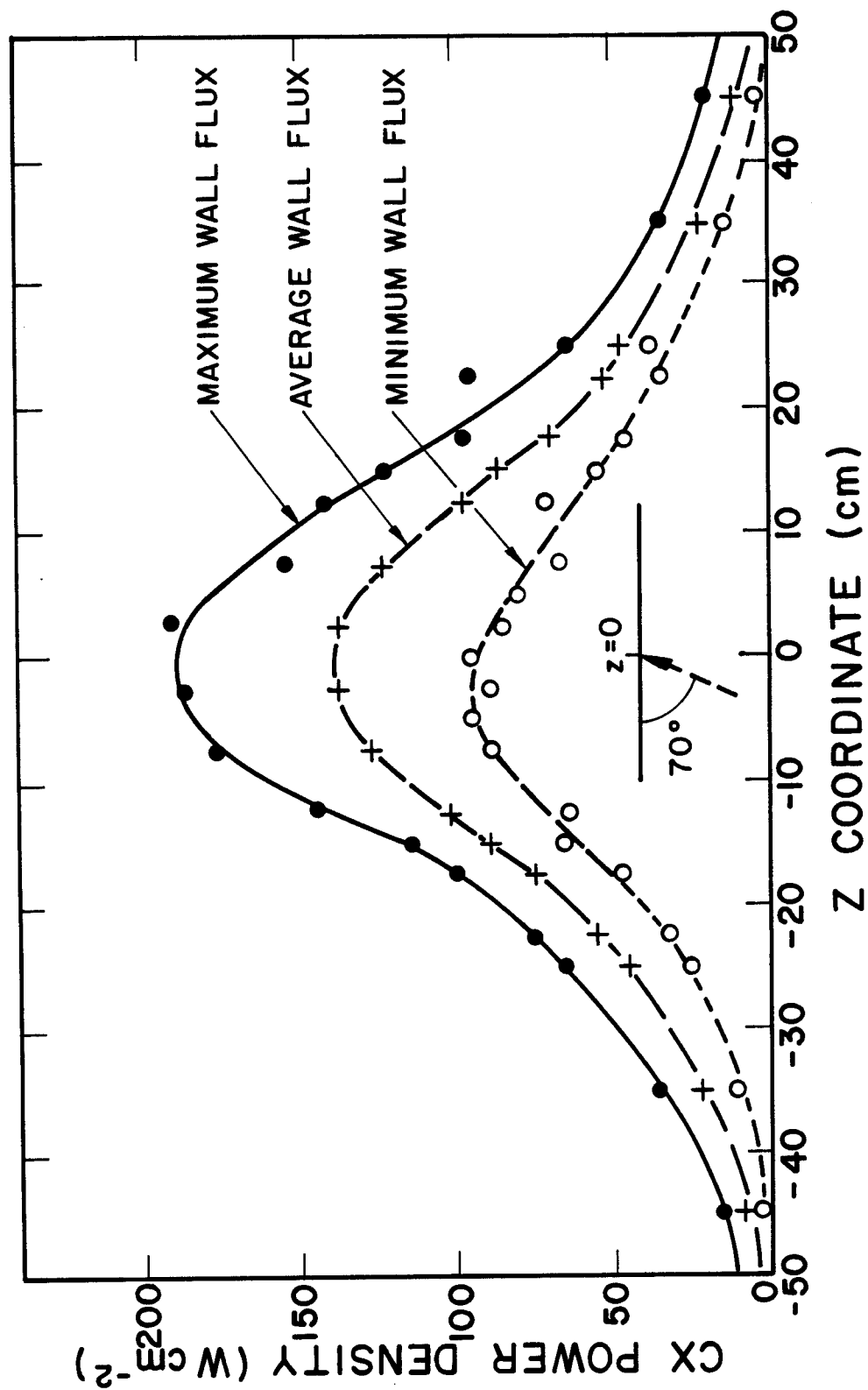
Fig. 6.2-4. Variation of maximum, minimum and average first wall CX heat fluxes as a function of the axial (z) coordinate for the low energy central cell beam. The beam intersection point is at z = 0.

butions exhibited in the earlier phases of the machine design where strong forward peaking was observed. Similar backward peaking was observed in the Technology Demonstration Facility (TDF).[4] It is also interesting to note that the distribution in Fig. 6.2-2 for the single beam is quite symmetric about the y-axis. This is to be expected in view of the incident beam direction. The slight deviations from true symmetry which can be seen are, of course, attributable to Monte Carlo statistics (~ 10% here).

For the composite distribution for four beams in Fig. 6.2-2, the backward peaking has been somewhat ameliorated by the superposition of multiple beams. However, the composite heat fluxes are still dominant in the general backward direction. This backward peaking is interesting in that when TASKA-M proceeds through startup, the neutral heat flux will progress from strongly forward peaked at low plasma densities to backward peaked at full plasma conditions.

Generally, for a single isolated CX interaction, the product neutral has a higher probability of forward emission because the CX cross section is large for particle pairs with small relative velocities.[11] In other words, an incident neutral with a given direction of travel is more likely to charge-exchange with a plasma ion having a velocity vector in the same direction. However, those forward peaked CX neutrals directed into the bulk of a dense plasma have a strong chance of undergoing a further interaction (either CX or ionization) before escaping. In addition, the incident neutral beam will be attenuated exponentially in the plasma, thus the primary CX production rate decreases along the chord length of the incident beam through the plasma. Therefore, in general, for a high energy beam and/or low plasma line density, the polar CX flux tends to be forward peaked. Conversely, for lower energy beams and/or higher plasma line densities, the CX heat flux at the first wall tends to a maximum in the backward direction. As the beam trapping fraction approaches 100%, strong backward peaking would be expected.

With these above physical arguments an account can be made for the backward peaking from the high energy beams in TASKA-M. The plasma density is relatively high and beam absorption is fairly good. In addition, compared with the interim phases of the machine design, the mean hot ion energy is lower (84 keV compared with 112 keV). Therefore, forward directed CX products have a good chance of absorption before penetrating to the opposite wall, leaving backward-directed CX neutrals to dominate the angular distribution.

In the event of a higher plasma density, lower beam energy or lower plasma hot ion energy, we would expect very strong peaking in the backward direction. The low energy central cell beam, for example exhibits strong backward peaking which is to be expected in view of the high beam trapping fraction (> 99%). Note also that a high trapping fraction with a low beam energy implies an intense CX source region localized in the first few cm of plasma on the incident beam side.

These high peak CX heat fluxes at the first wall present some significant technology problems. Clearly, the first wall heat loads of nearly 500 W cm^{-2} are too large given the current and near term status of high heat flux technologies. Neutral beam dumps based on the "Hypervapotron" principle are currently being incorporated on JET for heat loads of ~ 1-1.5 kW cm^{-2} under quasi-steady-state (~ 20 s) conditions.[12] Similarly, MFTF-B will incorporate tubular beam dumps probably based on the swirl-flow principle and with power density capabilities in the same range.[13] However, beam dump designs such as these have a rather bulky configuration and could not conceivably be integrated around the first walls of TASKA-M where space is at a premium.

In test facilities such as TASKA-M where true steady-state operation is envisaged and where component reliability is a key requirement, heat loads should be limited to water-cooled first wall surfaces to certainly no more than a few hundred W cm^{-2}. In the STARFIRE conceptual tokamak reactor design, for example, maximum surface heat loads to the water-cooled limiter were restricted to ~ 240 W cm^{-2}.[14]

6.2.3.6 Variation of CX Heat Fluxes with First Wall Radius. As an alternative to reconfiguring beam parameters and/or geometries, for the high energy central cell beams, the most effective method of reducing the peak heat loads in Fig. 6.2-3 is to simply increase the radius of the first wall. This would only be necessary in the vicinity of the beam interaction region and would not, therefore, be detrimental to neutron wall loading levels elsewhere in the machine. Accordingly, further MCNEUT runs were performed for TASKA-M employing various first wall radii.

In Fig. 6.2-5, we compare the axial (z) distribution of the maximum CX heat flux in TASKA-M at a new wall radius of r_w = 70 cm with that for the original radius of r_w = 25 cm for the interim design. Note that the peak CX heat flux has been reduced from ~ 470 W cm^{-2} for r_w = 25 cm to a much more accep-
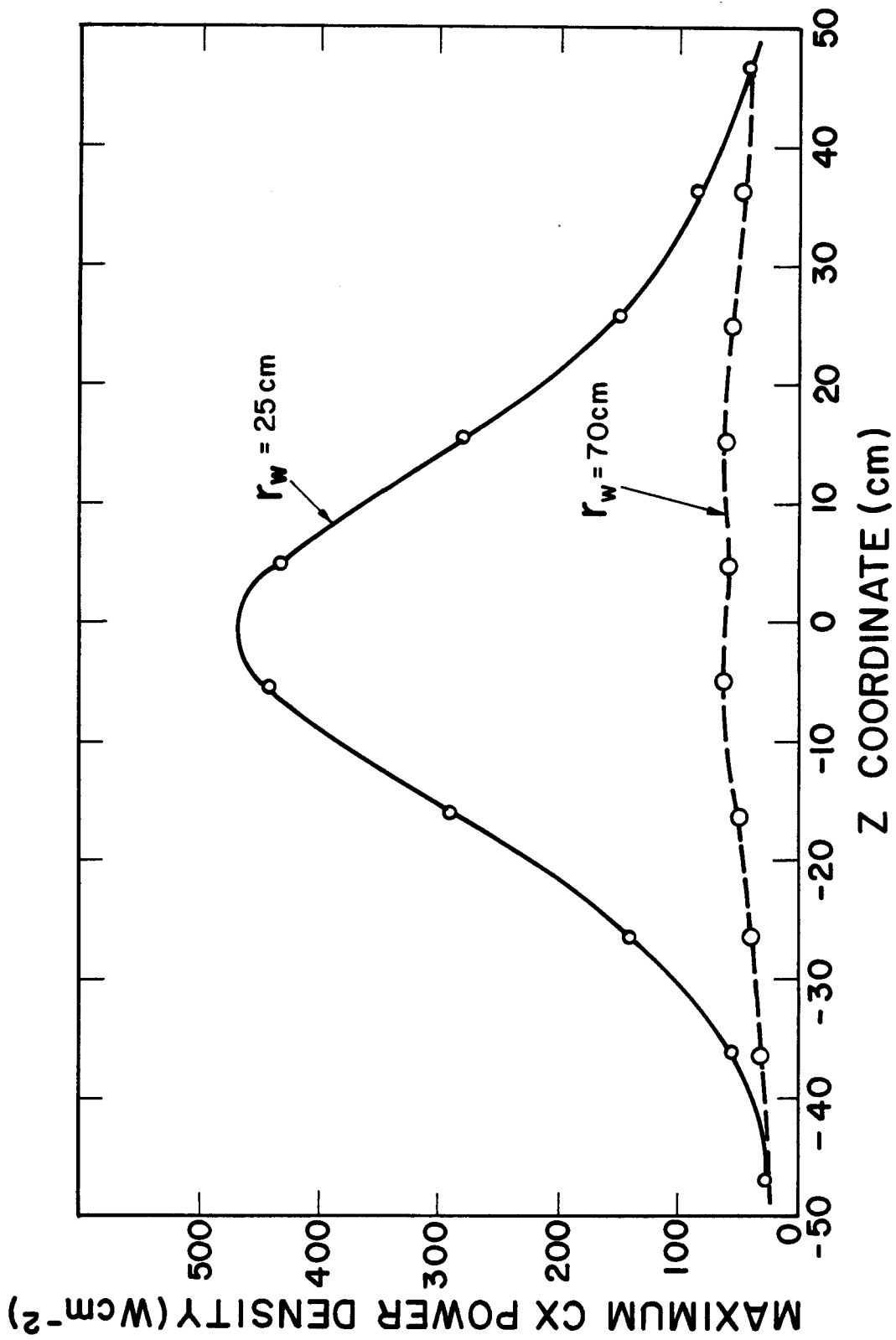
Fig. 6.2-5. Effect of the radius of the first wall on the axial distribution
of the maximum CX first wall heat flux for the high energy
central cell beams.

table value of ~ 65 W cm^{-2} for $r_w = 70$. Note also that this reduction in heat flux with increasing radii is considerably greater than the $1/r_w$ scaling which would be expected from a line source emission. This is due to the distributed nature of the CX emission across the volume of the plasma. Given the problems of integrating high heat flux surfaces at the first wall, it was felt that this latter peak heat load of less than 70 W cm^{-2} was a reasonable design goal. Accordingly, a recessed first wall of 70 cm was specified in the vicinity of the beam interaction region.

6.2.3.7 Conclusions on CX Heat Fluxes. In conclusion, we have seen that first wall CX heat fluxes from neutral beam injection in TASKA-M can attain peak values of several hundred W cm^{-2}. The angular distributions can be forward or backward peaked, relative to the incident beam direction, depending on the characteristic parameters of the beam/plasma system. For the final system design parameters, fluxes tend to be backward peaked. Accurate characterization by Monte Carlo methods of the heat flux distributions, both azimuthally and axially, is important for the prediction of hot spots on the first wall surface. One effective method of reducing the peak power densities at the first wall is to recess the first wall in the vicinity of the beam interaction region and taper it back to the original dimensions at axial coordinates where CX loads have fallen to acceptable levels. In view of the fact that space is usually at a premium at the first wall of any fusion device, further work is needed in developing sophisticated high heat flux surfaces with compact dimensions for incorporation in regions such as these.

References for Section 6.2.3

4. L.J. Perkins, "Monte Carlo Studies of Charge-Exchange First Wall Heat Fluxes from Neutral Beam Injection in Tandem Mirror Reactors," submitted to J. Fusion Energy (1983).

5. G.A. Carlson and G.W. Hamilton, "Wall Bombardment Due to the Charge Exchange of Injected Neutrals with a Fusion Plasma," in Proc. of First Top. Mtg. on the Technology of Controlled Nuclear Fusion, San Diego, CA (April 1974).

6. T.H. Batzer et al., "Conceptual Design of a Mirror Reactor for a Fusion Engineering Research Facility (FERF)," Lawrence Livermore National Laboratory, UCRL-51617 (1974).

7. J. Hovingh and R.W. Moir, "Efficiency of Injection of High Energy Neutral Beams into Thermonuclear Reactors," Lawrence Livermore National Laboratory, UCRL-51419 (1973).

8. R.L. Miller, "Monte Carlo Simulation of Neutral Beam Injection for Mirror Fusion Reactors," Ph.D. Thesis, University of Illinois (1979).

9. M.H. Hughes and D.E. Post, "A Monte Carlo Algorithm for Calculating Neutral Gas Transport in Plasmas," J. Computational Physics 28, 43 (1978).

10. T.B. Kaiser, Magnetic Fusion Energy Quarterly Report, October-December 1977, Lawrence Livermore National Laboratory, UCRL-50551-77-4 (1978).

11. R.L. Freeman and E.M. Jones, "Atomic Collision Process in Plasma Physics Experiments," United Kingdom Atomic Energy Authority-Culham Laboratory, CLM-R 137 (1974).

12. Joint European Torus (JET) Annual Report, January-December 1981, JET Joint Undertaking, Culham, UK (1982).

13. R.R. Stone, Lawrence Livermore National Laboratory, private communication (1981).

14. C.C. Baker et al., "STARFIRE - A Commercial Tokamak Fusion Power Plant Study," Argonne National Laboratory, ANL/FPP-80-1 (1980).

6.2.4   Neutral Beam Vacuum System (Fig. 6.2-6)

6.2.4.1 Overview

In order to limit beam losses due (Fig. 6.2-7) to reionization and scattering, the gas density in the neutral beam boxes and neutral beam ducts must be kept at a very low pressure. The operating pressure will be in the range of several 10^{-4} mbar in the neutralizer region and approx. 2×10^{-5} mbar in the duct.

The vacuum system of the neutral beam injectors and the neutral beam ducts is composed of cryopumps, Roots pumps or rotating plunger pumps, and turbomolecular pumps, plus control and isolation valves. Fig. 6.2-8 shows a neutral beam injector with the ion sources, neutralizer, ion sweep magnet, ion dump, calorimeter target diagnostics, and collimators. With the exception of the ion sources and the ion dump, all parts are installed in a rack located inside the neutral beam box. The ion sources and the ion dump are mounted separately from the back of the box. In order to reduce the dose rate outside the box, which originates from neutron activated parts inside, the neutral beam injector is shielded. Magnetic shielding of the box will be necessary due to stray fields. The amount of shielding is estimated in chapter 9.4.

The neutral beam injector is subdivided into three vacuum regions (see Fig. 6.2-9):   .

- Stage 1 contains the ion source, accelerator, neutralizer, sweep magnet, and ion dump.

- The calorimetric target is located in stage 2.
  Stages 1 and 2 are separated by a sheet metal wall with openings for the neutral beams.

- Stage 3 is formed by the beam duct connecting the box and the plasma chamber.
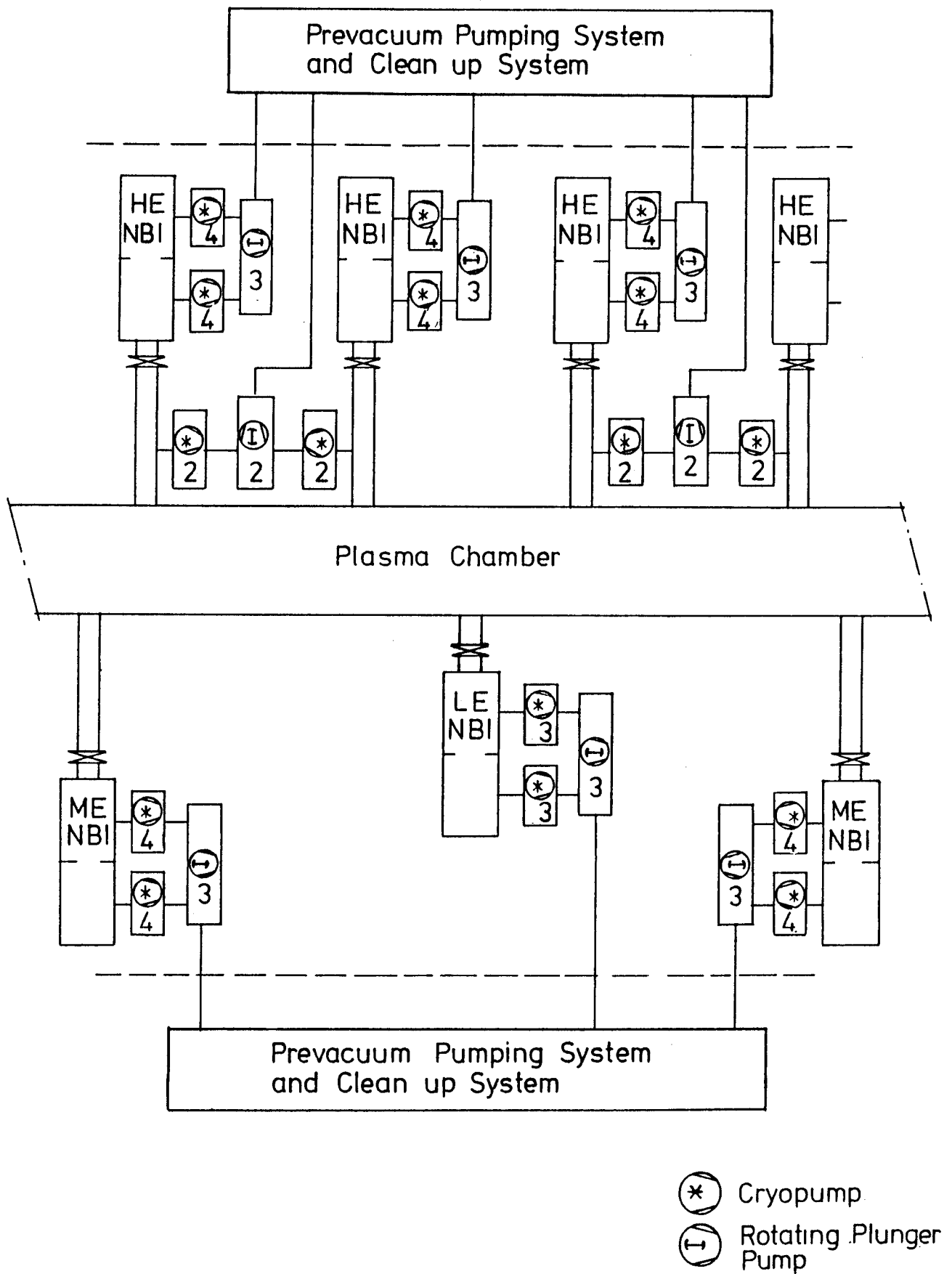
Fig. 6.2-6 General NBI Vacuum System
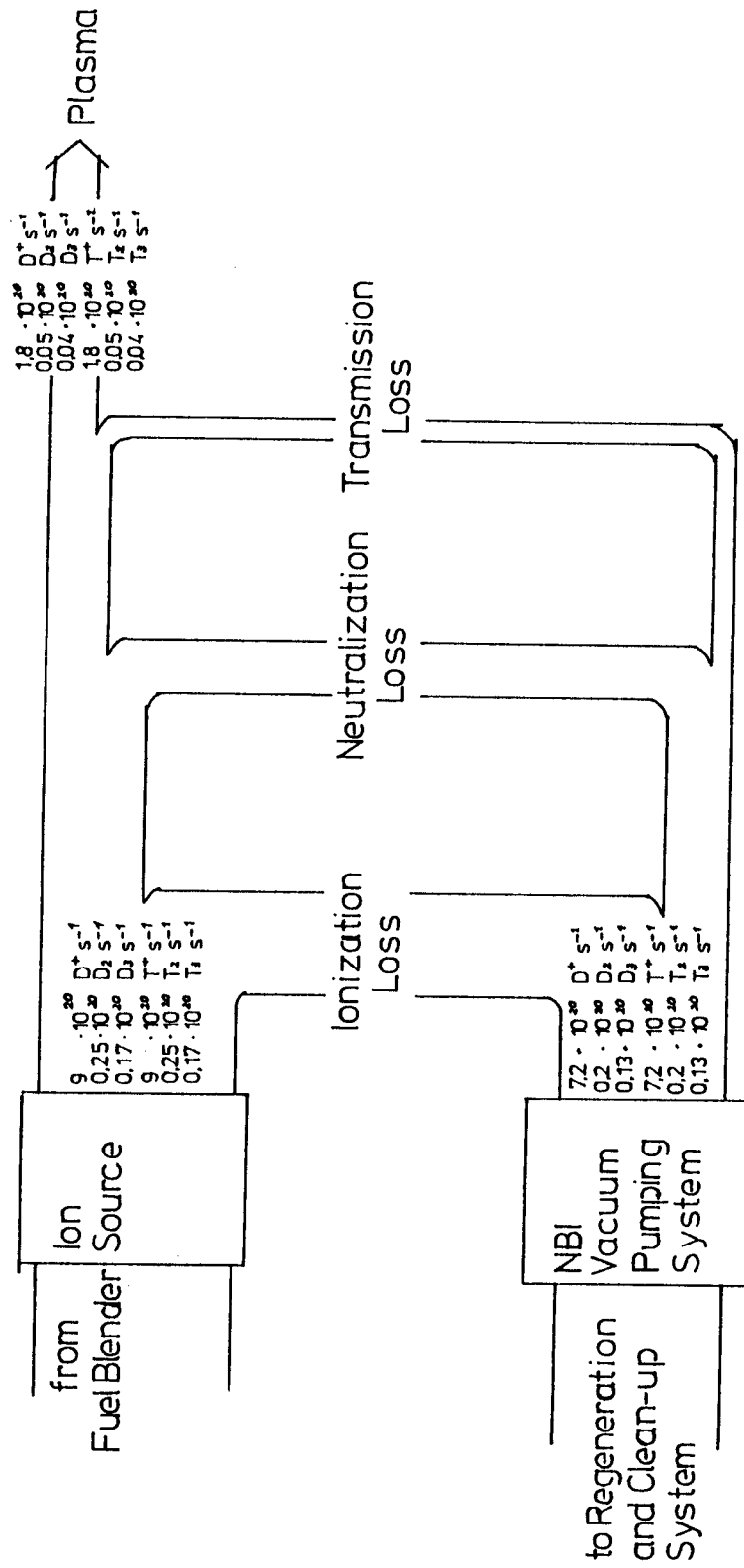
Fig 6.2-7   Gas Molecule Flow in the HE-NBI
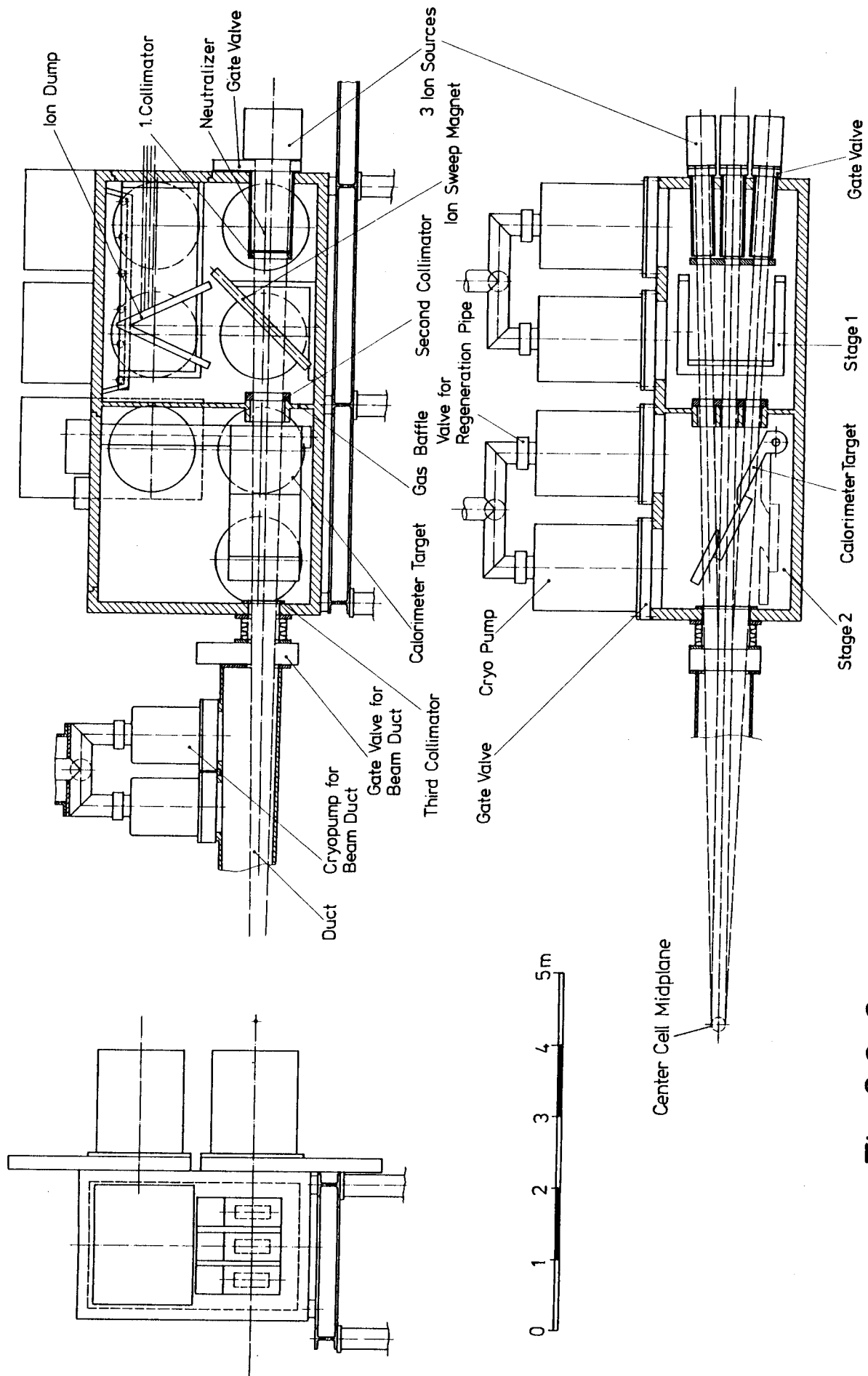
Fig. 6.2-8 HE-NEUTRAL BEAM INJECTOR

Ion Dump
1. Collimator
Neutralizer
Gate Valve
3 Ion Sources
Ion Sweep Magnet
Second Collimator
Gas Baffle
Valve for
Regeneration Pipe
Calorimeter Target
Gate Valve for
Beam Duct
Third Collimator
Cryopump for
Beam Duct
Duct
Gate Valve
Cryo Pump
Stage 1
Stage 2
Calorimeter Target
Gate Valve
Center Cell Midplane

0 1 2 3 4 5m
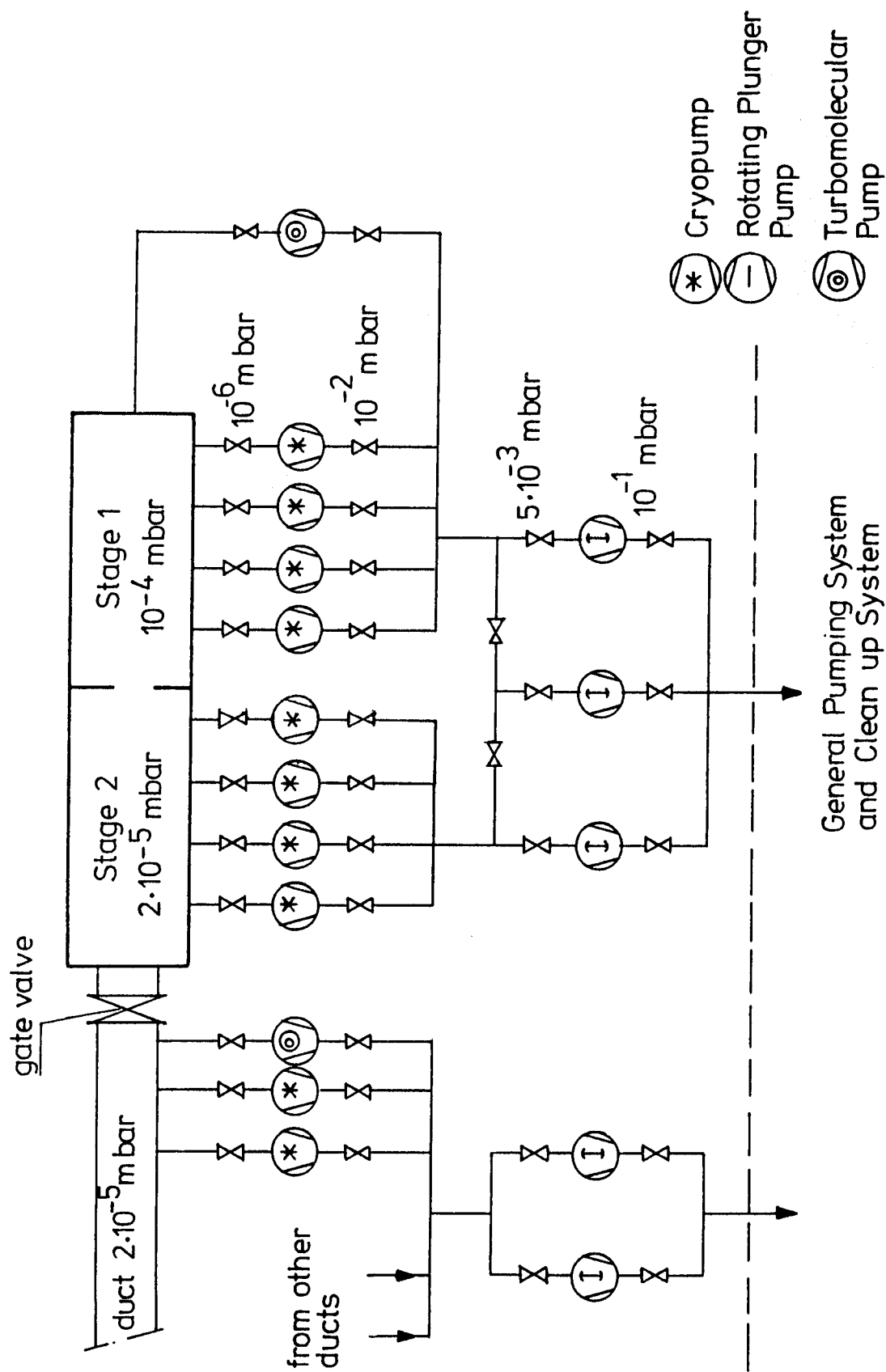
Fig. 6.2-9 NBI-Vacuum System (HE – NBI)

The injector box and the beam duct can be shut vacuumtight by means of a gate valve. In this way, the injector box can be disconnected without breaking the vacuum in the box and the plasma chamber / beam duct unit.

The ion sources can be exchanged individually after separation from the injector box by means of gate valves.

The neutral beam injectors must be designed for steady state operation. Excess gas can be removed from the injector box to achieve a low gas pressure, as mentioned above, either by Zr-Al getter panels /15/ or by liquid He cryopanels. Getter panels have the advantages of being insensitive to thermal variations, releasing no gases, and of being less sensitive to neutron bombardment. Their operating temperature is 670 K, the regeneration temperature 970 K /2/. On the other hand, the gettering surface is approximately 1.5 to 2 times larger than the cryopump surface, which makes it necessary to set up the getter panels inside the box while the cryopumps /16/ are located outside and can be separated from the box by gate valves /17/. These valves will be closed during the regeneration of a cryopump. As opposed to the operation / regeneration separation mechanism at the getter panels /2/ the gate valve closes very tightly. Consequently, the regeneration pressure can be kept at a higher level of approx. 10^{-3} mbar, thus simplifying the regeneration system for the cryopumps. Furthermore, getter panels are sensitive to poisoning by oxygen, especially at higher temperatures. Oxidation is irreversible. However, poisoning cannot be excluded, and since the capital costs of the getter panels ($ 3 million) and the cryopump system ($ 3.5 million) are in the same range, an exchange of the panels would double their original capital costs. The operating costs are higher for cryopumps due to the consumption of liquid He at 4 K. Nevertheless, after comparing the pros and cons, we selected cryopumps as the reference case. For the data, see Table 6.2-3.

Table 6.2-3   Vacuum System Parameters for Neutral Beam Injectors
              at the Sources

		HE-NBI	ME-NBI	LE-NBI	Remarks
Location		Central Cell	Anchor	Central Cell	
P_e / NBI	MW	12.6	8.4	1.0	
E	keV	90	73	12	
Gas flow Torr·l/s					
Stage 1		38,6	31,1	18,0	
Stage 2		6,0	5,6	} 6,8	
Duct		2,5	2,1		
Vacuum pressure mbar					
Stage 1		10^{-4}	10^{-4}	10^{-4}	
Stage 2		2×10^{-5}	2×10^{-5}	2×10^{-5}	
Duct		2×10^{-5}	2×10^{-5}	2×10^{-5}	
Cryopumps					
Stage 1	number	3(+1)	3(+1)	2(+1)	() for regeneration
	Pumping speed l/s	1.5×10^5	1.5×10^5	1.2×10^5	
Stage 2	number	3(+1)	3(+1)	2(+1)	() for regeneration
	Pumping speed l/s	1.5×10^5	1.5×10^5	1.5×10^5	
Duct	number	1(+1)			with stage 2
	Pumping speed l/s	1.5×10^5			

6.2.4.2 High Energy Neutral Beam Injectors (HE-NBI)

Stage 1 of the HE-NBI's is equipped with four cryopumps, each with a pumping capacity of 150,000 l/s. Three of them will be in operation while one will be regenerated. Stage 2 is identical to stage 1. Both cryopumps of the beam duct have pumping capacities of 80,000 l/s and operate alternately.

6.2.4.3 Medium Energy Neutral Beam Injectors (ME-NBI)

Stages 1 and 2 of the ME-NBI's are equipped with four and three cryopumps respectively, each of 150,000 l/s pumping capacity. Three and two pumps, respectively, each will be in action while the third one will be regenerated. The beam duct is very short and is pumped by the anchor vacuum chamber.

6.2.4.4 Low Energy Neutral Beam Injector (LE-NBI)

The vacuum system of stage 1 consists of three cryopumps, each with a pumping capacity of 120,000 l/s; two of the pumps operate while the third one is regenerated. Due to the dimensions of the beam duct its flow resistance is small. Thus, it was possible to combine its vacuum system with that of stage 2. The two cryopumps, each with a pumping capacity of 150,000 l/s, are operated alternately.

6.2.4.5 Regeneration System

The main fraction of the pumped gases will be hydrogen isotopes. This
allows the regeneration system to be simplified. To release the hydrogen
gas it is sufficient to warm up the liquid-helium cooled pumping surfaces
from 4 K to 30 K. Roots pumps and / or rotating plunger pumps can be used
to pump the gas released. These pumps allow an ultimate pressure of 10^{-3}
mbar to be attained. The operating pressure of the cryopumps, approx.
10^{-6} mbar, will be achieved by cooling the pumps to their operating
temperatures. By this means the loading of the cryosurfaces is negligible.

In order to evacuate each NBI after breaking the vacuum, they are equiped
with an additional turbomolecular pump. The ultimate pressure of this pump
will be approximately 10^{-5} mbar in the NBI-box.

These pumps provide the following advantages:

-   The cryopumps will not be contaminated by impurities
    which cannot be removed at regeneration
    temperatures of 30 K.

-   Therefore, the surfaces of the cryopumps are almost
    free from oxygen molecules which would react with
    tritium and hydrogen to form HTO.

-   Helium penetrating into the ducts by backstreaming,
    which is not pumped by LHe-cryopumps can be removed
    by means of the turbomolecular pumps.

References for Section 6.2.4

1. "Status of Tandem Mirror Confinement", D. E. Baldwin and the TMX-U Group, UCRL 89771, Aug. 30. 1983.

2. "TASKA-Tandem Spiegelmaschine Karlsruhe, a Tandem Mirror Fusion Engineering Test Facility", TASKA-Team, KfK 3311/1 UWFDM-500, June 1982, pp. 223-234.

3. "Development of an Ion Source for Long-Pulse (30 sec) Neutral Beam Injection" Menon et al. Proc. of the 12th Symp. on Fusion Technology, Aachen 1982, p. 1375.

4. L. J. Perkins, "Monte Carlo Studies of Charge-Exchange First Wall Heat Fluxes from Neutral Beam Injection in Tandem Mirror Reactors", submitted to J. Fusion Energy (1983).

5. G. A. Carlson and G. W. Hamilton, "Wall Bombardment Due to the Charge Exchange of Injected Neutrals with a Fusion Plasma" in Proc. of First Top. Mtg. on the Technology of Controlled Nuclear Fusion, San Diego, CA, (April 1974).

6. T. H. Batzer et al., "Conceptual Design of a Mirror Reactor for a Fusion Engineering Research Facility (FERF)", Lawrence Livermore National Laboratory, UCRL-51617 (1974).

7. J. Hovingh and R. W. Moir, "Efficiency of Injection of High Energy Neutral Beams into Thermonuclear Reactors", Lawrence Livermore National Laboratory, UCRL-51419 (1973).

8. R. L. Miller, "Monte Carlo Simulation of Neutral Beam Injection for Mirror Fusion Reactors", Ph. D. Thesis, University of Illinois (1979).

9. M. H. Hughes and D. E. Post, "A Monte Carlo Algorithm for Calculating Neutral Gas Transport in Plasma", J. Computational Physics $\underline{28}$, 43 (1978).

10. T. B. Kaiser, "Magnetic Fusion Energy Quarterly Report", Oct.-Dec. 1977, Lawrence Livermore National Laboratory, UCRL-50551-77-4 (1978).

11. R. L. Freeman and E. M. Jones, "Atomic Collision Process in Plasma Physics Experiments", United Kingdom Atomic Energy Authority-Culham Laboratory, CLM-R 137 (1974).

12. Joint European Torus (JET) Annual Report, January-December 1981, JET Joint Undertaking, Culham, UK (1982).

13. R. R. Stone, Lawrence Livermore National Laboratory, private communication (1981).

14. C. C. Baker et al., "STARFIRE - A Commercial Tokamak Fusion Power Plant Study", Argonne National Laboratory, ANL/FPP-80-1 (1980).

15. Zr-Al Getter Panels (86 % Zr, 14 % Al); Trade Name St101, manufactured by S.A.E.S. Getters S.p.A., Via Gallarate 215, 20151 Milan, Italy.

16. Leybold-Heraeus GmbH & Co KG, Köln; Badkryopumpe NW 1200, Zeichnung 931 20 006.0, Kryopumpe für quasi-kontinuierlichen Plasmabeschleuniger, U. Bieger, H. Tuczek, KFA Jülich; H.-J. Forth, Leybold-Heraeus; Vakuum-Technik, Heft 1/2 (1970).

17. J. Vetrovec, "TDF unpublished report", TRW-Energy Development Group, One Space Park, Redondo Beach, CA 90278 (1983).

6.3 Electron Heating in TASKA-M

6.3.1 Introduction

Additional electron heating power is advantageous in the TASKA-M tandem mirror to decrease the electron drag on the ions which substantially lowers the required neutral beam power, and to increase the electron temperature which enhances the midplane potential dip. This dip traps warm ions which stabilizes the loss cone distribution caused by the injected ions in a mirror configuration. In conclusion, electron heating provides substantial improvement in overall machine power requirements and microstability properties as discussed in Sections 3.1-3.4 and 3.6 of the report.

The methods for direct radiofrequency heating of electrons in mirror plasmas include: (1) electron cyclotron heating (ECRH), $\omega \approx \omega_{ce}$; (2) electron Landau and transit-time damping via the ion cyclotron range of frequencies (ICRF), $\omega \lesssim 4 \omega_{ci}$; and (3) electron Landau damping of lower hybrid waves (LHRF), $\omega \gtrsim \omega_{LH}$. Of these three, electron cyclotron heating is usually the most direct for tandem mirrors but the overdense ($\omega_{pe}/\omega_{ce} > 1$) high $\beta \simeq 50\%$ properties of TASKA-M which yield high fusion output make this wave's penetration problem for heating in the central cell quite difficult. The ion cyclotron frequency range waves require elevated electron temperatures ($T_e \gtrsim 2$ keV) and the absence of ion resonances at substantial concentrations $\omega \neq n\omega_{ci}(\bar{r})$ in the regions of substantial wave power flux where $\bar{r}$ denotes the spatial position where a harmonic resonance could be present in the plasma interior. In addition, below the fundamental resonances, low frequency coil excitation is required and substantial plasma cross sections given by $\bar{n}a^2$ (where $\bar{n}$ is the average plasma density and a is the plasma radius) as required for good coupling and is well satisfied in the central cell of the TASKA-M device. Finally, lower hybrid waves can heat electrons or provide current drive via electrons as observed in tokamaks. Although the electron heating results were moderately successful, the problem of wave spectrum and penetration with substantial Landau damping through the plasma edge at the elevated electron temperatures ($T_e \simeq 14$ keV) of TASKA-M are presumed to eliminate it from serious consideration for the purpose of this design study.

This section on electron heating of the plasma will concentrate primarily on the ion cyclotron frequency range method for heating electrons with a brief

mention of electron cyclotron frequency heating in the accessible lower density, low β transition region.

6.3.2 Electron Heating Physics

6.3.2.1 Electron Cyclotron Resonance Heating (ECRH)

The formulation of wave coupling, propagation, and absorption are presented in this section. We start with the rationales for choosing the various heating zones in the machine. The relevant assumed plasma operating parameters are shown in Table 6.3-1.

A 6 cm central cell annular halo plasma is required between the hot plasma edge and the walls (see Section 3.8). In addition, power balance calculations show an electron heating power required to achieve the steady state operating characteristics of 12.4 MW. Figure 6.3-1 illustrates the overall potential (ϕ) and magnetic field (B) structure on the axis which can be used to visualize the electron heating regions.

The previous table indicates that the central cell beta corrected steady-state electron cyclotron frequency is 83 GHz with a $\omega_{pe}/\omega_{ce}(\beta_0)$ value equal to 1.8. This means that steady-state gyrotron sources of 83 GHz with a single tube power output of 250 kW for a 12.4 MW total would require at least 50 gyrotrons. These sources are not currently available but may become available in a period of five to ten years. It should also be noted that this is a central cell minimum frequency and that non-β corrected cyclotron resonance such as for startup would require tubes at a frequency of 117 GHz, clearly well above the near term state of the art. In addition, even if the gyrotron sources were available, $\omega_{pe}/\omega_{ce}(\beta_0)$ values are near 1.8 for the high β TASKA-M central cell parameters. As discussed by Audenaerde and Scharer[1] and others, overdense plasmas such as this are very difficult to penetrate with electron cyclotron wave power due to wave cutoff effects for oblique launching angles. Even for nearly axial propagation relative to the magnetic field, recent work by Lam, Scharer and Audenaerde[2] has shown that for overdense mirror plasmas, electron cyclotron wave energy can diverge radially before reaching cyclotron resonance regions due to radial density gradients. Thus we do not support the use of electron cyclotron central cell heating for the overdense TASKA-M parameters based on near-term technological requirements and wave penetration problems.

Table 6.3-1. TASKA-M - Plasma Parameters for RF Heating

Parameter	Central Cell	Transition	Anchor
B_{min} (T)	4.2	2.18	1.02
B_{max} (T)	17.5	(17.5, 2.7)	2.7
n_e (cm^{-3})	3.5×10^{14}	2.6×10^{13}	2.6×10^{13}
T_e (keV)	14.0	14.0	14.0
$\bar{E}_i$ (keV)	84.1	7.3	60.3
r_p (cm)	12.1	$(17.7)_{eff}$	$(24.4)_{eff}$
r_W (cm)	25	$(36)_{eff}$	37
β	0.5	0.05	0.5
$f_{ce}(\beta_0)$ (GHz)	83	56	20
$\omega_{pe}/\omega_{ce}(\beta_0)$	1.8	0.83	2.33
$f_{cT}(\beta_0)$ (MHz)	15 (z = 0)	10	no tritium
	15 (z = 1 m)		
	35 (z = 2.2 m)		

The use of electron cyclotron heating in the anchor region is also not desirable since the plasma is even more overdense; $\omega_{pe}/\omega_{ce}(\beta_0)$ = 2.33 in this region. The steady-state cyclotron frequency is 20 GHz in this region allowing the use of high power steady-state klystrons which are currently available at up to 500 kW levels. The near axial wave launching access in the anchor region is improved near the ends of the machine. However, questions about good electron heat flow from the anchor to the central cell region given the complex magnetic and potential structure of TASKA-M and the diverging of axially launched electron cyclotron wave energy before reaching the resonance zone in overdense plasmas make this alternative much less than ideal.

Finally, the transition region for electron heating is the most desirable if this scheme is used. As shown on the table, β-corrected cyclotron frequencies of 56 GHz are required. The plasma is not overdense even at the lowest field point of 2.2 T. Oblique propagation of the X mode in this region will allow good wave penetration and absorption. However, the lack of steady-state 1 MW or 250 kW gyrotrons operating at 56 GHz required to make this scheme attractive for a near-term technology device makes this approach

Fig. 6.3-1

TASKA-M COIL CONFIGURATION, POTENTIAL AND MAGNETIC FIELD
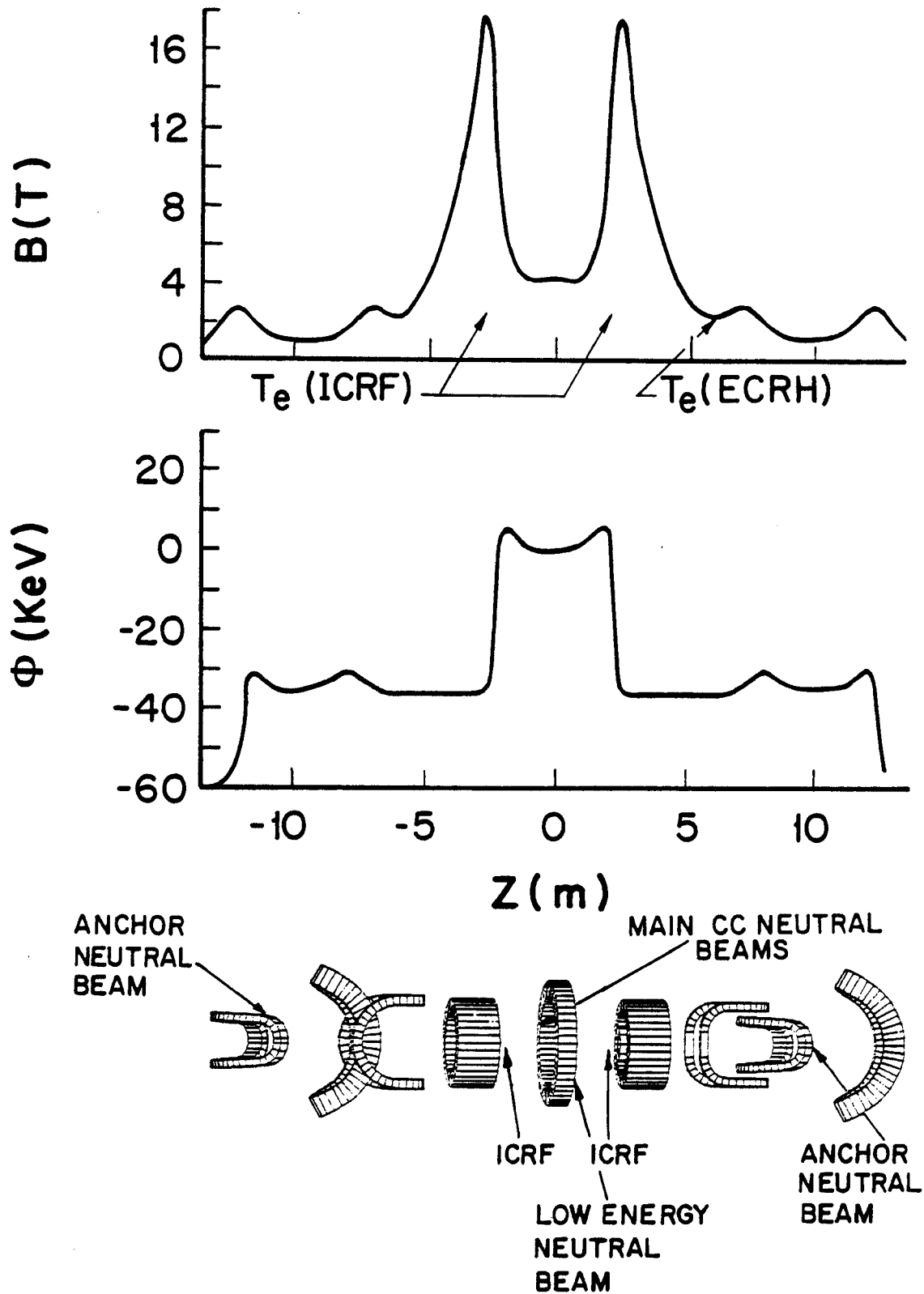
questionable. In addition, physics questions about electron trapping near the transition minimum, electron heat transport to the central cell and velocity space considerations must be analyzed before it can seriously be proposed for the longer term future.

6.3.3 Electron Heating in the Ion Cyclotron Range of Frequencies (ICRF)

The most successful radiofrequency heating experiments for plasmas to date have been primarily in tokamaks in the ion cyclotron frequency range. On the PLT tokamak Hwang et al.[3] have coupled 3.4 MW for several hundred milli- seconds at densities of 3 x 10^{13} cm^{-3} with a 2 keV ion temperature rise and a similar electron heating primarily due to electron drag on the fast ion tail. Wave coupling efficiencies $\nu_C = P_C/P_G = 80\%$ have been achieved with heating efficiencies P_H/P_C of about 60% ($P_H = \Delta(nkT_i)/\tau_\epsilon$) at the second hydrogen ion cyclotron harmonic $f = 2 f_{CH} = 42$ MHz corresponding to resonance at the center of the machine. On the TFR tokamak[4] substantial direct electron heating, $\Delta T_e = 1$ keV, has been observed for a hydrogen/deuterium plasma with densities of $n = 1.5$ x 10^{14} cm^{-3} at RF power levels of 600 kW. The heating process is attributed to mode conversion from the fast magnetosonic wave propagating on the high field side to an ion Bernstein mode which is rapidly electron Landau damped. It should also be mentioned that electron heat transport in tokamaks is highly anomalous and sensitive to machine conditions. This condition re- quires a careful experiment to test direct electron heating via ICRF. Other experiments utilizing Landau damping on electrons from lower hybrid waves have been observed on tokamaks to heat electrons such as JFT-2 (1981). Today's current drive experiments have shown promising results involving an inter- action with fast electrons. Also surface wave excitation by ICRF antennas has been shown to directly heat electrons on the Phaedrus[5] tandem mirror and other tokamak experiments.

In the theoretical area electron Landau and transit-time heating via ICRF has been studied by Stix,[6,7] by Scharer, McVey and Mau[8] and by Scharer, Beyer, Blackfield and Mau[9] for a tokamak reactor. The basic result for power absorption per unit volume can be expressed as

$$P_e = \frac{\pi^{1/2} \epsilon_o (\omega_{pe}/\omega_{ce})^2 v_e \omega^2 \tilde{B}_z e^{-(\omega/k_\parallel v_e)^2}}{4 k_\parallel} \qquad \frac{watts}{cm^3} \qquad (6.3\text{-}1)$$

where $\tilde{B}_z$ is the wave magnetic field parallel to the static field and the other plasma quantities take their usual definition. The spatial wave absorption can be obtained approximately from the wave quality factor with the electron absorption treated as a wave cavity loss term, Q_{erf},

$$Q_{erf} = \frac{\omega_r}{\omega_i} = \frac{\omega U_S}{P_e} = \frac{\omega \omega_{ce}^2}{\pi^{1/2} V_A^2} \frac{4k_\parallel e^1}{2\mu_o \varepsilon_o \omega_{pe}^2 k_\perp^2 v_e} \tag{6.3-2}$$

where U_S is the time averaged fast wave energy density, V_A is the Alfvén velocity and $\omega \simeq k_\parallel v_e$ is assumed. Thus, the axial damping decrement for TASKA-M steady-state parameters becomes

$$L_e \text{ (damping decrement)} = \frac{1}{k_i} = k_\parallel Q_{erf} = 10\text{-}20 \text{ cm} \tag{6.3-3}$$

with the wave strongly damped and an electron heat distribution over a large volume and velocity class due to the launched $k_\parallel$ spectrum.

The antennas used to couple the waves require a moderate density and lower temperature to ensure wave propagation over most of the transverse cross section and to isolate the antennas from the hot ion core. We, therefore, propose a 10 cm annulus halo with $\langle n \rangle = 5 \times 10^{12}$ cm^{-3} determined by the $n_\parallel^2 = R$ cutoff condition for the fast wave and $T_{edge} \lesssim 100$ eV. The general density for cutoff for the fast wave can be expressed as

$$n_{DT}\big|_{cutoff} = 1.3 \times 10^{11} k_\parallel^2 \frac{(\omega + \omega_{ci})}{\omega} \tag{6.3-4}$$

where $k_\parallel$ corresponds to the dominant part of the $k_\parallel$ spectrum, ω is the frequency of the ICRF wave and ω_{ci} is the ion cyclotron frequency.

The density and total plasma radius ($n_c r_p^2$) of the central cell for TASKA-M make the radial mode structure very good for efficient fast magnetosonic wave coupling from antennas. There are many perpendicular wavelengths over the hot plasma core plus halo plasma such that

$$k_\perp^F r_p = (\omega/V_A) r_p \geqslant 10\text{-}20 \tag{6.3-5}$$

even for frequencies below the minimum tritium resonance.

For the TASKA-M device, to ensure that the ICRF power flow is primarily to the electrons, we have to ensure that the ion resonances for deuterium and tritium as well as any <u>substantial</u> ion impurities are not present in the vicinity of the antenna and RF power flow region. In addition, the electron temperature should be well elevated ($T_e \gtrsim 2$ keV) before the antenna excited parallel phase velocity for the fast magnetosonic wave is comparable to the parallel electron thermal velocity for substantial electron damping to occur. We expect that electron-electron and electron-ion collisions over the length of TASKA-M at higher density will rapidly isotropize the electron distribution. At lower electron temperatures such as is the case for startup, ion resonances further from the antenna regions can be used to initially heat the plasma with electron absorption dominating at higher temperatures when the plasma reaches steady-state conditions. To ensure dominant electron heating, the wave frequency should be chosen below the beta-corrected tritium ion cyclotron resonance in regions of strong wave excitation $f_{cT}(\beta_0) = 15$ MHz.

One could also consider setting the wave frequency between lower ion cyclotron harmonic resonances (f = 25 MHz) for the deuterium-tritium plasma but the close spacing due to axial gradients in the central cell magnetic field makes this difficult to achieve without some ion heating. Some direct ion absorption at lower temperatures during startup could be quite beneficial. Even at the elevated temperatures of the full operating characteristic, the volumetric electron Landau and transit-time damping between the antennas could dominate over the axially localized heating near the ion resonance. If a 25 MHz design were used, a 0,π phasing for adjacent antennas would yield a desired spacing of $d_A(0,\pi) = \lambda_\parallel/2 = \pi v_e/\omega = 90$ cm. Another alternative is to operate at frequencies well above the lower beta-corrected, central cell (z = 0 $\rightarrow$ 2.2 m) ion cyclotron resonances where ion absorption is predicted to be very weak; $f \gtrsim 3\ f_{ci}(\beta) \simeq 200$ MHz. This higher frequency allows more versatility in wave launcher design in that antennae or waveguide launchers could be considered. However, no plasma experimental work in this range has been carried out.

It should also be mentioned that the transition region could also be considered for coupling and heating via these waves. However, the lower wave frequencies required for heating outside the central cell region and the non-

circular cross section of the plasma makes this alternative less desirable for wave coupling and heating than in the central cell.

Thus we propose to excite fast magnetosonic waves below the beta corrected tritium cyclotron resonance $f \lesssim f_{cT}(\beta)$ as a base case or well above the lower ion cyclotron resonances $f \gtrsim 3 f_{cD}(\beta)$ in the region where the antennas are located as an option for electron heating in TASKA-M. The $k_{\parallel}$ spectrum of the antennae will also be used for fast wave mode selectivity in the lower frequency case.

6.3.4 ICRF Antenna Design for Electron Heating

We now consider the appropriate antenna design and layout for the TASKA-M device for the low frequency $f \lesssim f_{cT}(\beta)$ case. As noted in Section 6.3.2 a total electron heating input level of 12.4 MW is required. We consider a four coil set of antennas with an assumed coupling efficiency of 90% and a heating efficiency of 80% based on previous high power experiments in this frequency range on PLT[3] and TFR.[4] The total RF power output from the RF generators would then be 17.2 MW which can be produced with a source efficiency of about 80% requiring 21.5 MW from the D.C. high voltage power supplies. A single antenna would then be required to couple 3.9 MW to the plasma. This is surely somewhat above the current state of the art which is in the range of 0.75 MW coupled for the half-turn narrow antennas on PLT and TFR. However, improvements utilizing wider antennas with improved center feeds, feedthrough, and Faraday shield designs can be expected in the near future. New antenna designs for PLT, TFR, JET, Doublet III-D, and TFTR are being made at total powers up to 50 MW which can reasonably be expected to increase the current maximum antenna surface power flux by a factor of four. The PLT antennas which were end fed and not optimized have produced RF power fluxes of 0.5 kW/cm^2 whereas current lower hybrid launchers have reached 10 kW/cm^2. An antenna design flux of 2 kW/cm^2 is used for this study. Thus, a single antenna properly matched could theoretically couple

$$P/antenna = S \times \pi \times D \times W = 2 \ kW/cm^2 \times \pi \times 40 \ cm \times 25 \ cm = 6.3 \ MW \qquad (6.3-6)$$

where D is the antenna diameter and W is the antenna width. This is more than the TASKA-M coupled design value of 3.9 MW but it is recognized that this is clearly a maximum design. If near term experimental progress were not able to

reach this value then additional antennas could be installed in the central cell or transition zone to reach the 12.4 MW absorbed power level.

A water cooled 15 cm O.D. coax of low impedance Z_0 = 20 ohms is used to provide high power transfer from the generators to the antenna. If the voltage standing wave ratio (VSWR) in the section of the coax between the antenna and matching system were too high, then a larger 23 cm O.D. coax would have to be used to accommodate the higher voltages. To match the generator impedance to the antenna, a stub matching system located outside the one meter radius blanket and shield central cell section is proposed. Figures 6.3-2 and 6.3-3a show the overall antenna unit, coaxial feeds and matching generator unit. Water cooling of the copper and stainless steel coil is shown together with a low Z graphite or base water cooled metal Faraday shield. A neutron shielded vacuum window is shown in Fig. 6.3-2 with gas pressurization (perhaps SF_6 or a lower neutron activated gas) behind the window to reduce RF breakdown properties.

The cross section of the coil and shield would be 25 cm width by a maximum of 10 cm depth to keep the antenna well away from the indented machine walls. An axial cut in the blankets of about 35 cm by 10 cm depth is indicated to allow good magnetic flux coupling to the plasma with minimal reduction due to image currents in the walls. Figure 6.3-3b shows an alternative slot design which has been used for heating at 100 kW levels in the ICRF range by Shvets et al. at Kharkov on a stellarator which might be more compatible with the reactor situation than coils if it can be developed further. The simplicity of a gap excitation and flat large surface area excitation would be attractive if higher power operation without breakdown and more analysis of the coupling spectrum were carried out.

Finally, if a high frequency scheme, $f \simeq$ 200 MHz, were used then possible waveguide or compact adjacent cavity resonant systems could be envisioned to couple the power. However, only lower hybrid tokamak experiments with no experimental work and little detailed analysis of this scheme in the ICRF range have been done so that it is not considered in detail for the purpose of this design.

The wave frequency, antenna dimensions, axial location as well as their relative placement in regard to the plasma will affect the coupling and heating through the wave spectrum $(k_\perp, k_\parallel)$ generated. In the simplified analysis

RF PARTICLE
SHIELD DETAIL
GRAPHITE OR
COOLED
METAL

15

I

10   20   26 cm

PLASMA

HALO

A

A

10

H₂O   25   H₂O

SECTION A-A (cm)

GENERATOR

RF MATCH
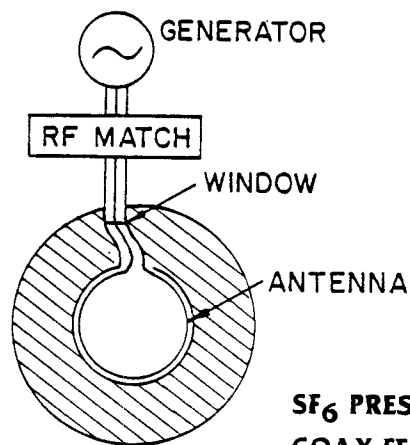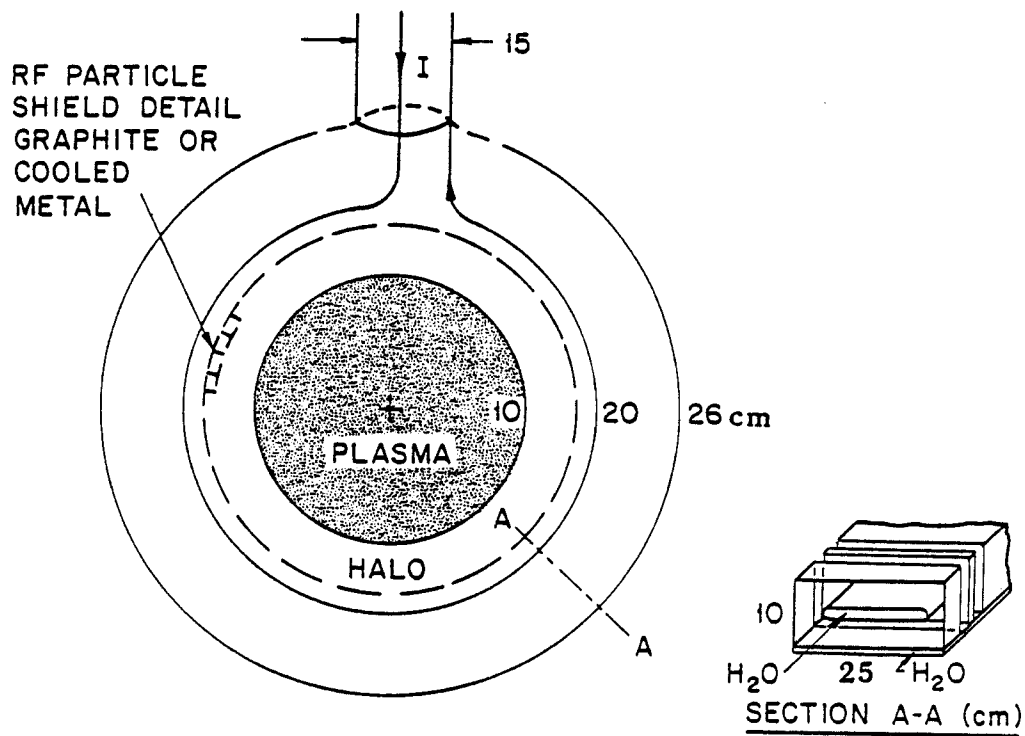
WINDOW

ANTENNA

SF₆ PRESSURIZED LOW IMPEDANCE
COAX FEED WITH OFFSET AND
WINDOW. EXTERNALLY MATCHED

Fig. 6.3-2   TASKA-M ICRF (T$_e$) antenna reference design for 15 MHz
          at 3.9 MW in plasma.
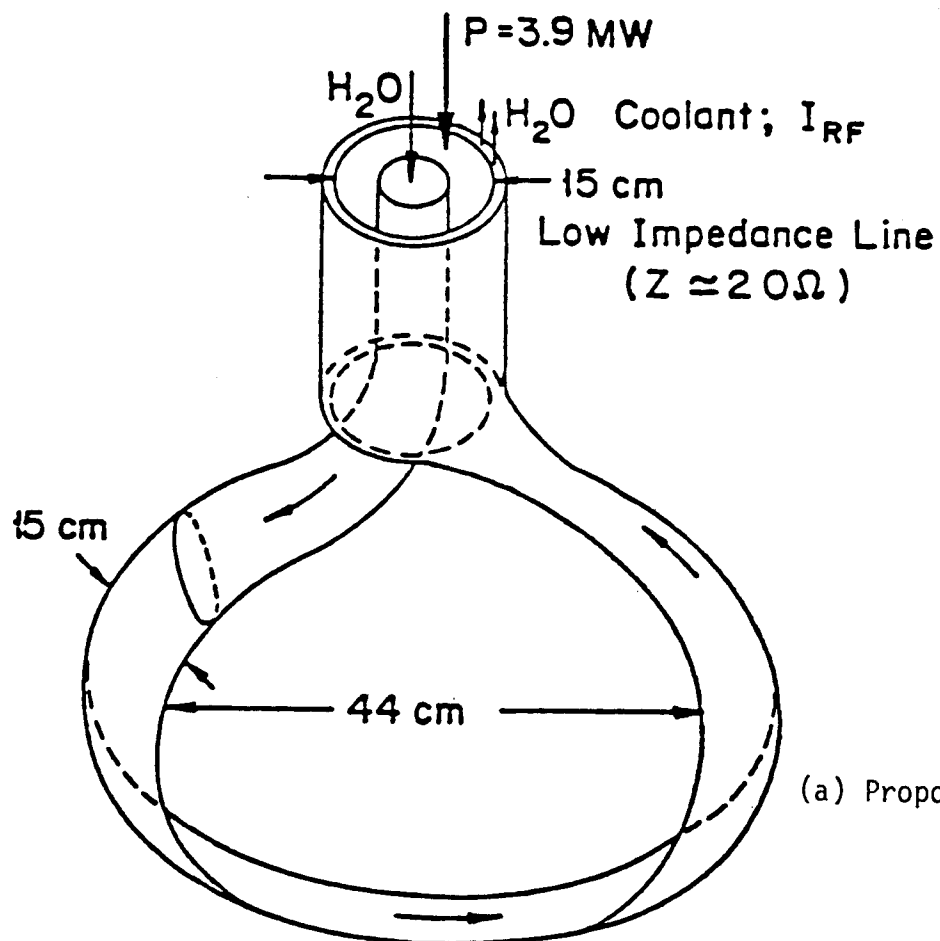
(a) Proposed Antenna Design
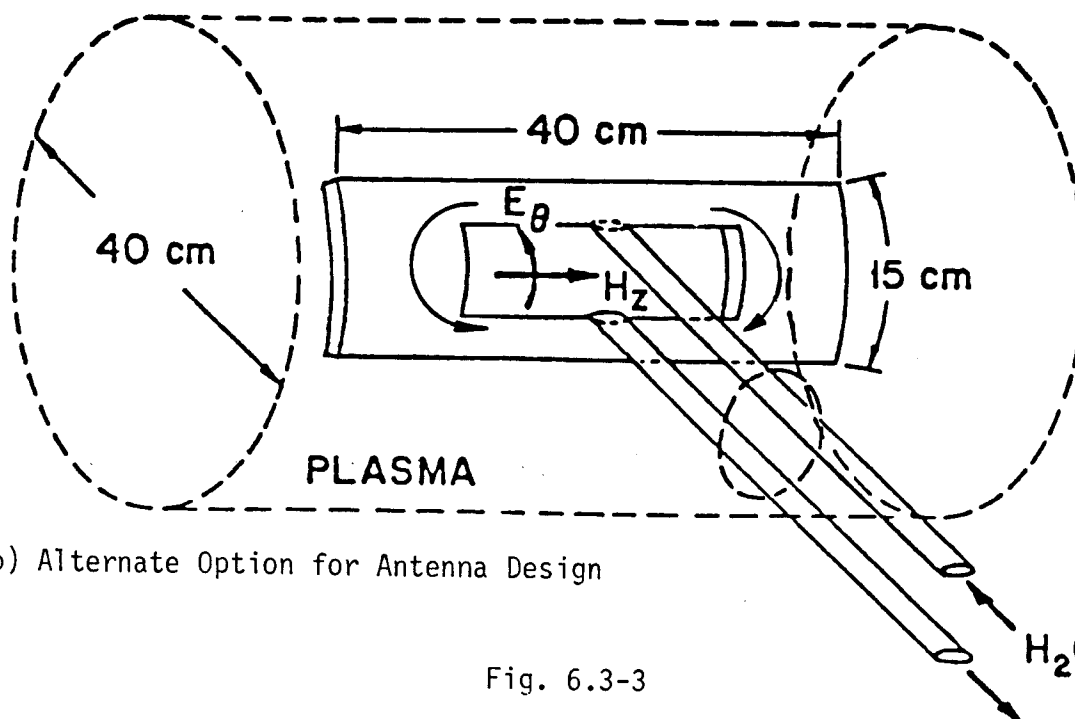
(b) Alternate Option for Antenna Design

Fig. 6.3-3

presented here, we determine the dominant part of the $k_\parallel$ spectrum through the antenna spacing and phasing so that the fast magnetosonic wave will be strongly damped at the steady state operating characteristics of TASKA-M, namely $T_e = 14$ keV. The convenient adjacent antenna coil spacing of 90 cm and operation at 15 MHz requires a $(0°,90°)$ phasing on the adjacent antenna drive to resonate with the bulk of the electron thermal distribution and Landau damp. This requires that the antenna spacing, d_A, be determined by the equation

$$d_A(0,90^0) = \lambda_\parallel/4 = \pi v_e/2\omega .$$ (6.3-7)

The frequency of the antenna is chosen as 15 MHz which is below the local tritium resonance near the $z = 1$ m location of the first antenna. This base design has an excitation frequency of 15 MHz, an antenna center-to-center spacing of 90 cm, a 0,90° adjacent phasing and a total power coupled of 15.5 MW.

It should be mentioned that the β-corrected magnetic field imposes a fairly low frequency of the generator $f = 15$ MHz to be below the tritium resonance. This has a detrimental effect on the antenna's radiation resistance for the moderate diameter of the TASKA-M plasma. Operation at a higher frequency would tend to improve the antenna coupling with attendant complications for power fraction coupled to the electrons and ions and would require a different antenna excitation scheme. The detailed antenna design shown in Fig. 6.3-3a would have to be modified to efficiently couple power to the electrons for the 200 MHz wave case. At these higher frequencies they could be well accomodated in the TASKA-M axial layout.

The placement of the ICRF antennas in the overall machine is shown in Fig. 6.3-4. The antenna center line placements are at $z = 1.2$ m and $z = 2.1$ m. This was done to keep the antennas away from the neutral beam charge exchange flux, beam path and dump. Each antenna location was chosen to lie within a single blanket module to allow for simpler removal and replacement.

Fig. 6.3-4: Placement of the ICRF antennas in the overall machine
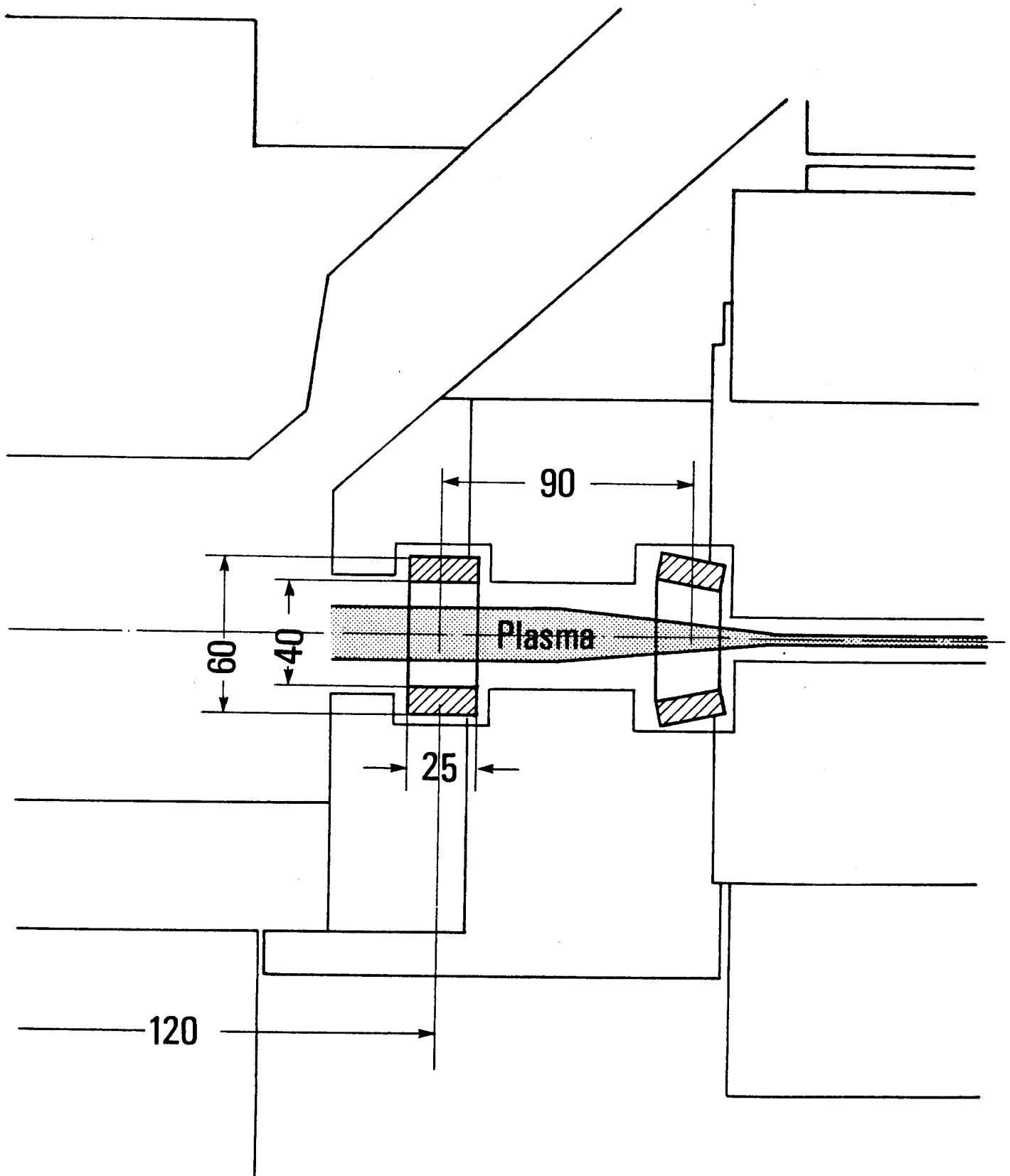
6.3.5 Power Generator for ICRF

After the experimental results obtained during the last 5 years on TFR /10/, PLT /11/ and JFT-2 /12/, heating in the ion cyclotron range of frequencies (ICRF) appears as one of the most powerful and reliable methods for plasma heating. The basic principles have been confirmed by experiment, good heating efficiency has been observed of both the ions and the electrons and the different damping mechanisms suggested by theory have been shown to apply in a wide range of density, temperature and magnetic field. On TFR, the rf power sources developed by European companies were operated in the power range between 1 and 2 MW. Each of the two output amplifiers includes a single Thomson CSF TH 518 power tetrode. Those tubes were capable of transmitting up to 1.5 MW RF power in pulses of 0.1 s duration in a broad range of frequencies (50 - 85 MHz).

High power, high energy ICRF experiments are presently in preparation for TEXTOR /13/, ASDEX /14/ and JET /15/. For TEXTOR, an RF power source capable of 3 s operation at 1.5 MW was satisfactorily developed at 27 MHz. For ASDEX, RF sources are under construction with 2 x 1.5 MW during 10 s between 30 - 115 MHz, and for JET, several units at 2 x 1.5 MW with long pulse capability ($\simeq$ 20 s) in the frequency range of 25 to 55 MHz. Consequently, the state of the art in high power generator technology in the frequency range of 25 to 90 MHz allows an RF power of about 1.5 MW per tube.

The cost of ICRF generators should be rated at about 0.3 \$ per Watt. The total cost per Watt of complete and fully automated ICRF systems (lines, generator, power supplies, control) should still be considerably higher (1 to 2 \$/Watt), but much lower than other RF heating schemes.

As far as area requirements are concerned, it can be noted that the two 1.5 MW-3 s units for TEXTOR, comprising the various amplifier stages, the control units and the cooling aggregates, are housed in two cells measuring 3.6 m x 4.2 m x 8.5 m each. A floor area of about 3000 m^2 for the d.c. power supplies appears to be adequate.

The main characteristics of the ICRF equipment, determined by the requirements of TASKA-M power balance, are the following:

Total RF power coupled to the plasma:	12.4 MW
Total RF output power of the generators:	17.2 MW
RF pulse duration:	steady state
Frequency:	15 MHz

RF power transmitted to each coupling system: 4.3 MW

Number of antennas: 4

Field on axis near antennas: 4.2 T

Extrapolation from existing high power ICRF heating will require a certain extent of developments:

1. Development of a 5 MW quasi-c.w. tube or use of a combination of presently available $\leq$ 1.5 MW units by means of 3 dB couplers.

2. Development of antenna structures and transmission lines to carry the significant thermal load due to the quasi-c.w. operation.

Consequently, if a combination of 2 x 1.75 MW units is used, the RF power source will consist of 4 units. The output power of each unit is obtained by a low power solid state broad band amplifier, driver stages and two high power output amplifiers. A possible block diagram of a power unit as discussed for Tore Supra /16/ is given in Fig. 6.3-5. The operating frequency can be adjusted continuously over a certain range by tuning the amplifier cavities. This scheme allows a matching of the antenna impedance by frequency modulation.

Each tetrode of the output cavity for Tore Supra will be supplied by a 25 kV-100 kA power supply with dynamic voltage regulation. This will allow the optimization of the RF output power level of the tetrode and limitation of the anode dissipation power under VSWR > 1 conditions caused by a change of the antenna loading impedance.

6.3.6 <u>Transmissions lines</u>

To transfer more than 1 MW of active RF power to the antenna, precautions against breakdown in coaxial lines have to be taken since the peak voltage on the line will be > 20 kV, depending on the coupling characteristics of the antenna with the plasma. For that reason a 15 cm O.D. coaxial line between the generator and the antenna may not be sufficient and the choice of a 23 cm O.D. line has to be made. Fig. 6.3-6 gives the possible lay-out of the coaxial lines between the generator and the antennas. The line consists of elbows, demountable elements, gas barriers and rigid straight sections. The total line should be pressurized protected against overvoltages or voltage breakdown.

Fig.6.3-5 : Schematic diagram of a 3 MW, 45 MHz unit proposed for Tore Supra

6.3.7 Matching System
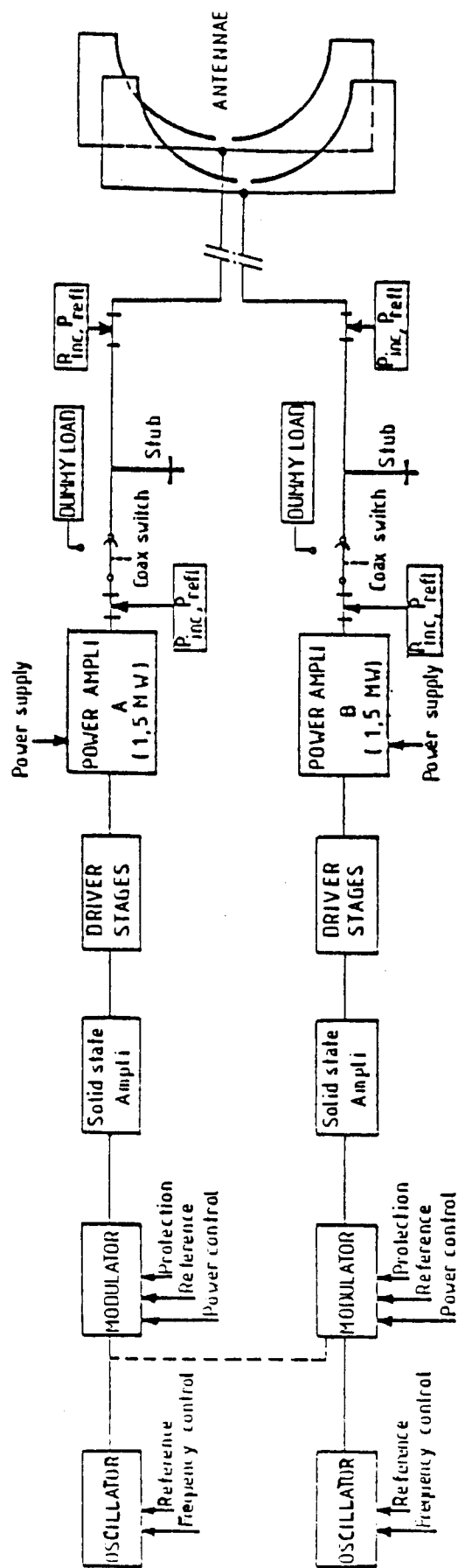
To match the antenna impedance to the output impedance of the RF generator,
tuning with two stubs, placed as near as possible to the antenna, was used
on TFR. It had the advantages of a short coaxial transmission line between
the tuning circuit and the antenna, loaded with high VSWR. A disadvantage
of this scheme was that tuning during RF pulses (30 s every 5 min) had to be
performed by changing the electrical length of the stub, i.e. by mechanically
moving the stub short circuits under high RF current conditions. Therefore,
tuning with one stub and modulating the frequency was also considered on TFR
and JET.

Tuning stubs, adapted to cover a 36 - 65 MHz range of frequencies, require a
length of 2.5 m. Those, as well as the various components of the transmission
lines are currently available from industry. For TASKA-M, the transmission
and matching system should be developed according to the results of current
high power experiments. It will be located outside the blanket and shield of
the central cell. A remote matching system could also be considered for TASKA-M
since it is not desirable to locate matching elements near the reactor core,
e.g. a broad band generator using frequency tuning.

Fig. 6.3-6: Lay-out of the coaxial lines between the generator
             and the antenna for Tore Supra
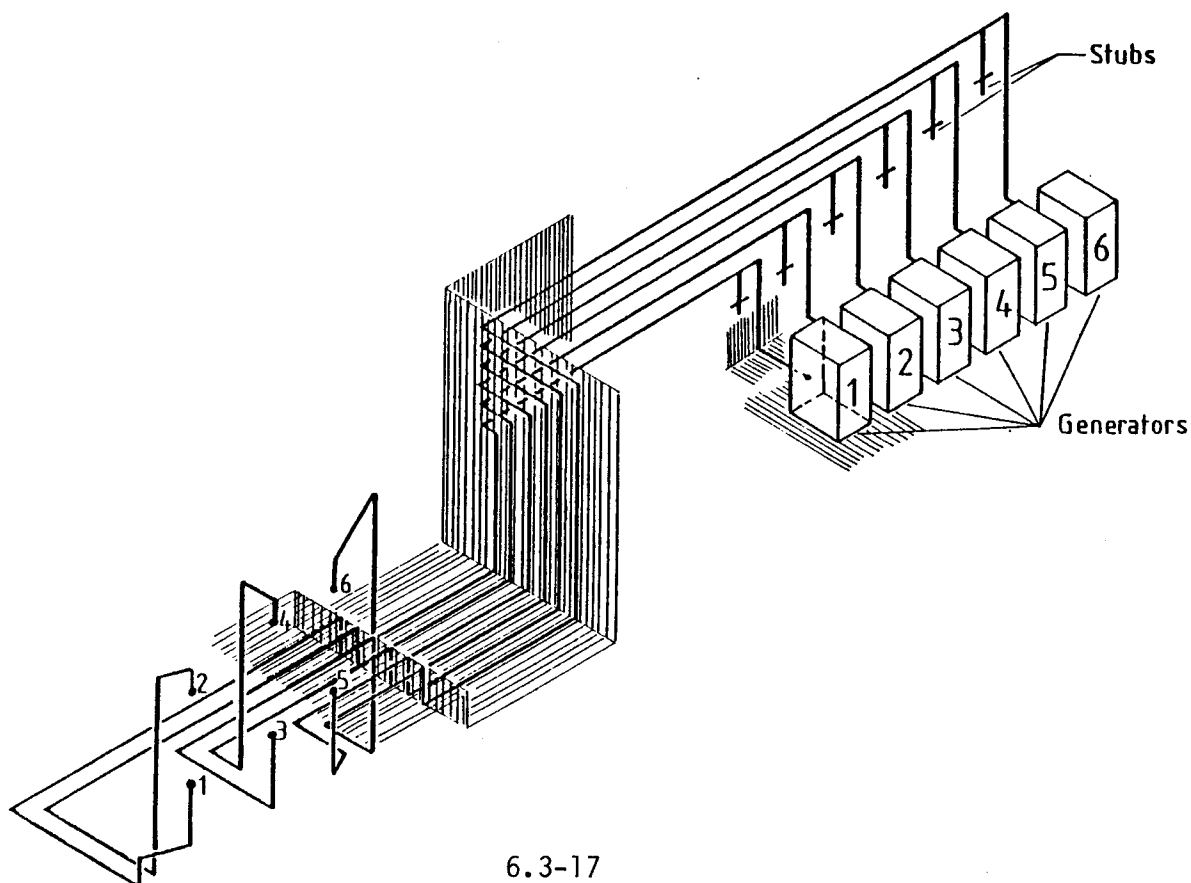
References for Section 6.3

1. K. Audenaerde and J. Scharer, "Electron Cyclotron Resonance Heating in Tandem Mirror Plasmas", Nuclear Technology/Fusion $\underline{2}$, 623 (1982).

2. N. Lam, J. Scharer and K. Audenaerde, "Electron Cyclotron Heating in Weakly Relativistic Realistic Tandem Mirror Plasmas", submitted to Physics of Fluids (1983).

3. D. Hwang et al., "High Power ICRF and ICRF Plus Neutral Beam Heating on PLT", Proc. 9th Conf. on Plasma Physics and Contr. Nuclear Fusion Research $\underline{II}$ (1982) 3.

4. TFR Group, "Dominant Role of Wave Conversion Mechanism in TFR Ion Cyclotron Heating Experiments", Proc. 9th Conf. on Plasma Physics and Controlled Nuclear Fusion Research, $\underline{II}$ (1982) 15.

5. L. Yujiri (MIT), private communication (1983).

6. T. Stix, PPPL Report-1298 ($\omega < \omega_{ci}$) Fast Wave Heating of a Plasma - Consideration of Two Frequency Regimes (1976) and Varenna Proceedings on Plasma Heating; invited paper on RF Heating, p.7 (1976).

7. T. Stix, Nuclear Fusion $\underline{15}$, 737 (1975).

8. J. Scharer, B. McVey, and T. K. Mau, Nuclear Fusion $\underline{17}$, 297 (1977).

9. J. Scharer et al., Nuclear Fusion $\underline{19}$, 117 (1979).

10. Equipe TFR, Plasma Physics, Vol. $\underline{24}$, No. 6, p. 615 (1982).

11. J. Hosea et al., Proc. 3rd Joint Varenna-Grenoble Int. Symp. Vol. I, p. 213.

12. JFT-2 Group, Proc. 3rd Joint Varenna-Grenoble Int. Symp. Vol. I, p. 259 (1982).

13. K. H. Knobbe, H. Noeldge and the ICRF heating team of Textor, Proc. 12th Symp. of Fusion Technology, Pergamon Press 1982, p. 1353.

14. F. Braun et al., Proc. 12th Symp. Fus. Techn., Pergamon Press 1982, p. 1393.

15. JET Annual Report 1981, EUR 7950 EN, p.62.

16. Proposal Tore Supra, Fontenay-aux-Roses, Mai 1983.

7. Vacuum- and Exhaust System

7.1 Introduction

The vacuum- and exhaust system is used in two distinct modes:

a) Before operation it has to evacuate the whole interior of the machine to generate the vacuum condition for start up ($<10^{-6}$ mbar).

b) During operation it has to ensure that the neutral gas pressure and the content of high Z-material in the plasma chamber is kept at the low level required for the fusion process.

The technical design objectives are mainly determined by the operational, i.e. the exhaust conditions. To fulfil these requirements, a particle stream corresponding to the particle stream supplied by the neutral beam-injectors (NBI) for plasma heating and fuel supply must be exhausted in such a way that the gas composition and the gas content in the machine remains constant with time. Fig. 7.1-1 is a schematic representation of the particle streams observed during operation of the machine (see also Table 7.1-1). The injected neutral particle streams of the high energy and anchor NBI's (2 and 4 in Fig. 7.1-1) split in three paths when they come in contact with the plasma: in shine through fractions of neutral particles which pass the plasma without interaction (6 and 7), in trapping fractions which sustain the fusion plasma and become a part of it and in charge exchange fractions which strike the first wall and form the halo plasma. The low energy NBI (3) creates no shine through fraction. A plasma stream equivalent to the sum of the trapping fractions and the charge exchange fractions leaves the machine axially (5) and has to be extracted from the end cells (9) together with the thermalized shine through fractions of the anchor NBI's (8). The thermalized shine through fraction (10) of the high energy NBI's is removed directly from the central cell.

Besides these process streams, additional gases must be exhausted which might enter the machine via leaks from outside, or which might be released from the numerous gas or liquid containing components inside the machine, e.g. superconducting coils, coolant pipes, blanket modules etc. Furthermore, it cannot be excluded at present, that even after start up during a certain time some noticeable amounts of gases are still released from the very large surfaces of the internal components.

The majority of particles to be exhausted during operation occur as directed neutral particle beams and plasma streams which must be converted first to thermal gas. Specially designed dump plates, bombarded by the particle beams and plasma streams serve this purpose. Because of their

FIG. 7.1-1 PROCESS PARTICLE AND GAS STREAMS (Values see Tab. 7.1-1)

Tab. 7.1-1: Process Particle and Gas Streams (g/s)
(see also Fig. 7.1-1)

Energetic Particle Input by Neutral Beam Injectors (NBI)
(Species atomic)

	Deuterium	Tritium	Helium	Remarks
(1) Total particle input	5.95E-3	4.04E-3	--	part. trapping fractions:
(2) Input by four high energy NBI	2.69E-3	4.04E-3	--	0.924
(3) Input by one low energy NBI	1.04E-3	--	--	1.000
(4) Input by two anchor NBI	2.21E-3	--	--	0.365

Energetic Particle Flow to Beam Dumps

	Deuterium	Tritium	Helium	Remarks
A. End dumps (Plasma/Halo)				
Contribution from four high energy NBI	1.79E-3 / 7.03E-4	2.69E-3 / 1.06E-3	--	
Contribution from one low energy NBI	6.69E-4 / 3.68E-4	--	--	
Contribution from two anchor NBI	5.35E-4 / 2.68E-4	--	--	
Contribution from fusion process	--	--	1.60E-5	
(5) total flow for two end dumps	2.99E-3 / 1.34E-3	2.69E-3 / 1.06E-3	1.60E-5	
total flow for one end dump	1.50E-3 / 6.70E-4	1.34E-3 / 5.28E-4	8.00E-6	
B. Central cell dumps				
Contribution from four high energy NBI	2.05E-4	3.07E-4	--	
(6) total flow for four central cell dumps	2.05E-4	3.07E-4	--	
total flow for one central cell dump	5.11E-5	7.68E-5	--	
C. Anchor dumps				
Contribution from two anchor NBI	1.41E-3	--	--	
(7) total flow for two anchor dumps	1.41E-3	--	--	
total flow for one anchor dump	7.03E-4	--	--	
Total flow to beam dumps	5.95E-3	4.06E-3	--	

Thermal Gas Output by Exhaust System
(Species molecular)

	Deuterium	Deut.-Tritium	Tritium	Helium	Remarks
A. End cell					
(8) Contribution from one end dump (Plasma+Halo)	1.38E-3	1.98E-3	6.88E-4	8.00E-6	
Contribution from one anchor dump	7.03E-4	--	--	--	
(9) total flow from one end cell	2.08E-3	1.98E-3	6.88E-4	8.80E-6*	*includes 10% safety margin to provide for leakages from SC coils and cryosurfaces
B. Central cell					
Contribution from four central cell dumps	1.03E-4	2.55E-4	1.54E-4	--	
(10)total flow from central cell	1.03E-4	2.55E-4	1.54E-4	--	
(11)Total gas output	4.26E-3	4.20E-3	1.53E-3	1.76E-5	

(Output values are taken from Tab. 7.3-1 and 7.3-2)

extraordinary loading conditions these beam dumps (BD) constitute one of the most critical component of the whole machine and consequently one of the most important component of the whole exhaust system. In Sec. 7.2 these aspects are covered in more detail.

The gas pressure in the vicinity of these dump plates must be kept close to the neutral gas pressure in the halo to limit the amount of reflux of cold thermalized gas and sputtered plate material to the plasma (see also Subsect. 7.1.3). For the axial plasma dumps this requirement would also apply if the end dump region were used to test direct converter components. The gas pumping requirements during operation are met with appropriate pump chains. Their first stages consist of cryopumps which have to be frequently regenerated.

The same pump chains are used for the evacuation process before start up. However, to remove the bulk of the contained gas efficiently when starting with approximately atmospheric pressure some additional pump sets for pre-evacuation are provided. In Sect. 7.3 the gas pumping facilities are described.

The operational sequence during the evacuation process and the total time required to reach the start up conditions is strongly determined by the design concept of the main vacuum boundary. Unlike most of the previous experimental fusion facilities the "outer wall" concept is selected here, similar as it will be realized in the US Tandem Mirror Fusion Test Facility (MFTF). Fig. 7.1-2 presents a schematic draft of the two different design concepts with inner and outer vacuum wall.

The advantage of the "outer wall" concept is that it avoids vacuum tight welds with highly irradiated materials close to the plasma and that it allows volumetric and geometric changes of the materials and structural parts by irradiation induced swelling and creep. For this purpose adequately wide clearances and gaps between all adjacent components are provided in the inner region. The support and the precise alignment of the components is performed by the outer structure of the machine, which is essentially not affected by irradiation. Also the main vacuum boundary is located outside the main neutron shielding.

The disadvantage of this design concept with respect to the vacuum conditions is easily shown: There are numerous individual components with large surface areas within the vacuum boundary which have to be degassed when the start up vacuum is generated. Baking out to accelerate degassing of the materials and discharge cleaning of the surfaces as commonly used in

Typical plasmaphysic experiments
(JET, TFTR, etc., not MFTF-B)

TASKA-M concept (schematic)

Atmosphere

Air or N_2

Vacuum region (H,D,T)

Air or N_2

Atmosphere

Plasma

Plasma

Inner Wall Concept

Outer Wall Concept

1 Coils
2 Shielding
3 FW cooling system (CO_2; H_2O)
4 Liquid He / N_2

5 Insert for instrumentation, plasma heating, material tests etc.
6 Test blanket
7 Guard vessel
— Vacuum boundary
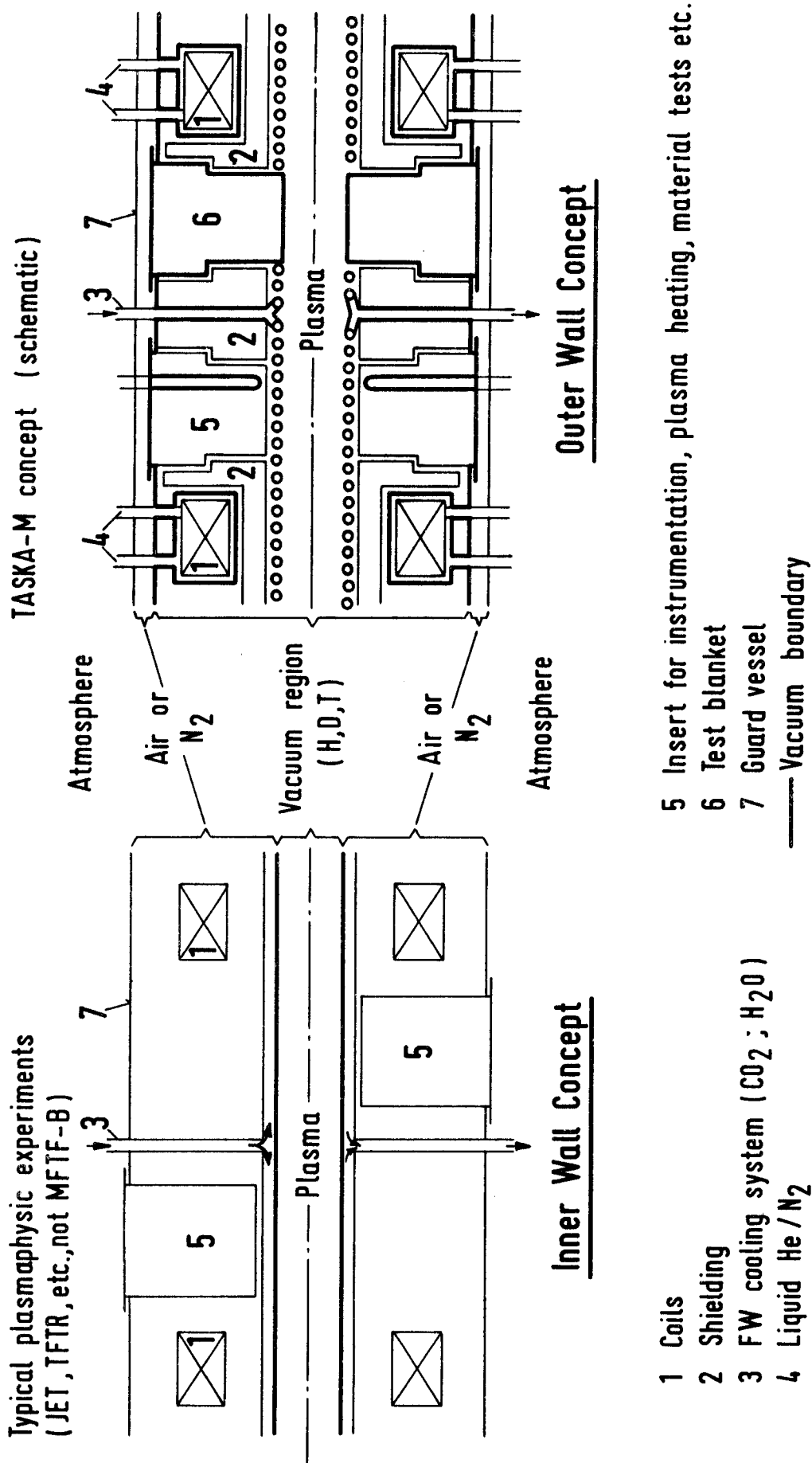
FIG. 7.1-2   TWO DESIGN CONCEPTS OF THE VACUUM BOUNDARY

the previous fusion facilities with a smooth inner vacuum wall is applicable here only to a very limited extent. Therefore, in any case, the first evacuation of the facility will require a comparatively long time and it cannot be excluded, that even some time after start up a certain amount of impurity gas is still liberated, as mentioned before. In this context, a specific effect should be mentioned here for which quantitative information is not available at present. The sharp increase of ionizing radiation within the facility after start up will lead to a drastic increase of the gas desorption rate /1,2/. The burst of gas generated in this way must be removed also by the vacuum and exhaust system, respectively, without an undue impact on the plasma condition. Finally, the possibility of inner leaks, which are difficult to detect and to locate, is another burden of this design concept.

In MFTF-B an additional getter process inside the machine is used to support the vacuum facilities. Unfortunately, for long continuous operation, as in the present case, this method cannot be applied.

In a DT burning fusion facility the outer wall concept has also serious impacts on the repair schemes, because all components within the vacuum boundary become radioactively contaminated. Probably, also the amount of tritium withheld in this way from the fuel cycle must be considered.

There is no question, that a final quantitative assessment of the vacuum process for a plant designed according the "outer wall" concept needs additional specific experimental investigations and much more in depth studies as could be carried out within the scope of this work. However, it is expected, that the large cryopump capacity of a mirror fusion device and the large cross sections of the gas flow paths will be advantageous in generating and sustaining the required vacuum conditions under these aggravated requirements given by the outer wall concept.

References for Section 7.1

1. O. Gröbner, et.al.: "Studies of photon induced gas desorption using synchrotron radiation", Vacuum 33 (1983) 7, p. 397-406

2. R.S. Vaughan Watkins et.al.: "An appraisal of glow discharge treatment of copper surfaces by the techniques of electron stimulated desorption", Vacuum 28 (1978) 10/11, p. 459-465

7.2 Beam and End Dumps
7.2.1 Overview

In the process of neutral beam heating of the plasma, the trapping of the incident neutral particles is not complete. Depending mainly on particle energy, plasma density, and path length, a substantial fraction of particles penetrates the plasma without interaction and has to be collected at appropriate heat sinks, the so-called beam dumps (BD). In TASKA-M, BDs are needed for each of the four HE-NBIs being focused at the mid point of the central cell (CC) and for the two Anchor-NBIs. According to their location the BDs will therefore be referred to as CC-BD and Anchor-BD respectively. There is a third tye of NBI, the LE-NBI in the CC, which, due to its low energy and power and thus neglegible shine through fraction, is assumed to not require additional means besides the water cooled first wall. Finally the end loss particles fanning out into both end cells have to be thermalized by adequate collectors, the so-called end dumps. The end dumps are exposed to plasma particles, i.e. ions and electrons, in contrast to the BDs, which only see neutral particles and neutrons.

Overall design requirements based on the envisaged operational modes and the specific TASKA-M NBI parameters are established in the following Subsect. 7.2.2. The design concepts for the CC-BD, the Anchor-BD and the end dumps, all based on the water cooled Hypervapotron /1/ heat sink, are described in Subsect. 7.2.3.

The phenomena to be considered in beam and end dump design are the following: (1) <u>Max. heat flux and heat flux distribution</u>- Since there is a large discrepancy between the heat flux per unit area within the shine through beam and the allowable heat flux at the dump surface, the heat flux has to be attenuated. The methods employed here are the geometric dispersion of the beam behind the focus and the inclination of the dump surface relative to the beam axis. The resulting maximum and average heat fluxes are evaluated in Subsect. 7.2.4. (2) <u>Heat transfer and power absorption</u> - The allowable heat flux referred to in item (1) is set by the achievable plate/coolant heat transfer in steady state condition. During transients, as for instance at start up, the maximum structural temperatures as well as stress and fatigue effects may be the life limiting factors. This will be briefly addressed in Subsect. 7.2.5. (3) <u>Sputtering of the dump surfaces</u> - The high energy particle impact leads to high erosion rates, which, according to present knowledge, will dictate predominantly the achievable life time of the dump surfaces. For the CC-BD and the Anchor-BD the sputtering

yields available in the open literature reveal acceptable life times, as shown in Subsect. 7.2.6. At the end dumps however, the erosion process is much more complicated due to recycling and impurity sputtering phenomena. These effects have been neglected in the present analysis. (4) <u>Gas exhaust and required duct sizes</u> - The particle flow impinging onto the dump surface is considered to be thermalized and completely released as neutral molecular gas. To prevent considerable back flow into the plasma, the gas has to be pumped continuously at sufficiently low pressures. Thus the dump design has to provide adequate exhaust space, which is evaluated in Subsect. 7.2.7.

The T permeation into the dump coolant flow is investigated in Subsect. 8.4.1. No work was performed in this study on DT and DD neutron generation in addition to what was done in the TASKA study /2/, Sect. VIII.3.6.

7.2.2 Design Philosophy

As design basis for the BDs three operational modes have been defined, i.e. normal operation, calibration and start up (Tab. 7.2-1).

Table 7.2-1: BEAM AND END DUMP OPERATIONAL MODES

Operational Mode	Plasma Density	Dump Power to be absorbed		
		CC-BD	Anchor-BD	End Dump
Normal Operation	nominal	$(1-f_T)P_{inj}$	$(1-f_T)P_{inj}$	P_{el}
Calibration	zero	$.33\ P_{inj}$	$.5\ P_{inj}$	zero
Start up	zero	P_{inj}	P_{inj}	zero

f_T = Trapping fraction

P_{inj} = Injected beam power per NBI

P_{el} = End loss power at one end

In the normal operation mode TASKA-M is assumed to run steady state, at rated power. The BDs are exposed to the shine through fraction of the injected beam power, and the end dumps see the rated end loss power. The calibration mode is needed to calibrate, adjust and check out the NBI and BD systems without plasma prior to start up. The idea is to turn on the individual sources within each NBI sequentially, so that only one out of three sources, as in the case of the HE-NBI, or one out of two sources, in the case of the Anchor-NBI, is operating at a time, leading to a time average power at the dumps of 1/3 or 1/2 of the nominal injected power respectively. During start up, as the third operational mode, the full injected power is needed, and the plasma is expected to ramp up from zero to nominal. For simplicity it is assumed that the beam dumps are exposed to the rated injected beam power during the start up mode, which is terminated by either a normal operation mode or a shut down, if the plasma is not developing as specified. It should be noted, that calibration and start up in this sense do not enhance the heat load at the end dumps (except transients) and are hence not considered there.

The mission time in the three operational modes is, of course, very different. As a goal, the dumps should withstand normal operation for at least 0.25 full power years. Thus the design has to be developed with respect to the long term effects (heat rejection, sputtering) and replacement primarily for this mode. The calibration periods may accumulate up to several hours during the dump life time and are relevant with regard to the maximum allowable quasi steady state heat load. For start up it has been estimated (Sect. 3.9), that the plasma density builds up within about 80 ms. So for the maximum duration of the start up mode defined above, 200 ms seem to be reasonable, provided the diagnostics and scram system is fast enough, as required for plant protection.

Besides these general rules, the neutral beam parameters and the plasma parameters (Tab. 7.2-2) provide the design basis for the dumps. Tab. 7.2-2 contains in the first block the parameters established by the physics basis (Chap. 3). In the second block, the relevant NBI design data (Sect. 6.2) are compiled, based on our present knowledge. The third block lists, besides the fundamental assumptions on beam focusing, some derived key variables pertinent to the dump design.

One of the most important parameters is the maximum allowable heat flux at the dump surface. Primarily with reference to the experience gained in the NBI development for JET /1/, a maximum heat flux of 5 MW/m^2 for the

Tab. 7.2-2: TASKA-M NEUTRAL BEAM AND PLASMA PARAMETERS RELEVANT TO BEAM AND END DUMP DESIGN

		Neutral Beam Parameters		Plasma End Loss Parameters
		HE-NBI	Anchor-NBI	
Neutral Species D/T/He	(Atom-%)	50/50/0	100/0/0	62.5/37.3/0.2
Grid Voltage	(kV)	90	73	–
Average Particle Energy D/T/He	(keV)	81	66	105/126/185
Injected Power per NBI or per end	(MW)	5.2	3.5	15
Beam Angle relative to CC Axis	(deg)	45	50	0
Trapping Fraction		.924	.365	–
Plasma Diameter and width, respectively	(m)	.242	$\approx$ .28	.87/7.37[1]
Number of Neutral Beam Injectors		4	2	–
Number of Sources per NBI		3	2	–
Beam Source Envelope Area	(m^2)	1.1x.5	.5 x .65	–
Source Distance from Focus	(m)	12	12	–
Divergence Angle	(deg)	0.48	0.6	–
Mode of Focus at Intersection[2]		point	point	Subsect. 7.2.4
Foot Print Diameter at Intersection[2]	(m)	0.20	0.251	–
Average Beam Power Density at Intersection	(MW/m^2)	166	71	–
Total Particle Flow Rate per BD or end	(10^{20}/s)	4.0	3.3	7.1

[1] Refers to minor and major ellipse axis, respectively, at a distance 19.5 m from the midpoint of TASKA-M

[2] Defined as the intersection of the main beam ₵ and the plasma ₵

normal operation mode and 10 MW/m^2 for the calibration mode has been chosen. The first figure is equal to half the design value adopted for JET (10 MW/m^2) and reflects additional margin for the continuous operation of TASKA-M. The figures are related to the selected design concept, the Hypervapotron, as described in the next Subsect. 7.2.3. For the start up mode, no maximum heat flux is established because of the thermal inertia effects. The maximum surface temperature will be the limiting factor (Subsect. 7.2.5).

7.2.3 Design Concept

As design concept for the beam dumps the Hypervapotron cooling technique was chosen. This has been developed by Thomson CSF in France for anode cooling of high power electrode tubes and is utilized in the JET project for NBI ion dumps and for limiters /1/. Successful experience is available with steady state dissipation up to 10 MW/m^2, the burn-out limits being near 18 MW/m^2 in the JET design /3/. The advantage of the Hypervapotron technique, if compared to a tubular array with highly turbulent water flow /2, 4/, is the low pressure drop and relatively thick front wall with regard to sputtering losses.

The Hypervapotron principle is easily explained, though the detailed heat transfer mechanism from the wall to the coolant is complex and subject to optimization. The water flow is perpendicular to macroscopic grooves. Vapour bubbles are formed near the bottom of the grooves, are ejected into the subcooled bulk flow and recondense. The grooves are refilled with liquid water, and the process starts over again.

A schematic diagram of the beam dump element is shown in Fig. 7.2-1. Typical dimensions are proposed for this application with reference to /1/ as first approach and will not be further substantiated in this study. An appropriate number of such elements is arranged to form the CC-BD, the Anchor-BD, and the end dump inserts as described below. Reference material is a chromium copper alloy (with approx. 1 % Cr) because of its excellent thermal conductivity and its promising strength properties. An alternative would be plating the surface with a material of higher strength, e.g. Molybdenum. In the following subsections, both versions are evaluated. The design data for the CC-BDs, Anchor-BDs and end dumps are listed in Tab. 7.2-3.

The CC-BD concept is shown in Fig. 7.2-2 through 7.2-4. The fingerlike BDs are designed as individual inserts (one insert for each of the four HE-NBI lines) penetrating the vacuum boundary at an angle of 60
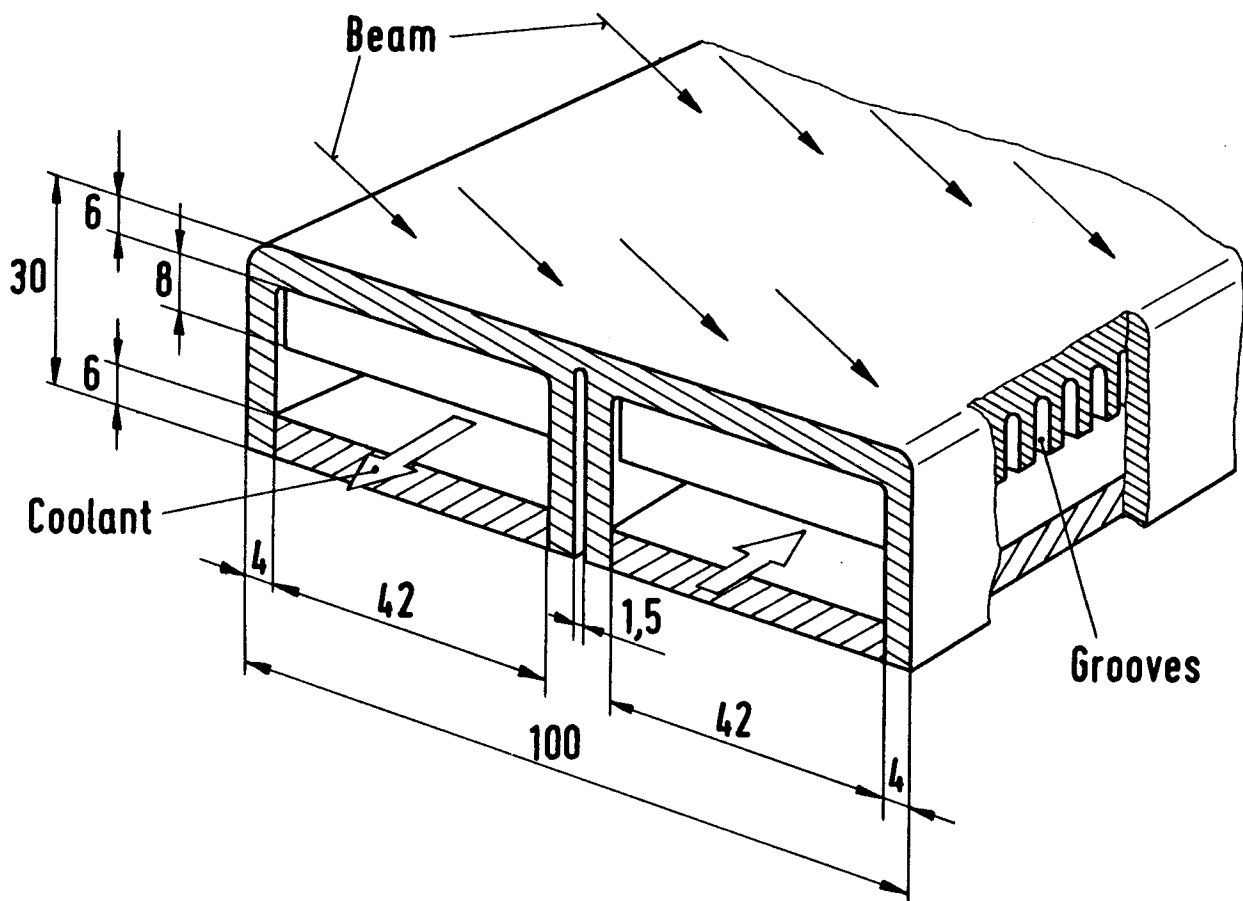
(Dimensions in mm)

FIG. 7.2-1 SCHEMATIC DIAGRAM OF THE HYPERVAPOTRON
BEAM DUMP ELEMENT
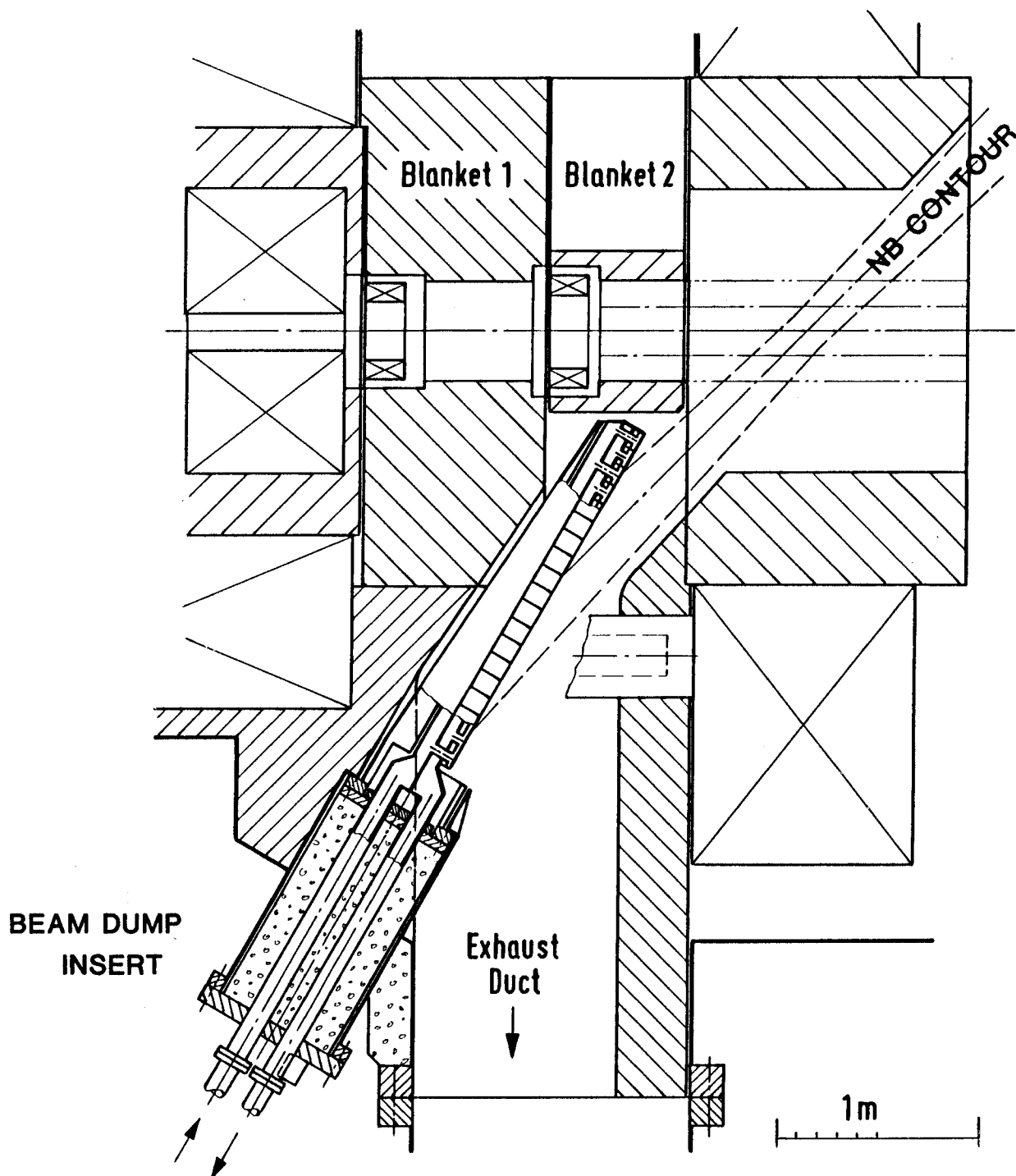
FIG. 7.2-2 TASKA-M CENTRAL CELL BEAM DUMP AND
EXHAUST DUCT CONCEPTUAL DESIGN
(Vertical Cross-Section)

B

≈ 750

1600

A   A

Beam ₵

100

Typical
Coolant
Flow Path

Beam
Foot
Print

Scale 1:10

75°

Incident Beam

71°

View B
Scale 1:5

Section A-A

520

Dimensions in mm
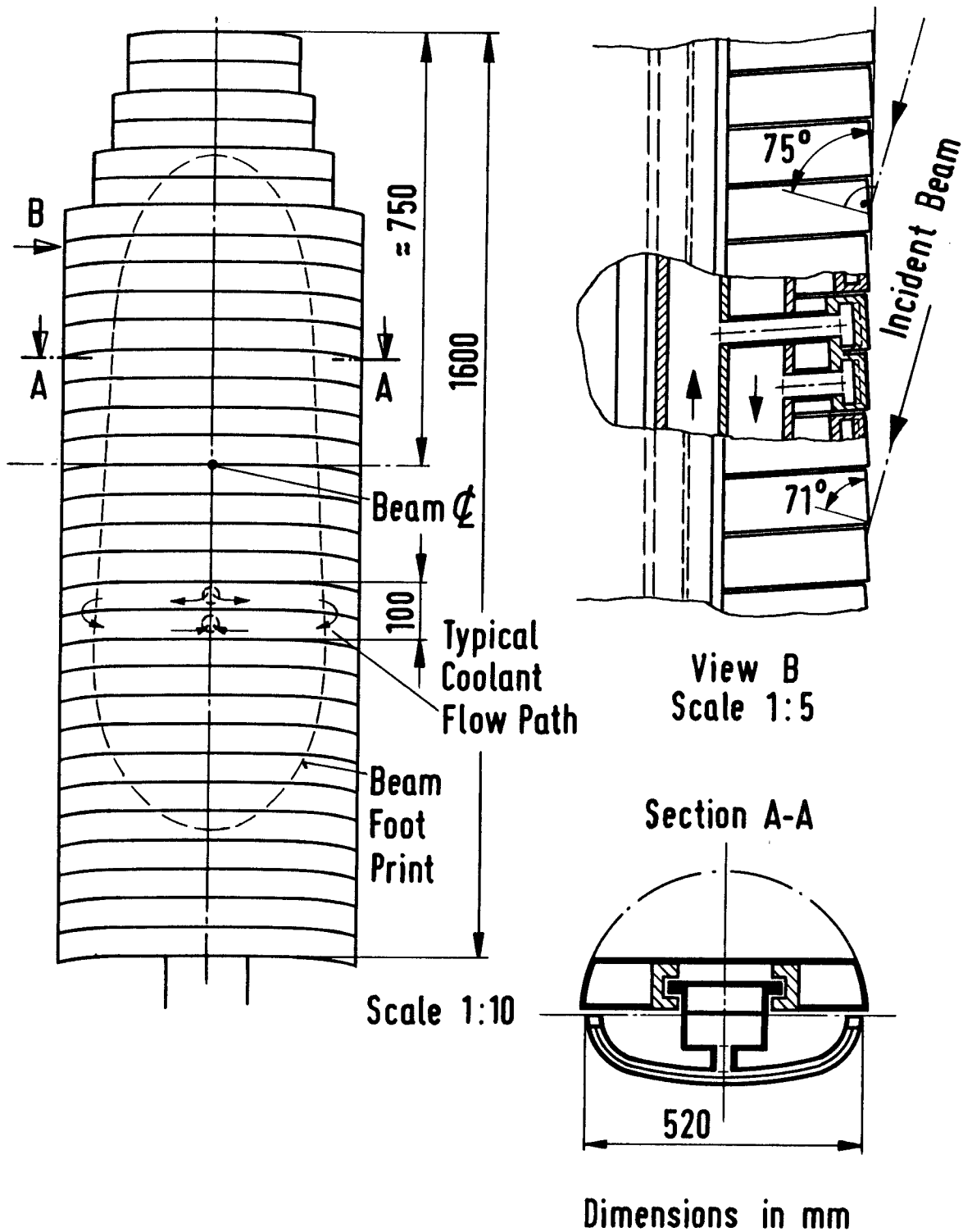
FIG.7.2-3 TASKA-M CENTRAL CELL BEAM DUMP
HYPERVAPOTRON CONCEPTUAL DESIGN

4 Identical Beam Dump Inserts

Blanket 1

Blanket 2

Exhaust Duct

1m

KfK
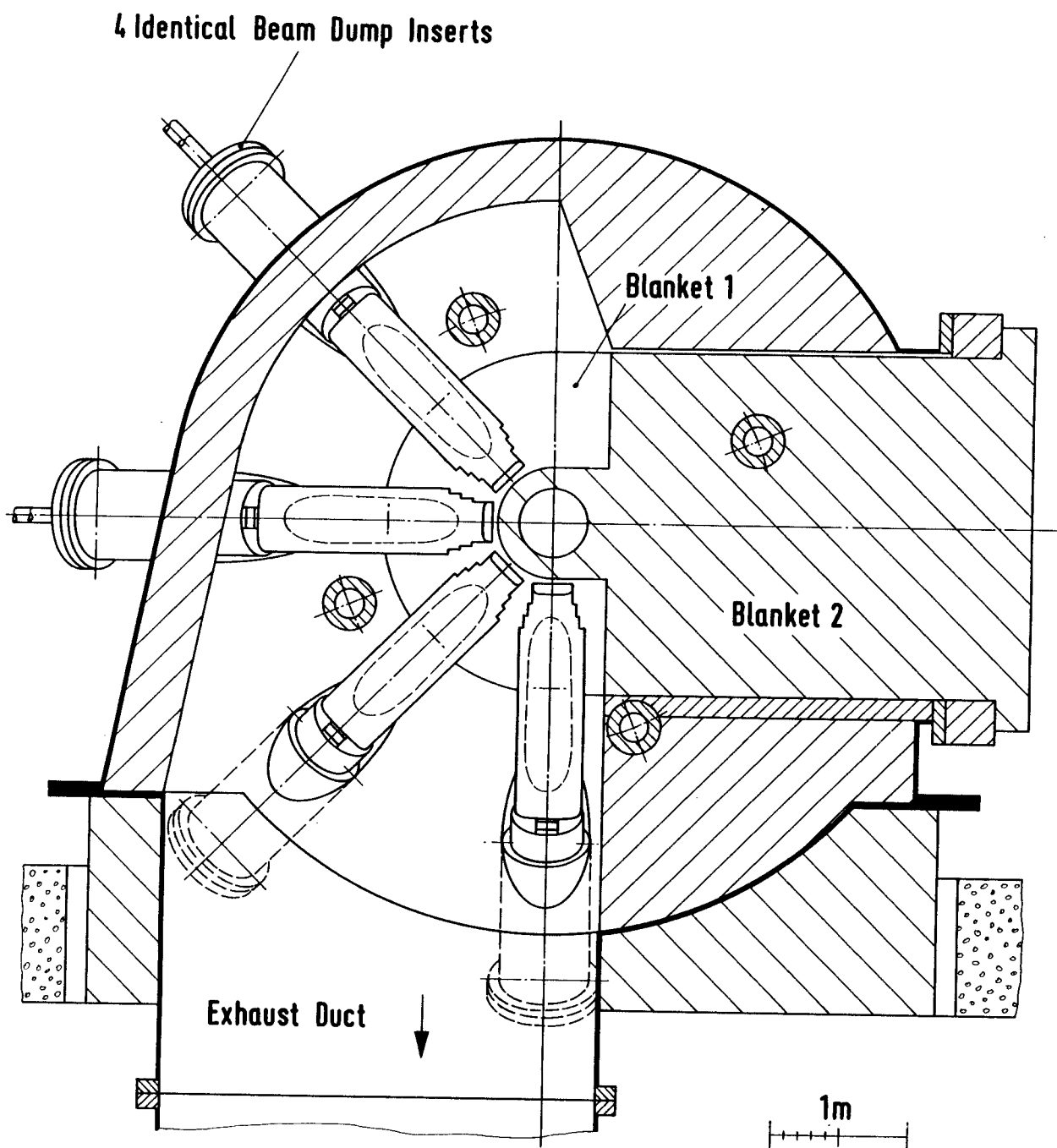
FIG 7.2-4 TASKA-M CENTRAL CELL BEAM DUMP AND EXHAUST DUCT
CONCEPTUAL DESIGN (Vertical Cross Section)

degrees, relative to the plasma axis (Fig. 7.2-2). The normal to the heated surface forms an angle relative to the beam axis of 75 degrees, resulting in a nominal foot print contour as shown in Fig. 7.2-3. Adding some margin of about 6 cm for beam and beam dump misalignment in each direction (perpendicular to the beam axis) leads to the required BD size of roughly 1.6 m x 0.52 m for the cooled structure.

The cooled structure is composed of parallel Hypervapotron elements supported at a central manifold for coolant supply to the individual elements. The manifold in turn is guided in a support structure allowing for differential thermal expansion. Coolant is fed to the elements into the upper chamber, is reversed at the element ends into the lower chamber and returned to the exit manifold (Fig. 7.2-3). The elements are shaped like a compound curve in order to further enlarge the incident angle in the edge region, where the power density in the shine through beam is the highest (Subsect. 7.2.4), particularly in case of misalignment of the beam and plasma axes. Another design feature is the tilting of the Hypervapotron elements relative to the gross BD surface in order to allow a certain staggering to avoid heat and particle flux peaks at the leading edges by shadowing. This reduces the effective angle from 75 degrees to approx. 71 degrees, and must be considered when surface effects such as sputtering and transient heating are investigated (Subsect. 7.2.5 and 7.2.7).

The arrangement of the four CC-BDs according to the NBI positions is shown in Fig. 7.2-4 in an end view. The inserts are penetrating into a common exhaust chamber, from where the thermalized gas is extracted downwards via a large exhaust duct (Subsect. 7.2.7). The downward direction was chosen to ease the shielding of the strong 14 MeV neutron flux leaving the CC. The BD inserts comprising the Hypervapotron assembly, manifolds, support structure, shielding plug, coolant piping and instrumentation are installed via nozzles and can be replaced by means of special transfer flasks, compatible with the overall maintenance scheme as described in Sect. 11.2.

The anchor-BDs are essentially of the same design as the CC-BDs, though the size and shape are different corresponding to the heat load to be dissipated. Furthermore pumping of the neutralized gas is achieved by the end cell evacuation system, so that no separate exhaust duct is necessary (Fig. 7.2-5). The main design data resulting chiefly from the choice of the inclination angle and other geometric restrictions are tabulated in Tab. 7.2-3.

Distance from Machine ℄ (m)

Transition Coil

Maintenance
Insert

To End Cell
Evacuation System
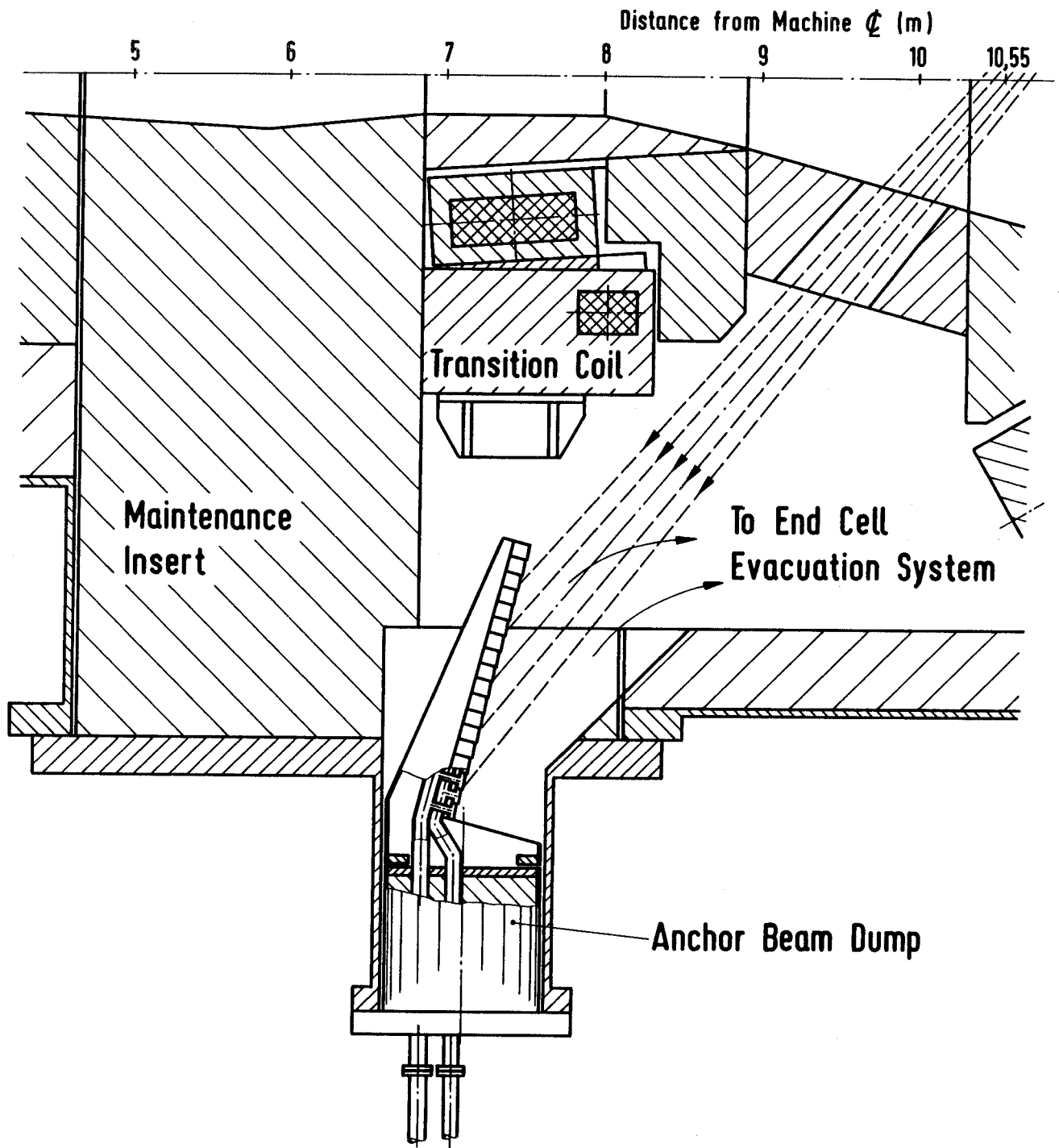
Anchor Beam Dump

FIG. 7.2-5 TASKA-M ANCHOR BEAM DUMP CONCEPTUAL
DESIGN

Tab. 7.2-3: TASKA-M BEAM AND END DUMP DESIGN DATA

Beam Dump Concept		CC-BD	Anchor-BD	End Dump
		Hypervapotron	Hypervapotron	Hypervapotron
Gross Inclination Angle rel. to Beam Axis	(deg)	75	65	0
Effective Inclination Angle of BD Segments	(deg)	71	60	0
Dump Distance [1] from Focus and Midpoint, resp.	(m)	1.7	5.0	19.5
Foot Print Area at Dump	(m^2)	0.41	0.77	5.03
Foot Print Envelope Dimensions	(m x m)	0.4 x 1.16	0.58 x 1.48	≈ 0.87 x 7.36
Dump Dimensions (width x length)	(m x m)	0.52x 1.60	0.7 x 1.8	Fig. 7.2-6
Total Dump Heat Load				
During normal operation, incl. CX	(MW)	0.45	2.22	15
During calibration	(MW)	1.72	1.75	–
Flow Rate of Primary Cooling Water	(1/s)	20	26.5	20.3
Coolant Inlet Temperature	(°C)	60	60	60
Bulk Coolant Temperature Rise	(K)	20	20	20
Coolant Inlet Pressure	(bar)	<6	<6	<6
Coolant Pressure Drop	(bar)	<2	<2	<2
Reference Material of Dump Elements		Cu,1%Cr	Cu,1%Cr	Cu,1%Cr
Maximum allowable Surface Temperature	(°C)	450	450	450
Depth Sputtering Yield Design Limit	(mm)	1	1	1
Expected Sputtering Life Time	(FPY)	.8	.8	7.4

1) at intersection of main beam axis with BD surface

The end dumps have to dissipate the high power of 15 MW per end, more than 99 % being in the plasma region and the rest in the halo region. To accommodate this power at acceptable heat fluxes, the strong spread of the plasma fan in the end cells is used at the expenses of a large collector area which, in essence, will face an elliptical foot print with a high aspect ratio. A modular end dump collector is proposed, consisting of parallel overlapping inserts similar to the BD design. The inserts are arranged in the following manner (Fig. 7.2-6).

- insert axes being parallel to the minor ellipse axis,
- collector surface beyond the design heat flux limit curve,
- collector width similar to BD width, i.e. approx. 0.5 m,
- overlapping of the inserts at least 5 cm (perpendicular to field lines),
- minimal pitch between inserts sufficient for manipulation, i.e. approximately 1 m.

The central inserts can be removed for plasma direct convertor tests. The advantage of this concept is obvious: small units, easy replacement, individual replacement frequency, similarity to BDs, variable in the scope of plasma direct convertor tests. A panorama view of the end dump inserts and the produced plasma foot print is shown in Fig. 7.2-7. As can be seen, the Hypervapotron section is intended only to cover the plasma region plus an adequate margin. In the halo region of the individual inserts a simpler design is sufficient, since the heat flux is very low.

7.2.4 Heat Flux Evaluation

The radial power distribution within the incident beam is usually assumed to be Gaussian (or due to collimator effects chopped Gaussian), the parameters of which depend on source geometry, divergence angle, focusing mode, distance from the source etc. Due to the radius dependent trapping efficiency in the plasma, the power profile in the shine through beam is even more complex and it may further be complicated by the curved beam dump surface. To estimate the maximum local heat flux at the dump surface, the empirical formula (Eq. 7.2-1) has been used. This is based on an average power density in a reference plane of the incident beam, which is being corrected by a number of factors accounting for the radial profile, geometric dispersion, trapping fraction, inclination angle and power condition.
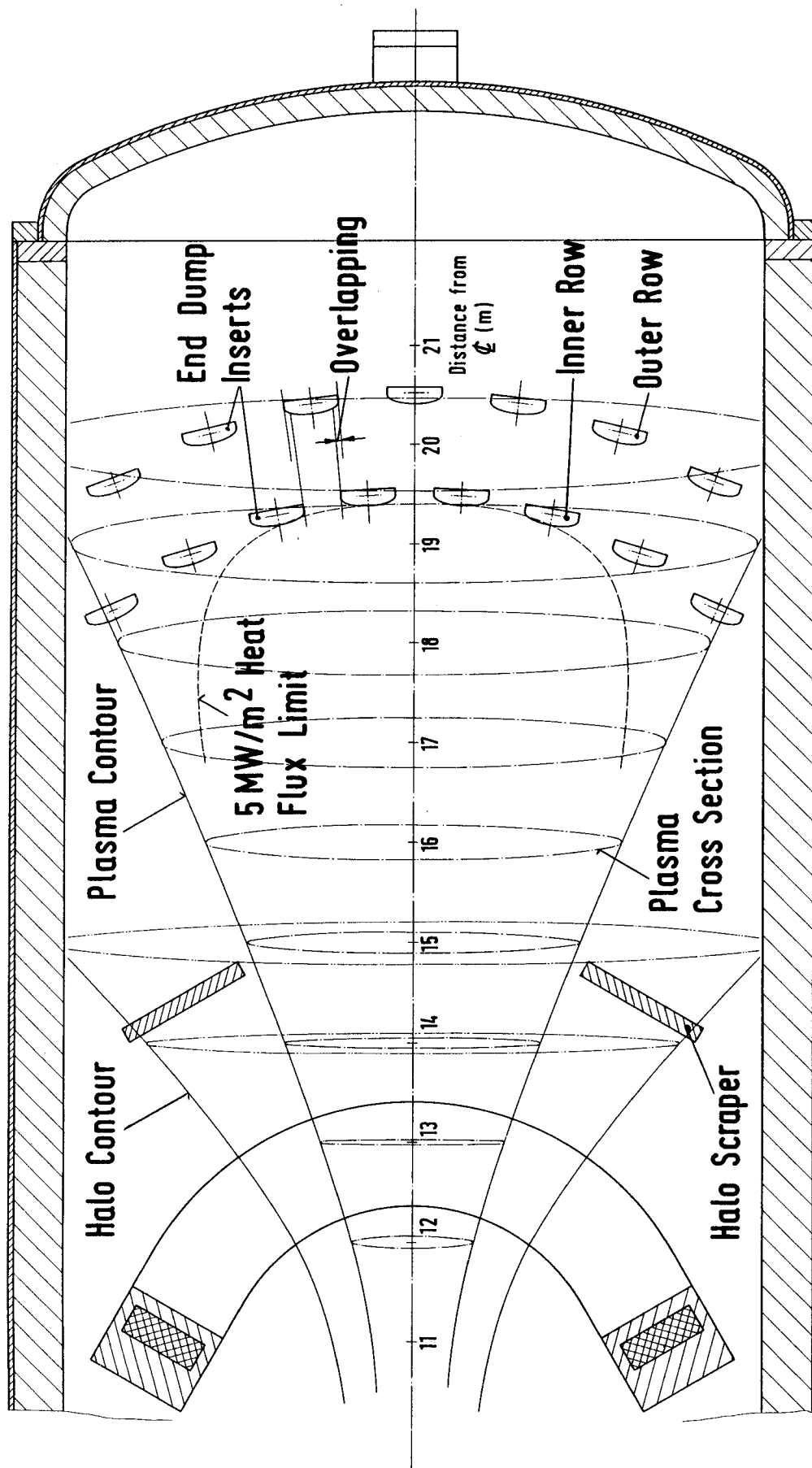
FIG. 7.2-6 SCHEMATIC DIAGRAM OF THE END DUMP ARRANGEMENT

Plasma Foot
Print

End Dump Inserts

Inner Row
(typical)

Outer Row
(typical)

Halo
Foot Print

to Cryo Pumps
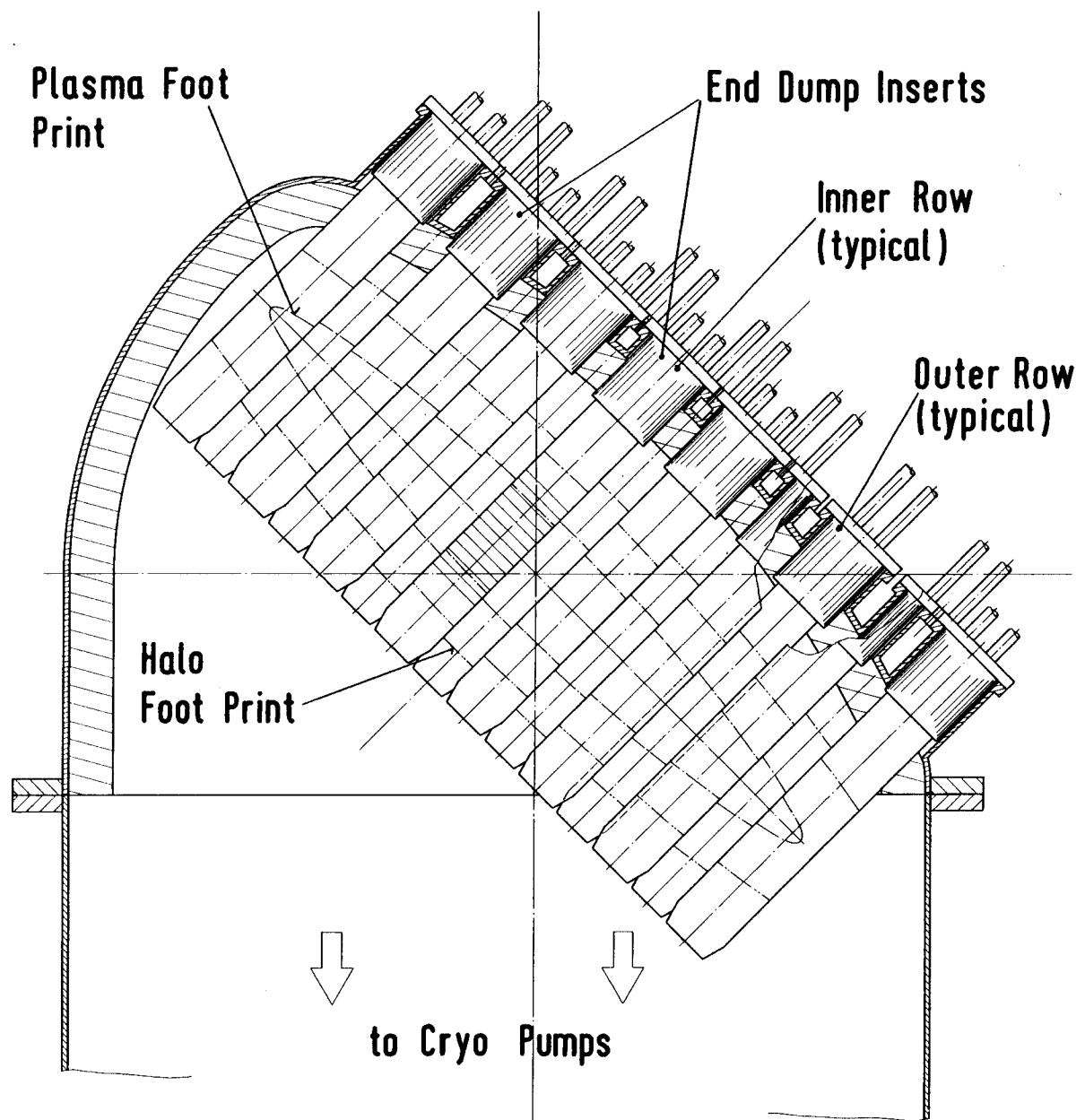
FIG. 7.2-7   PANORAMA VIEW OF THE END DUMP FOOT PRINT

$$\max \chi = (P_{inj}/A_o) \cdot f_{Peak} \cdot f_{Geo} \cdot f_{Thru} \cdot f_{Incl} \cdot f_{Power} \qquad (7.2\text{-}1)$$

$\max \chi$ = Max. local heat flux at dump surface

P_{inj} = Nominal injected power per NBI, Tab. 7.2-2 (for the end dumps it is the axial power loss per end, P_{el})

A_o = Beam cross section in a reference plane

f_{Peak} = Peaking factor accounting for planar power distribution incl. uncertainties

f_{Geo} = Geometric dispersion factor

f_{Thru} = $(1-f_T)$ Shine through factor, where f_T trapping fraction

f_{Incl} = Attenuation factor due to inclination angle

f_{Power} = Ratio of actual to nominal injected power

The results listed in Tab. 7.2-4 show, that the maximum heat flux at the CC-BD during normal operation (2.5 MW/m^2) is only half as high as the design limit established in Subsect. 7.2.2, however during calibration, 8.7 MW/m^2 are obtained, which is close to the design limit in the calibration mode. This is therefore the limiting steady state operational mode. The high transient heat flux of 26.3 MW/m^2 during start up will be discussed in Subsect. 7.2.5. For the anchor-BD we are close to the design limit in normal operation, whereas during calibration there is a margin of more than a factor 2. Even the transient heat flux of 8.6 MW/m^2 could be dissipated continuously. The end dumps are designed to be loaded at the design limit of 5 MW/m^2 in normal operation. This applies to the four central inserts of the inner row (Fig. 7.2-6). The central inserts of the outer row are exposed to a maximum heat flux of about 3.5 MW/m^2. This shows, that the maximum heat flux could be reduced by further optimization.

The assumptions employed in evaluating the factors of Eq. 7.2-1 for the three dump types (CC-BDs, anchor-BDs and end dumps) and for the different operational modes as defined in Tab. 7.2-1 are summarized below.

Table 7.2-4: MAXIMUM LOCAL HEAT FLUX AT THE BEAM DUMP AND END DUMP (max χ)
AND FACTORS AFFECTING IT

| Dump | Operational Mode | Factors Eq.(7.2-1) | | | | | max χ (MW/m^2) |
		f_{Peak}	f_{Geo}	f_{Thru}	f_{Incl}	f_{Power}	
CC-BD	Normal Operation	2.0	0.3	.076	.33	1.0	2.5
	Calibration	1.6	0.3	1.0	.33	.33	8.7
	Start up	1.6	0.3	1.0	.33	1.0	26.3
Anchor-BD	Normal Operation	1.4	.152	.635	.5	1.0	4.8
	Calibration	1.6	.152	1.0	.5	0.5	4.3
	Start up	1.6	.152	1.0	.5	1.0	8.6
End Dump	Normal Operation	1.7	1.0	1.0	1.0	1.0	5.0

Nominal Injected Power P_{inj} and End Loss Power P_{el}

For the neutral beam injectors the nominal injected power is derived by the physical requirements (Tab. 7.2-2). The end loss power, which has to be dissipated at the end dumps, results from the following power balance for TASKA-M.

HE-NBI x trapping fraction	=	20.88 MW x 0.92	=	19.2 MW
LE-NBI x trapping fraction	=	0.6 MW x 1	=	.6 MW
ME-NBI x trapping fraction	=	2 x 3.5 MW x 0.37	=	2.6 MW
Electron Power				12.4 MW
Fusion Power in α- particles		6.8 MW x 0.2	=	1.36 MW
HE-NBI charge exchange loss			= -	5.63 MW
LE-NBI " " "			= -	0.18 MW
ME-NBI " " "			= -	0.41 MW

Total power loss to both ends   29.94 MW

Total power loss per end, P_{el} 15   MW

Beam Cross Section A_0 in the Reference Plane

The reference plane for the neutral beams is taken as the focus plane (see Paragraph "Geometric Dispersion Factor" below). The cross section is

thus $A_0 = 20^2 \cdot \pi/4 = 314$ cm^2 for the HE-NBI and $A_0 = 25.1^2 \cdot \pi/4 = 495$ cm^2 for the anchor-NBI. For the end dumps, the reference plane is taken at 19.5 m away from the mid point of TASKA-M, where the plasma cross section is an ellipse with a minor semi axis of 43.5 cm and a major semi axis of 368 cm, resulting in a cross section $A_0 = 50326$ cm^2.

Peaking Factor f_{peak}

This is the ratio of the maximum heat flux to the average heat flux through the plane considered (perpendicular to the beam axis). In case of the CC-BD and for normal operation it is assumed, that the effects of the incident beam power profile (Gaussian) and of the plasma density profile $(1- (r/R)^3$, r = distance from plasma axis, R = plasma radius) compensate each other, so that only the path length within the plasma determines the shine through profile. Adopting present parameters (plasma radius = 12.1 cm, beam radius in focus plane = 10 cm) yields a peaking factor of approx. 1.6. Since, however, the power peak is at the lateral edges of the foot print, and very sensitive to an offset between beam and plasma axes, a factor $f_{peak} = 2.0$ was assumed for this case. In case there is no plasma (calibration and start up mode), a peaking factor of 1.6 has been esti- mated, assuming a Gaussian distribution with a standard deviation of 70% of the beamlet divergence, (beamlet divergence is the divergence angle from Tab. 7.2-2 multiplied by the distance of the plane considered from the source) and all beamlets focused to a single point.

In the anchor beam the trapping fraction is very low (0.37), thus the profile of the shine through beam is, to a first approximation, similar to the profile in the undisturbed incident beam with the tendency to be flat- tened. For the latter the peaking factor is 1.6, as explained above. Taking into account some deduction for flattening, $f_{peak} = 1.4$ seems to be ad- equate for the power profile at the anchor-BD during normal operation. In the calibration and start up mode $f_{peak} = 1.6$ applies.

For the end dumps it is assumed, that the power profile is identical to the density profile within the plasma and that the density profile is unchanged with the axial coordinate, also in the end cells, where the plasma cross section is elliptic. Thus the profile is proportional to $(1-(r/R)^3)$ as explained above, R being the major or the minor semi axis depending on the direction. The integration of such a power profile yields a peaking factor of 1.7.

Geometric Dispersion Factor f_{Geo}

The NBI sources are assumed to be point focused, i.e. to the point of intersection of the plasma and NBI axes (Fig. 7.2-8). Due to the divergence angle of each beamlet, the foot print is circular in the focus plane (perpendicular to the beam axis) and enlarges to a rectangle with rounded corners in each plane behind the focus. The foot print area A (ζ) as a function of the distance from the focus is derived by simple geometric rules with reference to Fig. 7.2-8, and the geometric dispersion factor f_{Geo} is defined as the ratio of the foot print size in the reference plane (ζ = o) to the foot print size at the point of interest. For the beam dumps this is the intersection of the beam axis with the beam dump surface.

Using the parameters for the source envelope dimensions from Tab. 7.2-2 and for the dump distance from focus, yields a geometric dispersion factor f_{Geo} = 0.3 for the CC-BD and f_{Geo} = 0.152 for the anchor-BD.

For the end dumps the reference plane is chosen at 19.5 m from the mid point of TASKA-M, where the maximum loaded inserts have been placed (Fig. 7.2-6). Therefore the dispersion factor is by definition equal to unity.

Shine Through Factor f_{Thru}

The shine through factor is the supplement of the trapping fraction to unity. Trapping fractions are given in Tab. 7.2-2.

Attenuation Factor due to Inclination f_{Incl}

This factor is defined as

$$f_{Incl.} = \cos \phi \qquad (7.2-2)$$

where ϕ is the particle incidence angle measured to the dump surface normal. Due to beam dispersion and curvature of the dump surface, ϕ varies across the foot print. However both effects are small or zero at the point of maximum heat flux and are therefore neglected. Thus the nominal effective inclination angle at the beam center line as listed in Tab. 7.2-3 has been used in Eq. (7.2-2).

Power Factor f_{Power}

The power factor f_{Power} is the ratio of the actual to nominal injected power, the numerator of which varies with the different modes of operation as described in Subsect. 7.2.2 and as listed in Tab. 7.2-4.
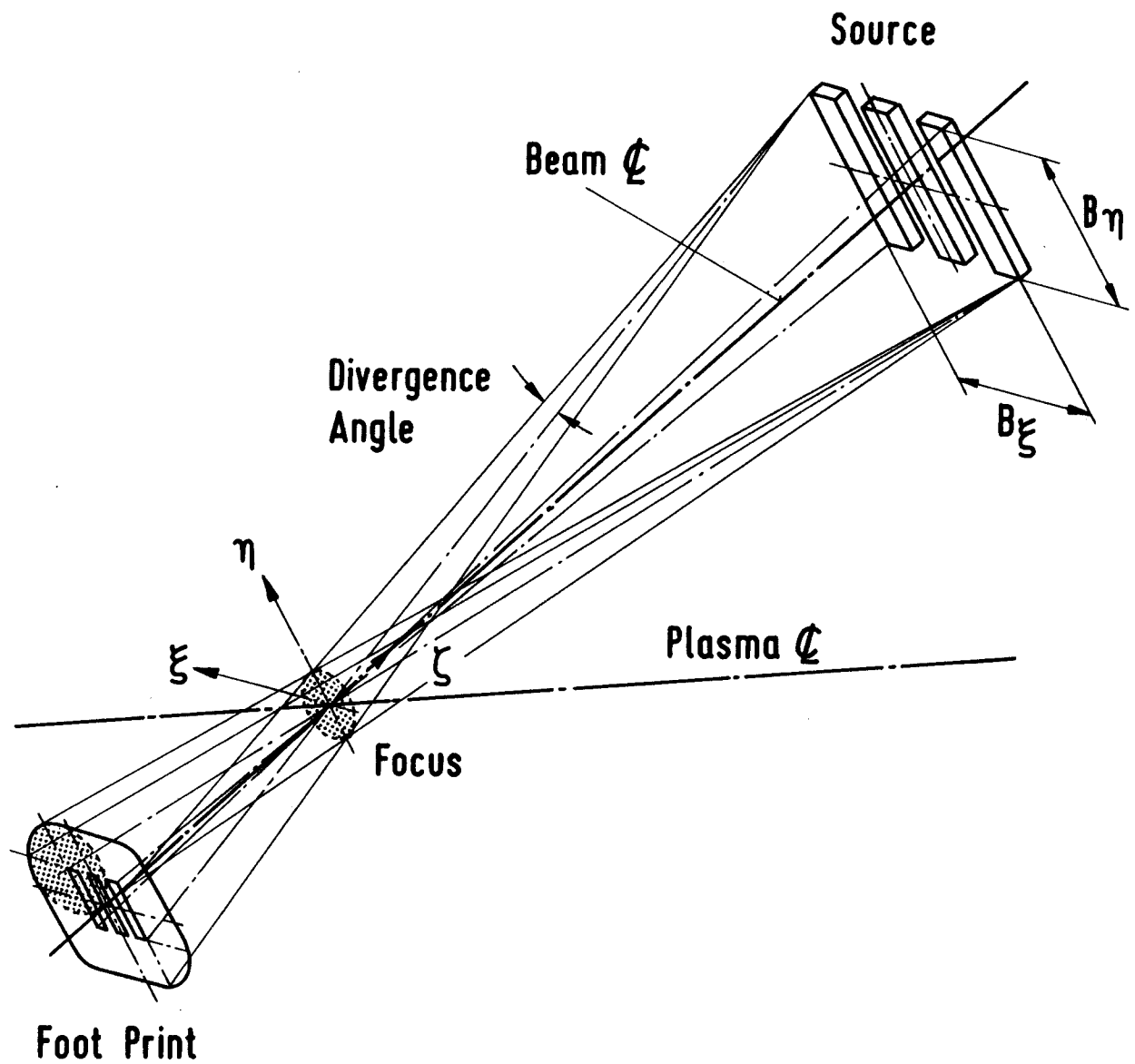
**FIG. 7.2-8 NEUTRAL BEAM FOOT PRINT IN A PLANE
PERPENDICULAR TO NBI-AXIS (Schematic)**

7.2.5 Thermohydraulic and Thermomechanical Performance
Required Coolant Flow

The cooling water is supplied to the individual Hypervapotron elements via the central inlet and outlet manifold, where orifices in the inlet nozzles provide for flow adjustment, corresponding to the integral heat load applied to the different elements. The flow path within the elements is described in Subsect. 7.2.3. In the following the required mass flow rate and the associated flow velocity and pressure drop will be characterized for the heaviest loaded element (termed as the hot element) and for the total beam dump.

In the CC-BD the hot element is located in the middle region of the dump, where the beam axes meets the dump surface. The heated surface area is $0.1 * 0.38$ m^2 = 0.038m^2 (Fig. 7.2-3) and the maximum steady state heat flux is 8.7 MW/m^2 in the calibration mode (Tab. 7.2-4). Assuming that the average heat flux at the hot element is 80% of the maximum value, leads to a total heat load of 0.264 MW. In order to dissipate this amount of heat a water flow rate of 2.1 l/s is necessary at a 30 K temperature rise. The bulk velocity in the Hypervapotron channel (Fig. 7.2-1) is 2.5 m/s and the pressure drop is in the order of 0.1 bar.

The total heat load applied to the CC-BD is 1.74 MW, requiring a water flow rate of 20 l/s at a 20 K temperature rise. The lower temperature rise of 20 K for the whole BD as compared to the 30 K value chosen for the hot element accounts for orificing uncertainties.

For the anchor-BD and the end dump the procedure is the same as for the CC-BD, and since the heat loads are similar, the results are in the same range. The required water flow rate for the hot element is 1.8 l/s and 2.2 l/s for the anchor-BD and for the end dumps, respectively. For the total beam dump insert the required water flow rates are 26.5 l/s and 20.3 l/s correspondingly. It should be noted, that in the case of the end dump the given values refer to the hot inserts, which are located in the inner row next to the plasma axis (Fig. 7.2-6). All the other inserts, in particular the central insert in the outer row, obtain less power due to overlapping and radial profile effects.

Steady State Surface Temperature

The temperature drop in a 6 mm Cu wall at a heat flux of 8.7 MW/m^2 (maximum steady state heat flux for the CC-BD, Tab. 7.2-4) is about 135 K. Assuming at the water side in the Hypervapotron grooves a wall temperature

of approximately 200 °C leads to a peak surface temperature of 335°C for the CC-BD in the calibration mode. During normal operation, the surface temperature will be in the range 230 to 250 °C. At the anchor-BDs and the end dumps the surface temperature will be somewhat higher (about 275°C) during normal operation . These numbers will not change significantly in case of a 1 mm thick Mo plating instead of the pure Cu version.

Transient Surface Temperature

Prior to the start up transient, the BDs are considered isothermal at approximately 60°C, which is the assumed coolant inlet temperature for steady state operation. During the transient, the surface temperature rise is determined by the thermal inertia only. Fig. 7.2-9 shows the transient surface temperature rise of a plate with infinite thickness at an arbitrary heat flux of 10 MW/m^2 for different wall materials. Applying the curve for copper at a heat flux of 26.3 MW/m^2 (Tab. 7.2-4) we find a temperature rise of about 350 K after 200 ms, at which time the plasma should be established (Subsect. 7.2.2). Thus we obtain a surface temperature peak of 410 °C, which then decays to the steady state temperature profile discussed above. As can be seen from Fig. 7.2-9 the transient temperature rise for other materials is higher than for copper, e.g. for molybdenum it is twice as high, leading to a peak surface temperature of 710°C. For the anchor-BD the transient peak load (8.6 MW/m^2) is much lower and is therefore covered by the CC-BD case.

It should be noted, that if for some reason the initial temperature is higher than 60°C, as for instance after a brief interruption, the peak temperatur could exceed design limits. This case would have to be investigated in more detail.

Thermal Stress

The thermal stress during the start up transient is to a first approximation equal to /5/:

$$S = \frac{\alpha \cdot E \cdot \Delta T}{(1 - \nu)} \qquad (7.2-3)$$

where α thermal expansion, E Young's modulus, ΔT transient surface temperature rise discussed in the previous paragraph, ν Poisson's ratio. For Cu (α = 17·10^{-6} K^{-1}, E = 120 GPa, ν = 0.3, ΔT=350 K) we obtain S $\simeq$ 1000 MPa, which is about twice as high as the double yield strength. In the case of Mo (α = 5.4·10^{-6} K^{-1}, E=300 GPa, ν = 0.32, ΔT = 650 K) we obtain S $\simeq$ 1500 MPa being
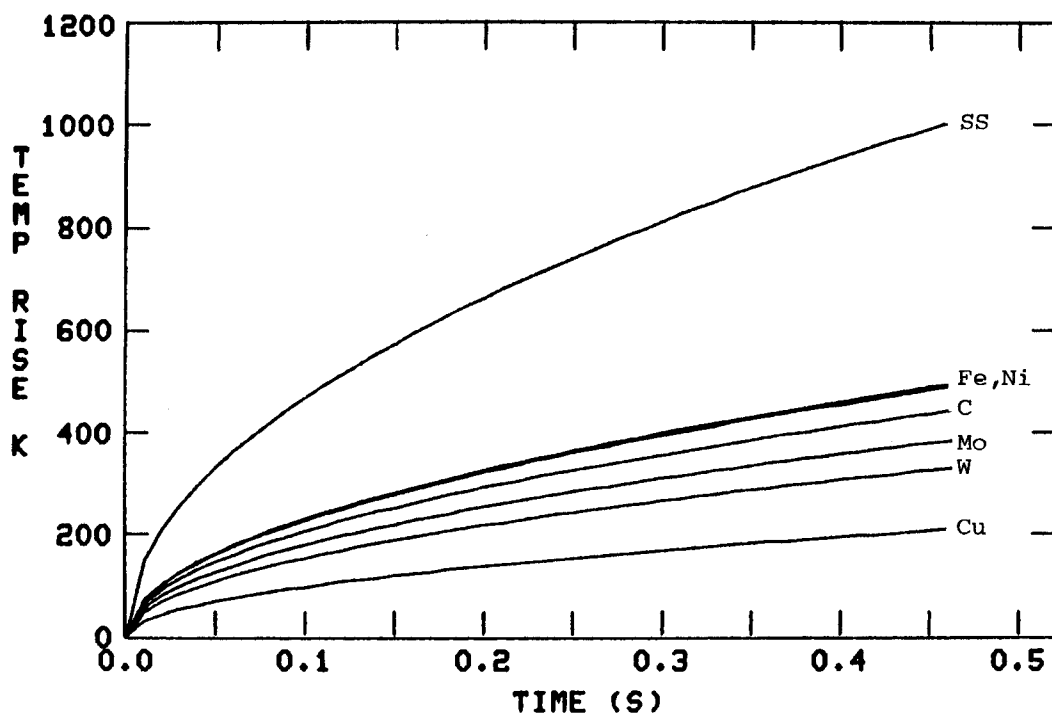
Fig. 7.2-9: Transient Surface Temperature Rise of a Plate with
infinite Thickness at a Heat Flux of 1 kW/cm^2
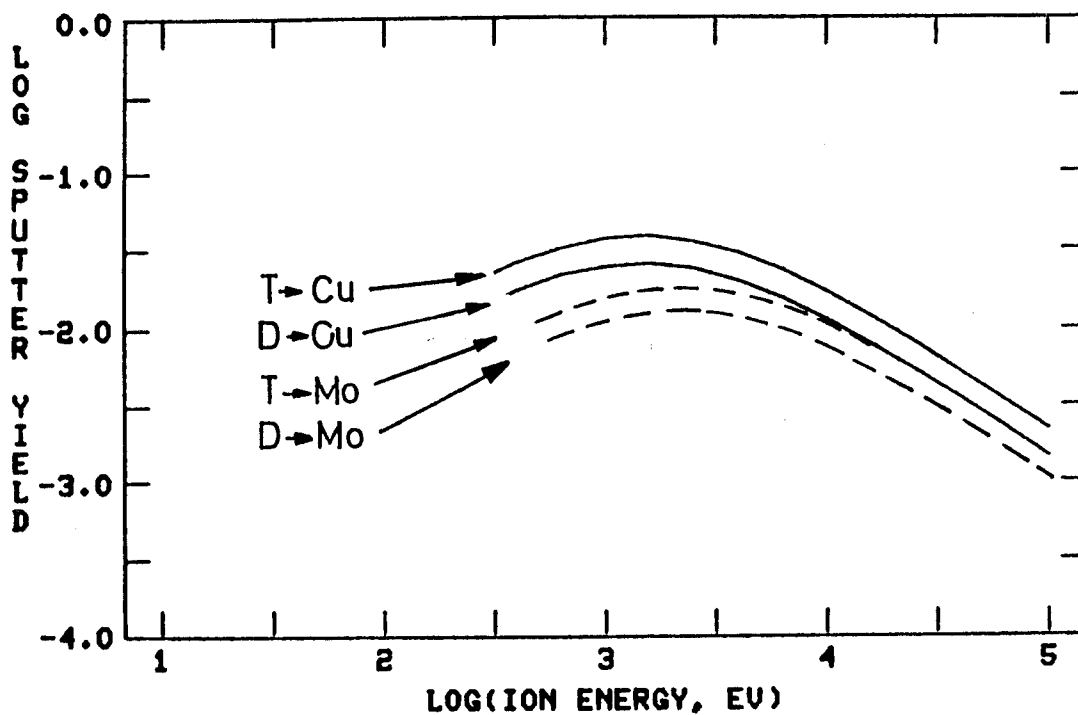
Fig. 7.2-10: Computed Sputtering Yield at normal Incidence
according to Eq. (7.2-6). Material Constants
for Cu (Mo): U_o = 3.52 (6.8) eV, M_2=63.5 (95.9)

close to the double yield strength. Thus, we cannot exclude surface cracks after a certain number of load cycles. At the anchor-BDs the transient thermal stresses are reduced to one third of the above values due to the lower heat flux.

In steady state operation the temperature and stress distributions within the Hypervapotron structure are very complex and have not yet been evaluated. However, applying a simple flat plate model with a linear temperature gradient, reveals thermal stresses below 200 MPa for the present BD and end dump design, which should be acceptable. An additional fatigue problem could arise with the concept of bonding a Mo layer onto a Cu substrate because of the different thermal expansion coefficients.

7.2.6 Sputtering and Lifetime

The wall erosion rate $\Delta w / \Delta t$ due to D,T ion bombardment (physical sputtering) has been calculated by use of Eq. (7.2-4)

$$\Delta w / \Delta t = \frac{M_2}{\rho \cdot L} (i_D S_D + i_T S_T) \qquad (7.2-4)$$

where M_2 target mass number, ρ target density, L Avogadro's number, i incident ion flux per unit area and S sputtering yield. Subscripts D and T refer to the D and T particle streams, respectively. The sputtering yield S in turn is a function of ion enery E and incident angle ϕ and is approximated by the empirical formula

$$S(E,\phi) = S(E,\phi=0) \cos^{-n} \phi \qquad (7.2-5)$$

where $S(E, \phi = 0)$ sputtering yield at normal incidence and n empirical constant. We assumed n = 1.8. The functions $S(E, \phi =0)$ are available in the literature for many ion-target combinations from measurements /6/ and can be numerically approximated by a model proposed by Smith /7/,

$$S(E,\phi=0) = \frac{20}{U_0} Z_1^2 Z_2^2 \frac{M_1}{M_2} \frac{E}{(E+50 \cdot Z_1 \cdot Z_2)^2} \qquad (7.2-6)$$

where S is in atoms per incident ion, and the incident particle energy E (Tab. 7.2-2) and surface binding energy U_0 are both in electron volts. Z and M are atomic and mass numbers with the subscripts 1 and 2 refering to the incident particles and target atoms, respectively. Fig. 7.2-10 shows the sputtering yield $S(E, \phi = 0)$ according to Eq. (7.2-6) for Copper and Molybdenum, which, in the energy regime $E > 1$ keV, are in reasonable agreement with available experimental data /6/.

In order to calculate the maximum local erosion rate, max. $\Delta w/\Delta t$, we have to use correspondingly in Eq. (7.2-4) the maximum local incident ion flux per unit area, max i, which can be derived in the same way as the maximum local heat flux using Eq. (7.2-1) by substituting P_{inj} by the D and T particle flow rate to the dumps, I_D and I_T, respectively (Tab. 7.2-2). In the case of the end dumps the additional small fraction of He particles (0.2%) has been added to the T fraction for simplicity.

Applying the above procedure for Copper as the reference material and for Molybdenum as a candidate plating material leads to the sputtering results listed in Tab. 7.2-5. The following constants were used for Cu (Mo): M_2 = 63.5 (95.9), Z_2 = 29 (42), ρ = 8.93 (10.2) g/cm^3, U_o= 3.52 (6.8) eV.

Table 7.2-5: BEAM AND END DUMP SPUTTERING RESULTS FOR CU AND MO SURFACE

	CC–BD		Anchor–BD		End Dump	
	Cu	Mo	Cu	Mo	Cu	Mo
Maximum Wall Erosion Rate (10^{-9}cm/s)	3.8	3.5	4.0	3.8	.43	.4
Sputtering Life Time (FPY)	0.8	0.9	0.8	0.8	7.4	8.0
Total Volume Sputter Rate (cm^3/FPY)	190	180	580	560	400	380

It follows from Tab. 7.2-5, that the sputtering life time for the CC-BDs and for the Anchor-BDs and for both materials is about the same, i.e. approximately 0.8 full power years (FPY), assuming a maximum allowable material loss of 1 mm. For the end dump the maximum wall erosion rate is about one order of magnitude lower than for the BDs. This is due to the lower particle flux per unit area and because of the normal particle incidence (ϕ =0 in Eq. 7.2-5). Thus the sputtering life time for the end dumps is expected to be in the order of 8 FPY, given an allowable wall loss of 1 mm. It should be noted, however, that due to the curvature of the surface of the individual end dump inserts the incidence angle increases towards the edges from ϕ = 0 up to ϕ = 90 degrees (Fig. 7.2-6), leading to enhanced

edge erosion. This can be compensated for by appropriate wall thickening in the edge regions.

The total sputtered volume, expected to be collected somewhere in the exhaust chambers, is in the order of 190 cm^3/FPY for one CC-BD and about 580 cm^3/FPY for one Anchor-BD. For one end dump (all 15 inserts) this amounts to approximately 400 cm^3/FPY (excluding the sputtering due to the halo end losses, which is estimated to be in the order of 15% of the plasma sputtering).

It should be noted, that the uncertainty of the sputtering assessment may be half an order of magnitude to both sides, which would have to be compensated for by adjusting the accumulated operating time and the allowable material loss, respectively, in the final analysis. Nevertheless it shows, that the target life time of 0.25 FPY can be easily attained.

7.2.7 Exhaust Channels

The philosophy of the CC evacuation system as described in Subsect. 7.3.2 is to keep the neutral gas pressure at the CC-BDs sufficiently low to prevent a net back flow from the BDs into the CC via the beam port (Fig. 7.2-11). Given a pressure in the CC, p_1, and a reasonable pressure at the exhaust channel exit, p_4, the required exhaust channel size can then be derived by empirical pressure drop calculations for the molecular flow regime as developed in /8/. For this assessment the shine through fraction of the high energy neutral beam is assumed to be released from the BD surface as a source term $\dot{M}$ and has to be pumped as a neutral gas through the exhaust channel.

Appling this model yields a required exhaust channel cross section at the exit of about 0.5 m^2 per one CC-BD, if the following data are employed: $p_1 = 3*10^{-5}$ mbar (this was a first result obtained from physics calculations, which later on was revised by applying a refined model, Subsect. 3.8.8),$p_4 = 6.6*10^{-6}$ mbar, $\dot{M}$ = 0.13 mg/s, molecular weight = 5, gas temperature = 500 K (this corresponds roughly to the BD surface temperature, Subsect 7.2.5). Since in the early design phase of the CC evacuation system there was the tendency to not only pump the shine through fraction of the HE-NBIs but also an appreciable amount of charge exchange (CX) gas from the CC, the exhaust channel cross section at the exit was chosen to be 0.8 m^2 per BD (instead of 0.5 m^2, if no CX gas had to be pumped). This leads to a cross section of the common exhaust channel of 4* 0,8 m^2 = 3,2 m^2, as it is designed in Figures 7.2-2 and 7.2-4.
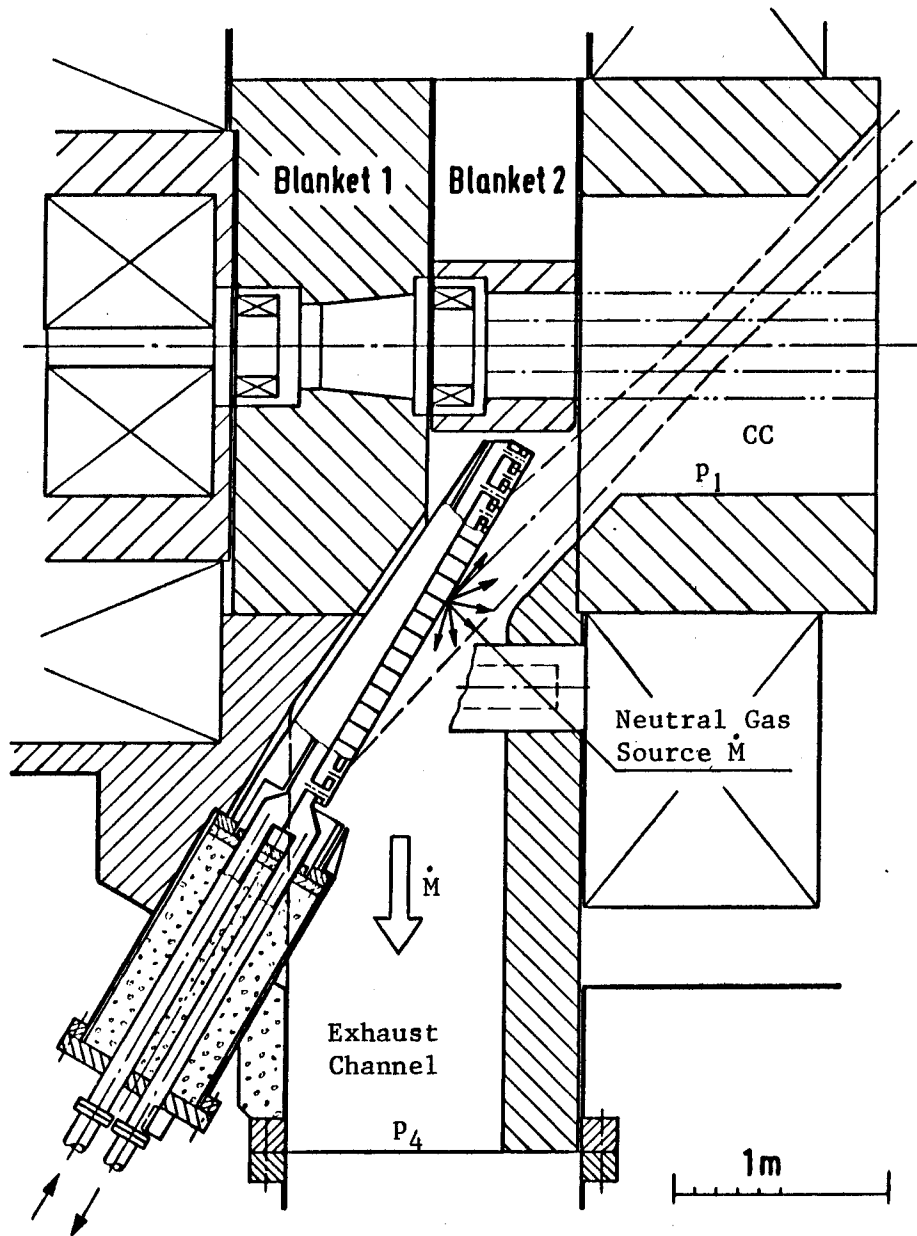
Fig. 7.2-11: Neutral Gas Pumping Model to determine the Exhaust
Channel Cross Section: Given p_1, p_4 and the Neutral
Gas Source Term $\dot{M}$, there shall be no net back flow
from the BD to the CC

Recent calculations of the halo pumping capability as described in Subsect. 3.8.8 revealed, that the halo is a very efficient pump for CX neutral gas from the recessed CC chamber to the end cells, and may even allow a certain back flow from the BDs via the CC chamber into the halo. If this could be proved, the exhaust channel size could be reduced to about 2 m^2 or even less. In this case also the cryopumps for the CC evacuation system (Fig. 7.3-4) could be reduced. However the gain in cryo surface would have to be added to the end cell evacuation system (Sect. 7.3).

The anchor-BDs do not have a separate evacuation system. The neutralized gas flows directly to the end cell evacuation system as indicated in Fig. 7.2-5.

References for Section 7.2

1. R. Haange: "Design of Calorimeter and Ion Dump for JET Neutral Injection Beam Line"; Proc. 9th Symp. on Engineering Problems of Fusion Research, Chicago, Oct. 1981, IEEE 81CH1715-2 NPS, p. 1352

2. B. Badger, F. Arendt, H.M. Attaya et al.:"TASKA - Tandem Spiegelmaschine Karlsruhe, A Tandem Mirror Fusion Engineering Test Facility"; Draft of KfK 3311, UWFDM-500, (1982)

3. H. Falter: JET Joint Undertaking, private communication

4. C.C. Thompson, D.H. Polk, D.J. McFarlin, R.R. Stone: "Heat Exchanger Concepts for Neutral Beam Calorimeters"; Proc. 9th Symposium on Engineering Problems of Fusion Research, Chicago, Oct. 1981, IEEE 81CH1715-2 NPS

5. R.J Roark: "Formulas for Stress and Strain", McGraw-Hill Book Co. New York and elsewhere, Fourth Edition , 1965

6. J. Roth, J. Bohdansky, W. Ottenburger: "Data on Low Energy Light Ion Sputtering", IPP 9/26, 1979 , Garching

7. D.L. Smith: "Physical Sputtering Model for Fusion Reactor First-Wall Materials", Journal of Nuc. Mat. 75 (1978), 20-31

8. S. Buch: "Einführung in die allgemeine Vakuumtechnik", Wissenschaftliche Verlagsgesellschaft MBH. Stuttgart 1962

7.3   Gas pumping Facilities

7.3.1 General Aspects

During operation the gas pressure in the annulus surrounding the plasma (in the so-called "Halo") and in the end cells must be kept below approximately 10^{-5} mbar. This requires a continuous removal of the supply gas streams, of all leak flows and of the gas quantities which may be liberated from the large internal surfaces. The evacuated gas must be compressed up to nearly atmospheric pressure before it is fed to the Tritium reprocessing system (See chapter 8).

Vacuum systems for such purpose usually consist of three different pumps. The first stage of such a pump train works in molecular flow regime (high vacuum), that is the pressure range below 10^{-3} mbar. Other pump types must be used in the medium pressure range between 10^{-3} mbar and 1 mbar. Forepumps work in the coarse vacuum range from 1 mbar up to 1000 mbar. The dominant factors for the design of the pumps last mentioned are the influence of gas pressure forces, heat loads and leak flows.

A short review of available pump types is given below in the sequence of their suction pressure region.

Typical high vacuum pumps are cryopumps, turbomolecular pumps, getter pumps and diffusion pumps.

Cyropumps are mainly used in fusion plants for first stages of pumping trains. Their advantages are: adaptability to high flow rates, no oil contamination, low price, especially if the refrigeration device is also needed for superconducting coil cooling.

Cryocondensation at 4.2 K is suitable for pumping all gases to pressures lower than 10^{-6} mbar, except Hydrogen and Helium. H_2 and He can be pumped by cryosorption and cryotrapping pumps. Cryosorption is explored extensively, especially with MS-5A absorption material (which is a resin bonded in organic molecular sieve /1; 2; 3; 4/). Cryotrapping uses an additional process gas, e.g. Ar, so that the H_2 and He becomes embedded in the solid Ar deposits. In both methods the ratio between H_2 and He must be considered. Generally, the H_2 fraction must be small, otherwise implanted He is displaced again by the excess H_2. For cryotrapping of one He atom about 30 Ar atoms are necessary. H_2, D_2, and T_2 have to be condensed before the gas stream reaches the trapping surface to exclude He-displacement.

The cryotrapping process seems to be preferable for the present conditions compared to the cryoadsorption process. In this way the disadvantages related to the latter, i.e. the ignition risk and the deterioration of the

adsorption material with increasing number of regeneration cycles, are avoided. Other pumps working in the molecular flow regime are ion- and titanium-sublimation pumps. However, getter pumps are restricted in their life time and the pumped gases are not completely recoverable.

Turbomolecular pumps are limited at present in suction flow to about 5000 l/s. These pumps are equipped with oil lubricated bearings so that the pumped gas may become somewhat contaminated, which is unacceptable for operation in a closed T-circuit. Only smaller units are fitted with magnetic bearings and fulfil the demand for not contaminating the gases. Generally, all molecular pumps need forepumps to establish the outlet pressure below 10^{-1} mbar.

With diffusion pumps, the contamination problems are even more aggravated. They would need additional provisions against oil-backstreaming and oil-carryover and it is uncertain whether the performance and the effectiveness of such provisions would be adequate.

For the medium pressure range roots pumps are suitable because they can be sealed hermetically. Special types with separately sealed gear boxes should be available when they are demanded /6/.

Forepumps that work in the viscous flow regime have to be hermetically sealed. The use of lubricants in contact with the gasstream is restricted. For this purpose metal bellows and diaphragm pumps are available from commercial sources and have been used extensively /7/. Scroll pumps are suitable for low volume flows. They can be used in the medium pressure regime also /8/. Larger pumps of this design show good volumetric efficiencies and can exhaust directly to atmospheric pressure. Rotating plunger pumps can be used for preevacuation purposes with lower risk of tritium contamination.

The pressure level at which the vacuum pumps of the high, the medium and the coarse vacuum range interface is a question of optimization. The cryopump process e.g.,allows in principle a high compression ratio. However, restrictions are given by the design details, e.g. the size of the dead space, the tightness of the vacuum valves, and the cooling and heating requirements. Detailed investigations of this kind could not be carried out within this work. All respective decisions were made on a qualitative basis taking into account existing vacuum installations and other design studies in the field of fusion engineering. Numerous alternative concepts seem feasible, e.g. the exclusive application of cryopumps in two successive stages shows some promise.

7.3.2 Design concept

The flow sheet of the gas pumping facilities is given in Fig. 7.3-1. Three different kinds of pump trains satisfy the exhaust requirements during operation:

- the D, T end cell trains which pump the majority of the gases (one train at each end cell)
- the He end cell trains using the Ar cryotrapping process (one train at each end cell)
- the D, T central cell trains (two parallel trains)

The subdivision of the whole pumping system allows the adaptation for the different gas compositions and independent operational sequences for each subsystem, e.g. for regeneration.

Each pump train is equipped with one or more cryopumps (data and design calculation see Subsect. 7.3.3), one turbomolecular pump, one boosterpump and one forepump. All mechanical pumps work without lubricant or are hermetically sealed against them to avoid contamination of the recycled gas. This and the required T-compatibility will require special R & D work. Additional pumps are connected to the He cryotrapping panels to allow the removal of He and Ar separate from D and T. These trains consist of a turbomolecular pump , a booster pump, a rotating plunger pump and a final cryopump cooled by liquid nitrogen. In these cryopumps the Ar is stripped from the stream, so that it is available for reuse after regeneration of these panels.

Redundancy requirements for cryopanel regeneration are met as follows: cross over pipes between the D, T and the He end cell trains and a smilar cross over connection between the two central cell trains provide two independent systems for each cryopump. There is no redundancy in each of the He/Ar removal systems. However, it is assumed, that the process characteristic and the regeneration sequence of these systems will allow to perform most of the routine repairs during plant operation.

As indicated in the flow sheet, the end cell cryopumps are installed within the vacuum boundary of the machine. In this way large gas ducts on the suction side of these pumps are avoided. To the contrary, the central cell cryopumps are located outside because of space and neutron shielding requirements. Ducts of relatively large cross section are necessary here. After the first compresssion stage carried out with the cryopumps, the duct sizes become generally moderate.

Pre-evacu-ation System | **Endcell Evacuation System** | **Beamdump Evacuation System** | **Endcell Evacuation System**

Ar Inlet

Ar Inlet

D,T to Regeneration
Ar to Reuse
He to Exhaust
to Offgas System

D, T, He Cryopump for Endcell
D, T Cryopump for Endcell
D, T Cryopump for beam dump

TM Pump
Boosterpump
Metalbellow Pump

Rotating Plunger Pump
Argon Trap
Oil Trap
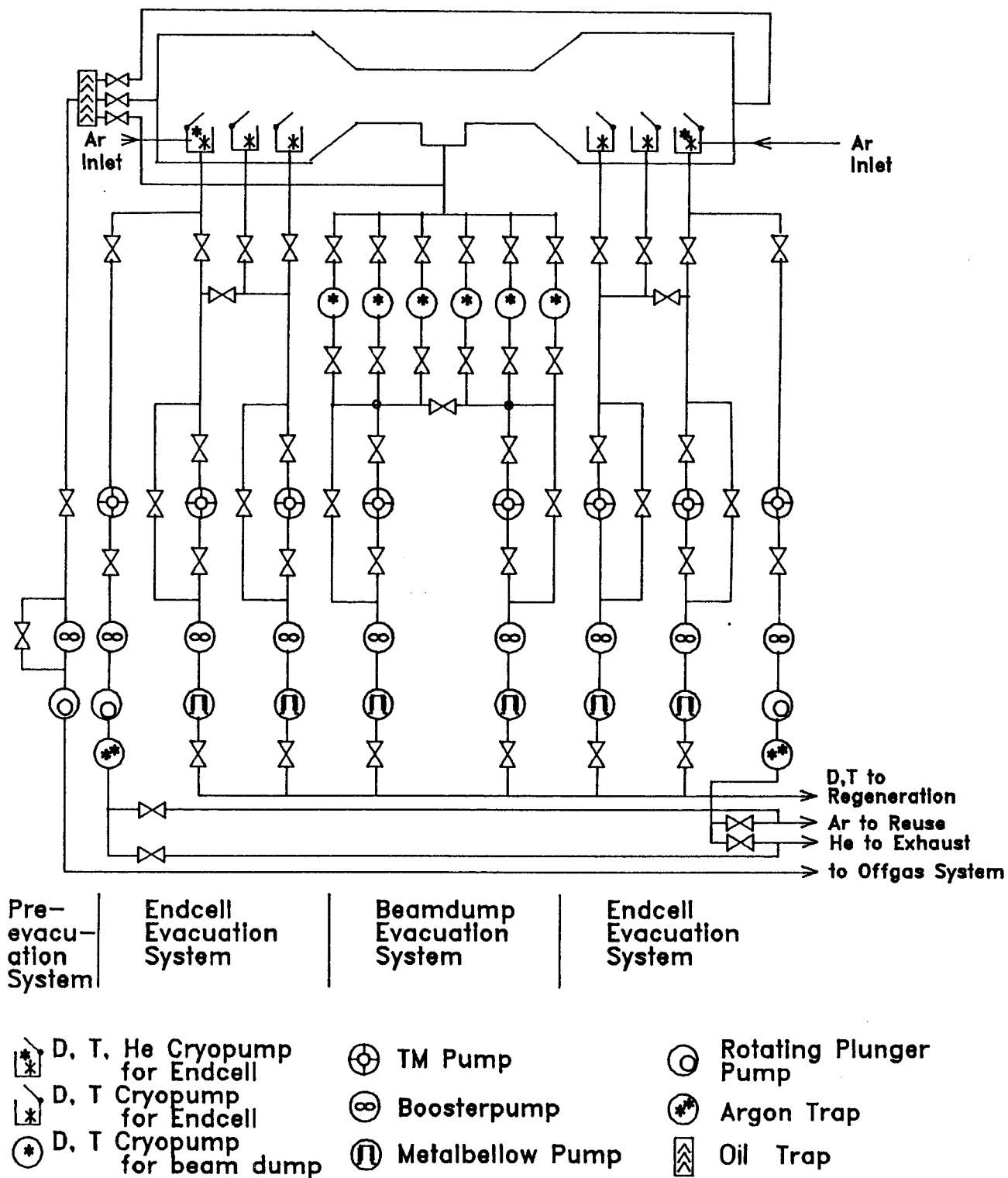
FIG. 7.3-1 VACUUM AND EXHAUST SYSTEM

For preoperational evacuation of the plant down to a pressure of approximately 10^{-3} mbar an additional start up vacuum system is provided, which feeds its effluent to the radioactive off gas systems. When this pressure level is reached, the other pump trains are started, first with non operating cryopumps. Finally, the cryopumps are activated to get the required start up vacuum within the facility of $\lesssim 10^{-6}$ mbar.

Regeneration of the cryopumps must take place during plant operation. To allow this, the total cryosurface of each subsystem is subdivided into a number of independent modules, and valves are installed also on the suction sides. After closing the inlet valve and the cryogenic system of one module, the respective cryopanel will heat up by radiative and convective heat transfer. In this way the condensed gas becomes liberated and the gas pressure in front of the cryopanels increases. The pressure gain is large enough so that the gas can be evacuated directly by the booster pump, while bypassing the turbomolecular pump. The turbomolecular pump is used finally to remove the rest of the gas and to decrease the gas pressure within the module to an adequately low level to allow to start the next operational cycle. All modules are regenerated successively in the same way.

The design basis for dimensioning the components are the process gas flow rates given in Fig. 7.1-1 and Tab. 7.1-1. Additional gas loadings as a result of leaks and residual degassing of internal parts and surfaces are not taken into account, because it is assumed that these contributions are negligible within the accuracy of this conceptual design study and in view of the comparatively large process gas streams. An exception was made only for the relatively low He process flow rate. This rate was increased by 10% as provision against possible He leaks of the liquid He cooled coils or in the cryopumps.

The cryopumps of the end cell systems for D, T and for He are located in the lower region of the end cells to minimize pressure loss. The pump pits are separated from upper parts of the end cells by water cooled shields, shaped like a coarse louvre type baffle. These shields are used to prevent excessive thermal radiation, to condense sputtered metallic atoms, and to catch coarse particles. The gas entrance of each pump pit can be closed by lids during regeneration.

Fig. 7.3-2 shows in a cross section the principal arrangement of one D, T cryopump. The total length of the vessel is 7 m, the length of the cryosurface 6,25 m. With 0.8 m height of the condensing panel, each pump contains about 10 m^2 cryosurface. In each end cell 8 pumps of this type are

Water Cooled
Cover Grid

Lid

Baffle

Condensing
Panel

LHe-Reservoir

Thermal
Shield

Thermal
Insulation

LN$_2$-Reservoir

1600
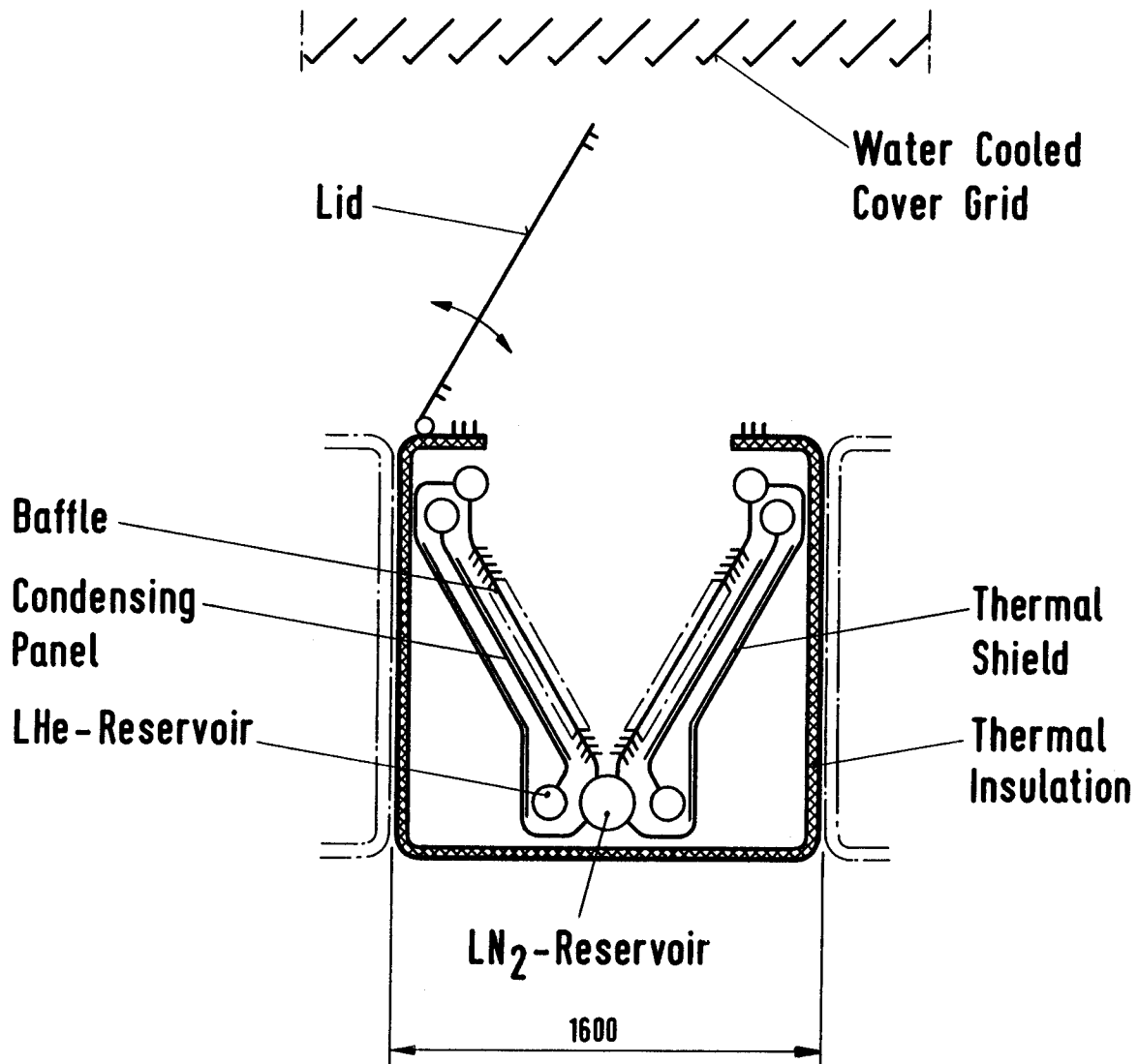
FIG. 7.3-2   D-T-CRYOPUMP (Cross Section)

Water Cooled
Cover Grid

Lid

1st Baffle

2nd Baffle

Ar - Injection
Grid

Condensing
Panel

Thermal
Shield

LN₂-Reservoir

Thermal
Insulation

LHe - Reservoir

1400
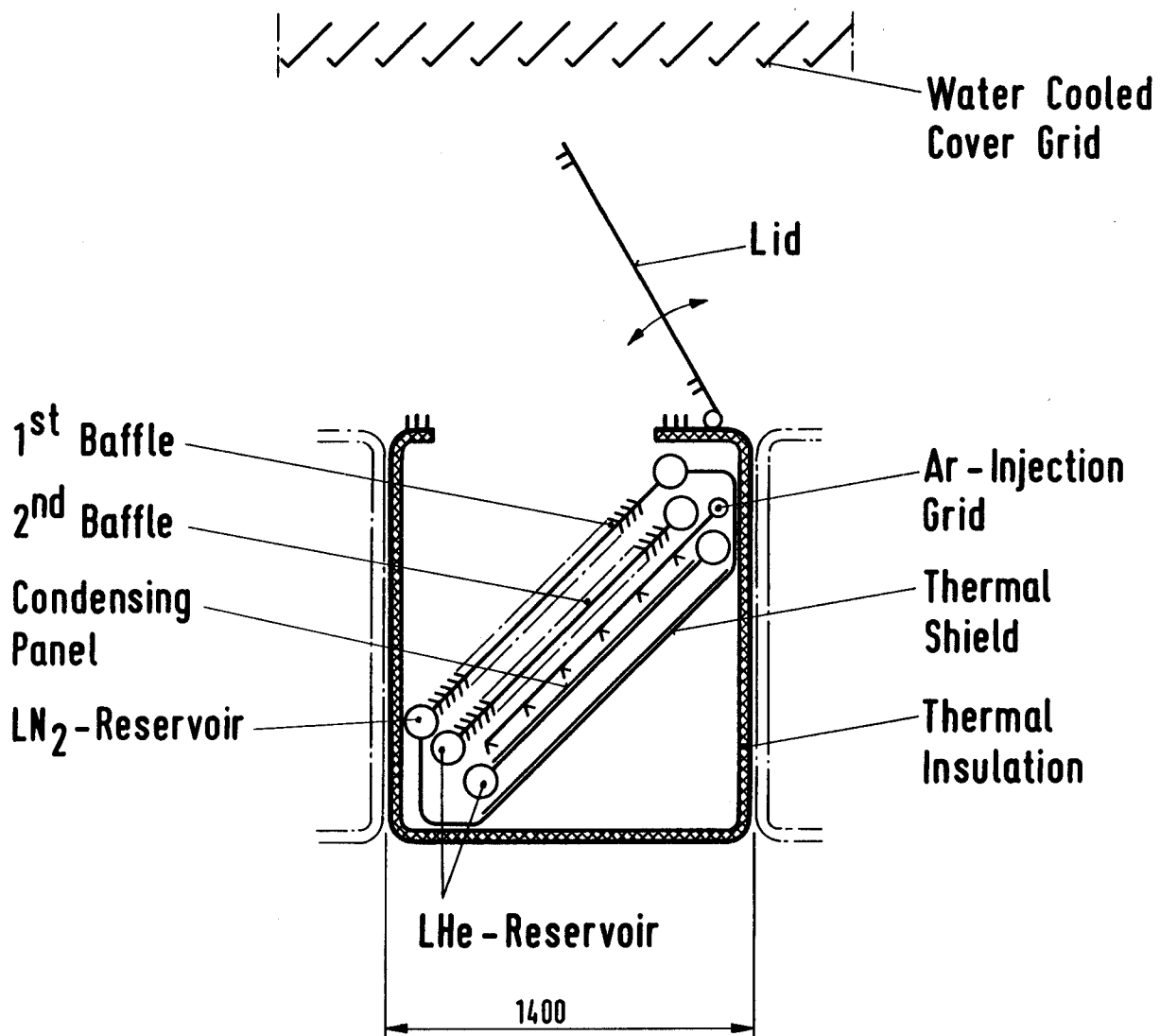
FIG. 7.3-3   HE - CRYOPUMP (Cross Section)

installed . The total pumping area of about 80 m^2 per end cell includes the reserve of approximately 25 % required for regeneration.

The He cryopump shown in Fig. 7.3-3 is of similar design. However, the additional Ar feed and distribution system in front of the cryosurface and a second baffle cooled by liquid He are necessary here.This baffle prevents the condensation of D and T on the cryotrapping surface. Two pumps with a cryotrapping surface of about 6 m^2 each are installed in each end cell. One of them is in operation, while the other one can be regenerated.

The regeneration process consists of the following steps:
1. sealing of pump vessel lid;
2. draining of lHe from cryosurface cooling system;
3. opening of cryopump outlet valve to connect the regeneration pump train (All pumps of the train work without interruption to keep their working temperature);
4. evacuation of released gases while bypassing the TM-pump (in this way the required elevated pressure level in the cryopump is maintained);
5. evacuation of the residual gas via TM-pump;
6. closing of cryopump outlet valve;
7. refilling of lHe circuit and cooling down of cryosurface;
8. reopening of pump vessel lid.

The pressure in the cryopump during regeneration should be discussed in some more detail. This pressure results from the balance between the gas flow released from the cryosurface, which depends on the heat transfer from the LN$_2$ cooled baffle and the backside shield to the cryoplate, and the gas flow extracted by the pump train, which is determined by the flow versus suction pressure characteristic of the pump train. Because the convective term of the heat transfer depends also on the gas pressure, the pressure in the cryopump actually feeds back to both sides of this balance. Such scheme can result in an unstable behavior and lead to an unacceptably high pressure burst causing a gas back flow to the plasma chamber via the imperfect seals of the vessel lid. To prevent this,the pumping characteristic of the pump train must be adapted to the thermal behaviour of the cryopumps. A pressure rise to about 10^{-2} mbar during regeneration should not be exceeded. This requires a pumping speed of aproximately 2000 m^3/h for a gas release time of about 30 min.

The CC evacuation system differs from the end cell system mainly in a lower suction pressure, the need of pipework for distribution, and no He pumping capability. Fig. 7.3-4 shows the external arrangement of

VIEW A

Main Floor

Cryogenic Supply

5 m

0

Central Cell Outlet Port

Regeneration Pipes

A

Guide Bearing

Roller Support

Cryopump Vessel
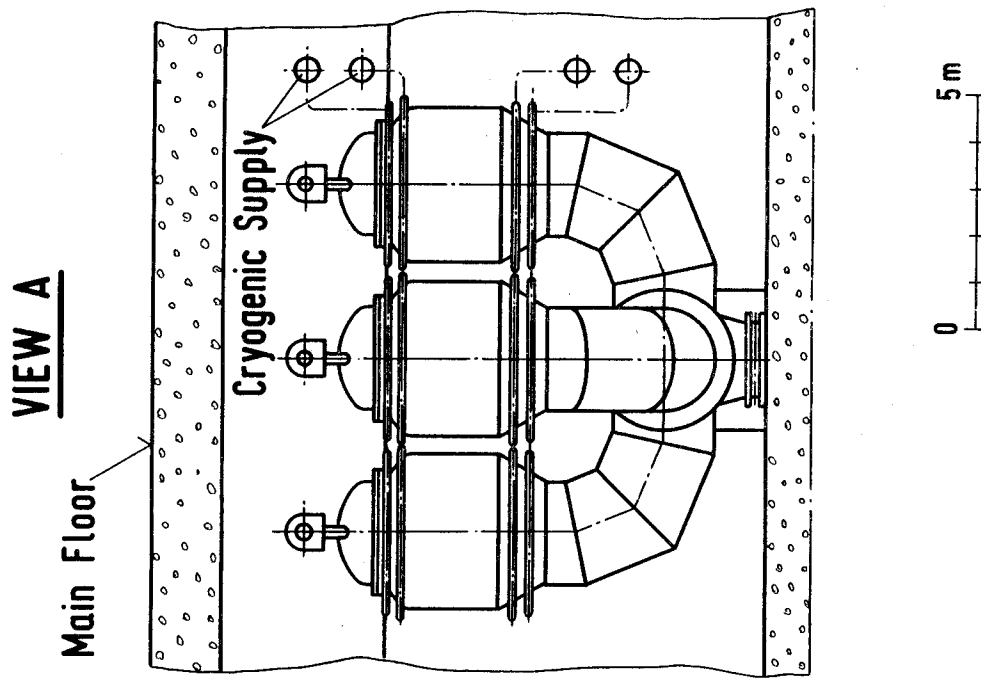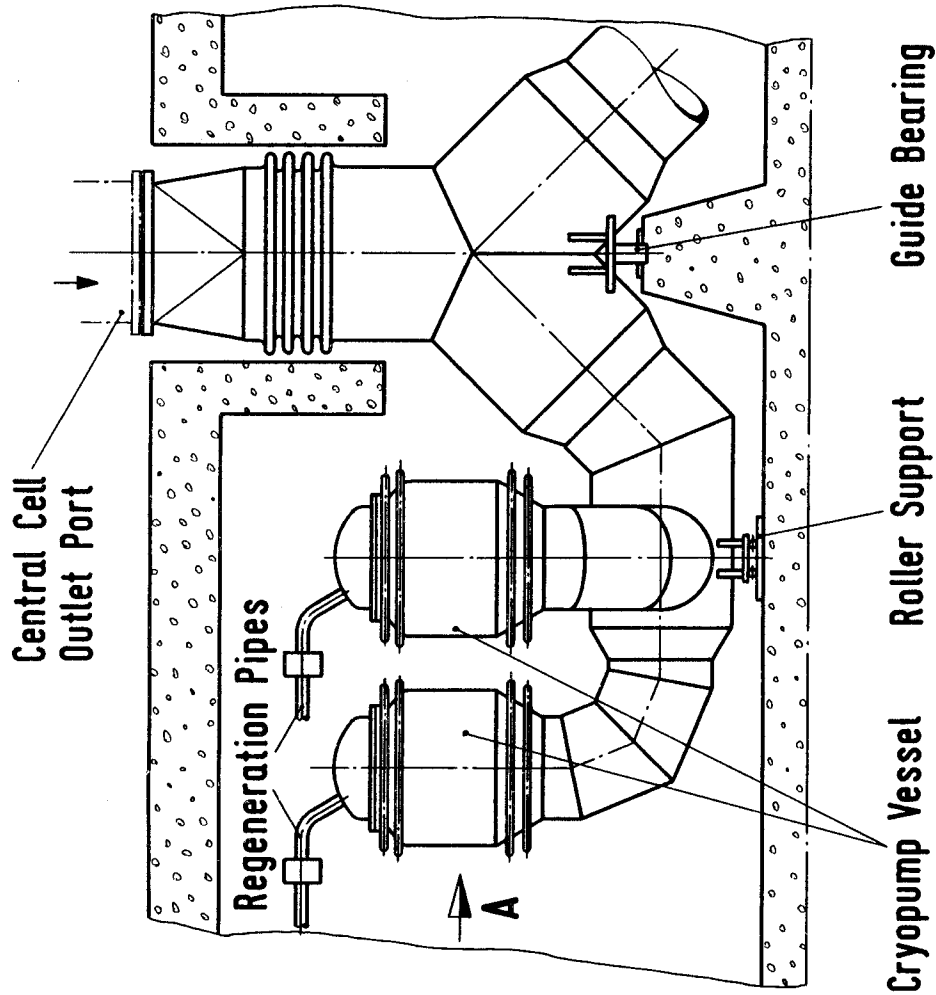
FIG. 7.3 -4 VACUUM DUCT AND CRYOPUMP ARRANGEMENT OF CENTRAL CELL EVACUATION SYSTEM

the cryopumps. All components are located below the main floor. The central duct is fitted to the outlet port with metal bellows to allow for thermal expansion, and distributes into two legs. Each leg supports 3 pump vessels with integrated valves.

The distance of the pumps from the outlet port eliminates all problems of additional radiation heating of cryosurface. It is expected that the deposition of sputtered material occurs before it reaches the pumps. A cross section of the cryopumps with the integrated valve mechanism is shown in Fig. 7.3-5. In the operational position, the valve dome is lifted by an elevator located in the upper section. The cylindrical cryosurface is protected by a chevron baffle at the inside and a lN_2 cooled shield at the outside. The cooling of the condensation area occurs by boiling He. Both cooling systems consist of a lower cryogenic collector, a system of coolant pipes for heat removal from the baffle and from the condensation surface and an upper collector for separation of liquid and gaseous cryogenics. The whole CC evacuation system consists of 6 pumps, 4 working while 2 are in regeneration mode.

The regeneration process of the CC cryopumps is essentially the same as for the end cell pumps described before. Sealing of the pump vessel is performed here by lowering the valve dome inside the pump vessel. It is expected, that with this valve design a better tightness can be reached than with the lids used in the end cell pumps. Consequently, during the regeneration process a higher gas pressure within the pump is tolerable. This offers some advantages, because the regeneration process is faster and the duct cross section of the pump train can be kept smaller due to the higher compression ratio of the cryopumps. The gas pressure in the cryopump during regeneration could be controlled also by active measures, such as heating systems for the cryopanels or throttling devices in the pump train. However, it is preferable if the requirement can be satisfied by the inherent characteristics of the whole system as described before.

The cycle time of the cryopumps must be defined with regard to (1) the maximum amount of tritium stored on the cryosurfaces, because this amount increases the total tritium inventory of the plant, (2) the risk potential in case of a major leakage with air intake and (3) the reduction of the pumping speed by an increasing layer of solid matter on the cryosurfaces. A qualitative assessment (see Subsect. 7.3.3) shows that for the actual conditions of this study the last two arguments are relatively unimportant because they gain weight only with extremely long cycle times or abnormal
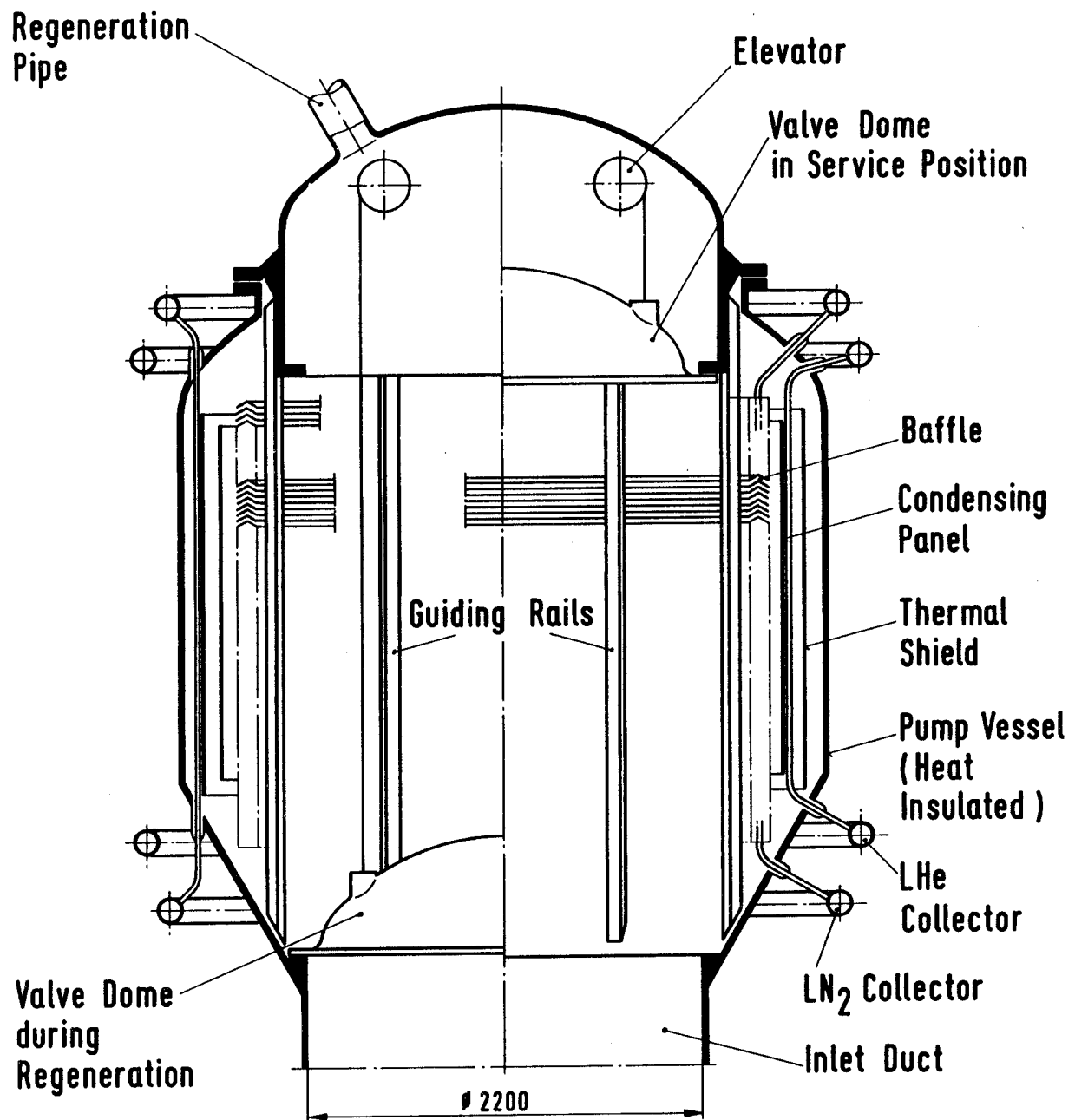
FIG. 7.3-5   CENTRAL CELL CRYOPUMP (Cross Section)

operating conditions. On the other hand short cycle times tend to increase cryogenic consumption. A cycle time of 8 hours and a time interval of about 2 hours to carry out the regeneration process seems to be an acceptable ratio for all cryopumps. Additional performance figures of the cryopumps are given in Subsect. 7.3.3.

7.3.3 Cryopump Assessment

For the pumping speed of a clean cryosurface the following equation holds /5/:

$$s = 36,38 \cdot a \cdot A \sqrt{T/M} \; (1 - p_s/p) \qquad (m^3/s)$$

with p gas pressure in front of cryosurface, p_s saturation gas pressure at surface temperature, T gas temperature in K, M molecular weight, A cryosurface size in m^2, a sticking coefficient, that is the ratio of the number of gas molecules which "stick" on the surface (i.e. become frozen) to the number of incident molecules.

In applying this equation for actual engineering tasks some additional problems must be considered. For instance, the assumption of a Maxwell distribution of the moving gas particles in front of the cryosurface is valid only if the cryosurface is small compared to the size of the vacuum chamber and for a uniform wall temperature of the vacuum chamber. This is not true in the present case. Other problems arise because the flow resistance within the gas conduit from the source (the dump surfaces) to the cryosurfaces must be taken into account. The available formulas are also based on a Maxwellian particle distribution before and after each single flow resistor. In reality, this assumption is violated and distinct streaming effects will take place. Therefore precise calculations in this field require the application of Monte Carlo methods.

If a gas mixture is pumped by a cryosurface as in the present case the situation becomes even more complex because the pumping speeds of the gas fractions differ and may not correspond to the delivered mass ratios. To get steady state conditions, a corresponding shift in the partial gas pressure ratios will take place in the gas conduit in front of the cryopump.

For a first assessment of the required size of the cryosurfaces a simplified method was used. In this calculation, the gas path is subdivided

into a number of subsequent sections, which represent the major resistors and a Maxwellian particle distribution is assumed throughout the gas conduit. For these conditions, the available simple formulas can be used /5/. This method leads to a certain overestimation of the pressure drops and the size of the cryosurfaces. Therefore, no extra safety margins were applied. The results of this calculation are listed in Tab. 7.3-1 and 7.3-2.

The calculation starts with the determination of the source term. The fuelling and exhaust flow rates within the facility are given in Tab. 7.1.1. At the end dump and beam dump plates the atoms recombine to molecules whereby also a DT fraction is generated /10/. The reference gas temperatures for the calculation of the energy throughputs were estimated to 330 K (mean value within the end cells) and 300 K (at machine outlet port). These temperature values are also used for the calculation of the flow conductances of the first sections of the flow paths. The gas temperatures for the subsequent sections are determined by the wall temperatures of the preceding sections.

The conductance values result from the following equation /5/:

$$C_i = A_i * w_i * v_i/4 \qquad (m^3/sec)$$

A = Flow Cross section $\qquad (m^2)$
w = Clausing Factor
v = $145,51 * (T/M)^{1/2}$
   = Mean particle velocity $\qquad (m/sec)$
T = Gas temperature $\qquad (K)$
M = Molecular weight
i = flow path section number $(i=1...n)$

The clausing factors for the cover grid and the chevrons depend on the geometric configuration of the baffle plates. If the inclination angle, the pitch and the width of the plates is such, that optical shine through in the main flow direction is just suppressed and the gap length is large compared to the gap width and plate pitch, respectively, then the situation is simplfied. In this case, the clausing factor depends exclusively on the inclination angle. For the present study, these conditions are postulated and inclination angles of 45 degrees for the cover grid plates and of 60 degrees for the chevron type baffles are assumed. The clausing factors for

Tab. 7.3-1 : End Cell Exhaust

		Deuterium	Deut.-Tritium	Tritium	Helium	Remarks
Gas sources:						
A. End dumps						*includes 10% safety margin to provide for leakages from SC coils and cryosurfaces
Incident atomic mass flow	(g/sec)	2.17E-3	-	1.87E-3	8.00E-6	
Released molecular mass flow	(g/sec)	1.38E-3	1.98E-3	6.88E-4	8.00E-6	
B. Anchor beam dumps						
Incident atomic mass flow	(g/sec)	7.03E-4	-	-	-	
Released molecular mass flow	(g/sec)	7.03E-4	-	-	-	
Total gas energy throughput (at 330 K)	(mbar*mE3/sec)	1.43E-2	1.08E-2	3.12E-3	6.04E-5*	
Flow path conductance:						
A. Cover grid, H2O cooled (300 K)						
Gas entrance temperature	(K)	330	330	330	330	
Flow cross section	(mE2)	49	49	49	49	
Mean particle velocity	(m/sec)	1322	1182	1079	1322	
Clausing factor	(-)	0.4	0.4	0.4	0.4	
Conductance	(mE3/sec)	6476	5792	5288	6476	
B. 1st Chevron, liqu. N2 cooled (77 K)						
Gas entrance temperature	(K)	300	300	300	300	
Flow cross section	(mE2)	66	66	66	6	
Mean particle velocity	(m/sec)	1260	1127	1029	1260	
Clausing factor	(-)	0.27	0.27	0.27	0.27	
Conductance	(mE3/sec)	5614	5021	4584	510	
C. 2nd Chevron, liqu. He cooled (5 K)						
Gas entrance temperature	(K)	-	-	-	77	
Flow cross section	(mE2)	-	-	-	6	
Mean particle velocity	(m/sec)	-	-	-	638	
Clausing factor	(-)	-	-	-	0.27	
Conductance	(mE3/sec)	-	-	-	259	
Total flow path conductance	(mE3/sec)	3007	2690	2455	179	
Pumping speeds:						
Gas entrance temperature	(K)	77	77	77	5	
Cryosurface size	(mE2)	66	66	66	6	
Mean particle velocity	(m/sec)	638.4	571.0	521.2	162.7	
Sticking factor	(-)	1	1	1	1	
Upper bound pumping speed (Surface temperature 5K)	(mE3/sec)	10534	9422	8601	(244)	
Effective pumping speed	(mE3/sec)	2339	2092	1910	(103)	
Gas pressures:						
Saturation pressure at surface	(mbar)	1.39E-7	1.29E-8	1.19E-9	(0)	
Partial pressure in end cell	(mbar)	4.97E-6	4.12E-6	1.29E-6	5.85E-7	
Total end cell pressure	(mbar / Torr)		1.10E-5 / 8.25E-6			

Tab. 7.3-2 : Central Cell Exhaust

		Deuterium	Deut.-Tritium	Tritium
Gas sources:				
Incident atomic mass flow	(g/sec)	2.05E-4	-	3.07E-4
Released molecular mass flow	(g/sec)	1.03E-4	2.55E-4	1.54E-4
Gas energy throughput (at 300 K)	(mbar*mE3/sec)	6.33E-4	1.26E-3	6.33E-4
Flow path conductance:				
Gas temperature	(K)	300	300	300
Mean particle velocity	(m/sec)	1256	1123	1025
A. Vertical duct				
Internal diameter	(m)	3.7	3.7	3.7
Characteristic length	(m)	7.25	7.25	7.25
Conductance	(mE3/sec)	1219	1090	994
B. Branch Pipes (two pipes parallel)				
Internal diameter	(m)	3.2	3.2	3.2
Characteristic length	(m)	8.00	8.00	8.00
Conductance	(mE3/sec)	1568	1402	1279
C. Ellbows (four ellbows parallel)				
Internal diameter	(m)	2.3	2.3	2.3
Characteristic length	(m)	4.25	4.25	4.25
Conductance	(mE3/sec)	1950	1743	1591
D. Chevron, liqu. N2 cooled (77 K)				
Flow cross section	(mE2)	54.8	54.8	54.8
Clausing factor	(-)	0.27	0.27	0.27
Conductance	(mE3/sec)	4645	4153	3790
Total flow path conductance	(mE3/sec)	457.4	409.0	373.1
Pumping speeds:				
Gas entrance temperature	(K)	77	77	77
Mean particle velocity	(m/sec)	636.2	568.8	519.1
Cryosurface size	(mE2)	54.8	54.8	54.8
Cryosurface temperature	(K)	5	5	5
Sticking factor	(-)	1	1	1
Upper bound pumping speed	(mE3/sec)	8716	7792	7112
Effective pumping speed	(mE3/sec)	435	389	355
Gas pressures:				
Saturation pressure at surface	(mbar)	1.39E-7	1.29E-8	1.19E-9
Partial pressure at CC outlet port	(mbar)	1.60E-6	3.27E-6	1.79E-6
Total pressure at CC outlet port	(mbar / Torr)	6.65E-6 / 4.99E-6		

the circular ducts of the CC-exhaust depend on the length to diameter ratio of the respective section. Bends are of no concern because of the molecular flow regime.

For the total flow path conductances the following equation holds:

$$C_g = 1/(\Sigma \; 1/C_i)$$

The upper bound pumping speeds follow from the equation given at the beginning of this Subsection, neglecting the flow conductivities of the gas paths ($p \gg p_s$; $1-p_s/p \approx 1$). The effective pumping speeds take into account the real flow path conductance, according to

$$S_{eff} = 1/(1/S + 1/C_g)$$

Based on the effective pumping speeds it now has to be checked whether the assumed cryosurface sizes, the geometric parameters of the flow paths and the chosen temperature values result in acceptable total gas pressures within the end cell and at the CC outlet port. The pressure drops for the different gas fractions are given by the simple equation

$$\Delta p = p/S_{eff}$$

with p = gas energy throughput for end cell and outlet port temperatures, respectively.

These pressure drops are added to the saturation gas pressure at the cryosurface to get the partial pressures in the end cell and at the CC machine outlet port. Finally, the summarized partial gas pressures determine the total gas pressure within the end cell and at the CC-machine outlet port. The numerical values in Tab. 7.3.1 and 7.3.2 have to be fixed by an iterative process according to the requirements set forth in Sect. 7.1 for the end cell and in Subsect. 7.2.7 for the central cell.

The D_2, DT and T_2 saturation pressures at the cryosurface were calculated according to formulas and coefficients given in /10/. It is shown, that their influence on the results is negligible, because the values are 2 to 3 orders of magnitude smaller than the values of the pressure drops and partial pressures, respectively.

For the Ar cryotrapping process of the He pumps the He pressure in front of the cryosurface cannot be easily defined. It is assumed, that 100%

of the approaching He and Ar particles are captured (sticking factor 1, pressures ~0). Consequently the He partial pressure in the end cell depends only on the He pressure drop. As design goal it was specified, that the He partial pressure in the end cell can climb up to max. 5% of the total gas pressure and that such a He enrichment is acceptable for the plasma behavior. The cryosurface size of the He pumps and the respective geometric parameters of the flow path selected lead to a reference He partial pressure fraction of 4%. For comparison the He content of the incident mass flow amounts to 2% .

The assumption, that the large D_2, DT, T_2-cryosurfaces of the end and central cell exhaust do not pump any amount of He is a conservative one. Actually, also these surfaces will probably trapp significant fractions of He simultaneously with the gases mentioned before. The He figures given in Tab. 7.3-1 should be considered therefore as upper bound.

The thickness of the layer of condensed matter at the cryosurfaces increases with time at a rate of:

$$d = m/(A^* \rho),$$

with m condensed mass flow, A cryosurface size, ρ density of condensed layer. After the specified duty time of 6 hrs the thickness amounts to d= 0.02 mm for the end cell cryopumps and d= 0.003 mm for the CC cryopump (for the mean value of ρ = 100 kg/m^3 according to /5/). It is understood that such small values will not impair the heat transfer rate from the condensing gas to the liquid helium coolant.

The total mass of all hydrogen isotopes stored at the cryosurfaces under the conservative and unrealistic assumption that all pumps work in phase is, before regeneration, 116 g at the end dump pump and 15 g at the four CC pumps.

For a first rough estimation it is assumed that the design pressure of the end cell and the CC cryopump casings is 2 bar and a hydrogen - air explosion can yield a maximal pressure increase by a factor of 8. Consequently, it must be checked, whether at a pressure level of 0.25 bar the concentration of the hydrogen isotopes can be kept below the explosion limit of 4 Vol. % /11/ in case of a larger air leak in the vacuum boundary, because such an incident would impair the thermal insulation of the cryopumps and lead to the evaporation of the hydrogen isotopes condensed on the cryosurfaces.

The above mentioned masses of the frozen hydrogen isotopes correspond to a gas volume at 0.25 bar; 330 K of

$$v = (m * 22.4 / M * 1000) * (330/273) * (1.01325/0.25)$$

$$= 2.7 \ m^3 \ \text{for the end cell} \\ = 0.33 \ m^3 \ \text{for the CC cryopumps} \quad \left.\right\} \text{(for M = 5)}$$

Corresponding to these figures, the end cell volume amounts to approximately 1000 m^3 (7m width,10 m height, 16 m length) and the volume of the four CC cryopumps to approximately 100 m^3 (3.2 m diameter, 3.2 m height). Consequently, the concentration of the hydrogen isotopes in air reaches only some 0.3 Vol. %, which is well below the before mentioned limit. However, in a detailed safety analysis also abnormal operating conditions, such as operating the cryopumps at higher pressures of the hydrogen isotopes or over longer cycle times, and other effects, such as uncomplete mixing with the incoming air, would have to be considered. Nevertheless, for the present stage of the study it can be stated, that the design concept selected will not result in undue safety problems.

References for Section 7.3

1. P.W. Fisher, J.S. Watson: "Cryosorption pumping of Deuterium by MS-5A at temperatures above 4.2 K for fusion reactor application"; Journal of Vacuum Science and Technology 15 (1978) 2, p 741 - 744

2. P.W. Fisher, J.S. Watson: "Cryosorption pumping of 95% Deuterium - 5% Helium on molecular sieve-5A at 4.2 K"; Proceedings of the 7th Symposium on Engineering Problems of Fusion Research, Knoxville, Te, USA (1977) p. 1816-1819

3. T.S. Chou, H.J. Halama: "Cryopumping of Deuterium Hydrogen and Helium mixtures on smooth 4.2 K surfaces"; Proceedings of the 7th International Vacuum Congress and the third International Conference on Solid Surfaces, Vienna, Austria (1977), p. 65-71

4. C.F. Dillow, J. Palacios: "Cryogenic pumping of Helium, Hydrogen, and a 90% Hydrogen - 10% Helium Mixture"; Journal of Vacuum Science and Technology 16 (1979) 2

5. R.A. Haefer: "Kryo-Vakuumtechnik"; Springer Verlag, Berlin, Heidelberg, New York (1981)

6. P. Duval: "Diffusionspumpen, Turbomolekularpumpen oder Kryopumpen?" Vakuum Technik; 31 (1982) 4

7. Don O. Coffin: "A Tritium Compatible High Vacuum Pumping System"; Journal of Vacuum Science and Technology 20 (1982) 4

8. J.E. McCullough and F. Hirschfeld: Mech. Eng. 101 (1979) 46

9. Landold-Börnstein: "Zahlenwerte und Funktionen aus Physik, Chemie, Astronomie, Geophysik und Technik", IV. Band; 4. Teil; Bandteil B; Springer Verlag Berlin-Heidelberg-New York (1967)

10. P.C. Souers: "Cryogenic Hydrogen data pertinent to magnetic fusion energy" UCRL-52628 (1979), Lawrence Livermore Nat. Lab., USA

11. K. Nabert, G. Schön: "Sicherheitstechnische Kennzahlen brennbarer Gase und Dämpfe", 2. Auflage, Deutscher Eichverlag GmbH. Berlin (1963)

8. TRITIUM SYSTEM

8.1 Overview

8.1.1 Fuel Rates

The sole method of fuel delivery to the plasma is by means of the 4 D/T neutral beam injectors in the central cell. Because of the small burnup, 0.3% of fuel during each transit through the plasma, large amounts of fuel must be recycled each day; see flow diagram Fig. 8.1-1.

The complete flow diagram for the fuel cycle, Fig. 8.1-2, indicates that the recycled fuel must be purified and the hydrogen isotopic compositions re-adjusted before the fuel is returned to the D/T NBI's. In addition, a storage unit for a continuous supply of tritium fuel is required because the test tritium breeding blankets are not designed to supply the required fuel, 1.03 g T/FPd (full power day).

In addition to recycle of the fuel, deuterium and tritium gases are re-cycled within the NBI's because of the gas inefficiencies in the NBI's. The complete flow D/T system requires an extensive recycle network as shown, Fig. 8.1-2, and discussed in this section.

8.1.2 Tritium Inventory

Each of the equipment items shown in Fig. 8.1-2 has some residual tritium inventory during operation. This amount of tritium has been assessed in Table 8.1-1. These inventories should be kept as low as possible because of the radiological hazards of tritium and the initial cost of tritium. Of the total tritium inventory 206.7 g are needed to provide the active inventory to the fuel cycle components. If all the recycle components are operating satis-factorily, a simple relationship[1] shows that the machine can be started using only the active inventory to saturate all the components in ~ 4 FPd. During this time the fusion test facilities will consume 4.12 g T; therefore, a total of ~ 211 g T is required to start the test facility plus a 30 day fuel supply (31 g) to keep it operational. At a cost of 10^4/g T this represents an initial cost of 2.4 million dollars. At the time the test facility is de-signed, reliability studies of the fuel cycle components will be required in order to determine if this minimal startup inventory is adequate.

After the initial startup, the test facility will require 1.03 g T/FPd or 3.8 million dollars/FPY for the tritium fuel cost.

Table 8.1-1. Tritium Inventory

Location	T (g)
Active inventory	206.7
HE-NBI cryopanels	115.5
Central cell cryopanels	4.2
End plasma exhaust	
D/T cryopanels	49.0
He cryopanels	5.5
Fuel cleanup unit	2.5
Isotope separation system	30.0
Inactive inventory	66.
Fuel storage (30 day supply)	31.0
Structure (end-of-life)	< 1.0
Coolant water (end-of-life)	34.0
Blanket test modules	
Liquid lithium	5.8
Liquid LiPb	0.01
Ceramic pellets/yr	25.0

PLASMA FUEL CYCLE (Flow rate g/d)
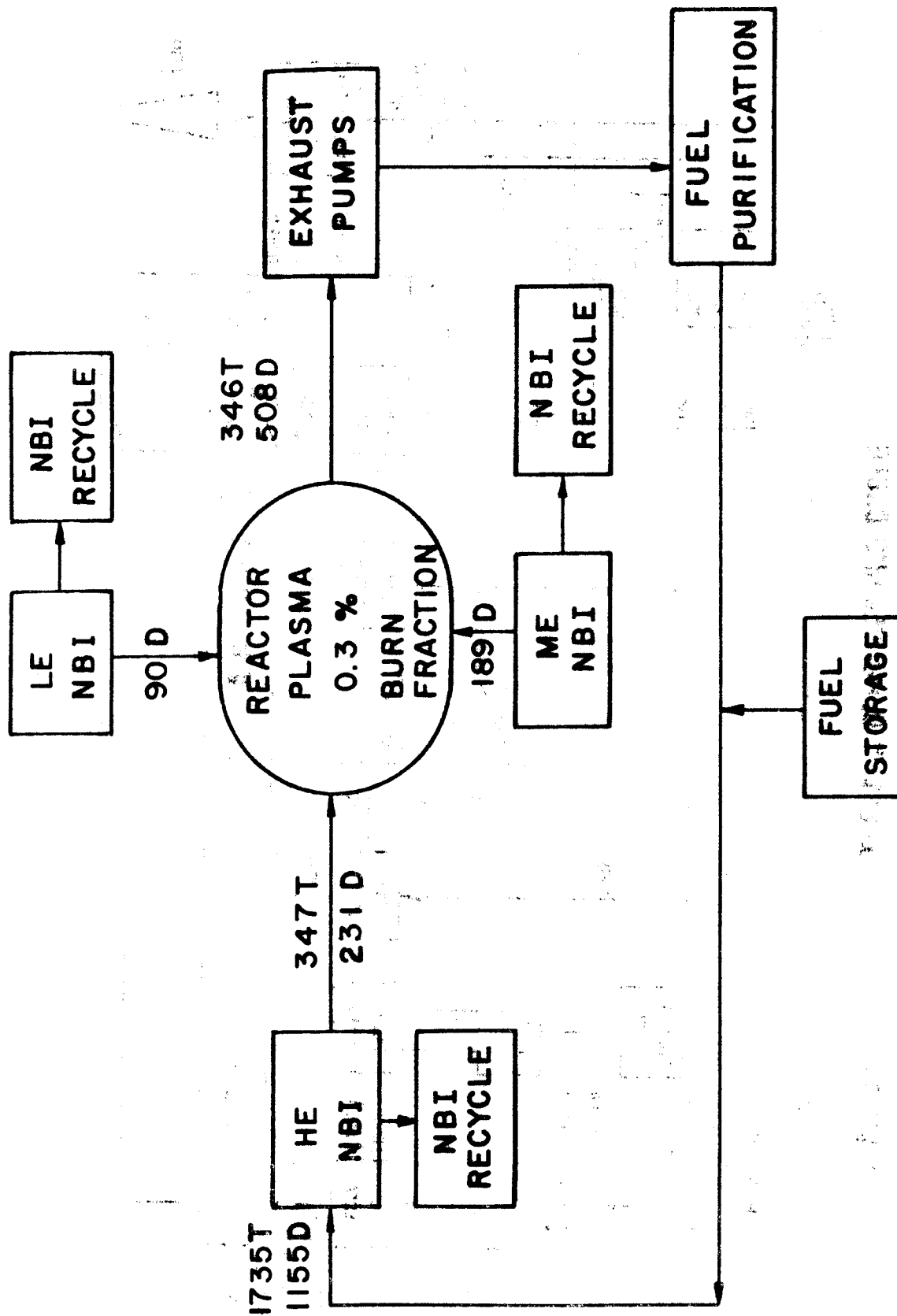
Fig. 8.1-1
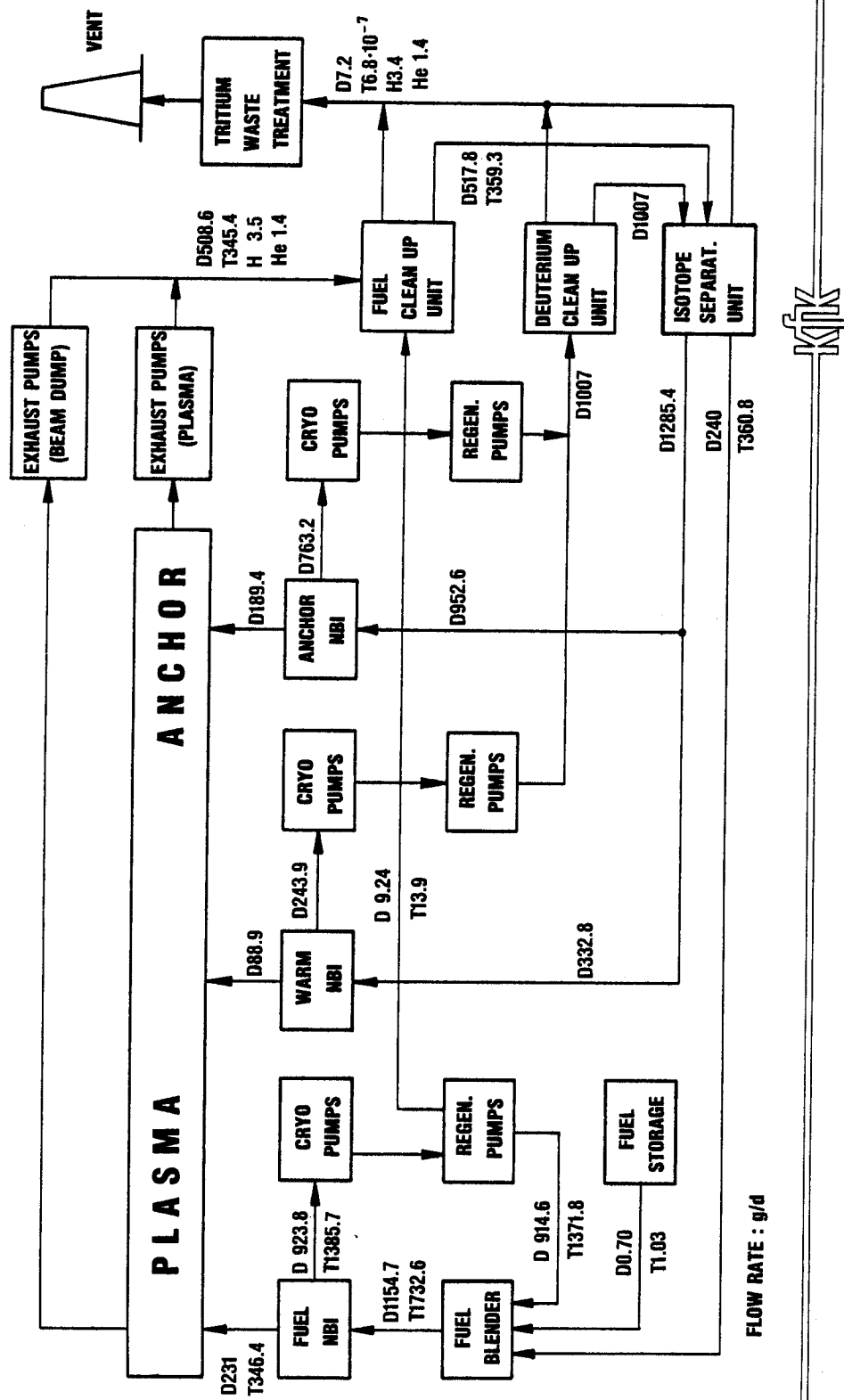
TASKA-M REPROCESSING CYCLE

FIG. 8.1-2 :

8.2 Fuel and Exhaust Systems

8.2.1 Neutral Beam Injectors (NBI)

8.2.1.1 D/T Fuel (HE-NBI). The sole method of fueling the test facility is by use of the 4 high energy, 90 kV NBI's located in the central cell. These injectors provide a combined power of 20.88 MW to the plasma at an average particle energy of 81 keV. The total beam flux of 258 A delivers a 50:50 mixture of D + T particles. The amount of fuel delivered is $\sim 8.05 \times 10^{20}$ T_0/s (4.01 mg/s) and $\sim 8.05 \times 10^{20}$ D_0/s (2.68 mg/s). Because of the small fraction of fuel which undergoes fusion, $\sim 0.3\%$, the majority of this fuel must be recovered by the vacuum system at the two end dumps.

The gas efficiency of these NBI's is assumed to be only 20%, i.e. neutral particles injected into the test facility compared to the gas atoms (supplied as molecular gas) to the NBI. The 4 NBI cryopanels are, therefore, accumulating fuel at the rate of 5.35 m mole/s ($D_2 + T_2$). As the panels are recycled this will also be the rate of release. Because the minimum time to recycle the cryopumps is ~ 2 hours, the inventory of fuel on the panels during this period is 115.5 g T_2 and 77.0 g D_2. In addition to the undelivered fuel on the cryopumps, these pumps also capture molecules which drift into the beam duct from the halo gas surrounding the plasma, at a pressure of 10^{-6} mbar and 673°K. Of particular concern is the protium impurity at a concentration of 1% in the plasma halo, which accumulates at the rate of $\sim 3.15 \times 10^{-8}$ mole H_2/s. If the H content, and other chemical or sputtered impurities did not accumulate on these cryopumps the entire off-gas from the cryopumps could be recycled to the NBI without purification; however, it is desirable to maintain the H atomic fraction of the fuel $< 10^{-3}$. The H content of the NBI cryopanels would reach 10^{-3} H atomic fraction in 140 recycles; therefore, a 1% side-stream of the cryopanel off-gas is diverted to the fuel cleanup system for chemical purification and removal of protium. The composition and flow rate of this side-stream is shown, Table 8.2-1. Because the H/(D + T) ratio is $\sim 10^{-3}$, the side-stream contains 8.8×10^{-8} g atoms H, mostly as HD.

8.2.1.2 NBI's Containing Only Deuterium. This category includes the one LE-NBI which supplies the warm beam ions to the central cell and the two ME-NBI's (one at each end) which supply the sloshing-ion density in the anchor regions. The gas efficiency of the LE-NBI is 27% while that of the ME-NBI is 20%. Because of the low gas efficiencies, a large amount of D_2 collects on the

Table 8.2-1. Compositions of Flow Streams from Plasma Exhaust and NBI Regeneration

| Molecular Species | Plasma Exhaust[a] μ mole/s | Neutral Beam Injectors (Cryopanel Regeneration) | | |
		HE-NBI[b] μ mole/s	LE-NBI[c] μ mole/s	ME-NBI[c] μ mole/s
H_2	8.7×10^{-2}	---	---	---
HD	33.4	5.4×10^{-2}	2.1×10^{-2}	1.05×10^{-2}
HT	7.8	5.4×10^{-2}	1.0×10^{-2}	0.5×10^{-2}
D_2	1009.2	13.4	2210	706
DT	911.2	26.7	1.5	0.8
T_2	208.3	13.4	---	---

CO, NO
$C(H,D,T)_4$ } ~ 3.0
$N(H,D,T)_3$
Argon

a) μmole/s $= 10^{-6}$ mole X_2/s
b) 1% recycle
c) 100% recycle

----

cryopumps in these NBI's and is subsequently released upon regeneration of the pumps. As shown in Table 8.2-1, each of the cryopumps of these three beam ducts will also trap impurity gas molecules which diffuse from the halo gas near the plasma at the rate of 7.4×10^{-7} mole DT/s, 1.05×10^{-8} mole HD/s and 0.5×10^{-8} mole HT/s. In this case, the atomic fraction T compared to D is ~ 5 $\times 10^{-4}$. It is desirable to keep this ratio $< 10^{-3}$ (T/D) so that the tritium contamination in the NBI is as low as possible for maintenance. These cryopump panels would reach the limit of tritium contamination in ~ two regeneration cycles; therefore, all of the gases adsorbed on these cryopumps are sent for chemical purification and the removal of tritium after each regeneration

cycle, according to the flow rate given in Table 8.2-1. These gases should not significantly increase the size of the Isotope Separation System because they can be inserted into the cascade of the distillation columns at a low tritium concentration point.

8.2.2 Exhaust Pumps

8.2.2.1 End Dumps. The cryopumps for the end cells are designed to be enclosed within the vacuum chamber; consequently, the pumps must be fitted with tight sealing covers which must be closed when the pump is being regenerated. Helium cooled cryopanel pumps are used to pump the hydrogen isotopes. For each end cell six of these pumps are in active use while two additional pumps are being regenerated. All of the cryopumps operate for 6 hours and are regenerated for 2 hours. The steady-state tritium inventory in these pumps is 49.0 g. The composition and flow rates of these gases are shown in Table 8.2-1. The protium H concentration is 1% of the total g·atoms D + T.

Two additional compound cryopumps are installed in each end cell to evacuate helium by the co-deposition of argon. These pumps also condense some D/T on cryobaffles in front of the argon panels. The inventory of tritium on the cryopanels is 5.5 g when two pumps are in use and two are being regenerated, based upon a 8-hour cycle.

8.2.2.2 Central Cell Beam Dump Pumps. The D/T neutral beam particles which shine through the plasma and impinge upon the beam dump rebound as thermalized molecular hydrogen species. These molecules are evacuated from the central cell by the use of cryopumps, four pumps active while two pumps are being regenerated. For a duty time of 8 hours (a regeneration time of 2.7 hours, duty time of 5.3 hours) the inventory of tritium is 4.24 g.

8.3 Fuel Reprocessing Systems

The fuel reprocessing system must chemically purify and isotopically adjust the hydrogen isotopes so that purified and blended fuel of the proper composition is recycled to the fuel injectors. The successful operation of this system is required with low tritium inventories because for this test facility > 99.7% of the fuel injected into the test facility must be recycled. In addition, the fuel reprocessing system accepts and purifies for recycle the gases condensed on the cryopanels within the NBI's. The flow diagram for the fuel reprocessing system, Fig. 8.1-2, specifies the types of apparatus re-

quired and the flow rates. These components and their tritium inventories are discussed in the following sections.

8.3.1 Fuel Cleanup Unit (FCU)

The FCU is required to remove in a continuous process the non-molecular hydrogenic constituents from the plasma exhaust gases listed in Table 8.2-1. In addition to the nearly 1 mole % H_2 impurity in the plasma exhaust, nearly 0.1% of additional impurities, carbon, oxygen, nitrogen and argon from the helium condensation pumps, appear as the chemical species shown in the table. The small amount, 1%, of the gases sent for purification from the D/T NBI's is blended with the plasma exhaust stream for cleanup because it has a similar composition.

Several chemical processing schemes[2] have been suggested for use in the FCU in order to remove the chemical impurities from the mixed hydrogen isotopic gases. The simplest and perhaps the least costly process, namely cryogenic adsorption of the impurity gases, is the primary method suggested for this test facility. In this process, the gas stream flows through a column of type 5A molecular sieves (MS) cooled in liquid nitrogen, 77°K. In this column the compounds CH_4, NH_3, H_2O, and argon from the helium cryopumps are more strongly absorbed than the hydrogen molecules. The effluent from the column is monitored until the most volatile impurity begins to appear, at which time the inlet stream is switched to a freshly regenerated column so that only purified gases flow to the Isotope Separation System (ISS).

The size of these columns can be estimated from TSTA data in which 1.6 kg MS is utilized for 356 moles H_2/d; therefore, the present columns should contain 860 g MS. Such columns containing the impurity gases, CH_4, NH_3, and Ar at 77°K also contain some mixed hydrogen isotopes at the concentration of 35 cm^3 (STP) H_2/g MS. As a result, the TASKA-M columns contain

$$860 \text{ g MS} \times \frac{35 \text{ cm}^3 \text{ } H_2}{\text{g MS}} = 1.35 \text{ moles } (D_2 + T_2) \text{ .}$$

Because the exhaust contains ~ 31% atomic % T, the regenerated gases from each column contains ~ 2.5 g T/d. This quantity of tritium would be too large to discard with the impurity gases; therefore, the loaded column is regenerated by slowly warming to ambient temperature so that the molecular hydrogenic species are preferentially desorbed before the chemical impurities. This

process is repeated through several adsorption/desorption cycles until the major fraction of the molecular hydrogen is sufficiently pure to introduce to the ISS.

Finally, the tritium bearing chemical species, such as CT_4 and NT_3 must be prepared for disposal. These gases are accumulated in a surge tank and monitored for their tritium content. If their tritium value were low, the gases would be sent to a Tritium Waste Treatment (TWT) system which would oxidize all the tritium to water and adsorb it on a desiccant. The volatile gases from the TWT are sufficiently low in tritium that they can be released; however, the tritiated water on the desiccant, which is retained for radioactive disposal, is usually too dilute to recover tritium economically. Consequently, if the impurity gases contain a large amount of tritium, they will be oxidized in a closed system so that all the tritiated water is recovered with minimal dilution. This water is subsequently decomposed by either electrolysis or by reactive metal, such as hot uranium, so that molecular hydrogenic species are formed and nonvolatile uranium oxide and nitrides are retained. The hydrogen gases are sent to the ISS for enrichment of the tritium.

A separate FCU is utilized for the chemical purification of the principally deuterium gases which are released from the cryopanels from the deuterium NBI's. These gases are similarly passed through a molecular sieve (MS) column at 77°K for the adsorption of the impurities and the purified hydrogenic gases are sent to the ISS. The size of the MS column in this case, which must process 252 moles D_2/d, should contain 1.15 kg MS. When one of these columns is ready for regeneration it will contain 1.8 moles D_2 plus a small amount of DT, e.g. 2×10^{-3} mole DT. As a result, the tritium inventory is ~ 6 mg T per column. The regenerated gases from this column are, subsequently, routed to the front end of the FCU for the plasma exhaust because the chemical impurities are small compared with those in the plasma exhaust.

8.3.2 Isotope Separation System (ISS)

The three part-streams arising from the fuel NBI and the exhaust (beam dump and plasma), the warm NBI and the anchor NBI are combined after the precleaning into two feed streams for the isotope separation system (Fig. 8.3-1).

The two feed streams with the composition as shown in table 8.3.-1 are decomposed in the ISS into three product streams.

Table 8.3-1: Feedstream composition (chemical equilibrium at 300 k)

	H	HD	HT	D	DT	T	
Fuel + exhaust	4.E-5	0.0151	3.2E-3	0.46	0.42	0.1	atom
Warm + anchor	-	-	-	1	-	-	fraction

The pure D- and T-components are recycled for addition to the D- and D/T-fuel streams. The protium separated is delivered to the offgas system. The quantity of protium is not specified in this study but for ISS design it is important to know which components are in the feed. That has a strong influence on the column configuration. Secondly the concentration range is of importance, therefore a reasonable value of 3.5 g/d is estimated.

Table 8.3-2 indicates the required composition of the product streams to be supplied by the isotope separation unit.

Table 8.3-2: Purity of product streams (atom fraction)

Waste $\qquad$ $T/(H + D)$ $\quad < 10^{-2}$ or better

Deuterium (D_2) $\quad T/D < 10^{-3}$ $\left.\begin{array}{l} \\ \\ \end{array}\right\}$ $\dfrac{H}{H + D + T} < 5 \cdot 10^{-4}$

Tritium ($DT + T_2$) $\quad T/D > 1$

ISOTOPE SEPARATION SYSTEM

FIG. 8.3-1

DEUTERIUM NEUTAL BEAM RETURN

D1007.1

D7.2

H 3.5
D335.1
T 1.9

EXHAUST

H 3.5
D518.5
T360.3

COLUMN I

EQUILIBRATOR I

H 3.5
D1349.4
T 1.9

H1.5·10⁻⁴
D183.4
T358.4

COLUMN II

H 3.5
D1292.7
T 1.1·10⁻²

EQUILIBRATOR II

H 3.8·10⁻⁵
D56.7
T1.8

VENT

H3.4
D7.2
T6.9·10⁻⁷

COLUMN III

H 0.1
D1285.5
T1.1·10⁻²

DEUTERIUM NEUTRAL BEAM

H 1.9·10⁻⁺
D240.1
T360.3

DEUTERIUM TRITIUM NEUTRAL BEAM

FLOW RATE : g/d

KfK

8.3-5
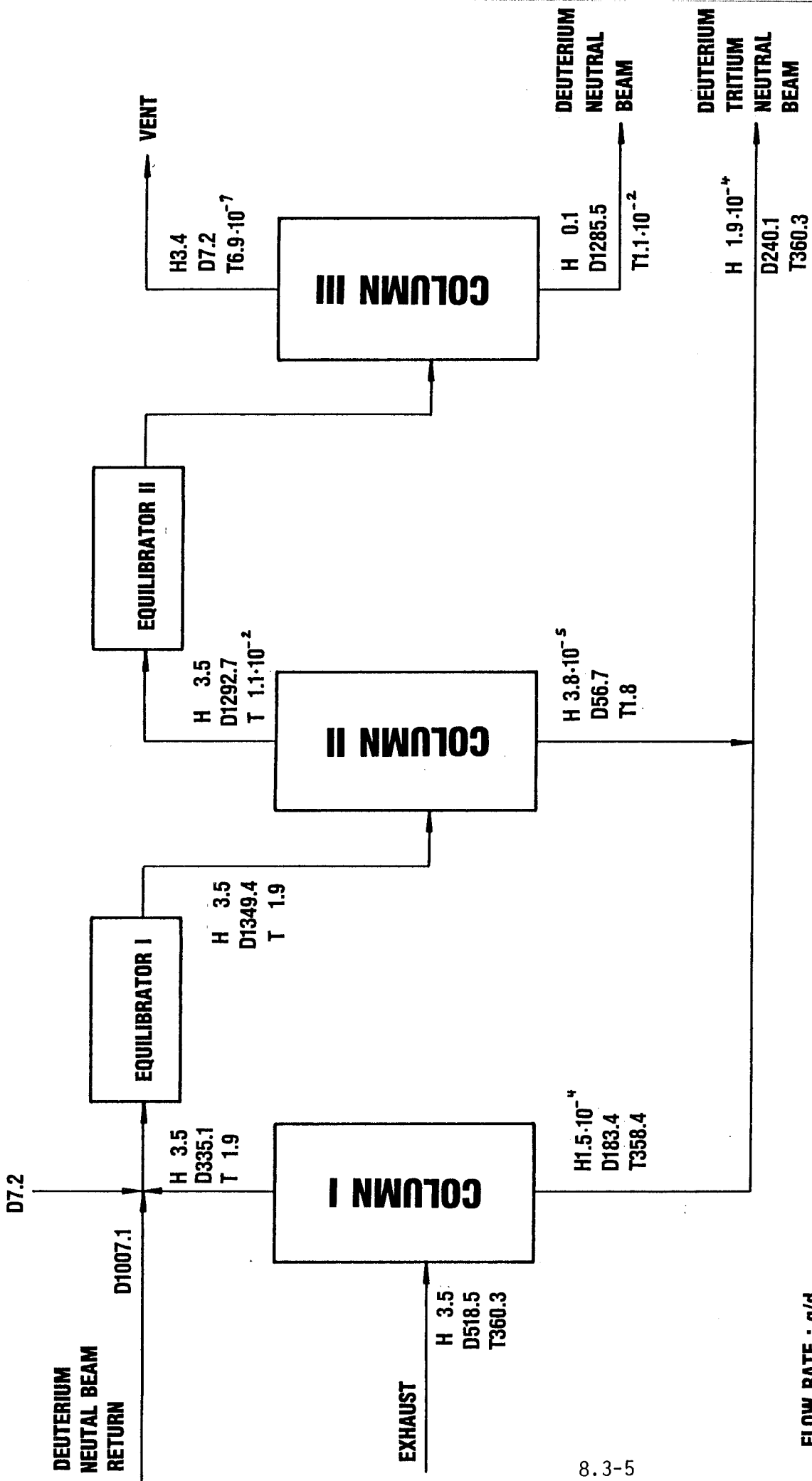
In TASKA-M, the technique of multi-stage distillation is used for isotope separation. The separtion effect is achieved on the basis of the sufficiently large difference in vapor pressure of the hydrogen isotopes (in the order of decreasing vapor pressures: H_2, HD, HT, D_2, DT, T_2).

The number of columns connected is determined roughly by the number of product streams required, while the purity of the streams is a function of the number of separation stages per column.

A column system has been calculated by means of the DEREK computer program /3/, the input and output streams of which meet the present TASKA-M specifications with a minimum activity inventory and minimum number of columns. Significant change in that specifications especially in product stream composition and purities require new calculations and design.

The DEREK program computes a cascade consisting of ideal separation stages; Table 8.3-3 shows the input and output parameters, respectively.

Figure 8.3-2 shows the liquid and vapor concentration of the hydrogen isotopes on each theoretical stage in column 1.

Table 8.3-3:   Input and output data of the DEREK code

Input	Output
columns pressure	Temperatur profile
Feed composition	Concentration profile
Number of theoretical stages	Activity inventory
Number of feed stage	Condenser and reboiler duty
Reflux ratio	Column geometry
Product streams	

The catalysts installed between the columns to shift the isotopic equilibrium were computed by means of the ISEQ program /4/.
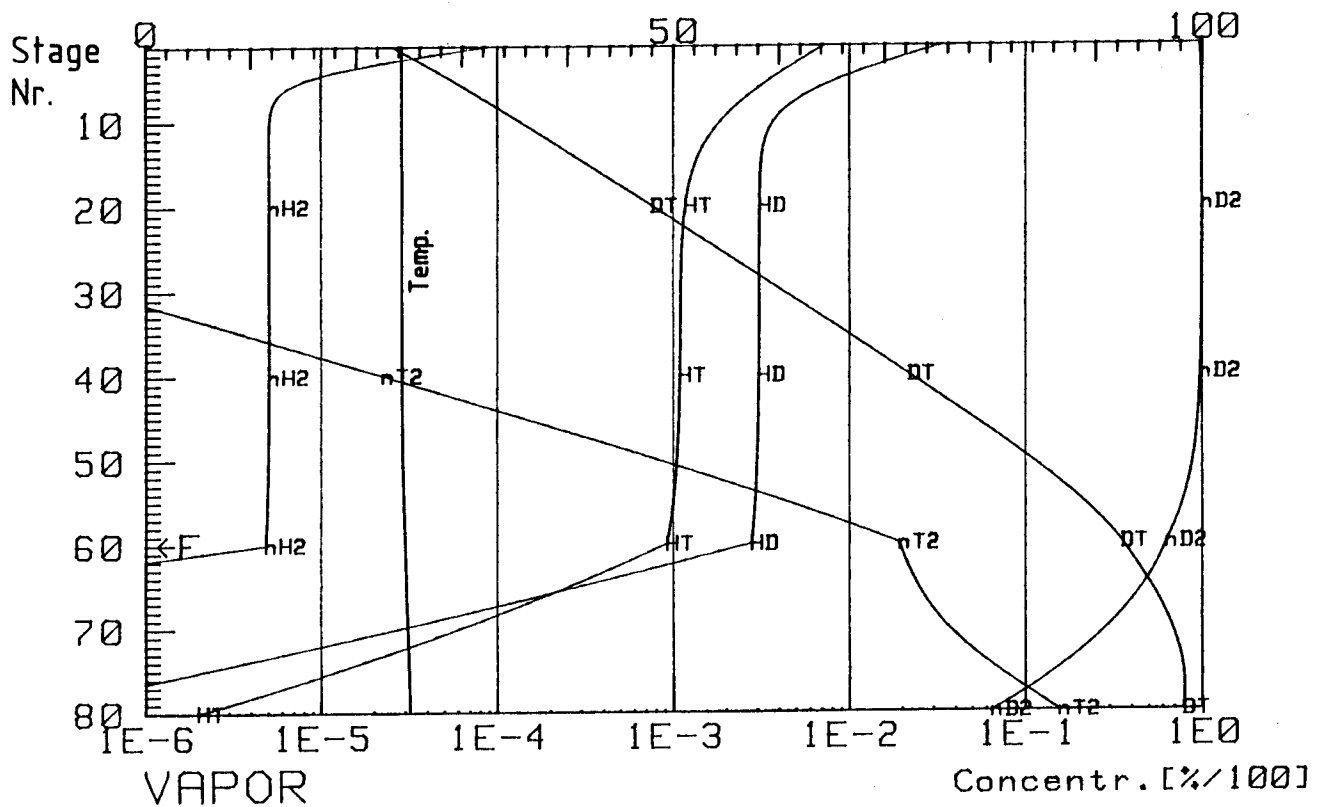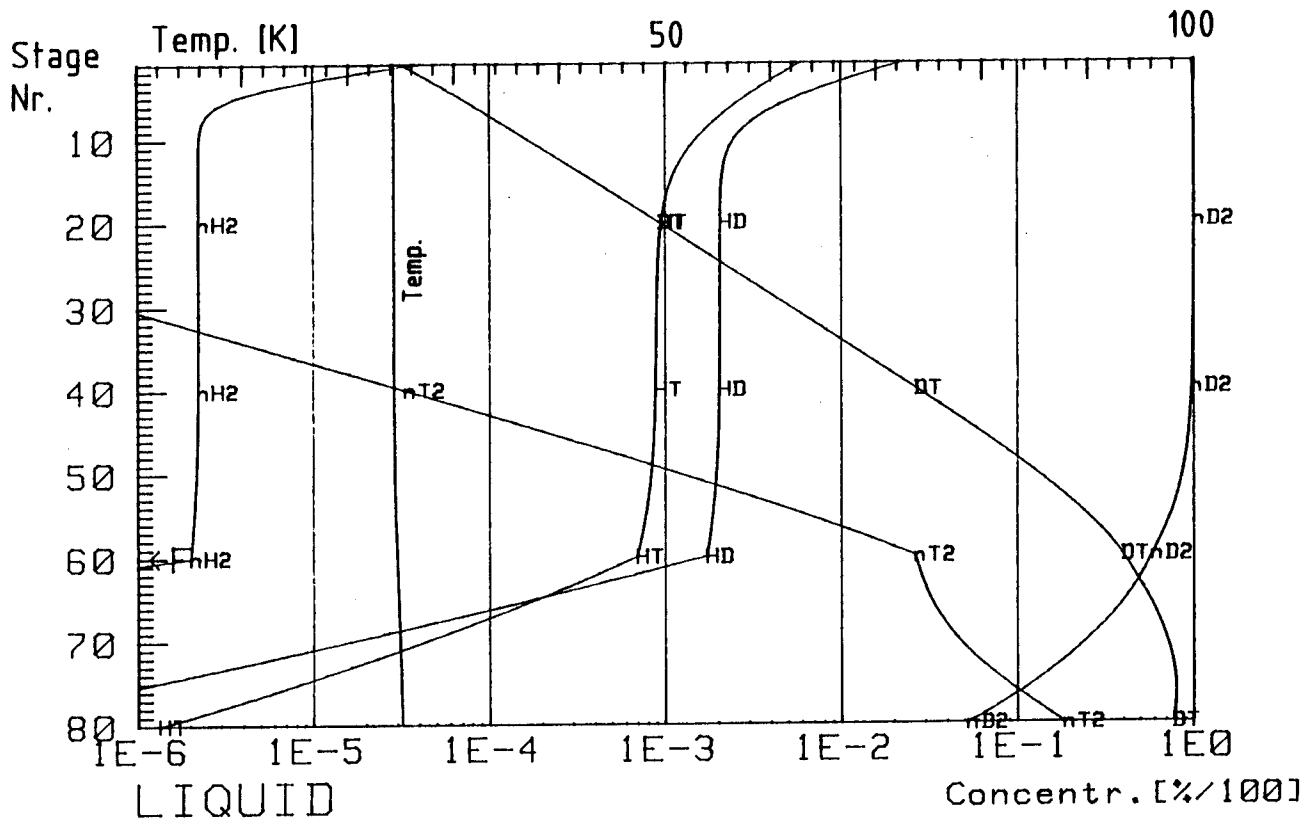
FIG. 8.3-2   CONCENTRATION PROFILES COLUMN 1

The design data as computed are summarized in the table below.

Table 8.3-4:   Design data

		Column		
		1	2	3
Diameter	mm	24	35	18
Length	mm	4000	3000	2500
No. of theor. Stages		80	60	50
Feed stage		60	45	7
Reflux ratio		30	17	500
Activity Inventory	Ci	286780	10791	3
Condenser Duty	Watt	63	137	31

All columns use as packings stainless steel helices 3 mm in diameter and
3 mm long. The length of a practical stage containing these packings is
about 50 mm (HETP - high equivalent of a theoretical plate).

The process computed comprises three series-connected separation columns
generating the gas streams for the D-neutral beam, the DT-neutral beam,
and the offgas system.

In the first column, the exhaust stream coming from the fuel cleanup stage
and contaminated essentially only with H is decomposed into a fraction
rich in tritium (bottom) and depleted in T (top). The T-D mixture extrac-
ted through the bottom only contains approx. 1 vppm of H, while the distil-
late contains 3600 vppm of T. To this distillate stream is added the
reflux stream of D-NBI coming from the deuterium cleanup stage, which
consists of essentially pure D with approximately 600 vppm T.

In the second column, the deuterium stream containing H and T is largely
stripped of T, which required the protium existing as HT to be transferred
into DT by shifting the chemical equilibrium in accordance with

$$HT + D_2 - HD + DT;$$

DT can be separated sufficiently well from the H-isotopes.

The shift in equilibrium is achieved by feeding D_2 to the distillate from column 1 and by means of a catalyst at room temperature /4/. This additional D stream is approx. proportional to the H concentration in the feed streams of column 1. The bottom product of the first and second column together makes up the D/T-NBI feed stream. In the third column the D-stream contaminated with H and T is decomposed into the offgas stream containing only 0.03 vppm of T and the D-NBI feed streams with 208 vppm H and 6 vppm T.

He, traces of which are contained in the exhaust as "fusion ash", goes into the waste stream as a gas together with the protium. The He-contamination of the NBI feed streams is < 1 vppm.

The total activity inventory of the isotope separation unit is approx. 30 g of tritium, the required refrigeration capacity of the columns is approx. 230 W.

8.3.3 Fuel Blending

High purity tritium fuel $(DT + T_2)$ from the ISS must be blended in the proper proportions with the deuterium supplied by the ISS to form an atomic ratio $T/D \sim 1$. The desired T/D composition of the fuel will depend upon the efficiency of the NBI's to feed mixed fuel and the operational characteristics sought by the test facility operator. To these constituents must be added D_2 and T_2 from storage to compensate for fuel no longer available because of: (1) consumption in the fusion reactions, (2) loss by permeation into both the test facility structure and coolant water, and (3) loss by chemical reactions in the reprocessing apparatus. This blending operation will be performed initially in a batch mode at a Blending Station. This station consists of a large surge tank equipped with agitators in order to thoroughly mix the gases. The composition of the tank will be determined before and after mixing by use of a mass spectrometer. Also, aliquots of the gases will be supplied to thermostatted chambers for P-V-T measurements and their tritium content determined by use of a beta gauge. With experience this blending can be done, perhaps, with the use of accurately calibrated flow gauges, pressure measurement devices, the mass spectrometer and the beta gauge. This blended fuel is sent to the D/T NBI inlet tanks.

8.3.4 Fuel Storage and Receiving

Both T and D fuel must be supplied from external sources to start the test facility. Also a continuous supply of fuel is required during operation because fuel is either consumed in the fusion process or lost in the reprocessing system. Tritium breeding in the test modules is not sufficient to supply fuel at the rate at which it is burned in the test facility. For instance, the test facility consumes 1.03 g T/FPd (full power day) while the tritium breeding in the liquid metal test module is only 20% of this amount; see Section 10.3.5.2.

The high purity deuterium fuel can be stored in high pressure cylinders using the same precautions as for the industrial storage and use of hydrogen. Special precautions must be taken, however, for the storage of tritium because of its radioactive character. As a result the tritium supply is stored in a vault-type room which is serviced by an atmospheric detritiation system. The majority of the tritium is stored as a solid metallic tritide such as uranium tritide. In this form a large quantity of tritium can be stored in a rela-

tively small space and at a low pressure. The tritium is released when the metallic compound is heated to approximately 400°C for uranium. Because of the time involved in heating the UT_3 to release the tritium, some tritium is stored for immediate use in the gaseous form in metallic cylinders at less than atmospheric pressure.

Both the gaseous form and the UT_3 accumulate He-3 at the tritium decay rate, and the He-3 is transferred with the T_2. The helium must be separated from the tritium by use of a series of adsorption/desorption steps using uranium powder as the absorbant. In this manner, T_2 free of He-3 is delivered to the Fuel Blender as needed.

Because tritium fuel must be constantly supplied to this test facility a special receiving station will be required. This station must contain: (1) a glovebox to receive the shipping containers and couplings to adapt the ship-ping vessel to the fuel system; (2) apparatus to transfer the tritium from the shipping cask to the storage containers, (3) instruments to assay the quantity and chemical purity of the tritium; and (4) apparatus for temporary storage of the tritium before transfer to the storage vault. This system is similar to the Tritium Storage and Delivery System[5] fabricated for use at the TFTR lo-cated at PPPL.

8.4 Tritiated Water Inventory
8.4.1 Tritium Permeation Into Coolant Water

Water coolant is utilized in numerous locations in this reactor to pro-tect structural materials from overheating. When metallic structural materi-als are in the plasma chamber, tritium contamination of the coolant water occurs by permeation of tritium from the plasma halo gas through the structure because of the ease by which hydrogen (tritium) permeates most metals at moderate temperatures. At low tritium partial pressures ($< 1.3 \times 10^{-4}$ mbar) in the halo gas and moderate temperatures (100-500°C), the tritium permeation rate into the coolant water is usually insignificantly small. Much higher tritium permeation rates are possible, however, when energetic tritium ions from the plasma impinge upon the structural material. Such critical areas occur in this reactor at three locations, namely: (1) the End Plasma Dumps, (2) the HE-NBI beam dumps, and (3) the Central Cell insert. Estimates are presented in this section regarding the tritium permeation at each of these

locations and related information regarding the tritium inventory in these structures.

Several analytical transport models have been proposed recently for evaluating the steady state tritium inventory, recycle rate and permeation rate for surfaces exposed to energetic tritium ions. These models include the effects of implantation depth, diffusion, thermal gradients, recombination barriers to the release of tritium at the front and rear surfaces and tritium trapping at defects in the structure caused by ion bombardment or neutron displacement. For this study several example calculations were performed in each of the critical areas by use of the computer code, named DIFFUSE, prepared by M.I. Baskes.[6] While the formalism of this code is exact, uncertainties in the relationship between neutron displacements and the number and energy depth of traps cause the results to be only qualitative at this time, as is discussed in the following.

8.4.1.1 End Plasma Dump. The energetic tritium ion loss to the two end dumps is $\sim 5 \times 10^{20}$ s^{-1} at an energy of 125 keV. These ions are intercepted by water-cooled copper plates which have ~ 9.8 m^2 of surface area exposed to the ions. The ions penetrate the copper to a depth of 1.27×10^{-4} cm and diffuse toward the front and rear surfaces. Because the neutron flux is small at the end cell, no tritium traps were considered in the copper. Use of the DIFFUSE code indicated that after one year, the permeation rate to the rear surface was constant at 2.08×10^{10} T atoms/cm$^2 \cdot$s. The total accumulation rate in the coolant water is ~ 9 Ci/d. The tritium inventory in the copper was, also, constant after one year, at 4×10^{16} T atoms/cm^2; the total tritium in this structure is only 20 mg.

8.4.1.2 Beam Dumps. The four copper beam dumps, 4.3×10^3 cm^2 each, intercept the "shine-through" from the HE-NBI; therefore, each beam dump intercepts 1.5×10^{19} T ions/s at 90 keV. These ions are implanted into the copper and diffuse toward the front and rear surfaces. The initial permeation into the coolant water is ~ 1.5 Ci/d. The beam dumps, however, are located in the central cell and receive neutron irradiation from the plasma which causes atom displacement and eventually leads to the formation of traps for the diffusing T atoms. When these traps occur, the diffusing of tritium to the water coolant is severly restricted. For instance, use of the DIFFUSE computer code based upon 1% atomic concentration of traps and a trap depth of 1 eV indicated that

no tritium diffused to the rear surface. Instead, a large inventory of tritium was trapped at the rate of 3 x 10^{18} T atoms/cm^2·yr which had penetrated approximately 0.02 cm into the copper. When this tritium inventory was scaled for the lifetime (~ 8 yr) of the machine, nearly 2.06 g (T) was found to be trapped in the 4 beam dumps, if they had remained in the reactor for its lifetime. Further analysis is necessary, therefore, to determine if the 0.02 cm thick front surface of the copper retained its structural integrity and good thermal conductivity properties when it is loaded with such a large amount of tritium (hydrogen) and a comparable amount of deuterium. At this time, it would appear prudent to change the beam dumps frequently, so that the neutron damage is not high and the tritium inventory is only 3 mg for all the copper.

8.4.1.3 Central Cell Insert. The wall at the center of the reactor has been recessed to 70 cm in order to withstand the high heat load from ion bombardment caused by charge-exchange (CX) of the HE-NBI particles with the plasma. These CX ions deposit 5.63 MW on the first wall of this insert which is formed from water-cooled tubes fabricated from the ferritic alloy HT-9. The D and T ions at 90 keV energy penetrate the steel to a depth of 1.02 x 10^{-4} cm and then diffuse to the front and rear of the steel tube wall. The tritium permeation in the ferritic steel reaches a steady-state value in ~ 12 days; consequently the coolant water receives tritium at the rate of 105 Ci/d.

This central cell insert, however, is directly exposed to the neutrons emitted from the plasma; consequently, atomic displacements in the steel form traps to the diffusing tritium. For instance, use of the DIFFUSE code for 1% atomic concentration of traps with an energy depth of 1 eV indicated that in 0.5 yr no tritium had diffused to the rear surface. In fact, the profile of the tritium in the steel indicated it had not progressed far beyond its computed injection depth. The tritium inventory in the steel, however, was very high. If the inventory were extrapolated to the lifetime of the machine, ~ 8 yr, the tritium inventory in the steel would be 128 g. The integrity of the steel with this amount of tritium and a similar amount of deuterium needs to be assessed. These tubes should probably be changed frequently so that the neutron damage remains low; therefore the tritium inventory would be < 1 mg (T).

8.4.2 Tritiated Water Removal Unit

As noted in the previous discussion and summarized in Table 8.4-1 the quantity of tritium which permeates into the coolant water changes markedly depending upon the length of time the beam dumps and the central cell insert remain in the reactor. Because of the large tritium inventory, and its unknown effect upon the metallic structural properties, a reactor lifetime residence of these two components in the reactor is probably not advisable. In such a case, the tritium diffusion in these components would not be trapped by damage caused by neutron irradiation; consequently, the total tritium permeation to the coolant water would be $\sim$ 117 Ci/d (3.4 x 10^5 Ci in the reactor lifetime). If the coolant water from these three components were combined, approximately 2.4 x 10^5 kg, the concentration of tritium in the water at end of reactor life would be $\sim$ 1.5 Ci/kg. Experience at D_2O cooled fission reactor plants[7] indicate that tritium concentration at this level in coolant water < 100°C does not cause excessive tritium contamination of plant personnel. At this time, therefore, a Tritium Water Removal Unit at this site does not appear to be necessary. This issue will need more further study whenever this test reactor site is designed. Such a study must also consider the disposal of the 130 m^3 of coolant water containing $\sim$ 34 g of tritium.

Table 8.4-1. Tritium Permeation to Coolant Water and Inventory in Metal for High Heat-Flux Components

Component	Frequent Replacement[a]		Reactor Life	
	Permeation T (Ci/d)	Inventory T (g)	Permeation T (Ci/d)	Inventory T (g)
End plasma dumps	10	0.02	10	0.02
Beam dumps	2	1 x 10^{-3}	$\sim$ 0	2[b]
Central-cell insert	105	3 x 10^{-5}	$\sim$ 0	128[b]

[a] Time interval needs to be assessed based upon decreases of structural strength and thermal conductivity.

[b] Hypothetical extrapolation.

References for Chapter 8

1. F. Carré, E. Proust and A. Rocaboy, "Analysis of Tritium Requirements for a Power Reactor," Nuclear Technology/Fusion 4, 93-98 (1983).

2. E.C. Kerr, J.R. Bartlit and R.H. Sherman, "Fuel Cleanup System for the Tritium Systems Test Assembly: Design and Experiments," Proc. ANS Topical Mtg. Tritium Technology in Fission, Fusion and Isotopic Applications, Dayton, OH, April 1980, pp. 115-118.

3. B. Misra and A. Maroni, "Multicomponent Isotopic Separation and Recirculation Analysis," ANL-76-92, Argonne National Laboratory (Jan. 1976).

4. P.C. Souers, "Cryogenic Hydrogen Data Pertinent to Magnetic Fusion Energy," UCRL-52682, Lawrence Livermore National Laboratory (March 15, 1979).

5. H. Phillips, L. Yemin, N. Youssef, C. Pierce, R. Watkins, W. Wilkes, J. Gill, "Tritium Storage and Delivery System for the Tokamak Fusion Test Reactor," Proc. ANS Topical Mtg. Tritium Technology in Fission, Fusion and Isotopic Applications, Dayton, OH, April 1980, pp. 353-359.

6. M.I. Baskes, "DIFFUSE 83," U.S. DOE Report, SAND 83-8231 (June 1983).

7. M. Abdou et al., "Documentation for Tritium Contamination of the Reactor Hall Environment," in U.S. FED-INTOR, Phase 2A Workshop, W.M. Stacey, Jr., Ed., Vol. II, Chapter VIII.D, pp. 123-132 (October 1982).

9. THE MAGNET SYSTEM OF TASKA-M

9.1 Introduction

The design of the TASKA-M magnets follows the same guidelines as in
the TASKA-study [1] and uses the same constraints in the magnetic data.
The aim of TASKA-M was to decrease the costs while retaining a reasonable
test volume compared with TASKA. Another plasma configuration is used,
so the magnets are smaller, less numerous and therefore cheaper.

In TASKA-M the field requirement in the central cell is 4.2 T at the mid-
plane; the high field hybrid mirror coil gives 17.5 T at the mirror throat.
The minimum field in the transition region was required to be about 2.2 T.
The anchors should have a mirror ratio of 2.5 to 3 with a minimum field
of about 1 T. This high mirror ratio was required to provide good con-
finement of the sloshing ions in the anchors.

The EFFI code [2] was used to calculate the electromagnetic character-
istics of the magnet coil system.

9.2 General Magnetic Characteristics

The magnet set of TASKA-M consists of

- 1 central cell coil (CCC)

- 2 high field hybrid mirror coils (choke coils). Each consists of a
  normal conducting insert, a Nb_3Sn part and a NbTi outer part (BC1, BC2).

- 2 transition coils (RCP1, RCN2)

- 2 Yin-Yang sets (CESN1, CESP1 and CESN2, CESP2).

Fig. 9.2-1 shows a computer drawing of the magnet set with the names of
the magnets and the magnetic field magnitude B along the z-axis
(machine axis). The central cell coil and the choke coils are solenoidal
type magnets. All the anchor magnets are C-shaped coils.

Table 9.2-1 lists the magnetic field at various cardinal points on
the axis.

Table 9.2-1: Special B-values

z [m]	B [T]	Comment
0	4.2	Center of TASKA-M
2.75	17.5	Maximum on-axis field; mirror
6.35	2.18	Transition region; minimum
7.4	2.72	1st anchor maximum ,
10.2	1.02	Minimum anchor field
12.8	2.67	2nd anchor maximum

Fig. 9.2-2 shows the field lines in the x-z plane (top) and y-z plane
(bottom). The lines start at z = 0 m, x = 0.125 m (plasma radius),
z = 0 m, x = 0.25 m (wall radius) and z = 0 m, y = 0.125 m and
0.25 m.
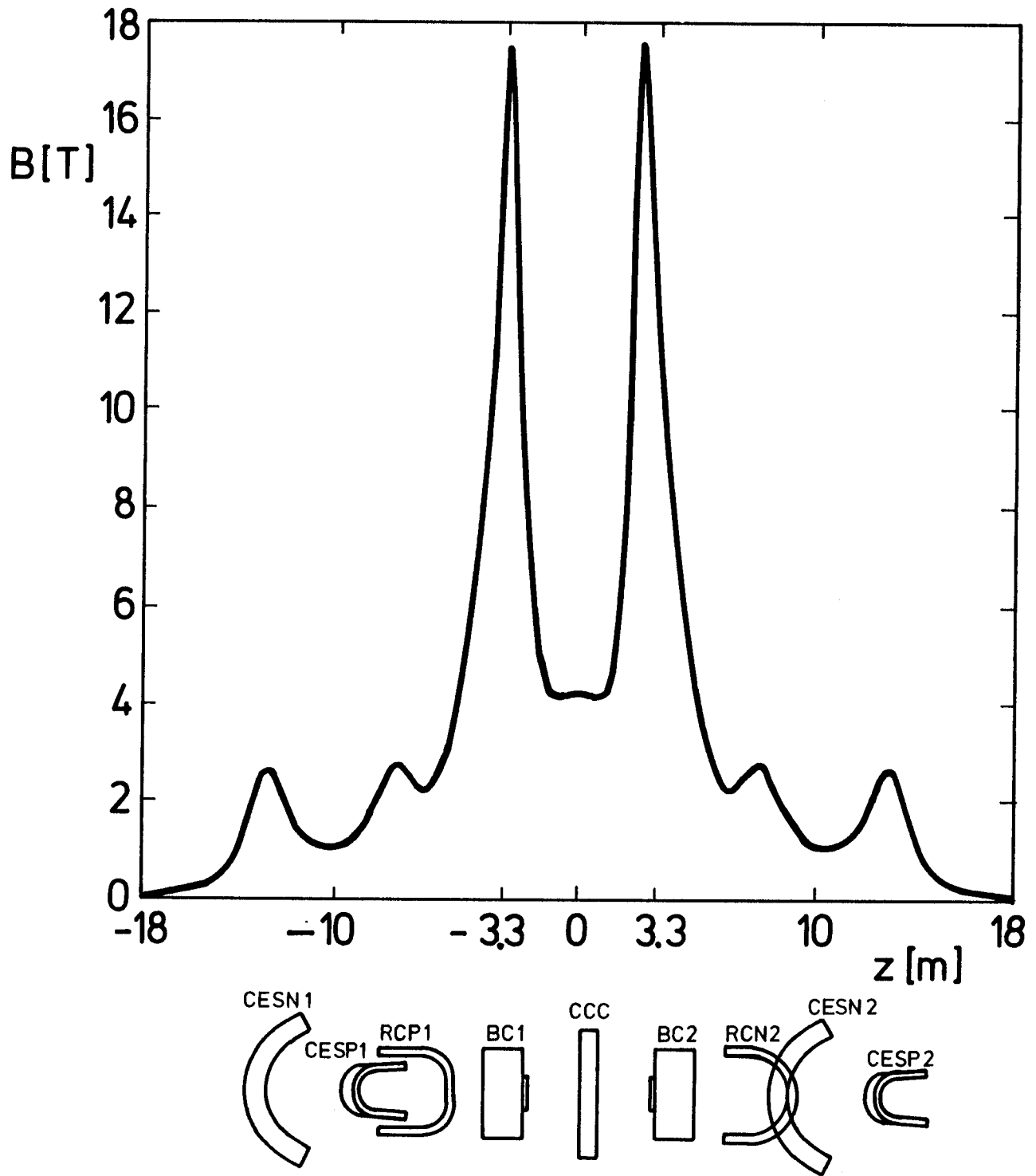
Fig. 9.2-1: Magnet system of TASKA-M and axial magnetic field profile
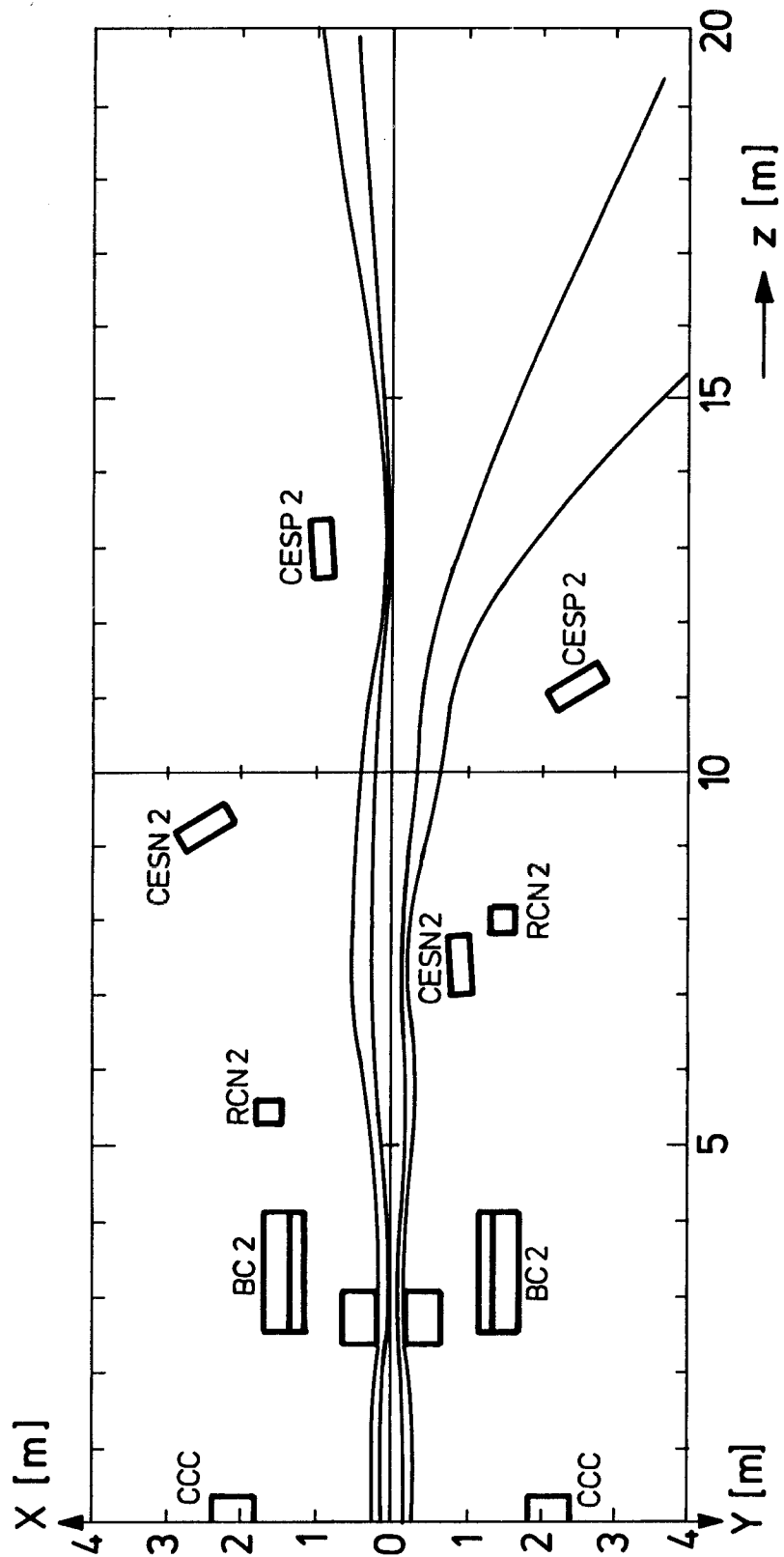
Fig. 9.2-2: Field Lines in x-z and y-z planes

A critical area is the small radius corner inboard of the normal conducting insert coil, where the magnetic field is 13 T. At this location the beta-corrected plasma radius is 6.2 cm and the α-particle gyroradius is 2.1 cm. Allowing two gyroradii between the plasma and the wall gives a space of 4.5 cm for the structural material of the normal conducting coil.

The field line fan in the end cell is elliptic because there is no recircularising coil outside of the anchor cell. Allowing an average power density of 300 W/cm^2, a beam dump can be placed at about 20 m from the center of the machine (assuming a total power of 15 MW streaming into each end of the machine). (See Chapter 7.2.3).

Table 9.2-2 and 9.2-3 contain the magnet data.

Table 9.2-2 shows significant data of the solenoidal coils forming the central cell. TASKA-M uses only one central cell solenoid instead of three in TASKA. The choke coils are much smaller than in TASKA due to a smaller plasma radius and lower field requirement, and they are more compact. The amount of Nb$_3$Sn conductor which was the most expensive part of the TASKA choke coil, is much smaller; it is only one fifth of the winding mass of the TASKA Nb$_3$Sn coil. In addition, the total weight of the winding of one of the choke coils is about 50 t, which eases the maintenance of such a coil.

Table 9.2-3 gives the data of the C-shaped coils. In each anchor there is one reversed C-coil and two squeezed C-coils forming the Yin-Yang set. All the squeezed C-coils have the same geometry, but two have a current density of 2500 A/cm^2 and two of only 1530 A/cm^2. All the electrical data are similar to the data used in TASKA, especially for the superconductors.

Fig. 9.2-3 shows the resulting forces (MN) during normal operation. Compared with TASKA the forces in TASKA-M are much lower, especially in the Yin-Yang region.

As the design procedure is the same as in the TASKA-study, only some specific problems are discussed in the following to avoid repetition.

These items are the design of the high field hybrid coil and the magnetic shielding of the neutral beam injectors. No detailed conductor design is presented, because all the conductors are similar to those in the TASKA report, e.g. Fig. 9.2-4 shows a possible scheme of Al-stabilized conductors for solenoids in TASKA-M.

Table 9.2-2: Solenoidal Coils of TASKA-M

	Unit	Central Cell Coil	NC-Insert	Choke Coil Nb$_3$Sn-Coil	Choke Coil NbTi-Coil
Center of Coil(s)	z	m	0	± 2.7	± 3.3	± 3.3
Inner Radius	a_1	m	1.8	0.15	1.15	1.34
Outer Radius	a_2	m	2.4	0.65	1.31	1.70
Radial Thickness	T	m	0.6	0.5	0.16	0.36
Axial Width	W = 2b	m	0.7	0.7	1.6	1.6
Mean Radius	$\bar{A}$	m	2.1	0.4	1.23	1.52
Average Winding Length	$\bar{L}$	m	13.2	2.52	7.73	9.55
Volume	V	m^3	5.54	0.9	2.0	5.5
Filling Factor of Winding λ			0.8	0.6	0.8	0.8
$\lambda\rho$ (estimated)		t/m^3	5.6	5.4	5.6	5.6
Mass (estimated)		t	31.0	4.75	11.0	31
Current Density	(λJ)	A/cm^2	2180	2200	2380	2750
Ohmic Losses	P	MW		18.0		
Ampère Turn	N·I	10^{6}A-turn	9.2	7.7	6.1	15.9
Ampère metres		10^{3}kAm	122	19.5	47.1	152
B_{max} at Conductor		T	7.4	18	12	8.2
Self-Inductance L/N^2		10^{-6}H/N^2	5.5	0.36	2.05	2.7
Stored Self-Energy E_s	(λJ)	MJ	232	10.65	38.2	337
$\sigma_{max} = (B \cdot r)_{max} \cdot (\lambda J)$		MPa	290	133	330	300
Number of Coils			1	2	2	2

Table 9.2-3: Data of C-shaped Coils

	Unit	Reversed C-Coils (RCP1 + RCN2)	Squeezed C-Coils (CESN1+CESP2 (CESP1+CESN2))
"Minor Radius"	m	1.44	0.58
Average Minor Radius	m	1.62	0.735
"Major Radius"	m	0.82	2.085
Average Major Radius	m	0.97	2.485
Center of Coil on Z-Axis	m	6.35	10.45
Half Opening Angle θ	degrees	90	60
Width in Direction of Minor Radius	m	0.36	0.3
Thickness in direction of major radius	m	0.3	0.8
Length of Straight Section	m	1.0	0.17
Current Density λJ	A/cm^2	2500	2500 (1530)
B_{max} at Conductor	T	5	6
Mean Turn Length $\bar{L}$	m	18.3	20.8
Volume V	m^3	2.0	5.0
Filling Factor λ		0.8	0.8
estimated $\lambda \cdot \rho$	t/m^3	5.6	5.6
Winding Mass (estimated)	t	11.0	28.0
Ampère Turns $N \cdot I$	10^6 A-t	2.7	6.0 (3.7)
Ampère Metres	10^3 kAm	50.0	125.0 (77.0)
Self-Inductance L/N^2	10^{-6} H/N^2	8.87	5.32
Stored Self-Energy E_s	MJ	33.0	96.0 (36.0)
Number of Coils		2	2 (2)

Fig. 9.2-3: Resulting forces in MN during normal
operation (1 MN corresponds to approx. 100 t)

REINFORCED EPOXY
INSULATION

SS

NB-TI-ROEBELBAR
OR
NB₃SN-BRONZE-MONOLITH
PREREACTED

PUREALUMINUM WITH
EXTENDED SURFACE
SOLDERED TO SS

CU-STRIPS FORMING HE-CHANNELS
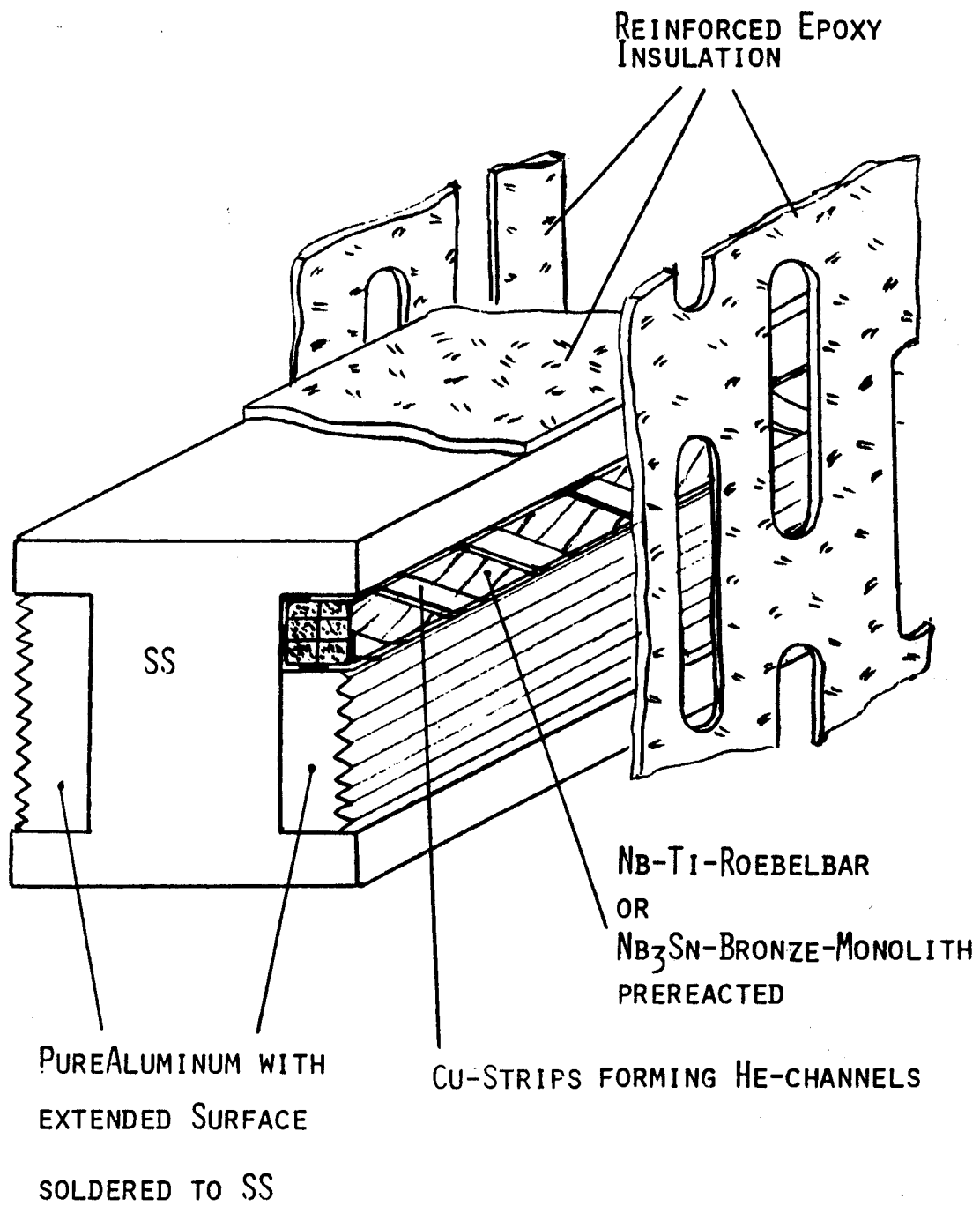
Fig. 9.2-4:   Scheme of Al-stabilized conductors for
              solenoids in TASKA-M

9.3 The High Field Hybrid Coil

9.3.1 Superconducting background coil

The high field hybrid coil consists of three individual parts; the innermost coil is normal conducting. The outer coils are a Nb_3Sn coil and a NbTi coil, respectively. Fig. 9.3-1 shows a cross section of the hybrid coil. The normal conducting insert is moved towards the central cell.

The maximum magnetic field of the Nb_3Sn part is less than 12 T. Therefore, the requirements are less stringent than in TASKA and we may use higher current densities than in TASKA. For 12 T we can use $5x10^4$ A/cm² as a current density value for Nb_3Sn and bronze. The overall current density in the coil is about 2400 A/cm², so we have a high reserve for stabilization, structural material, insulation and cooling channels.

The maximum field of the NbTi coils occurs at the inner corners as shown in Fig. 9.3-1. The field is less than 8.2 T. Therefore, we can use a convenient value of $7x10^4$ A/cm² for the current density in the superconductor NbTi.

9.3.2 The design of the normal conducting insert coil

Designing the normal conducting coil one has to take into account several constraints, such as the space available for the magnet. Using the standard optimization procedure described in /3/ and taking into account that the plasma size defines the minimum inner radius of the coil to be 0.15 m, the result was a coil producing a magnetic field of 5.9 T for an overall current density of J_{ov} = 2200 A/cm². This current density is limited by the power dissipated in the coil volume. A value of about 20 W/cm³ is chosen which is easily feasible in a pancake with two conductors in parallel.

The field contribution of 5.9 T was too low to get the 17.5 T design value. A field contribution of about 9.3 T is needed by the normal conducting coil. Therefore, the power optimization as described in [3] was not directly applicable.
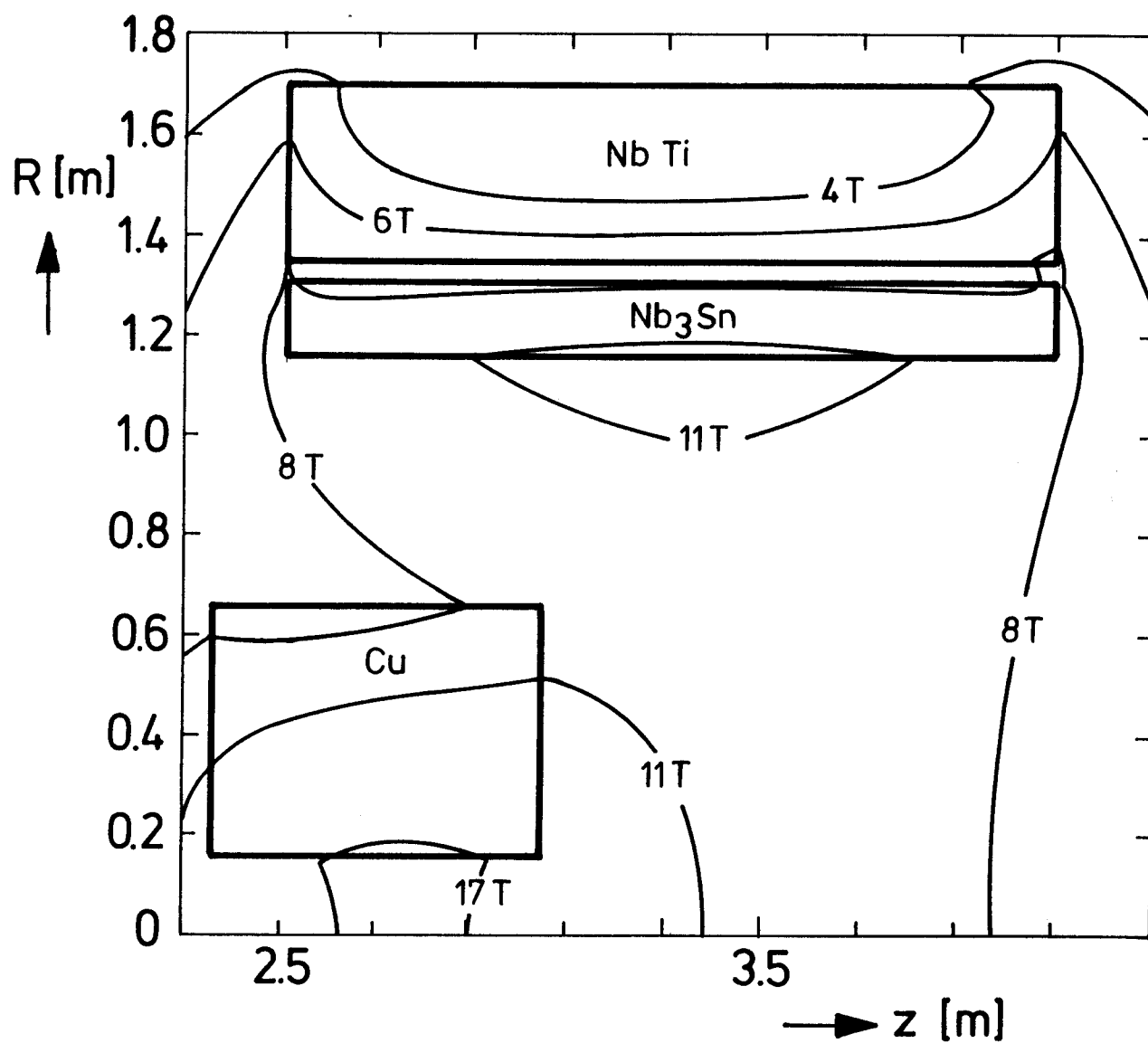
Fig. 9.3-1: Contours of the magnetic field strength
in the vicinity and within the choke coil

Nested cylinders with variable current density in the radial direction were used in TASKA. To define the current densities and the optimum geometry a problem orientated optimization was used. The formula for the magnetic field in the center of the coil is [3]:

$$B_0 = \lambda \cdot J \cdot a_1 \cdot \mu_0 \cdot \beta \cdot \ln \frac{\alpha + (\alpha^2 + \beta^2)^{1/2}}{1 + (1 + \beta^2)^{1/2}}$$

and for the power consumed:

$$P = \lambda \cdot J^2 \cdot \rho \cdot a_1^3 \cdot 2\pi\beta \cdot (\alpha^2 - 1)$$

where

λ = filling factor

J = current density in the conductor

a_1 = inner radius

β = b/a_1

b = half axial length of the coil

α = a_2/a_1

a_2 = outer radius

ρ = specific resistivity of the conductor

μ_0 = $4\pi \cdot 10^{-7} \frac{Vs}{Am}$

The aim is to get the maximum field for a given power. Thus, the function

$$\Phi(J,\beta) = \lambda J a_1 \mu_0 \beta \ln \frac{\alpha+(\alpha^2+\beta^2)^{1/2}}{1+(1+\beta^2)^{1/2}} + \lambda_1(P-\lambda J^2 \cdot \rho \cdot a_1^3 \, 2\pi\beta(\alpha^2-1))$$

is considered and the well known Lagrange multiplier technique is used. Form the partial derivatives

$$\frac{\partial \phi}{\partial J} = 0 \qquad \text{and} \qquad \frac{\partial \phi}{\partial \beta} = 0$$

and consider a_1 and α as free parameters and λ and ρ as independent of the current density J.

Two equations are obtained:

$$\mu_0 \ln \frac{\alpha+(\alpha^2+\beta^2)^{1/2}}{1+(1+\beta^2)^{1/2}} = \lambda_1 \cdot J \cdot \rho \, a_1^2 \, 4\pi(\alpha^2-1)$$

and

$$\lambda_1 J \cdot \rho\, a_1^2\, 2\pi(\alpha^2-1) = \mu_0\, \ln \frac{\alpha+(\alpha^2+\beta^2)^{\frac{1}{2}}}{1+(1+\beta^2)^{\frac{1}{2}}}$$

$$+ \mu_0\beta^2 \left[\frac{1}{\alpha(\alpha^2+\beta^2)^{\frac{1}{2}} + \alpha^2+\beta^2} - \frac{1}{(1+\beta^2)^{\frac{1}{2}} +1+\beta^2} \right]$$

By elimination of the current density a condition for an optimum parameter set of (β,α) is obtained:

$$\ln(\alpha+(\alpha^2+\beta^2)^{\frac{1}{2}}) + \frac{2\beta^2}{\alpha^2+\beta^2+\alpha(\alpha^2+\beta^2)^{\frac{1}{2}}} = \ln(1+(1+\beta^2)^{\frac{1}{2}}) + \frac{2\beta^2}{1+\beta^2+(1+\beta^2)^{\frac{1}{2}}}$$

With the definition of the function

$$C(\alpha;\beta) = \ln(\alpha+(\alpha^2+\beta^2)^{\frac{1}{2}}) + \frac{2\beta^2}{\alpha^2+\beta^2+\alpha(\alpha^2+\beta^2)^{\frac{1}{2}}}$$

the condition is:

$$C(\alpha;\beta) = C(1;\beta)$$

This condition is numerically solved. The result is used for the design of the normal conducting coil.

A solution with two cylinders and two current densities (the maximum was $J_{ov} = 2200$ W/cm²) could be found. However, the thickness of the outer cylinder is very thin and therefore, a one cylinder solution was adopted for simplicity.

In addition, a Bitter type design of the normal conducting insert was examined, showing comparable electrical data and power dissipation as the helically wound coil. A decision between the two options should only be made after a detailed design, including an assessment of the radiation damage problem of the insulation as discussed in the TASKA-Report [1] and in Chapter 5 of this report.

Fig. 9.3-2 shows a tentative conductor design for the normal conducting insert coil and Table 9.3-1 contains the geometrical data. Magnesium oxide (MgO) in compacted powder form is used as insulation in the normal conducting insert. According to the neutronics results the lifetime of the normal conducting coil is over 10 FPYs, if a 10 v/o swelling in the insulator is allowed. A more radiation resistant insulator, Spinel $(MgAl_2O_4)$, was also considered. It seems to be the most desirable material for high stress and high irradiation applications.
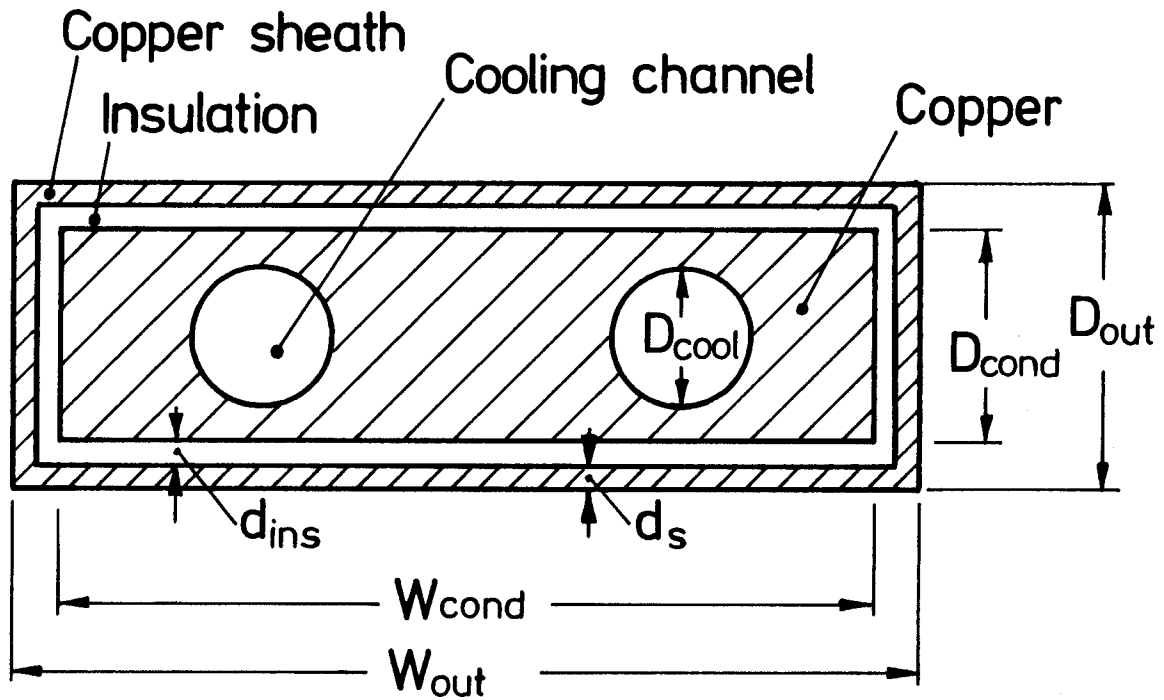
Fig. 9.3-2: Tentative conductor cross section of
the normal conducting insert coil
(not to scale).

Table 9.3-1: Conductor data of the normal conducting
insert coil

Core and sheath material	Cu
Insulation	MgO
D_{out}	20 mm
D_{cond}	16 mm
W_{out}	60 mm
W_{cond}	56 mm
d_{ins}	1.3 mm
d_s	0.7 mm
D_{cool}	9.0 mm

9.4 Magnetic Shielding of Neutral Beam Injectors

Due to the high stray fields in the outer region of the machine magnetic shielding of the components of the neutral beam injector is necessary. The critical components are the ion source, the neutralization and the sweep magnet/ion dump regions. The magnetic field magnitude due to stray fields in these regions varies from about 0.1 T to 0.02 T as seen in Fig. 9.4-1. The aim of this section is to estimate the influence of the needed magnetic shielding material on the costs of the machine.

One important quantity is the shielding factor S, i.e. the ratio of the magnetic field without shielding to the magnetic field with shielding at one point in space. If a penetrating field (magnetic field with shielding) of $1 \div 2 \times 10^{-4}$ T is required, the shielding factors are about 500 to 1000.

Using formulas and data of references [4,5,6] the shielding factor of a single cylinder is estimated (see Fig. 9.4-2). For a permeability $\mu \gg 1$ and a magnetic field perpendicular to the axis of the cylinder the shielding factor S is given by

$$S = \frac{\mu}{4} \left(1 - \frac{D^2}{(D+2d)^2} \right) + 1$$

for long cylinders. D is the inner diameter and d is the wall thickness of the cylinder. For

$$x = \frac{d}{D}$$

S is given by

$$S = \mu \frac{x(1+x)}{(1+2x)^2} + 1$$

For effective shielding the shielding factor must be $S \gg 1$. For big cylinders (D in the order of 100 cm) and reasonable wall thicknesses (d in the order of 1 cm) the ratio $x = d/D$ is much smaller than 1. So S in the case considered is

$$S = \mu \cdot x$$
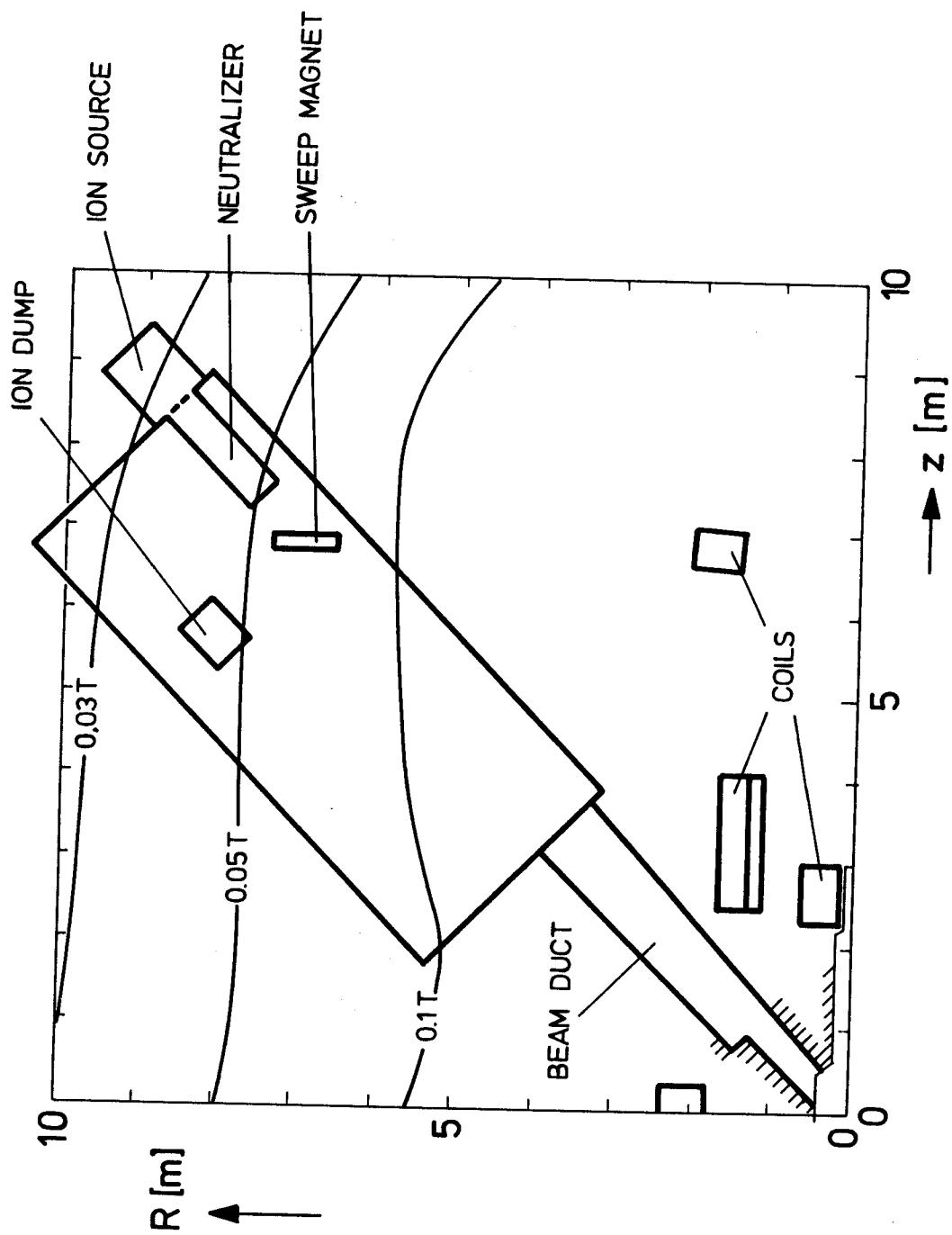
Fig. 9.4-1: Neutral beam arrangement and magnetic stray fields
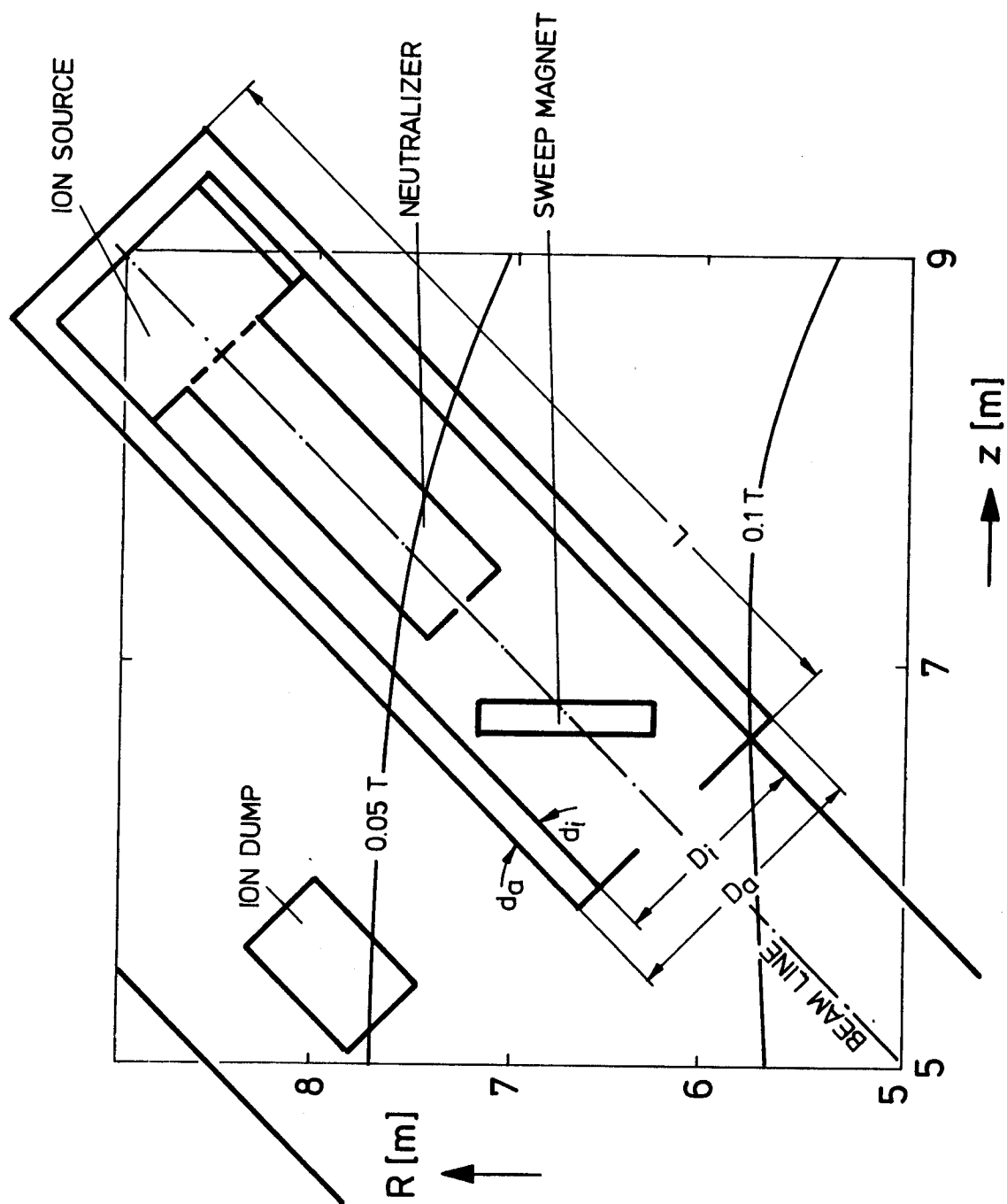
Fig. 9.4-2: Arrangement of cylindrical shields

For x = 0.01 and $\mu \approx 25000$ (MUMETALL [4]) the shielding factor for a
single cylinder is estimated to be 250. A wall thickness of about 4 cm
would give a shielding factor of about 1000 as required. With a cylinder
length of about 4 m the volume of the required shielding material would
be about 53×10^4 cm^3 and with a density of 8.6 g/cm^3 the total weight
would be 4600 kg. At a price of 20 US$/kg for MUMETALL [7] the cost of
the shielding material is about 10^5 US$ per neutral beam injector. This
seems to be an upper limit because the required shielding factor varies
from 1000 to about 250 along the cylindrical tube, so the shield thick-
ness can be adapted along the cylinder.

This estimate neglects the influence of cross sections differing from
a circle. For example, the correction factor for a square is 0.7 [6].
For field components parallel to the axis of the cylinder the correction
factor would be about 0.25. Also the influence of openings is neglected.
A detailed calculation for a double shield taking into account a square
cross section, parallel field components and the influence of openings
gives for an average shielding factor of 750 the result of 1 t/m shield-
ing material (MUMETALL). That is about the same amount of material as in
the case of single cylinder shielding. Similar shielding factors occur in
the neutral beam injectors of JET.

9.5 Conclusions

The magnet system in TASKA-M is much simpler than that used for the TASKA design. In particular the choke coil is smaller and cheaper, because the plasma radius is lower and the field requirement is 17.5 T in TASKA-M instead of 20 T in TASKA. The goal to have only 12 T at the Nb_3Sn conductor is attained and the electrical data are comparable with Nb_3Sn coils already tested. But the diameter of these coils is characterized by a half meter bore.

All the NbTi superconducting coils have electrical data comparable with existing tested magnets. Also the size is in the same order of magnitude as for tested magnets.

A sufficient data base is not available for the normal conducting insert coil, especially for the behaviour of the ceramic insulation in a high magnetic field and high 14 MeV neutron flux environment. In this respect, more experimental work is needed.

References for Section 9.

1. TASKA-Tandem Spiegelmaschine Karlsruhe, A Tandem Mirror Fusion Engineering Test Facility, KfK 3311/1 and KfK 3311/2 and UWFDM-500

2. S.J. Sackett, EFFI, A Code for Calculating the Electromagnetic Field, Force and Inductance in Coil Systems of Arbitrary Geometry, Lawrence Livermore National Laboratory, Livermore, California, UCRL-52402 (1978)

3. D.B. Montgomery, Solenoid Magnet Design, Wiley-Interscience, 1969

4. Magnetische Abschirmungen, Firmenschrift FS-M9, Ausgabe 1975, Vacuumschmelze GmbH, Hanau

5. R. Boll and L. Borek, Elektromagnetische Schirmung, NTG-Fachberichte, VDE-Verlag GmbH, 1000 Berlin, Bd. 76 (1980), Technische Informationsblätter M38, Vacuumschmelze GmbH, Hanau, Federal Republic of Germany

6. A. Mager, Großräumige magnetische Abschirmungen, Journal of Magnetism and Magnetic Materials 2 (1976), p. 245-255

7. Vacuumschmelze GmbH, Hanau, FRG, private communication, 13.4.1983

10. TESTING MODULES

10.1 Introduction

One of the main functions of the TASKA-M facility is to provide a nuclear test bed for the magnetic fusion program. This role is meant to supplement other ex-reactor facilities and provide an integrated test of components in a complex nuclear environment. It is important to emphasize the integrated nature of the testing that TASKA-M provides. Simply irradiating small size materials samples in a neutron flux can be accomplished in fission reactors, small DT neutron sources, or high energy neutron sources like FMIT. However, using large specimens in a thermal, stress and chemical environment similar to what they will face in a fusion reactor requires large volume, high fluence, high energy neutron environments. At the present time, there are no such facilities operating, being built, or even being actively designed. Only pre-conceptual reactor studies such as TASKA, TASKA-M, INTOR, or TDF can provide this function to the fusion program.

Another very important function of TASKA-M is to provide a test bed for fusion blanket designs. Such blankets can be tested separately with regard to magnetic field, stress, corrosion, neutronic, and thermal hydraulic effects but none of the facilities now in place, or envisioned to be in place over the next 10-15 years can test all of these effects while the blanket is being bombarded with a high flux (~ 1 MW/m^2) of neutrons. The synergistic effects of corrosion, stress, and neutron induced mechanical property changes can be tested in no other way except through a TASKA type facility. Licensing authorities will most certainly want to see the results of such integrated effects before even considering the safety of fusion power plants.

Finally, TASKA-M will also give very realistic tests of high heat flux components (beam dumps), neutral beams, RF launchers and antenna, normal conducting coils, superconducting magnets, vacuum pumps, and direct convertors. Each of these components could be tested outside of the reactor with respect to thermal and corrosive behaviors, but we know of no such facility which could test a reactor size component with a fusion reactor neutron spectrum and flux.

The above discussion should graphically illustrate why an integrated neutron producing test reactor facility like TASKA-M is needed. The question is not why such a facility should be built, it is only when.

10.2 Materials Modules

10.2.1 Philosophy

The main goal in the materials test modules is to provide a large volume test zone for testing specimens in a high fusion neutron flux. To that end we tried to maximize the exposure of the specimens to the neutron environment while maintaining reasonable access to the test cells. These objectives are sometimes at cross purposes and compromises had to be made which, at times, reduced both the test volume and integrated damage level. It is felt that future analysis of the machine performance, and the cost per specimen should be conducted to see whether such compromises are cost effective. At the present time we feel that the proper balance has been struck between engineering simplicity and level of data obtained and the present design actually provides more test volume than is required by even liberal test matrices.

10.2.2 Test Matrix and Test Module Design Considerations

The test matrix for materials irradiations in TASKA-M is similar in scope to those developed for the INTOR and TASKA testing programs.[1,2] The TASKA-M test matrix is a representative list of materials test specimens and the associated environmental and irradiation conditions. Given a test matrix, along with the physical and neutronics features of the reactor, the experiment designer can design a specific test module or modules to physically contain and environmentally control the necessary number of materials test specimens. The test matrix specifications and the resultant test module design are then used to define the mechanical and operational requirements of the testing program.

10.2.2.1 Test Matrix. The TASKA-M matrix specifies the type of materials tests with detail on specimen numbers, irradiation temperatures, fluences, stress, changeout frequencies and postirradiation testing conditions. The test matrix provides a means to compare the volume needed to carry out a specific materials testing scenario with the volume available for testing in TASKA-M. Also the frequency of specimen changeout can be quantified and its effect on the overall reactor availability estimated.

The test matrix is shown in Table 10.2-1. The presumed scope of the testing specified in the test matrix is that one or two candidate materials have been identified (through extensive fission reactor and accelerator source screening programs) for the various applications (first wall, structural, insulators, etc.). The first portion of the test matrix (qualification and

Table 10.2-1. Materials Test Matrix for TASKA-M*

Module 4

Test Types	Mat.[a] Var.	Dup.[b]	Temp.[c]	Fluence[d]	Postirradiation Conditions	Total Specimens (Assume 50-50 Mix of Ferritic & Austenitic Alloys)	Total Capsules[e]	Sub-Total
Material Qualification								
Tensile/Ductility	3	2	4	3	4 Rate/Temp.	288	14	
Fatigue Life	2	2	4	3	2 Strain Levels	96	3	
Fatigue Crack Growth	2	2	4	3	2 Stress Levels	96	1	
Fracture Toughness								
-- Charpy	2	2	6	2	6 Temperatures	288	2	
-- Compact Tension	2	2	3	2	2 Temperatures	48	4	24
Engineering Scoping								
Tensile/Ductility	5	3	6	4	4 Rate/Temp.	1440	6	
Fatigue Life	5	2	4	2	2 Strain Levels	160	4	
Fatigue Crack Growth	5	2	4	4	2 Stress Levels	320		
Fracture Toughness								
-- Charpy	3	2	6	4	6 Temperatures	864	4	
-- Compact Tension	3	2	2	4	2 Temperatures	96	1	
Swelling/Microstructure	10	5	10	5	2	5000	1	
Creep/Stress Rupture	6	2	4	[6]	6 Stress Levels	288	2	18
Other Materials[f]								
Fatigue Life	5	2	4	4	2 Strain Range	320	8	
Tensile/Ductility	15	3	6	4	4 Rate/Temp.	4320	16	
Dimensional Stability	15	4	6	3	3 Post-Tests	7200	36	
Creep/Creep Rupture	10	2	6	[4]	4 Stress Levels	480	2	
Fracture Toughness	3	2	2	2	6 Temperatures	144	2	
Electrical Properties	6	3	3	4	3 Tests	648	4	
Thermal Conductivity	6	3	4	4	2 Tests	576	6	74
						22,576	116	
					Total No. of Specimens		Total No. of Capsules to Hold Specimens	

Module 4 only; Module 3 used for surface effects and dynamic in-situ testing.
[ ] 1 specimen used to obtain 6 fluence measurements.

[a] Materials x variations

[b] Duplication

[c] Number of irradiation temperatures

[d] Fluence Levels

[e] Capsule volume-390 cm^3

[f] Ceramics, electrical, and heat sink materials

engineering scoping) was developed for candidate first wall materials and other structural components receiving high exposure and the second portion of the test matrix was developed for other high exposure applications such as high heat flux components, armor, and RF. The test matrices reveal why large numbers of specimens are needed to provide design data.

In the test matrix, the types of tests are listed in the left hand column, and important test parameters are summarized as column headings across the top. The first parameter is "materials x variations" and refers to the number of base (candidate) materials and the number of variations in heat treatment or different conditions such as weldments to be tested. The second column refers to duplication of specimens, primarily to verify the reproducibility of data. In some cases such as specimens for swelling and phase stability, the duplication also allows for attrition in the postirradiation preparation of samples. The next two columns refer to the two basic parameters of irradiation temperature and fluence. The numbers of separate irradiation temperatures and goal fluences are given in these columns.

Typically, parallel tests are performed at several irradiation temperatures in order to map expected temperature-dependent behavior over the range of interest. Usually, linear dependence of materials properties on temperature is not expected, especially near ceiling temperatures (about which useful service is not expected).

The microstructure of materials is often studied at more temperature conditions than are mechanical properties because swelling and phase stability are quite sensitive to temperature, and the more complete characterization of microstructures with temperature (and fluence) provides a qualitative guide for interpolating a coarser matrix of observations on materials properties. For example, microstructural observations were performed at intervals of about 50°C in irradiation tests supporting alloy development for the U.S. breeder program. In the test matrices for TASKA-M, the number of irradiation temperatures varies from two temperatures for some mechanical properties tests to ten temperatures for observations of swelling and phase stability.

Irradiation experiments typically include tests to a goal fluence, representing end-of-life conditions if possible, and several interim fluences. Irradiation experiments are expensive and take a long time. Consequently, preliminary predictions of material behavior are used for redirecting experi-

mental objectives and for preliminary design data, pending corroboration with data at high fluences. However, the extrapolation of low fluence data to predict properties at high fluences can be grossly misleading. A rule of thumb is extrapolation by less than a factor of two in fluence (for moderate fluence levels, i.e., exceeding incubation doses for property changes) is sometimes acceptable but certainly not always. Data at several values of moderate to high fluences are required to accurately define trends, especially where the properties after irradiation are only marginally acceptable. Five goal fluences are appropriate for some tests in TASKA-M on structural materials (components using "other" materials were assumed to be more easily replaceable than the first wall and have lower lifetime fluences).

The column headed "Postirradiation Conditions" refers to test conditions after the specimens have been removed from the reactor. For example the strain ranges in fatigue tests are conditions in postirradiation tests. Another example is for tensile tests where both the strain rate and the post-irradiation test temperature are variables. Typically, postirradiation tensile tests are performed at the irradiation temperatures, at a temperature slightly above the irradiation temperature and at the temperature expected in the material during refueling or during repair. Designers use these data to predict behavior during operation and for fault conditions such as overheating and seismic response.

In the case of creep tests, the other "condition" is stress. The current techniques for in-reactor creep tests utilize sealed tubes pressurized to different stress levels. The diameters of the tubes are measured at several intervals of fluence after which the specimens are again placed in the reactor for further exposure.

The last two columns give the total number of specimens and the number of irradiation capsules (see Section 10.2.2.2.3 for capsule description) required to contain the specimens within the facility's testing module.

It was assumed that one-half of the qualification and scoping specimens were ferritic alloys (e.g., HT-9) and one-half austenitic (e.g., 316 SS) alloys. The major difference in testing ferritics and austenitics is the increased number of fracture toughness specimens required to determine the effect of irradiation on the ductile to brittle transition temperature in ferritic steels.

10.2-4

The total number of specimen capsules in TASKA-M is significantly reduced over that in TASKA (116 vs. 252) due to (1) a reduction in the required volume of tensile, fracture toughness and creep specimens and (2) the availability of module three for in-situ and/or surface effects tests. Recent analysis[3] in the U.S. Fusion Materials Program has shown good correlation between many of the smaller specimens currently used in irradiation tests and those that are significantly larger. For example, half-size Charpy specimens have been used in the TASKA-M test matrix while full-sized Charpy specimens which require nearly eight times the volume were used in the TASKA and INTOR matrices.

In view of recent in-reactor dynamic fatigue crack growth testing results[4] that have shown in-situ and postirradiation test results to be very similar, and because of the relatively high cost of such tests it is believed that significant efforts will be made to minimize the volume required for such tests in the future.

10.2.2.1.1 Test Matrix Related Operations. The fluence requirements specified in the TASKA-M test matrix necessitate test module removal from the test facility at periodic intervals. The number and time between removals is a function of (1) the test matrix goal fluences and (2) the rate at which damage is accumulated over the necessary specimen volumes.

Figure 10.2-1 illustrates the variation of the dpa rate throughout a specimen capsule at the midplane of module 4. Based on the peak dpa rate available in TASKA-M, the resultant capsule discharge sequence will be as illustrated in Fig. 10.2-2. The specimens will be discharged from the reactor at 2, 5, 15, 25 and 50% of the final 78 dpa level achieved after a 7.8 FPY estimated life of the device. Lower dpa levels will be obtained in specimens in zones A and B of the capsule as indicated in Fig. 10.2-3. The capsule discharge sequence is based on an initial test module loading of 116 capsules. At each interim examination, approximately 20 capsules are removed from the test module for specimen analysis. Twenty fresh capsules are then loaded into the test module for further irradiation along with the ~ 100 previously irradiated capsules which remained in the test module. This operational sequence was selected to minimize the total time required to achieve the specified goal fluences. Table 10.2-2 summarizes some salient test matrix results and operational frequences.

ASSUMPTIONS

1.34 MW/m² Peak Neutron Wall Loading

Center Plane of Module
50% NaK, 50% SS

A = Structural Materials
    dpa = 8±2
B = Other Materials
    dpa = 4±2

MODULE WALL
SPECIMEN CAPSULE

dpa PER FPY

9

6

3

0

0 2 4 6 8 10 12 14 16 18 20 cm

DISTANCE INTO TEST MODULE

A   B
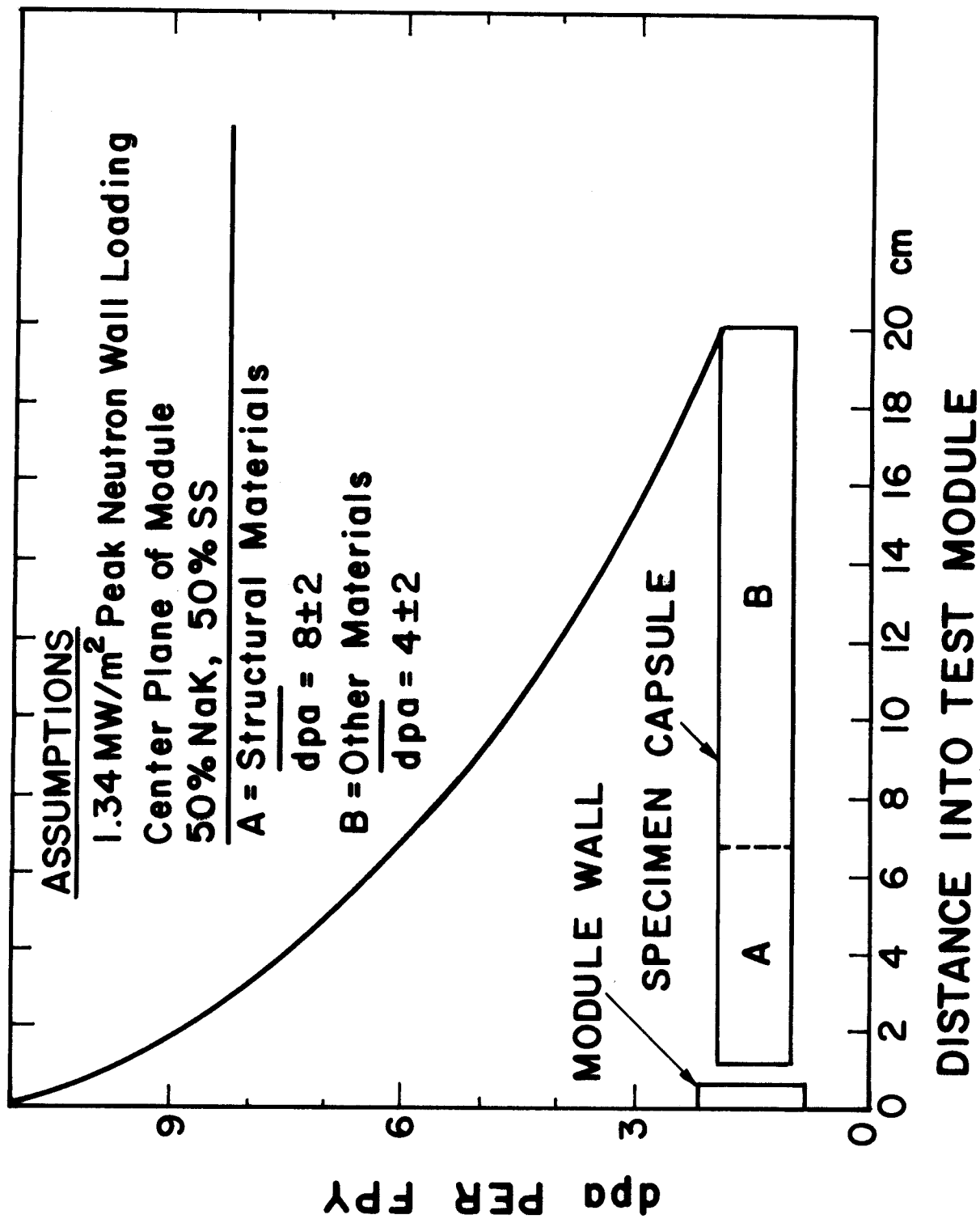
Fig. 10.2-1. Dpa variation throughout a capsule located at the peak neutron wall loading.
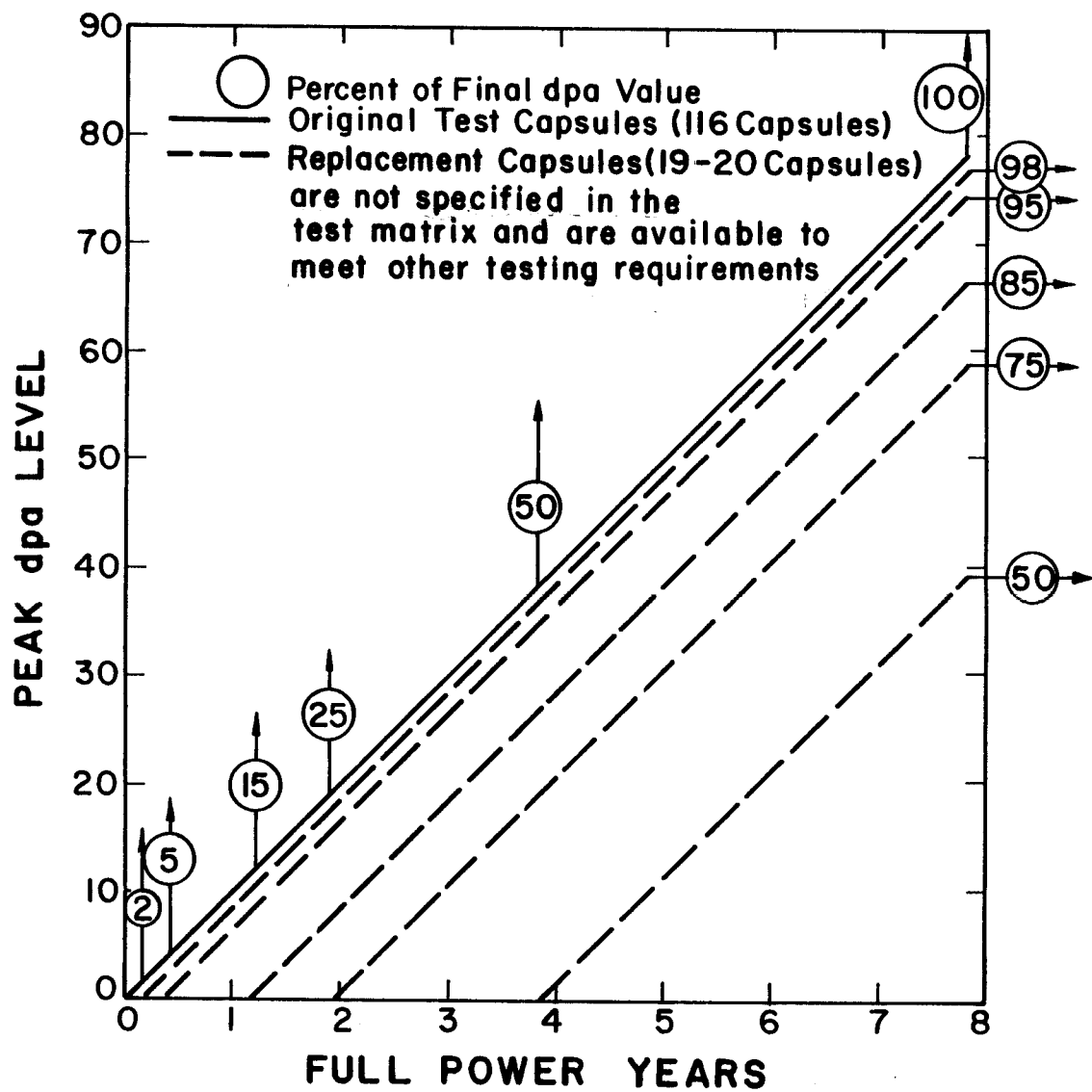
Fig. 10.2-2 The capsule discharge scheme.
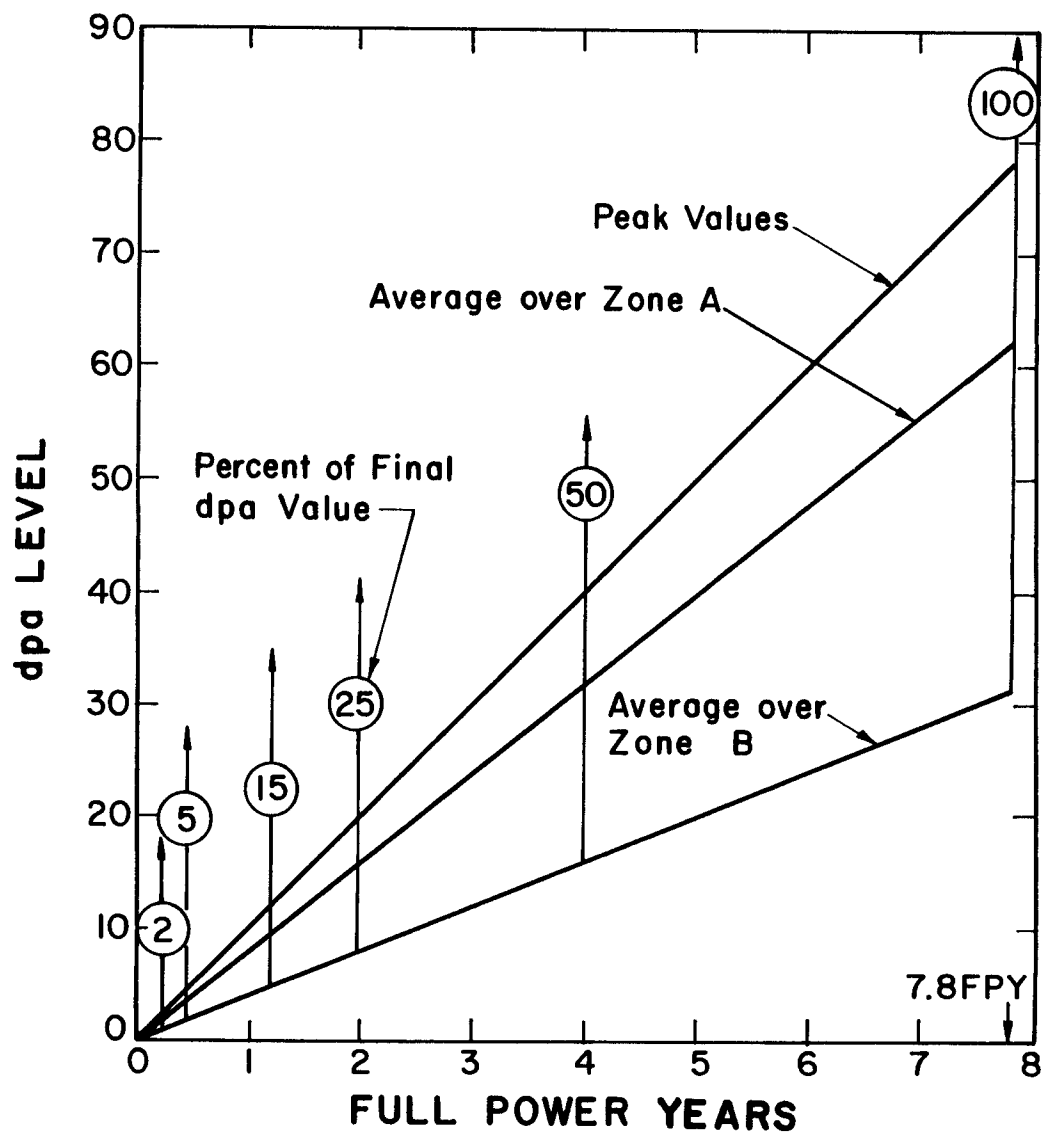
Fig. 10-2-3.   Dpa levels obtained in different zones of the capsule.   Numbers
in circles represent the percent of final dpa value obtained.

Table 10.2-2. Parameters Derived From TASKA Test Matrix

Item	Value
1. Number test modules (TM) in TASKA-M	1
2. Number specimen capsules in TM	180*
3. Time to achieve goal fluence (FPY)	7.8
4. Average time between TM changeouts from reactor (FPd)[+]	475
5. Minimum time between TM changeouts (FPd)[+]	85
6. Maximum time between TM changeouts (FPd)[+]	1424

*Mirror and tokamak specimens considered. Only 116 capsules are required as per Table 10.2-1.
[+]Full power days.

10.2.2.2 Materials Test Blanket No. 4. The materials test blanket no. 4 is the hardware that contains the materials test specimens and provides environmental containment as specimens are irradiated in the TASKA-M. Figure 10.2-4 illustrates the key features of the test module concept design for TASKA-M. The key components of the materials test blanket no. 4, that will be referred to often in this section, are the (1) specimen capsule which contains the groups of individual materials specimens, and (2) the annular test module which acts as the heat sink and holding fixture for specimen capsules.

The test module concept must be consistent with the requirements of the test matrix (see Section 10.2.2.1) and with the mechanical and neutronics characteristics of the TASKA-M reactor. The reactor configuration therefore strongly affects the test module design and conversely the test module will have an impact on the availability, floor space, services, access, remote handling and operations required by TASKA-M.

10.2.2.2.1 Test Module Design Criteria. The test module is based on the following general design requirements:
1. Reliability
2. Minimum specimen temperature variation
3. Quick turnaround (reconstitution).

**TASKA-M
TEST MODULES**

**ARRANGEMENT OF TEST
MODULES IN CENTRAL CELL**

PLASMA AXIS

MATERIALS TEST BLANKET NO. 4

MATERIALS TEST BLANKET NO. 3

INSTRUMENT AND COOLANT LINE SHIELD PLUG

ANNULAR CONICAL CYLINDER TEST MODULE WITH 180 CAPSULE TUBES

VACUUM SHROUD

TEST SPECIMEN CAPSULE

MATERIALS TEST BLANKET NO. 4

MODULE SHIELD PLUG
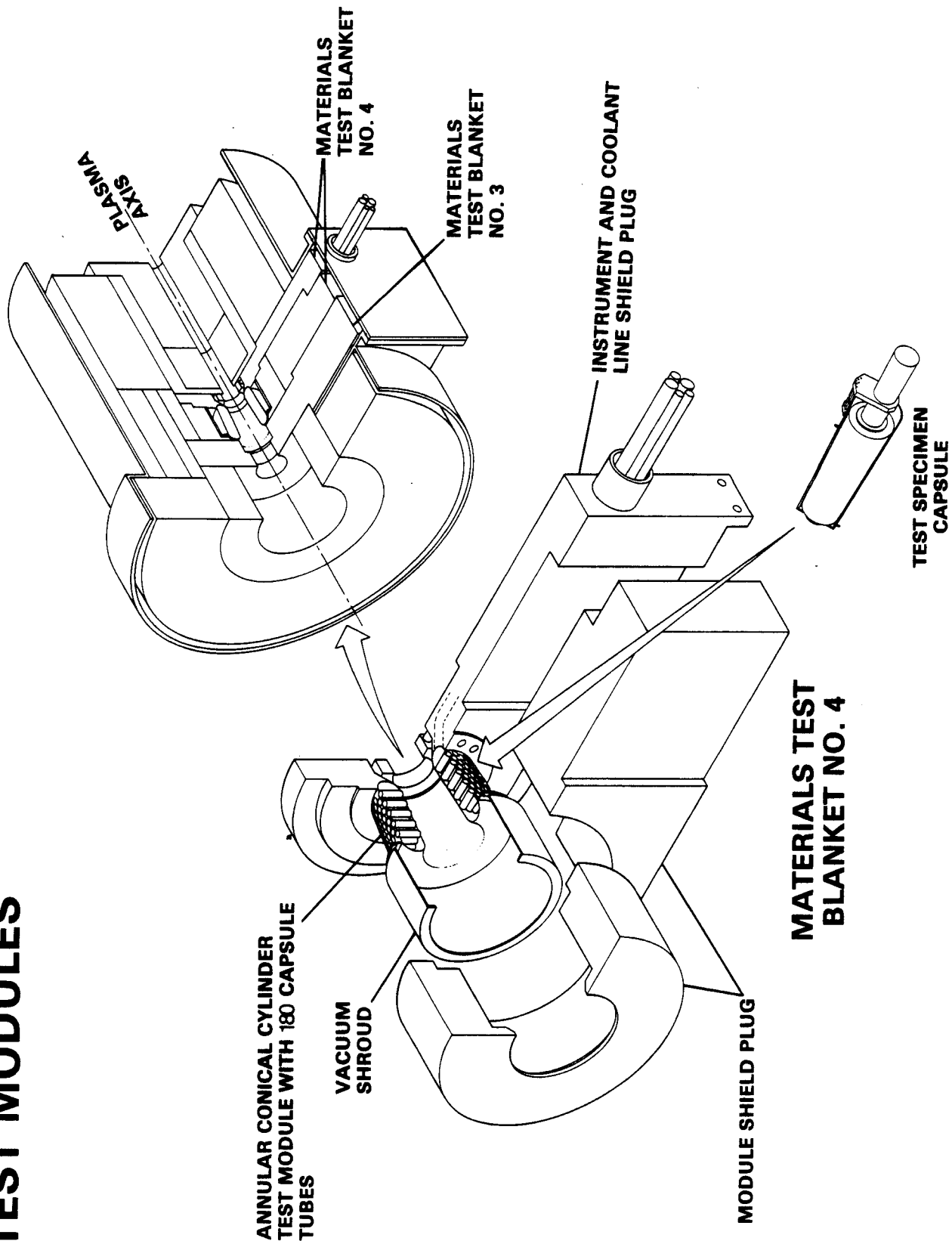
Fig. 10-2-4. Major components of the materials test module.

Based on the above general test module requirements and features of the conceptual TASKA-M reactor design, the following more detailed criteria (Table 10.2-3) were established to guide the test module design. The above requirements and criteria are consistent with the TASKA-M test matrix and were established as a result of materials testing experience gained through involvement in (1) the fast breeder reactor program, and (2) design studies supporting the Fusion Materials Irradiation Test Facility, the INTOR Study, and the TASKA conceptual design.

10.2.2.2.2 Arrangement of Test Modules in TASKA-M. Four different testing facilities are provided in the TASKA-M central cell. These are the liquid metal blanket, the solid breeder blanket, materials test blanket no. 3, and materials test blanket no. 4. Materials test blanket no. 4 will be referred to simply as the materials test module which is designed to test a wide variety of structural materials as defined in the design criteria (Table 10.2-3). This materials test module is nested next to and underneath materials test Blanket No. 3 and together with it forms the vacuum boundary. Materials test module no. 3 is subjected to a very high plasma surface heating rate ranging from ~ 1 W/cm^2 at the interface between modules 3 and 4 to ~ 85 W/cm^2 at the other side of the module. It will require water surface cooling and can be ideally used for high heat flux component testing. Design of module no. 3 is not considered further in this section.

10.2.2.2.3 Test Module Design Details. The major components of the TASKA-M materials test module, shown in Fig. 10.2-4, are the helium cooled heat sink (annular test module), the biological shield and the specimen capsules. The temperature within each of the 180 specimen capsules is predetermined by engineering the thermal barrier between the specimen capsule and the heat sink. Individual capsules can be independently accessed and are designed to operate at a predetermined temperature within the range of 350 to 650°C. The total irradiation volume within the module is 70.6 liters. Table 10.2-4 lists the detailed test module design values determined during the initial conceptual design.

Test Module. TASKA-M allocates one reactor opening for the materials test module together with materials test blanket no. 3. These modules are inserted into TASKA-M horizontally through a rectangular opening in the vacuum vessel. The annular test module consists of an HT-9 (ferritic alloy), helium

Table 10.2-3. Design Criteria

1. Test module shall permit simultaneous irradiation of an array of specimen capsules within the first 20 cm of blanket region. Maximum axial reactor opening is 91 cm.

2. Test module components shall have a design lifetime of at least four full power years.

3. Temperature range available for designing specimen capsule shall be 350-650°C with a calculated variation in specimen temperature of less than 10°C.

4. Each specimen capsule shall have independent temperature control and monitoring capability.

5. Test modules shall be capable of accepting previously irradiated specimens and undergoing reconstitution.

6. A portion of the test module shall interface directly with the plasma chamber. There will be no separate first wall between test module and plasma.

7. Test module shall interface with the adjoining blanket and shield and be consistent with the TASKA-M concept, and with biological shielding requirements.

8. Test module design shall maximize utilization of the available flux-volume.

Table 10.2-4. Design Values for Test Module #4

REACTOR OPENING
- Maximum axial opening of 90 cm

TEST MODULE
- Material of Construction: HT-9
- Size: Inside radius - 18 to 22 cm (conical)

  Outside radius - 38 to 42 cm (conical)

  Length - 55 cm (end to end) 42.4 cm straight section
- No. of Capsule Tubes: 180
- Total Heat Generation: 572 kW
- Coolant: Helium at 3448 kPa and 125°C
- Flow Rate: 33.7×10^3 ℓ/min
- Coolant Pipe Size: 12.5 cm diameter
- Instrumentation Per Capsule Tube: 2 pair thermocouple leads - chromel alumel

  2 gas leads - 0.158 cm diameter for gas gap control

SPECIMEN CAPSULE
- Material of Construction: 316 SS
- Size: 5 cm diameter by 20 cm long
- Specimens: Various shapes packed to 50% of capsule volume in NaK (22/78)
- Instrumentation: (2) 0.168 cm diameter stainless steel sheathed MgO insulated thermocouples
- Sealing: All welded construction with bellows for NaK expansion
- Gas Gap: Variable annulus 0.018 - 0.100 cm filled with helium or neon or mixtures of the two gases

filled pressure vessel structure which is penetrated by 180 capsule holes. The capsule holes are arranged with their long axes along radial lines with the open end of the capsule hole facing away from the plasma. The capsule holes are arranged in eight rows. These are grouped as four pairs of tubes which are on a triangular pitch between pairs and which are in line outside of pairs. Helium flows parallel to the module axis inside the module, perpen-

dicular to, and outside of, the capsule holes. Instrumented specimen capsules shown in Fig. 10.2-4 can be inserted in any of the 180 capsule holes. The specimen capsule outside diameter is spaced from the inside wall of the capsule hole by a gas cap. This gap becomes "sealed" when the specimen capsule is inserted into the capsule hole.

Neutron and gamma heat deposited in the test specimens is transferred by conduction via the NaK liquid metal to the capsule wall, across the insulating gap, through the outer wall, which is cooled on the outside by the circulating helium system. Two 1.6 mm O.D. tubes are provided to access the insulating gap near the top and bottom of each of the 180 capsule holes. These tubes can provide inert gas to the insulating gap space. Two (2) lines are provided to the gap to permit either a static or dynamic supply of gas. In addition, they allow for on-line changeout of gas.

Two pair of thermocouple leads are connected to each of the 180 capsule holes and are routed between capsules along the outside front surface of the module. The electrical leads terminate in an electrical connector which is positioned near the entry of each capsule hole. This connector becomes mated with the specimen capsule thermocouple leads when the capsule is inserted in the capsule hole. The electrical leads (360 pair of thermocouples) and tubes (360) are routed from the module, along the helium coolant lines through stepped openings in the shield plug. From there they are run to instrument cabinets located in the experiment support area.

Coolant system. The helium coolant system is designed to remove heat from the test module structure and the specimen capsules contained within it. Helium, while not as good as water or sodium from a heat removal standpoint, is inert, relatively easy to handle and has minimal impact on the dpa-volume because it does not degrade the high energy neutrons.

The helium coolant path through the test module is divided into two zones by a 1/16 in. thick flow divider which is concentric with the first wall. The flow divider is located 1.8 cm radially outward from the first wall and also serves to support the lower ends of the 180 capsule tubes. Helium enters from the 12.5 cm diameter inlet pipe to a plenum which connects the space between flow divider and first wall, flows across the test module lower section (parallel to the axis) where it cools the high heat flux first wall and the lower portions of the capsule tubes. At the other side the helium reverses

flow and enters the upper module section where it cools the test module structure and the upper portion of the capsule tubes.

To evaluate the performance of the helium cooled test module the temperature profile from the bulk helium coolant to the center of the specimen capsule was calculated. Figure 10.2-5 illustrates the results of one such calculation for the case in which the total heat removed from the specimen capsule was uniformly averaged over the capsule wall area (i.e., heating gradients were not considered). The average neutron induced heating rate was assumed to be approximately 4.94 W/cm^3 over the capsule volume at the axial location corresponding to the peak neutron wall loading. For the materials within the capsule, 4.94 W/cm^3 corresponds to 1.13 W/g. Table 10.2-5 summarizes the temperature profile date for the average case (Fig. 10.2-5).

Table 10.2-5. Test Module Temperature Profile

BASIS: Avg. Heating Rate + 1.13 W/g (Max. = 1.68 W/g)
Bulk Helium ΔT = 50°C
Helium Convective Heat Transfer
Coefficient = $1420 \dfrac{W}{(m^2)(^0K)}$

	Temp. °C Average	Temp. °C Maximum
Helium Inlet	100**	100**
Bulk Helium ΔT	50	50
Helium Outlet	150	150
Helium Film ΔT	48	72
Capsule Tube Outside	198	222
Capsule Tube ΔT	6	9
Capsule Tube Inside	204	231
Gas Gap ΔT (Variable)	109-409	64-364
Specimen Capsule ΔT	37	55
Capsule Center	350-650	350-650

**Provides ΔT of 75°C to cool with water at 25°C.
+Based on 1.34 MW/m^2
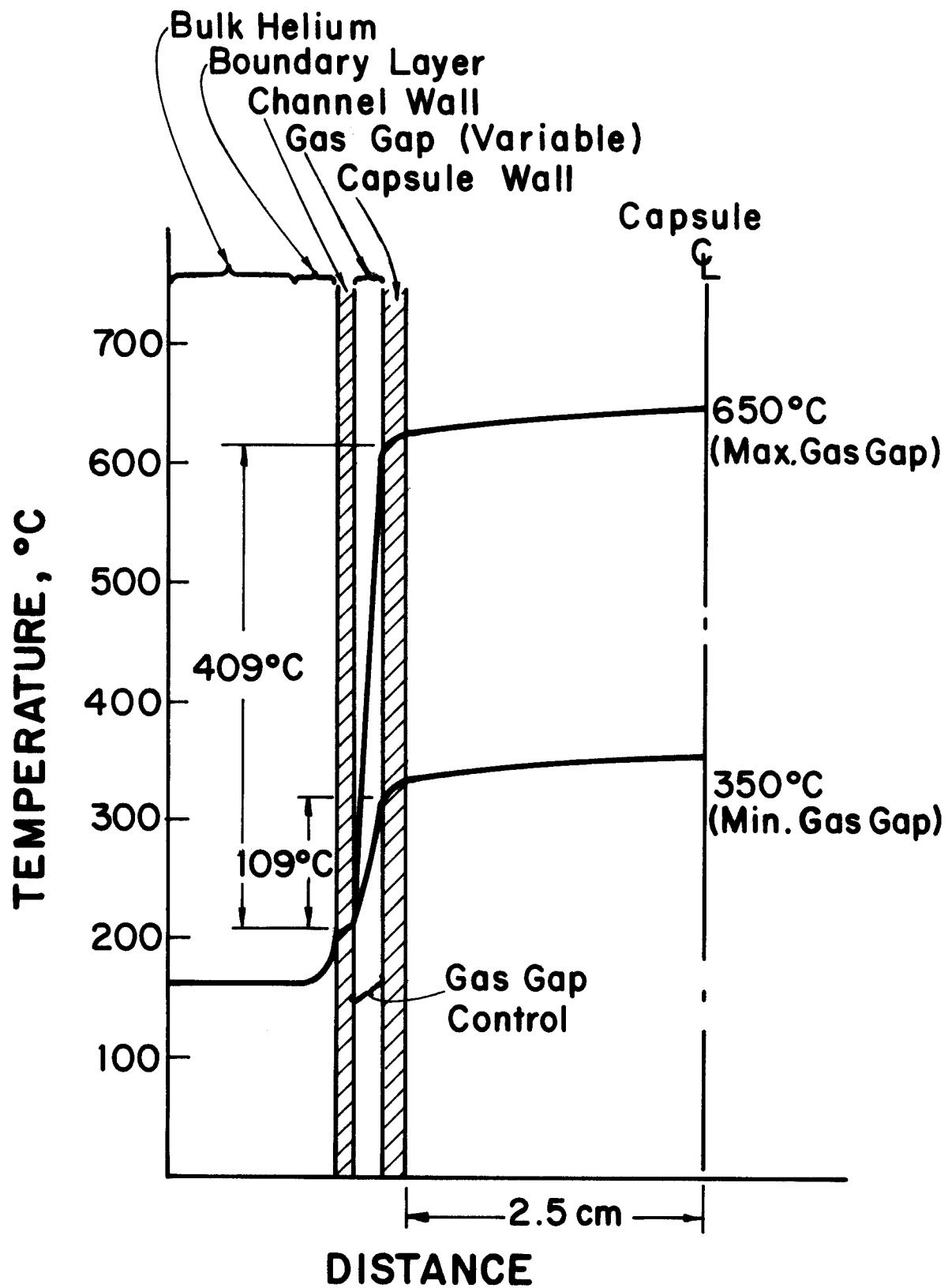
Fig. 10.2-5.   Temperature profile from helium coolant into specimen capsule.

As heat flows from inside the specimen capsule to the helium coolant it encounters its greatest resistance at (1) the engineered gas gap, and (2) at the boundary layer between the helium coolant and the outside of the capsule hole. The thermal conductivity of the engineered gas gap can be controlled by varying the composition of gas (helium and neon) within the gap. By varying the mixture of the two gases, it is possible to vary the thermal conductivity (K), and hence the temperature drop across the gap (ΔT), by approximately +100%, -50%. This allows the temperature of the capsule to be controlled to a certain degree. The range of control is, however, strongly dependent upon the magnitude of the ΔT across the gap. As illustrated in Fig. 10.2-5 for the case in which the capsule centerline temperature is 650°C, the ΔT gap (409°C) represents a significant fraction of the total temperature drop between the capsule and bulk helium coolant. For a low temperature capsule (350°C) the ΔT gap (109°C) is a smaller fraction of the total ΔT, hence, temperature control will not be as good. For the peak location this ΔT reduces to 64°C which may not result in adequate temperature control at the peak heating rate capsule location.

Specimen Capsule (Fig. 10.2-6). Each specimen capsule is a circular stainless steel cylinder 5 cm in diameter by 20 cm long. Material test specimens are positioned inside each capsule. A NaK liquid metal heat transfer bond is provided between test specimens and the capsule wall. Each capsule is provided with two or more chromel-alumel thermocouples for measuring test specimen temperature. The capsule wall thickness is adjusted during fabrication to provide a gap between it and the capsule hole. This gap is sized so that when it is filled with a particular insulating gas it will provide the desired test specimen temperature. This gap can be of uniform width or it can be stepped along the capsule axis to compensate for different heating rates between the front and the back ends of the capsule. The top of each capsule includes a cylindrical canopy which seals the gap when the capsule is inserted in the tube. A metal bellows with a compressible space is provided for thermal expansion of the NaK bond.

To cover the entire temperature range (350-650°C) requires a relatively high and low thermal conductivity media in the gap. Helium and neon were selected - helium because of its good thermal conductivity and neon because of its lower thermal conductivity and reduced activation (compared to argon).
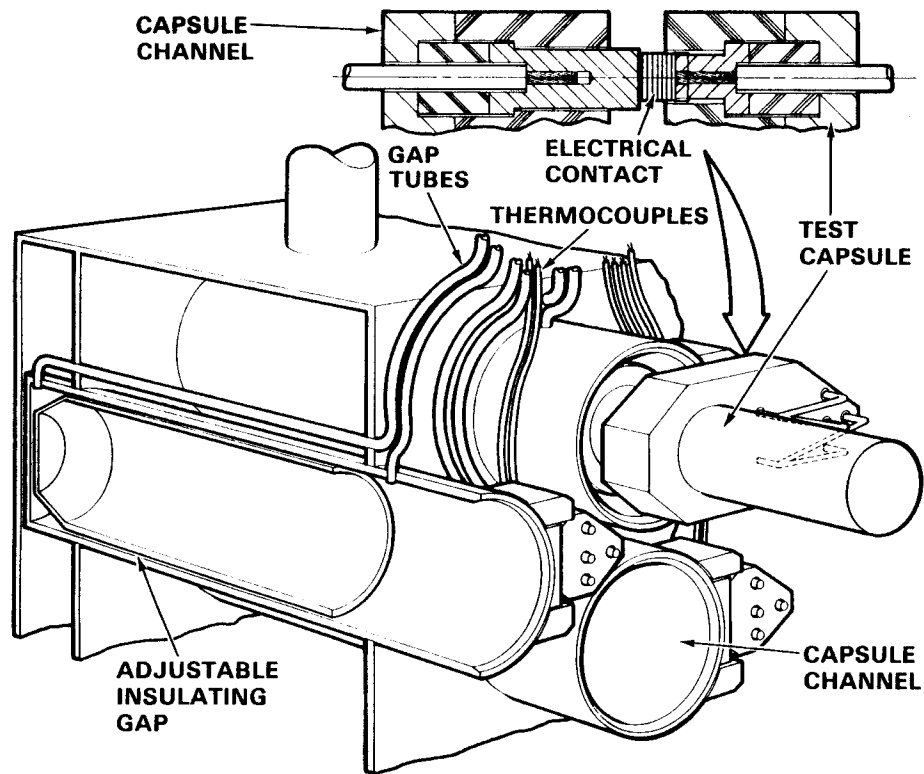
Fig. 10.2-6.   Major components of the specimen capsule.

The practical range of gas gaps is approximately 0.0175 to 0.10 cm. A 0.0175 cm gap is believed to be the minimum controllable gap width from a fabrication standpoint and for gap widths above approximately 0.10 cm convection starts adding to conduction which makes temperature prediction less reliable.

In summary, for gas gap widths ranging from 0.0175 to < 0.10 cm filled with an atmosphere of helium or neon, the range of average specimen capsule temperatures is 350 to 650°C. For that portion of the specimen capsule receiving the maximum neutron heating rate ($\sim$ 7.4 W/cm^3) the attainable specimen capsule temperatures are also 350-650°C. (This assumes no axial heat transfer -- only radial.) Hence, the initial design concept can meet the specified low temperature criteria of 350°C.

10.2.2.3 Test Module Operation and Handling. The frequency of test module removal is a function of the test matrix fluence requirements discussed in Section 10.2.2.1 and the reliability of the test module. If one looks only at the fluence requirements the materials test module will be removed from the reactor and transported to a disassembly hot cell every $\sim$ 460 full power days (Table 10.2-2). There will be additional removals from the reactor as random failures occur within the test module and test module control and data acquisition equipment.

When problems and failures occur within the test module the entire test module will have to be removed from the test facility for repair. The design does not accommodate maintenance internal to the vacuum flange while in the test facility. Therefore, in order to maximize TASKA-M availability a second test module should always be available for insertion when the primary module requires repair. The transfer of the module from the test facility to the disassembly hot cell should be a simple, efficient operation with minimal impact on other systems. Removal of the shielded module will require a counterweighted horizontal handling machine. This machine will be moved next to the TASKA-M test module no. 3 and no. 4 port. After removal of the vacuum cover the modules will be bolted to the handling machine. The handling machine will remotely remove the test modules horizontally from the reactor.

The operations required to remove a test module from TASKA-M are given in Table 10.2-6.

Table 10.2-6. Operations Required For Test Module Removal From Reactor

Operation	Comment	Approximate Time to Complete Operations (hr)
1. Following reactor shutdown and cooldown period, disconnect helium piping and instrument leads.	Hands on operation.	16
2. Unbolt flange from vacuum boundary of machine.	Hands on.	4
3. Unbolt large module coverplate from pipe penetration flange.	Hands on.	4
4. Swing coverplate over helium piping and remove. Protect sealing surfaces.	Hands on.	8
5. Secure handling fixture to test module. Slide entire test module from reactor (from side).	As soon as removal begins operations become remote.	4
6. Transfer test module to hot cell for disassembly (or load TM into a large cask for transfer).	Totally remote viewing and handling.	3
7. Place test module in rotating, indexing figure in hot cell.	Hot cell operation utilizing crane, electromechanical and master slave manipulators.	8
8. Remove shield plug and shear vacuum cover seal which covers specimen capsule tubes.	Remote operation.	16-32
9. Withdraw specimen capsules from capsule holes and replace with new capsules.	Utilize rotating removal machine which indexes on each row of capsule holes.	24-48
10. Verify integrity of test module and all specimen capsules. Leak test system, service lead continuity check.	All systems and components must be verified operable.	48-120
11. Replace vacuum cover and weld, reassemble shield plug to module. Prepare for transfer back to reactor.	----	48-72
	Total Time:	183-319 hrs.

The times estimated are actual working hours (assumes 60 minutes are worked each hour) assuming success-oriented operations.

10.2.2.4 Summary and Conclusions. A materials testing scenario for TASKA-M
was presented in the form of a test matrix. The test matrix lists the type of
materials test, the irradiation temperatures, goal fluences and details re-
lating to stresses and postirradiation test conditions. It was shown that the
entire TASKA-M test matrix consisting of nearly 23,000 test specimens could be
completed in approximately eight full power years utilizing on the average
less than two-thirds of the volume in a single test module. The maximum flu-
ence achieved by any group of specimens is over 50 dpa.

The test module was designed to contain and thermally control the test
specimens within the vacuum boundary of the reactor. Helium was chosen as the
bulk heat removal fluid because it has the least moderating effect upon the
neutrons and therefore results in the greatest dpa-volume for a given test
module space envelope. Helium is acceptable from a heat removal standpoint;
however, further design optimization will be required to verify the limits of
test module operation.

The operation impacts of materials testing upon TASKA-M should be minimal
as long as reliable test modules can be designed and fabricated. The test
module concept presented in this section requires minimal handling in the
vicinity of the reactor -- the majority of test module remote operations occur
during test module disassembly which occurs in hot cell facilities removed
from the reactor operating gallery.

10.2.3 Neutronics Analysis

Neutronics calculations have been performed to determine the specimen
damage profiles and testing capability of the materials testing modules in
blankets #3 and #4. Profiles of the power density resulting from neutron and
gamma heating in the modules have also been determined as they are required
for proper design of the cooling system. The materials test modules are
cooled by helium gas. Water coolant is not used because of the increased
damage gradients resulting from higher neutron attenuation in water.

Test module #3 is 55 cm wide and consists of two segments; the first is
23 cm wide with an inner radius of 25 cm while the other is 32 cm wide with an
inner radius of 32.5 cm. The wall is recessed to a radius of 32.5 cm to
accommodate the ICRF antenna. The outer radius of the module is 45 cm imply-
ing that one of the segments has a thickness of 20 cm while the other is only
12.5 cm thick. While the four main central cell neutral beam ducts do not

penetrate the test modules, the low energy neutral beam penetration reduces the volume of module #3 by 4.5%. In addition, the ICRF antenna coax penetration accounts for a 1.6% reduction in the volume of module #3. This yields a volume of 186 liters for module #3. Module #4 has a tapered inner wall with the radius decreasing from 22 cm to 18 cm in order to achieve high neutron fluences. The back of the test module has a radius of 42 cm. The module is 53 cm wide with a total volume of 227 liters.

The test capsules are 5 cm in diameter and have different lengths depending on their location in modules #3 and #4. The axis of the capsule is placed perpendicular to the plasma axis implying that the spacing between capsules will increase as one moves toward the back of the module. Although a detailed design was made only for module #4, both modules #3 and #4 will be considered in the neutronics analysis and assumptions about the design of module #3 will be made. For the purpose of performing the neutronics calculations we assumed that 341 capsules are used in module #3 while 220 capsules are used in module #4. This provides 93 and 90.7 liters of test capsule volume in modules #3 and #4, respectively. The test capsules, therefore, represent 50 and 40% of the total volumes of modules #3 and #4, respectively. These parameters are given for the preliminary design used in the neutronics calculations. However, the final mechanical design resulted in reducing the test volume and number of capsules as indicated at the end of this section. The neutronics results will be modified to account for this volume reduction. The capsules are assumed to consist of 50 vol.% Nak, which is used as a thermal contact material, and 50 vol.% 316 SS, which represents the specimens and capsule structural material. The module structure is assumed to represent 20% of the module volume and is made of HT-9. The helium gas coolant occupies the remaining volume of the test module. Table 10.2-7 gives the locations, dimensions, volumes and compositions of the two materials test modules.

In the relatively short central cell of TASKA-M, the D-T neutron source has a strong axial variation as indicated in Fig. 5.1-1. The linear source strength increases from a value of 5×10^{15} n/cm s at the reactor midplane to a peak value of 9.6×10^{15} n/cm s at a point 170 cm from the midplane. This peak occurs near the center of test module #4. The source strength drops rapidly as one moves farther from the reactor midplane. This source axial variation together with the axial variation of the wall radius results in an

Table 10.2-7. Some Key Parameters for the Preliminary Design
of the Materials Test Modules

	Module #3	Module #4
Axial location of test zone, cm	80 ≤ z ≤ 135	137 ≤ z ≤ 190
Width of test zone, cm	55	53
Inner/outer radius for test zone, cm	25-32.5/45	18-22/42
Module volume, ℓ	186	227
Number of capsules	341	220
Total capsule value, ℓ	93	90.7
Module composition (vol.%)		
HT-9 module structure	20%	20%
Helium coolant	30%	40%
316 specimen and capsule structure	25%	20%
NaK thermal contact material	25%	20%

even stronger axial variation of the neutron wall loading along blankets #3 and #4 devoted for materials testing as shown in Fig. 5.1-3. The average neutron wall loadings for test zones #3 and #4 are 0.69 and 1.226 MW/m^2, respectively. Notice that the segment of blanket #4 behind the ICRF antenna has a very low wall loading averaging only 0.387 MW/m^2 and hence is not utilized for materials testing. The neutron wall loading in the materials test module #3 varies between a minimum of 0.6 MW/m^2 and a maximum of 0.78 MW/m^2. Module #4 has a minimum neutron wall loading of 1 MW/m^2 and a peak of 1.34 MW/m^2.

One-dimensional coupled neutronics and photonics calculations have been performed to give preliminary estimates for the radial variation of power density and damage rate in the test capsules. In these calculations a first wall radius of 20 cm, which corresponds to the midplane of module #4, was used. A 3 mm thick HT-9 module wall was used followed by a 19.7 cm thick test zone consisting of 25 vol.% 316 SS, 25 vol.% NaK, and 50 vol.% He. A shield made of 90 vol.% 316 SS and 10 vol.% H_2O was used behind the test zone. The discrete ordinates code ONEDANT[5] was used to model the problem in cylindrical geometry using the P_3S_8 approximation. A coupled 46 neutron-21 gamma group

cross section library based on the VITAMIN-C data library[6] and the MACKLIB-IV-82 response library[7] was used.

Figure 10.2-7 gives the radial variation of dpa and helium production rates in steel. The results are normalized to a unit wall loading. The module and capsule walls have a total thickness of 13 mm implying that the specimen exposed to the highest irradiation level is placed at a depth of 13 mm from the surface of the module facing the plasma. Using a peak neutron wall loading of 1.34 MW/m^2 implies that the peak dpa and helium production rates in the test specimens are 11.2 dpa/FPY and 120 He appm/FPY, respectively. However, smaller values are expected from the three-dimensional calculation since in the one-dimensional model the neutron source is assumed to have uniform axial distribution.

Figure 10.2-8 gives the radial variation of power density in both NaK and 316 SS. Notice that the power density in steel is a factor of ~ 5 higher than that in NaK. This is primarily due to the higher density and larger gamma absorption. Using the peak wall loading of 1.34 MW/m^2 indicates that the peak power density due to nuclear heating in the module wall is 13.1 W/cm^3. The peak power densities in the NaK and 316 SS of the test capsules are 2.8 and 12.7 W/cm^3, respectively. The peak power generated in a 20 cm long capsule is 1.71 kW. These values are conservatively larger than those expected from the detailed three-dimensional calculations.

Three-dimensional neutronics calculations have been performed for the materials test modules. The continuous energy Monte Carlo code MCNP[8] was used together with cross section data based on the ENDF/B-V evaluation. The geometrical model used in the calculations is illustrated in Fig. 10.2-9. For simplicity, azimuthal symmetry was assumed and the penetrations for the low energy neutral beam and the ICRF antenna coax were not included. This represents only ~ 2.7% of the total volume of test modules #3 and #4. Since these penetrations exist in the low fluence module (#3), their impact on the damage rate averaged over both modules will be negligible. However, when we determine the testing capability of the device represented by the volume integrated damage, we account for these penetrations by using the available test volume which excludes the penetration volume. Also, not included in the model are the ICRF antennas. These are very thin with an effective copper thickness of 8 mm and water thickness of 5 mm. This was estimated to reduce the damage in
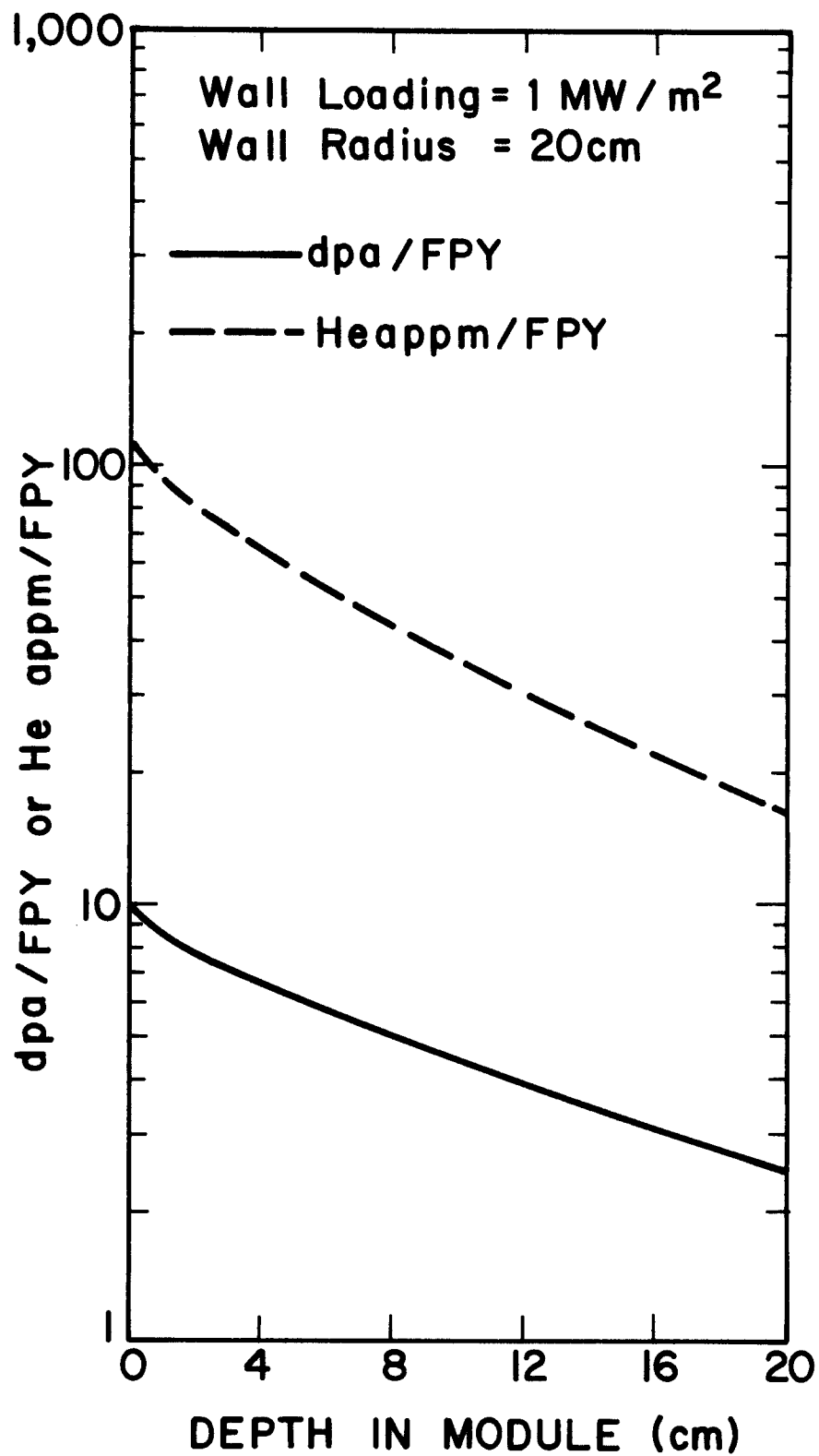
Fig. 10.2-7.   Radial variation of dpa and helium production rate in steel as
obtained from the one-dimensional calculation.
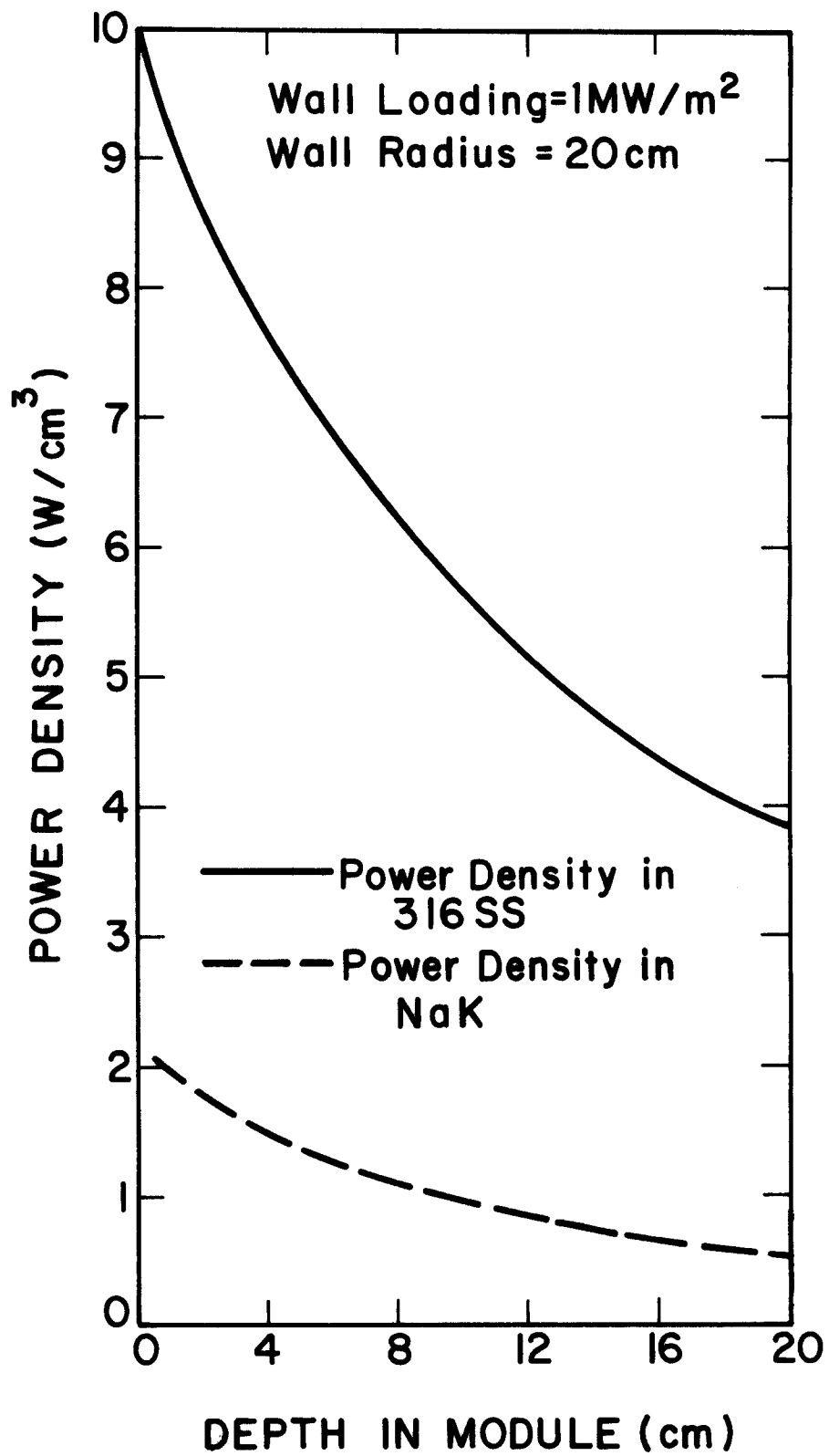
Fig. 10.2-8. Radial variation of power density in NaK and 316 SS as obtained
from the one-dimensional calculation.
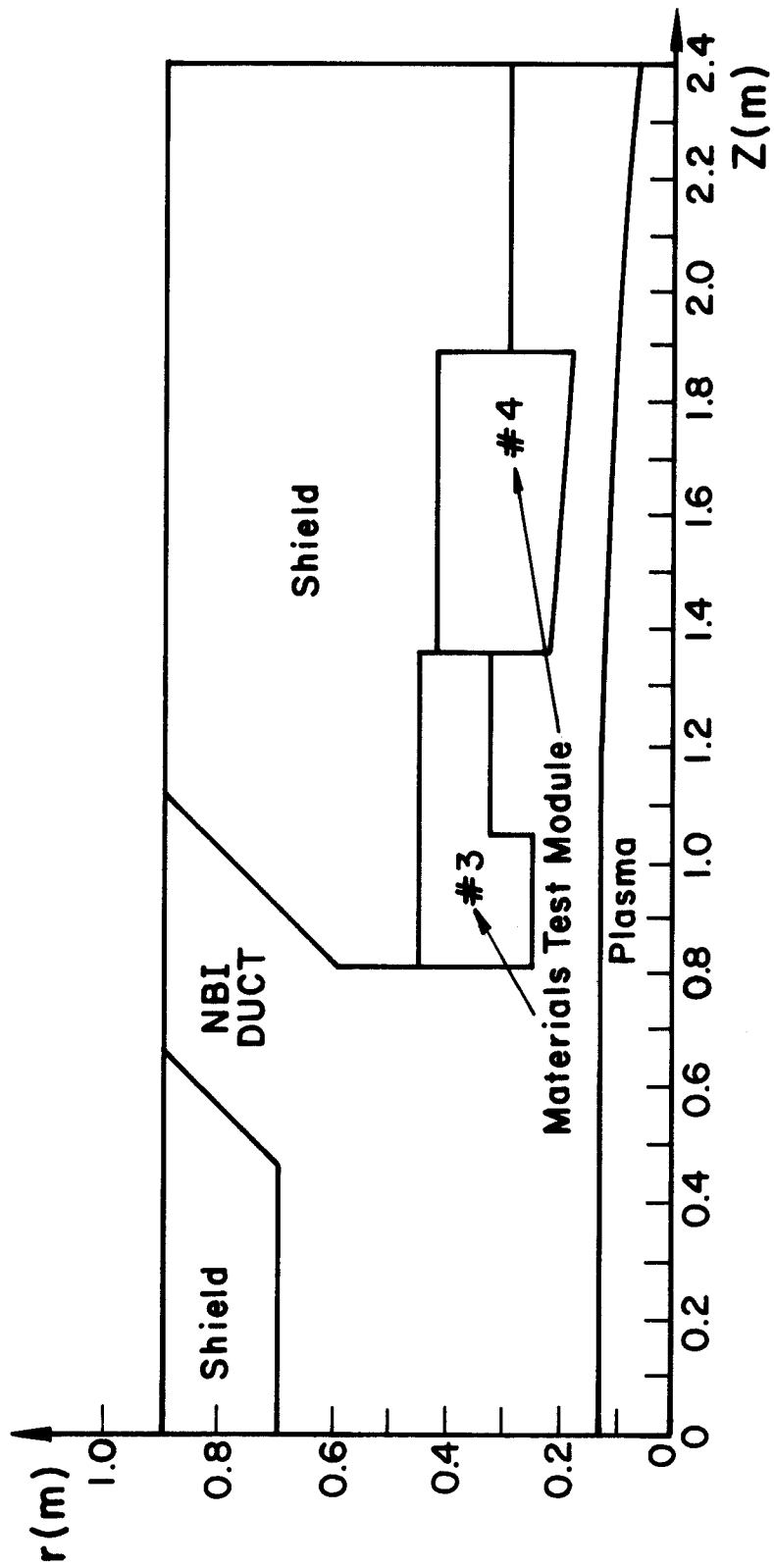
Fig. 10.2-9.   Geometrical model used in the MCNP calculations.

the segment of the test module behind the antenna by less than 10%. Since this will affect only a portion of the thin segment of module #3 the impact on the calculated overall testing capability is expected to be very small.

Since the source is symmetric about the midplane, a reflecting boundary was used to properly account for the contribution from source neutrons generated in the other side of the machine. Uniform smeared nuclide densities were used throughout modules #3 and #4. However, different compositions were used in the two modules as given in Table 10.2-7. The modules were divided into 50 cells per module to determine the damage profiles. 40,000 histories were used in the calculations yielding statistical uncertainties of less than 0.5% in the integral damage values for each of the modules. The statistical uncertainties in the local damage rates are less than 2%. An isotropic neutron source was sampled from the axial variation of source strength and plasma radius shown in Fig. 5.1-1.

Because of the limited central cell space and the neutron source peaking in TASKA-M, no attempt was made to utilize the REGAT[9] concept. However, the recession of the wall to accommodate the ICRF antenna results in some REGAT effects in modules #3 and #4 due to the direct source neutrons impinging on the sides of the modules. In order to assess this effect, two sets of calculations were performed for module #4. In one set, the actual geometry was modeled while in the other set the wall was not recessed in the zones adjacent to the test module such that no direct source neutrons will impinge on its sides.

Table 10.2-8 gives the average dpa and helium production rates in module #4 obtained in the two sets of calculations. It is clear that a gain of only 0.5% in average dpa rate is obtained by allowing direct source neutrons to impinge on the sides of the module. The gain in average helium production rate is 6%. The effect on helium production is more pronounced than that on dpa as the threshold energy for the (n,α) reaction is much higher than that for dpa. A much larger gain ($\sim$ 40%) was obtained using the REGAT design in TASKA.[10] The reason is that while in TASKA, the neutron source was axially uniform, the neutron source peaks near the center of module #4 in TASKA-M with much fewer source neutrons produced on the sides of the module. However, more REGAT effect is expected in the thick segment of module #3 due to the contribution from the source peak to the damage at the side of the segment at z =

Table 10.2-8. Average dpa and Helium Production Rates
in Test Module #4 Obtained Using Different Calculational Models

	Average dpa Rate (dpa/FPY)	Average He Production Rate (He appm/FPY)
One-dimensional calculation	5.13	39.10
Three-dimensional calculation		
Unrecessed surrounding zones	4.09	37.72
Recessed surrounding zones	4.11	39.98

103 cm. Included also in the table are the results obtained from the one-dimensional calculation normalized to the average wall loading of 1.226 MW/m^2 in module #4. The higher values obtained from the one-dimensional calculation are related to the axial variation of source. Using the average wall loading in the one-dimensional calculation properly accounts for the total number of source neutrons crossing the module wall. However, in the actual three-dimensional calculation with the peaked source distribution most of these neutrons are incident perpendicular to the wall and have a larger chance to penetrate all the way to the shield behind the test module. The effect is less pronounced for helium production which occurs only at high neutron energies ($\gtrsim$ 1 MeV).

The effect of using neutron multipliers in the surrounding shield was also investigated. A shield that consists of 80 vol.% multiplier, 10 vol.% 316 SS, and 10 vol.% H_2O was considered. Be and Pb were considered as neutron multipliers. The results obtained by three-dimensional calculations are given in Table 10.2-9 in comparison with the results obtained using a stainless steel shield. Pb results in higher average dpa rates than Be. This is due to the fact that while the neutrons produced from (n,2n) reactions in Pb are emitted isotropically, the neutrons are preferentially emitted in the forward direction in the case of Be with a smaller fraction of them returning into the test module. However, the gain in average dpa rate is very small and does not justify the added complexity in the shield design. Furthermore, using a neutron multiplier results in reducing the average helium production rate. This is attributed to the fact that the neutrons produced in the (n,2n) reaction

10.2-29

Table 10.2-9. Effect of Using Neutron Multipliers in the
Shield on Average Damage Rate in Module #4
Obtained From Three-Dimensional Calculations

	Average dpa Rate (dpa/FPY)	Average He Production Rate (He appm/FPY)
316 SS shield	4.11	39.98
Be shield	4.11	39.42
Pb shield	4.16	38.91

have energies in the low MeV region where the (n,α) cross section is quite small. The effect is more pronounced for Pb due to the softer spectrum of the neutrons produced in the $(n,2n)$ reaction. Therefore, there is no incentive for using a neutron multiplier in the shield.

The dpa and helium production profiles in modules #3 and #4, obtained from the three-dimensional Monte Carlo calculations using the geometrical model of Fig. 10.2-9, are given in Figs. 10.2-10 and 10.2-11. These profiles reveal that the peak dpa and He production rates in the test modules are 10 dpa/FPY and 120 He appm/FPY, respectively. The dpa rates drop to a value of ~ 1.5 dpa/FPY at the back of the module. The helium production rate drops to ~ 10 He appm/FPY. Table 10.2-10 lists some of the key damage parameters in modules #3 and #4.

Coupled neutronics and photonics calculations for the two materials test modules were performed to determine the power density profiles. A peak power density of 4 W/cm^3 occurs in module #4. Notice that this gives the power per unit volume of the module which was considered to consist of a homogeneous mixture of NaK, steel and He. The corresponding peak power density in the test capsule is 6.67 W/cm^3. This is about 14% less than the 7.75 value obtained using the one-dimensional model. This is expected due to the assumed uniform axial source distribution in the one-dimensional model. The average power density in the test modules is 1.3 W/cm^3 which corresponds to an average capsule power density of 2.17 W/cm^3 compared to a value of 3.16 W/cm^3 obtained from the one-dimensional calculations.
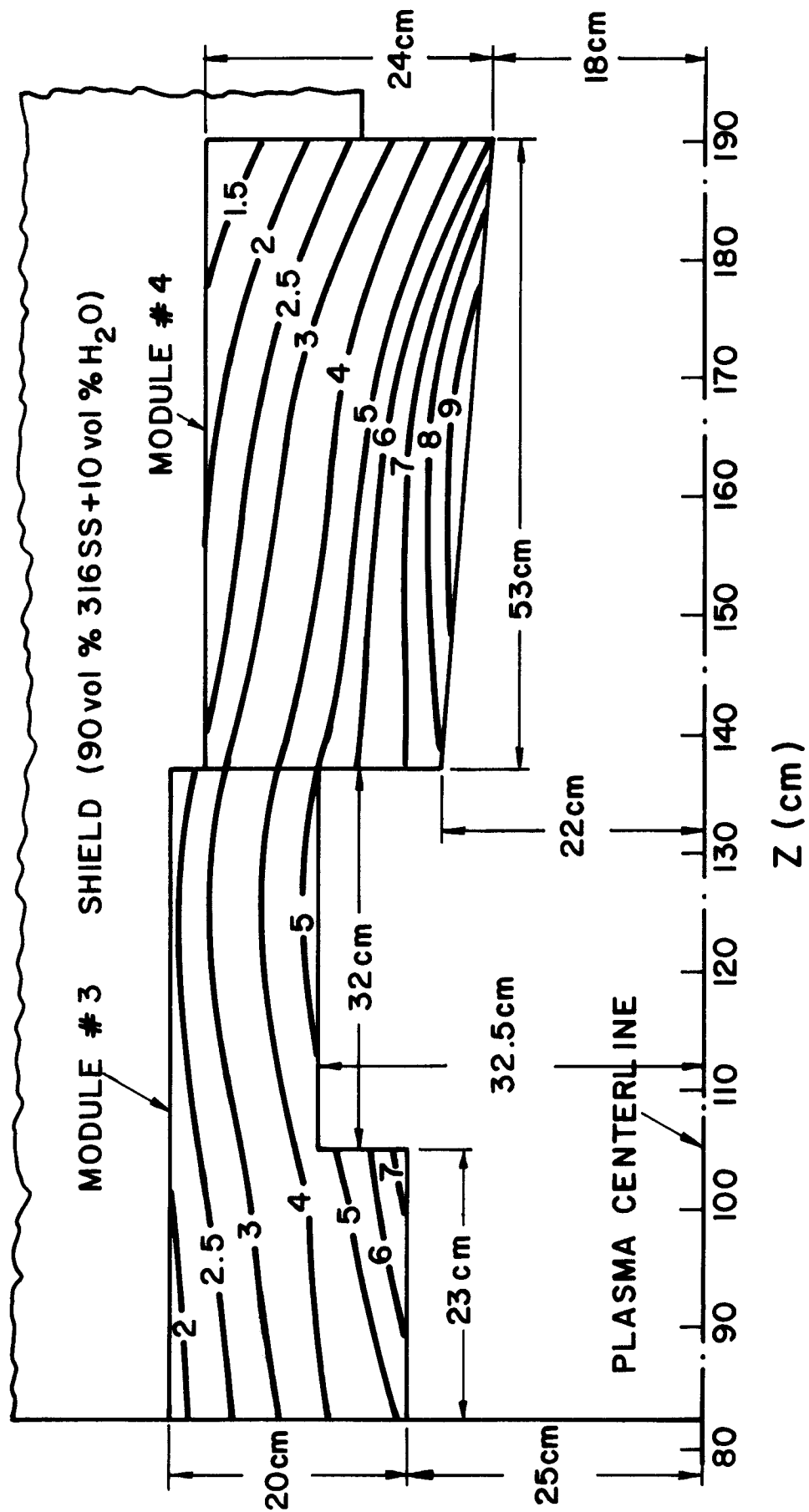
Fig. 10.2-10. Equal dpa rate (dpa/FPY) contours in the test modules.
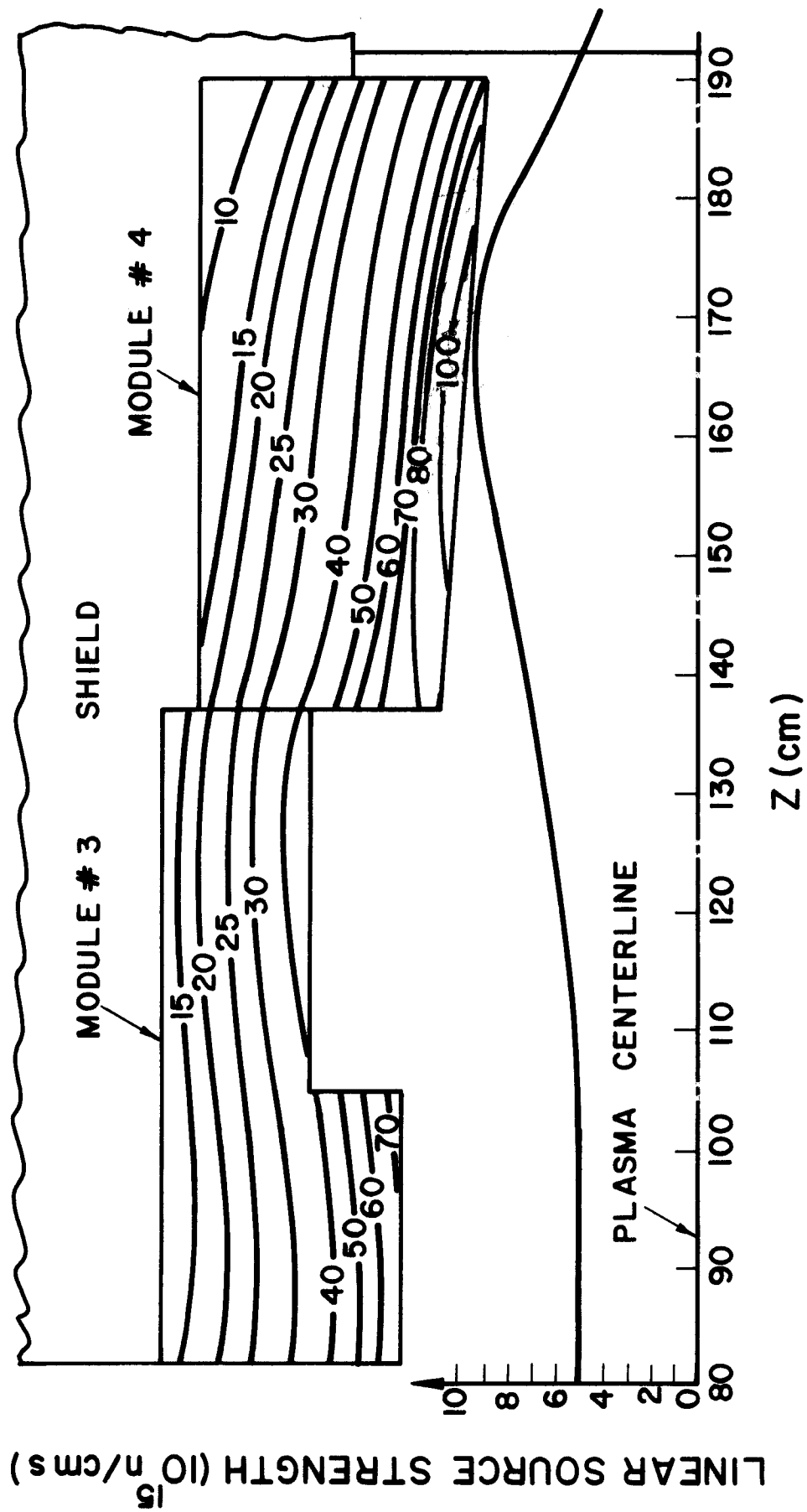
Fig. 10.2-11. Equal He production rate (He appm/FPY) contours in the test modules.

Table 10.2-10. Key Damage Parameters for the Materials Test Modules

	Test Module #3	Test Module #4
Peak dpa rate (dpa/FPY)	7.5	70
Minimum dpa rate (dpa/FPY)	2	1.5
Average dpa rate (dpa/FPY)	3.38	3.92
Peak He production rate (He appm/FPY)	70	120
Minimum He production rate (He appm/FPY)	15	10
Average He production rate (He appm/FPY)	29.5	35.1

Another way of expressing the damage in the test specimen is to sum the product of the damage level times the volume of the test zone that can produce that damage level. This parameter accounts for the number of specimens that can be irradiated to high levels. It can be calculated by multiplying the average damage level by the total test capsule volume in the module. This number reflects the total space available not only for specimens but also for temperature, stress, and environmental control. We have assumed that TASKA-M will operate on the following schedule.

Year	% Availability
1	10% (hydrogen operation)
2-3	15%
4-7	25%
8-20	50%

Therefore, the device is expected to operate for 7.8 FPY.

Because of the large pressure of the helium gas coolant, the final module design employs two hemispherical heads at both ends of the modules. This results in removing two rows of capsules from each module. The number of capsules in module #4 is reduced to 180 while the number in module #3 becomes 276. The total volumes of the capsules utilized in modules #3 and #4 are 74.5 and 70.6 ℓ, respectively. The average damage rates are expected to be higher than those obtained from the three-dimensional calculations where it is assumed that the whole module width is utilized for testing. On the other hand, lower damage rates are expected in module #3 due to use of a separate water cooled first wall that can handle the large surface heat flux. The three-

Table 10.2-11. Volume Integrated Damage in the Final Design
of the Materials Test Modules

	Module #3	Module #4
# of capsules	276	180
Total capsule volume (ℓ)	74.5	70.6
Maximum dpa rate (dpa/FPY)	5.5	10
Average dpa rate (dpa/FPY)	3.38	3.92
Cumulative dpa-ℓ	1960	2160
Maximum He production rate (He appm/FPY)	70	120
Average He production rate (He appm/FPY)	29.5	35.1
Cumulative He appm-ℓ	17140	19330

Table 10.2-12. Dpa-ℓ Values per FPY of Operation in Different Facilities

INTOR	182
TASKA	1510
FMIT	5
RTNS-II	0.0003
TASKA-M	530

dimensional results were used to determine the values for the volume inte-
grated damage accumulated at the end of life of the device given in Table
10.2-11 for both modules. The total dpa-ℓ value obtained in TASKA-M is 4100.
This corresponds to 530 dpa-ℓ per FPY of operation. Table 10.2-12 gives a
comparison between the values of dpa-ℓ obtained per FPY of operation for the
different proposed fusion facilities. While the value for TASKA-M is only 35%
of that in TASKA,[1] the dpa-ℓ figure of merit in TASKA-M is a factor of ~ 3
higher than that in INTOR[11] and much higher than the corresponding values in
FMIT[12] and RTNS-II.[13] The time integrated dpa and dpa-ℓ values for TASKA-
M are given in Fig. 10.2-12. It can be seen that in the 7.8 FPY operating
scenario, the maximum accumulated damage in steel is ~ 78 dpa.
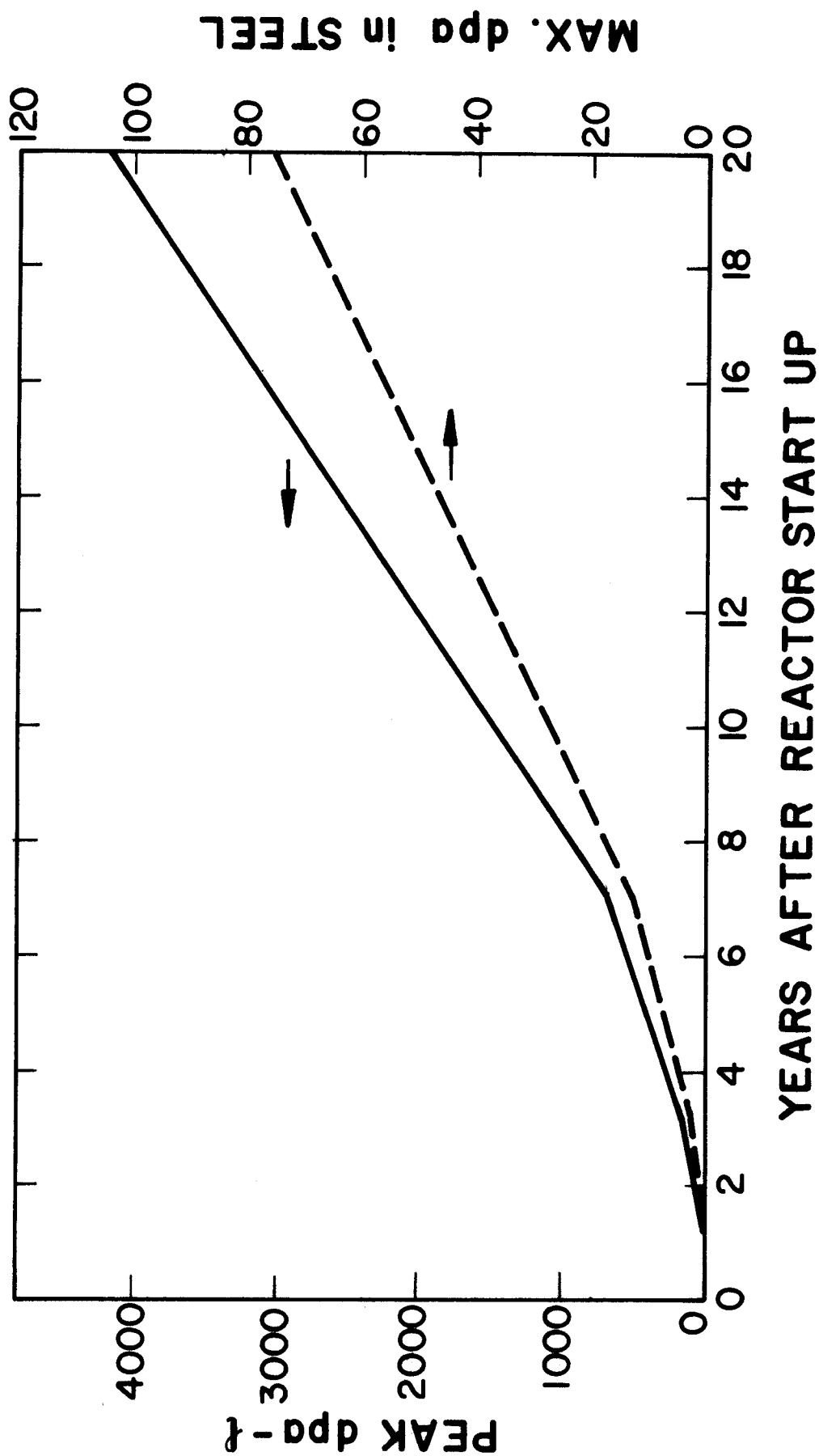
Fig. 10.2-12. Accumulated damage parameters for TASKA-M.

References for Section 10.2

1. TASKA-Team, "TASKA-Tandem Spiegelmaschine Karlsruhe, A Tandem Mirror Fusion Engineering Test Facility," KfK 3311/1,2 UWFDM-500, June 1982.

2. W. M. Stacey, Jr., et al., "USA Conceptual Design Contribution to the INTOR Phase-I Workshop," INTOR/81-1, June 1981.

3. N. F. Panayotou, E. K. Opperman, "Specimen Size Effects and Fusion Materials Research," ADIP Semiannual Progress Report DOE/ER-0045/8, Sept. 1982.

4. A. M. Ermi, "Results of the MFE-5 In-Reactor Fatigue Crack Growth Experiment," ADIP Semiannual Progress Report, DOE/ER-0045/7, March 1982.

5. R. O'Dell, F. Brinkley, Jr., and D. Marr, "User's Manual for ONEDANT: A Code Package for One-Dimensional Diffusion-Accelerated, Neutral-Particle Transport," LA-9184-M, Los Alamos National Laboratory (1982).

6. "VITAMIN-C, 171 Neutron, 36 Gamma-Ray Group Cross Section Library in AMPX Interface Format for Fusion Neutronics Studies," DLC-41B, RSIC Data Library, Oak Ridge National Laboratory (1977).

7. "MACKLIB-IV, 171 Neutrons, 36 Gamma-Ray Group Kerma Factor Library," DLC-60B, RSIC Data Library, Oak Ridge National Laboratory (1982).

8. "MCNP - A General Monte Carlo Code for Neutron and Photon Transport," LA-7396-M, Los Alamos National Laboratory (1981).

9. M. Sawan, D. Sze and G. Kulcinski, "An Improved Materials Testing Module for Magnetic Fusion," Proc. 9th Symposium on Engineering Problems of Fusion Research, Chicago, IL, Vol. II, pp. 1797 (1981).

10. M. Sawan, "Neutronics Analysis for the Materials Testing Module of TASKA," Trans. Am. Nucl. Soc. 41, 515 (1982).

11. W.M. Stacey et al., "INTOR," Georgia Tech Report No. USA-INTOR/81-1 (1981).

12. E. Opperman, HEDL, private communication (1983).

13. "Guide for Experimenters - RTNS-II," M-094, Lawrence Livermore Report (March 1982).

10.3 Liquid Metal Modules

10.3.1 Philosophy

The main objective of TASKA-M is to provide a large volume for use in technology testing. Although the device itself, including the physics on which it is based does not have to extrapolate to a power reactor, most of the technology features should be reactor relevant. One of the salient technology features in TASKA-M is the development, testing and qualification of blanket concepts which are particularly suitable for power reactors. Information such as tritium breeding and energy multiplication only depend on the source of radiation, the geometry of the blanket and the materials used. Such information is generic to all reactor concepts. Surface wall heating, however, is different in a tandem mirror than in a tokamak. Thus, such data would not be universally applicable to all reactor concepts. In TASKA-M, space has been provided for testing both liquid metal and solid breeder blanket concepts.

There are many aspects to testing and qualification of a blanket concept for ultimate use in a power reactor. Obviously safety and environmental acceptability are close to the top of the list. Other obvious aspects are structural, thermal, neutronic and chemical. All the other aspects fit into subcategories of the ones listed above.

The successful use of liquid metals in the fast breeder program has carried over into fusion power research. It is not surprising, therefore, that liquid metals have been serious candidates as blanket materials in fusion power reactors from the earliest days of fusion research and still are today. The two leading candidates are $Li_{17}Pb_{83}$ with a melting temperature of 235°C and Li which has a melting temperature of 180°C. Both self-cooled and separately cooled liquid metal blankets are under consideration for fusion. The self-cooled liquid metal blanket is ideally suited for the central cell in tandem mirrors, and thus, the blanket design proposed for testing in TASKA-M is self-cooled. The higher surface heating and large MHD pressure drop due to the higher magnetic field in a tokamak may preclude the use of self-cooled liquid metal blankets on the inboard side because of excessive pumping power losses.

Tests relating to safety and environmental issues need not be performed in a test reactor and will not be conducted in TASKA-M. Structural, thermal, neutronic and chemical issues relating to material compatibility, corrosion,

tritium permeability, containment and extraction are tests that must be performed within a test reactor because they are influenced by the neutronic environment. These tests will be performed in TASKA-M.

Two blanket modules, one utilizing $Li_{17}Pb_{83}$ and the other Li are designed to fit in the same slot within the central cell shown in Fig. 10.3-1. They will be tested consecutively. Both are self-cooled once-through tubular designs, with a single inlet and outlet connection. The $Li_{17}Pb_{83}$ module has seven rows of tubes and the Li module, ten rows of tubes. The structural material is the ferritic steel HT-9. The modules are designed to accommodate an ICRF antenna located in close proximity to the plasma. Because the antenna effectively acts as a limiter, issues of plasma-wall interactions are critical and it must be capable of being removed from the device with a minimum of effort. These and other considerations will be discussed in the following sections.

10.3.2 Structural Design

10.3.2.1 General Description. The design of the liquid metal blanket in TASKA-M draws on the experience gained in earlier tandem mirror studies such as WITAMIR[1] and TASKA.[2] Although the designs all differ slightly, they share the once-through tubular concept and all have a single inlet and outlet header.

The liquid metal blanket test module consists of rows of tubes distributed axially, running from an upper manifold to a lower manifold as shown in Fig. 10.3-2. Breeding material comes in through a horizontal header at the top, distributes axially within the upper manifold with the aid of the magnetic field, then flows through the tubes around the plasma collecting in the lower manifold and exiting through the outlet header. The inner radius is 22 cm, the axial length is 83 cm and the thickness is 45 cm for the $Li_{17}Pb_{83}$ module and 64 cm for the Li module. The structural material is the ferritic steel HT-9. Material fractions by volume are 7% structure, 73% breeding material and 20% void.

All the tubes have an outer diameter of 7.04 cm and a wall thickness of 1.6 mm. The axial spacing from tube center to center is 7.3 cm and the radial spacing is 6.32 cm. At the point where they connect to the manifold, the tubes neck down to a diameter of 5.2 cm. This provides more space for welding on the inside of the manifold. Figure 10.3-2 shows that the first row of
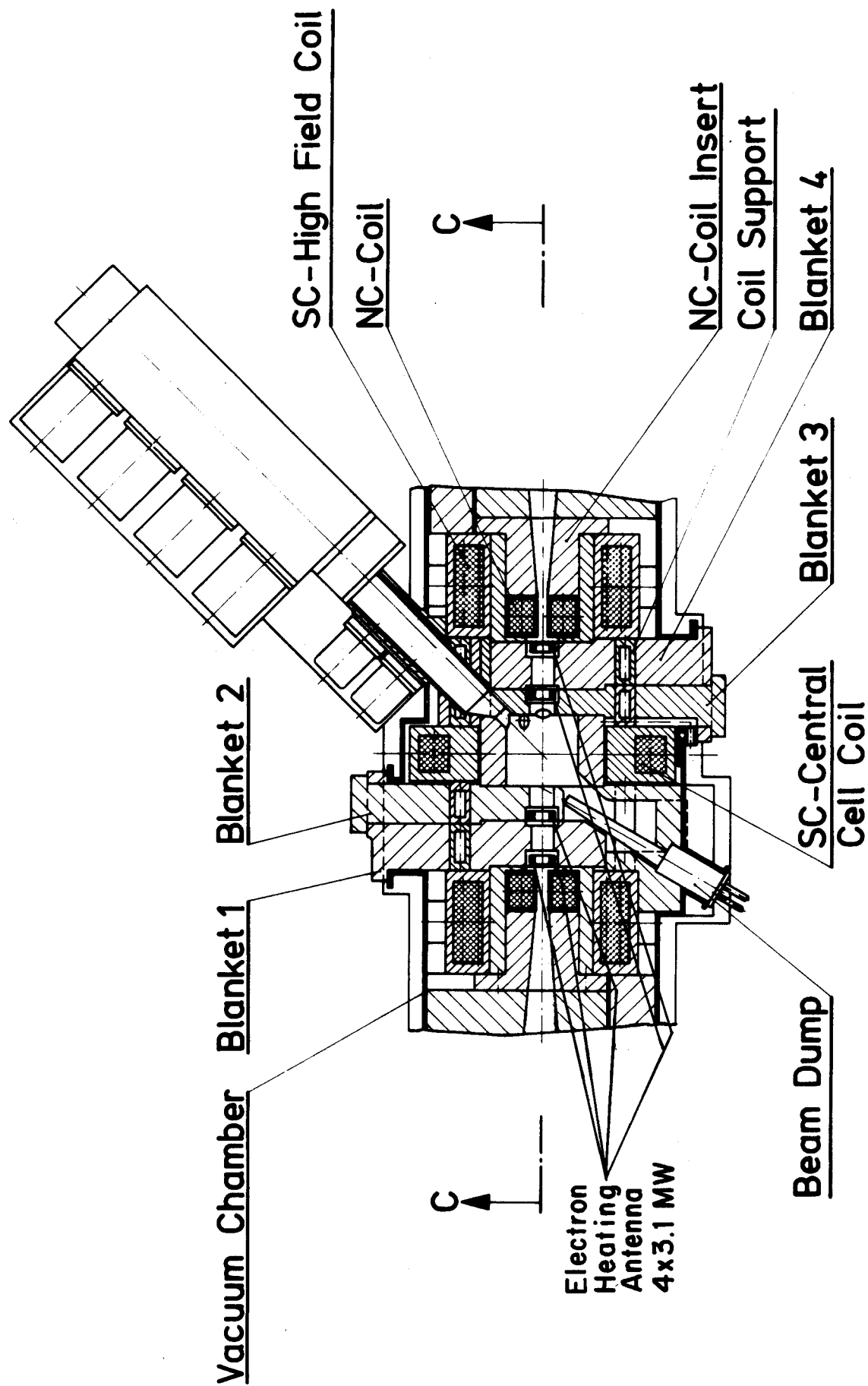
Fig. 10.3-1. Cross section of the central cell.

Vacuum Chamber   Blanket 1   Blanket 2

SC-High Field Coil

NC-Coil

C

NC-Coil Insert

Coil Support

Blanket 4

Blanket 3

SC-Central
Cell Coil

Beam Dump

Electron
Heating
Antenna
4x3.1 MW

C
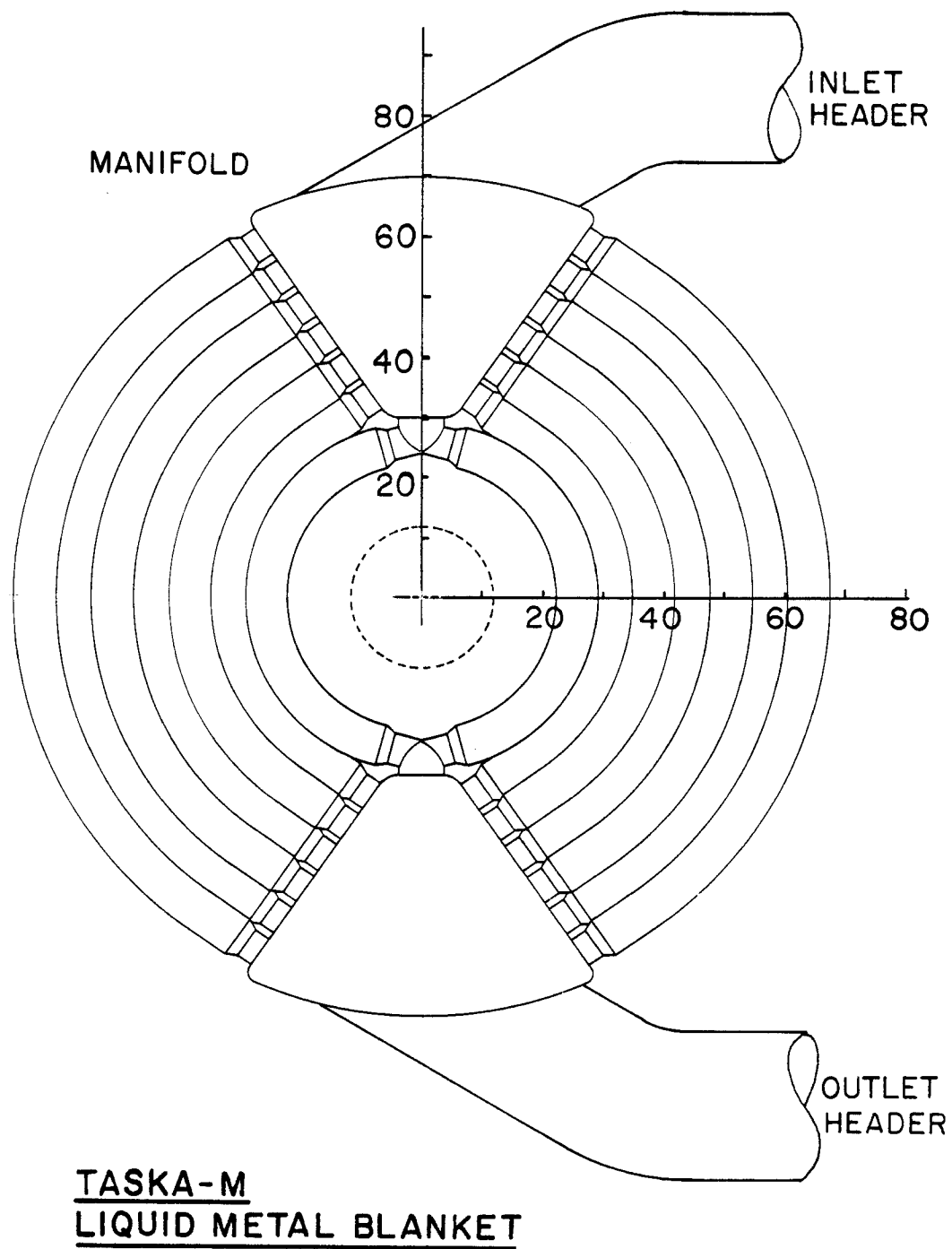
Fig. 10.3-2.   Plan view of LiPb blanket module.

tubes is manifolded through a special fitting designed to supply breeding ma-
terial to both sides of the tube simultaneously. This design is unique to
TASKA-M and is done for several good reasons. Firstly, the small plasma
radius in TASKA-M makes it very difficult to make sharp bends in the front
tubes at the connection points to the manifold. Secondly, the special fitting
is designed to avoid stagnation points at the flow separation and thus allevi-
ates the probability of hot spots.

Table 10.3-1 gives the parameters of the liquid metal blanket module both
for $Li_{17}Pb_{83}$ and Li.

Figure 10.3-3 shows the liquid metal blanket module as part of the as-
sembly used to support it and insert it into the test reactor. The assembly
consists of the module, integral reflector/shield and the seal flange. Hori-
zontal insertion is used to fit the assembly into the test reactor. The as-
sembly flange then makes a seal to the reactor vacuum chamber. Figure 10.3-3
shows the ICRF coaxial feed penetrating the flange through an insulating fit-
ting. In reality, a separate flange/shield/reflector assembly would be used
such that the ICRF would be removed independently of the blanket module.

The Li blanket module will have ten rows of tubes per side instead of
seven. A completely new assembly will be needed to accommodate it. However,
the space within the reactor and the components in it will not need to be
modified. That is to say, the Li blanket assembly will fit into the same slot
as the $Li_{17}Pb_{83}$ blanket assembly and the two will be completely interchange-
able.

10.3.2.2 ICRF Antenna Integration. Plasma heating by ICRF requires that
antennas be situated within the central cell in close proximity to the plasma.
One of the antennas falls within the axial span occupied by the liquid metal
module. To accommodate the ICRF antenna, four of the front tubes have to be
eliminated, to provide space on the sides and in the back of the antenna. Two
schemes have been considered for integrating the antenna within the blanket
module. Figure 10.3-4 shows a scheme where the antenna is supported on a
horizontal coaxial feedthrough and Fig. 10.3-5 is a cross section at midplane
for the same case. It can be seen that altogether 26 tubes had to be elimi-
nated. Although the fact that the antenna is supported on a cantilever is a
drawback, a major advantage of this scheme is that the blanket module need not
be removed for servicing the antenna. In the second scheme, the antenna is

Table 10.3-1. Parameters of Liquid Metal Blanket Modules

	$Li_{17}Pb_{83}$	Li
First wall radius, cm	22	22
Axial extent, cm	83	83
Blanket thickness, cm	45	63.9
Number of tube rows/side	7	10
Total number of tubes*	148	210
Tube outer diameter, cm	7.04	7.04
Tube inner diameter, cm	6.72	6.72
Axial tube spacing, cm	7.30	7.30
Radial tube spacing, cm	6.32	6.32
Outer diameter of transition section, cm	5.20	5.20
Inner diameter of transition section, cm	4.92	4.92
Length of transition section, cm	2.8	2.8
Material fractions		
HT-9 structure, %	7	7
Breeding material, %	73	73
Void, %	20	20
Mass of full module, tonnes	7.50	1.60
Mass of empty module, tonnes	0.54	0.94

---

*This number is prior to tube removal for ICRF antenna.
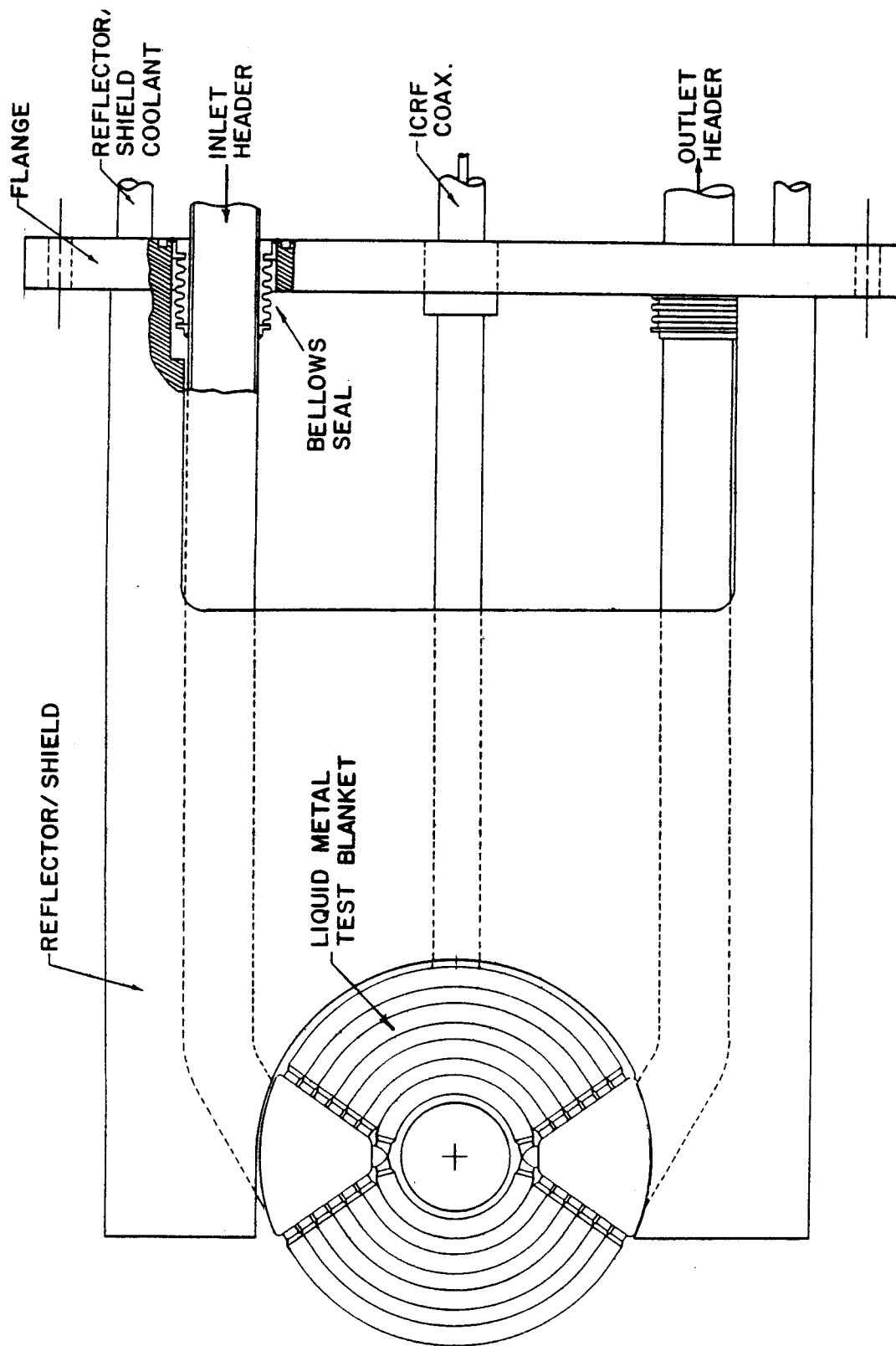
Fig. 10.3-3. View of liquid metal blanket module assembly.
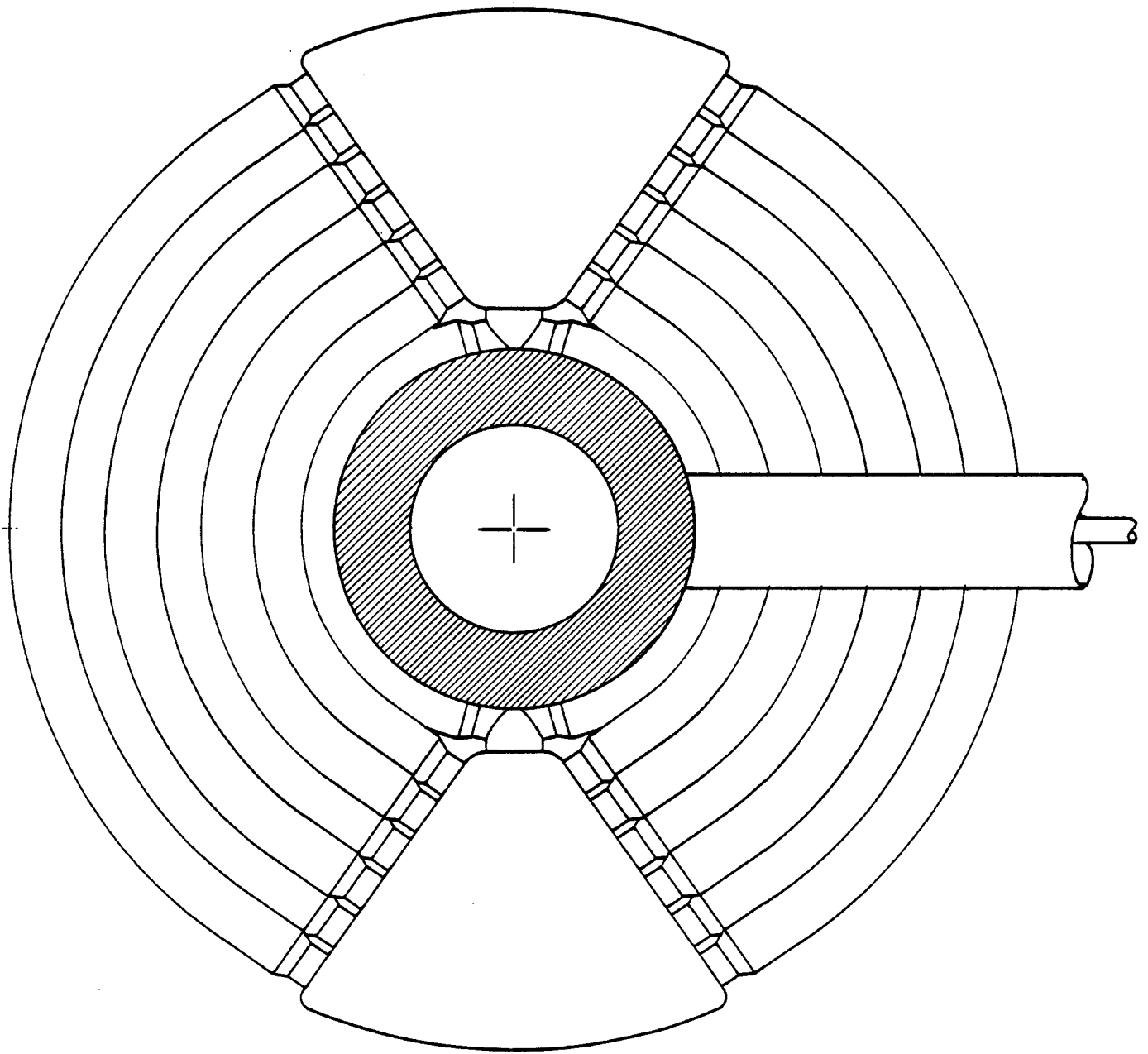
ICRF ANTENNA / BLANKET INTEGRATION

SCHEME I

Fig. 10.3-4.   Plan view of horizontally supported antenna.

ICRF ANTENNA

PLASMA

MIDPLANE CROSS SECTION
SCHEME I
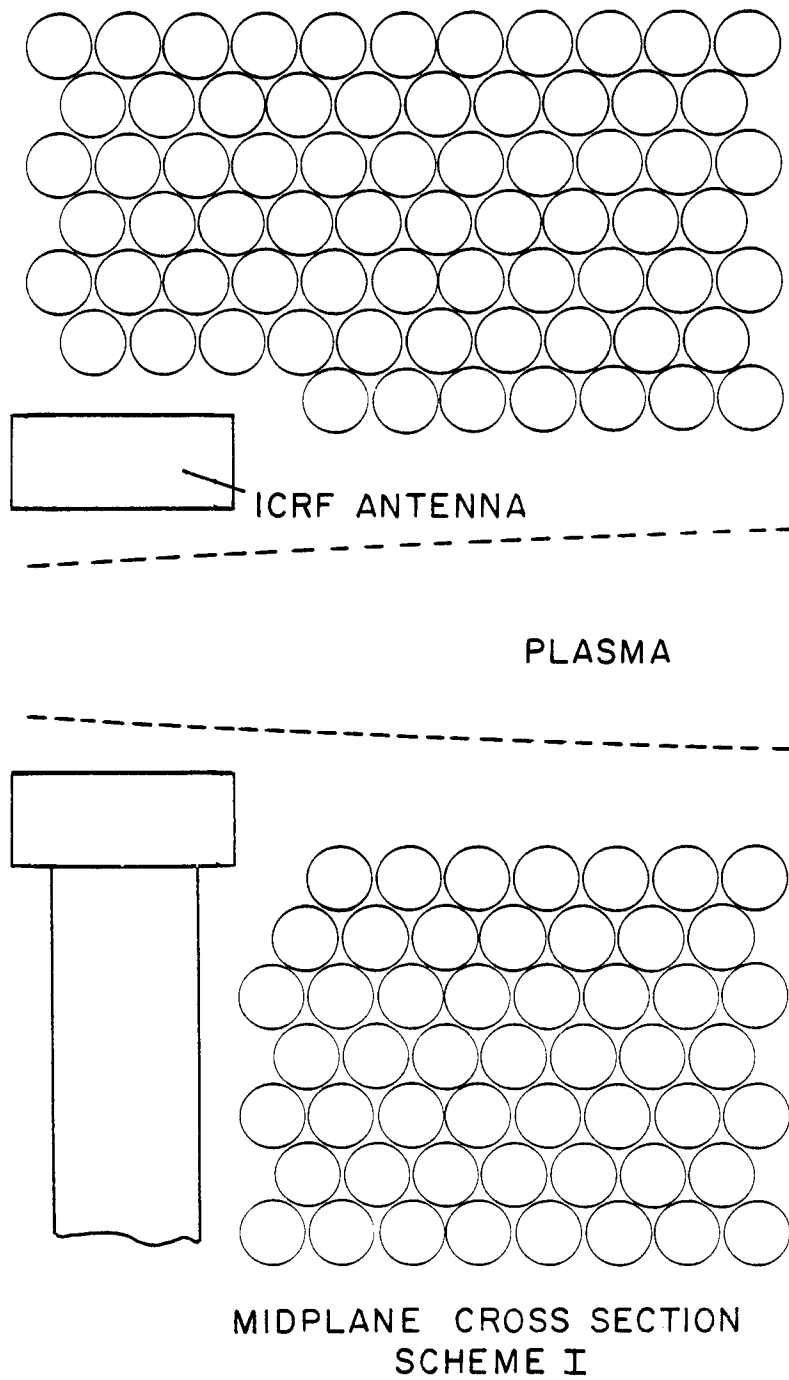
Fig. 10.3-5.   Cross section of horizontally supported antenna.

supported on a vertically located coaxial feedthrough as shown in Figs. 10.3-6 and 10.3-7. Fourteen tubes are eliminated and the upper manifold is notched to make space for the coaxial feedthrough. In this design the antenna is effectively suspended from the top, a very good way to support it. However, because the antenna and the blanket are interlocked, both have to be removed together. Thus, in order to service the antenna, the blanket module has to be removed as well. This can be a very serious handicap if the lifetime of the antennas due to sputtering is short. Table 10.3-2 summarizes the advantages and disadvantages of the two schemes.

10.3.2.3 Stresses. The blanket modules are supported on the bottom manifold with the load path going through the reflector, vacuum chamber and then to external structure supporting the central cell. In the case of the $Li_{17}Pb_{83}$ module, the total mass is ~ 7.5 tonnes. An analysis has been made to determine the stresses on the front tubes for the $Li_{17}Pb_{83}$ case. The tube was modeled as a continuous ring fixed on the bottom and built-in on rollers (capable of vertical movement) at the top. It is loaded at the top by the weight of the manifold and along its length by the mass of the tube and the breeding material as shown in Fig. 10.3-8.

Figure 10.3-9 is a free body diagram of the front tube where P is the vertical force, N_1 the horizontal force and M_1 the moment at the bottom fitting. Summation of the moments about the point of analysis yields the following equation:

$$M = -M_1 - N_1 r(1 - \cos \phi) + P(r \sin \phi) - \omega r^2 (\phi \sin \phi + \cos \phi - 1) \quad (10.3-1)$$

where M is the moment at the section at angle ϕ, r the average radius of curvature and ω the tube mass per unit length.

To solve for M_1 and N_1 we make use of the expression for flexural energy,

$$U = \int \frac{M^2 r}{2EI} d\phi \quad (10.3-2)$$

where E is the modulus of elasticity and I the moment of inertia. From this we obtain the boundary conditions

$$\frac{\partial U}{\partial M_1} = 0 \qquad \text{therefore} \int M \frac{\partial M}{\partial M_1} \partial \phi = 0 \quad (10.3-3)$$

Table 10.3-2. Advantages and Disadvantages of the
Two Methods of Antenna Integration

Scheme	Advantages	Disadvantages
Horizontal Support	• Antenna can be removed w/o moving blanket module • Simple manifold	• Lower breeding • Undesirable support method
Vertical Support	• Higher breeding • Desirable support method	• Blanket must be removed for servicing antenna • Complicated upper manifold

----

and

$$\frac{\partial U}{\partial N_1} = 0 \qquad \text{therefore} \int M \frac{\partial M}{\partial N_1} \partial\phi = 0 \qquad (10.3\text{-}4)$$

Integrating Eq. 10.3-1 from $0 < \phi < \pi$ and setting it equal to zero according to Eq. 10.3-3 we obtain,

$$0 = -M_1\pi - N_1 r\pi + 2Pr . \qquad (10.3\text{-}5)$$

From the second boundary condition, we can solve for N_1. Since $\partial M/\partial N_1 = r(1 - \cos \phi)$, we get

$$\int M \frac{\partial M}{\partial N_1} \partial\phi = \int Md\phi + \int M(-\cos \phi) \, d\phi = 0 .$$

From Eq. 10.3-5 $\int M \, d\phi = 0$, thus we integrate the second term $\int_0^\pi M(-\cos \phi) \, d\phi = 0$ and obtain:

$$N_1 = \frac{\omega r}{2} .$$

Substituting in Eq. 10.3-5 we solve for M_1

$$M_1 = \frac{2Pr}{\pi} - \frac{\omega r^2}{2} .$$

10.3-11
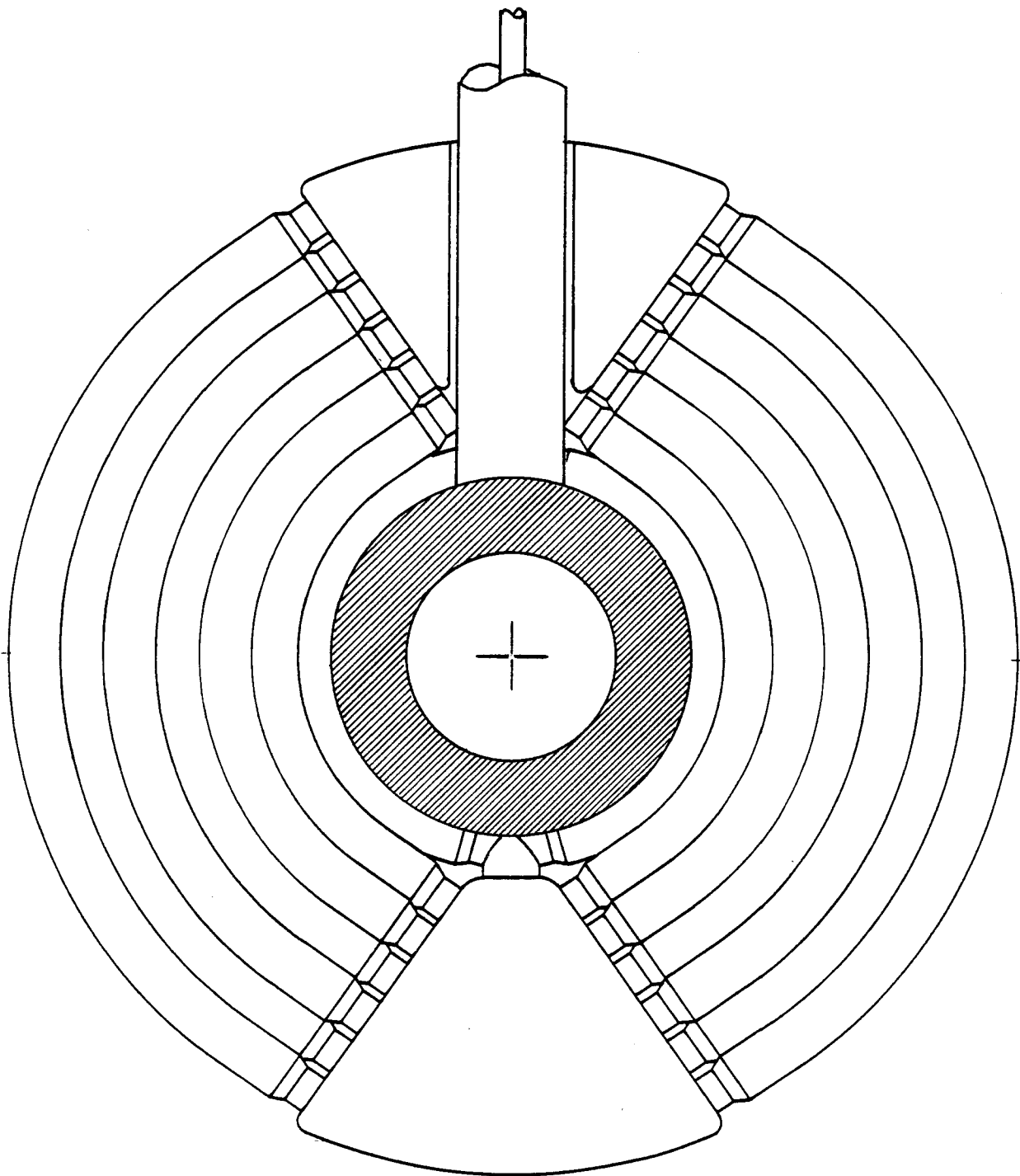
ICRF ANTENNA / BLANKET INTEGRATION

SCHEME II

Fig. 10.3-6.   Plan view of vertically supported antenna.

MIDPLANE CROSS SECTION
SCHEME II
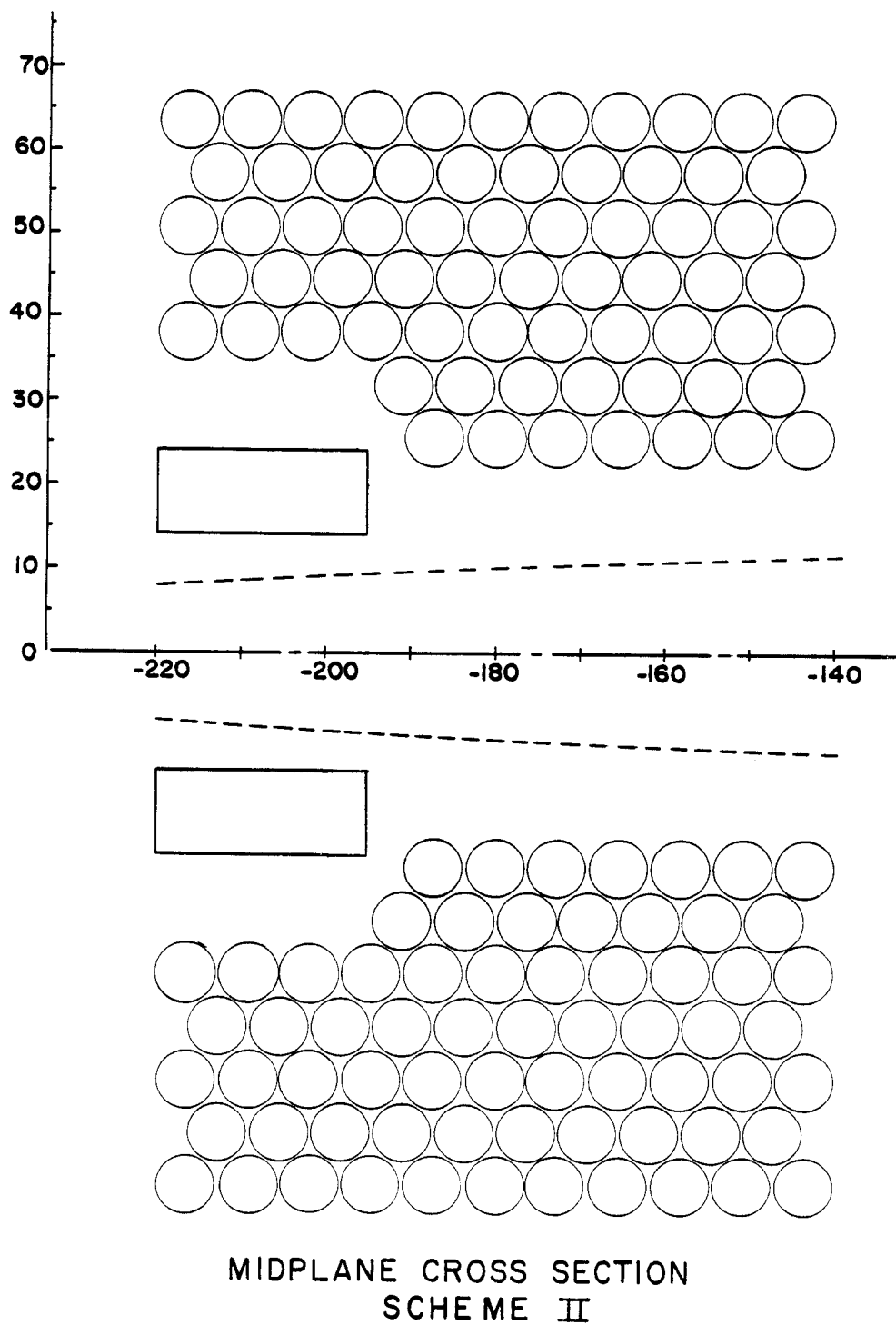
Fig. 10.3-7.   Cross section of horizontally supported antenna.
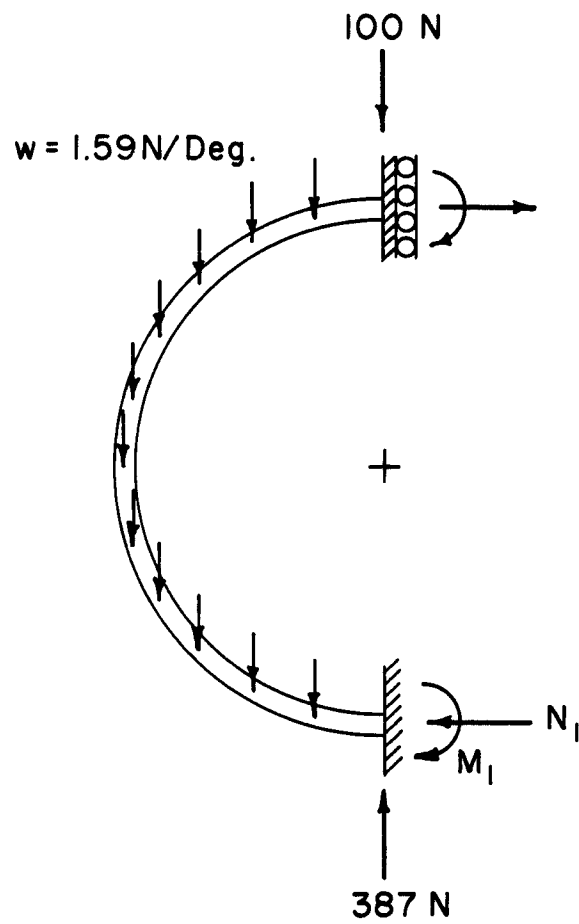
Fig. 10.3-8.   Model of front tube in the module.
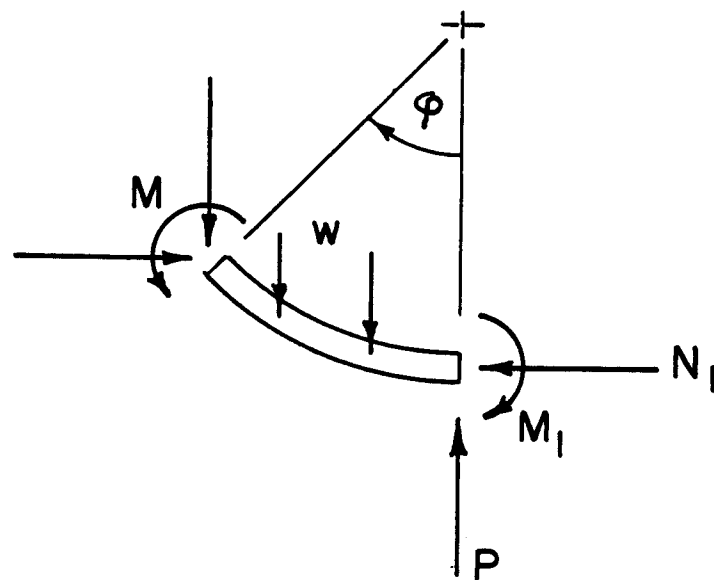
Fig. 10.3-9.   Free body diagram of front tube in the blanket.

These values of N_1 and M_1 can now be used in Eq. 10.3-1 to calculate the bending moments at any point on the tube. Further, the vertical and horizontal reactions at each section are resolved into normal forces (tangent to the radius of curvature) and shear forces (perpendicular to the radius of curvature). The following force and moment convention is used:

Normal forces: Compressive forces are negative (-)

                     Tensile forces are positive (+)

Shear forces: Directed away from center, negative (-)

                     Directed toward center, positive (+)

Moments: Producing tension on inner surface (-)

                     Producing compression on inner surface (+).

The resulting normal and shear forces, and the moments for $0 < \phi < \pi$ calculated every 15° are listed in Table 10.3-3.

The negative bending moment at $\phi = 0$ indicates that the inner surface of the tube is in tension at that point due to the forces acting on it from the mass of the $Li_{17}Pb_{83}$. The maximum bending moment, however, occurs at $\phi = 135°$ and produces a compressive stress in the inner surface.

The maximum blanket operating pressure is ~ 0.7 MPa which produces a hoop stress of ~ 15 MPa and a longitudinal stress of 7.5 MPa. Only the longitudinal stress adds directly to the tube bending stresses. Table 10.3-4 gives the bending stresses and the total stress (exclusive of thermal) on the inside and outside surfaces of the front tube as a function of the angle ϕ. Positive values are tensile.

Figure 10.3-10 is a plot of the stresses in the front tube for the $Li_{17}Pb_{83}$ blanket module as a function of the angle ϕ. The maximum stresses occur at the upper transition section at $\phi = 180°$ and are 31.25 MPa compressive on the inner surface and 43.85 MPa tensile on the outer surface. The maximum design stress intensity for HT-9 at 550°C is 110 MPa taken as 2/3 of the yield strength. It can be seen that the stresses are far below this value.

The effect of the thermal stresses will be to put the inner surface into further compression and the outer into further tension. In the worst case the stresses can double in magnitude. This, however, still leaves a large margin of safety with respect to the maximum design stress intensity.

Table 10.3-3.   Normal Forces, Shear Forces and Moments on the First Tube of the $Li_{17}Pb_{83}$ Module as a Function of the Angle ϕ

ϕ (degrees)	Normal Force (N)	Shear Force (N)	Moment (Nm)
0	45.58	386.6	-51.17
15	137.90	338.53	-8.57
30	208.87	270.61	17.60
45	254.90	190.44	42.14
60	274.80	106.03	63.89
75	269.81	-25.12	82.03
90	243.28	-45.53	96.08
105	200.12	-100.81	105.89
120	146.53	-137.23	111.64
135	89.14	-153.60	113.59
150	34.41	-150.75	112.46
165	-11.96	-131.48	108.69
180	-45.58	-100.00	102.85

Normal Force: Compressive (-), Tensile (+)

Shear Force: Toward center (+), Away from center (-)

Moment: Producing tension on inner surface (-), Producing compression on inner surface (+)

Table 10.3-4. Bending and Total Stresses on the First Tube of the $Li_{17}Pb_{83}$ Module as a Function of the Angle ϕ

ϕ (degrees)	Bending Stresses (MPa)	Total Stress* on Inside Surface (MPa)	Total Stress* on Outside Surface (MPa)
0	±18.68	25.38	-11.98
15	±1.47	9.26	6.32
30	±3.03	5.07	11.13
45	±7.25	0.99	15.50
60	±10.99	-2.70	19.28
75	±14.11	-5.83	22.39
90	±16.53	-8.33	24.73
105	±18.22	-10.14	26.30
120	±19.21	-11.29	27.13
135	±19.54	-12.30	26.78
150	±19.35	-11.95	26.75
165	±18.70	-11.23	26.17
180	±37.55	-31.25	43.85

Tensile stress (+)

Compressive stress (-)

*Total stresses with the exception of thermal stresses.
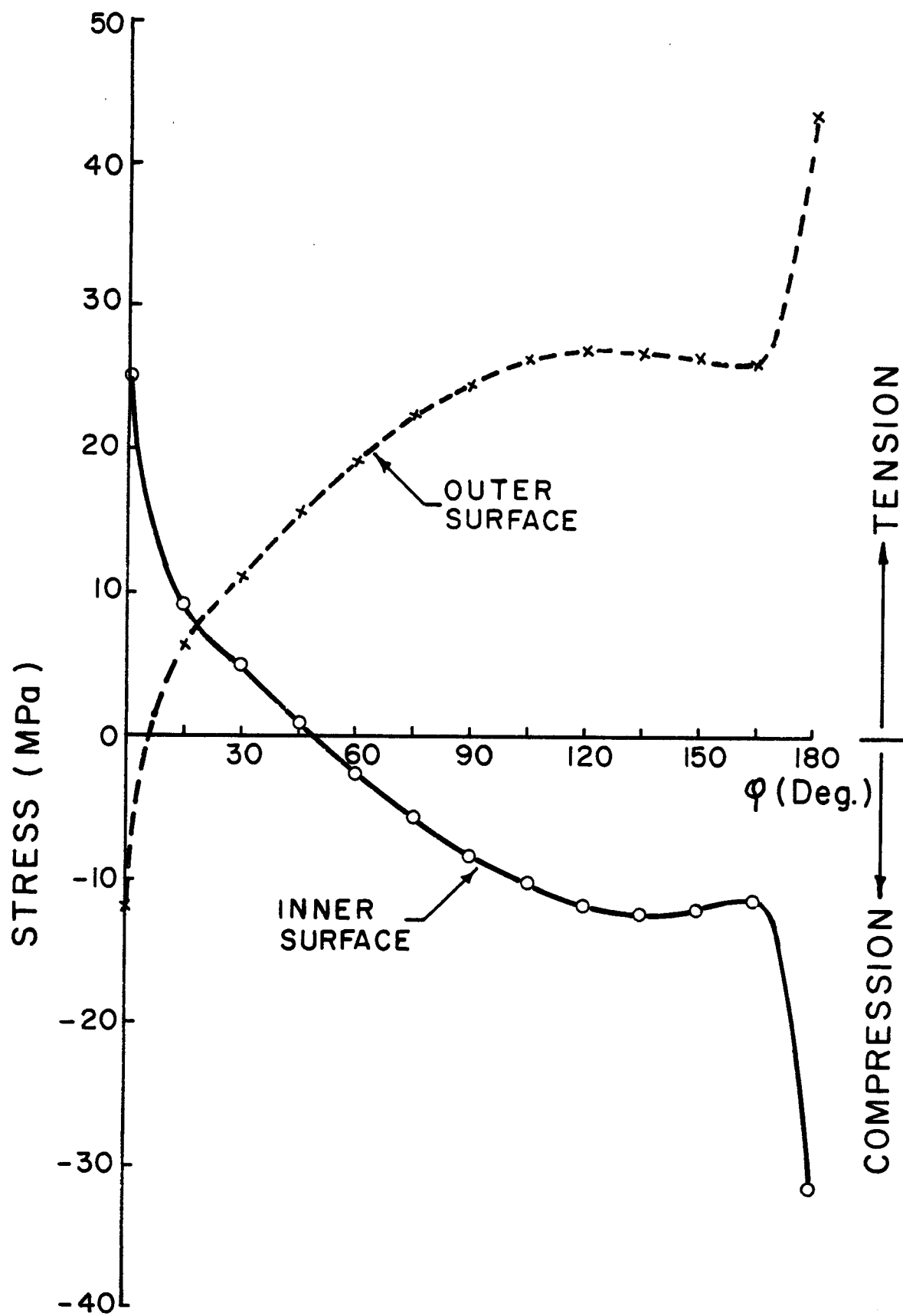
Fig. 10.3-10. Total stress in the front tube as a function of the angle φ.

10.3.3 Neutronics

Neutronics analysis has been performed for blanket #1 which is utilized for liquid metal blanket testing. The blanket is self-cooled implying that the liquid metal breeder acts also as the coolant. A tubular design was considered in which the liquid metal flows in tubes made of the ferritic steel alloy HT-9 with an outside diameter of 7.04 cm and an inside diameter of 6.72 cm. The tubes are arranged with axial and radial spacings of 7.30 and 6.32 cm, respectively. This corresponds to an average blanket volumetric composition of 73% liquid metal, 7% HT-9, and 20% void. A uniform inner wall radius of 22 cm is considered except for a 30 cm wide zone in which the wall is recessed to a radius of 29 cm for locating the ICRF antenna. The total width of the test module is 83 cm. The axial variation of the neutron wall loading is shown in Fig. 5.1-2. The peak and average wall loadings are 1.22 and 0.85 MW/m^2, respectively.

The primary goal of the neutronics analysis is to design blanket test modules which have reactor relevant neutronics parameters. Local tritium breeding ratios $\geq$ 1.15 and energy multiplications $\geq$ 1.3 are required. The required tritium breeding ratio exceeds unity by a margin that allows for tritium losses and radioactive decay and possible data uncertainties and calculational deficiencies. A large value of energy multiplication is required because of its impact on the overall cost of energy in a power reactor. Previous analysis[3] indicated that using the manganese steel Fe-1422 (14 wt.% Mn, 2 wt.% Ni and 2 wt.% Cr) as a reflector at the back of the blanket enhances the overall energy multiplication considerably. Notice that the energy multiplication is defined as the ratio of the total recoverable energy deposited in both the blanket and reflector to the fusion neutron energy of 14.1 MeV per D-T fusion. A Fe-1422 reflector that is cooled by 5 vol.% water is used in this design.

The two leading liquid metal breeder candidates, namely, liquid lithium and $Li_{17}Pb_{83}$, are considered. Two separate modules were designed to fit in the same slot designated for liquid metal blanket testing. A series of one-dimensional neutronics calculations has been performed to determine the proper enrichment and thickness for the two blanket test modules. The total blanket and reflector thickness was fixed at 90 cm. In the calculations, a 50 cm thick shield was used. Two atom fractions of ^6Li in lithium, namely 7.42%

(natural lithium) and 90%, were considered. The one-dimensional discrete or-
dinates code ONEDANT[4] was used to model the problem in cylindrical geome-
try. We used the P_3S_8 approximation with a coupled 46 neutron-21 gamma group
cross section library based on the VITAMIN-C data library[5] and the MACKLIB-
IV-82 response library.[6]

Figure 10.3-11 gives a plot of the tritium breeding ratio T versus the
energy multiplication M for Li and $Li_{17}Pb_{83}$ blankets with different Li enrich-
ments and blanket thicknesses (Δ_B). It is clear from these results that the
best neutronics performance in which large values of T and M can be obtained
simultaneously can be achieved when highly enriched lithium is used in
$Li_{17}Pb_{83}$. On the other hand, there is no incentive for increasing the enrich-
ment in the liquid lithium blanket beyond the natural abundance of 7.42% ^6Li.
Therefore, the liquid lithium blanket module is designed with natural lithium
while the $Li_{17}Pb_{83}$ blanket utilizes lithium enriched to 90% ^6Li.

Figure 10.3-12 shows the variation of the tritium breeding ratio with
blanket thickness for the two modules. A blanket thickness of 63.9 cm which
corresponds to ten rows of tubes was chosen for the liquid lithium module.
This yields a tritium breeding ratio of 1.19. For the Li-Pb module a thick-
ness of 45 cm is used with seven rows of tubes resulting in a tritum breeding
ratio of 1.15. Table 10.3-5 gives a summary of the design parameters and
tritium production results for both modules. It is clear that in the Li-Pb
module a negligible amount of tritium is produced via the $^7Li(n,n'\alpha)t$ reaction
due to the domination of the Pb(n,2n) reaction in the high energy range. On
the other hand, about 44% of tritium production is contributed by ^7Li in the
liquid lithium module because of its large atomic fraction. The radial vari-
ation of the volumetric tritium production rate in both modules is shown in
Fig. 10.3-13. The results are normalized to a unit wall loading and are given
per unit volume of the tubes. The results indicate that a lower tritium pro-
duction rate occurs at the front of the Li-Pb blanket than at the front of the
Li blanket. This is attributed to the large nuclide density of Pb and the
small density of ^7Li which is responsible for most of the breeding at high
neutron energies. However, as one moves deep in the blanket, the neutron
energy spectrum softens considerably resulting in a large contribution from
^6Li. This is reflected in a larger tritium production rate in the highly
enriched Li-Pb module. The local peaking at the back of the blanket due to

Table 10.3-5. Comparison Between Design Parameters and
Tritium Production Results for Li and Li-Pb Blanket Modules

	Li Blanket	Li-Pb Blanket
Lithium Enrichment (% ^{6}Li)	7.42	90
Blanket Thickness (cm)	63.9	45
Number of Tube Rows	10	7
Reflector Thickness (cm)	26.1	45
Tritium Breeding (Tritons/fusion)		
^{6}Li(n,α)t	0.67	1.15
^{7}Li(n,n'α)t	0.52	0.002
Total	1.19	1.15
Tritium Production Rate (Triton/s)		
Per Unit Wall Loading Per 1 m Width	7.28×10^{17}	7.04×10^{17}

neutron reflection is more pronounced in the Li-Pb case since the reflected neutrons will have a considerably soft spectrum.

Table 10.3-6 gives the results for the nuclear heating in MeV per D-T fusion in the blanket and reflector zones of the two blanket modules. The overall energy multiplication is 1.371 in the Li blanket and 1.344 in the Li-Pb blanket. While 58% of the total nuclear heating is due to gamma heating in the Li-Pb blanket, gamma heating represents only 35% of the total heating in the Li blanket. This is due to the large gamma absorption in lead. The power per 1 m width is also given for the two blanket modules normalized to 1 MW/m^2 wall loading. For a unit wall loading the peak power density in the first wall is 6.91 W/cm^3 for the Li blanket and 6.22 W/cm^3 for the Li-Pb blanket.

The radial variation of the power density in the Li blanket and reflector is illustrated in Fig. 10.3-14. The results are normalized to 1 MW/m^2 wall loading and are given per unit volume of the tubes. Most of the contribution to nuclear heating in the blanket comes from neutron heating via absorption in lithium. The small gamma heating contribution results from gamma production and subsequent gamma absorption in the structure. In the metallic reflector nuclear heating is dominated by gamma heating. Figure 10.3-15 shows the
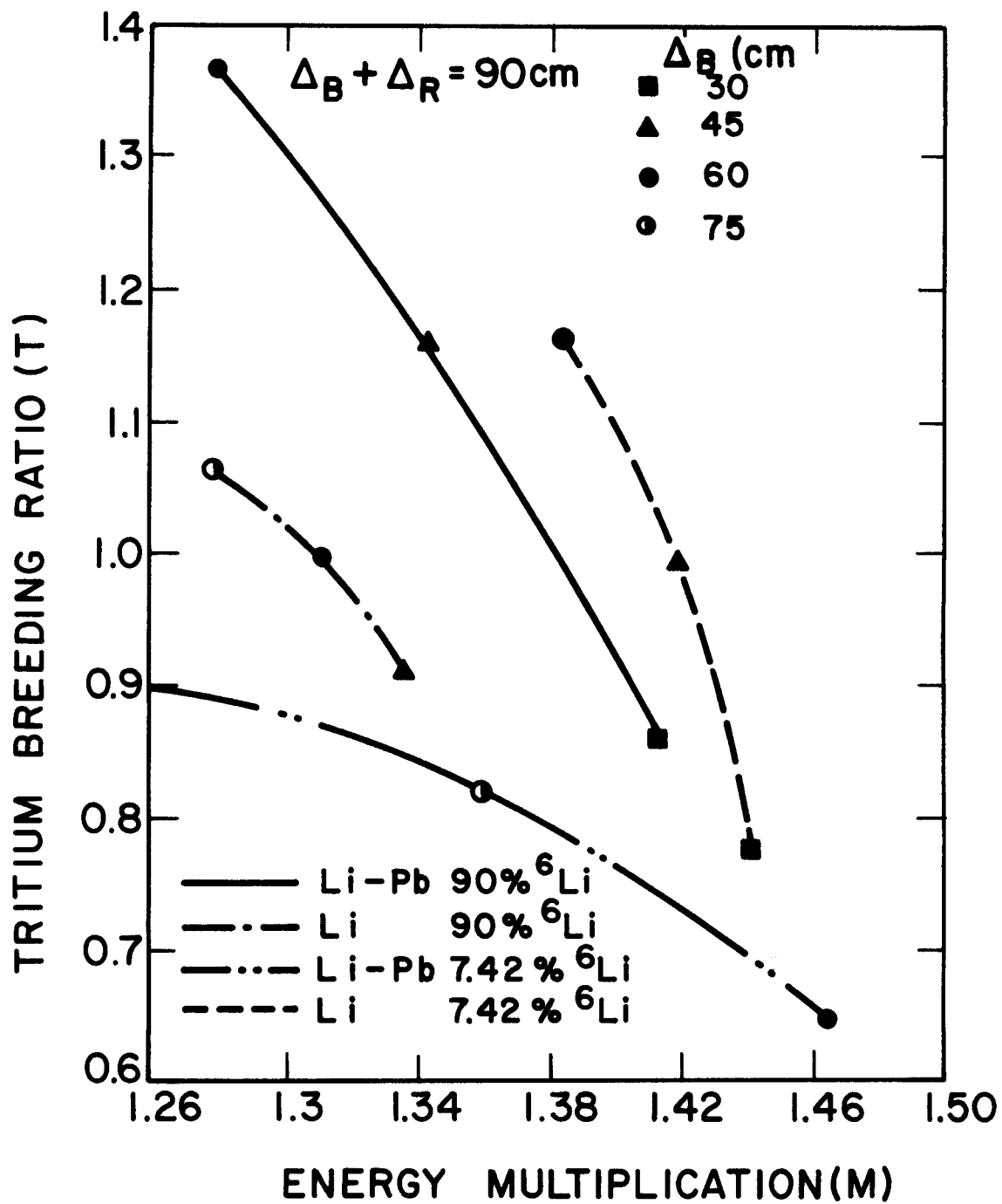
Fig. 10.3-11. The T-M plot for Li and Li-Pb blankets with different Li
enrichments and thicknesses.
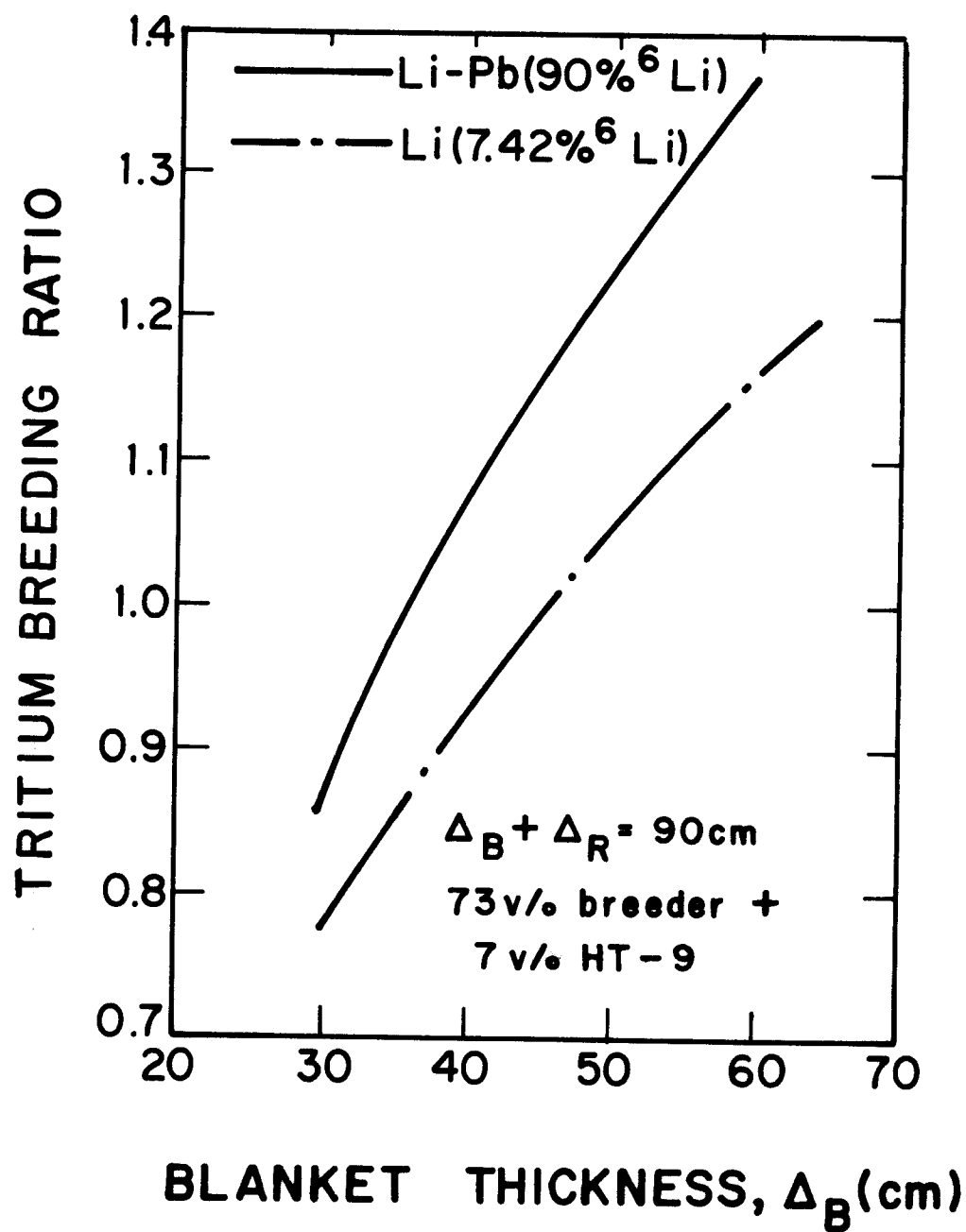
Fig. 10.3-12. Variation of tritium breeding ratio with blanket thickness.
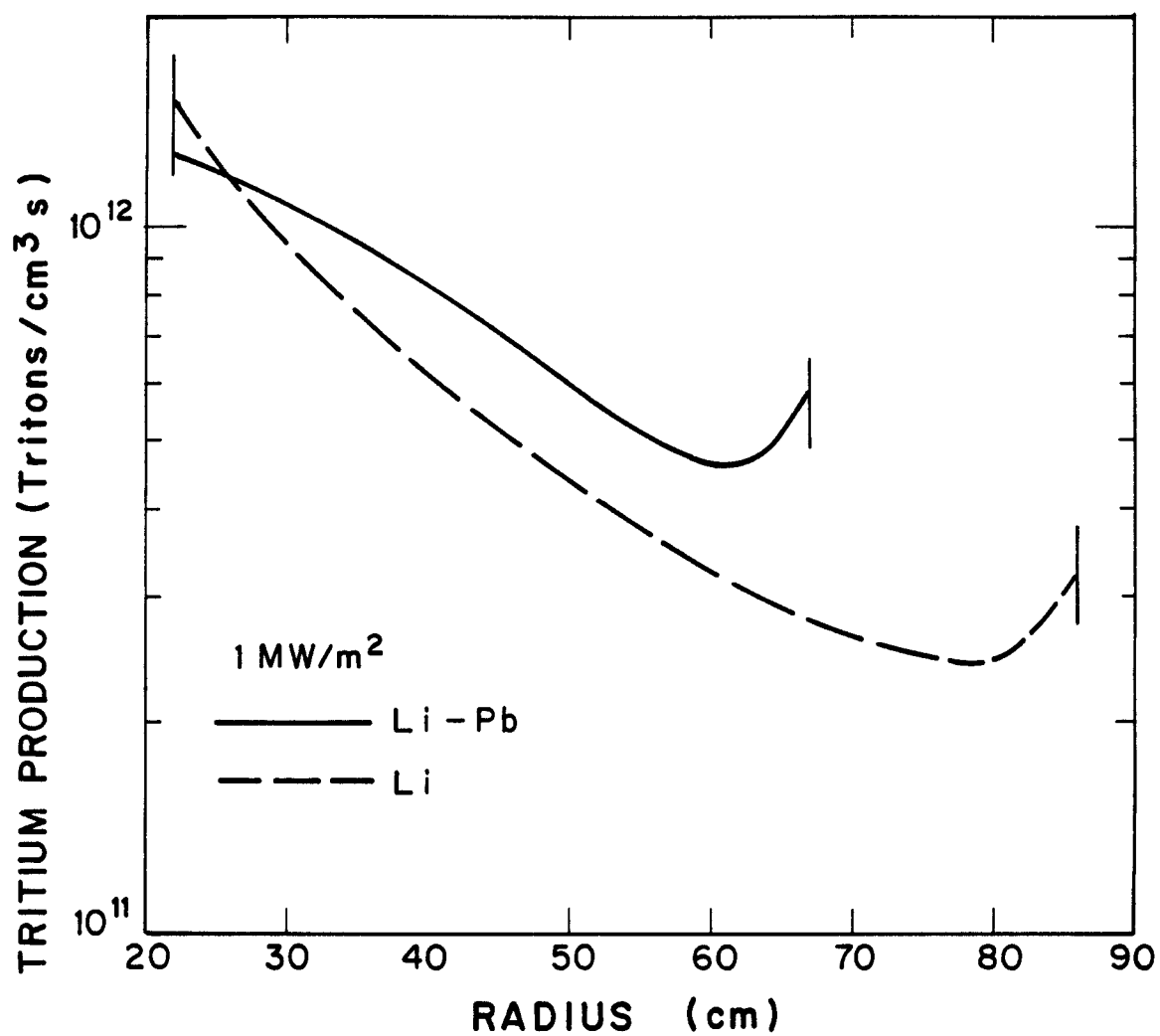
Fig. 10.3-13. Radial variation of tritium production rate.
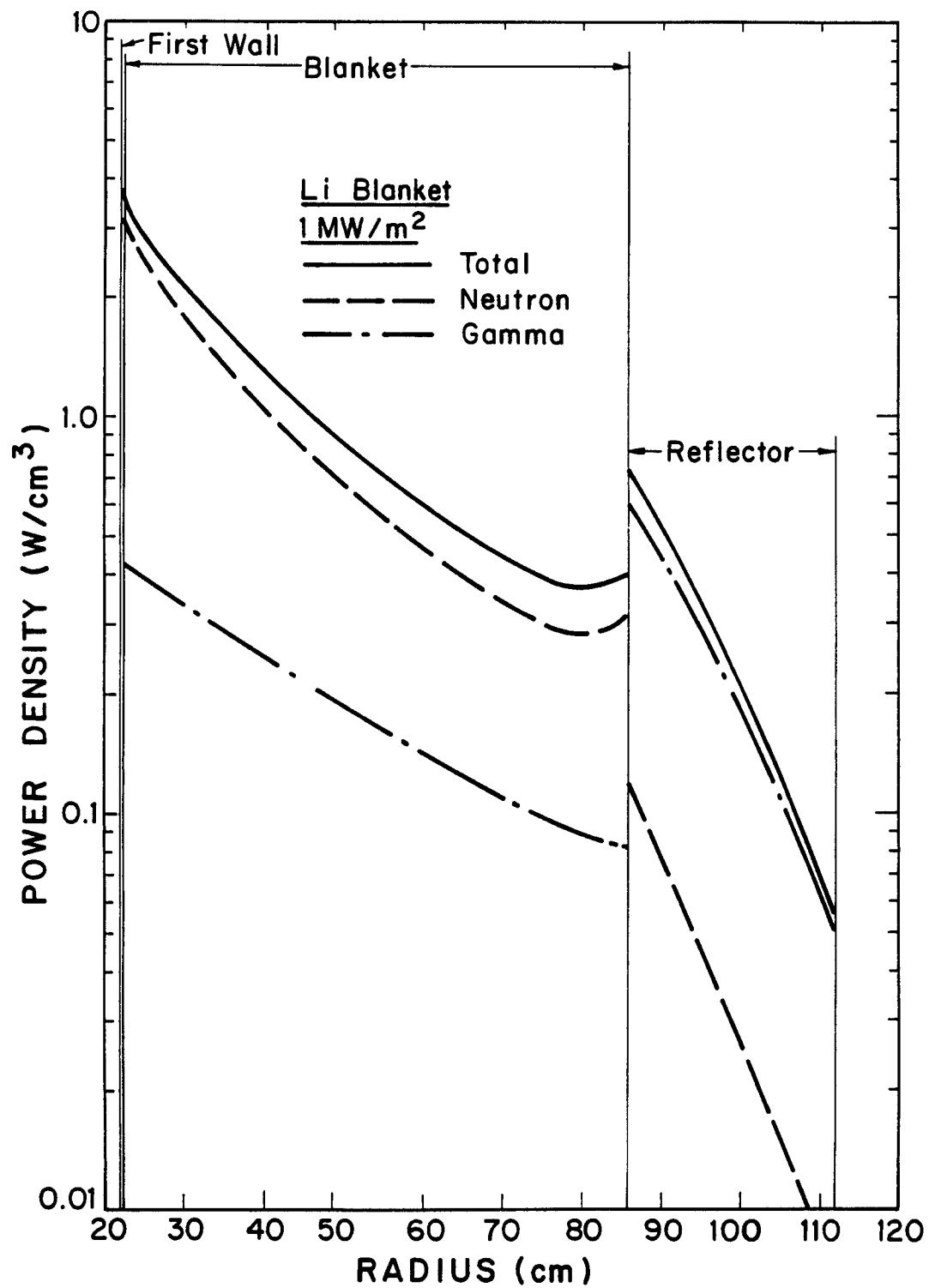
Fig. 10.3-14. Radial variation of power density for the Li blanket.
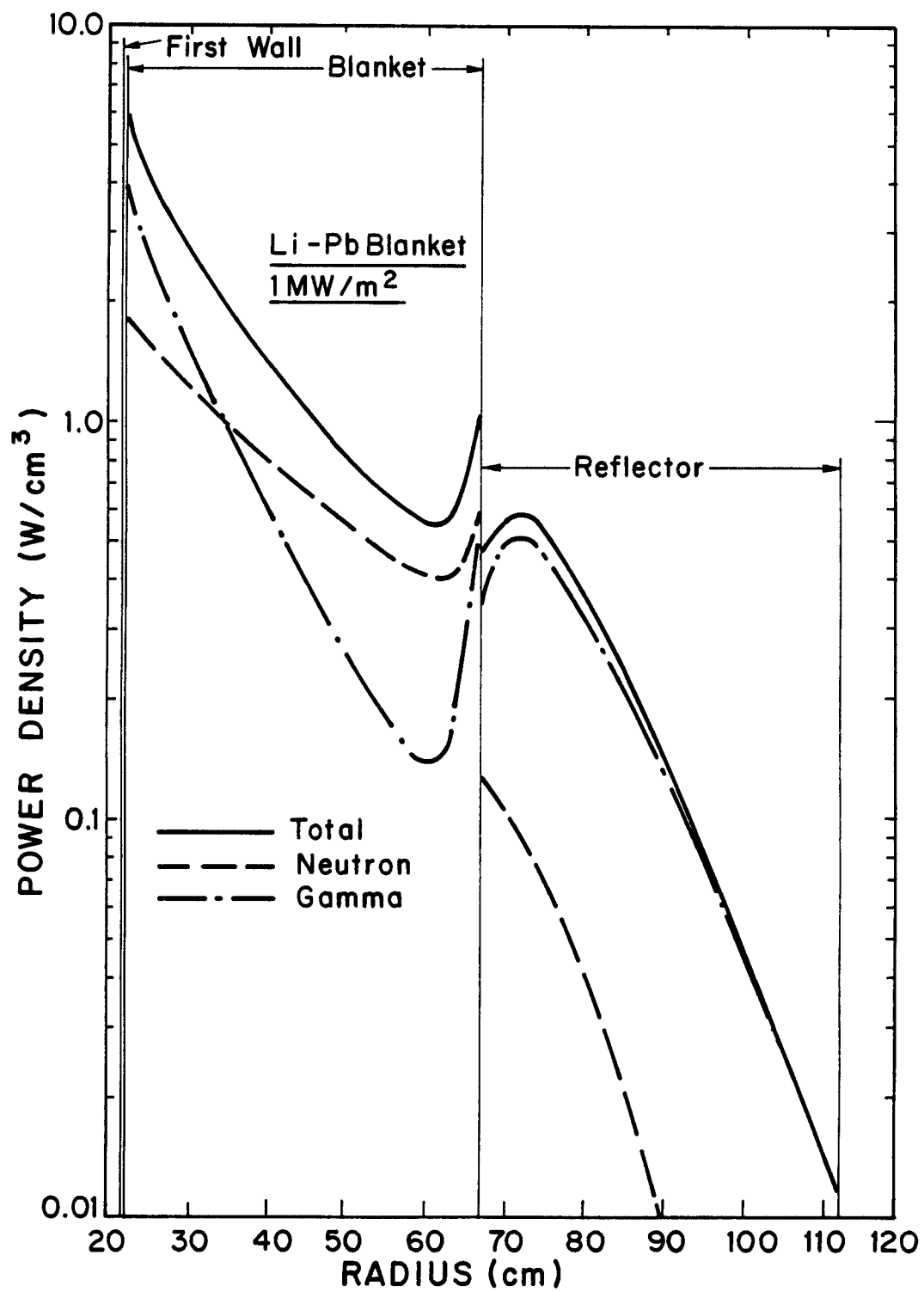
Fig. 10.3-15. Radial variation of power density for the Li-Pb blanket.

Table 10.3-6. Nuclear Heating Results for the Li and Li-Pb Blanket Modules

	Li Blanket	Li-Pb Blanket
Nuclear Heating (MeV/fusion)		
Blanket		
Neutron	11.85	7.31
Gamma	2.95	6.41
Total	14.80	13.72
Reflector		
Neutron	0.61	0.70
Gamma	3.93	4.53
Total	4.54	5.23
Total Recoverable Energy	19.34	18.95
Energy Multiplication	1.371	1.344
Power Per Unit Width (MW/m) for 1 MW/m^2 Wall Loading		
Blanket	1.45	1.35
Reflector	0.45	0.51
Total	1.90	1.86

radial power density variation for the Li-Pb case. Unlike the Li case, large gamma heating occurs in the Li-Pb blanket due to the strong gamma absorption in lead. The pronounced peak at the back of the blanket is attributed to the absorption in lead of the gammas generated in the metallic reflector. It is this strong gamma absorption in lead that results in shifting the peak power density in the reflector away from the interface with the blanket.

Due to the large axial variation of the neutron wall loading along the first wall of the blanket module, the power density in the module will vary axially as well as radially. The radial variation of power density was obtained from the one-dimensional calculations with the axial variation of wall loading to get an estimate for the r and z dependence of the power density instead of performing expensive two-dimensional calculations. The power density at the first wall ($r = r_w$) is considered to be proportional to the wall loading. Hence

$$P(r_w, z) = P_f \Gamma_n(z) \ ,$$ (10.3-6)

where P_f is the front power density for a unit wall loading. We assume that the blanket is thick enough such that the axial variation in power density at the front of the module will disappear at the back of the module resulting in a uniform axial distribution. The power density at the back of the module is, therefore, given by

$$P(r_w + \Delta_B, z) = P_b \overline{\Gamma}_n \ ,$$ (10.3-7)

where P_b is the back power density for a unit wall loading and $\overline{\Gamma}_n$ is the average wall loading for the module.

At a given axial position z, the power density is assumed to decrease exponentially with r according to the relation

$$P(r,z) = \frac{r_w}{r} P(r_w, z) \ e^{-(r-r_w)/\lambda(z)} \ .$$ (10.3-8)

The factor r_w/r is used to account for the cylindrical geometry. Note that the 1/e folding distance λ is allowed to vary with z to account for the different axial distributions at the front and back of the module. The values of P_f and P_b can be determined by fitting the radial variation in the blanket at unit wall loading to an exponential form as indicated by Eq. 10.3-8. Using Figs. 10.3-14 and 10.3-15 we get values for P_f of 3.7 and 5.7 W/cm^3 for the Li and Li-Pb blankets, respectively. The corresponding values for P_b are 0.3 and 0.5 W/cm^3. Setting $r = r_w + \Delta_B$ in Eq. 10.3-8 and substituting for $P(r_w, z)$ and $P(r_w + \Delta_B, z)$ from Eqs. 10.3-6 and 10.3-7 we get

$$\lambda(z) = \Delta_B / \ln \left[\frac{r_w}{r_w + \Delta_B} \frac{P_f \Gamma_n(z)}{P_b \overline{\Gamma}_n} \right] \ .$$ (10.3-9)

Substituting in Eq. 10.3-8 yields the power density distribution

$$P(r,z) = \frac{r_w P_f \Gamma_n(z)}{r} \left[\frac{(r_w + \Delta_B) P_b \overline{\Gamma}_n}{r_w P_f \Gamma_n(z)} \right]^{(r-r_w/\Delta_B)} \ .$$ (10.3-10)

Although this formula was derived for a uniform wall radius, it can still be used for the TASKA-M blanket module, where the wall is recessed by only a few centimeters to accommodate the ICRF antenna. In this case r_w and Δ_B will be allowed to vary with z in Eq. 10.3-10. However, one must keep in mind that Eq. 10.3-10 is not perfectly accurate as it does not account for power density peaking at the back and sides of the module due to reflection from the surrounding shield. The power density profiles obtained using Eq. 10.3-10 are shown for the Li and Li-Pb blanket modules in Figs. 10.3-16 and 10.3-17, respectively.

10.3.4 Thermal Hydraulics

10.3.4.1 MHD Effects. The dominant force on a conducting fluid across the magnetic field lines is the MHD force. The effect of the MHD force is to increase the pressure drop and retard heat transfer by suppressing turbulence. In a D-T fusion reactor blanket, with the breeding material serving also as the coolant, the only severe heat transfer problem occurs at the first wall. For TASKA-M, the first wall surface heat load is < 10 W/cm^2. The effects of MHD on heat transfer are, therefore, not critical and the heat transfer calculations can be carried out by assuming no turbulence. The MHD pressure drop will increase the stress in the blanket and also increase pumping power. The lower neutron wall loading in TASKA-M compared to a power reactor allows a lower coolant velocity which in turn will reduce the MHD pressure drop. Its magnitude and effects, however, still have to be assessed.

It is well known that whenever an electrically conducting fluid flows across field lines, eddy currents will appear wherever curl [v x B] is non-zero. This produces a retarding force which causes extra pressure drops in the fluid. These pressure drops will be classified here into two categories,[7] the Hartmann and end-of-loop effects.

The Hartmann pressure gradient arises in fully-developed laminar flow with a uniform transverse magnetic field. For such a flow between parallel plates, in a uniform magnetic field normal to the plates, the pressure gradient is given by the following equation:[8]

$$ -\frac{dP}{dx} = \frac{\mu v}{a^2} \left[\frac{H_\perp^2 \tanh H_\perp}{H_\perp - \tanh H_\perp} + \frac{H_\perp^2 C}{1+C} \right] \qquad (10.3\text{-}11) $$
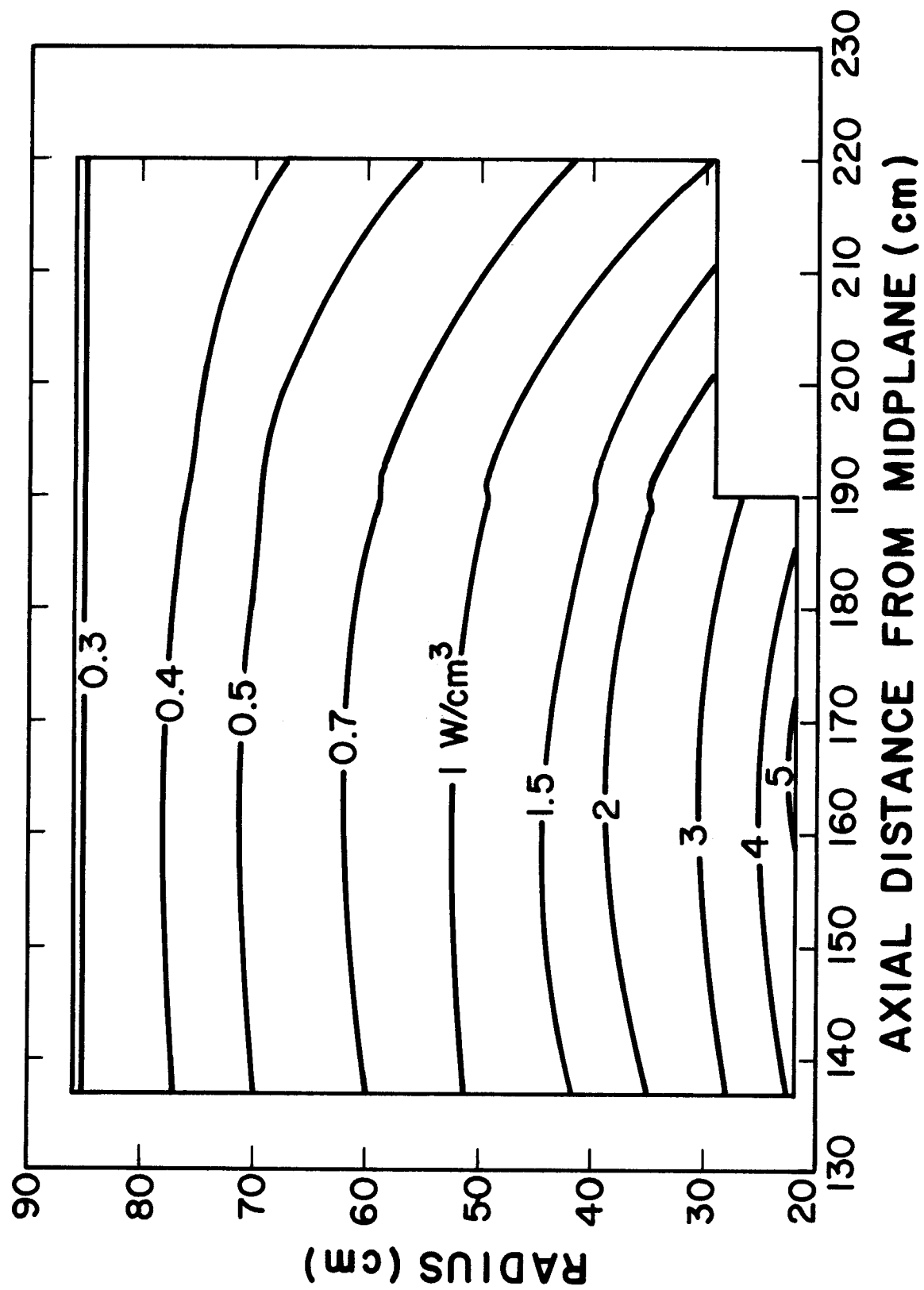
Fig. 10.3-16. Equal power density (W/cm³) contours for Li blanket.
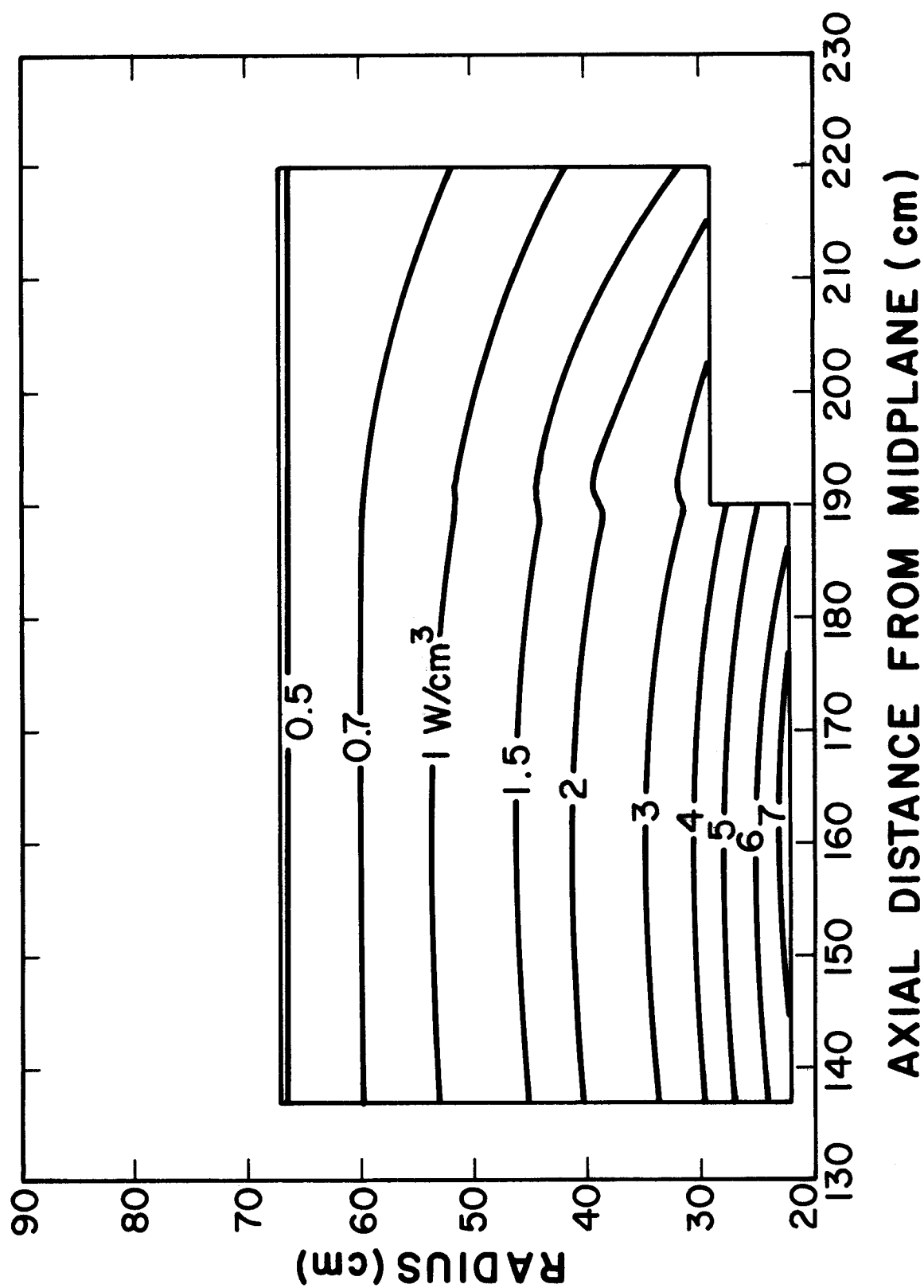
Fig. 10.3-17. Equal power density (W/cm³) contours for Li–Pb blanket.

where μ = viscosity

      v = coolant velocity

      C = wall conductance ratio, $\sigma_w t_w / \sigma a$

      a = channel half-width

      H = Hartmann number; $H \equiv \dfrac{B^2 a^2 \sigma}{\mu}$

     σ_w = electrical conductivity of the wall material

      σ = electrical conductivity of the coolant

    t_w = wall thickness.

When the fluid is in a channel with a conducting wall and under large magnetic fields (H >> 1 + 1/C), the last term of Eq. 10.3-11 dominates, giving

$$-\frac{dP}{dx} = \frac{vB_\perp^2 \sigma_w t_w}{a(1 + C)} .$$ (10.3-12)

If the wall is strong enough to withstand the pressure and the corrosion of the liquid metal, the value of C is usually on the order of 10^{-2} or larger; hence, Eq. 10.3-12 is an excellent approximation in the present range of Hartmann numbers (H ≈ 10^5).

The end-of-loop effects are caused by gradients of [$\underline{v}$ x $\underline{B}$] in the flow direction. The resulting pressure drops are given approximately by the following equation[8]

$$\Delta P = K_{PIE} \frac{\sigma b_{av}}{v_{av}} \Delta(v^2 B_\perp^2) .$$ (10.3-13)

Here b is the mean half-width of the local cross section in the direction normal to $B_\perp$ while the subscript av indicates the arithmetic average of values for initial and final cross sections (or velocities). The coefficient K_{PIE} has been presented by Hoffman and Carlson[7] for flows in tubes and ducts with varying $B_\perp$; the results are summarized in Figs. 10.3-18 and 10.3-19. The same plots are used here to estimate K_{PIE} for changes of velocity and channel width; in this estimation L_F is taken as the downstream length of the region of varying $vB_\perp$.

The MHD pressure drops for the $Li_{17}Pb_{83}$ and Li coolants are calculated from Eq. 10.3-12 and 10.3-13, based on data summarized in Table 10.3-7. The results are summarized in Table 10.3-8 for the LiPb blanket. The calculations

Table 10.3-7. Liquid Metal Test Module Parameters

	LiPb	Li
Average wall loading, MW/m^2	0.84	0.84
Peak wall loading, MW/m^2	1.22	1.22
Energy production rate, MW/m / MW/m^2	1.35	1.45
Module width, m	0.83	0.83
Inner/outer radius, cm	22/67	22/85
Breeder/coolant	LiPb	Li
Local tritium breeding ratio	1.15	1.19
Blanket energy production, MW	0.95	1.02
Reflector energy production, MW	0.36	0.32
Magnetic field, tesla	4.2	4.2
Module neutron power, MW	0.96	0.96
Tritium production rate, g/d	0.21	0.22

are based on a local magnetic field of 4.2 tesla. The resulting pressures are shown in Fig. 10.3-20. The largest pressure drop occurs in the feed and discharge tubes due to the high local velocity. This pressure drop has been reduced by using a laminated tube structure, with a sleeve 1 mm thick, which is insulated from the main structural tube. The thin inner wall reduces the Hartmann pressure drop as can be seen from Eq. 10.3-12. The liquid metal testing module thermal hydraulic parameters are given in Table 10.3-9.

10.3.4.2 Heat Transfer Calculations. The temperature profile in the coolant tube can be calculated by assuming only conduction. This can be justified due to the MHD effects on suppressing of turbulence. The most severe heat transfer problems occur in the first row of tubes. The energy deposited in the first row of tubes consists of a volumetric component due to nuclear heating and a surface heating load from the plasma.

For a slab geometry with a constant velocity, constant surface heat flux, and exponential volumetric heat flux, the temperature profile can be calculated by:

Table 10.3-8. Summarized MHD Pressure Drop Calculations for LiPb Module

	v, m/s	r, cm	L_F/b	K_{PIE}	t_w, mm	L, m	ΔP_E	ΔP_M	$\sum \Delta p$
								MPa	
Feed pipe	0.13	10	10	0.1	5	3	0.06	0.11	0.17
Feed pipe turns to manifold	0.13	10	2	0.15	--	--	0.1	--	0.1
Manifold turns to blanket tube	0.025	3.5	2	0.15	--	--	0.01	--	0.01
Blanket tube	0.025	3.5	--	--	1.6	0.69	--	0.01	0.01
Blanket tube turns to manifold	0.025	3.5	2	0.15	--	--	0.01	--	0.01
Manifold turns to discharge pipe	0.13	10	2	0.15	--	--	0.1	--	0.1
Discharge pipe	0.13	10	10	0.1	5	3	0.06	0.11	0.17
TOTAL									0.57

Table 10.3-9. Liquid Metal Testing Module Thermal - Hydraulic Parameters

	LiPb	Li
Blanket power, MW	0.95	1.02
Blanket coolant	LiPb	Li
Coolant temperature, °C	300/450	300/450
Coolant flow rate, kg/hr	1.37×10^5	5.8×10^3
Maximum structural temp., °C	512	500
Maximum coolant velocity, cm/s	2.5	1.8
MHD pressure drop (MPa)[*]	0.57	0.45
Maximum blanket pressure (MPa)[**]	0.42	0.35
Pumping power, kW	2.3	1.4
Reflector power, MW	0.36	0.32
Reflector coolant	H_2O	H_2O
Coolant temperature, °C	80/150	80/150
Coolant flow rate, kg/hr	4400	3900

[*] Total MHD drop from entrance to exit from blanket module.

[**] Maximum blanket pressure can be less than total MHD drop because half of MHD drop occurs at exit from blanket.
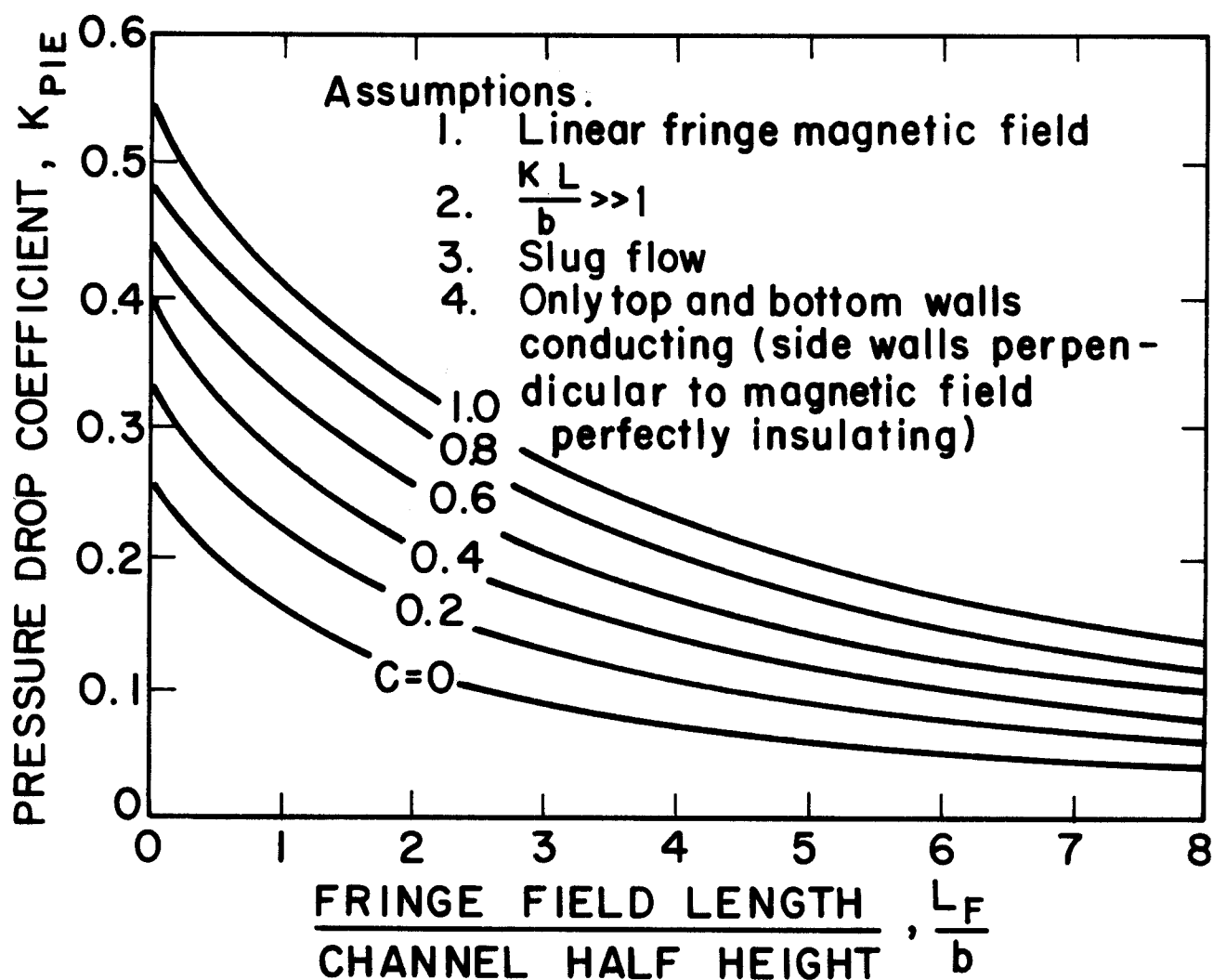
Fig. 10.3-18. Pressure drops due to entrance and exit eddy current for linear
fringe magnetic fields separated by a long region of uniform
magnetic field.
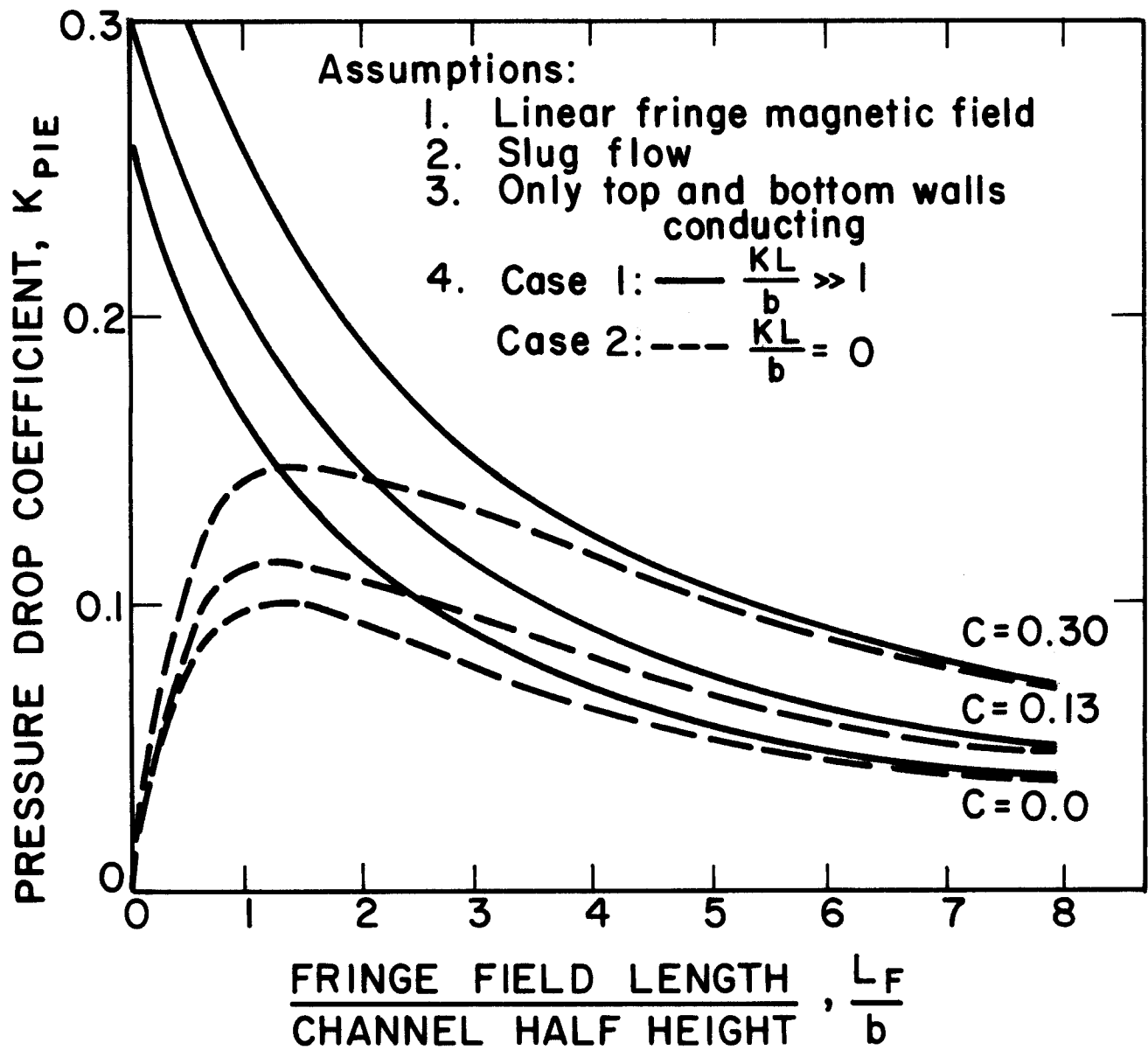
Fig. 10.3-19. Pressure drop due to entrance or exit eddy currents.

Fig. 10.3-20. MHD pressure drops in liquid metal blanket for LiPb and Li.
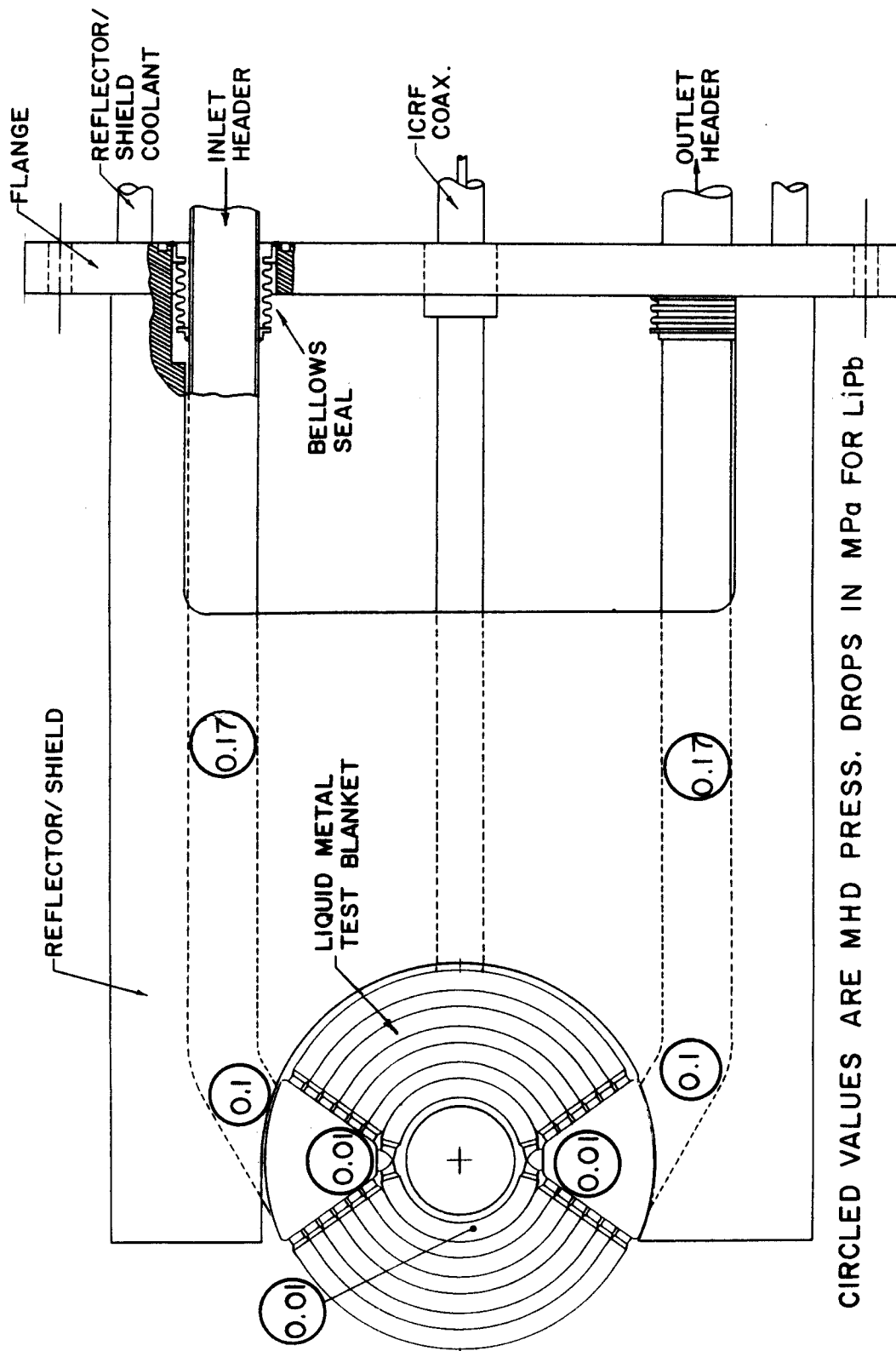
CIRCLED VALUES ARE MHD PRESS. DROPS IN MPa FOR LiPb

$$T = \frac{W_o R^2}{K} \left\{ \frac{1}{b} (1 - e^{-b}) \frac{\alpha t}{R^2} \right.$$

$$+ \sum_{n=1}^{\infty} [1 + (-1)^n e^{-b}] \frac{2b}{\mu_n^2 (b^2 + \mu_n^2)} \cos \mu_n \frac{x}{R} \left[1 - e^{-\mu^2 n^2 \frac{\alpha t}{R^2}} \right] \left. \right\}$$

$$+ \frac{2 W_s}{K} (\alpha t)^{1/2} \text{ierfc} \left[\frac{x}{2(\alpha t)^{1/2}} \right] \tag{10.3-14}$$

in which $\mu_n = n \pi$ $\qquad\qquad W_v = W_o e^{-b(x/R)}$ $\qquad\qquad$ (10.3-15)

W_v is the nuclear heating rate

x is the distance from the surface

b is a constant defined by Eq. 10.3-15 and equal to 0.54

W_o is a constant defined by Eq. 10.3-15 and equal to 6.7 W/cm^3

R is thickness of the slab is 7 cm

K is thermal conductivity, equal to 0.22 W/cm-K

α is thermal diffusivity, equal to 0.156 cm^2/s

t is y/V_o

y is distance from entrance

V_o is coolant velocity, equal to 2.5 cm/s

W_s is surface heating, equal to 10 W/cm^2

This equation can be used to calculate the complete temperature profile within each tube of the blanket. The first wall is subjected to a relatively large surface heating from the plasma and, consequently, has a more severe heat transfer problem. The equation to calculate the first wall temperature, at x = 0, can be simplified to the following form

$$T_o - T_{in} = 3.4 t + 22.4 t^{1/2} .$$

At the exit, t = 27.6 s, and T_o = 512°C. This is high but judged to be acceptable.

10.3.5 Test Program

10.3.5.1 Introduction. For the TASKA-M blanket, a number of engineering tests have to be performed. A list of the engineering tests is tabulated in Table 10.3-10. The purpose of the tests is to subject a complete test blanket system to a fusion environment. The results of the engineering tests will provide the information required to construct and operate the blankets for the next generation of fusion devices.

The flow diagram of the TASKA-M liquid metal blanket module and heat rejection system is shown in Fig. 10.3-21. The cycle involves a heat rejection system for normal operation and a test module for engineering testing. The heat rejection system consists of an intermediate heat exchanger (IHX), with a helium secondary coolant. A low temperature heat exchanger operates in the range of 100 ~ 150°C. This low temperature will ensure minimum tritium leakage to the water coolant. The tritium will be recovered from the primary coolant by a well-established system; perhaps not highly efficient. A possible method for tritium removal in the LiPb is vacuum pumping. The tritium leaked into the intermediate coolant can be oxidized and removed by molecular sieve techniques.

Table 10.3-10.   Information To Be Obtained from the Test Program

- Temperature Distribution
- Pressure Distribution
- Corrosion
- Corrosion Product Transport
- Corrosion Product Cleanup
- Tritium Production
- Tritium Recovery
- Tritium Isolation
- Neutron Heating
- Nuclear Spectrum
- Material Activation and Decay Heat
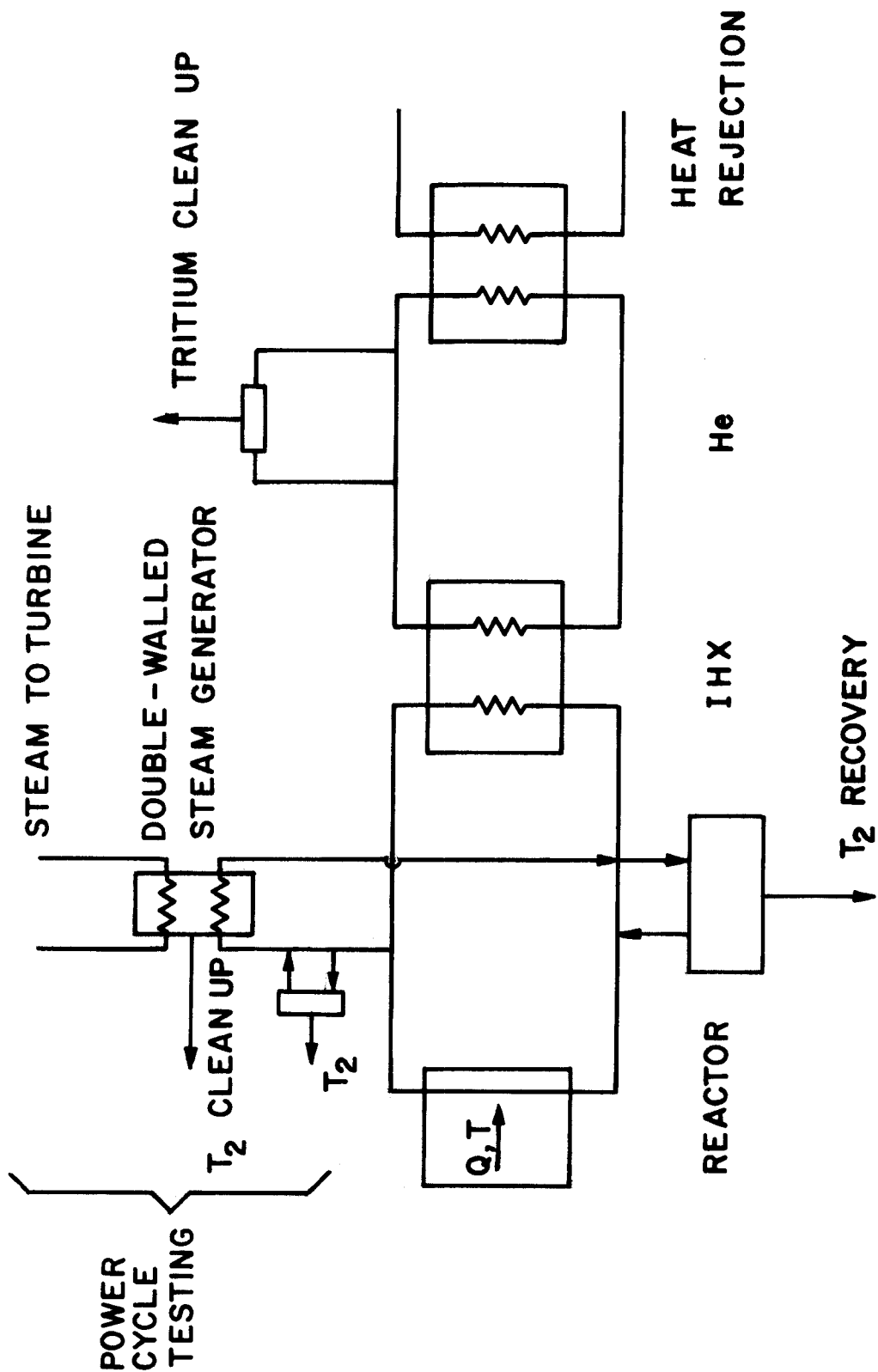
Fig. 10.3-21. TASKA-M Testing Power Cycle.

The testing program will also study various methods of tritium recovery, tritium isolation, steam generator operation, and corrosion product cleanup. This is a small part of the whole engineering system and operating conditions can be varied to study the effect of different parameters.

The instrumentation for the module will be required to obtain the test data for eventual correlation. The most important data are velocity, temperature, pressure and tritium concentration. The bulk information for these can be obtained by many conventional methods. From this information, the energy production and tritium breeding rates can be calculated and compared to the neutronic calculation. However, if local pressure, temperature, velocity and tritium concentration are required, the instrumentation required will be far more complicated. Such information would be useful to calibrate the neutronics calculation and to predict MHD effects, and is valuable to the blanket design.

10.3.5.2 Tritium Recovery from Liquid Metal Test Blankets

Individualized tritium recovery systems have been designed for the liquid lithium and the liquid lithium-lead alloy test blankets. The proposed recovery systems utilize conservative designs which can be thoroughly tested before the breeder blankets are installed. For this reason a separate test module is located on each of the liquid metals circuits so that additional techniques may be investigated. The proposed heat transfer system, Fig. 10.3-21, utilizes an intermediate helium circuit in order to separate the tritium-bearing liquid metal from the water-cooled heat rejection circuit. The parameters used in this study for each of the three heat transfer circuits and the two heat exchangers are given in Table 10.3-11.

Although the primary goal of these experiments is the demonstration of tritium breeding and recovery in liquid metal breeders, it is equally important to demonstrate that this objective can be met in an environmentally acceptable manner. This objective requires that tritium losses to the water coolant be controlled to a limit which is representative of a full-scale fusion power plant. The Blanket Comparison Systems Study[12] suggests that tritium losses to water coolant should be < 100 Ci/d per 4000 MW (thermal), i.e. 2.5×10^{-2} Ci/d·MW(th); a more restrictive environmental study[13] suggests that total tritium losses from a fusion plant should be < 10 Ci/d per plant, i.e. $\sim 3 \times 10^{-3}$ Ci/d·MW(th) to environmental cooling water. The

Table 10.3-11. Parameters for the Liquid Metal Heat Transfer System

Liquid Li Test Blanket

Structural material: ferritic steel
  (HT-9)
Temperature: 450/300°C
Mass Li: 2×10^3 kg
Flow rate: 5.8×10^3 kg/hr
Pressure, T_2: 1.3×10^{-10} mbar
Tritium removal system: absorption
  on yttrium

Intermediate Heat Transfer Circuit

Coolant: Helium
Structural material: ferritic steel
  (HT-9)
Temperature: 450/300°C
He Mass: 1.45×10^3 moles
He flow rate: 4.6×10^3 kg/hr
He pressure: 50 atm
Tritium removal system: T_2O
  adsorption

Liquid LiPb Blanket

Coolant/Breeder: $Li_{17}Pb_{83}$
Structural material: ferritic steel
  (HT-9)
Mass LiPb: 2.1×10^4 kg
Flow rate: 1.37×10^5 kg/hr
Temp.: 450/300°C
Pressure, T_2: 1.3×10^{-4} mbar
Tritium removal system: vacuum
  degassing

Water Coolant Circuit

Coolant: H_2O
Structural material: ferritic steel
  (HT-9)
Temp.: 150/100°C
H_2O mass: 4.3×10^3 kg
H_2O flow rate: 1.71×10^4 kg/hr.
H_2O pressure: 6 atm.
Heat rejection: water (ambient
  temperature)

Intermediate Heat Exchanger

Type: tube-in-steel
Material: ferritic steel, HT-9
Tube surface area: 30 m^2
Tube thickness: 1.65 mm

Water-Cooled Heat Exchanger

Type: tube-in-steel
Material: ferritic steel, HT-9
Tube surface area: 11 m^2
Tube thickness: 2 mm
Tritium diffusion barrier factor: 10

initial goal set for this study was to limit the tritium loss to the water coolant at < 3 x 10^{-3} Ci/d for this 1 MW(th) system. This goal requires a tritium partial pressure < 1.3 x 10^{-10} mbar in the intermediate circuit. Tritium removal systems were then designed for each liquid metal breeder blanket which would meet the tritium loss rate goal.

10.3.5.2.1 Liquid Lithium Breeder. Because of the high solubility at low pressure of hydrogen (tritium) in liquid lithium, several extraction systems[14] have been proposed for the recovery of tritium. The technique of tritium transfer directly from the liquid lithium in contact with yttrium metal foil was chosen for this study for the following reasons: (1) low tritium concentrations in lithium can be obtained without the need for hydrogen isotope dilution; (2) no foreign chemicals are introduced into the lithium; and (3) experimental thermodynamic and kinetic data exist.

With the proposed tritium pressure of 1.3 x 10^{-10} mbar in the intermediate, helium circuit, further tritium removal in the helium was avoided when a tritium removal system was designed to limit the tritium pressure to the same value in the liquid lithium. Based on the Sievert's constant for tritium in liquid Li[15] (K_S = 7.13 x 10^4 wppm·mbar$^{-1/2}$ at 400°C), the low tritium pressure desired, 1.3 x 10^{-10} mbar, has the additional benefit that the tritium concentration is low, 0.818 wppm, and the total tritium inventory in the lithium is only 1.64 g.

Initially, it was assumed that the tritium extraction could be accomplished by the diversion of only 0.3% of the Li flow to a yttrium trap at 250°C so that the tritium pressure upon exit liquid from the trap was 1.3 x 10^{-11} mbar and the concentration 0.259 wppm·T/Li. Based upon the Sievert's constant for tritium in yttrium[15] (1.93 x 10^9 wppm·mbar$^{-1/2}$), a full day's tritium generation, 0.22 g tritium, could be accommodated in 275 g yttrium. It has been experimentally determined,[16] however, that the mass transfer rate, β, is very small, ~ 10^{-5} cm/s at 250°C, where β is defined by the following relationship,

$$\ln \frac{c}{c_o} = -\beta \frac{S}{V} t \qquad (10.3-16)$$

where: c_o = initial concentration T in Li
        c = final concentration T in Li

β = mass transfer constant

s = surface area of yttrium

v = volume of lithium

t = residence time.

Because $v = \dot{m}t$, where $\dot{m}$ is the mass flow rate of Li to the TRS (Tritium Removal System) and the residence time must equal this flow time, the relationship becomes,

$$\ln \frac{c}{c_0} = -\beta \frac{s}{\dot{m}} .$$

For the appropriate values given in the previous paragraph for c_0, c, β and $\dot{m}$, s = 1.0 x 10^6 cm^2; the thickness of the yttrium foil to supply this area is 1.2 x 10^{-4} cm when the foil is considered to have two reactive surfaces; however, the volume of Li covering the foil is only 9.1 cm^3. Clearly, a greater volume of Li is required to cover and flow over the Y surface.

In order to obtain more Li in the TRS, a greater fraction (20%) of the total Li flow was diverted to the TRS; consequently, a smaller detritiation of the Li was needed. The concentration of T in Li upon exit from the TRS is 0.810 wppm and the concentration (T in Y) is 2.5 x 10^3 wppm. As a result the weight of Y required decreased to 88 g to absorb 1 FPd tritium generation. By use of Eq. 10.3-16, s_Y = 6.3 x 10^5 cm^2, which could be provided by yttrium foil with a thickness of 6.4 x 10^{-5} cm (reactive on both sides) and the foil is covered by 644 cm^3 Li. In order to have unrestricted flow channels through the foil channels the Li inventory was increased by 10^3, making the TRS contain ~ 0.64 m^3 Li, not an unreasonable size. The yttrium foil thickness was increased by 10 to 6.4 μm. With some development work, such high surface area yttrium flakes could be fabricated.

After one full power day usage, the lithium flow is diverted to a second yttrium trap and the loaded yttrium trap is regenerated. Recovery of tritium from the yttrium requires that all the lithium must be drained from the trap and the tritium released by vacuum degassing or purging with argon at high temperature. Experiments in the removal of tritium from yttrium in flowing argon indicate that the desorption reaction is very slow,[17] probably due to a tenacious oxide surface barrier on the yttrium surface, therefore, at 900°C only 10% of the tritium was assumed to be released in 12 hr. As described

previously, the yttrium foil was fabricated ten times thicker than required; consequently, after several recycle operations the yttrium will contain 2.20 g (T) of which 10% (0.22 g), one day's tritium generation, is released upon each recycle. This retention of tritium in the yttrium does increase the tritium inventory to 4.18 g (T) when two traps are used alternately.

As previously discussed no further removal of tritium is required in the intermediate helium circuit when the lithium test blanket is in use. With an assumed oxide barrier on the water-cooled heat exchanger (which reduces the tritium permeation by a factor of 10), the tritium loss to the coolant water is only 2×10^{-3} Ci/d, within the initial goal.

10.3.5.2.2 $Li_{17}Pb_{83}$ Test Blanket. The heat transfer system for the lithium-lead alloy test blanket is identical to that used for the lithium test blanket, shown in Fig. 10.3-21. In fact, the intermediate helium circuit and the water-coolant circuit can be the same for each experiment with only the primary liquid metal breeder blanket, and possibly the intermediate heat exchanger, requiring replacement for each liquid metal.

The liquid LiPb alloy test circuit has a permanent TRS for the removal of tritium at the rate it is generated in the breeder. Also, in the circuit is a test module TRS which can be used to conduct special tritium removal techniques and also to test concepts such as double-walled heat exchangers. The present study is limited to design and performance of the permanent TRS and the potential loss of tritium to the water coolant.

The partial pressure of tritium in equilibrium with solutions of tritium in LiPb alloy is much higher at the same T concentration than in the liquid lithium. As a result, the T concentration in solution must be kept very small in order to maintain acceptably low T_2 partial pressures. The technique of tritium transfer to yttrium metal in contact with the liquid metal, which was useful in the lithium system to maintain low tritium concentration, cannot be used with the LiPb alloy because of Y-Pb compound formation. Of the remaining extraction techniques, only vacuum degassing or gas sparging appear to be reasonably developed technologies. This study focuses on the use of vacuum degassing for the TRS, although no experimental studies exist presently on any of the possible tritium removal techniques.

Previous study of vacuum degassing of the LiPb alloy indicated[18] that 1.3×10^{-4} mbar pressure was an achievable lower limit for the entire liquid

metal circuit. Based upon the Sievert's constant[19] of 1.6 x 10^{-2} wppm·mbar$^{-1/2}$ at 400°C, the T concentration of the alloy is 1.8 x 10^{-4} wppm, which yields an inventory in the entire alloy blanket of only 4 x 10^{-3} g (T).

The Tritium Removal System by vacuum degassing of the liquid alloy must remove tritium at the rate it is generated, 0.21 g/d, therefore, 40% of the liquid alloy flow is diverted to the TRS kept at a T_2 pressure of 1.3 x 10^{-6} mbar. As a result, the concentration of T in the alloy is reduced from 1.8 x 10^{-4} wppm to 1.8 x 10^{-5} wppm. A pump speed of 1.6 x 10^4 ℓ/s is required at 1.3 x 10^{-6} mbar.

The required surface area of the liquid alloy pool is determined by use of Eq. 10.3-16, in which β has been approximated[18] to be 10^{-1} cm/s based upon observations of H removal from molten steel. The 3.3 m^2 surface area required is accomplished with a circular pool of 1 m radius. For a 10 s residence time in this vacuum chamber the depth of the alloy is 4.6 mm. Agitation is necessary to induce rapid bottom to top circulation in the liquid.

At the T_2 pressure of 1.3 x 10^{-4} mbar in the liquid metal, the intermediate helium loop would also attain the same T_2 pressure at steady-state. Because the HX to the water coolant operates at a lower temperature and includes an oxide barrier in the water side of the HX tubes which decreases permeation by ~ 10 fold, the permeation rate to the water is 1.75 Ci/d. While this tritium loss is acceptable for this test blanket, it needs to be reduced in order for the test to be representative of a full-scale reactor. This reduction is accomplished by the use of a TRS in the helium circuit.

In order to reduce the T_2 pressure in the helium loop, oxygen at a pressure of 1.3 x 10^{-2} mbar is introduced in order to form T_2O where the equilibrium constant at 400°C is defined by the relationship,

$$K_P = \frac{[P_{T_2O}]}{[P_{T_2}]\cdot[P_{O_2}]^{1/2}}$$

and $\qquad$ K_P = 2 x 10^{13} atm$^{-1/2}$ for H_2.

If K_P for T_2 is similar and the T_2O pressure is kept at 1.3 x 10^{-3} mbar by use of a molecular sieve dessicant column, then the T_2 pressure is

$\sim 10^{-14}$ mbar; the fraction of the He flow, f, which must be diverted to the drying column is determined by the relationship

$$f = \dot{T} \left[(X_{in} - X_{out}) \cdot \dot{m}(He) \times \frac{6 \text{ g } T_2/\text{mole } T_2O}{4 \text{ g He/mole He}} \right]^{-1}$$

where: $\dot{T}$ = tritium generation rate

$\dot{m}(He)$ = helium flow rate

X_{in}, X_{out} = the mole fraction of T_2O into and out of the desiccant column, respectively.

For this calculation the tritium generation rate is the permeation of T_2 from the liquid metal loop which is 2.26×10^{-3} mole T_2/d. The mole fractions of T_2O were determined from the partial pressures of T_2O and He; the other parameters are given in Table 10.3-11. A steady state pressure of 6.5×10^{-4} mbar T_2O was taken as representative of a regenerated molecular sieve drying column operating at 95°C. The fraction of helium flow diverted to the drying column is only 0.6%. A full day's tritium inventory on the drying column before regeneration would contain only 1.4×10^{-2} g (T). The total tritium in the helium circuit is only 2.3×10^{-4} g, mostly as T_2O.

With the use of the technique of the additional TRS in the helium, the permeation of tritium to the coolant water is a very low 2×10^{-5} Ci/d. This TRS provides a significant reduction in the tritium loss to the water. It also provides a safety system in the event that the TRS in the liquid lithium-lead alloy or the liquid lithium circuits becomes inoperable. In such an event the flow to the TRS in the helium circuit could be increased while the primary TRS was being repaired. For this reason, additional dessicant columns for standby use are recommended for the He-TRS circuit.

The design parameters for the TRS's in the liquid lithium test blanket, the liquid lithium-lead test blanket, and in the helium circuit are summarized in Table 10.3-12.

The tritium inventory and the loss of tritium to the coolant water for the two liquid metal test systems are summarized in Table 10.3-13. As noted in the table, the tritium inventory in the liquid lithium-lead alloy is very small.

Table 10.3-12. Parameters for Tritium Removal Systems (TRS)

Liquid Lithium Blanket

Tritium removal technique: yttrium absorption

Daily operation: 1 column in use, 1 column in regeneration

Fraction of flow to TRS: 20%

Temperature TRS: 250°C

Tritium partial pressures

Entrance: 1.3×10^{-10} mbar

Exit: 1.29×10^{-10} mbar

Tritium concentration

Entrance: 0.818 wppm

Exit: 0.810 wppm

Yttrium flakes

Weight: 880 g

Surface area: 630 m^2

Thickness: 6.4 μm

T_2 Removal from Y: vacuum degassing @ 900°C

Liquid LiPb Blanket

Tritium removal technique: vacuum degassing

Operation mode: continuous

TRS

Fraction of coolant flow: 40%

Temperature: 300°C

Tritium partial pressures

Entrance: 1.3×10^{-4} mbar

Exit: 1.3×10^{-6} mbar

Tritium concentration

Entrance: 1.8×10^{-4} wppm

Exit: 1.8×10^{-5} wppm

Dimensions: circular cylinder

Surface area: 3.1 m^2

Radius: 1.0 m

Depth, alloy: 4.6 mm

Gas flow: 2.1×10^{-2} mbar-ℓ/s

Pump speed: 1.6×10^4 ℓ/s @ 1.3×10^{-6} mbar

Intermediate Heat Transfer Circuit

Heat transfer fluid: helium

Tritium removal technique: oxidation with catalyst and adsorption of T_2O

Fraction of helium flow to TRS: 0.6%

Operation mode: continuous oxidation; desiccant; 1 in use, 1 in recycle daily

Partial pressure in helium:

$T_2 = 10^{-14}$ mbar

$T_2O = 1.3 \times 10^{-3}$ mbar

$O_2 = 1.3 \times 10^{-2}$ mbar

Desiccant meaterial: molecular sieves

Temperature: 95°C

TRS Pressure T_2O inlet: 1.3×10^{-3} mbar

outlet: 6.5×10^{-4} mbar

Table 10.3-13. Tritium Inventory and Loss Rate for Liquid Metal Heat Transfer Systems

Liquid Li Test System

Tritium loss to coolant water: 2×10^{-3} Ci/d

Inventory	T (g)
Li blanket	1.64
Y getter	4.18
Total	5.82

Liquid LiPb Test System

Tritium loss to coolant water: 1.5 Ci/d without intermediate TRS

2×10^{-5} Ci/d with intermediate TRS

Inventory	T (g)
LiPb blanket	4×10^{-3}
He circuit	2×10^{-4}
Desiccant	1.2×10^{-2}
Total	0.0142

10.3.5.3 Corrosion Product Transport

Corrosion and corrosion product transport may be a critical issue in a liquid metal blanket. It may limit the maximum operating temperature of a liquid metal and this limits the thermal efficiency of the power cycle. Both MHD effects and radiation effects may affect the corrosion rate. Therefore, an integral test in the proper environment is very important.

The best test would be similar to a corrosion experiment in a conventional system. A coupon is inserted in the high temperature region to study the corrosion rate. The weight change of the coupon, as well as the composition change near the exposed surface will be measured as a function of temperature, velocity and exposed time. The measurement of the deposition is more difficult. One way is to ease the heat rejection system in the test section. The velocity and friction factor will be varied as deposition occurs. The operation of a valve is another good indication of the corrosion

product deposition. However, the best method of observing the deposition of the corrosion product is to cut open the cold section of the loop and measure the deposition of various materials. The thickness, porosity, and composition of the deposition can all be measured at various locations.

If the corrosion problem is judged to be too severe for continued operation of the coolant loop, either a corrosion inhibitor can be added to the coolant, or a cold trap for the corrosion product can be added. It was found that 100 ~ 200 ppm of Al or Mg will significantly reduce the corrosion rate in Li[9] or Pb[10], respectively. On the other hand, the MARS study recommended[11] the use of a cold trap to keep the corrosion product concentration in the primary loop always below the saturation concentration at the lowest temperature of the loop. The cold trap system employed a regenerator heat exchanger attached to cool a side stream of the coolant to a relatively low temperature and precipitate out the corrosion products. It is not possible at this time to pick which method to use to minimize corrosion, since either method will certainly have to be tested conventionally before it will be incorporated into the TASKA-M system.

References for Section 10.3

1. B. Badger et al., "WITAMIR-I, A University of Wisconsin Tandem Mirror Reactor Design," University of Wisconsin Fusion Engineering Program UWFDM-400 (Sept. 1980).

2. B. Badger, W. Heinz, et al., "TASKA - Tandem Spiegelmachine Karlsruhe, A Tandem Mirror Fusion Engineering Test Facility," University of Wisconsin Fusion Engineering Program Report UWFDM-500, KfK-3311, FPA-82-1 (March 1982).

3. J.H. Huang and M.E. Sawan, "Neutronics Analysis for the MARS Li-Pb Blanket and Shield," Nucl. Technology/Fusion, 4/2/3, 835 (1983)

4. R. O'Dell, F. Brinkley, Jr., and D. Marr, "User's Manual for ONEDANT: A Code Package for One-Dimensional Diffusion-Accelerated, Neutral-Particle Transport," Los Alamos National Laboratory, LA-9184-M (1982).

5. "VITAMIN-C, 171 Neutron, 36 Gamma-Ray Group Cross Section Library in AMPX Interface Format for Fusion Neutronics Studies," DLC-41B, RSIC Data Library, Oak Ridge National Laboratory (1977).

6. "MACKLIB-IV, 171 Neutron, 36 Gamma-Ray Group Kerma Factor Library," DLC-60B, RSIC Data Library, Oak Ridge National Laboratory (1982).

7. M.A. Hoffman and G.A. Carlson, "Calculation Techniques for Estimating the Pressure Losses for Conducting Flows in Magnetic Fields," USAEC Report UCAL-51010, 1971.

8. G.W. Sutton and A. Sherman, Engineering Magnetohydrodynamics, McGraw Hill, N.Y., 1956.

9. P.F. Tortorelli et al., "Corrosion Inhibition in Systems of Li with Ni Bearing Alloy," Proceedings of the 8th Symposium on Eng. Problems of Fusion Research, Vol. 3, IEEE 79CH1441-5 NPS, p. 1610.

10. A.J. Romano et al., "The Investigation of Container Materials for Bi and Pb Alloys, Part 1, Thermal Convection Loops," USAEC Report BNL-811, 1963.

11. B.G. Logan et al., "Mirror Advanced Reactor Study," LLNL Report, to be published.

12. M. Abdou et al., "Blanket Comparison and Selection Study," Section II.3, U.S. DOE Document ANL/FPP/TM-177 Draft (September 1983).

13. S.J. Piet and M.S. Kazimi, "Implications of Uncertainties in Modeling of Tritium Releases from Fusion Reactors," Proc. ANS Mtg., Tritium Technology in Fission, Fusion and Isotopic Applications, April 1980, Dayton, Ohio, pp. 25-31.

14. V.A. Maroni, "Tritium Processing and Containment Technology for Fusion Reactors: Perspective and Status," Proc. ANS Second Top. Mtg., Tech. Controlled Nuclear Fusion, Sept. 1976, Richland, Wash., CONF-760935-P3, pp. 799-818.

15. S.D. Clinton and J.S. Watson, "The Solubility of Tritium in Yttrium at Temperatures from 250 to 400°C," J. Less-Common Metals 66, 51-57 (1977).

16. J.B. Talbot, "Recovery of Tritium from a Liquid Lithium Blanket," Proc. Amer. Inst. Chem. Eng. Symposium Series No. 208, 77, 58-63 (1981).

17. J.S. Talbot and J.D. Clinton, "Liquid Lithium Blanket Processing Studies," Proc. IEEE 8th Top. Mtg. Eng. Problems in Fusion Reactors, 1979, pp. 389-393.

18. K.E. Plute, E.M. Larsen, L.J. Wittenberg and D.K. Sze, "Tritium Recovery from Liquid Lithium-Lead by Vacuum Degassing," Nuclear Tech./Fusion 4 (No. 2), 407-414 (1983).

19. Y.C. Chan and E. Velekis, "A Thermodynamic Investigation of Dilute Solutions of Hydrogen in Liquid Li-Pb Alloys," Proc. Third Top. Mtg. Fusion Reactor Materials, September 1983, Albuquerque, NM, in press.

10.4.   Solid Breeder Blanket

10.4.1   Introduction

10.4.1.1 General Scope

The solid breeder test blanket is one out of four test modules (blanket
No. 2 in Fig. 10.4-1) located at the central cell of TASKA-M, Fig. 4.1-2. A decision
has been made that this module should serve as a test bed for all kinds of
solid blanket materials rather than as a breeding blanket. There are mainly
two reasons for this:

a) There are still a number of candidate breeder materials under discussion.
   Therefore it is desirable to have the possibility to exchange the materials
   inserted into the high flux region adjacent to the plasma (without disas-
   sembling the blanket).

b) The space available for the test blanket is limited. It is an annulus with
   the following dimensions:
   - inner radius 0.25 m
   - outer radius 0.40 m
   - length   0.43 m

Especially the small blanket thickness of 0.15 m makes it impossible to obtain
a breeding ratio near unity. The size and shape of the available space does
not allow a complete design typical of a breeding blanket in a larger fusion
device, but it allows to test the operation of the key blanket components,
namely the materials with its cooling and tritium breeding and extraction
principle.

To show how this can be carried out in TASKA-M, as example the test blanket
No. 2 is introduced which includes simultaneously some new ideas.

10.4.1.2 The Qualities of the chosen Concept

An important problem in designing a solid breeder blanket is the confinement
of tritium on one hand and the possibility of tritium extraction on the other
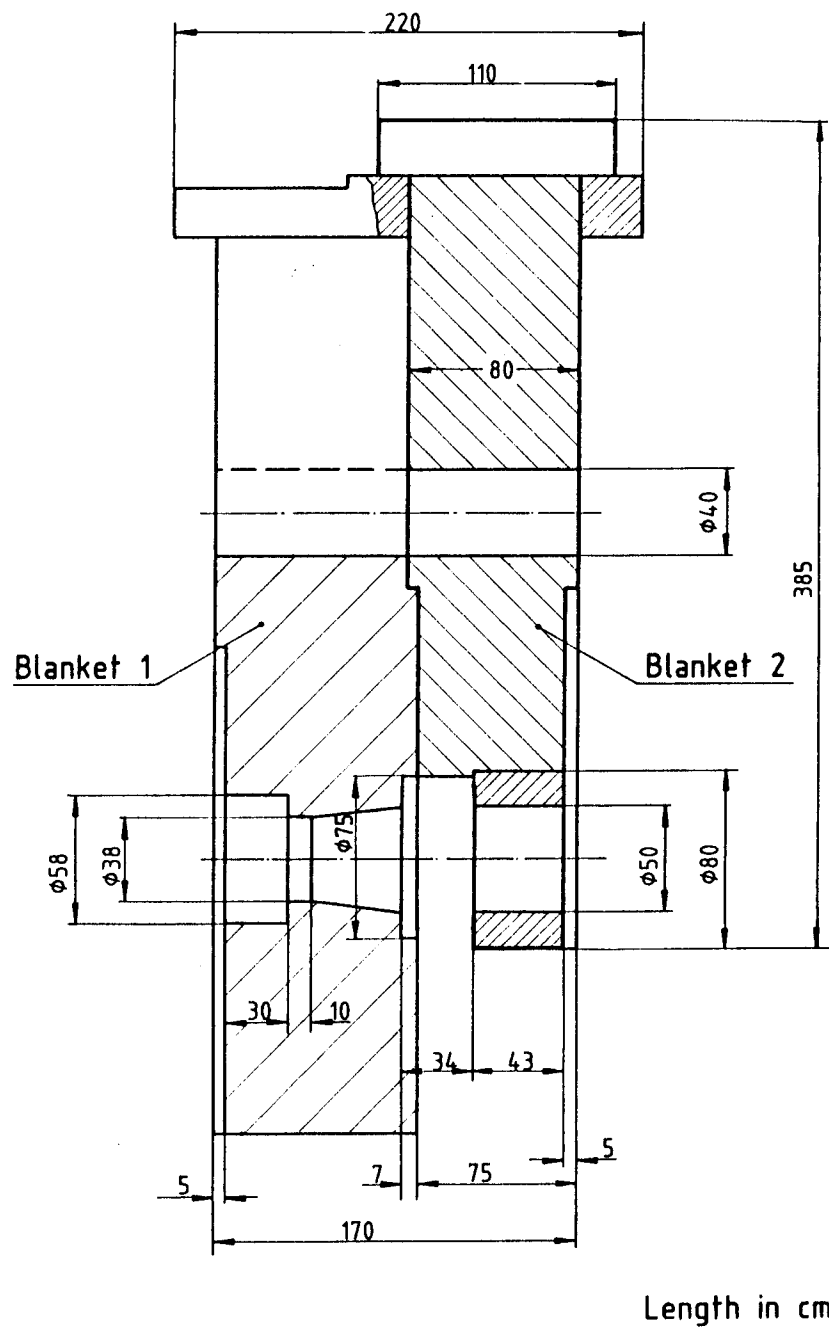
Fig. 10.4-1. Overall View of the Blanket Modules

Length in cm

hand. The usually proposed method of tritium extraction is to have helium flowing through the breeder material and extract the tritium on line from the helium. To accomplish this, quite a large number of connecting tubes inside the blanket and to the outside are necessary. To avoid the problems associated with this solution a blanket concept has been proposed /1/ which exhibits the following features:

- The blanket consists of a mixture of Li-ceramic breeder spheres with lead spheres, which are both confined by steel shells.
- The balls are filled in stainless steel tubes, which are coiled up around the plasma; the balls are cooled by pressurized water at 10 MPa pressure (300 ^{O}C).
- Tritium extraction is made by continuous or batchwise removal of balls and heating them to the temperature required for tritium extraction.

This concept has the following advantages:
1. The advantage of liquid breeders, namely, the decoupling of tritium production and extraction with the possibility of optimizing the tritium extraction process,
2. the advantages of ceramic breeders, namely,
   - the use of a much less corrosive material than liquid metal,
   - no problems of a radioactive liquid metal hazard,
3. the use of a totally canned breeding material, which remains canned even in a pressure tube rupture accident.
4. The quality to replace the breeding balls or the test spheres in a short time.

The problem associated with this concept is the difficulty to obtain a high breeding ratio due to the small volume fraction of breeder material.

For a breeder material test bed however the breeding ball concept offers a number of advantages while the disadvantage of the lower breeding ratio is not important. Therefore it has been used for the test blanket described in this report.

10.4.2   Design Description

10.4.2.1 Overview

The central cell of TASKA-M has been designed as a permanent structure with openings for the four test modules. The position of the four modules can be seen in Fig. 4.1-1.   These test modules slide into openings from both sides like drawers. Each blanket test module consists of the blanket zone, the reflector zone, the shielding zone and the outer flange with the vacuum seals. Fig. 10.4.-1 shows the outer dimensions of the two blankets. Transfer flasks have been designed which permit the exchange of test modules under vacuum conditions. To accomplish this, the test modules have to be designed for removal without disconnecting any internals, e.g. cooling lines and mechanical attachments.

One important goal in designing the solid breeder test blanket was the possibility to exchange the breeder material fast and easily without disassembling the module. This has been accomplished by designing a machine for insertion and withdrawal of the breeding balls and spheres for all desired blanket materials in a short time and, if necessary, even during operation.

Another important goal stated for the design was a high margin for increasing power by operating at a high pressure of the coolant up to 100 bar. All components can cope with about twice of the rated power. The dimensions chosen for the blanket region allow a linear swelling rate of up to 5 %.

In order to get a reliable design there are no welds or sharp bends in the high flux region. The number of penetrations through the vacuum flange has been minimized. All these penetrations remain welded permanently. This means, that they don't have to be disconnected when the blanket module is exchanged.

10.4.2.2 Blanket Zone

The breeding material is contained in spherical shells with an outer diameter of 30 mm. These balls are filled into pressure tubes made of SS 316 and with an inner diameter of 34 mm and a 3 mm wall thickness. The pressure tubes are coiled up around the plasma. There are 4 layers of coils, each of them having about 9 windings. This arrangement can be seen in Fig. 10.4.-2 and 3 showing the 4 layers of coils, their access tubes and the reflector/shield region. Each layer gets a different neutron flux since they are arranged concentrically. The content of each layer can be exchanged separately in order to avoid mixing of breeding balls with different neutron fluences. To accomplish this, each layer has separate access tubes (inlet and outlet) for breeding balls and cooling water. There are 4 inlet and 4 outlet tubes penetrating the vacuum flange. Access tubes and the windings of the coils have the same dimensions. They are welded together outside the high flux region. The length of the 4 pressure tubes is 20 to 25 m, leading to a content of 650 to 850 balls each. Balls and tubes are cooled by pressurized water. The innermost coil forms the first wall and is heated at the inner side by a surface heat flux in addition to the volumetric heat generation in the tube wall and the balls.

The coils are attached to the reflector by clamps in a way that thermal expansion and swelling do not cause additional stress. Fig. 10.4.-3 shows a cross section of the coils and the attachment to the reflector. The clamp used for the attachment can be seen in Fig. 10.4.-4.

The geometric dimensions of the blanket are summarized in Table 10.4-1

Reflector Cooling Water
Manifold

Boron Carbide
Rod Bundles

Access Tubes

2 900

2 500

250

3 450

400

Reflector Cooling Tubes

Blanket Tubes

500

800
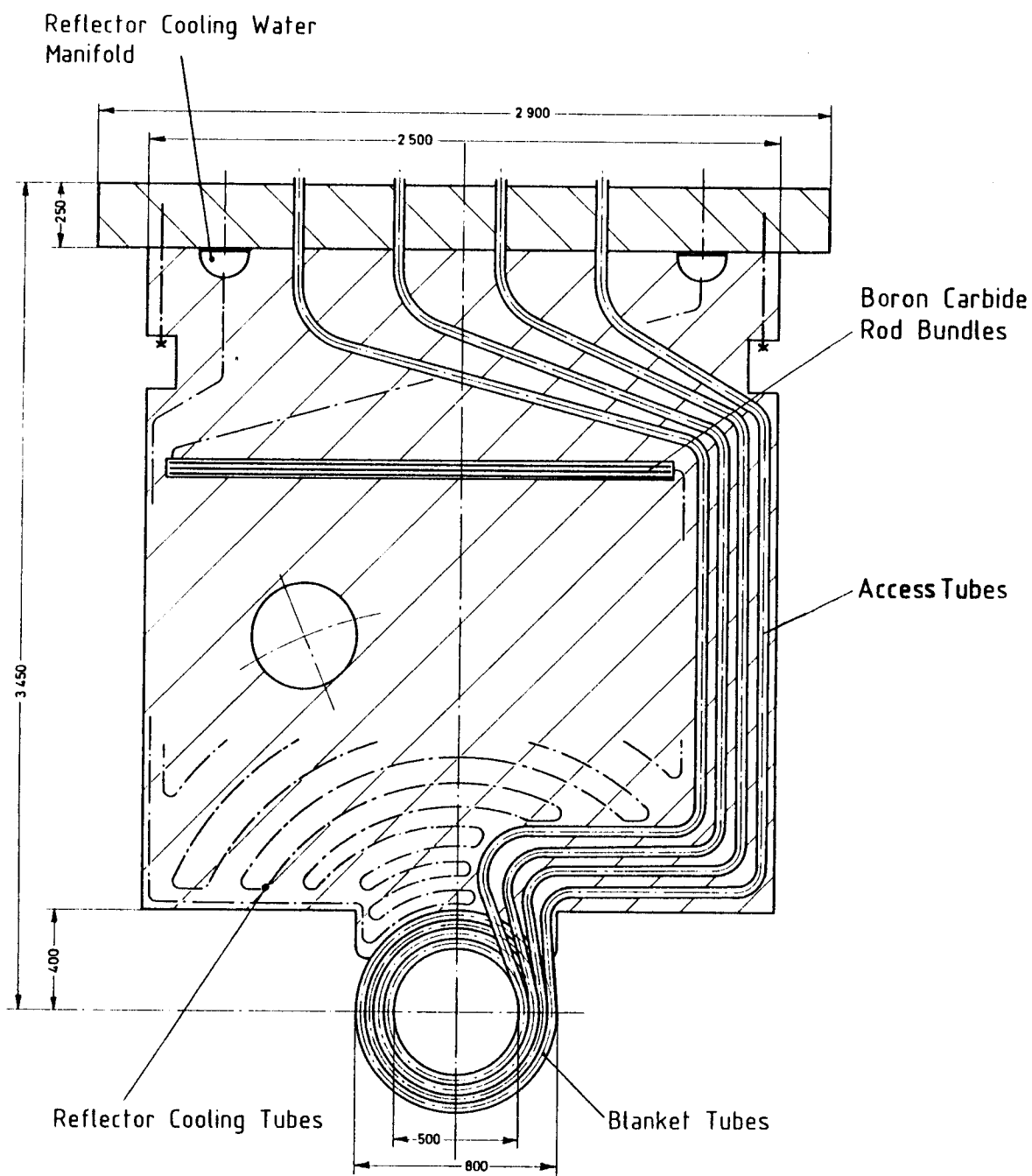
Fig. 10.4-2 Basic Arrangement of the Blanket and the Reflector/Shield
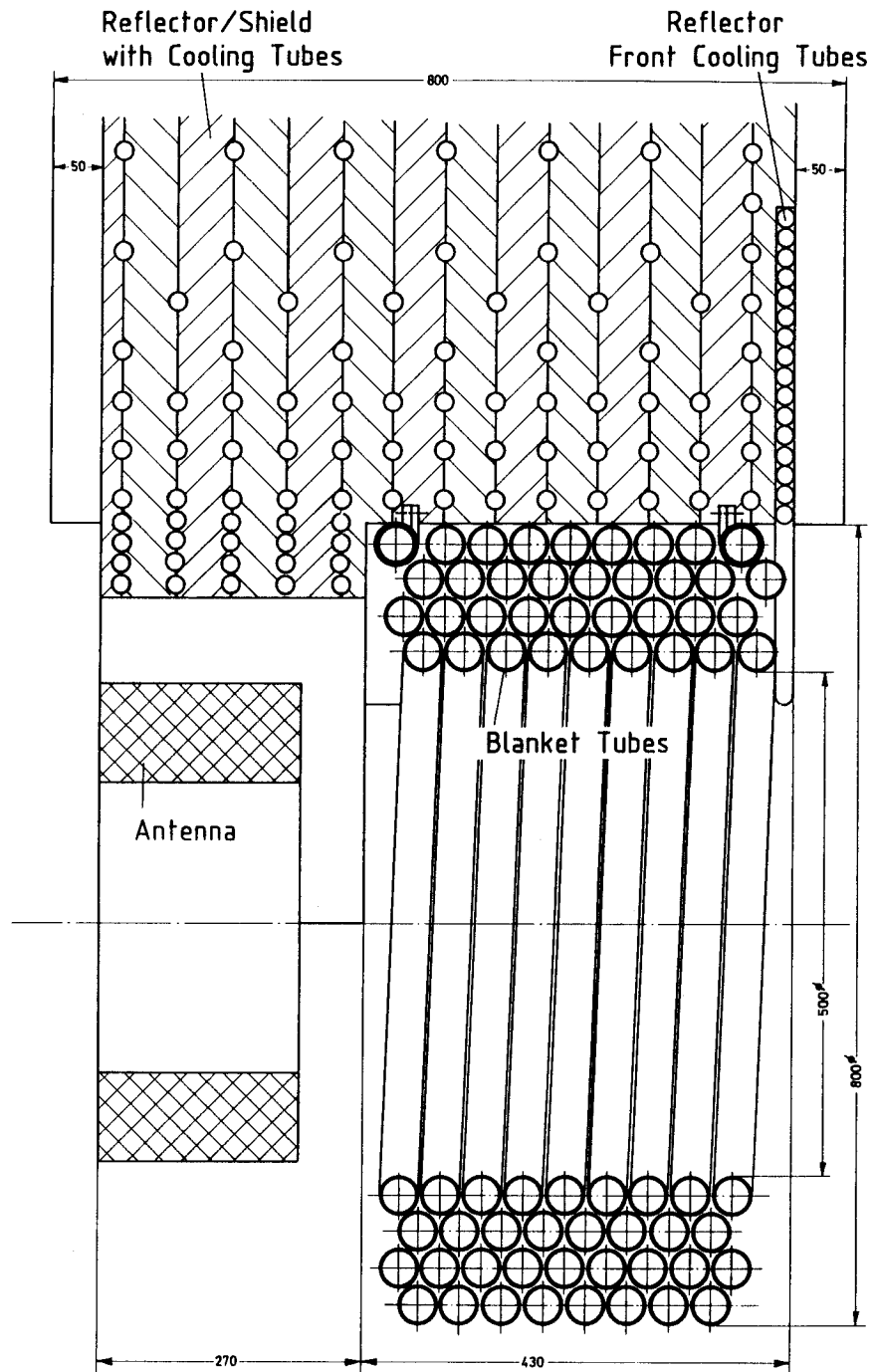
Fig. 10.4-3 Cross Section of Blanket and Reflector
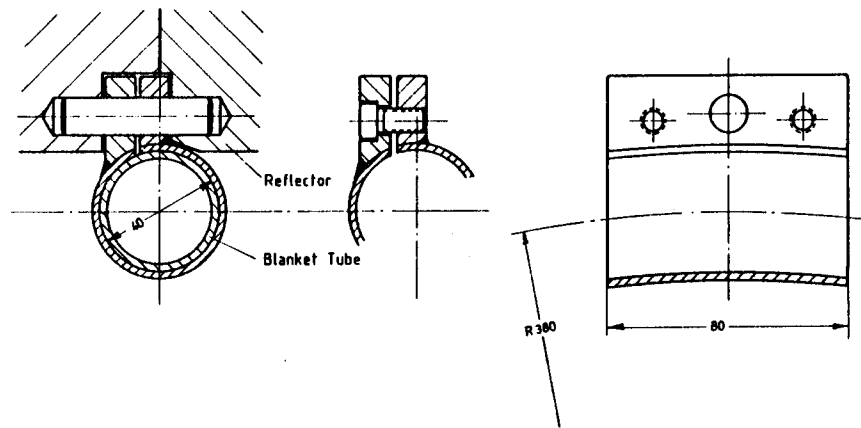
Fig. 10.4-4 Clamps for the Attachment of the Blanket to the Reflector
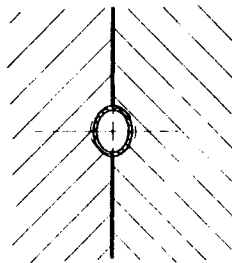
Fig. 10.4-5 Cross Section of a Cooling Tube after Clamping between
Reflector Plates (schematically)

Table 10.4-1: Geometry of Breeding Ball Blanket

a) Breeding Zone

outer radius	40 cm
inner radius	25 cm
length	43 cm
tube outer diameter	40 mm
tube wall thickness	3 mm
tube length	20 - 25 m
tube material	SS 316
breeding ball diameter	30 mm
wall thickness of the shell	2 mm
shell material	SS 316
breeding material	Li_2O

volume fractions in the breeding zone

breeding material	20 %
steel	32 %
water	28 %
void	20 %

b) Reflector/Shield

plate thickness	50 mm
plate material	SS 316
cooling tube outer diameter	22 mm
cooling tube wall thickness	1 mm
cooling tube material	SS 316

10.4.2.3 Reflector and Shield Zone

The reflector and the shield zone are composed of flat steel plates which are bolted together. Cooling tubes are located between the plates. This can be seen in Figs. 10.4-2 and 3. The cooling tubes are embedded in grooves of non-circular cross section. The original circular tubes are deformed to an elliptical shape by clamping them between the plates in order to obtain a good thermal contact between tubes and plates. Fig. 10.4-5 shows a cross section of a cooling tube after deformation. An additional contact pressure is caused by the coolant pressure which tries to bend back the tube to a circular cross section. The plate thickness and the spacing between the tubes depends on the volumetric heat generation and the allowable temperature variation in the plates.

The heat generation by neutrons and gammas decreases strongly with increasing distance from the plasma(see Figs. 10.4-12 and 13),but nevertheless the plate thickness has been kept constant in order to keep fabrication as simple as possible. Only the spacing between the tubes is adjusted to the local heat generation.

There is a considerable heat flux to the front surface of the reflector facing the neutral beam ducts, caused by charge exchange particles. This surface is covered by separate cooling tubes as can be seen in Figs. 10.4-3 and 6.

Boron carbide rods are located near the vacuum flange of the blanket module to increase neutron shielding. Fig. 10.4-7 shows the arrangement of two rows of boron carbide rod bundles schematically.

There is one inlet and one outlet manifold for the cooling water located at the backside of the shield. All cooling tubes are welded to these manifolds after assembling the reflector / shield plates. A cross section of the manifold is shown in fig. 10.4-8. From the manifolds there is only one inlet as well as one outlet tube penetrating the vacuum flange. These penetrations are sealed by welding after bolting together the plates and the vacuum flange. One disadvantage of this reflector design is the rather large surface area of the plates which may increase the outgassing time. If this is a problem, the plates can easily be sealed at their circumference.

Reflector Front
Cooling Tubes

Blanket Tubes

400

250

700
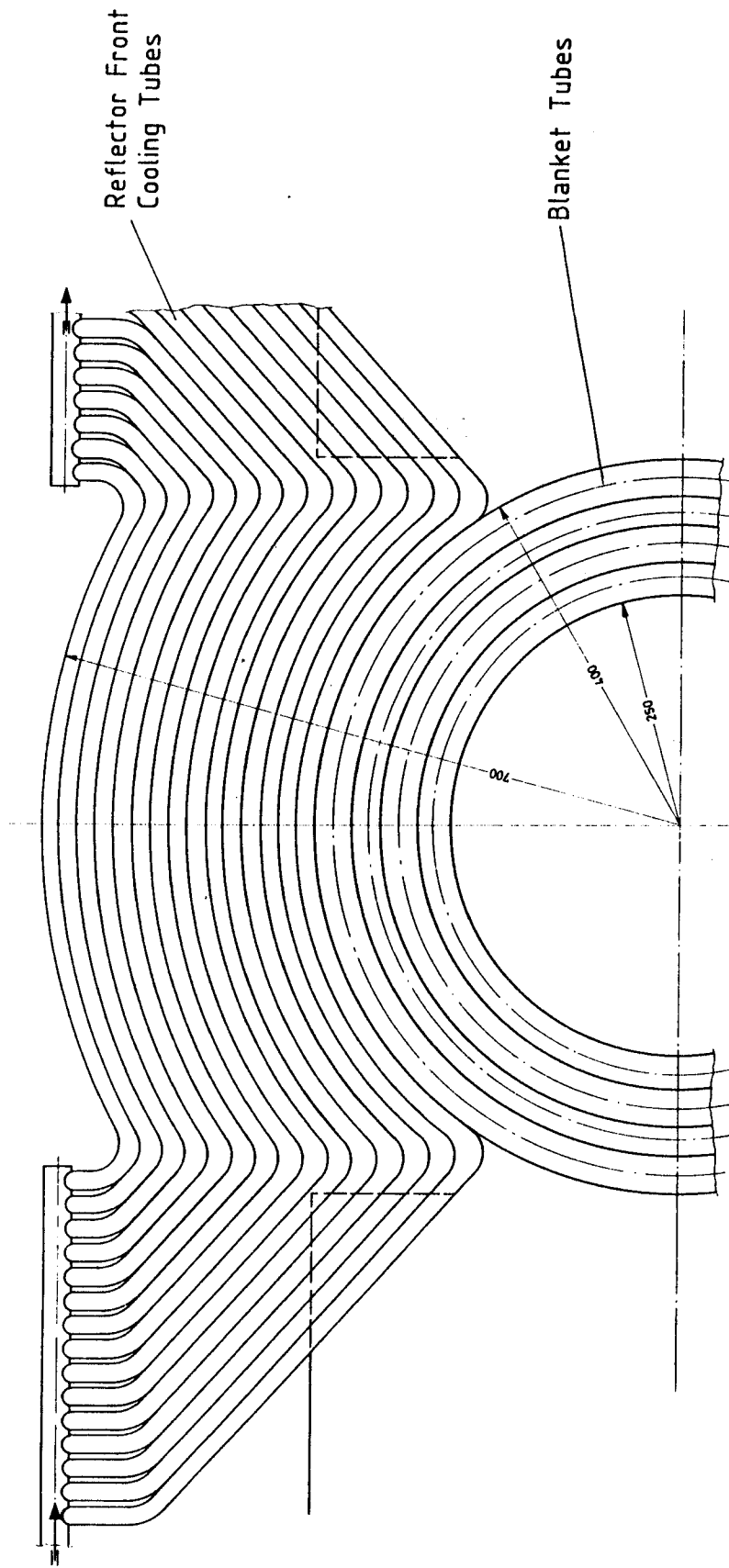
Fig. 10.4-6 Cooling Tubes at the Front Surface of the Reflector
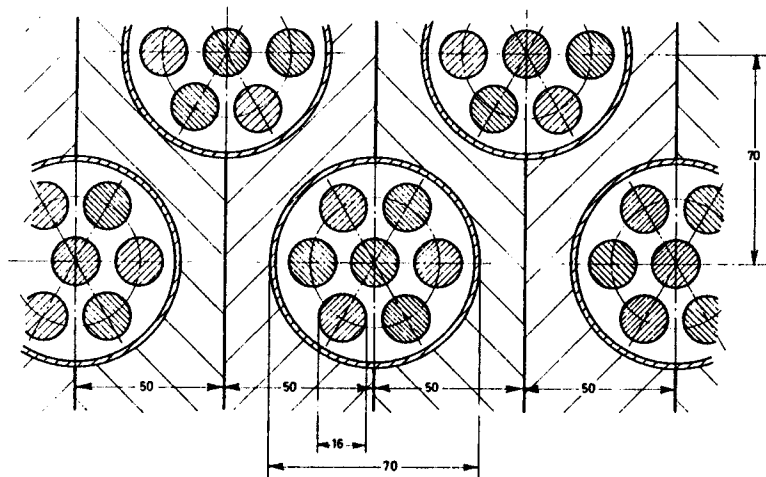
Fig. 10.4-7 Water Cooled Boron Carbide Rod Bundles
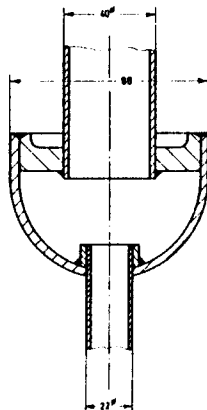
Fig. 10.4-8 Cross Section of the Cooling Water Manifold

10.4.2.4 Refilling Machine

Each of the 8 access tubes to the blanket is closed by a separate valve block, containing two double valves for closing the cooling water line and the ball exchange line. The refilling machines are flanged to those valve blocks after removing blank flanges. All flanges are designed for remote handling. Fig. 10.4-9 shows the valve blocks and the refilling machines attached to the blanket access tubes at the outer side of the vacuum flange. A cross section of a valve block and a refilling machine can be seen in Fig. 10.4-10.

Identical machines can be used for insertion and withdrawal of the breeding balls. The machine designed for batchwise exchange is operated hydraulically using the cooling water as working fluid. It is a closed system without sliding seals in order to avoid any leakage of tritiated water. The housing of the machine is designed for the full operating pressure but the hydraulic pump has to deliver a differential pressure only to overcome friction between ball and tube. The normal mode of operation of the refilling machine is to push one ball after the other into the tube and let balls come out at the other end of the tube with the same frequency. A system of interlocks has been designed for this purpose, which is operated hydraulically too. It is anticipated that it takes less than one hour to exchange the balls contained in one of the four layers of blanket tubes. Provisions have been made to empty the ball exchange lines and to check the tightness of the valves at both sides prior to disconnecting the refilling machines.

10.4.3 Neutronic Calculations

In the neutron and gamma transport calculations, the one-dimensional discrete ordinate code, ONEDANT /8/, is used with the University of Wisconsin 46-neutron, 21-gamma group cross-section set condensed from the ENDF/B-IV based Vitamin C and MACKLIB libraries in P_3, S_8-approximations.   The actual shape of the TASKA-M test pebble blanket module is modeled in the code by cylindrical geometry (fig. 10.4-11)with homogenized regions. The breeding zone contains then: 32 % SS 316, 28 % H_2O, 20 % breeding medium (Li_2O) and 20 % void. The reflector/shield consists of 95 % SS and 5 % water.

Reflector Cooling
Water Flange

Flanges of Access
Tubes

Cooling water

Ball
Container

Ball
Container

Pump
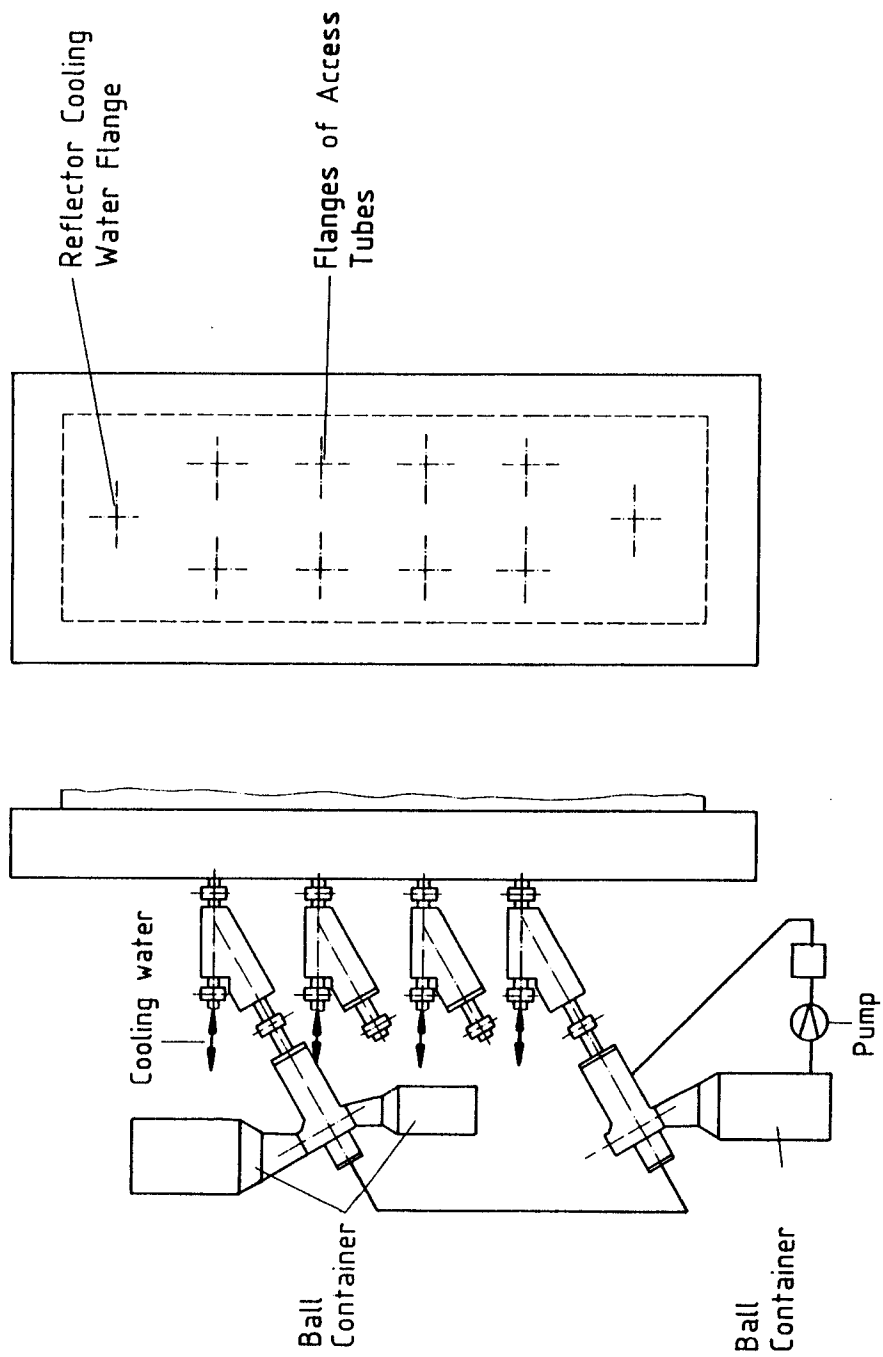
Fig. 10.4-9 Attachment of the Valve Blocks on the Refilling Machine

10.4-14
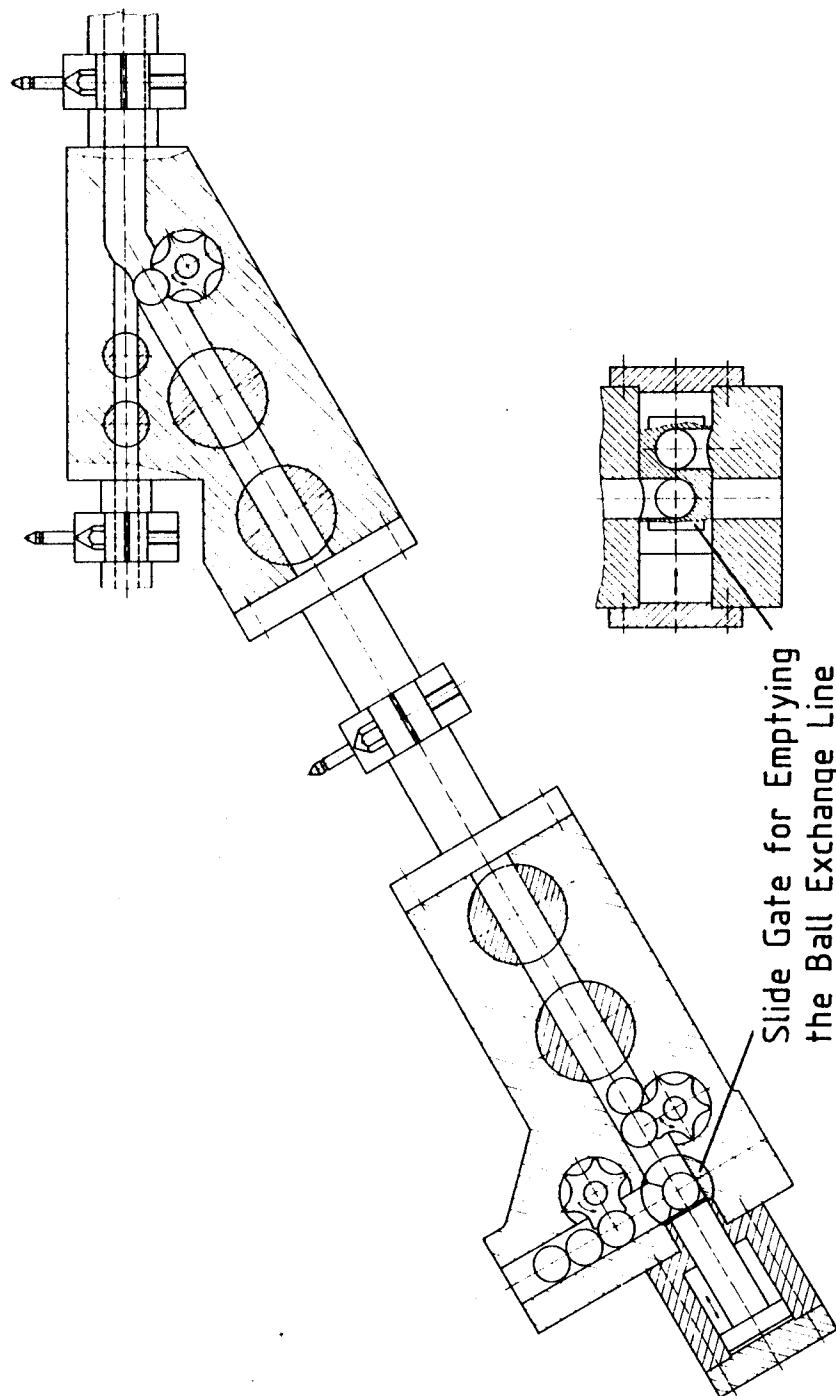
Fig. 10.4-10 Cross Section of a Valve Block and a Refilling Machine

Slide Gate for Emptying
the Ball Exchange Line

The objective of the calculations is to provide necessary data for the design of the blanket cooling system and to give an indication of the breeding ratio expected.

It should be mentioned that the one-dimensional cylindrical geometry must be assumed as rather rough approximation with respect to rather small lateral real dimensions. This is even true if the zone structure homogenization does not influence the calculated results for the given circumstances (Spheres diameter of 3 cm, not very soft spectrum). Therefore, more accurate results can be provided only on the basis of three-dimensional calculations which consider the mutual influence of neighbouring modules. Nevertheless, present evaluation of the radial power distribution (Figs. 10.4-12 and 13) may be recognized as satisfactory for the preliminary design of the cooling system.

The following energy multiplication factors M have been calculated

a) Blanket Region

    Breeding Zone $M = 0.81$

    Reflector/Shield Zone $M = 0.5$

    Total $M = 1.31$

b) Antenna Region $M = 1.53$

Another interesting result of the neutronic calculation is the tritium production rate. The total breeding ratio, using enriched Li with 30 % ^{6}Li and 90 % of the theoretical density has a surprisingly high value of 0.71 combined of 0.66 ^{6}Li(n,α)T and 0.05 ^{7}Li$(n,n'\alpha)$T. The neutronics data are summarized in Table 10.4-2.

10.4.4 Thermal Hydraulic Analysis

Separate cooling cycles have been designed for the blanket and the reflector/ shield region. The analysis is restricted to the module itself since all requirements and problems involved in the design of heat exchangers and piping systems are common with other parts of the machine and similar fusion devices. The detailed thermal hydraulic data are assembled in Tab. 10.4-3.

Table 10.4-2: Neutronics of Breeding Ball Blanket

Tritium breeding per Neutron

$^6\mathrm{Li}(n,\alpha)T$	0.659
$^7\mathrm{Li}(n,n'\alpha)T$	0.054
total breeding ratio	0.713

energy multiplication

in breeding zone	0.81
in reflector/shield behind breeding zone	0.5
breeding zone + reflector	1.31

reflector/shield behind antenna	1.53

Breeding
Zone

Reflecting
Shield

25   40   Radius (cm)   150

a) Blanket Region

Antenna   Reflecting
                 Shield

14 24 32,5   Radius (cm)   150
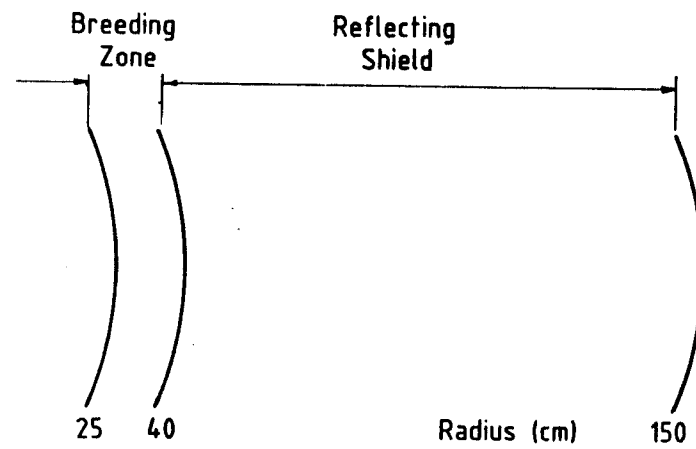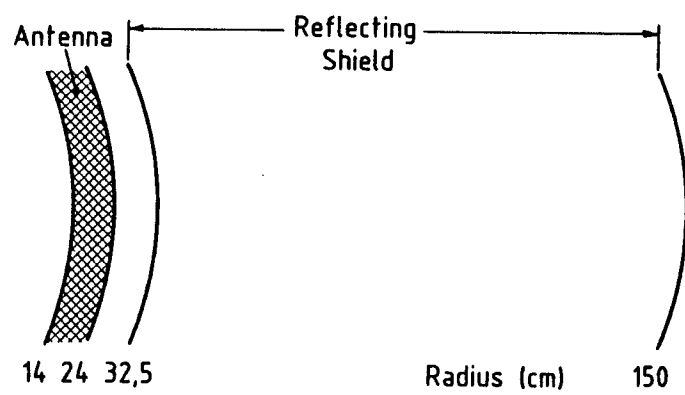
b) Antenna Region

Fig. 10.4-11 Calculational Scheme of the Test Module
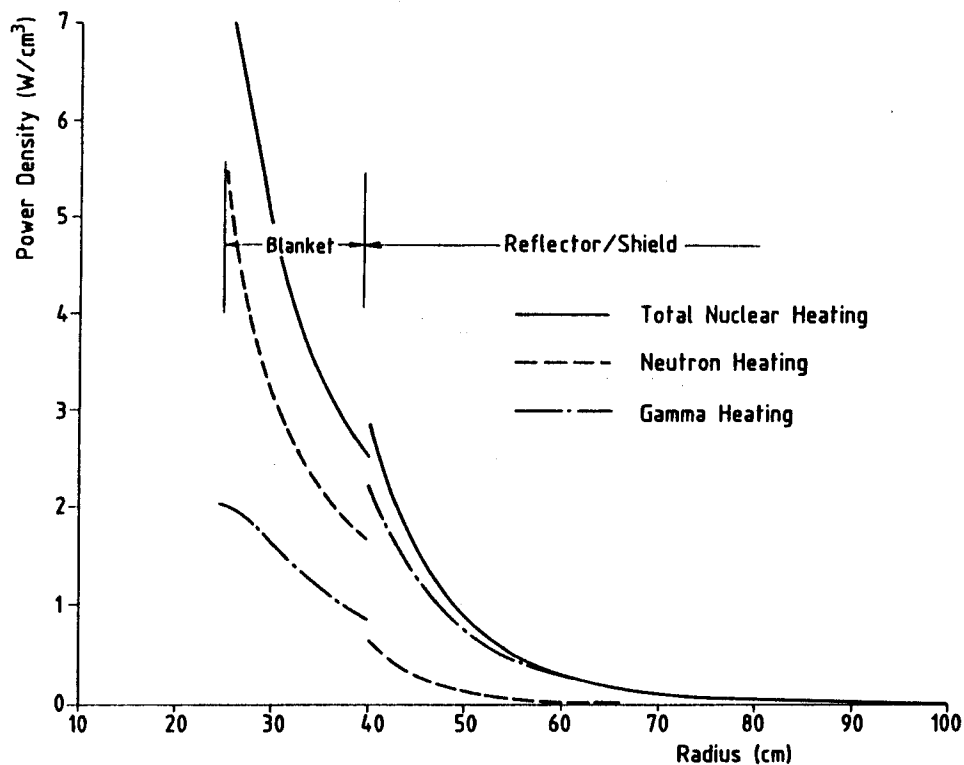
Fig. 10.4-12 Heat Generation in the Blanket Region
(Normalized to 1 MW/m^2 Neutron Wall Loading)
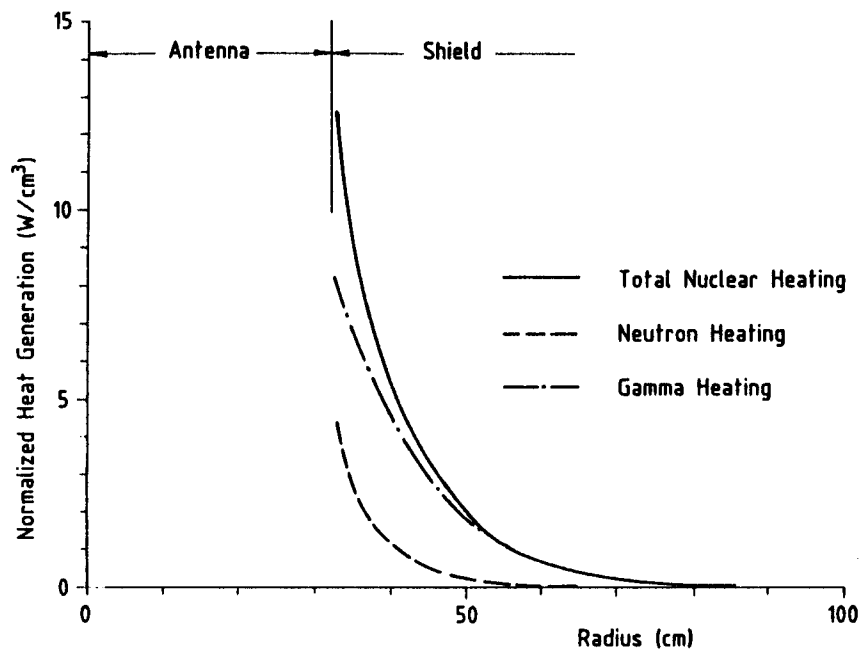
Fig. 10.4-13 Heat Generation in the Reflector/Shield behind the Antenna
(Normalized to 1 MW/m^2 Neutron Wall Loading)

Tab. 10.4-3: Thermal Hydraulic Data

Thermal Load:

average neutron wall loading
    breeding zone   0.73 MW/m^2
    antenna zone   0.638 MW/m^2

peak wall loading in antenna zone   0.74 MW/m^2

total heat generation in
breeding zone   380 kW

total heat generation in
reflector/shield behind breeding zone   130 kW

total heat generation in reflector/shield
behind antenna   270 kW

Cooling Water:

a) Breeding Zone
    total mass flow rate   1.8 kg/s
    inlet pressure   5 MPa
    inlet temperature   150 °C
    pressure drop   2 MPa
    temperature rise   50 K

b) Reflector/Shield Zone
    total mass flow rate   2 kg/s
    inlet pressure   3 MPa
    inlet temperature   40 °C
    temperature rise   50 K

10.4.4.1 Blanket Cooling

The breeding ball blanket suggested for a larger Tokamak reactor /1/ is cooled by boiling water. In that system a pressure of 10 MPa leads to steam conditions at the turbine (after a heat exchanger) identical to a Boiling Water Reactor. For the breeding material test bed in Taska-M, however, there is no need to design a power cycle at all. Therefore subcooled water at 5 MPa is used as a coolant.

The heat generation in the breeding material and the heat fluxes at the ball and tube surfaces are sufficiently low, to avoid any heat transfer problems. Therefore, the analysis is restricted to the determination of coolant mass flow rate and pressure drop in the blanket tube. Only the first row of tubes has been analyzed, since, the heat input is considerably lower for the following rows.

Coolant Mass Flow Rate

The average neutron wall loading in the solid breeder test blanket is 0.73 MW/m^2 as can be seen in fig. 5.1-2. Assuming a surface heat flux density of q" = 0.05 x 0.73 MW/m^2 and a first wall surface of 0.6 m^2, the surface heat load to the first row of tubes is 22 kW. The volumetric heat generation in the blanket region is shown in Fig. 10.4-12 for a normalized neutron wall loading of 1 MW/m^2. The average value for the first 3.75 cm (equivalent to the homogenized first row of tubes) is 6.4 W/cm^3 or, with the average neutron wall loading of 0.73 MW/m^2, q''' = 4.67 W/cm^3. This leads to a volumetric heat generation of 112 kW. The total heat input to the first row therefore amounts to 134 kW. Between inlet and outlet a coolant temperature rise of 50 K has been chosen, resulting in a mass flow rate of 0.6 kg/s.

The total heat generation in the breeding region is 380 kW, leading to a total coolant mass flow (at ΔT = 50 K) of 1.8 kg/s.

Coolant Pressure Drop

The breeder balls have a diameter of 30 mm and fit into the pressure tube
with a radial gap of 2 mm. This is a rather complicated coolant channel
geometry where the calculated velocity varies between w_{max} = 3.6 m/s
w_{min} = 0.8 m/s between the spheres. The pressure drop is caused mainly by the
flow separation in the part where the velocity decreases, leading to a small pressure
recovery. It is rather difficult to estimate theoretically a recovery factor
and the friction pressure drop for the given case. Therefore, a benchmark
experiment has been performed in a 1:1 geometry to determine the drag
coefficient. A detailed description of this test is reported in /2/. A drag
coefficient of ξ = 0.5 has been calculated from the measured data for one
ball and the given Re-number of 10^5. Using this coefficient, the pressure
drop in the inner blanket tube containing about   n = 750 balls is

$$\Delta p = \rho/2 \cdot w_{max}^2 \cdot n \cdot \xi \approx 2 \text{ MPa}, \quad \text{with } \rho \text{ density}$$

10.4.4.2 Reflector/Shield Cooling

The thickness of the reflector plates is determined by the volumetric heat
generation since cooling tubes are located between plates only. For a conservative
lay-out the shielding provided by the antenna is neglected.
Fig. 5.1-2 shows a maximum neutron wall loading in this part of 0.74 MW/m^2.
Using the radial power distribution in Fig. 10.4-13 a maximum local heat
generation density of 9 W/cm^3 is calculated.

The closed packed arrangement of cooling tubes near the first wall surface
as shown in Fig. 10.4-3 results in a maximum temperature variation inside
the plates of less than 100 K. The thermal stresses caused by this
temperature variation are not too large since the plates do not carry any
mechanical load.

A good thermal contact between plate and cooling tube is maintained by
clamping the tubes between the plates in non-circular grooves. The tempe-
rature difference between tubes and plates is small, the temperature level
low, therefore the thermal stresses are not critical.

To determine the cooling water flow rate in one tube, the heat generation in the plate with the highest thermal load has to be calculated. This heat generation is

$$\dot{Q}_p = \Gamma_n \cdot M \cdot \pi \cdot D \cdot t_p \cdot 0,5$$

with Γ_n neutron wall loading 0.74 MW/m^2

      M energy multiplication in reflector/shield 1.532

      D diameter in the antenna region 0.65 m

      t_p plate thickness 0.05 m

$$\dot{Q}_p = 0.058 \text{ MW}$$

A water velocity of 0.5 m/s has been assumed, resulting in a mass flow rate of 0.15 kg/s.

The inlet conditions of the cooling water are
    $T = 40 \,^{\circ}C$; $p = 3$ MPa

A heat input of 58 kW results in a temperature rise of 90 K.

If the same water velocity is used in all the 13 tubes, the total water flow rate is $\approx$ 2 kg/s. With a total heat generation in the reflector/ shield of 400 kW a temperature rise in the cooling water after mixing is calculated to 50 K.

10.4.5   Stress Analysis

10.4.5.1   Stress and strain distribution in a thin-walled pressurized tube with unsymmetrical irradiation creep.

Blanket tubes in the zone of the first wall of a fusion reactor are exposed to high doses of fast neutrons. Because of internal pressure irradiation creep will occur mainly in the front of the tube and can cause a re- distribution of the originally uniform stresses in the cross-sectional area.

For calculations it is assumed that the front side of the tube is irradiated with an uniform intensity I_0, the back side with the lower intensity I_1.

For stress computations it is sufficient to consider only the unsymmetrical portion of intensity

$$I = I_0 - I_1 \tag{1}$$

The accompanying intensity distribution assumed is shown in Fig. 10.4-14. The blanket tubes are wound around the plasma like a coil so that plane strain can be assumed in the cross section. Fig . 10.4-15 shows a tube element with the acting stresses σ_φ, σ caused by the internal pressure p.

From the assumption of a "thin-walled tube" it follows, that
a) the radial stresses σ_ρ can be neglected,
b) the pipe will remain circular in shape during creep deformations.
The circumferential membrane load is given by

$$\sigma_\varphi = PD/2h \tag{2}$$

where D is the diameter of the tube and h the thickness of the tube wall. The axial equilibrium condition

$$\sigma_1 \, F/2 + \sigma_2 \, F/2 = PD^2 \, \pi/4 \qquad\qquad ; F = \pi \, Dh \tag{3}$$

leads to
$$\sigma_1 + \sigma_2 = \frac{PD}{2h}$$

In the left tube section irradiation creep occurs. The axial creep rate is

$$\dot{\varepsilon}_{1c} = \frac{3}{2} \, B \, \sigma_v^{\,n-1} \, S_1 \qquad \text{with B the proportional factor} \atop \text{for creep rate} \tag{4}$$

where the stress deviator S_1 is defined by

$$S_1 = \sigma_1 - \frac{1}{3} \, (\sigma_1 + \sigma_\varphi + \sigma_\rho) = \frac{2}{3} \, \sigma_1 - \frac{1}{3} \, \sigma_\varphi \tag{5}$$

and the effective stress σ_v by

$$\sigma_v = \frac{1}{\sqrt{2}} \, \sqrt{(\sigma_1 - \sigma_\rho)^2 + (\sigma_1 - \sigma_\varphi)^2 + (\sigma_\rho - \sigma_\varphi)^2} \tag{6}$$

10.4-24

At temperatures below 400 ^{O}C where swelling can be neglected the creep rate is proportional to stress, that means n = 1 /3/. So Eq. (4) is simplified to become

$$\dot{\varepsilon}_{1_C} = \frac{3}{2} B S_1 = B (\sigma_1 - \frac{1}{2} \sigma_\varphi) \qquad (7)$$

and the circumferential creep rate becomes

$$\dot{\varepsilon}_C = B(\sigma_\varphi - \frac{1}{2} \sigma_1) \qquad (8)$$

Since the tube is wound like a coil, imposing plane deformation, the deformation rates are identical in both tube sections, i.e.

$$\dot{\varepsilon}_1 = \dot{\varepsilon}_2 \qquad (9)$$

Superposition of elastic strain rates and creep rates gives

$$\dot{\varepsilon}_1 = \frac{1}{E}(\sigma_1 - \mu \dot{\sigma}_\varphi) + B (\sigma_1 - \frac{1}{2} \sigma_\varphi) \qquad (10a)$$

$$\dot{\varepsilon}_2 = \frac{1}{E} (\sigma_2 - \mu \dot{\sigma}_\varphi) \qquad ; \dot{\sigma}_\varphi = 0 \qquad Eq. (2) \qquad (10b)$$

Combination of eq. (10) and eq. (9) yields

$$\frac{1}{E} \dot{\sigma}_1 + B \sigma_1 - \frac{1}{2} B \sigma_\varphi = \frac{1}{E} \dot{\sigma}_2 \qquad (11)$$

Differentiation of eq. (3) referring to time t gives

$$\dot{\sigma}_2 = - \dot{\sigma}_1$$

and results in

$$\dot{\sigma}_1 + \frac{BE}{2} \sigma_1 = \frac{BE}{4} \sigma_\varphi \qquad (11a)$$

The solution of this linear differential equation is

$$\sigma_1 = e^{\frac{-BE}{2} t} \left| \frac{BE}{4} \sigma_\varphi \int e^{\frac{BE}{2}t} dt + C \right| = \frac{\sigma_\varphi}{2} + C e^{\frac{-BE}{2}t} \qquad (12)$$

Since at the moment of loading (t = 0) $\sigma_1 = \sigma_2 = \sigma_\varphi /2 \left|_{t = 0} \right.$

is fulfilled, the integration constant C becomes

C = 0

and the stresses are independent of time

$$\sigma_1 = \sigma_2 = \frac{1}{2} \ \sigma_\varphi \tag{13}$$

Result: Irradiation creep does not create any stress redistribution, if swelling can be neglected (n = 1) and the tube can be assumed as thin-walled.

The axial strain is given by

$$\varepsilon_1 = \frac{1}{E} (\sigma_1 - \mu \ \sigma_\varphi) = \frac{1}{E} (\frac{1}{2} - \mu) \ \frac{PD}{2h}$$

The projected blanket tubes have an outer diameter of 40 mm and a wall thickness of 3 mm. For the desired internal pressure of 5 MPa the stresses are given by eqs. (2) and (3)

$$\sigma_1 = 16,7 \ N/mm^2 = 16,7 \ MPa$$

$$\sigma = 33 \ N/mm^2 = 33 \ MPa$$

The circumferential creep deformation can be calculated by

$$\varepsilon_{\varphi c} \approx S \ \sigma \ \Phi \ t \tag{14}$$

where Φt is the neutron fluence and $S \approx 2 \cdot 10^{-6} (MPa^{-1} \ dpa^{-1})$ a mean value for some stabilized stainless steels /4/.

10.4.5.2 Deformation of the Breeding Ball Shell

The breeding material is contained in spherical shells with assumed wall thickness
of 2 mm. Those shells are loaded by

a) an outer overpressure of 5 MPa

b) a point load caused by the pressure drop in the cooling water.

Considering the relatively thick wall of the shell, the external overpressure
is of no concern. The pressure drop of 2 MPa however, results in a point
load of 1.4 kN, acting at the last ball in flow direction. In calculating
this force, any friction between balls and tube has been neglected. The
stresses and deformations caused by the point load have to be determined
in order to assure the integrity of the shells.

Loading of a spherical shell by a single load is described in /5,6 /. Reference
is made to a great number of experiments and methods of calculations.
According to those references such a load does not constitute a risk
implying an abrupt failure by collapsing of the shell. An increase of
the load above an elastic limit causes the shell to bulge permanently and
the deformation increases continuously with the load.

Using the methods of elastic calculations according to /7/, the stresses
and elastic deflections have been calculated for the following values

outer radius of sphere	R = 15 mm
wall thickness	h = 2 mm
radius of load	r = 0.5 mm
load	F = 1.4 kN

The results of this calculation are a maximum stress of σ = 700 N/mm^2 = 700 MPa
and a deflection of δ = 0.009 mm for a half shell and therefore for one
shell 0.018 mm. This stress implies that the yield stress of SS 316
is exceeded locally and plastic deformation will occur.

It is rather difficult and uncertain to calculate the amount of plastic
deformation in the given case. Using the method explained in /6/ for
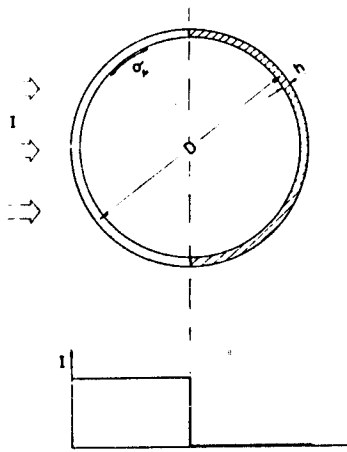
Fig. 10.4-14 Intensity Distribution
for Irradiation Induced
Creep in the Blanket
Tube
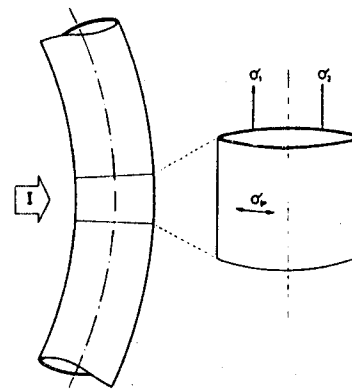
Fig. 10.4-15 Blanket Tube with Acting Stresses
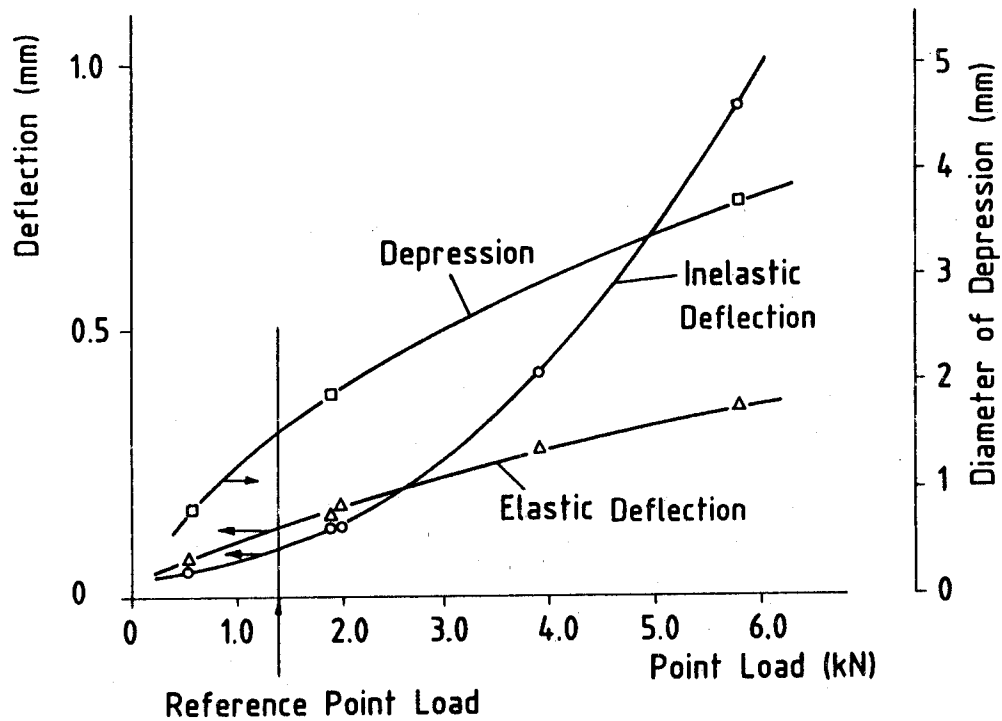
Fig. 10.4-16 Deformation of the Breeder Ball Shell

example, a minimum load of 6.3 kN would be necessary to obtain plastic deformation at all.

Therefore, a benchmark experiment has been performed to determine the load-deformation relationship for the shell, using a 1:1 geometry. Spherical shells made of annealed SS 316 were pressed between two hardened solid balls of the same diameter in a guiding tube. The load has been varied between 0.56 and 5.8 kN. As functions of the load for one shell the

- elastic deflection
- inelastic deflection
- diameter of the remaining depression
were measured.
The results of the tests are shown in Fig. 10.4-16. Indicated are the values for a load of 1.4 kN, namely a

- elastic deflection of 0.13 mm
- inelastic deflection of 0.09 mm
- diameter of depression of 1.5 mm

Those minimal plastic deformations do not endanger the integrity and coolability of the breeding balls.

10.4.6 Tritium Production and Extraction

It is a main advantage of a breeding ball concept that the tritium breed remains inside the steel shell of the breeding ball, for in this case the tritium extraction can be separated from the cooling process. A high retention - that means a minimum of tritium losses through the steel shell - is reached by the following features:

- Under the operating conditions at up to 300 ^{o}C a thin oxide layer will establish at the outer surface of the steel shell. This will reduce the permeability of T by a factor of 10 to 100 compared with pure steel.

- By adding to the solid breeder material a small portion of Nb as volume getter material, the partial pressure of T inside the ball can drastically be reduced. At 300 ^{o}C the pressure is reduced by a factor of about 10^4 and at room temperature even of larger than 10^{10}.

The tritium extraction can easily be done by heating the balls up to 800 ^{o}C in a special recovery system outside the reactor. At this temperature the outgassing of T is favoured by the following facts:

- The oxide layer at the outer surface of the steel shell decays at 800 ^{o}C and the permeation of T only depends on the permeability of pure steel which is high at this temperature.

- The reduction of the T partial pressure inside the ball by the getter material is low at 800 ^{o}C (only about a factor of 13). That means a strong increase of the partial pressure which also increases the outgassing of T.

After the tritium extraction by heating up, the breeding balls can be inserted again into the blanket region. The total endurance of the balls inside the blanket module is limited by the helium pressure which increases constantly with the time because helium is not able to be outgased by heating and it also cannot be sorbed by a getter material.

In the case of enriched Li (30 % of ^{6}Li) and 10 % void in the blanket balls the total tritium production is 25 g/fpy. It will be breed 10 mg tritium in the ball with the highest rating. In two month full power this ball reaches 1.67 mg tritium and 2.2 mg helium. At 300 ^{o}C in the ball exists a helium pressure of 3 MPa (by a tritium pressure lower than 1 mbar), this leads to a tensile stress of 10 N/mm^2=10 MPa in the wall of the sphere.

The combination of the two effects: establishing of the oxide layer and absorption of T by the getter material results in good retention of T. Assuming a reduction factor of only 10 by the oxide layer the tritium loss into the cooling water is lower than 1 % of the total tritium breed at 300 ^{O}C. At room temperature - that means during stand-by times of the machine - the losses are nearly negligible.

10.4.7 Test Program

In accordance with the philosophy about the solid breeder test blanket as outlined in Section 10.4.1.1, no specific test matrix has been designed.

To fill all balls with enriched Li_2O is only one possible test case, leading to the highest tritium production. The blanket design offers a large flexibility for varying the test parameters. There are more than 2,500 balls in the blanket. Each of them can be filled individually either with breeding or nonbreeding material. It is also possible to adjust the temperature of each material probe over a wide range by use of an intermediate layer of metallic felt or another thermal insulator between shell and test material. Another way of temperature control is to use different fill gases having different thermal conductivities.

In order to correlate precisely the irradiation results to the neutron flux, there is a desire to monitor the flux and the spectrum. This can be accomplished by putting balls filled with flux monituring probes in selected positions.

References for Section 10.4

1. Küchle, H:
   The breeding ball concept, to be published in NED-Fusion (1983)

2. Marten, K.:
   Pressure drop measurements for the spherical shell blanket of
   TASKA-M. Internal Paper, unpublished (1983), KfK Karlsruhe.

3. Ehrlich, K.:
   Irradiation creep and interrelation with swelling in austenitic
   stainless steels; Journ. of Nucl. Materials 100 (1981), 149-166.

4. Schneider, W., Herschbach, K., Ehrlich, K.:
   Interdependence of in pile creep and void swelling in Ti- and Nb-
   stabilized stainless steels; ASTM STP 782, 1982, 30-42

5. Raujan, G.V.:
   Edge Zone Expansions for Thin Shells with Application to 1.)
   Torispherical Pressure Vessel and 2.) Large Deflection of Sphere
   with Point Load: Stanford University, Ph.D. 1977, Applied Mechanics.

6. Oliveira, J.G., Wierzbichi, T.:
   Crushing Analysis of Rotationally Symmetric Plastic Shells
   J. of Strain Analysis 17 (1982), 229.

7. Britisch Standards Institution, BS 5500:1976
   Specification for Unfired Fusion Welded Pressure Vessels,
   Appendix G, p. G/25, Issue 2, April 1978

8. O'Dell, R., Brinkley, F. jr., Marr, D.:
   User's Manual for ONEDANT: A Code Package for One-Dimensional
   Diffusion-Accelerated, Neutral-Particle Transport,
   Los Alamos National Laboratory, LA-9184-M (1982).

11. Maintenance

11.1 Maintenance Classification

In accordance with the TASKA study /1/, the major subsystems and components are categorized into four general classes as a function of their lifetimes.

Classes	Expected lifetime
1	The life of the machine
2	$\geq$ 3 full-power years (FPY)
3	$\leq$ 3 FPY
4	Very short life (e.g. samples of material test blankets)

In addition to dependence on lifetime, a distinction should be made between scheduled and unscheduled replacements due to random component failures. Four typical cases have been selected to demonstrate the feasibility of maintenance jobs, i.e., the replacement of

- Test blankets
- Beam dumps
- Neutral beam injector components, especially neutral beam source, and
- Yin/Yang coils.

The reason for selecting these components is the frequency of scheduled replacements in the first three cases, and the complexity of the replacement in the fourth case. All these components are characterized by a high radiation dose, which necessitates remotely controlled handling techniques.

Table 11.1-1   Maintenance categories as a function of lifetimes /1, 2/

System	Class 1 Full lifetime	Class 2 Lifetime ≥3 FPY	Class 3 Average lifetime <3 FPY
Building and support structures	x		
Shield	x		
Vacuum vessel	x		
Breeder test blanket			/x/
Material test blanket			/x/
Central cell insert		/x/	(x)
Coils	x	(x)	(x)
Insert coils	x	(x)	(x)
Cryopumps	x	(x)	

/x/ scheduled replacement   (x) replacement in case of failures

11.1-2

Table 11.1-1   Maintenance categories as a function of lifetimes (continued)

System	Class 1 Full lifetime	Class 2 Lifetime ≥3 FPY	Class 3 Average lifetime <3 FPY
Neutral beam injector, total		(x)	
NBI – ion source			/x/
NBI – ion dumps		(x)	(x)
ICRH		/x/	(x)
Beam dumps			/x/
Diagnostics		/x/ (x)	/x/ (x)
Heat exchanger		(x)	
T-system		(x)	
Maintenance equipment	x	(x)	(x)

/x/   scheduled replacement   (x)   replacement in case of failures

11.2   Short Lifetime Components

11.2.1   Introduction

Components of Class 4, such as samples inserted in the material test
blanket or breeding test blanket 2, can be exchanged rather easily by
suitable methods during operation. All other components, except the
maintenance equipment, must be replaced during scheduled or unexpected
shutdown periods because of radiation and high magnetic fields during
operation.

Taking into consideration, the safety issues associated with maintenance,
the replacement of the following typical Class 3 components is described:
Test blankets, beam dumps, and neutral beam injectors, with the ion
sources in particular.

11.2.2   Safety During Maintenance

With regard to the safety aspects, the question arises whether or not
to use a protective containment chamber attached to the machine during
replacement of components /3/. Risks associated with component exchanges
include

- radiation doses originating from neutron induced activation of
  components and corrosion products in coolant circuits,

- emission of tritium and airborne contamination from neutron activated
  components into the environment during maintenance operations and,
  consequently, accumulation of contaminated products in the reactor
  hall,

- environmental impact on the machine vacuum and the components during
  replacement operations, especially if the superconducting coils are not
  warmed up. Since the liquid N_2-shield for the coils, acts as a
  cryopump, the vacuum chamber can be contaminated with impurities.

The masses and sizes of main components to be handled are listed in Table 11.1-2.

Table 11.1-2   Main components –
                 estimated sizes and removable weights *)

	size (m)	removable weight (t)
Vacuum chamber (section)	5.5x4.5x4	17
Breeding test blanket (1)	4.45x2.50x0.88	35
Central cell coil	5.16 Ø x 1.06	110
High field coil	3.70 Ø x 2.06	73
Yin/Yang coil	6.5x3.2x2.95	52
Transition coil	4.05x3.85x3.45	35
Beam Dump	0.65 Ø x 3.5	6
Central cell insert	2.45 Ø x 1.36	38
NC-coil insert	1.95 Ø x 2.1	40

*) may include shields, supports, etc.

The analysis of typical maintenance tasks in the following sections is intended to outline some critical operations and to demonstrate feasibility. Undoubtedly, there are numerous other maintenance tasks which must be investigated as to their impact on component design. Generally speaking it can be assumed that the maintenance problems are well within present capabilities.

The problem of radiation doses can be solved without the use of a shielded protective containment. It is sufficient to increase the wall thickness of the reactor hall to provide biological shielding and carry out all the operations inside by remotely control, if the radiation dose is unacceptably high for manned access.

Contamination of the reactor hall from the machine, or contamination of the vacuum chamber with environmental impurities, can be prevented with the use of an air lock. The size and the mode of operation of the air lock depends on the tasks to be performed. This makes it possible to carry out the work under vacuum or inert gas conditions. The advantage in the former case is that the machine vacuum will not be interupted during exchange operations and, consequently, the evacuation time for restarting the machine will be reduced. On the other hand, use of an inert gas in the vacuum chamber and the air lock at atmospheric pressure makes it possible to reduce the wall thickness of the air lock and helps to achieve the seal tightness required. In this reason, the latter scheme is chosen for the replacement of those components, which require long shutdown times, e.g. blankets.

11.2.3 Test Blankets and Beam Dumps

The blankets inside the vacuum chamber face the plasma directly, forming the first wall with their inner surfaces. Besides their replacement according to a maintenance schedule, exposure to extreme thermal and radiation loads can make their candidates for frequent exchange.

Aside from the preliminey work in blanket replacement, the main operations are

- breaking the blanket seal,
- removing the blanket,
- transporting the blanket to a storage cell or hot cell,
- transporting and installing a new blanket,
- restoring vacuum tightness,
- evacuating the chamber.

The following steps should be taken to insure vacuum tightness and ease subsequent evacuation:

- The machine vacuum should only be broken under inert gas conditions.

- Because of the large blanket, openings, lip welding should be used.

- These welded joints must be checked with regard to tightness.

To insure these requirements, a combination of a welded joint and a metal gasket seal is proposed (see Fig. 11.2-1). After insertion of the blanket into the reactor, the gasket seal in affected against the vacuum chamber flange by means of bolts. This operation can be performed with tools inside the air lock. Subsequently the air lock is removed and the joint welded. The metal gasket protects the vacuum chamber from impurities such as welding vapor and allows a tightness check to be performed.

To break the blanket seal, the gasket flange is initially tightened by the flange bolts and then the welded joint is cut. The air lock is then attached to the machine and after unbolting, the blanket can be withdrawn.

Various methods of blanket handling were investigated in previous studies /2, 3/. The use of permanently installed roller tails on the blanket or in the vacuum chamber is questionable, because of the need for lubricants in the vacuum. One possible solution could be the use of roller chains /4/. To remove the blanket, a pair of chains is introduced through blanket openings which are normally closed. Then the guide track for the chain mounted at the bottom of the vacuum chamber is mechanically lifted from the outside and the blanket is withdrawn.

Flasks can be used to transport blankets. Because of the high radiation level from the blankets after an operating time of 2 or 3 full-power years, the shielding an the flasks must be very thick to permit access of personnel during transportation. Thus, remotely controlled transport in less shielded transport flasks is preferred. The transport flasks can also serve as the air locks. For this purpose, the transport flask is attached directly to the machine (Fig. 11.2-2) or connected to a transfer unit, which can be attached to the machine (Fig. 11.2-3).
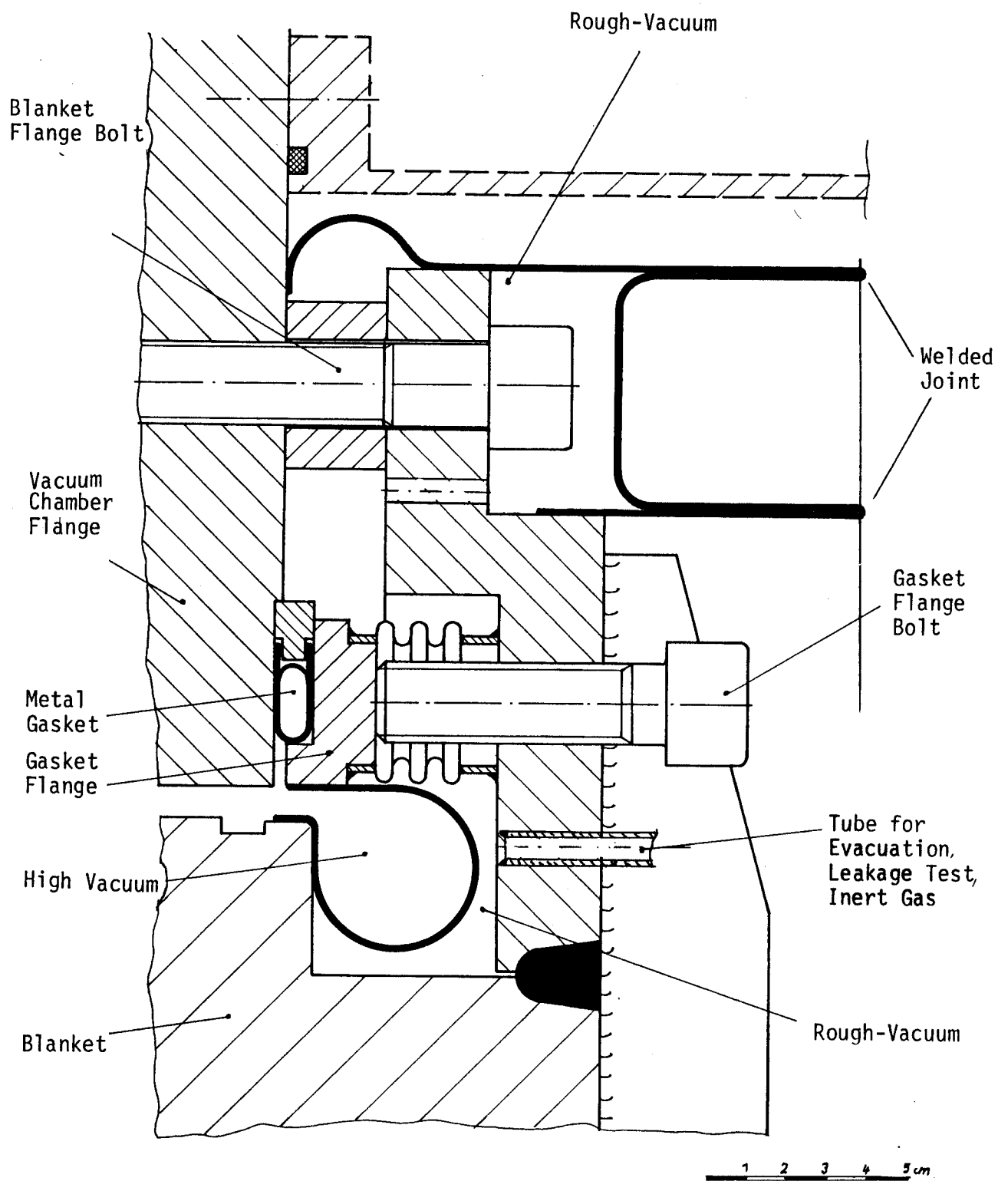
Fig. 11.2-1   Blanket Flange Gasket
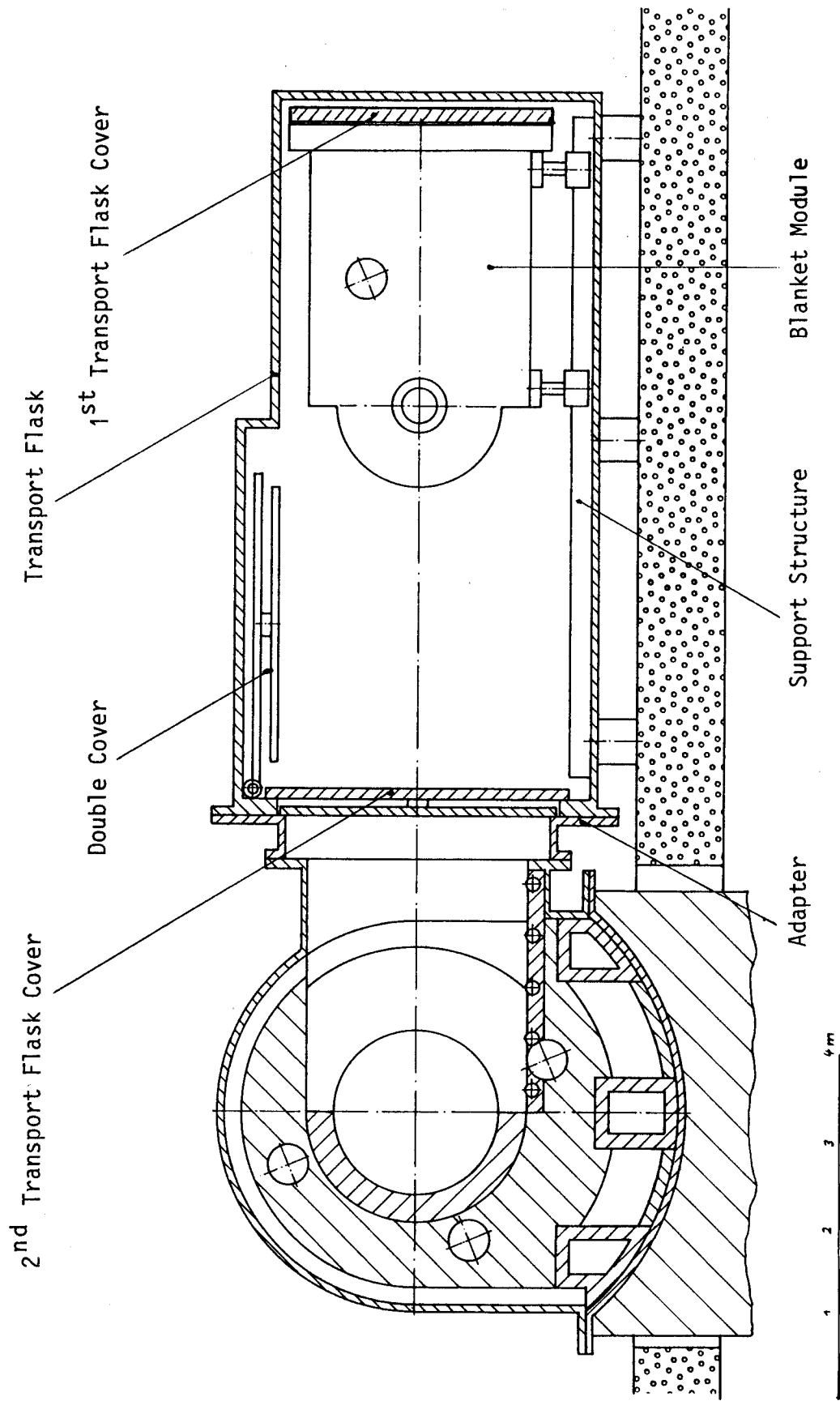
Fig. 11.2-2 Exchange of Blanket Module

Labels in figure:
- 2nd Transport Flask Cover
- Transport Flask
- 1st Transport Flask Cover
- Double Cover
- Blanket Module
- Support Structure
- Adapter

Double Cover

Machine
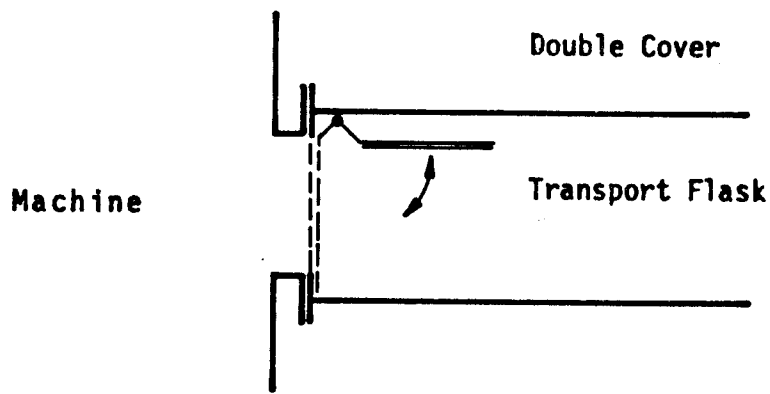
Transport Flask

Transport Flask with Integrated Transfer Unit

Machine

Transport Flask
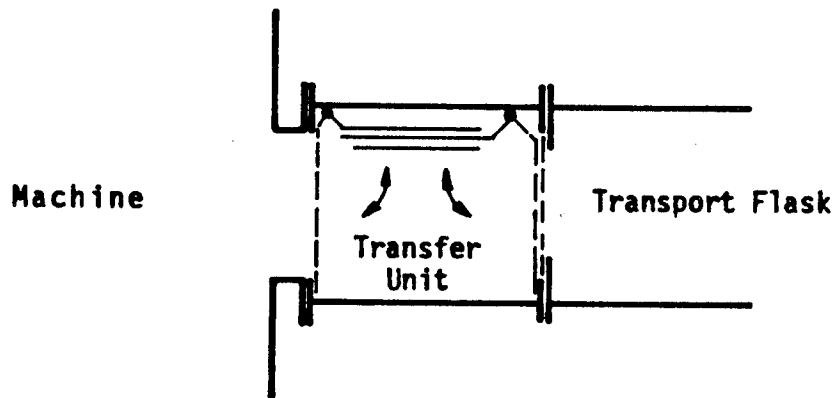
Transfer
Unit

Transport Flask with Additional Transfer Unit

| TU | TF |
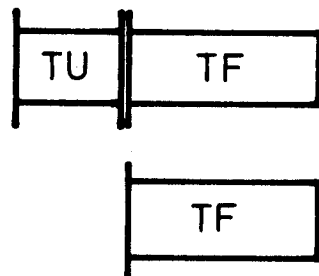
Transfer Unit

+

Two Transport Flasks

| TF |

| TU | | TF |
| | | TF |
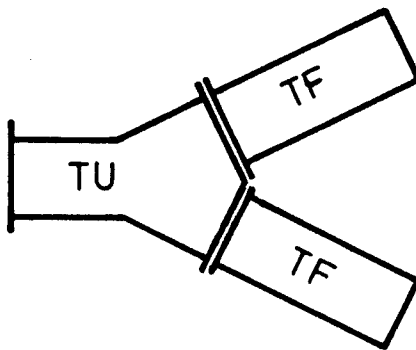
Transfer Unit

+

Two Simultaneous
Connectable Transport
Flasks

Fig. 11.2-3   Use of Transport Flask

In the first case, double covers close the machine and the flask are needed; tools and devices for sealing the blanket opening as well as the exchange equipment are integrated. Consequently, the transport flask becomes very large, heavy and quite expensive. Furthermore if more than one flask is used they must all be fully equipped for blanket exchanging. In the second case, a transfer unit will be set up between the machine and the transport flask. This transfer unit contains all the exchange equipment and is equipped with double covers closing the transfer unit at both ends and the transfer flask as well. The unit remains attached to the machine during the blanket exchange.

In order to reduce the shutdown time, two transport flasks or one double transport flask can be employed /4/. Figure 11.2-3 shows the blanket exchange sequence when the operation is performed with one transfer unit and two transport flasks.

Beam dumps are exchanged in a similar way as blankets. The only differences are the smaller dimensions and the lower weight, which allows smaller transport flasks to be used. In view of these facts and because of the exchange frequency of about once every two years, it is assumed that the beam dumps will be replaced under vacuum conditions.

11.2.4 Neutral Beam Injector

The TASKA-M machine will have seven neutral beam injectors. Next to the beam dumps, parts of the neutral beam injectors are the components of the facility to be replaced most frequently. Figure 11.2-4 is a schematic diagram of the injector. The ion sources and the ion dumps are fitted with covers attached to another cover from the back. Also attached to this cover is a rack with a neutralizer, ion sweep magnet, collimators, and calorimetric target diagnostics.
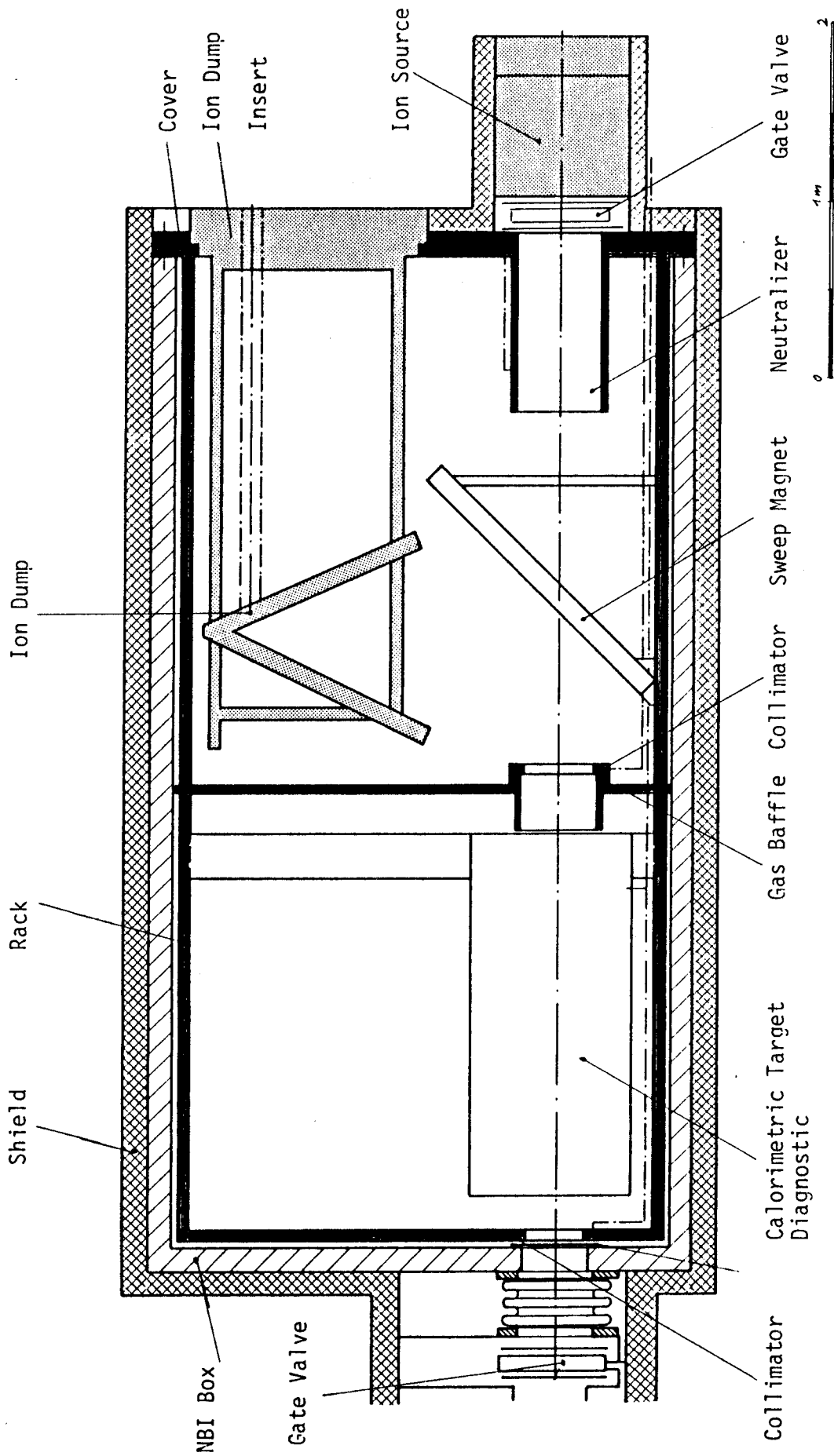
Fig. 11.2-4   Neutral Beam Injector (Scheme with Insert Components)

Cover
Ion Dump
Insert
Ion Source
Gate Valve
Neutralizer
Sweep Magnet
Gas Baffle Collimator
Calorimetric Target Diagnostic
Collimator
Gate Valve
NBI Box
Shield
Rack
Ion Dump

11.2.4.1 Exchange of Ion Sources, Cryopumps, and the Ion Dump

In order to avoid a breakdown of the vacuum in the neutral beam box on the one hand, and tritium contamination originating from the ion source on the other hand, the ion source is separated from the neutral beam box by a special isolation valve.
After removal of the shielding, the supply connections are cut, the bolts holding the cover are unscrewed and, after attaching the exchange device to the cover, the cover is withdrawn along with the source. The assembly of a new source is accomplished in the reverse sequence. The neutral beam cryopumps can be replaced in a similar manner. Isolation valves of the same type as those used for the ion sources prevent contamination of the environment during the exchange.

The ion dump with the cover attached and inserted into the neutral beam box must be exchanged by means of a vacuum tight transport flask equipped with double covers. The method is similar to a blanket exchange and thus is not explained in detail here.

11.2.4.2 Replacement of Neutral Beam Internals

With the exception of the ion dump, all internals are arranged on a rack and fitted with a cover which closes and seals the back of the neutral beam box. If parts of these internals are to be exchanged, the isolation valve between the neutral beam box and the duct must be closed. As the internals will be activated and contaminated, replacement and repair must be performed in a protective containment.

One way of doing this is by attaching an air lock to the neutral beam box which is equipped with all the tools needed for replacement and repair. Aside from the dimensions of this air lock it must also be considered that the neutral beam injectors are arranged around the facility. Therefore, it may be better to separate the replacement and the repair jobs. The repair can be done in a hot cell. For replacement and transportation a flask can be used. A double cover protects the NBI box cover surface against contamination (see Fig. 11.2-4 and 11.2-5).

Neutral Beam Injector

TASKA-M

Valve closed

NBI (Shielding) Box

Hot Cell

Parking Position of NBI-Box
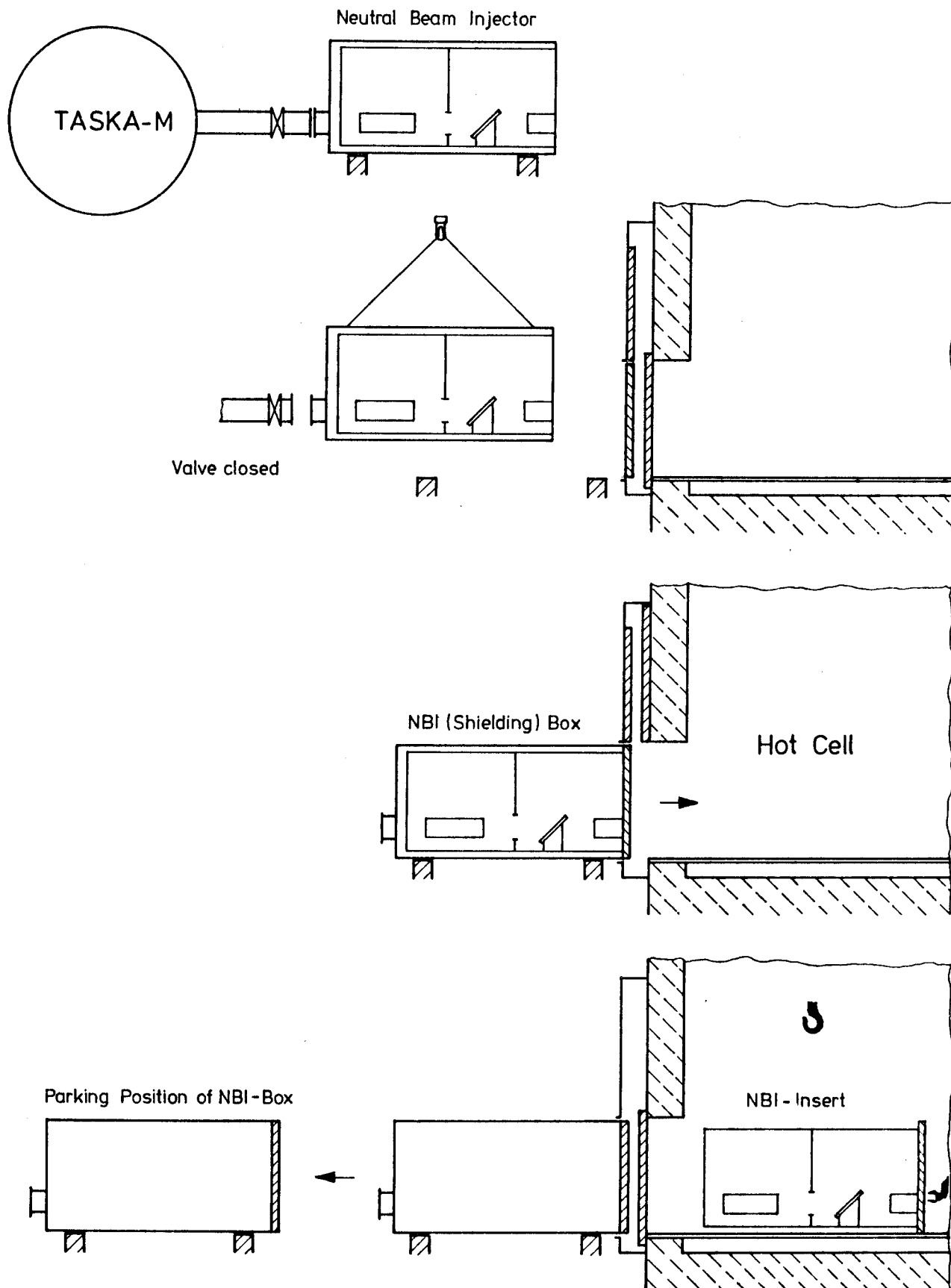
NBI - Insert

Fig. 11.2-5   Exchange of NBI-Insert

The disadvantage of this method stems from the need to transfer the rack twice, first from the box into the transport flask and then from the transport flask into the hot cell. To avoid this and, at the same time, reduce costs, the neutral beam box itself can double as the transport flask (see Fig. 11.2-5). One disadvantage as compared with the previous method will be that not only the isolation valve in the duct, but also the isolation valve between the neutral beam box and the cryopumps must be closed and the cryopumps must be disconnected. The sequence for this exchange procedure is more or less similar to the replacement of a blanket.

11.3   Large Components

11.3.1   Introduction

Besides the routine operations described above there is another category of operations to be investigated. Their difficulty arises from the weight of the components, their complexity and the techniques needed for their replacement. Typical examples of this kind of components are the Yin/Yang coils.

11.3.2   Yin/Yang Coils

The Yin/Yang coils located between the high field coils and the end dump are arranged inside the vacuum chamber like all the other coils. They are shielded against radiation by insert shields. The injection point of the medium energy neutral beam injector lies between the Yin/Yang coils, where the beam dump is also inserted (Fig. 11.3-1). This figure also shows the separation lines of the vacuum chamber. The segments of the chamber are clamped and tightness is insured by lip welding.
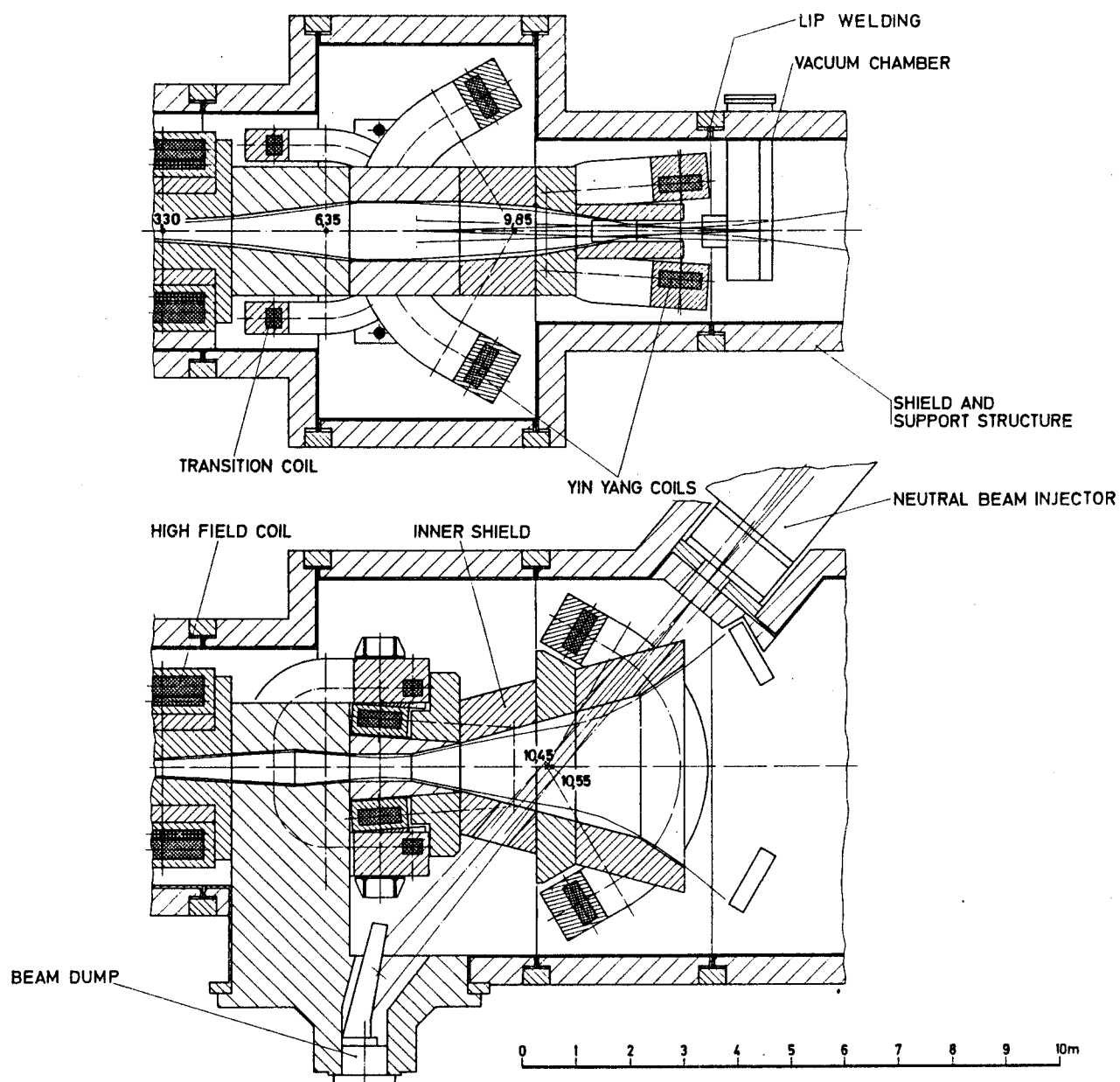
Fig. 11.3-1 Anchor and Transition Region

LIP WELDING

VACUUM CHAMBER

330 6,35 9,85

SHIELD AND
SUPPORT STRUCTURE

TRANSITION COIL

YIN YANG COILS

NEUTRAL BEAM INJECTOR

HIGH FIELD COIL

INNER SHIELD

10,45
10,55

BEAM DUMP

0 1 2 3 4 5 6 7 8 9 10m

11.3-2

The coils must be exchanged in case of failure. This will entail a shutdown period of several months. First the coils must be deenergized and the peripheral components, like neutral beam injector, support structures and the beam dumps, must be removed. After cutting the supply lines and unscrewing the clamps, a cutting and welding machine is installed /1/. The basic unit guided on tracks can be assembled with a cutting or a welding head. Once the welded joints are cut and the upper vacuum chamber segment removed by a crane, the upper shield and then the coil support structure can be dismantled.

Parts of the inner shield can be withdrawn independently of the coils. Others are removed together with the coil by means of a crane.

Before a new coil and chamber unit can be installed the dimensions of the vessel must be checked and the weld joint must be prepared. The installation of a new coil must be followed by the alignment of the coil, which can be accomplished by means of auxiliary hydraulic cylinders and optical measurement methods. Finally, the vacuum chamber can be welded and clamped.

REFERENCES to Chapter 11

1. TASKA-Team:
   "TASKA Tandem Spiegelmaschine Karlsruhe", Chapter X,
   Kernforschungszentrum Karlsruhe and University of Wisconsin /
   Fusion Associates, KfK 3311/1-2, UWFDM-500 (June 1982)

2. J.N.Doggett, et al.:
   "Proceedings of the 28th Conference on Remote Systems Technology",
   University of Californie Lawrence Livermore National Laboratory,
   CRSTBJ 26 1-460 (1978)

3. D.Leger, J.L.Royer, J.Vertut:
   "Protection, Maintenance and Wastes",
   Commissariat àl'Energie Atomique, ARD 1/044/EI (July 1983)

4. F.Farfaletti-Casali:
   "Critical Issues - European Contributions to the INTOR -
   Phase II A Workshop",
   Vol III, EUR FU BRU/XII-132/82/EDV 30 (December 1982)

12. COSTS

12.1 Introduction

As in TASKA, the direct costs developed for TASKA-M are based on the format adopted for INTOR. The accounts are divided into the following categories:

Acct. 1.1   Vacuum chamber, blanket and shield

Acct. 1.2   Magnets

Acct. 1.3   Plasma heating

Acct. 2.0   Reactor support systems

Acct. 3.0   Buildings

Reactor support systems include the following:

Acct. 2.1   Electrical

Acct. 2.2   Auxiliary cooling

Acct. 2.3   Instrumentation and control

Acct. 2.4   Fuel handling and storage

Acct. 2.5   Maintenance equipment

Acct. 2.6   Heat transport

Acct. 2.7   Reactor vacuum

Acct. 2.8   Radwaste treatment

Acct. 2.9   Thermal dumps

Acct. 2.10   Reactor support structure

Acct. 2.11   Special Materials

Acct. 2.12   Miscellaneous

Most of the unit costs and cost algorithms were obtained from the "INTOR - Summary of Cost/Schedule/Manpower" report, FEDC-M-81-SE-062. Costs which were not available from INTOR were taken from PNL-2987 "Fusion Reactor Design Studies: Standard Cost Estimating Rules," issued by Pacific Northwest Labs and DOE; the "Unit Cost Documentation" WFPS-TN-057 issued by ORNL with Westinghouse and industrial sources. Some costs were also obtained from TDF. Identification of the source will be as follows: INTOR, PNL/DOE, WFPS, INDUSTRY and TDF.

The costs are based on 1983 dollar levels, or inflation adjusted values when previous analyses were used.

12.2 Individual Accounts and Unit/Base Costs

Acct. 1.1   Vacuum Tank, Blanket and Shield

	Material	Quantity $(10^3$ kg)	Unit Cost ($/kg)	Source	Total ($ x 10^6)
Vacuum Tank*	304 SS	306.6	23.3	TDF	7.14
	304 SS	585.4	15	TDF	8.78
Central Cell Shield**	HT-9	0.49	80	TDF	0.04
Insert	HT-9	29.8	10	INTOR	0.30
CC Shield	Fe-1422	120	10	INTOR	1.20
	B_4C	0.62	35	TDF	0.02
End Plug Shield**	Fe-1422	22.2	80	TDF	1.78
	Fe-1422	52.1	20	TDF	1.04
	B_4C	2.4	35	TDF	0.08
Biological Shield	Concrete	2540 m^3	$350/$m^3$	PNL/DOE	0.89
					21.27

---

*More complex segments have a higher unit cost.

**Any part of the shield exposed to plasma has a water cooled first wall which has a unit cost of $80/kg.

Acct. 1.2   Magnets

The costs of recent big projects such as LCT and MFTF have been used as the basis for the estimates.   The unit costs used are the following:

1 - Superconductor

NbTi cryostable, reinforced $14.5/kAm at 6 T

$19.3/kAm at 8 T

Nb_3Sn cryostable, reinforced $34.5/kAm at 10 T

$41.4/kAm at 12 T

2 - Winding costs $46/m of wound conductor

3 - Coil case $46/kg

4 - Intercoil structure $13.8/kg

5 - Normal conducting coil $55.2/kg

6 - Pretesting and special cryogenic engineering   20% of items 1, 2 & 3

We assume a coil case of 6 cm thickness with 6 cm free space between winding pack and case. The following table summarizes the TASKA-M magnet costs:

Cost 10^6 \$	CCC	NC	Barrier Coil Nb_3Sn	NbTi	Reserved C-Coil	Squeezed C-Coil	
Superconducting costs	2.4		1.95	3.0	0.72	1.82	
Winding costs	0.6		0.22	0.7	0.23	2.42	
			2.2	3.7			
Coil case costs	1.0		1.0		0.82	1.33	
Normal conducting coil costs	---	0.3	---		---	---	
Pretesting and special cryogenic engineering	0.8		1.3		0.36	0.75	
Per coil total	4.8		8.3		2.13	4.5	
Number of coils	1		2		2	4	
Costs	4.8		16.6		4.3	18	43.7×10^6 \$
Intercoil structure							15.0
							58.7×10^6

Acct. 1.3 Plasma Heating

Neutral Beams

	Energy (keV)	Power (MW)	Unit Cost (\$/W)	Source	Total (\$ x 10^6)
High energy - CC	90	20.8	2	INTOR	41.6
Medium energy (anchors)	66	7	2	INTOR	14.
Low energy - CC	12	0.6	2	INTOR	1.2
					56.8

RF Heating

	Frequency (MHz)	Power (MW)	Unit Cost (\$/W)	Source	Total (\$ x 10^6)
ICRF	25	15.6	2.2	INDUSTRY	34.32
					91.12

Acct. 2.0 Reactor Support Systems

Acct. 2.1 Electrical

This account is divided into three parts: power supply switching and energy storage, basic wiring and distribution at the reactor and balance of plant electrical requirements. These costs were scaled from TDF using power requirement scaling.

		$ x 10^6
1.	Power supply switching and energy storage	4.00
2.	Electrical wiring and distribution	12.00
3.	Balance of plant electrical requirements	15.00
		31.00

Acct. 2.2 Auxiliary Cooling

System	Type	Power	Basis	Source	Total ($ x 10^6)
Magnet & vacuum system cooling	Cryogenerator	7.5 MWe		KfK	13.59
End dumps	Water	14.8 MW$_{th}$	algorithm	INTOR	0.32
Neutral beam dumps	Water	2.67 MW$_{th}$	algorithm	INTOR	0.08
Shield	Water	4.5 MW$_{th}$	algorithm	INTOR	0.12
ICRH antenna	Water	6.0 MW$_{th}$	algorithm	INTOR	0.15
Normal inserts	Water	17.8 MW$_{th}$	algorithm	INTOR	0.37
Cooling tower	Water/air	45.8 MW$_{th}$	algorithm	INTOR	1.73
					16.36

Acct. 2.3 Instrumentation and Control

This account was also scaled from TDF which was a fairly detailed estimate. It breaks down in the following way:

	$ x 10^6
Reactor instrumentation and control	23.00
Balance of plant instrumentation	2.00
	25.00

Acct. 2.4 Fuel Handling

System	Capacity g/day	Costing Basis	Source	Total $ \times 10^6$
Piping	1860	algorithm	INTOR	1.47
Isotopic separation	1860	algorithm	INTOR	1.55
Glove box	1860	algorithm	INTOR	6.45
Miscellaneous	1860	algorithm	INTOR	1.89
Emergency detritiation	18000 m^3/hr	algorithm	INTOR	6.30
Water detritiation			ONTARIO HYDRO	5.00
T_2 storage	500 g	$80,000/unit	PNL/DOE	0.08
Total				22.74

Acct. 2.5 Maintenance Equipment

Item	Source	Total $ \times 10^6$
Overhead bridge crane	KfK	1.0
Component handling machine	KfK	2.21
Shielded cabin	KfK	0.99
Manipulator unit	KfK	1.10
2 work platforms	KfK	0.22
Temporary shielding	KfK	0.22
NBI turnover machine	KfK	0.55
Blanket carriage/barrier coil support structures	KfK	0.33
Cutting/welding unit	KfK	0.99
Auxiliary remote equipment	KfK	2.76
20 hot cell work stations	KfK	3.31
Active service area bridge crane	KfK	0.66
Overhead manipulator system	KfK	2.43
Supplementary tools and devices	KfK	2.89
Total		19.66

Acct. 2.6 Heat Transport

	Material	Capacity	Source	
Piping and valves	Steel	1.4×10^6 kg/hr		10.00
Pumps	Steel	1.4×10^6 kg/hr	PNL/DOE	2.45
Total				12.45

Acct. 2.7 Reactor Vacuum

System	Type	Capacity	Cost Basis	Source	Total $ x 10^6
DT pumps in CC	cryocond.	10^7 ℓ/s	Algorithm	INTOR	3.00
DT pumps in end plug	cryocond.	6.34×10^6 ℓ/s	Algorithm	INTOR	1.90
He pumps in end plugs	cryosorp.	1.03×10^5 ℓ/s	Algorithm	INTOR	0.50
TMP		10^4 ℓ/s x 8	175×10^3 ea.	PNL	1.40
Regeneration	roots blower	10^5 ℓ/s x 9	$44. \times 10^3$ ea.	PNL	0.40
Metal bellows pumps		10^4 ℓ/s x 6	44.5×10^3 ea.	PNL	0.27
Valves		D = 1.2 m, N = 35	153×10^3 ea.	INTOR	5.36
		D = 0.5, N = 15	69×10^3 ea.	INTOR	1.04
Piping & ducts			$20/kg	PNL	2.50
					16.37

Acct. 2.8 Radwaste Treatment

This account was taken to be equal to TDF, or 3×10^6.

Acct. 2.9 Thermal Dumps

	Area (m^2)	Unit Cost ($/m^2$)	Source	Total $ x 10^6
End dumps	60	8000	TDF	0.48
CC NB dump	5	8000	TDF	0.04
Anchor NB dump	2	8000	TDF	0.02
Total				0.54

Acct. 2.10 Reactor Support Structure

Intercoil structure was included in the magnet costs. The remaining structure is estimated at 500 tonnes at \$15/kg, amounting to \$7.5 x 10^6.

Acct. 2.11 Special Materials

The initial tritium inventory is included in this account. It is equal to 220 g at \$10,000/g or \$2.2 x 10^6.

Acct. 2.12 Miscellaneous Plant

This account covers items not directly identified. We use TDF as a guide here, allocating \$10 x 10^6.

Acct. 3.0 Buildings

Building	Volume	Unit Cost	Source	Total $ x 10^6
Reactor hall	56,000 m^3	algorithm	INTOR	37.05
Lock area & active comp. inter. storage	12,000 m^3	297/m^3	INTOR	3.58
Active dismant. maint. & testing	12,000 m^3	297/m^3	INTOR	3.58
Active waste cond. & temp. storage	12,000 m^3	297/m^3	INTOR	3.58
Inactive assem. testing	12,000 m^3	297/m^3	INTOR	3.58
Inactive storage	12,000 m^3	297/m^3	INTOR	3.58
Vacuum & cryogenic systems	11,000 m^3	297/m^3	INTOR	3.28
Cooling & DT reprocess.	20,000 m^3	297/m^3	INTOR	5.94
Control	4,500 m^3	297/m^3	INTOR	1.34
Administration	15,000 m^3	88/m^3	INTOR	1.32
Diesel Generator Bldg.	5,000 m^3	88/m^3	INTOR	0.44
Total				67.27

12.3 Summary of Accounts

		$ x 10^6
1.1	Vacuum tank blanket/shield	21.27
1.2	Magnets	58.70
1.3	Plasma heating	91.12

Support Systems

2.1	Electrical	31.00
2.2	Auxiliary cooling	16.36
2.3	Instrumentation and control	25.00
2.4	Fuel handling	22.74
2.5	Maintenance equipment	19.66
2.6	Heat transport	12.45
2.7	Reactor vacuum	16.37
2.8	Radwaste treatment	3.00
2.9	Thermal dumps	0.54
2.10	Reactor support structure	7.50
2.11	Special Materials	2.20
2.12	Miscellaneous plant	10.00
3.0	Buildings	67.27
	Total Direct Costs	405.18

In addition to the direct costs, certain percentages for indirect costs such as engineering, assembly and contingency have to be accounted for. As an example in INTOR these consisted of 45% and 15% of the direct costs for engineering and assembly respectively, and 30% of the direct and indirect costs for contingency.

12.4 Annual Operating Costs

The operating costs for TASKA-M are made up of operation and maintenance, tritium costs and power costs. Operation and maintenance is taken as 3% of the total direct costs, a value which seems to be consistent with major installations of this nature. Tritium costs are based on a burnup rate of 1.03 g per full power day and an annual decay rate of 12 g at a cost of $10,000/g. The initial T_2 inventory was included as a direct cost. Presumably, it will be available for resale at plant shutdown. Power consumption is made up of two components, that required during reactor operation and that which is needed continuously. Cost of power is taken as 45 mills/kWh. Table 12.4-1 gives the breakdown of the power requirements.

The availability for TASKA-M is taken the same as in INTOR but the final period is extended to 20 years instead of 15 years. Thus the availability is 10% for the first year, 15% for the second and third year, 25% for the fourth to seventh year and 50% for the eighth to twentieth year. Tritium and power costs are based on this availability schedule. Table 12.4-2 summarizes the operating costs.

Table 12.4-1. Power Consumption in TASKA-M

Component	During Reactor Operation (MWe)	During Reactor Downtime (MWe)
Neutral Beams	70	---
ICRF	25	---
Normal Conducting Coils	36	---
Cooling for Normal Conducting Coils	10	---
Vacuum System	5	4
Magnet Cryogenerators	5	5
Cooling for Dumps	10	---
Other Cooling Systems	2	1
Auxiliary Requirements	3	2
Totals	166	12

Table 12.4-2. Summary of Operating Costs

Year	Avail. (%)	O & M ($ x 10^6)	Annual T_2 ($ x 10^6)	Annual Power ($ x 10^6)	Total Annual ($ x 10^6)
1	10	13	0	10.6	23.6
2-3	15	13	0.68	13.6	27.3
4-7	25	13	1.05	19.6	33.6
8-20	50	13	1.98	34.6	49.5

The levelized annual operating cost for the 20 years is $42.8 x 10^6. We have assumed that the normal coils which consume a total of 46 MWe can be turned off during reactor downtime.

12.5 Perspective on Costs

It is instructive to compare the costs for TASKA-M with TASKA and give a commentary on some of the differences. Table 12.5-1 gives a summary of the total direct costs for both systems.

In some cases the differences are due to the smaller size and scope of TASKA-M, such as in the blanket/shield, magnets, plasma heating, auxiliary cooling, heat transport, reactor support structure and buildings. Other differences simply reflect a better knowledge or understanding of the system

Table 12.5-1. Comparison of Direct Costs for TASKA-M and TASKA

Account		TASKA-M (1983) $ x 10^6	TASKA (1981) $ x 10^6
1.1	Blanket/Shield/Vacuum Chamber	21.3	46.3
1.2	Magnets	58.7	227.9
1.3	Plasma Heating	91.1	269.6
2.1	Electrical	31.0	25.0
2.2	Auxiliary Cooling	16.4	19.3
2.3	Instrumentation & Control	25.0	25.0
2.4	Fuel Handling	22.7	16.7
2.5	Maintenance Equipment	19.7	20.3
2.6	Primary Heat Transport	12.5	22.0
2.6	Secondary Heat Transport	---	5.5
2.7	Reactor Vacuum	16.4	16.1
2.8	Radwaste Treatment	3.0	0.1
2.9	Thermal Dumps	0.7	0.3
2.10	Reactor Support Structure	7.5	13.5
2.11	Special Materials	2.2	---
2.12	Miscellaneous Plant	10.0	---
3.0	Buildings	67.3	80.36
	Total Direct Costs	405.5	788.0

involved. Such is the case in account 2.1, the electrical system. In TASKA, the equipment in this account was poorly identified and thus the value from INTOR was used. However, in TASKA-M, a scaling from TDF was used, where the systems were identified in some detail. Thus, the value in TASKA-M is more accurate. The same is true of the thermal dumps and radwaste treatment. Similarly, a miscellaneous plant equipment account of $10 x 10^6 is allocated for TASKA-M where none was used in TASKA.

In the case of instrumentation and control, the value for TASKA was an educated guess, whereas in TASKA-M it is scaled from TDF. Coincidentally, the numbers are the same. It is interesting to note that the cost of fuel handling is higher in TASKA-M than in TASKA. These values are based on an algorithm which gives the cost as a function of the fuel handled per day. Surprisingly, the fuel handled is somewhat higher for TASKA-M than for TASKA, in spite of the lower power level of TASKA-M. This is due to the lower burnup rate in TASKA-M. Furthermore, a water detritiation system has been included in TASKA-M, whereas in TASKA, this function was assumed to be performed offsite.

The accounts for maintenance equipment and reactor vacuum are very similar for both devices. Although the capacity of both systems is lower in TASKA-M, the inflation rate for the reasonably well identified equipment has driven the cost to the level of TASKA.

For the two devices to be comparable in costing procedure, it is felt that the following adjustments should be made to TASKA:

Account	Original $ x 10^6		Adjustment $ x 10^6		New Total $ x 10^6
2.1 Electrical	25.0	+	20	=	45
2.4 Fuel Handling	16.7	+	5	=	21.7
2.9 Radwaste Treatment	0.04	+	3	=	3.0
2.13 Miscellaneous Plant	0	+	13	=	13

These adjustments raise the total direct costs for TASKA to ~ $830 x 10^6. On this basis, the cost of TASKA-M is slightly less than half the cost of TASKA.

A final comparison of TASKA-M can be made to other recent test reactor proposals. Figure 12.5-1 graphically displays the quoted direct costs of 3

Figure 12.5-1

COMPARISON OF NEAR TERM TEST FACILITIES
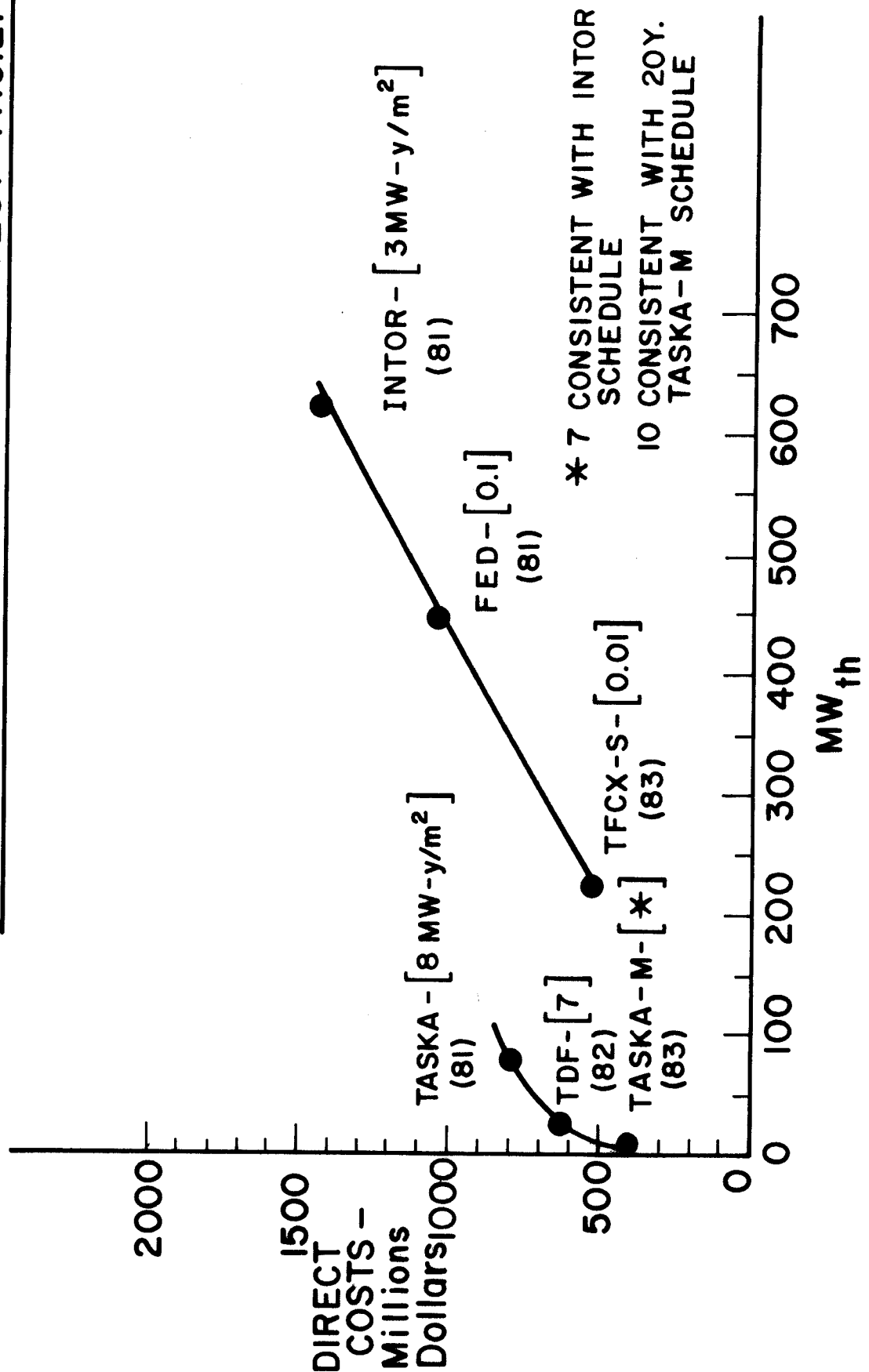
tokamak test facilities (INTOR, FED, and TFCX-S) and 3 tandem mirror test facilities (TASKA, TDF and TASKA-M). Also quoted on the figure is the year the cost estimates were made (1981-1983) and the cumulative maximum neutron fluence to the test modules in MW-y/m^2 (0.01-8). It can be seen that the tandem mirrors and tokamaks separate into two categories. Progressing from TFCX-S at 230 MW and 530 M$ one notes that only 0.01 MW-y/m^2 of neutron fluence is expected over the lifetime of the device. The FED device increased the neutron exposure by a factor of 10 to 0.1 MW-y/m^2 but the direct cost in 1981 $ exceeded 1 billion dollars. To get a respectable neutron fluence (3 MW-y/m^2) the INTOR device direct cost exceeded 1.4 billion dollars.

On the other hand, Fig. 12.5-1 demonstrates that tandem mirror facilities could achieve rather high neutron fluence levels (6-8 MW-y/m^2) at direct costs of 400-800 million dollars. The main difference between TASKA-M and TASKA is the inclusion of the thermal barrier. While the TASKA design is more reactor relevant, one must examine whether it is worth the extra 400 million dollars in the test phase of the fusion program. The final point of note in Fig. 12.5-1 is that the total DT power of the tandem mirrors can be made quite small, reducing the problems of tritium handling, thermal power and large re-actor components. It also relieves the necessity of breeding tritium for continued plant operation.

13. CONCLUSIONS

The TASKA-M conceptual design is the least expensive fusion technology test facility conceived to date which is capable of adequately testing key fusion reactor features and their integration in a neutron environment. These features include:

• Blanket technology

• Materials

• Superconducting magnets

• Plasma heating systems (both neutral beams and RF)

• Tritium loops

• Exhaust systems with high heat flux dumps

• Maintenance systems.

TASKA-M shows that a mirror-based facility can fulfill most engineering test objectives for both toroidal and mirror devices. To keep costs relatively low, the plasma volume, fusion power, and tritium inventory have been minimized by tailoring the plasma ion distribution and placing test modules around the two high neutron flux zones. The test volume and neutron flux are more than sufficient to test a variety of blanket schemes, and the neutron fluence is adequate for materials test purposes. In addition, TASKA-M requires the integration of magnets, blanket modules, neutral beams, and RF antennae, so it provides an excellent test of simultaneous operation of these systems in a neutron environment. The total input power to the plasma is about 44 MW, while the fusion power is about 7 MW, so the system is heavily driven. Internal tritium breeding is not required for continued plasma operation at that power level. Furthermore, energy breakeven is not critical to the engineering test goals and is not a feature of TASKA-M.

TASKA-M is intended to be a near-term test device, so we have relied on existing physics and technology with only moderate extrapolations. In particular, we have tried to keep as close as possible to the present experimental data base and theoretical understanding. Since the thermal barrier utilized in the earlier studies was a major cost-driver, but is not crucial to engineering testing goals, it is not present in TASKA-M.

As with the first study of any configuration, some problems remain to be clarified before proceeding with a construction proposal. For example, plasma

microstability and neutron damage to RF antennae and normal-conducting insert magnets are issues which require further experimental and theoretical work.

The primary result of the TASKA-M study is that the major engineering and materials test requirements of the fusion technology program can be fulfilled with a relatively small and inexpensive device. In addition, the TASKA-M design possesses the flexibility to adapt to issues relevant to other concepts. Since the cost of TASKA-M is low relative to other test facilities (approximately 400 million dollars), it might well be considered the next reasonable and necessary engineering step on the path to a demonstration reactor.

TASKA-M PARAMETER LIST

1. PHYSICS PARAMETERS

1.1 TASKA-M General Parameters

Neutron Wall Loading

Central cell midplane (at 0.25 m radius), MW/m^2	0.7
Central cell maximum, MW/m^2	1.3

Fusion Power, MW   6.8

Magnetic Fields

Central cell - midplane, T	4.2
Central cell - maximum, T	17.5
Transition region - minimum, T	2.2
Anchor - midplane, T	1.0
Anchor - maximum, T	2.7

Central Cell Dimensions

Length between magnetic field peaks, m	5.5
Length between density peaks, m	3.4
Wall radius in the test zone, m	0.22-0.25

Anchor Dimensions

Length between magnetic field peaks, m	5.4
Length between density peaks, m	3.4
Wall radius - midplane, m	0.37

Total Length of Vacuum Tank, m   50.

1.2 TASKA-M Neutral Beam and RF Heating Parameters

Central Cell

  High Energy Neutral Beams

Injection voltage, kV	90
Total injected power, MW	21
Injection angle, °	45
Species, D/T	0.5/0.5
Trapping fraction	0.92
Number of beam lines	4

Low Energy Neutral Beam

Injection voltage, kV	12
Total injected power, MW	0.60
Injection angle, °	70
Species	D
Trapping fraction	1
Number of beam lines	1

Anchor

Medium Energy Neutral Beams

Injection voltage, kV	73
Total injected power/anchor, MW	3.5
Injection angle, °	50
Species	D
Trapping fraction	0.37
Number of beam lines/anchor	1

RF Heating of Electrons by Landau Damping

Absorbed power, MW	12
Frequency, MHz	15

1.3 Particle Balance

Central Cell

Injected – HE NBI (50% D, 50% T), s^{-1}	1.6×10^{21}
Injected – LE NBI (100% D), s^{-1}	3.1×10^{20}
End loss ($\overline{E}$ = 125 keV), s^{-1}	1.1×10^{21}
End loss ($\overline{E}$ = 70 keV), s^{-1}	2.0×10^{20}
Charge exchange* ($\overline{E}$ = 84 keV), s^{-1}	4.2×10^{20}
Charge exchange* ($\overline{E}$ = 6 keV), s^{-1}	1.1×10^{20}
Shine through ($\overline{E}$ = 90 keV), s^{-1}	1.2×10^{20}

---

*The charge exchange particle current hits the side walls at the mean energy given and recycles as cold gas, which then reionizes in the halo and goes to the end plasma dump as ~ 600 eV ions.

Each Anchor

Injected - ME NBI (100% D), s^{-1}	3.32×10^{20}
End loss ($\overline{E}$ =90 keV), s^{-1}	7.8×10^{19}
Charge exchange* ($\overline{E}$ = 60 keV), s^{-1}	4.32×10^{19}
Shine through ($\overline{E}$ = 73 keV)	2.1×10^{20}

1.4   TASKA-M Plasma Parameters*

	Central Cell	Anchor
On-axis β	0.50	0.50
Radially-averaged β	0.30	0.30
Electron temperature, keV	14	14
Hot ion density, cm^{-3}	3.3×10^{14}	2.6×10^{13}
Hot ion sloshing density ratio	1.59	1.4
Mean hot ion energy, keV	84	60
Mean hot ion escape energy, keV	67	56
$(n\tau)$ - hot ions, s/cm^3	1.0×10^{13}	3.0×10^{12}
Warm ion density, cm^{-3}	3.0×10^{13}	2.6×10^{12}
Mean warm ion energy, keV	5.8	6.6
$(n\tau)$ - warm ions, s/cm^3	1.3×10^{12}	6.6×10^{11}
Potential (to ground), kV	59	24
Warm ion confining potential, kV	5.3	3.4
Plasma radius, cm	12	24
Radial profile exponent	3	3

---

* spatially dependent parameters are given on-axis at the midplane.

2. PLASMA HEATING AND FUELING

2.1 TASKA-M Neutral Beam Injector Requirements

	HE-NBI	ME-NBI	LE-NBI
Location	central cell	anchors	central cell
Injection angle, °	45	50	70
Primary energy, kV	90	73	12
Mean energy of neutral atom, keV	81	66	11
Ionization efficiency in source	0.5	0.5	0.5
Transmission efficiency	0.7	0.7	0.6
Neutralization efficiency	0.57	0.57	0.9
Neutral atom current/NBI, A_0	64	53	50
Species	$D^0 + T^0$	D^0	D^0
Power/NBI at plasma, MW	5.2	3.5	0.55
Power/NBI absorbed in plasma, MW	3.5	0.85	0.35
No. of ion sources per NBI	3	2	2
Total No. of NBI	4	2	1
I^+ per source, A	46.7	57.5	41.7
Extraction area per source, cm^2	20 x 50	20 x 50	20 x 50
Current density at source, A/cm^2	0.047	0.058	0.042
Beam divergence, °	±0.5	±0.6	±1x±2
Beam composition at plasma			
Full energy, %	83.3	83.3	83.3
1/2-energy, %	7.5	7.5	7.5
1/3-energy, %	9.2	9.2	9.2

2.2 Ion Cyclotron Range of Frequencies (ICRF)

Location	central cell
Number of antennas total	4
Antenna unit inner radius, cm	20
Antenna axial extent, cm	25
Antenna material	copper
Faraday shield material	stainless steel
Total (wall plug) power, MW	21.5
Power transmitted to antennae, MW	17.2
Coupled power, MW	15.5
Absorbed power, MW	12.4
Frequency, MHz	15
Wave mode	fast magnetosonic
Antenna coupling efficiency, %	90
Electron heating efficiency, %	80
Overall heating efficiency, %	72

2.3 Plasma Parameters for Alternative RF Heating Options

	Central Cell	Transition	Anchor
B_{min}, T	4.2	2.18	1.02
B_{max}, T	17.5	(17.5, 2.7)	2.7
n_e, cm^{-3}	3.5×10^{14}	2.6×10^{13}	2.6×10^{13}
T_e, keV	14.0	14.0	14.0
E_i, keV	84.1	7.3	60.3
r_p, cm	12.1	$(17.7)_{eff}$	$(24.4)_{eff}$
r_w, cm	25	$(36)_{eff}$	37
β	0.5	0.05	0.5
$f_{ce}(\beta_0)$, GHz	83	56	20
$\omega_{pe}/\omega_{ce}(\beta_0)$	1.8	0.83	2.33
$f_{cT}(\beta_0)$, MHz	15 (z = 0)	10	no tritium
	15 (z = 1 m)		
	38 (z = 2.2 m)		

3. MAGNETS

3.1 Solenoids

	Central Cell	Choke Coil	
		NbTi	Nb$_3$Sn
Superconducting Parts			
Function	C.C. field	mirror	
Number of coils	1	2	2
Minor radius, m	1.8	1.34	1.15
Major radius, m	2.4	1.70	1.31
Bundle cross section, m x m	0.7 x 0.6	1.6 x 0.36	1.6 x 0.16
Mean turn length, m	13.2	9.6	7.7
Volume of windings per coil, m^3	5.54	5.5	2.0
Weight of windings per coil, t	31	31	11
Overall current density, A/cm^2	2180	2750	2380
Ampere-turns, 10^6 A-turns	9.2	15.9	6.1
Self-inductance per N^2, 10^{-6} H/N^2	5.5	2.7	2.05
Stored self energy, MJ	232	595	
Operating temperature, K	4.2	4.2	4.2
Magnetic field on axis, T	4.2	8.3 (17.5 w/insert)	
Peak field at conductor, T	7.4	8.2	12
Superconductor	NbTi	NbTi	Nb$_3$Sn
Stabilizing material	Al	Al	Al
Structure material	SS	SS	SS
Normal Conducting Insert			
Conductor material			Cu
Number of coils			2
Volume, m^3			0.9
Overall current density, A/cm^2			2200
Ohmic dissipation, MW			18
Ampere-turns, 10^6 A-turns			7.7
Max. working stress, MPa			133
Stored self-energy, MJ			10.7
Ceramic insulation material			MgO powder
Operating temperature			350 K

3.2 C-Shaped Coils

	Transition	Anchor
Coil type	Reversed-C	Yin-Yang
Number of coils	2	2 (+2)
Function	Change of flux bundle cross-section	Magnetic well of anchor
Minor radius, m	1.44	0.58
Major radius, m	0.82	2.085
Sweep angle, degree	90	60
Bundle cross section, m x m	0.36 x 0.3	0.8 x 0.3
Mean turn length, m	18.3	20.8
Volume of windings per coil, m^3	2.0	5.0
Weight of windings per coil, t	11	28
Overall current density, A/cm^2	2500	2500 (1530)
Ampere-turns, 10^6 A-turns	2.7	6.0 (3.7)
Self-inductance per N^2, 10^{-6} H/N^2	8.9	5.3
Stored self-energy, MJ	33.0	96 (36)
Operating temperature, K	4.2	4.2
Peak field at conductor, T	5	6
Superconductor	NbTi	NbTi
Stabilizing material	3/4 hard Cu	3/4 hard Cu
Structure material	3/4 hard Cu	3/4 hard Cu

4. CENTRAL CELL AND TEST MODULE PARAMETERS

	LiPb/Li Module	Solid Breeder Module	Central Cell Insert
4.1 Composition			
Blanket structural material	HT-9	316 SS	NA
Blanket coolant	$Li_{17}Pb_{83}$/Li	H_2O	NA
Breeding material	$Li_{17}Pb_{83}$/Li	Li_2O	NA
Blanket composition, v/o			
Structure	7	32	NA
Coolant/breeder	73	28/20	NA
Void	20	20	NA
Reflector composition, v/o			
Structure	95	95	NA
Coolant	5	5	NA
Void			
Shield Material			
Material 1/coolant	$1422/H_2O$	$1422/H_2O$	$1422/H_2O$
Composition, v/o	90/10	90/10	90/10
Material 2	$1422/B_4C/H_2O$	$1422/B_4C/H_2O$	$1422/B_4C/H_2O$
Composition, v/o	10/10/80	10/10/80	10/10/80
4.2 Dimensions			
Central cell I.D., m	0.44/0.58	0.50	1.40
Blanket testing zone area, m^2	1.14	0.68	NA
First wall thickness,[+] mm	1.6	3.0	2.0
Blanket thickness, m	0.45/0.26	0.15	NA
Reflector thickness, m	0.4	0.4	0
Shield thickness, m	0.5	0.5	0.78

[+] Thickness of first wall tubing
NA = not applicable
N/A = not available

	LiPb/Li Module	Solid Breeder Module	Central Cell Insert
4.3 Neutronic Summary			
14 MeV neutron wall loading, MW/m^2	0.7...1.12	0.7...0.74	0.7**
Average 14 MeV neutron wall loading, MW/m^2	0.84	0.73	0.7**
Energy multiplication	1.371/1.344	1.31	NA
Local tritium breeding ratio	1.19/1.15	0.71	NA
Power in tubes forming first wall, MW	0.114	0.022	0.23
Power in breeding blanket, MW	1.32/1.29	0.38	NA
Power in reflector and shield, MW	0.36/0.32	0.27	NA
Max. first wall power density, W/cm^3	6.22/6.91	12	4.3
Max. blanket power density, W/cm^3	5.7/3.7	6.4	NA
4.4 Thermal Hydraulics			
Blanket temperature, °C			
Coolant inlet	300/300	150	NA
Coolant outlet	450/450	200	NA
Maximum structure temperature	512/500		NA
Minimum structure temperature	350/345		NA
Reflector temperature, °C			
Coolant inlet	80/80	40	NA
Coolant outlet	150/150	90	NA
Maximum structure temp.	170		NA
Blanket coolant conditions			
Maximum velocity, cm/s	2.5/1.8	N/A	NA
Maximum pressure drop,[†] MN/m^2	0.57/0.45	2.0	NA

[†] Including head pressure.
** at 25 cm radius.

Maximum pressure, MN/m^2	0.42/0.35	5.0	NA
Total coolant flow, kg/hr x 10^5	1.37/0.06	0.065	NA
Pumping power, kW	2.3/1.4		NA
Reflector Coolant Conditions			
Maximum pressure drop, MN/m^2	N/A		NA
Maximum pressure, NM/m^2	3.0	3.00	NA
Total coolant flow, kg/hr	4400/3900	7200	NA

4.5 Central Cell Materials

4.5.1 Fixed Blanket Structure

Material	HT-9	316 SS	NA
Average neutron wall load, MW/m^2	0.84	0.73	NA
Operating temp. range, °C	345-512		NA

4.5.2 Coolant

Material	LiPb/Li	H_2O	H_2O
Temp. range, °C	300-450	150-200	30-60
Velocity range, m/s	1.8-2.5	N/A	3.26
Pressure, MPa	0.35-0.42	5.0	0.4

4.5.3 Breeder

Material	LiPb/Li	Li_2O	NA
Temp. range, °C	300-450	N/A	NA
Velocity, m/s	1.8-2.5	NA	NA
Pressure, MPa	0.35-0.42	NA	NA

4.5.4 Reflector

Material	1422	1422	NA
Coolant	H_2O	H_2O	NA
Operating temp., °C	80-150	80-150	NA

4.5.5 Shield

Materials	$1422/B_4C$	$1422/B_4C$	$1422/B_4C$
Coolant	H_2O	H_2O	H_2O

4.6 Magnets

	SC-Solenoids	NC-Insert	C-Shaped Coils
Conductor	NbTi/Nb$_3$Sn	Cu	NbTi
Stabilizer	Al	NA	3/4 hard CU
Coolant	LHe	H$_2$O	LHe
Electrical insulation	gff epoxy	MgO powder	gff epoxy
Thermal insulation	Kapton	NA	Kapton
Structure	304 SS	316 SS	304 SS
Dewar	304 SS	NA	304 SS

4.7 Materials Test Modules

Width, m	0.53/0.55
Thickness, m	0.20/0.125-0.20
Area, m^2	0.69/1.01
Module volume, liters	217.4
Capsule volume, liters	70.6/74.5
Module structure and v/o	HT-9/20
Coolant and v/o	He/40
Specimen and capsule structure and v/o	316 SS/20
Thermal contact material and v/o	NaK/20
Average dpa per MW-yr/m^2 in capsule	3.92/3.38
Max. no. of capsules per module	180/276
Cumulative dpa·ℓ (7.8 FPY operation)	2160/1960
Average He appm per MW-yr/m^2	35.1/29.5
Cumulative He appm·ℓ (7.8 FPY operation)	19330/17140
Average power density, W/cm^3	1.3

5. NEUTRONICS

5.1. Geometrical Configuration and Average Wall Loading for the Test Modules

Blanket	Axial Location (cm)	Segment	Axial Width (cm)	Wall Radius (cm)	Average Wall Loading (MW/m^2)
Blanket #1	-220 < Z < -132	liquid breeder test	30	29	0.39
		liquid breeder test	53	22	1.11
		shield	5	32.5	0.72
Blanket #2	-130 < Z < -60	shield	27	32.5	0.64
		solid breeder test	43	25	0.73
Blanket #3	80 < Z < 135	materials test	23	25	0.74
		materials test	32	32.5	0.65
Blanket #4	137 < Z < 220	materials test	53	18-22	1.23
		shield	30	29	0.39

5.2 Radiation Effects in Superconducting Magnets of TASKA-M

	Inner Bore of Central Coil at Midplane	Inner Bore of Choke Nb$_3$Sn Coil	Inner Bore of Central Coil	
			At NBI Duct	At Beam Dump Duct
Stabilizer/dpa rate (dpa/FPY)	Al/5.2×10^{-6}	Al/5.6×10^{-7}	Al/8.1×10^{-5}	Al/2.5×10^{-5}
Electrical Insulator/ Dose after 7.8 FPY (rad)	epoxy/6.6×10^7	epoxy/ 9.4×10^6	epoxy/ 1.8×10^8	epoxy/ 9.4×10^7
Dose in aluminized Kapton after 7.8 FPY (rad)	1.1×10^9	3.2×10^7	3.2×10^9	1.6×10^9
Power density in winding pack (mW/cm^3)	0.005	0.001	0.038	0.0012
Superconductor/Fast neutron flux (n/m^2 per FPY)	NbTi/5×10^{19}	Nb$_3$Sn/ 3.5×10^{19}	NbTi/ 6.7×10^{20}	NbTi/ 2.1×10^{20}

5.2 (continued)

	Outer Bore of Choke NbTi Coil		Transition		Design
	At NBI Duct	At Beam Dump Duct	Coil	Anchor Coil	Limits
Stabilizer/dpa rate (dpa/FPY)	Al/9.8×10^{-5}	Al/4.4×10^{-5}	Cu/4.8×10^{-5}	Cu/6.4×10^{-5}	Al/10^{-4} Cu/3.1×10^{-4}
Electrical Insulator/ Dose after 7.8 FPY (rad)	epoxy/ 1.5×10^{8}	epoxy/ 6×10^{7}	polyimide/ 9.6×10^{8}	polyimide/ 1.3×10^{9}	gff epoxy/ 6×10^{8} gff polyimide/5×10^{9}
Dose in aluminized Kapton after 7.8 FPY (rad)	2.9×10^{9}	1.1×10^{9}	2.2×10^{9}	3.1×10^{9}	10^{10}
Power density in winding pack (mW/cm^3)	0.047	0.018	0.096	0.088	0.1
Superconductor/Fast neutron flux (n/m^2 per FPY)	NbTi/ 8.1×10^{20}	NbTi/ 3.6×10^{20}	NbTi/ 6.2×10^{20}	NbTi/ 7.8×10^{20}	NbTi/ 1.1×10^{22} Nb$_3$Sn/ 5.1×10^{21}

5.3 Radiation Effects in Normal Conducting Insert

Peak Neutron Fluence in MgO, n/m^2 per FPY, ($E_n > 0.1$ MeV) 4×10^{24}

6. EXHAUST AND VACUUM

6.1 Process Gas Streams

Total input by NBIs (atomic)

Deuterium, g/s	5.95×10^{-3}
Tritium, g/s	4.04×10^{-3}

Thermal gas output by exhaust system	D_2	DT	T_2	He
from one end cell, 10^{-3} g/s	2.08	1.98	0.69	8.8×10^{-3}
from central cell, 10^{-3} g/s	0.103	0.255	0.154	0
total from end cells and CC, 10^{-3} g/s	4.26	4.20	1.53	17.6×10^{-3}

6.2 Cryopumping System

	per End Cell		Central Cell
Total number of cryopumps	8	(2) [4]	6
Number cryopumps in operation/regeneration	6/2	(1/1)	4/2
Cryosurface size, m^2 [1]	66	(6)	55
Effective pumping speed, m^3/s			
for D_2	2339		435
for DT	2092		389
for T_2	1910		355
for He	103		---
Equilibrium pressure, 10^{-5} mbar	1.1		0.67 [2]
Assumed gas temperature, K	330		300 [2]

6.3 Beam and End Dump Data

	CC-BD	Anchor-Bd	End Dump
Collector plate concept		Hypervapotron	
Total number of dump inserts	4	2	15 per end
Inclination angle rel. to beam axis, deg.	75	65	0
Footprint area at dump, m^2	0.41	0.77	5.03
Dump dimensions, collector width/length, m	0.52/1.6	0.7/1.8	0.55/2.9
Total dump heat load			
during normal operation, MW	0.45	2.22	15
during calibration, MW	1.72	1.75	0

	CC-BD	Anchor-BD	End Dump
Max. local heat flux, MW/m^2			
during normal operation	2.5	4.8	5.0
during calibration	8.7	4.3	0
Flow rate of primary cooling water, ℓ/s	20	26.5	20.3 [3]
Coolant inlet temperature, °C	60	60	60
Bulk coolant temperature rise, K	20	20	20
Coolant inlet pressure, bar	< 6	< 6	< 6
Coolant pressure drop, bar	< 2	< 2	< 2
Reference material of collector		Cu-Cr Alloy	
Steady state surface temperature, °C	~ 240	~ 275	~ 275
Peak surface temperature at startup, °C	410	< 275	< 275
Sputtering yield depth design limit, mm	1	1	1
Expected sputtering lifetime, FPY	0.8	0.8	7.4

6.4 Neutral Beam Exhaust (Cryopanels)

	HE-NBI	LE-NBI	ME-NBI
H_2, 10^{-6} g/s	0	0	0
HD, 10^{-6} g/s	16×10^{-2}	6×10^{-2}	3×10^{-2}
HT, 10^{-6} g/s	22×10^{-2}	4×10^{-2}	2×10^{-2}
D_2, 10^{-6} g/s	5360	8840	2820
DT, 10^{-6} g/s	13350	7.5	4.0
T_2, 10^{-6} g/s	8040	0	0
Fraction to fuel cleanup, %	1	100	100
Internal recycle, %	99	0	0

---

[1] Operating pumps only

[2] At exhaust duct outlet port

[3] Refers to the hottest end dump insert

[4] Numbers in brackets refer to the additional He cryopumps

7. TRITIUM SYSTEMS

7.1 Fuel Reprocessing Systems
Fuel Cleanup Units

Technique   cryogenic (77°K) removal
                                                   of impurities

Molecular sieve columns (wt)
  Fuel exhaust, kg   0.86
  D_2 NBI exhaust, kg   1.15

Isotope Separation System

Technique   cryogenic distillation
Design Data

Parameter	Column #		
	1	2	3
Diameter, mm	24	35	18
Length, m	4	3	2.5
Theoretical stages	80	60	50
Feed stage	60	45	7
Reflux ratio	30	17	500
Inventory, g	28.7	1.08	~ 0
Condenser power, W	63	137	31

Effluent release 6.8×10^{-3} Ci/d

7.4 Tritium Inventory in Grams
Location

Active		206.7
HE-NBI cryopumps	115.5	
CC cryopumps	2.2	
End plasma exhaust		
D/T cryopumps	24.4	
He cryopumps	2.5	
Fuel cleanup unit	2.5	
Isotope separation system	30.0	

Inactive		66.0
Fuel storage (30 day supply)	31.0	
Structure (end-of-life)	< 1.0	
Coolant water (end-of-life)	34.0	
Test Modules		
Liquid Li	5.8	
Liquid LiPb	0.01	
Ceramic pellets/yr	25.	

7.3 Tritium Requirements

Startup (minimum), g	181
Operational (per year), g	380
Burn fraction, %	0.3

7.4 Tritium Loss to Coolant Water

End plasma dump, NBI beam dump, CC insert, Ci/d	117

7.5 Liquid Metal Tritium Removal Systems (TRS)

7.5.1 Liquid Li TRS

TRS technique	yttrium absorption column
Daily operation	1 column in use, 1 column in regeneration
Flow to TRS, %	20
TRS temperature, °C	250
Volume Li in TRS	0.64 m^3

T_2 Partial Pressure

Entrance	1.3 x 10^{-10} mbar
Exit	1.25 x 10^{-10} mbar

Yttrium Foil

Weight	880 g
Surface area	630 m^2
Thickness	6.4 μm
T_2 removal from Y	vacuum degassing at 900°C

7.5.2 Liquid LiPb Test Blanket

TRS technique	vacuum degassing
Operation mode	continuous
Fraction coolant to TRS	40%
TRS temperature	300°C

T_2 Partial Pressure

Entrance	1.3×10^{-4} mbar
Exit	1.3×10^{-6} mbar

Tritium Concentration

Entrance	1.8×10^{-4} wppm
Exit	1.8×10^{-5} wppm

TRS Dimensions

Configuration	circular cylinder
Surface area	3.3 m^2
Radius	1.0 m
Depth, LiPb	4.6 mm
Gas flow	2.1×10^{-2} mbar·ℓ/s
Pump speed at 1.3×10^{-6} mbar	1.6×10^4 ℓ/s

7.5.3 Intermediate Heat Transfer Circuit

Heat transfer fluid	He
TRS technique	continuous oxidation with T_2O adsorption on desiccant
Operational mode	recycle desiccant daily
Fraction flow to TRS	0.6%

Partial Pressure in He

T_2	1.3×10^{-14} mbar
T_2O	1.3×10^{-3} mbar
O_2	1.3×10^{-2} mbar

Desiccant Molecular Sieves: Molecular Sieves

Temperature	95°C absorption

T_2O Pressure in TRS

Entrance	1.3×10^{-3} mbar
Exit	6.5×10^{-4} mbar

7.5.4 Tritium Loss to Water Coolant Circuit

Liquid Li test module 2×10^{-3} Ci/d

Liquid LiPb test module   1.5 Ci/d w/o intermediate TRS

                2×10^{-5} Ci/d with intermediate TRS

8. REMOTE REPLACEMENT CHARACTERISTICS

8.1 Main Components - Estimated Sizes and Removal Weights*

	Size (m)	Removable Weight (t)	Estimated Life-time (FPY)
Vacuum chamber (section)	5.5 x 4.5 x 4	17	> 8
Breeding test blanket	4.45 x 2.50 x 0.88	35	≤ 3
Central cell coil	5.16 ∅ x 1.06	110	> 8
High field coil	3.70 ∅ x 2.06	73	> 8
Yin-Yang coil	6.5 x 3.2 x 2.95	52	> 8
Transition coil	4.05 x 3.85 x 3.45	35	> 8
Beam dump	0.65 ∅ x 3.5	6	< 3
Central cell insert	2.45 ∅ x 1.36	38	≈ 3
NC-coil insert	1.95 ∅ x 2.1	40	≲ 8

* may include shields, supports, etc.

∅ = diameter

9. COSTS

9.1 Direct Costs

Base Equipment	$ x 10^6
Vacuum tank blanket/shield	21.27
Magnets	58.70
Plasma heating	91.12

Support Systems	
Electrical	31.00
Auxiliary cooling	16.36
Instrumentation and control	25.00
Fuel handling	22.74
Maintenance equipment	19.66
Heat transport	12.45
Reactor vacuum	16.37
Radwaste treatment	3.00
Thermal dumps	0.54
Reactor support structure	7.50
Special materials	2.20
Miscellaneous plant	10.00
Buildings	67.27
Total Direct Costs	405.18

9.2 Power Consumption

Component	During Reactor Operation (MWe)	During Reactor Downtime (MWe)
Neutral beams	70	---
ICRF	25	---
Normal conducting coils	36	---
Cooling for normal conducting coils	10	---
Vacuum system	5	4
Magnet cryogenerators	5	5
Cooling for dumps	10	---
Other cooling systems	2	1
Auxiliary requirements	3	2
Totals	166	12

9.3 Operating Costs

Year	Availability (%)	Maintenance (leveled) ($ x 10^6)	Annual T_2 ($ x 10^6)	Annual Power ($ x 10^6)	Total Annual ($ x 10^6)
1	10	13	0	10.6	23.6
2-3	15	13	0.68	13.6	27.3
4-7	25	13	1.05	19.6	33.6
8-20	50	13	1.98	34.6	49.5